

Proceedings of the 8th IEEE Benelux Young Researchers symposium in electrical power engineering

Citation for published version (APA):

Jansen, J. W., & Roes, M. G. L. (Eds.) (2016). *Proceedings of the 8th IEEE Benelux Young Researchers symposium in electrical power engineering: YRS2016, 12-13 May, Eindhoven University of Technology*. Technische Universiteit Eindhoven.

Document status and date:

Published: 01/05/2016

Please check the document version of this publication:

- A submitted manuscript is the version of the article upon submission and before peer-review. There can be important differences between the submitted version and the official published version of record. People interested in the research are advised to contact the author for the final version of the publication, or visit the DOI to the publisher's website.
- The final author version and the galley proof are versions of the publication after peer review.
- The final published version features the final layout of the paper including the volume, issue and page numbers.

[Link to publication](#)

General rights

Copyright and moral rights for the publications made accessible in the public portal are retained by the authors and/or other copyright owners and it is a condition of accessing publications that users recognise and abide by the legal requirements associated with these rights.

- Users may download and print one copy of any publication from the public portal for the purpose of private study or research.
- You may not further distribute the material or use it for any profit-making activity or commercial gain
- You may freely distribute the URL identifying the publication in the public portal.

If the publication is distributed under the terms of Article 25fa of the Dutch Copyright Act, indicated by the "Taverne" license above, please follow below link for the End User Agreement:

www.tue.nl/taverne

Take down policy

If you believe that this document breaches copyright please contact us at:

openaccess@tue.nl

providing details and we will investigate your claim.

Current-Based ZVS Modulation Strategy for a 3-5 Level Bidirectional Dual Active Bridge DC-DC Converter

Georgios E. Sfakianakis, *Student Member, IEEE*

Electromechanics and Power Electronics (EPE) group
Department of Electrical Engineering
Eindhoven University of Technology (TU/e)
Eindhoven, The Netherlands
g.e.sfakianakis@tue.nl

Abstract—This paper presents a Zero Voltage Switching (ZVS) modulation strategy for the 3 Level – 5 Level (3-5L) Dual Active Bridge (DAB) DC-DC converter. The DAB accommodates a full bridge in the primary side and two 3-level T-Type bridge legs in the secondary side, linked by a high-frequency transformer and an inductor. A ZVS modulation strategy is presented, in which commutation inductances are utilized to extend the ZVS region to the entire operating range of the converter. The configuration of the secondary-side bridge allows further flexibility, compared to a full bridge configuration, to minimize the RMS current in the inductor. The nominal power of the converter is 2.8 kW with input voltage range from 8 V to 16 V, and output voltage range from 175 V to 450 V. The RMS currents of the 3-5L DAB are compared with those of a typical 3-3L full bridge - full bridge DAB, by applying the proposed modulation strategy in the 3-5L DAB, and a strategy proposed in literature in the 3-3L DAB.

Index Terms—DC-DC Converters, Dual Active Bridge, Zero Voltage Switching, Modulation Schemes.

I. INTRODUCTION

Power converters are widely used in powertrains of plug-in hybrid electric vehicles (PHEVs) and plug-in battery electric vehicles (PBEVs). DC-AC converters transfer power from the high-voltage (HV) batteries to the electric motors, an AC-DC converter connects the HV batteries to the grid (i.e. battery charger) and a DC-DC converter interfaces the low voltage (LV) batteries with the HV batteries (LV2HV interface). High power density and efficiency are required in such applications in order to increase the driving range and space utilization. Concerning the LV2HV interface, where a significant difference in the input and output voltage is imposed (12 V \rightarrow 400 V), the Dual Active Bridge (DAB) converter is a promising choice due to its soft-switching capability. The DAB can bring advantages by equalizing the input and output voltages using the transformer turns ratio (N). Moreover, the DAB is operated more efficiently when the output voltage referred to the primary side is equal to the input voltage ($N \cdot V_{DC,2} \approx V_{DC,1}$) [1], [2].

The DAB was introduced in [3] for the realization of high-efficiency, high-power-density, isolated DC-DC converters with buck-boost operation and bidirectional power flow

TABLE I
CONVERTER SPECIFICATIONS

LV Side	$V_{DC,1}$	$8 \text{ V} \leq V_{DC,1} \leq 16 \text{ V, nom. } 14 \text{ V}$
	$I_{DC,1,max}$	$\pm 200 \text{ A}$
HV Side	$V_{DC,2}$	$175 \text{ V} \leq V_{DC,2} \leq 450 \text{ V, nom. } 400 \text{ V}$
AC-link	$n_1/n_2 = N$	1/9
	L	$0.0683 \mu\text{H}$
	f_s	120 kHz

capability. Since then, various modulation strategies have been proposed for the traditional 3 Level - 3 Level (3-3L) full bridge - full bridge DAB, where the main objective is to minimize the RMS current of the inductor/transformer under full-operating-range zero voltage switching [4]–[6]. The extra voltage levels ($\pm V_{DC}/2$) of the 3-5L DAB provide more flexibility in the inductor/transformer current shaping, which leads to lower RMS current [7]. On top of that, the extra switches used for the extra levels need to be able to block only half the DC-bus voltage, which requires devices with half blocking voltage and typically less than half on-resistance.

In this paper, a 3-5L DAB [8] is considered for a Low-to-High voltage DC-bus, DC-DC interface converter. The input voltage range is $8 \text{ V} \leq V_{DC,1} \leq 16 \text{ V}$, the output voltage range is $175 \text{ V} \leq V_{DC,2} \leq 450 \text{ V}$, and the maximum input current is $\pm 200 \text{ A}$. Further details about the specifications are listed in Table I. In Section II, a detailed explanation is given for the DAB topology. Section III contains an analysis of the different switching modes, the mode selection procedure, as well as the derivations of the piecewise linear equations and the soft-switching constraints. The proposed modulation strategy is discussed in Section IV. In Section V, a comparison is performed between the 3-5L DAB and the traditional 3-3L DAB.

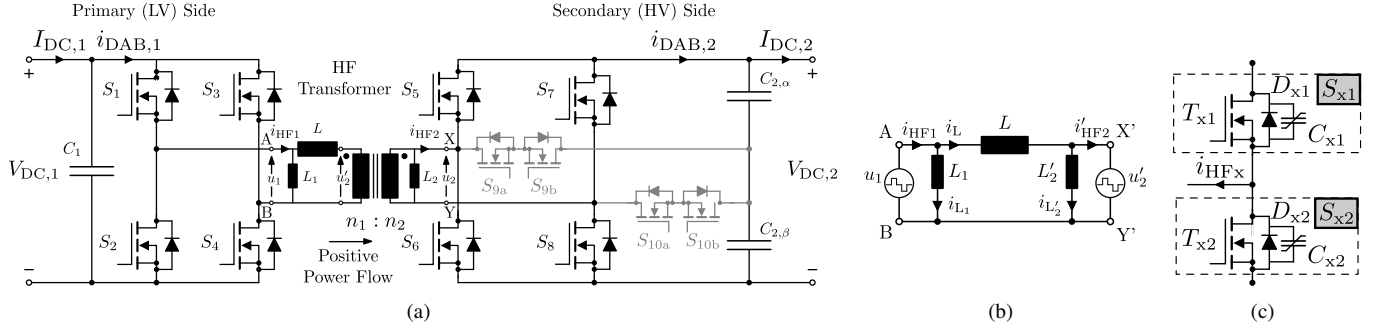


Fig. 1. (a) Circuit schematic of the 3-5L Dual Active Bridge converter [8], (b) Equivalent circuit of the Dual Active Bridge, and (c) DAB phase leg with parasitic capacitances.

II. 3-5L DAB CONVERTER TOPOLOGY

Fig. 1(a) shows the schematic of the considered 3-5L DAB [8], consisting of a full-bridge at the primary side (LV-side) and two T-Type bridge-legs at the secondary side (HV-side), coupled by a high frequency (HF) transformer and series inductor L . For the realization of the HV-side bridge, other options are possible like the Neutral Point Clamped (NPC) [9]–[12] or the flying capacitor bridge leg. However, this work focuses on the modulation strategy and does not further discuss implementation variants.

The operating principle of the 3-5L DAB is presented in [8]–[12], and it is similar to the operating principle of the traditional 3-3L DAB. Both active bridges produce phase-shifted edge resonant square wave voltages v_1 and v_2 at the terminals of the HF AC link (inductor and HF transformer), resulting in an inductor current i_L . Voltages v_1 and v_2 are also applied to the commutation inductances (L_1 and L_2), resulting in currents i_{L1} and i_{L2} , respectively, which enhance the ZVS operation [5] by injecting reactive current into the bridges without contributing to the power flow. The bridges transform the i_{HF1} and i_{HF2} into DC currents $i_{DAB,1}$ and $i_{DAB,2}$, on the primary and secondary side respectively. Fig. 1(b) shows the equivalent circuit of the considered DAB, where all quantities are referred to the primary side. The switching frequency is chosen $f_s = 120$ kHz in order to achieve compact converter design without excessive high-frequency losses.

The main inductor L , is chosen to be $L \approx 0.75 \cdot L_{\max}$, where L_{\max} is determined by the maximum input power of the DAB. According to [13], maximum positive DAB power is achieved when $\tau_1 = \tau_2 = \tau_{2B} = \pi$ and $\phi = \phi_B = \pi/2$, thus, the input current equation is (acc. to eqn. (14) of [13]):

$$I_{DC,1} = \frac{N \cdot V_{DC,2,\min}}{8 \cdot f_{s,\max} \cdot L}, \quad (1)$$

$$I_{DC,1} \geq I_{DC,1,\max} = 200 \text{ A}.$$

The result of solving the inequality of eqn. (1) for L , is the inequality $L \leq L_{\max}$, where L_{\max} is:

$$L_{\max} = \frac{N \cdot V_{DC,2,\min}}{8 \cdot f_{s,\max} \cdot I_{DC,1,\max}}. \quad (2)$$

III. SWITCHING CONTROL ANALYSIS

In the 3-3L DAB, the inductor current i_L is controlled by three variables, i.e. the pulse-width of the voltages v_1 and v_2 produced by the primary and secondary side active bridges and the phase shift between them. Depending on the sequence of the voltage edges (falling or rising), 12 unique switching modes are distinguished. In the 3-5L DAB, the extra voltage levels ($\pm V_{DC,2}/2$) of the secondary side bridge, increase the control variables to five. This results in more flexibility for the optimal shaping of the inductor current, but the total number of modes is increased to 40 and the analysis of the DAB is getting more complex.

Fig. 2 depicts general waveforms of v_1 , v_2 and i_L , i_{HF1} , i_{HF2} for the 3-5L DAB. The control variables are the pulse-widths τ_1 , τ_2 and τ_{2B} for the primary bridge, the secondary bridge half-DC voltage level and the secondary bridge full-DC voltage level, respectively. The phase shifts are defined with respect to the falling edge of the primary side voltage at $t = \pi/\omega_s$, being ϕ for the first level and ϕ_B for the second level. The physical limits of the control variables are,

$$\begin{aligned} 0 &\leq \tau_1, \tau_2, \tau_{2B} \leq \pi, \\ -\pi &\leq \phi \leq \pi, \\ -2\pi &\leq \phi_B \leq \pi, \end{aligned} \quad (3)$$

and for valid waveforms the following conditions should also apply:

$$\begin{aligned} \phi_B &\leq \phi, \\ \phi - \phi_B + \tau_{2B} &\leq \tau_2. \end{aligned} \quad (4)$$

A. Switching Modes Selection Procedure

To determine the optimal mode for each operating point and the corresponding control angles (τ_1 , τ_2 , τ_{2B} , ϕ and ϕ_B), an optimization algorithm (non-linear constrained minimization) is developed [14]. The constraints applied during the optimization process are the inequality soft-switching constraint (see section III-C), the physical limits of the control variables (eqns. (3)-(4)) and the input current $I_{DC,1}$ equality constraint ($I_{DC,1} = I_{DC,1,\text{ref}}$). The soft-switching constraints assure ZVS in every operating point and quasi zero switching losses.

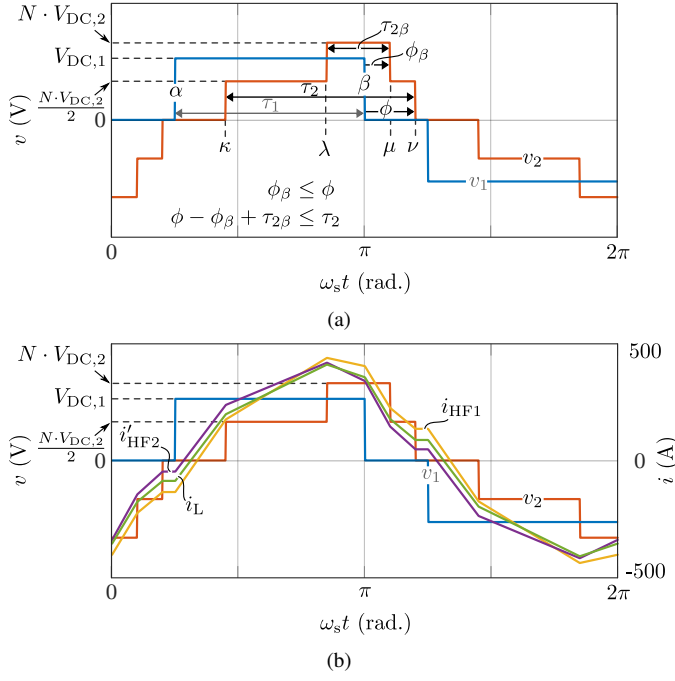


Fig. 2. General waveforms of v_1 , v_2 and i_L , i_{HF1} , i_{HF2} for the 3-5L DAB. The waveforms were obtained for $V_{DC,1} = 15.5$ V, $V_{DC,2} = 175$ V, $\tau_1 = \frac{3\pi}{4}$, $\tau_2 = \frac{3\pi}{4}$, $\tau_{2B} = \frac{\pi}{4}$, $\phi = \frac{\pi}{5}$, $\phi_B = \frac{\pi}{10}$, $f_s = 120$ kHz, $L = 0.0683$ μ H, $L_1 = 0.77$ μ H and $L_2 = 62.1$ μ H. Fig. 2(a) focuses on the control variables and the names of the edges and Fig. 2(b) on the currents in the inductors L , L_1 and L_2 .

Under ZVS operation, the conduction losses of the transistors account for the biggest part (≥ 50 %) of the total converter losses [15]. Thus, the objective function used in the optimization is related to the overall conduction losses and is calculated using the equation:

$$f_{obj} = I_{RMS,HF1}^2 + \frac{I_{RMS,HF2}^2}{N^2}, \quad (5)$$

where $I_{RMS,HF1}^2$ and $I_{RMS,HF2}^2$ are proportional to the primary and secondary side conduction losses, respectively.

The outcome of this optimization procedure is depicted in Fig. 3. By analyzing the outcome, only two modes (mode 21,11) are preferably used for positive power flow, and two modes (mode 21,31) for negative power flow. Waveforms of mode 21 and 11 are depicted in Fig. 4(a) and Fig. 4(b), respectively. The transition from mode 21 to 11 (i.e. from negative to positive phase-shift), makes using the commutation inductances necessary because the injected current in each bridge is contributing positively, in most cases, to meet the soft-switching constraints (see Section IV-B).

For brevity, only positive power flow is considered ($LV \rightarrow HV$) for the derivation of the analytical modulation strategy of Section IV. The analysis for reverse power flow is similar, since the secondary bridge waveform is mirrored for the

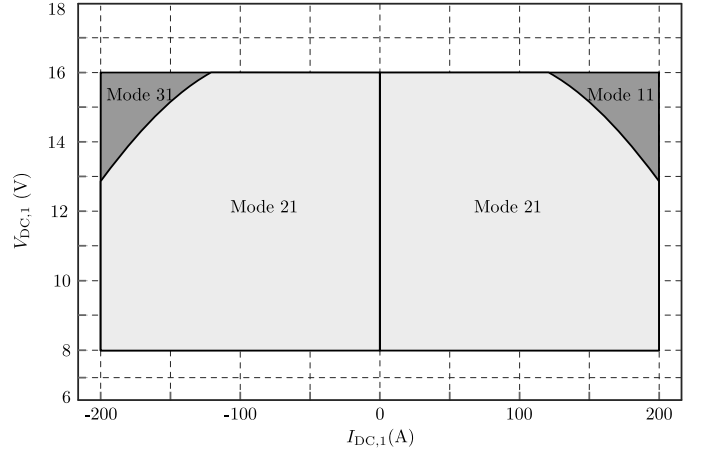


Fig. 3. Switching modes obtained from the numerical optimization algorithm. The output voltage is $V_{DC,2} = 175$ V.

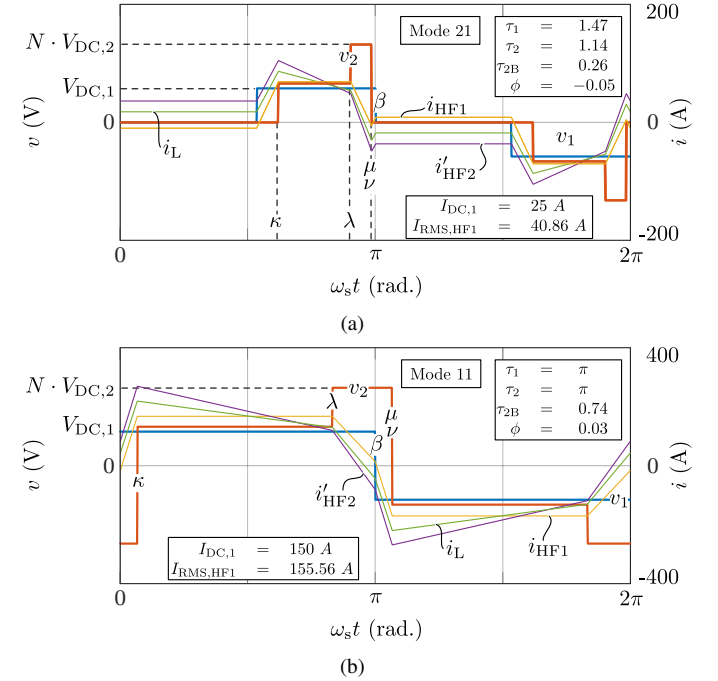


Fig. 4. Ideal voltage and current waveforms for (a) mode 21 and (b) mode 11. The waveforms are derived for: $V_{DC,1} = 8.5$ V, and $V_{DC,2} = 175$ V.

corresponding operating point¹. The strategy proposed in this paper is for positive power flow and is based only on modes 21 and 11.

B. Piecewise Linear Analysis

The results obtained from the numerical optimization are used as a basis to derive closed form analytical solutions for the control angles (τ_1 , τ_2 , τ_{2B} , ϕ and ϕ_B), which are presented

¹If the control angles for the operating point ($V_{DC,1}$, $V_{DC,2}$, $+I_{DC,1}$) are known, the control angles for the operating point ($V_{DC,1}$, $V_{DC,2}$, $-I_{DC,1}$) are calculated using $\tau'_1 = \tau_1$, $\tau'_2 = \tau_2$, $\tau'_{2B} = \tau_{2B}$, $\phi' = -\phi - \tau_1 + \tau_2$ and $\phi'_B = \phi' + \tau_{2B} - \tau_2$.

TABLE II
INPUT CURRENT ($I_{DC,1}$) EXPRESSIONS FOR MODE 21 AND 11

Mode 21	$\frac{N V_{DC,2} ((2\phi + \tau_1 - \tau_2) \tau_2 + (2\phi_B + \tau_1) \tau_{2B} - \tau_{2B}^2)}{4 L \pi \omega_s}$
Mode 11	$-\frac{N V_{DC,2}}{4\pi L \omega_s} [2\phi^2 - 2\phi(-\tau_1 + \tau_2 + \pi) + 2\phi_B^2 - 2\phi_B(-\tau_1 + \tau_{2B} + \pi) + 2\tau_1^2 - \tau_1 \tau_2 - \tau_1 \tau_{2B} - 4\pi \tau_1 + \tau_2^2 + \tau_{2B}^2 + 2\pi^2]$

in Section IV. The respective inductor currents, induced by v_1 and v_2' are depicted in Fig. 2(b) and derived by:

$$\frac{di_L(t)}{dt} = \frac{v_1(t) - v_2'(t)}{L}, \quad (6)$$

$$\frac{di_{L_1}(t)}{dt} = \frac{v_1(t)}{L_1}, \quad (7) \quad \frac{di_{L_2'}(t)}{dt} = \frac{v_2'(t)}{L_2'}. \quad (8)$$

Solving equations (6)-(8) in each interval within half the switching period and assuming steady state operation (i.e. $i_L(t) = -i_L(t + T_s/2)$, $i_{L_1}(t) = -i_{L_1}(t + T_s/2)$ and $i_{L_2'}(t) = -i_{L_2'}(t + T_s/2)$), results in the expressions for the currents at every switching instance $\theta_i = \{\alpha, \beta, \kappa, \lambda, \mu, \nu\}$, where $\theta_i = \omega_s t$ and $\omega_s = 2\pi f_s$. The bridge currents $i_{HF1}(t)$ and $i_{HF2}(t)$ are calculated using:

$$i_{HF1}(t) = i_L(t) + i_{L_1}(t), \quad (9)$$

$$i_{HF2}(t) = N \cdot i_{HF2'}(t) = N \cdot (i_L(t) - i_{L_2'}(t)). \quad (10)$$

The current expressions for mode 21 and mode 11, applying the aforementioned procedure for each mode, are summarized in Table V and in Table VI of the Appendix, respectively. By analyzing the conduction state of the switches, currents $i_{DAB,1}(t)$ and $i_{DAB,2}(t)$ can be derived from $i_{HF1}(t)$ and $i_{HF2}(t)$, respectively. Averaging $i_{DAB,1}(t)$ over a switching period T_s , yields the expressions for input current $I_{DC,1}$. Table II denotes the input current expressions for modes 21 and 11.

C. Soft-Switching Constraints

Zero-voltage-switching operation of the switches (acc. to Fig. 1(c), S_{x1} , S_{x2}), is explained for a voltage transition that is initiated by the turn-off of the transistor T_{x1} . The current i_{HFx} transfers the charge of the nonlinear parasitic capacitance C_{x2} (discharge) to the respective nonlinear parasitic capacitance C_{x1} (charge). By the time instant the Diode D_{x2} takes over the current, the transistor T_{x2} can be turned-on under ZVS. A minimum turn-off current is needed to complete the resonant transition within the dead-time interval and avoid voltage transition delay. The current-based soft-switching constraints for bridge currents i_{HF1} and i_{HF2} are summarized in Table III. A minimum commutation current value of 2 A is used for the primary and secondary side high-frequency switches ($I_{SS,Prim} = I_{SS,Sec} = 2$ A).

TABLE III
SOFT-SWITCHING CONSTRAINTS

Edge	Current Constraint	Type	Critical ZVS Constraints per Region			
			1	2	3	4
α	$i_{HF1}(\alpha) \leq -I_{SS,Prim}$	Rising				
β	$i_{HF1}(\beta) \geq I_{SS,Prim}$	Falling	x	x	x	x
κ	$i_{HF2}(\kappa) \geq I_{SS,Sec}$	Rising			x	
λ	$i_{HF2}(\lambda) \geq I_{SS,Sec}$	Rising	x			
$\nu \equiv \mu$	$i_{HF2}(\nu) \leq -I_{SS,Sec}$	Falling	x	x	x	x

IV. ANALYTICALLY DERIVED MODULATION SCHEME

The results of the numerical optimization are presented in Fig. 3. A close look into the results, shows that the optimizer chooses to keep the edges μ and ν in the same switching instant for both modes (21 and 11), leading to the constraint:

$$\phi = \phi_B, \quad (11)$$

as shown in Fig. 4.

In order to derive an analytical modulation scheme, the operating points were checked step-by-step and critical ZVS conditions were identified. For each operating point, in total three constraints should be identified, on top of the constraints denoted by the equation (11) and the input power expression (Table II), in order to be able to solve the system of equations towards the control variables (τ_1 , τ_2 , τ_{2B} , ϕ and ϕ_B). Following this procedure, five regions were identified, where every operating point of the same region has the same critical ZVS conditions, which are summarized in Table III². Fig. 5(a) depicts an overview of them and their boundaries. In Fig. 5(c) and Fig. 5(b) the critical switch commutation currents are shown as function of input current for $V_{DC,1} = 9$ V and $V_{DC,1} = 14.5$ V, respectively. Dashed lines denote commutation currents for $L_1 = \infty$, $L_2 = \infty$ and solid lines for finite L_1 and L_2 . The resulting ZVS conditions of the commutation currents that are not shown in Fig. 5(b) and Fig. 5(c) are either less important ($i_{HF2}(x) \gg I_{SS,Sec}$) or identical to ZVS conditions of another voltage edge ($(i_{HF1}(\alpha) \leq -I_{SS,Prim}) \equiv (i_{HF1}(\beta) \geq I_{SS,Prim})$).

A. Infinite L_1 and L_2

Starting from operating point 1 (OP1) of Fig. 5, the soft-switching constraints (edges β , λ , and ν) are satisfied. As it can be seen in Fig. 5(b) (dashed lines), each commutation current has the minimum required value for edges β and λ , and the maximum required value for the edge ν . Thus, from every soft-switching inequality constraint the equal part is true (" \leq ", " \geq " \rightarrow " $=$ "). The resulting system of equations for region 1

²Region 5 is separately discussed in the end of this section.

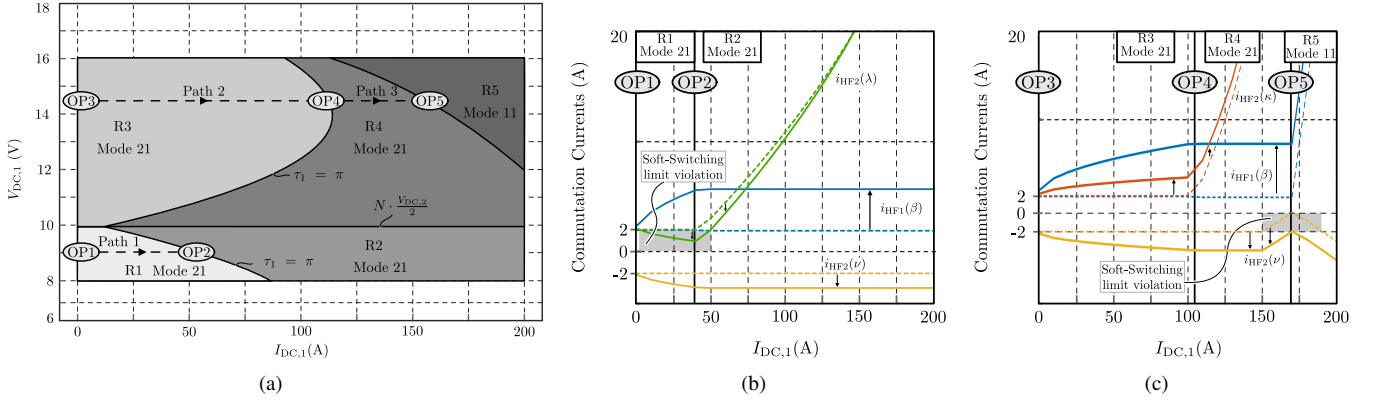


Fig. 5. (a) Overview of the five regions detailed in Section IV. Every operating point of the same region has the same critical ZVS conditions. Switch commutation currents as function of input current for (b) $V_{DC,1} = 9$ V and (c) $V_{DC,1} = 14.5$ V. Dashed lines denote switch commutation currents for $L_1 = \infty$ and $L_2 = \infty$, and solid lines for finite L_1 and L_2 values. The output voltage is $V_{DC,2} = 175$ V.

is depicted in Table IV and the expressions for the control variables are summarized in Table VII of the Appendix.

Using the region 1 expressions for the control variables and following path 1 of Fig.5(a) (i.e. keeping the same voltage and increasing the input current), at a certain operating point the pulse-width of voltage v_1 , is getting $> \pi$, which is beyond the physical limits and τ_1 is clipped to its maximum value ($\tau_1 = \pi$). This operating point (OP2) defines the boundary between region 1 and 2. In Fig. 5(b), it can be seen that the current $i_{HF2}(\lambda)$ is increasing as $I_{DC,1}$ increases, meeting the ZVS condition $i_{HF2}(\lambda) \geq I_{SS,Sec}$ until current $I_{DC,1}$ reaches its maximum value. The soft-switching constraint for edges β and ν are still satisfied in the minimum and maximum value, respectively. The system of equations for region 2 is depicted in Table IV, where the ZVS condition of edge λ is replaced with the condition $\tau_1 = \pi$. The resulting expressions for the control variables are summarized in Table VIII of the Appendix.

Fig. 5(c) (dashed lines) shows the switch commutation currents for edges β , κ , and ν for regions 3, 4, and 5. The same procedure is followed in region 3, starting from the operating point 3 (OP3). The soft-switching constraints are satisfied in their minimum required value for edges β and κ , and in the maximum required value for edge ν . A system of equations is solved (Table IV), resulting in the expressions for the control variables of Table IX of the Appendix.

Following path 2 of Fig.5(a) (i.e. $V_{DC,1} = 14.5$ V and increasing the input current), the control variables for every operating point are calculated using the region 3 expressions. At a certain operating point, the pulse-width of voltage v_1 becomes bigger than its physical limit ($\tau_1 > \pi$), which is impossible and thus, τ_1 is clipped to π . This operating point (OP4) defines the boundary between region 3 and 4. The soft-switching constraint for edges β and ν are still satisfied in the minimum and maximum value, respectively. The current $i_{HF2}(\kappa)$ is increasing as $I_{DC,1}$ increases, meeting the requirement $i_{HF2}(\kappa) \geq I_{SS,Sec}$ until current $I_{DC,1}$ reaches its maximum value. The system of equations that corresponds

to region 4 is summarized in Table IV and the control variables are calculated using the expressions³:

$$\begin{aligned} \tau_1 &= \pi, \\ \tau_2 &= \frac{e_7 - \sqrt{e_{11}}}{N^2 V_{DC,1} V_{DC,2}^2}, \\ \tau_{2B} &= \frac{e_7 + \sqrt{e_{11}}}{N^2 V_{DC,1} V_{DC,2}^2}, \\ \phi &= -\frac{L \omega_s (I_{SS,Prim} + I_{SS,Sec})}{V_{DC,1}}. \end{aligned} \quad (12)$$

which are also summarized in Table VIII of the Appendix. In this point, it is observed that the resulting expression of region 2 and region 4 are identical, but they are treated separately for practical reasons (distinction between $V_{DC,1} \leq N \cdot V_{DC,2}/2$ and $V_{DC,1} > N \cdot V_{DC,2}/2$).

Following path 3 of Fig.5(a) and calculating the control variables for every operating point using the expressions of region 4 results in the operating point 5 (OP5). In this operating point, the e_{11} term of equation (12) becomes negative and this causes the square root ($\sqrt{\cdot}$) to return a complex number. OP5 defines the boundary between regions 4 and 5 and the transition point from mode 21 to mode 11. Mode 21 is not able to transfer more power (under ZVS) and the optimizer selects to switch to mode 11.

In Fig. 5(c) (dashed lines, region 5), the soft-switching currents are satisfied for edges β ($i_{HF1}(\beta) \geq I_{SS,Prim}$) and κ ($i_{HF2}(\kappa) \geq I_{SS,Sec}$), while not for edge ν (assuming $I_{SS,Prim} = I_{SS,Sec} = 2$ A). This problem can be solved using finite values for commutation inductances (L_1 , L_2) and is discussed in Section IV-B. Another important consideration is to conserve smooth transition of the control variables from mode 21 to mode 11, because a sudden transition (i.e. discontinuous function of one or more control variable) causes an unwanted dynamic behavior of the DAB.

To calculate the control variables for region 5, the real part of the τ_2 and τ_{2B} equations is used. In this way, it is verified

³Expressions for e_{xx} elements are summarized in Table XI of the Appendix.

TABLE IV
SYSTEM OF EQUATIONS

Regions		
1	2 and 4	3
$i_{HF1}(\beta) = I_{SS,Prim}$	$i_{HF1}(\beta) = I_{SS,Prim}$	$i_{HF1}(\beta) = I_{SS,Prim}$
$i_{HF2}(\lambda) = I_{SS,Sec}$	$\tau_1 = \pi$	$i_{HF2}(\kappa) = I_{SS,Sec}$
$i_{HF2}(\nu) = -I_{SS,Sec}$	$i_{HF2}(\nu) = -I_{SS,Sec}$	$i_{HF2}(\nu) = -I_{SS,Sec}$

that the resulting control angles are close to the optimal control angles of the optimization procedure and smooth transition from mode 21 to mode 11 is achieved. Finally, the ϕ for region 5 is calculated using the input power equation of mode 11, while τ_1 remains equal to π . The expressions for the control variables used in region 5 are summarized in Table X of the Appendix.

B. Finite L_1 and L_2

In Fig. 5(c) (dashed lines), a ZVS limit violation is observed for edge ν ($i_{HF2}(\nu) < I_{SS,Sec}$). Therefore, finite L_1 and L_2 are used to enhance ZVS. The resulting commutation currents are depicted with solid lines in Fig. 5(b) and Fig. 5(c).

As discussed in [5], commutations inductances always enhance ZVS operation in the traditional 3-3L DAB. However in the case of the 3-5L DAB, L_2 depresses ZVS for edge λ , as can be seen in Fig. 5(b) (solid line). A trade-off is introduced for achieving ZVS in edge λ in region 1 and ν in region 5. In this paper, edge λ in region 1, is chosen to violate ZVS, because the resulting switching losses will be lower (lower voltage and current). However, ZVS is achieved in the entire operating range assuming $I_{SS,Prim} = I_{SS,Sec} = 0$ A.

Using the proposed strategy, soft-switching operation is achieved in the entire operating range ($I_{SS,Prim} = I_{SS,Sec} = 0$ A) of the 3-5L DAB. The analytical solution for every sub-region is available in the Appendix. The complete algorithm derived during this process is depicted in Fig. 6, showing how every operating point ($V_{DC,1}, V_{DC,2}, I_{DC,1}$) results in the appropriate region and solution set. The control variables τ_1 , τ_2 , τ_{2B} and ϕ are depicted in Fig. 7, as function of the input current for nominal and minimum input voltage. A continuous waveform can be seen for every variable which is necessary to avoid undesirable dynamic behavior.

V. COMPARISON TO 3-3L DAB

In order to demonstrate the advantages of the 3-5L DAB, a comparison is performed between the 3-5L DAB and the traditional 3-3L DAB. For the latter, the analytically derived modulation scheme from [5] is used. The basis for this comparison is the RMS value of the currents $i_{HF1}(t)$ and $i_{HF2}(t)$ over the entire operating range, using common system specifications (Table I). First, the maximum value of the commutation inductances that assures ZVS ($I_{SS,Prim} = I_{SS,Sec} = 0$ A) in the entire operating region is identified for each topology.

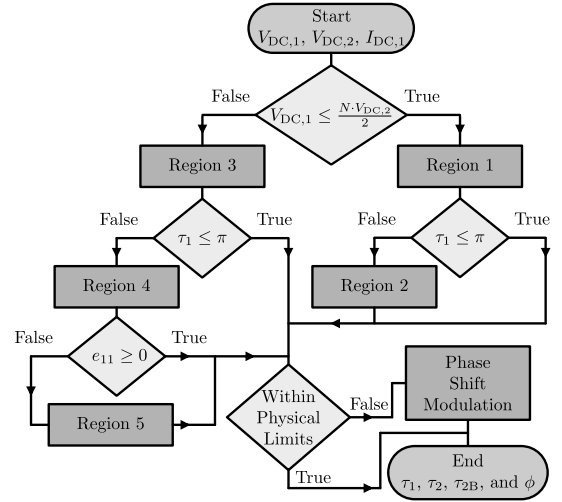


Fig. 6. Diagram of the calculation algorithm for the control angles τ_1 , τ_2 , τ_{2B} , ϕ and ϕ_B , given the operating point ($V_{DC,1}, V_{DC,2}, I_{DC,1}$).

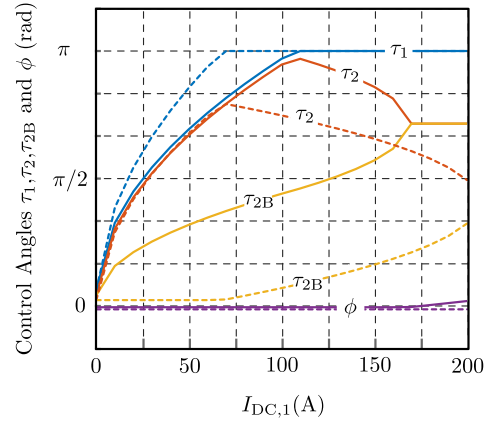


Fig. 7. Control angles τ_1 , τ_2 , τ_{2B} and ϕ , for nominal (14 V, solid line) and minimum (8 V, dashed line) input voltage. The output voltage is $V_{DC,2} = 175$ V.

Using these values, Fig. 8 is derived. Fig. 8(a) and Fig. 8(b) show the RMS values of the primary and secondary bridge currents for the traditional 3-3L DAB. Fig. 8(c) and Fig. 8(d) show the RMS values of the primary and secondary bridge currents for the 3-5L DAB, respectively. Fig. 8(e) depicts the percent difference between Fig. 8(a) and Fig. 8(c), and Fig. 8(f) depicts the percent difference between Fig. 8(b) and Fig. 8(d). For the derivation of Fig. 8(e) and Fig. 8(f) the following expression is used:

$$RMS\% = 100\% \cdot \frac{I_{RMS,HFx,3-5L}^2(v, i) - I_{RMS,HFx,3-3L}^2(v, i)}{I_{RMS,HFx,3-3L}^2(v, i)} \quad (13)$$

The advantage of the 3-5L DAB is mainly observed in the low-voltage, low-current region, where the squared RMS currents for both primary (Fig. 8(e)) and secondary (Fig. 8(f)) side bridges are up to 70% lower. On the contrary, in the high-voltage, high-current region there is no significant advantage because the secondary bridge is operated as a full bridge ($\tau_2 \approx$

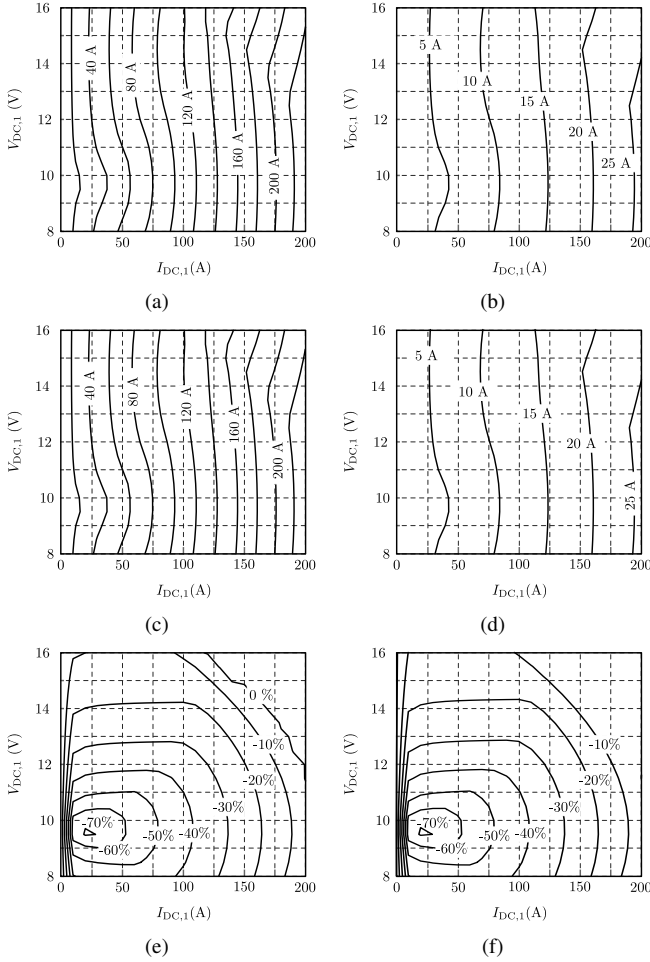


Fig. 8. RMS current of (a) LV-side bridge ($I_{RMS,HF1}$) and (b) HV-side bridge ($I_{RMS,HF2}$) of the 3-3L DAB topology. (c) and (d) show the RMS current of LV-side bridge ($I_{RMS,HF1}$) and HV-side bridge ($I_{RMS,HF2}$) of the 3-5L DAB topology, respectively. Figure (e) shows the percent difference of (a) and (c), and figure (f) shows the percent difference of (b) and (d), according to eqn. (13).

τ_{2B}).

VI. CONCLUSION

In this paper a modulation strategy for the 3 Level – 5 Level (3-5L) Dual Active Bridge (DAB) DC–DC converter, achieving ZVS in the whole operating range, is presented. An analysis of the possible switching modes is provided, as well as, a selection procedure to select the optimum mode for every operating point. Two modes are selected and by interpreting the results of the numerical optimization, a final switching control strategy is derived. Both bridges use commutation inductances in order to assure ZVS in the transition between modes. The proposed strategy is compared with a similar strategy derived for the traditional 3-3L DAB in literature. The comparison shows the advantage of the 3-5L DAB in the low-voltage, low-current region.

ACKNOWLEDGMENTS

This paper is part of the ADvanced Electric Powertrain Technology (ADEPT) project which is an EU funded Marie Curie ITN project, grant number 607361 [16].

REFERENCES

- [1] M. N. Kheraluwala, R. W. Gascoigne, D. M. Divan, and E. D. Baumann, "Performance characterization of a high-power dual active bridge DC-to-DC converter," *IEEE Transactions on Industry Applications*, vol. 28, no. 6, pp. 1294–1301, Nov. 1992.
- [2] F. Krismer and J. W. Kolar, "Efficiency-Optimized High-Current Dual Active Bridge Converter for Automotive Applications," *IEEE Transactions on Industrial Electronics*, vol. 59, no. 7, pp. 2745–2760, July 2012.
- [3] R. W. De Doncker, D. M. Divan, and M. H. Kheraluwala, "A Three-Phase Soft-Switched High Power Density DC/DC Converter for High Power Applications," in *IEEE Industry Applications Society Annual Meeting*, vol. 1, Oct. 1988, pp. 796–805.
- [4] G. G. Oggier, G. O. Garcia, and A. R. Oliva, "Modulation Strategy to Operate the Dual Active Bridge DC-DC Converter Under Soft Switching in the Whole Operating Range," *IEEE Transactions on Power Electronics*, vol. 26, no. 4, pp. 1228–1236, April 2011.
- [5] J. Everts, J. Van den Keybus, F. Krismer, J. Driesen, and J. W. Kolar, "Switching Control Strategy for Full ZVS Soft-Switching Operation of a Dual Active Bridge AC/DC Converter," in *IEEE 27th Annual Applied Power Electronics Conference and Exposition (APEC 2012)*, Feb. 2012, pp. 1048–1055.
- [6] J. Everts, F. Krismer, J. Van den Keybus, J. Driesen, and J. W. Kolar, "Optimal ZVS Modulation of Single-Phase Single-Stage Bidirectional DAB AC–DC Converters," *IEEE Transactions on Power Electronics*, vol. 29, no. 8, pp. 3954–3970, Aug. 2014.
- [7] P. A. M. Bezerra, F. Krismer, R. M. Burkart, and J. W. Kolar, "Bidirectional Isolated non-Resonant DAB DC-DC Converter for Ultra-Wide Input Voltage Range Applications," in *IEEE International Power Electronics and Application Conference and Exposition (PEAC 2014)*, Nov. 2014, pp. 1038–1044.
- [8] J. Everts and J. W. Kolar, "Elektrischer Leistungswandler zur DC/DC-Wandlung mit Dualen Aktiven Brücken," Swiss patent CH707553 (A2), August 15, 2014.
- [9] M. A. Moonem and H. Krishnaswami, "Control and configuration of three-level dual-active bridge DC-DC converter as a front-end interface for photovoltaic system," in *IEEE 29th Applied Power Electronics Conference and Exposition (APEC 2014)*, March 2014, pp. 3017–3020.
- [10] —, "Analysis and control of multi-level dual active bridge DC-DC converter," in *IEEE Energy Conversion Congress and Exposition (ECCE 2012)*, Sept. 2012, pp. 1556–1561.
- [11] A. Filba-Martinez, S. Busquets-Monge, and J. Bordonau, "Modulation and capacitor voltage balancing control of a three-level NPC dual-active-bridge DC-DC converter," in *IEEE 39th Annual Conference of Industrial Electronics Society (IECON 2013)*, Nov. 2013, pp. 6251–6256.
- [12] A. K. Tripathi, K. Hatua, H. Mirzaee, and S. Bhattacharya, "A three-phase three winding topology for Dual Active Bridge and its D-Q mode control," in *IEEE 27th Annual Applied Power Electronics Conference and Exposition (APEC 2012)*, Feb. 2012, pp. 1368–1372.
- [13] F. Krismer and J. W. Kolar, "Closed Form Solution for Minimum Conduction Loss Modulation of DAB Converters," *Power Electronics, IEEE Transactions on*, vol. 27, no. 1, pp. 174–188, Jan. 2012.
- [14] J. Everts, G. E. Sfakianakis, and E. A. Lomonova, "Using Fourier Series to Derive Optimal Soft-Switching Modulation Schemes for Dual Active Bridge Converters," in *IEEE 7th Annual Energy Conversion Congress and Exposition (ECCE 2015)*, Sept. 2015, pp. 4648–4655.
- [15] J. Everts, F. Krismer, J. Van den Keybus, J. Driesen, and J. W. Kolar, "Comparative Evaluation of Soft-Switching, Bidirectional, Isolated AC/DC Converter Topologies," in *Applied Power Electronics Conference and Exposition (APEC), 2012 Twenty-Seventh Annual IEEE*, Feb 2012, pp. 1067–1074.
- [16] A. Stefanskyi, A. Dziechciarz, F. Chauvicourt, G. E. Sfakianakis, K. Ramakrishnan, K. Niyomsatian, M. Curti, N. Djukic, P. Romanazzi, S. Ayat, S. Wiedemann, W. Peng, A. Tamas, and S. Stipetic, "Researchers within the EU funded Marie Curie ITN project ADEPT, grant number 607361," 2013–2017. [Online]. Available: adept-itn.eu

APPENDIX

TABLE VI
CURRENT EXPRESSIONS FOR MODE 11

$i_{\text{HF1}}(0) =$	$\frac{L_1 N V_{\text{DC},2}(-2\phi - 2\phi_{\text{B}} + \tau_2 + \tau_{2\text{B}}) - 2\tau_1 V_{\text{DC},1}(L + L_1)}{4L L_1 \omega_s}$
$i_{\text{HF1}}(\alpha) =$	$\frac{L_1 N V_{\text{DC},2}(-2\phi - 2\phi_{\text{B}} - 4\tau_1 + \tau_2 + \tau_{2\text{B}} + 4\pi)}{4L L_1 \omega_s}$ $- \frac{2\tau_1 V_{\text{DC},1}(L + L_1)}{4L L_1 \omega_s}$
$i_{\text{HF1}}(\beta) =$	$\frac{2\tau_1 V_{\text{DC},1}(L + L_1) + L_1 n V_{\text{DC},2}(2\phi + 2\phi_{\text{B}} - \tau_2 - \tau_{2\text{B}})}{4L L_1 \omega_s}$
$i_{\text{HF1}}(\kappa) =$	$\frac{2V_{\text{DC},1}(L + L_1)(2\phi + \tau_1 - 2\tau_2) + L_1 N V_{\text{DC},2}(\tau_2 + \tau_{2\text{B}})}{4L L_1 \omega_s}$
$i_{\text{HF1}}(\lambda) =$	$\frac{2V_{\text{DC},1}(L + L_1)(2\phi + 3\tau_1 - 2\pi) - L_1 N V_{\text{DC},2}(\tau_2 + \tau_{2\text{B}})}{4L L_1 \omega_s}$ $+ \frac{2V_{\text{DC},1}(L + L_1)(2\phi_{\text{B}} + \tau_1 - 2\tau_{2\text{B}})}{4L L_1 \omega_s}$
$i_{\text{HF1}}(\mu) =$	$+ \frac{L_1 N V_{\text{DC},2}(2\phi - 2\phi_{\text{B}} - \tau_2 + 3\tau_{2\text{B}})}{4L L_1 \omega_s}$ $+ \frac{2V_{\text{DC},1}(L + L_1)(2\phi_{\text{B}} + 3\tau_1 - 2\pi)}{4L L_1 \omega_s}$
$i_{\text{HF1}}(\nu) =$	$- \frac{L_1 N V_{\text{DC},2}(2\phi_{\text{B}} - 2\phi + \tau_2 + \tau_{2\text{B}})}{4L L_1 \omega_s}$

TABLE V
CURRENT EXPRESSIONS FOR MODE 21

$i_{\text{HF1}}(0) =$	$\frac{L_1 N V_{\text{DC},2}(\tau_2 + \tau_{2\text{B}}) - 2\tau_1 V_{\text{DC},1}(L + L_1)}{4L L_1 \omega_s}$
$i_{\text{HF1}}(\alpha) =$	$\frac{L_1 N V_{\text{DC},2}(\tau_2 + \tau_{2\text{B}}) - 2\tau_1 V_{\text{DC},1}(L + L_1)}{4L L_1 \omega_s}$
$i_{\text{HF1}}(\beta) =$	$\frac{2\tau_1 V_{\text{DC},1}(L + L_1) - L_1 N V_{\text{DC},2}(\tau_2 + \tau_{2\text{B}})}{4L L_1 \omega_s}$
$i_{\text{HF1}}(\kappa) =$	$\frac{2V_{\text{DC},1}(L + L_1)(2\phi + \tau_1 - 2\tau_2) + L_1 N V_{\text{DC},2}(\tau_2 + \tau_{2\text{B}})}{4L L_1 \omega_s}$
$i_{\text{HF1}}(\lambda) =$	$\frac{2V_{\text{DC},1}(L + L_1)(2\phi + \tau_1) - L_1 N V_{\text{DC},2}(\tau_2 + \tau_{2\text{B}})}{4L L_1 \omega_s}$ $+ \frac{2V_{\text{DC},1}(L + L_1)(2\phi_{\text{B}} + \tau_1 - 2\tau_{2\text{B}})}{4L L_1 \omega_s}$
$i_{\text{HF1}}(\mu) =$	$+ \frac{L_1 N V_{\text{DC},2}(2\phi - 2\phi_{\text{B}} - \tau_2 + 3\tau_{2\text{B}})}{4L L_1 \omega_s}$
$i_{\text{HF1}}(\nu) =$	$\frac{2V_{\text{DC},1}(L + L_1)(2\phi_{\text{B}} + \tau_1) - L_1 N V_{\text{DC},2}(2\phi_{\text{B}} - 2\phi + \tau_2 + \tau_{2\text{B}})}{4L L_1 \omega_s}$
$i_{\text{HF2}}(0) =$	$\frac{N V_{\text{DC},2}(L + L_2)(\tau_2 + \tau_{2\text{B}}) - 2L_2 \tau_1 V_{\text{DC},1}}{4L L_2 \omega_s}$
$i_{\text{HF2}}(\alpha) =$	$\frac{N V_{\text{DC},2}(L + L_2)(\tau_2 + \tau_{2\text{B}}) - 2L_2 \tau_1 V_{\text{DC},1}}{4L L_2 \omega_s}$
$i_{\text{HF2}}(\beta) =$	$\frac{2L_2 \tau_1 V_{\text{DC},1} - N V_{\text{DC},2}(L + L_2)(\tau_2 + \tau_{2\text{B}})}{4L L_2 \omega_s}$
$i_{\text{HF2}}(\kappa) =$	$\frac{N V_{\text{DC},2}(L + L_2)(\tau_2 + \tau_{2\text{B}}) + 2L_2 V_{\text{DC},1}(2\phi + \tau_1 - 2\tau_2)}{4L L_2 \omega_s}$
$i_{\text{HF2}}(\lambda) =$	$\frac{2L_2 V_{\text{DC},1}(2\phi + \tau_1) - N V_{\text{DC},2}(L + L_2)(\tau_2 + \tau_{2\text{B}})}{4L L_2 \omega_s}$ $+ \frac{N V_{\text{DC},2}(L + L_2)(2\phi - 2\phi_{\text{B}} - \tau_2 + 3\tau_{2\text{B}})}{4L L_2 \omega_s}$
$i_{\text{HF2}}(\mu) =$	$+ \frac{2L_2 V_{\text{DC},1}(2\phi_{\text{B}} + \tau_1 - 2\tau_{2\text{B}})}{4L L_2 \omega_s}$
$i_{\text{HF2}}(\nu) =$	$\frac{2L_2 V_{\text{DC},1}(2\phi_{\text{B}} + \tau_1) - N V_{\text{DC},2}(L + L_2)(2\phi_{\text{B}} - 2\phi + \tau_2 + \tau_{2\text{B}})}{4L L_2 \omega_s}$

TABLE VII
EXPRESSIONS FOR CALCULATION OF CONTROL VARIABLES FOR REGION 1

τ_1	$\frac{e_5 e_4 - \sqrt{e_4^4 e_3 L N V_{\text{DC},2} \omega_s}}{e_4^2 V_{\text{DC},1}(2V_{\text{DC},1} - N V_{\text{DC},2})}$
τ_2	$\frac{2(\sqrt{e_4^4 e_3 L N V_{\text{DC},2} \omega_s} + e_6)}{e_4^2 N V_{\text{DC},2}(N V_{\text{DC},2} - 2V_{\text{DC},1})}$
$\tau_{2\text{B}}$	$-\frac{2I_{\text{SS,Sec}} L \omega_s}{e_4}$
ϕ	$-\frac{L \omega_s (I_{\text{SS,Prim}} + I_{\text{SS,Sec}})}{V_{\text{DC},1}}$

TABLE VIII
EXPRESSIONS FOR CALCULATION OF CONTROL VARIABLES FOR REGION 2
AND 4

τ_1	π
τ_2	$\frac{e_7 - \sqrt{e_{11}}}{N^2 V_{\text{DC},1} V_{\text{DC},2}^2}$
$\tau_{2\text{B}}$	$\frac{e_7 + \sqrt{e_{11}}}{N^2 V_{\text{DC},1} V_{\text{DC},2}^2}$
ϕ	$-\frac{L \omega_s (I_{\text{SS,Prim}} + I_{\text{SS,Sec}})}{V_{\text{DC},1}}$

TABLE IX
EXPRESSIONS FOR CALCULATION OF CONTROL VARIABLES FOR REGION 3

τ_1	$\frac{e_{13} - \sqrt{e_{12}} V_{DC,1}}{e_4 V_{DC,1} (2 V_{DC,1} - N V_{DC,2})}$
τ_2	$\frac{I_{SS,Sec} L \omega_s (3 N V_{DC,2} - 4 V_{DC,1}) - \sqrt{e_{12}}}{e_4 (2 V_{DC,1} - N V_{DC,2})}$
τ_{2B}	$\frac{\sqrt{e_{12}} + I_{SS,Sec} L N V_{DC,2} \omega_s}{-e_4 N V_{DC,2}}$
ϕ	$-\frac{L \omega_s (I_{SS,Prim} + I_{SS,Sec})}{V_{DC,1}}$

TABLE X
EXPRESSIONS FOR CALCULATION OF CONTROL VARIABLES FOR REGION 5

τ_1	π
τ_2	$\Re\left(\frac{e_7 - \sqrt{e_{11}}}{N^2 V_{DC,1} V_{DC,2}^2}\right)$
τ_{2B}	$\Re\left(\frac{\sqrt{e_{11}} + e_7}{N^2 V_{DC,1} V_{DC,2}^2}\right)$
ϕ	$\frac{-\sqrt{e_{15} + e_{16}} + 2 N \tau_2 V_{DC,2} + 2 N \tau_{2B} V_{DC,2}}{8 N V_{DC,2}}$

TABLE XI
EXPRESSIONS FOR e_{xx} ELEMENTS

e_1	$2 I_{SS,Prim} + I_{SS,Sec}$
e_2	$I_{SS,Sec}^2 L N V_{DC,2} \omega_s$
e_3	$e_2 + 2 \pi I_{DC,1} V_{DC,1} (N V_{DC,2} - 2 V_{DC,1})$
e_4	$V_{DC,1} - N V_{DC,2}$
e_5	$L \omega_s \left(e_1 N^2 V_{DC,2}^2 - 3 e_1 N V_{DC,1} V_{DC,2} + 4 I_{SS,Prim} V_{DC,1}^2 \right)$
e_6	$e_4 I_{SS,Sec} L N V_{DC,1} V_{DC,2} \omega_s$
e_7	$N V_{DC,1} V_{DC,2} (\pi V_{DC,1} - 2 I_{SS,Prim} L \omega_s)$
e_8	$4 I_{SS,Prim} L^2 \omega_s^2 (N V_{DC,2} (I_{SS,Prim} + I_{SS,Sec}) - I_{SS,Prim} V_{DC,1})$
e_9	$N V_{DC,2} (e_1 + I_{DC,1}) - 2 I_{SS,Prim} V_{DC,1}$
e_{10}	$-\pi^2 e_4 V_{DC,1}^2$
e_{11}	$N^2 V_{DC,1} V_{DC,2}^2 (e_8 - 2 \pi e_9 L V_{DC,1} \omega_s + e_{10})$
e_{12}	$L N V_{DC,2} \omega_s (e_2 - 2 \pi e_4 I_{DC,1} (2 V_{DC,1} - N V_{DC,2}))$
e_{13}	$L \omega_s \left(-3 e_1 N V_{DC,1} V_{DC,2} + 2 N^2 V_{DC,2}^2 (I_{SS,Prim} + I_{SS,Sec}) \right) + L \omega_s \left(4 I_{SS,Prim} V_{DC,1}^2 \right)$
e_{14}	$4 \pi I_{DC,1} L \omega_s$
e_{15}	$(-2 N \tau_2 V_{DC,2} - 2 N \tau_{2B} V_{DC,2})^2$
e_{16}	$-16 N V_{DC,2} (e_{14} + N \tau_2^2 V_{DC,2} - \pi N \tau_2 V_{DC,2} + N \tau_{2B}^2 V_{DC,2}) - 16 N V_{DC,2} (-\pi N \tau_{2B} V_{DC,2})$

DESIGN AND APPLICATION OF A BOOTSTRAP CIRCUIT CONTROLLED BY PIC24 FOR A GRID INVERTER

Mohannad Jabbar Mnati ^{1,2}, Alex Van den Bossche ² and Jean Marie Vianney Bikorimana ^{2,3}

¹ Department of Electronic Technology, Institute of Technology Baghdad, Baghdad, Iraq,

E-mail: mohannad.j.mnati@ieee.org

² Electrical Energy Laboratory, Ghent University, Ghent, Belgium

E-mail: alex.vandenbossche@ugent.be

³ Department of Electrical and Electronics, University of Rwanda, Kigali, Rwanda

E-mail: jbikorimana@nur.ac.rw

Abstract— The standard bootstrap circuit consists of three important external components (diode, resistance and capacitor) for a PWM standard application. However, bootstrap circuits have shown some weakness such as having adequate components to allow a high performance. This article shows a bootstrap driver circuit using IR2112 to drive a power IGBTs inverter with a low energy consumption. In this paper, the PWM signal is generated by using a PIC24FJ128GA010 microcontroller and interfaced to the bootstrap circuit. The paper discusses the advantage and disadvantages of the bootstrap circuits.

Keywords— Bootstrap components, PIC24FJ128GA010, IGBT, driver circuit, IR2112.

I. INTRODUCTION

In driver circuits, it is necessary to turn ON/OFF and protect the power switches (MOSFETs, IGBTs, ..etc) from a shoot through current. The gate driver circuit consists of driver IC (IR2112) and a bootstrap circuit. Many papers have dealt with the bootstrap application circuit to drive the upper transistor [1][2][3][4]. The bootstrap gate drive circuit is a useful element for many converters. A block diagram of the IR2112 integrated circuit and external components are presented in Fig. 1.

The working principle of a bootstrap capacitor is as follow: (C_{boot}) has to be charged from the Vdc supply and store sufficient charge to provide power to the upper side driver circuit transistor [5]. The minimum capacitance value can be calculated by equation 1.

$$C_{boot}(\text{min.}) \geq \frac{Q_{BS(\text{total})}}{\Delta V_{BS}} \quad (1)$$

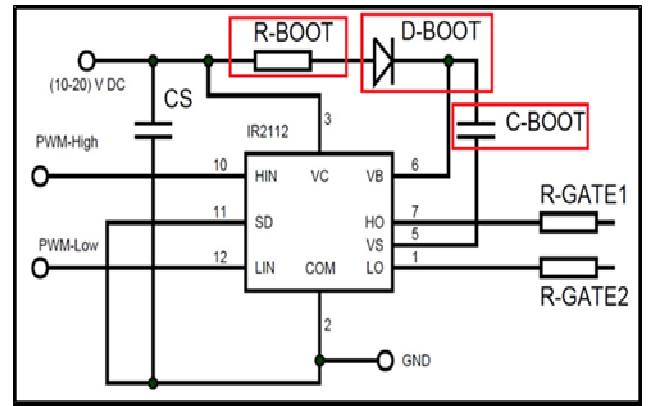


Fig.1. Bootstrap circuit (driver IC IR2112 and external element)

The gate drivers are fundamental for power electronic system in converters (DC/DC, DC/AC etc.). However, adequate techniques are needed to generate a suitable PWM to driver them. In this paper, A PIC24FJ128GA010 microcontroller has been employed to generates the control signals that are used as inputs to the IGBT driver circuit[6] because of its low power consumption.

II. BOOTSTRAP GATE DRIVER CIRCUIT

A. Bootstrap Driver IC (IR2112)

After considering the different options of IGBT driver ICs, the IR2112 in Fig. 2 was chosen. The rated voltage of the selected IC is up to 600V, with a gate driving current(+/-) of 200 mA / 420 mA and a gate driving voltage of 10-20V respectively, The turn ON time is 125ns whereas turn OFF time is 105ns [7].

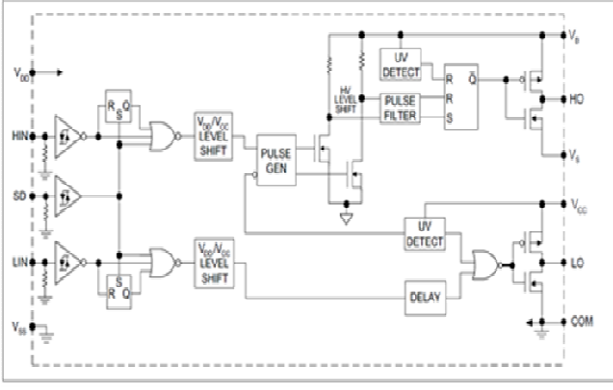


Fig. 2 IR2112 Block Diagram

B. Bootstrap External Component

The bootstrap circuit consists of three external components (R_{Boot} , D_{Boot} and C_{Boot}) as shown in Fig. 1.

1) *Bootstrap Resistance(R_{Boot}):* The first element in the bootstrap circuit is a bootstrap resistance as a small value connected in series with bootstrap diode(D_{Boot}). This resistance (R_{Boot}) is used to limit charger current flowing to bootstrap capacitor(C_{Boot}) [2].

$$R_{Boot} \leq \frac{T_{on}(lowerIGBT)}{4 \times C_{Boot}} \quad (2)$$

2) *Bootstrap Diode(D_{Boot}):* The bootstrap diode (D_{Boot}) provide route to charge bootstrap capacitor (C_{Boot}) and it must be able to have a fast recovery time to block the fed back voltage from this capacitor to driver power supply. There are some parameter that must be considered when choosing diode [8].

- T_{RR} = Reverse Recovery Time
- V_{RRM} = Maximum Repetitive reverse Voltage
- $I_{F(AV)}$ = Average Rectified Forward Current

3) *The main principle of bootstrap capacitor (C_{Boot}) is to store sufficient charge to supply the enough power exhaustion of IGBT gate driver and necessary gate charge to turn the upper side transistor "ON". The minimum bootstrap capacitor required can be calculated using the equation 1.*

$$Q_{BS(total)} = Q_g + Q_{LS} + (I_{LK,CAP} + I_{LK,GE} + I_{QBS} + I_{LK} + I_{LK,DIODE} + I_{LK,DS}) * T_{ON} \quad (3)$$

$$\Delta V_{BS} \leq (V_{DC} - V_F - V_{GE(min.)} - V_{CE(ON)}) \quad (4)$$

Where,

- Q_g : IGBT Turn on Required Gate Charge
- Q_{LS} : Charge required by The Internal Level Shifters
- $I_{LK,CAP}$: Capacitor Leakage Current
- $I_{LK,GC}$: Gate Leakage Current of The IGBT
- I_{QBS} : High Side Floating Supply Leakage Current
- I_{LK} : Bootstrap Circuit Leakage Current
- $I_{LK,DS}$: Bootstrap Diode Leakage Current
- ΔV_{BS} : Minimum Voltage Drop
- V_{DC} : Section logic voltage source
- V_F : Bootstrap Diode Forward voltage
- V_{LS} : Low – Side IGBT Drop Voltage
- $V_{CE(ON)}$: Minimum voltage Between V_C and V_E
- T_{ON} : Turning on Interval of lower IGBT

III. PROGRAMMABLE PWM CONTROLLER

PIC24FJ128GA010 microcontroller is the main unit used in the implementation to control the Half-Bridge. It is programmed by C language and using a MPLAB X IDE V3.15 software compiler for programing[6][9][10].

The control signals that are used as inputs to the IGBT driver circuit are generated by PIC24FJ128GA010 microcontroller. This controller was used because of its low power consumption, Pin terminals and the salient features are observed in Table 1.

TABLE I. Specifications of PIC24FJ128GA010

Device	Pins	Program Memory (Bytes)	SRAM (Bytes)	Timers 16-Bit	Capture Input	Compare PWM Output	UART	SPI	I2CTM	10-Bit A/D (ch)	Comparators	PWM/TSP	JTAG
PIC24FJ128GA010	100	128K	8K	5	5	5	2	2	2	16	2	Y	Y

PIC24FJ128GA010 is often used in industry, automotive applications, medical electronics applications and consumer electronics. The signal levels are directly compatible but they are not galvanic separated. Some applications do not need it. Therefore, in this case the bootstrap circuits have advantages.

IV. CALCULATION AND EXPERIMENTAL RESULTS

A. Mathematical Results

To accurately calculate the value of the bootstrap capacitor, equations 1,3 and 4 and following bootstrap circuit components, an switching frequency of 10kHz have been. (IRG4BC10UD Power IGBT[11], bootstrap diode DO-204AL (DO-41), Driver IC 2112).

Table 2 shows all the equations parameters used to calculate the bootstrap capacitor value. The values are from the datasheets.

TABLE 2. Bootstrap Component Parameters

Parameter was selected parameter of the data sheets			
Element	Value	Device	Notes
I_{QBS}	60 μA	IR2112	Driver IC
I_{LK}	50 μA	IR2112	
Q_{LS}	5nC 20nC		500-600V /1200V
Q_G	15 nC	IRG4BC10UD	IGBT Transistor
I_{GES}	100 nA	IRG4BC10UD	
$V_{CE(on)}$	2.6v	IRG4BC10UD	
V_{GE}	15v	IRG4BC10UD	
V_f	1.7 V	DO-204AL (DO-41)	Bootstrap Diode
$I_{KL,DIODE}$	10 μA	DO-204AL (DO-41)	
I_{LK_CAP}	0		Typical

The (C_{boot}) used in the present paper has been calculated as follows:

$$\Delta V_{BS} = 20 - 1.7 - 15 - 2.6 = 0.7V \quad \text{based on eq. (4)}$$

$$Q_{BS(total)} = \frac{(15 * 10^{-9}) + (5 * 10^{-9}) + 0 + (100 * 10^{-9}) + (60 * 10^{-9}) + (50 * 10^{-6}) + (10 * 10^{-6}) + 0}{(10 * 10^3)}$$

$$= 32.01nC$$

based on eq. (1)

Hence, a (C_{boot}) of 100nF can be used for the bootstrap driver circuit.

Fig. 3. Illustrates the minimum value of bootstrap capacitor depending on the switching frequency. Once the switching frequency varies from 5KHz to 50KHz, 100 times more, the used electrolytic capacitor ageing is (2 – 200)times more.

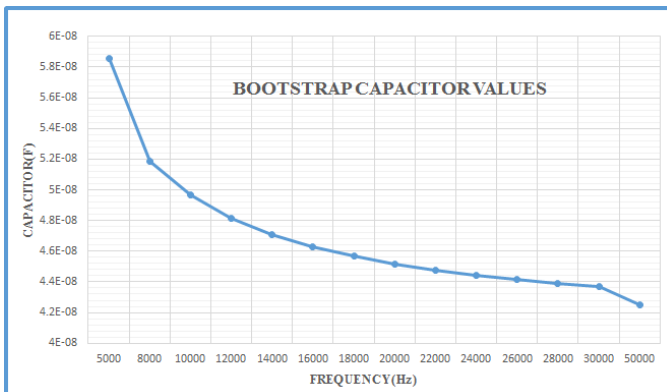


Fig. 3. Minimum Bootstrap capacitor

B. Experimental Results

The Final circuit diagram of the bootstrap circuit and Half-Bridge topology are shown in the Fig. 4.

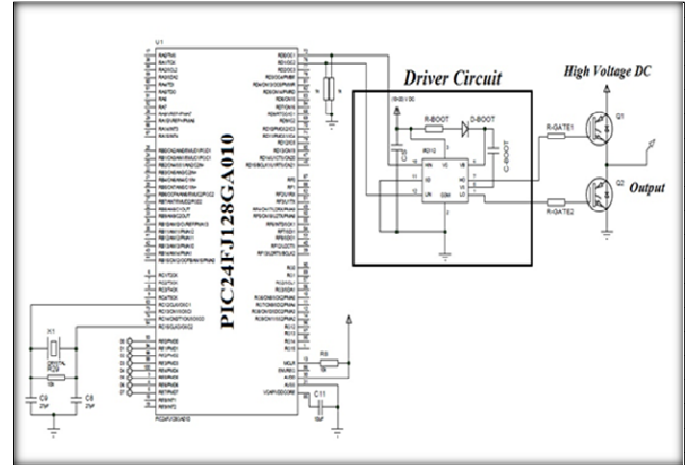


Fig. 4. Complete Half-Bridge Circuit

The practical circuit in the Fig. 5 explains the final bootstrap circuit, Half-Bridge IGBT and 5 volt voltage regulator are used to supply the driver IC (IR2112). However, if ON time of (10 ms) are considered, much higher values for charging are required.

Large electrolytic capacitor is connected in parallel with the bootstrap capacitor to improve the charge of the upper gate only and cope with long ON time of the upper transistor. The value of electrolytic capacitor can be calculate by multiply the bootstrap capacitor by factor 20 depended to the transistor and high DC link Voltage

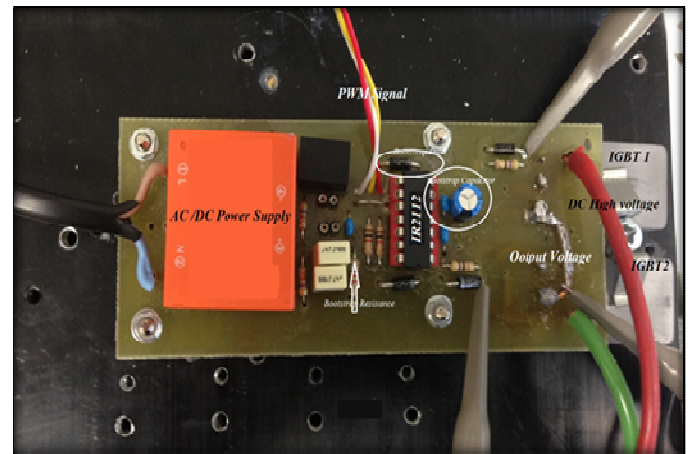


Fig. 5. Final Driver Circuit

Figures 6 through 8 show the experimental results for the bootstrap circuit of IGBT Half-Bridge without load.

Fig. 6 shows the PWM waveforms of the PIC24FG128GA010 and gate driver circuits without connect IGBT transistor, Ch1 and Ch2 output PWM of the microcontroller Ch3 and Ch4 the output PWM of the bootstrap driver circuit .



Fig. 6. Bootstrap capacitor depending on the

Fig. 7 shows the PWM waveforms of the PIC24FG128GA010 and gate driver circuits with IGBT transistor (half-bridge circuit), Ch1 and Ch2 output PWM of the microcontroller Ch3 and Ch4 the output PWM of the driver circuit. The main deferent between Fig 6 and Fig 7 is voltage of Ch4 (lower transistor) is lease than the voltage of Ch3 due to drop voltage across the freewheel diode .

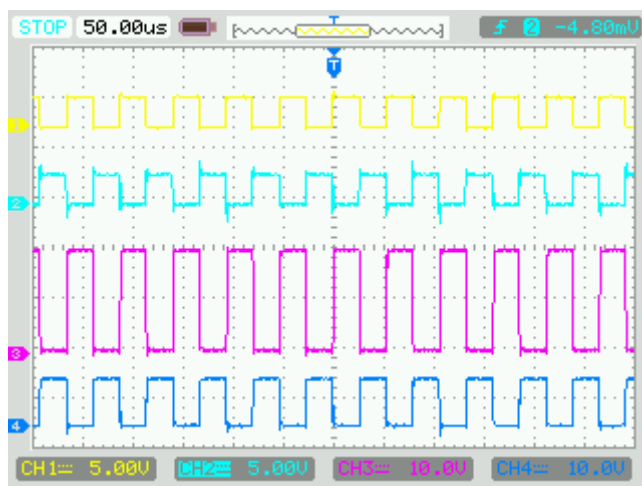


Fig. 7. PWM waveforms with connect IGBT

The voltage of the output of the driver circuit and half-bridge circuit is shown in the Fig. 8 , Ch1 and Ch2 is the PWM of the driver circuit and Ch3 is the output voltage of half-bridge circuit

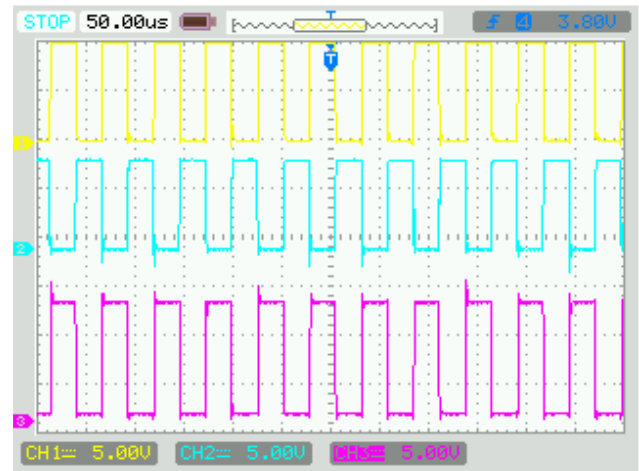


Fig. 8. Output waveform of Half-Bridge and driver circuit

The experiment shows that they are some advantages and disadvantages of the bootstrap circuits.

A. Advantages /Steght

- Low power consumption,
- No inductive components ,
- Low number of internal supplies.

B. Disadvantages /Weakess

- No galvanic separation,
- High reach current occurs in internal supplies,
- A long pulse is needed to charge the upper bootstrap capacitor.

V. conclusion

This paper present to design a bootstrap circuit based on power IGBT and IR2112 driver IC. The bootstrap resistance is first parameter of bootstrap circuit, series with bootstrap diode to limit charger current flowing to bootstrap capacitor. Then the paper showed how to calculate the bootstrap capacitor for different switching frequency. It presented the technique of connecting electrolytic capacitor in parallel with film capacitor in order to improve the of the upper gate. Moreover, the paper discussed the advantage and disadvantages of the bootstrap circuit. PIC24FJ128GA010 was used to generate control signals that are used as inputs to the IGBT driver circuit

REFERENCES

- [1] A. Seidel, M. Costa, J. Joos, and B. Wicht, "Bootstrap circuit with high-voltage charge storing for area efficient gate drivers in power management systems," *Eur. Solid-State Circuits Conf.*, pp. 159–162, 2014.
- [2] Fairchild Semiconductors, "Design and Application Guide of Bootstrap Circuit for High-Voltage Gate-Driver IC," 2008.
- [3] T. Y. Elganimi, "Design and Analysis of a Bootstrap Ramp Generator Circuit Based on a Bipolar Junction Transistor (BJT) Differential Pair Amplifier," vol. I, no. September, pp. 22–24, 2014.
- [4] S. Chung and J. Lim, "Design of Bootstrap Power Supply for Half-Bridge Circuits using Snubber Energy Regeneration," *JPE*, vol. 7, no. 4, pp. 294–300, 2007.
- [5] H. V Floating and M. D. Ics, "Application Note AN-978 Table of Contents," *Int. Rectifier*, vol. 2092, pp. 1–30, 1998.
- [6] G. Purpose and F. Microcontrollers, "Pic24Fj128Ga010 Family," *Microchip*, 2012.
- [7] I. I. Rectifier, "Datasheet IR2112," vol. 2112, pp. 1–18.
- [8] J. Zhu, W. Sun, S. Member, Y. Zhang, S. Lu, L. Shi, S. Zhang, and W. Su, "An Integrated Bootstrap Diode Emulator for 600-V High Voltage Gate Drive IC With P-Sub / P-Epi Technology," *518 IEEE Trans. POWER Electron.*, vol. 31, no. 1, pp. 518–523, 2016.
- [9] A. . Fallis, *ADVANCED PIC MICROCONTROLLER PROJECTS IN C*, vol. 53, no. 9. 2013.
- [10] Microchip Technology Inc., *MPLAB ® X IDE User ' s Guide*. 2012.
- [11] I. Gate, B. Transistor, U. Soft, and R. Diode, "IRG4BC10UD IRG4BC10UD," *Int. Rectifier*, pp. 1–11.

An Observer-based MPC Approach by Sensing Primary Signals in Transformer-isolated Converters

Ya Zhang, Marcel A. M. Hendrix and Jorge L. Duarte
Eindhoven University of Technology
Department of Electrical Engineering
P.O. Box 513, 5600MB Eindhoven, The Netherlands
ya.zhang@tue.nl

Abstract—A digital control method combining primary-side sensing, observer and model-predictive-control techniques is proposed. A conventional isolated Flyback converter is chosen for demonstrating the method. The only measured signal is the drain-source voltage over the switch. Following a procedure of signal processing, state estimation and constraint problem formulation, the controller determines the optimal duty cycle ratio. The advantages of the proposed method include minimal overshoot and fast stabilization, converter state restriction, and measurement network simplification.

Keywords— *Flyback, observer, primary side sensing, model predictive control, model mismatch*

I. INTRODUCTION

Because model-predictive-control (MPC) deals with constraints and optimizes stabilization trajectories, it is gaining increasing attention in power electronics as an alternative to traditional analog control [1]. An observer is adopted for state estimation when a plant faces difficulties or complexities in state measurements. It measures a part of the plant state variables and accordingly estimates the plant state [2]. The primary-side-sensing (PSS) technique requires no opto-coupler-based circuits and is commonly used in isolated power electronics [3], [4].

The work in this paper continues the research in [5], [6] and experimentally demonstrates the control method measuring the primary voltage in a Flyback converter. It measures the switch drain-source voltage, and by means of signal processing the output capacitor voltage is calculated. From that, an observer module estimates the state of the magnetizing inductor. Knowing the state of the converter, the model-predictive-control scheme can be applied.

The paper demonstrates the importance of taking into account measurement errors and model-mismatch while designing an observer. The state estimation is given based on a derived plant model. Mismatch between the model and how the actual plant behaves, influences the estimation accuracy. In addition to this, measurement error is inevitable in experiments and it adds up to the estimation error.

II. FLYBACK CONVERTER AND THE CONTROL DIAGRAM

A. Flyback Converter Model Derivation

It is assumed that the Flyback converter is ideal (no parasitic components) and lossless, as it is shown in Fig.1. The converter is therefore represented by three differential equations

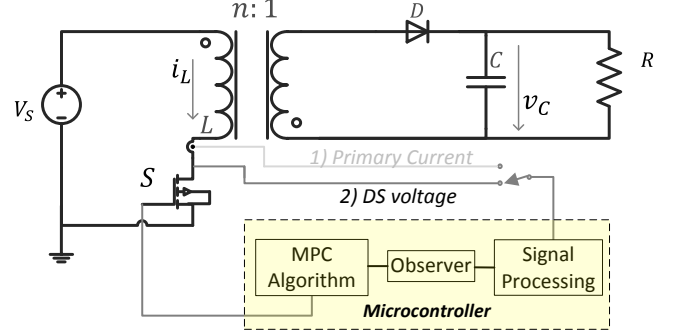


Fig. 1: System diagram

given in Table II, where i_L , v_C and D_t are the inductor current, capacitor voltage and duty cycle ratio value, respectively.

TABLE I: Flyback converter parameters

Definition	Symbol	Value	Unit
Magnetizing inductance	L	1.4	mH
Output capacitance	C	10	μF
Source voltage	V_s	100	V
Transformer transfer ratio	n	3	
Switching frequency	T_{sw}	10	μs
Load resistance	R	100	Ω

The converter parameters are summarized in Table I. It is presumed that the Flyback converter operates around a duty cycle ratio of $u_e = 0.6$ and it will result in a corresponding converter state given by $x_e = [0.2083A \ 25.00V]^T$, in continuous conduction mode (CCM). The first and second elements denote the averaged inductor current and the averaged capacitor voltage, respectively. They form the converter equilibrium point quantities:

$$u_e = 0.6, \\ x_e = [0.2083A \ 25.00V]^T. \quad (1)$$

Following a process of state space averaging, model linearisation and discretization illustrated in [6], we can get a

TABLE II: State space representation of the Flyback converter, switched model.

SS description	$\dot{x}_t = Ax_t + b_t$ $x_t = \begin{bmatrix} i_L \\ v_C \end{bmatrix}$,	Dwell time
Switch ON, diode OFF	$A = A_1, b_t = b_{t,1}$ $A_1 = \begin{bmatrix} 0 & 0 \\ 0 & \frac{-1}{RC} \end{bmatrix}$ $b_{t,1} = \begin{bmatrix} \frac{V_s}{L} \\ 0 \end{bmatrix}$	$D_t T_{sw}$
Switch OFF, diode ON	$A = A_2, b_t = b_{t,2}$ $A_2 = \begin{bmatrix} 0 & \frac{-n}{L} \\ \frac{n}{C} & \frac{-1}{RC} \end{bmatrix}$ $b_{t,2} = \begin{bmatrix} 0 \\ 0 \end{bmatrix}$	$D_{t,1} T_{sw}$
Switch OFF, diode OFF	$A = A_3, b_t = b_{t,3}$ $A_3 = \begin{bmatrix} 0 & 0 \\ 0 & \frac{-1}{RC} \end{bmatrix}$ $b_{t,3} = \begin{bmatrix} 0 \\ 0 \end{bmatrix}$	$D_{t,2} T_{sw}$

simplified model of the converter, given by

$$\begin{aligned} x_{k+1} &= A_d x_k + B_d u_k, \\ y_k &= C_m x_k, \end{aligned} \quad (2)$$

where C_m is the measurement matrix, y_k the measured value, and A_d, B_d are constant matrices represented by the Flyback converter parameters and the equilibrium point quantities, and x_k and u_k are discrete small signals given by

$$\begin{aligned} u_k &= D_t - u_e \\ x_k &= x_t - x_e. \end{aligned} \quad (3)$$

Because the capacitor voltage is the only measured variable fed into the micro-controller, as highlighted in Fig.1, the inductor current (associated with the first element of x_k) has no contribution to the measured value y_k . The measurement matrix is therefore given by

$$C_m = \begin{bmatrix} 0 & 1 \end{bmatrix}. \quad (4)$$

B. Observer-Based Model Predictive Controller

1) *Capacitor Voltage Calculation from DS Voltage* : When the switch is OFF and the diode is ON, the switch drain-source voltage is

$$v_{DS} = V_s + n v_C, \quad (5)$$

where V_s is the source voltage and n the transformer primary-to-secondary transfer ratio. Accordingly the capacitor voltage is calculated.

2) *Converter State Estimation by Observer*: Now that the capacitor voltage is known, we are able to estimate the converter state accordingly. The observer elaborated on in [2] is adopted, described by

$$\hat{x}_{k+1} = A_d \hat{x}_k + B_d u_k + L_m (y_k - C_m \hat{x}_k), \quad (6)$$

where \hat{x}_k is the estimation of x_k , and L_m is the observer feedback gain. Comparing (2) and (6) yields

$$x_{k+1} - \hat{x}_{k+1} = (A_d - L_m C_m)(x_k - \hat{x}_k). \quad (7)$$

Therefore, the observation design turns out to be a classic pole-placement problem, and that is, to place the eigenvalues of $(A_d - L_m C_m)$ within the unit cycle in the complex plane. The tunable parameter is L_m and A_d and C_m are constant matrices.

3) *MPC for Trajectory Restriction*: The algorithm is designed to fast stabilize the converter while considering the converter constraints and input efforts. Its mathematical description is to minimize the cost function defined by

$$\begin{aligned} F(x_0, U) &= x_N^T P x_N + \sum_{i=0}^{N-1} (x_i^T Q x_i + u_i^T R u_i), \\ \text{with } U &= [u_0 \ u_1 \ \cdots \ u_{N-1}]^T, \\ x_i &= A_d x_{i-1} + B_d u_{i-1}, \ i = 1, 2, \dots, N, \end{aligned} \quad (8)$$

where u_{i-1}, x_i are subjected to

$$\begin{aligned} u_{low,i} &\leq u_{i-1} + u_e \leq u_{high,i}, \\ \text{and } x_{low,i} &\leq x_i + x_e \leq x_{high,i}, \end{aligned} \quad (9)$$

and N is the prediction horizon; $u_{low,i,i=1 \dots N}$ and $u_{high,i,i=1 \dots N}$ are constraints about the input (associated with the duty cycle ratio); $x_{low,i,i=1 \dots N}$ and $x_{high,i,i=1 \dots N}$ are constraints about the state (associated with the inductor current and the capacitor voltage); P, Q, R are the weights on terminal state, the rest state, and the input, respectively [7].

III. IMPACTS OF MEASUREMENT ERROR AND MODEL MISMATCH ON OBSERVATION

The work in [5] demonstrates that the observer convergence time selection influences its performance. This section elaborates on additional criteria to assess an observer's performance: its abilities to deal with inevitable model mismatch and measurement errors.

A. Measurement Error

The analysis of measurement error is performed in absence of model mismatch. The normalized measurement offset error is defined as

$$\delta_y = \frac{\Delta y_\infty}{x_e(2)}, \quad (10)$$

where Δy_∞ is the static measurement error of the capacitor voltage, and $x_e(2)$ denotes the second element of x_e (the capacitor voltage at the equilibrium point). According to the analysis in section II-A, $x_e(2)$ can be also written as

$x_e(2) = C_m x_e$. The normalized observation offset error is defined as

$$\delta_{\hat{x}} = \begin{bmatrix} \frac{1}{x_e(1)} & 0 \\ 0 & \frac{1}{x_e(2)} \end{bmatrix} \Delta \hat{x}_\infty, \quad \text{with} \quad \Delta \hat{x}_\infty = [\Delta \hat{x}_\infty(1) \quad \Delta \hat{x}_\infty(2)]^T \quad (11)$$

where $\Delta \hat{x}_\infty$ is the state estimation error when the observer is in steady state. The observation error gain from the measurement error is defined as

$$G_{mag} = \frac{\delta_{\hat{x}}}{\delta_y}. \quad (12)$$

Next, we show a procedure to derive the algebraic expression of the observation error gain. When the observer is in steady state, equations

$$\begin{aligned} \hat{x}_{k+1} &= \hat{x}_\infty \\ \hat{x}_k &= \hat{x}_\infty \\ y_k &= y_\infty, k \rightarrow \infty \end{aligned} \quad (13)$$

hold for (6). When there is no measurement error, y_k and \hat{x}_k are zero. Therefore, the offset errors are $\Delta y_\infty = y_\infty - 0$ and $\Delta \hat{x}_\infty = \hat{x}_\infty - 0$. Substituting $\hat{x}_{k+1} = \hat{x}_k = \hat{x}_\infty = \Delta \hat{x}_\infty$ and $y_k = y_\infty = \Delta y_\infty$ into (6), and by comparing (11) and (10), we get the explicit algebraic expression of the error gain

$$G_{mag} = \begin{bmatrix} \frac{1}{x_e(1)} & 0 \\ 0 & \frac{1}{x_e(2)} \end{bmatrix} (I - A_d + L_m C_m)^{-1} L_m C_m x_e. \quad (14)$$

This gain is independent of the measurement offset error Δy_∞ and dependent on the chosen equilibrium point.

B. Observer Design by Pole Placement

The function of an observer is to estimate a system state in a certain time interval. The observer design by pole placement is simple and effective for linear models, as it is illustrated in [2]. Bessel Polynomials further simplify the observer design by indicating the pole locations. However, practical systems have imperfect models and are therefore sensitive to model derivation errors and measurement inaccuracies. Consequently, the effectiveness of observer design by pole placement can be compromised.

1) *Closed Loop Observer Design by Pole Placement*: the observer settling time $650\mu s$ is borrowed from [6] which demonstrated an effective current observer with the same observer settling time. Bessel polynomials are adopted for pole placement. The resulting observer gain matrix and its corresponding error gain factor are

$$\begin{aligned} L_{m,1} &= [-0.1056 \quad 1.1494]^T, \\ G_{mag,1} &= [-39.5568 \quad 0.1876]^T \end{aligned} \quad (15)$$

respectively. The error gain indicates that -1% offset error in measuring the voltage will lead to an estimation offset error of 39.5% in current, -0.187% in voltage, as highlighted by the blue small solid sphere in Fig.2.

Since the estimation error is linearly proportional to the measurement error, the observer becomes more inaccurate when the measurement error increases (see Fig.2 for the example of -5% measurement error). Please note that the observation error gain discussed here is oriented to the chosen equilibrium point given in (1).

2) *Open Loop observer*: An open loop observer (not feasible in practice) is obtained by setting the observer gain $L_{m,0} = [0 \quad 0]^T$. It means the observer disregards the information from the measurement, and there is no communication between the converter and the controller. Consequently, the measurement error has no influence on the estimation and from (12) we have $G_{mag,0} = 0$.

C. Observer Design Adaptation

An observer designed by pole placement is confined to coordinate the convergence speed. The tolerance to measurement and model derivation errors is not regarded or promised by this method. The observer obtained by the method of pole placement in section III-B1 is very sensitive to the measurement error. A open loop observer discards converter measurement information and makes itself very dependent on the correctness of the derived converter model. Hence, the observer is heuristically adjusted towards a small error gain G_{mag} (not a zero gain). The extreme design is to set the observer gain matrix $L = [0 \quad 0]^T$ (resulting in a zero error gain). It is not feasible in practice, but it indicates that an observer gain matrix whose elements are close to zero could be a solution. Please note that a small observer gain matrix (not zero) will prolong the observer convergence time from (7). This means that the MPC algorithm cannot give reasonable response in time and overshoots are possible.

An observer with a relatively small error gain is found after a series of manual attempts. The resulting observer gain matrix and its corresponding error gain factor are

$$\begin{aligned} L_{m,2} &= [-0.0106 \quad -0.0460]^T, \\ G_{mag,2} &= [1.0698 \quad -0.0612]^T, \end{aligned} \quad (16)$$

respectively. The observer with the adapted observer gain matrix is chosen because it yields a relatively small error gain. As a consequence, the observer becomes more tolerant to the measurement error compared to the one obtained by pole placement. Despite the fact that this observer results in 122ms observation settling time, it is adopted for the experiments and we have $L_m = L_{m,2}$.

D. Model Mismatch

1) *Switched Model and Simplified Model*: The premise for an observer design is an accurate model of the converter. Regardless of power loss and parasitic components, the most accurate model for the Flyback converter is the switched model

described in Table II. However, adopting this switched model makes an observer design very complex. A common solution is model simplification by means of averaging and linearisation.

As a consequence, the simplified linear model is not equal to the original switched model. According to the parameters in Table I, the pairs of the converter steady state (inductor current and capacitor voltage) and a given duty cycle ratio with these two different models are plotted in Fig.2: *Switched model* refers to the one described in Table II; *Simplified model* denotes the one in (2) given by $(x_\infty + x_e)$. Please note that the *Switched model* takes into account both continuous and discontinuous conduction modes, while the *simplified model* is the small signal model linearised at $D_t = 0.6$.

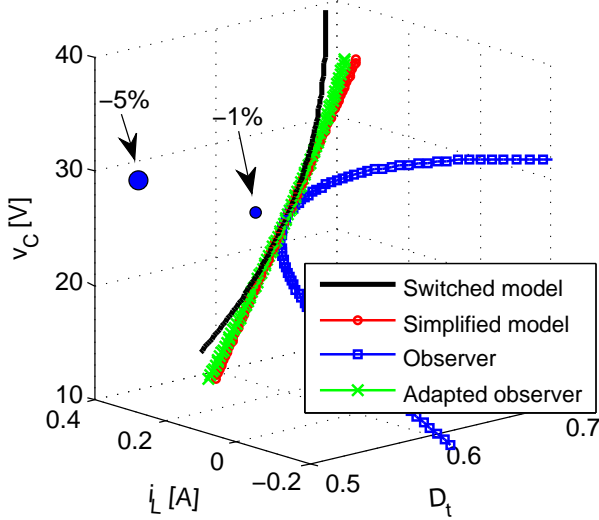


Fig. 2: Visualization of model mismatch and observation error

2) *Model-Based Observation*: The pairs of the converter steady state (inductor current and capacitor voltage) and a given duty cycle ratio with different observers are plotted in Fig.2: *Observer* indicates the estimated converter state $(\hat{x}_\infty + x_e)$ with $L_m = L_{m,1}$ and *Adapted observer* refers to the state with $L_m = L_{m,2}$. Both observers give estimation based on equation (6).

IV. EXPERIMENTAL RESULTS

A. Set-up Description and Implementation

Fig.3 shows the Flyback converter system. The type of the DSPACE is *DS1104 R&D Controller Board* associated with software *Control Desk 5.1*. The oscilloscope is *HDO 4024, 200MHz high definition oscilloscope 2.5Gs/s*. The parameters for the MPC algorithm are summarized in Table III.

B. Results and Discussion

Fig.4 and Fig.5 display the experimental results captured by the digital controller and by the oscilloscope, respectively. The converter initial state is set by feeding a constant duty cycle ratio value to the plant (in open loop). The reference is set in advance by the digital controller. At a certain moment,

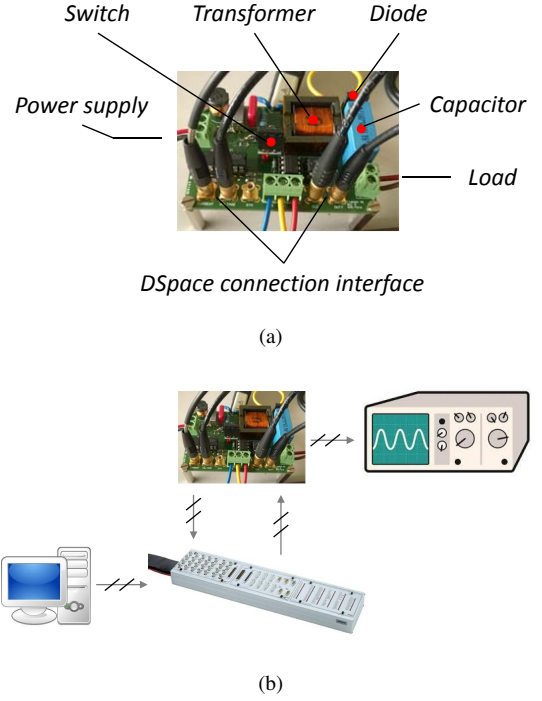


Fig. 3: Experimental set-up description: (a) Flyback converter board; (b) system connection diagram.

TABLE III: Controller parameters

parameter	value
weight on i_L	$\frac{1}{x_e(1)}$
weight on v_C	$\frac{100}{x_e(2)}$
weight on u	$\frac{1}{u_e}$
$u_{low,i=0 \dots N-1}$	0.1
$u_{high,i=0 \dots N-1}$	0.7
$x_{low,i=0 \dots N-1}$	$\begin{bmatrix} 0 & 0 \end{bmatrix}^T$
$x_{high,i=0 \dots N-1}$	$\begin{bmatrix} 0.6A & 34V \end{bmatrix}^T$
sampling time T_s	330 μ s
prediction horizon	5
control horizon	1

a *button* is pressed to close the control loop and the controller becomes active.

As it is shown in Fig.4, the red arrow points out the instant when the controller is activated. The reference is plotted in bold solid black line; the blue solid line with discrete dots refers to the observed trajectory of the converter.

The top curve of Fig.5 shows the trace of the Flyback converter primary current which is detected by a current probe in series with transformer primary side. The middle one is the averaged primary current which is obtained by using a shunt resistor with an analog low-pass filter. The bottom one is the capacitor voltage measured by a voltage probe placed in parallel with the load.

It can be seen in both figures that the converter state approaches the pre-set reference and the convergence trajectory stays in its pre-set margins. No objectionable overshoot is

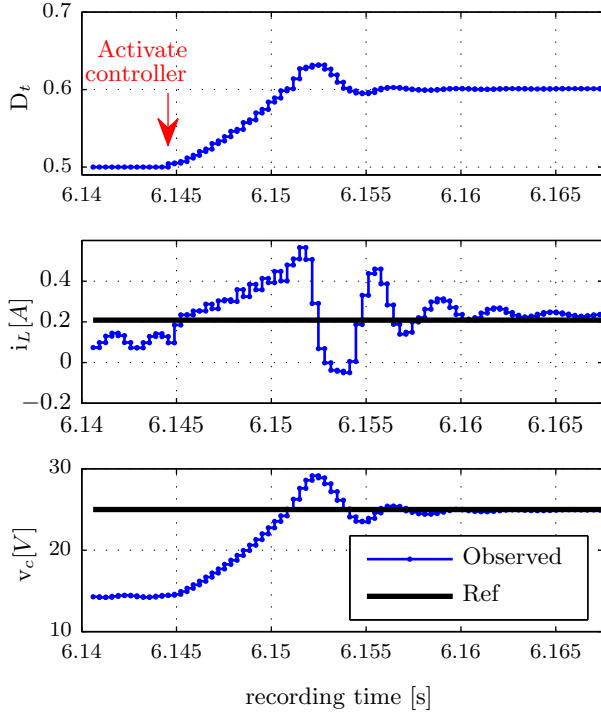


Fig. 4: Experimental results when using the adapted observer, captured by the digital controller. From the top to the bottom are duty cycle ratio, averaged inductor current and capacitor voltage.

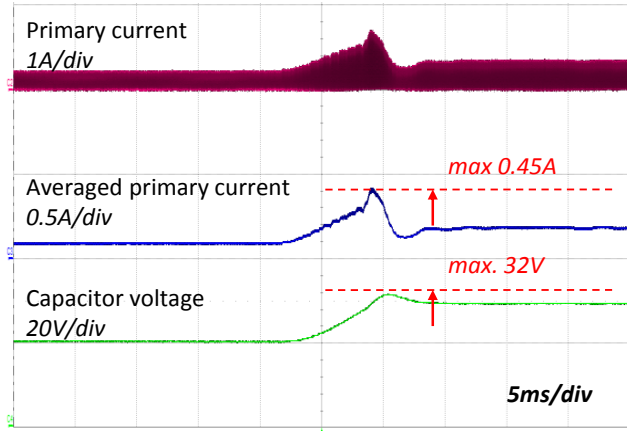


Fig. 5: Experimental results when using the adapted observer, captured by the oscilloscope. From the top to the bottom are primary current through the switch, averaged primary current and capacitor voltage.

simple pole-placement method is not sufficient to design a decent observer because it only takes into account observation speed and disregards the existence of modelling error and measurement error. It is essential to check the observer error gain before experiments. This paper demonstrates an effective voltage observer measuring the switch drain-source voltage in the Flyback converter.

It is recommended to use an observer which can compensate the mismatch between original and simplified models, at least not to enlarge the difference. Due to the existence of measurement errors, it is necessary to check the observer's tolerance to the measurement errors before applying it in practice.

REFERENCES

- [1] V. Spinu, A. Oliveri, M. Lazar, and M. Stora, "Fpga implementation of optimal and approximate model predictive control for a buck-boost dc-dc converter," in *Control Applications (CCA), 2012 IEEE International Conference on*, Oct 2012, pp. 1417–1423.
- [2] R. J. Vaccaro, *Digital control: a state-space approach*. McGraw-Hill New York, 1995, vol. 196.
- [3] C.-W. Chang, Y.-T. Lin, and Y.-Y. Tzou, "Digital primary-side sensing control for flyback converters," in *Power Electronics and Drive Systems, 2009. PEDS 2009. International Conference on*, Nov 2009, pp. 689–694.
- [4] X. Xie, J. Wang, C. Zhao, Q. Lu, and S. Liu, "A novel output current estimation and regulation circuit for primary side controlled high power factor single-stage flyback led driver," *Power Electronics, IEEE Transactions on*, vol. 27, no. 11, pp. 4602–4612, Nov 2012.
- [5] Y. Zhang, M. A. M. Hendrix, and J. L. Duarte, "Ccm flyback converter using an observer-based digital controller," in *2015 IEEE International Conference on Industrial Technology*, March 2015, pp. 2056–2061.
- [6] Y. Zhang, M. A. M. Hendrix, J. L. Duarte, and E. A. Lomonova, "Flyback converter using an observer-based digital controller," in *17th European Conference on Power Electronics and Applications*, August 2015.
- [7] V. Spinu, J. Schellekens, M. Lazar, and M. Hendrix, "On real-time optimal control of high-precision switching amplifiers," in *System Theory, Control and Computing (ICSTCC), 2013 17th International Conference*, Oct 2013, pp. 507–515.

visible. Because the measurement takes place on the converter primary side, no sophisticated feedback network is needed.

V. CONCLUSION AND RECOMMENDATIONS

The aim is to design an observer which is both fast and tolerant to measurement error and model mismatch. A

Basic Crossover Correction Cells

R. Baris Dai

Electrical Engineering Department
Eindhoven University of Technology
Eindhoven, The Netherlands
Email: b.r.dai@tue.nl

Jorge L. Duarte

Electrical Engineering Department
Eindhoven University of Technology
Eindhoven, The Netherlands
Email: j.l.duarte@tue.nl

Noud Slaats

Prodrive Technologies B.V.
Eindhoven, The Netherlands
Email: noud.slaats@prodrive-technologies.com

Abstract—In electric power processing converters for high-precision voltage supply, usually correction amplifiers are connected in series with a main low-accuracy power amplifier. As such, conventional switched-mode correction amplifiers have also to process the total current as delivered by the main amplifier. Therefore, switching semiconductors with high current rating have to be selected for implementing correction amplifiers. This paper proposes a solution this problem by separating the major part of the current delivered by the main amplifier from the current part that flows through the switches in the correction amplifiers. As a result, the switching semiconductors used in the correction amplifiers have a much reduced current rating, and the overall system efficiency can be increased.

I. INTRODUCTION

Cascading power amplifiers is a well-known method in high precision applications. In this method, the power amplification system consists of a main power amplifier supplying the bulk power, while other converters are connected in series or in parallel, and operating as correction amplifiers, aiming at achieving a high-quality output waveform. The correction amplifiers only process a small portion of the bulk load [1]. The cascading connection of two or more converters is also known as composite amplifiers, and the dependence on the passive filters is much less compared to single-stage power amplifiers. The fundamental idea for improving voltage output through composite amplifier realizations based on Voltage-Source Converters (VSC) or Current-Source Converters (CSC) is shown in Fig. 1. Systems that employ a shunt or series active power filters are notable examples of composite amplifiers.

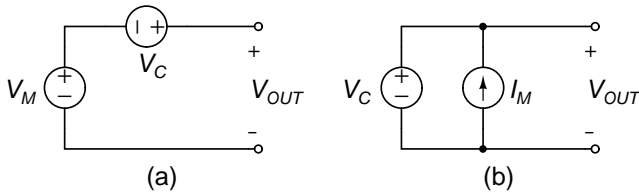


Fig. 1: (a) Series connection of a main VSC (V_M) with a correction VSC (V_C), and (b) a parallel connection of a main CSC (I_M) with a correction VSC (V_C) for voltage output composite amplifiers.

Even though the low efficiency of linear power amplifiers is a drawback, they are still used as amplifiers where high-fidelity is a priority, since a conventional switching power

amplifier cannot ensure this property. The composite power amplifier idea arose with the demand on a high efficiency and high-bandwidth AC power source by combining linear power amplifiers and switching power amplifiers. In this case switching converters are used as main amplifiers and amplifiers are used to perform the correction [2]. However, composite amplifiers may also employ another switching amplifier as the correction amplifier, aiming at even higher efficiency [3]. In view of Fig. 1, correction amplifiers have to process the full rated current if they are connected in series with the main amplifier (Fig. 1(a)), or they have to process full rated voltage if they are connected in parallel (Fig. 1(b)). As a result, conventional composite amplifiers are good for high precision and reduce the necessity to passive components, nonetheless they have to process the rated current or rated voltage.

II. BASIC CROSSOVER CELL OPERATION

Basic Crossover Correction Cell is a new electronic circuit for providing a high-precision voltage supply for electric loads, which operates with a main amplifier together with an arbitrary number of cascaded-connected correction amplifiers. In this new concept the correction amplifiers, referred to as Basic Crossover Correction Cells (B3Cs) in the following, are realized in such a way that the majority of the current delivered by the main amplifier does not circulate through the switches of the correction cells. As a consequence, B3Cs can be implemented with simpler (therefore cheaper) low-current rated semiconductor switches.

A Basic Crossover Correction Cell combines a shunt inductor in parallel with a VSC, as described in the following. For the sake of illustration, a cascaded connection of a main amplifier with two B3Cs is given in Fig. 2.

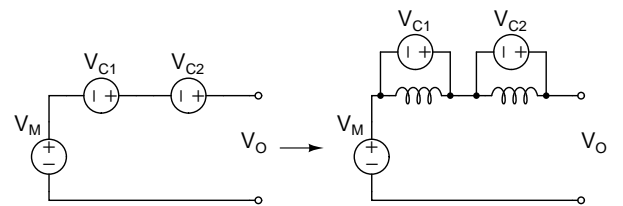


Fig. 2: Transformation of a composite amplifier from using conventional series correction amplifiers to using Basic Crossover Correction Cells (B3C).

A. System Structure

As part of a B3C, the VSC may be implemented with any kind of power electronic converter, under the condition that the average voltage provided by the VSC is zero (since there will be an inductor connected in parallel with the VSC terminals). The VSC internal impedance should be high for low-frequency harmonic current components (for instance, by deliberately placing a capacitor in series with the current path through the VSC).

Since the B3Cs are connected in series with the main amplifier, the shunt inductors (L_1 and L_2 in Fig. 2) create a low-impedance path between the main amplifier and the load output terminals for the low-frequency harmonic components of the current delivered by the main amplifier to the load. Therefore, by placing a VSC with high low-frequency input impedance in parallel with the shunt inductor, the major part of the load current will be naturally diverted to the shunt inductor, alleviating by this way the requirements for the semiconductor devices in the correction VSCs.

The resulting output voltage supplied to the load will be the summation of the momentary voltages of the main amplifier and correction VSCs ($V_M + V_{C1} + V_{C2}$ in Fig. 2). The voltage waveform patterns of the correction amplifiers are constructed such that together all the VSCs in series correct the distorted ripple voltage generated by the main amplifier. Voltage drops in the shunt inductors due to intrinsic resistance do not interfere on the resulting output voltage. As a consequence, the shunt inductors do not degrade the quality of the generated output voltage.

As an aside, the B3C inductors connected in series will also help to increase the filtering effect of eventual inductors already present in the load. That is to say, the current filtering requirements at the output will be less, and the total losses in the system will be reduced.

The crux of B3C is the parallel current path introduced by the shunt-inductors. There are already many solutions in the published literature on how to implement the required correction voltage patterns for the connection in series of the VSCs as correction amplifiers, such that the resulting output voltage presents high quality [4].

Altogether, B3Cs propose a novel approach for an arbitrary number of series-connected correction amplifiers leading to high precision, very low power consumption and quite modest requirements for the semiconductor devices.

B. Voltage Pulse Patterns

Considering the composite amplifier in Fig. 1(a), a possible method to improve the quality of the switched output voltage is sketched in Fig. 3, where the generated voltage pulse patterns for the B3C is detailed. It goes without saying that the desired voltage waveforms can be achieved by various alternative ways.

In Fig. 3 the switched voltage levels of the correction amplifier are shaped and synchronized with switched voltage levels of the main amplifier such that it reduces the pulsation gap of the output voltage by half at each correction stage. As a side

benefit, the effective frequency of the output waveform is increased by a factor of two, as also shown in Fig. 3.

Higher precision can be obtained by cascading more correction cells. In order to achieve the same benefits as in Fig. 3 with an arbitrary number of B3Cs in series, each correction amplifier should produce a symmetric voltage waveform with half of the magnitude and in same frequency of the voltage waveform at its input. This is illustrated in Fig. 4, where five correction cells are applied. It is possible to see that the amplitude of voltage ripple is reduced by half while ripple frequency is doubled at the output of each correction stage.

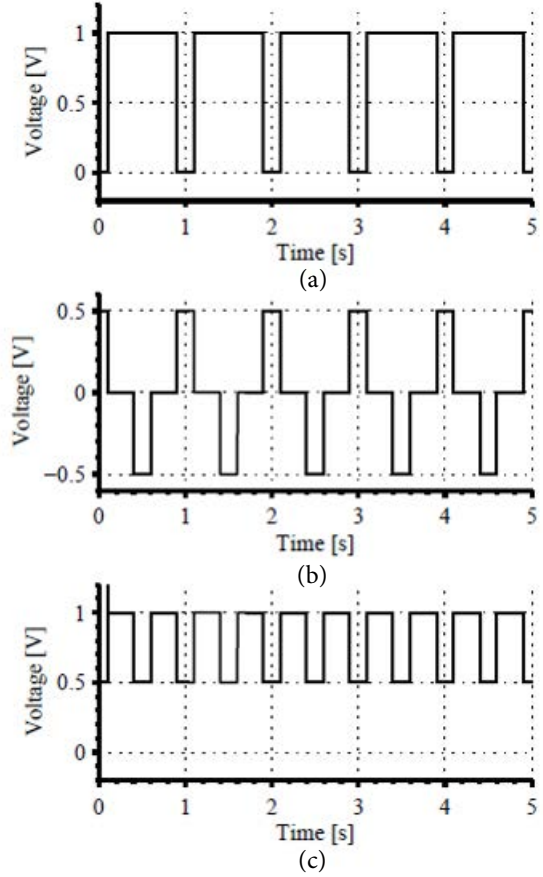


Fig. 3: (a) Output main switching converter, (b) voltage output of the correction amplifier, and (c) output voltage waveform.

III. BASIC CROSSOVER CORRECTION CELL IMPLEMENTATION

B3C is a concept that can be realized by any three-level switching power amplifier. For instance, a phase-shift-controlled Class-D amplifier can be used as B3C if capacitors are added in series in the current path of the amplifier, or any other method which ensures that only AC current will flow through the correction amplifier switches.

Another possible realization is a three-level converter that is shown in Fig. 5(a), which features zero-voltage switching for the switches over the full operation range for further

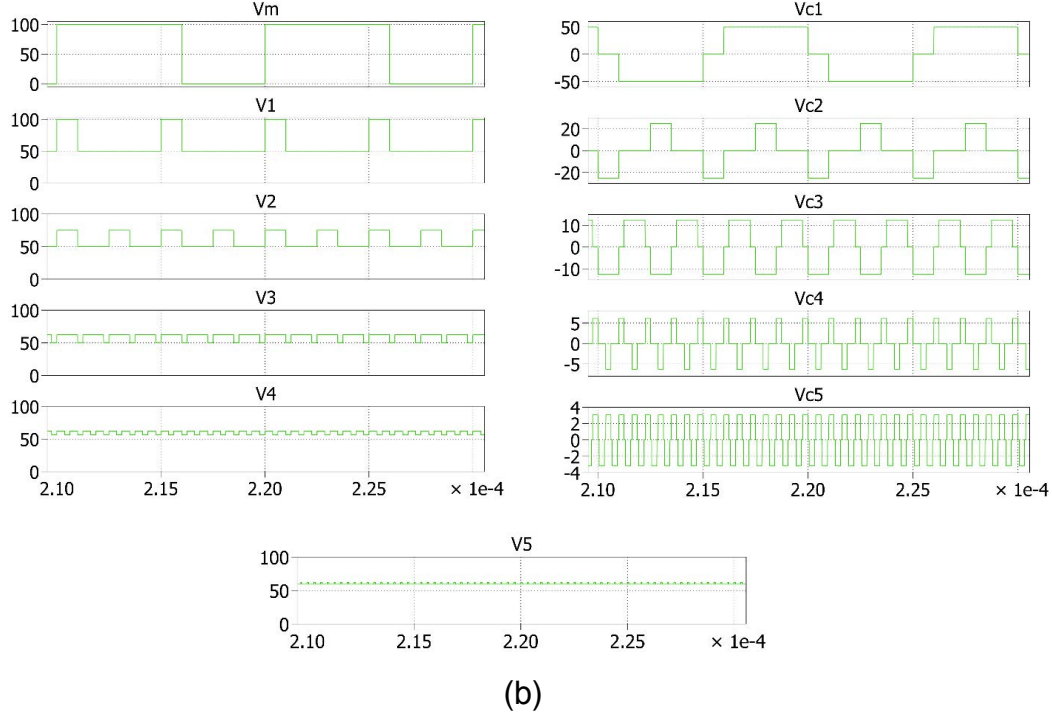
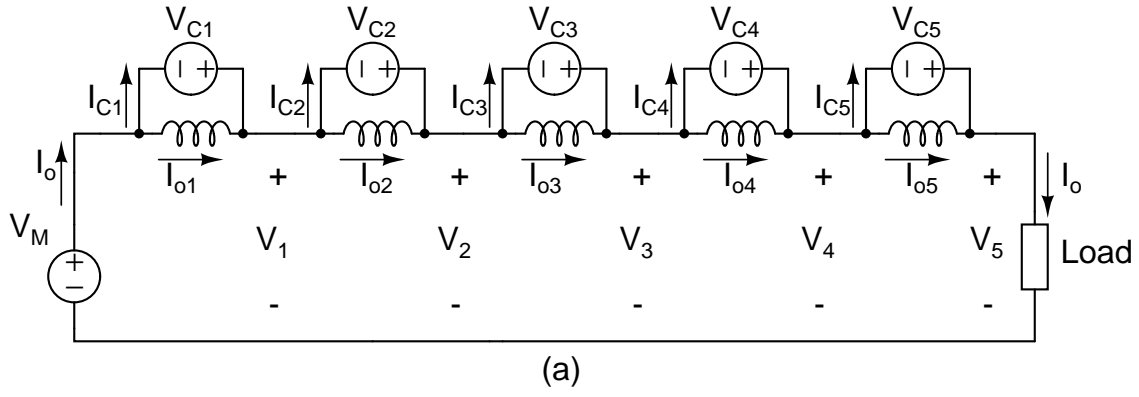


Fig. 4: (a) A composite amplifier with five B3Cs, and (b) voltage waveforms of the main amplifier (V_M) and output voltage levels after each correction stage ($V_1...V_5$) along with differential node voltages ($V_{C1}...V_{C5}$)

improvement in efficiency [5]. The B3C inductors, which create a low-impedance current path for the low-frequency components of the load current through the cell, are split in two parts, in order also to allow internal capacitor charge balance in the correction cell. Therefore, the topology in Fig. 5 requires few magnetic components.

A skilled person in the field can conceive other circuit implementations for the B3Cs. The essential aspect of the invention is the parallel current path introduced by the shunt-inductors in the correction cells.

It should be noticed in Fig. 5 that the internal floating DC voltage in the B3C is obtained from available AC sources through isolation transformers and simple diode rectification. The internal power consumption of the correction cells is much less than the load power since the correction cell only process

the ripple current. Moreover, the bigger the number of a cell in sequence, the less power it consumes since the rated voltage of the correction cells are reduced by half at each stage.

IV. CONCLUSION

In conclusion, B3C is an approach to reduce the output voltage ripple for high precision switching power amplification with very low power consumption, employing voltage source converters with very low current ratings compared to conventional correction amplifiers. It reduces the dependence on passive filtering with its multilevel operation with an uncomplicated cascading method that improves overall system efficiency. Key feature of B3Cs is the current divider, a shunt inductor connected to a VSC, which lets the VSC built with low-current semiconductors as it yields a low-impedance path

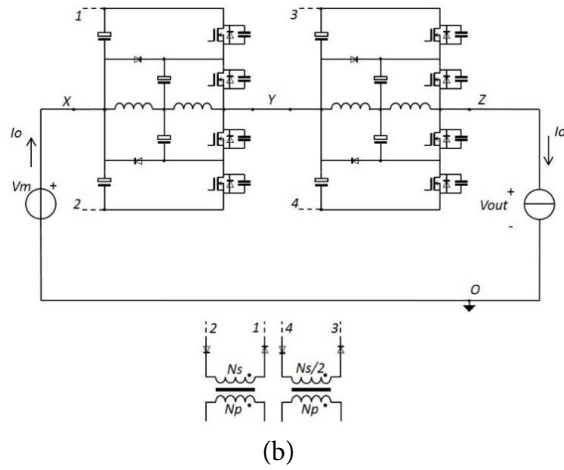
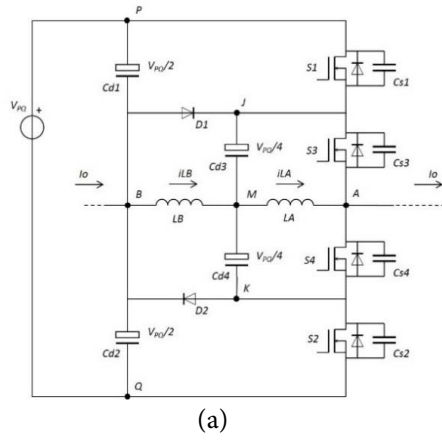


Fig. 5: (a) Phase-Shift-Controlled Three-Level Converter, and (b) B3C application of the converter. Note the low-impedance current path created by the inductors for low-frequency components of the load current I_o .

for the low-frequency component of the load current. A B3C can be built with any VSC topology whose average output voltage is zero.

ACKNOWLEDGMENT

This research is supported by the Dutch Technology Foundation STW, which is the applied science division of Netherlands Organisation for Scientific Research (NWO).

REFERENCES

- [1] G. B. Yundt, "Series- or Parallel-Connected Composite Amplifiers," *IEEE Transactions on Power Electronics*, vol. PE-1, no. 1, pp. 48–54, 1986.
- [2] G. S. Silva, R. C. Beltrame, M. L. S. Martins, L. Schuch, H. L. Hey, and C. Rech, "Hybrid AC Power Source based on Modular Multilevel Converter and Linear Power Amplifier," *IEEE Transactions on Power Electronics*, vol. 30, no. 1, pp. 216–226, 2015.
- [3] G. Gong, D. Hassler, and J. W. Kolar, "A comparative study of multicell amplifiers for AC-power-source applications," *IEEE Transactions on Power Electronics*, vol. 26, no. 1, pp. 149–164, 2011.
- [4] H.-h. Chiu, C.-m. Chen, M.-f. Tsai, and C.-s. Tseng, "A Novel Isolated Buck Converter with Output Voltage Ripple Reduction by a Complementary Square-Wave Scheme," in *6th IEEE Conference on Industrial Electronics and Applications*, 2011, pp. 1786–1790.

- [5] J. L. Duarte, J. Lokos, and F. B. M. van Horck, "Phase-Shift-Controlled Three-Level Converter With Reduced Voltage Stress Featuring ZVS Over the Full Operation Range," *IEEE Transactions on Power Electronics*, vol. 28, no. 5, pp. 2140–2150, 2013. [Online]. Available: <http://ieeexplore.ieee.org/lpdocs/epic03/wrapper.htm?arnumber=6287049>

Peer-to-Peer Control of Microgrids

Hamada Almasalma*, Jonas Engels*, Geert Deconinck
ESAT-ELECTA, KU Leuven, Kasteelpark Arenberg 10, 3001 Leuven, Belgium
EnergyVille, Thor Park 8300, 3600 Genk, Belgium
hamada.almasalma@kuleuven.be, jonas.engels@kuleuven.be

*Equally contributing authors

Abstract—In this paper, the motivation to develop microgrids as an effective solution for the control of distribution networks with high level penetration of Distributed Energy Resources (DERs) is discussed. As many different control methods for microgrids can be found in literature, this paper proposes a classification from highly centralized to distributed peer-to-peer control architectures. A peer-to-peer control paradigm is proposed as a way to control the distribution network with a high penetration of distributed energy resources. Different control algorithms suited for the proposed peer-to-peer control strategy are discussed.

Index Terms—Microgrid Control, Distributed Energy Resources, Peer-to-Peer Control, Distributed Coordination and Control.

I. INTRODUCTION

Growing concerns about energy sustainability, security of supply and an increasing penetration of renewable energy and other distributed energy resources (DERs), such as storage systems and electrical vehicles, are impacting the operation and the architecture of the electricity system. While currently placing a burden on the distribution grid, it is generally agreed that DERs could also be used for active grid control, thereby contributing to a stable and secure grid. To accomplish this, new control systems have to be designed that are able to fully harness the potential of the installed DERs [1]. This active monitoring and control of the distribution grid is commonly referred to as an essential part of the *smart grid*, which is regarded to be key in the future integration of electricity consumers, generators and those that do both (prosumers).

Current distribution networks are not designed to accommodate a large amount of DERs. A large penetration of DERs may create problems to maintain the quality of supply to all customers connected to the distribution network. Besides, the intermittent nature of DERs can create issues with the second-by-second balance of demand and supply. However, by coordinating the DERs, these issues could be resolved without the need for additional investments in grid infrastructure [2].

In the literature [3], the idea of a microgrid is an often mentioned alternative to controlling the whole distribution grid with a large amount of DERs. The main idea is that, when there are many DERs in a wide network, it can be

very complex and difficult to control. Thus, a potential way to manage this complexity is by breaking down the entire grid into a smaller microgrids, containing only a limited amount of DERs. This paper elaborates this idea and proposes an operational control paradigm for the future distribution grid, based on the concept of microgrids.

When considering such a microgrid and the coordination of multiple microgrids, different control methods can be found in literature [4]. This paper proposes a taxonomy of these control methods, from fully centralized to completely decentralized. A highly decentralized control method, the peer-to-peer control architecture, is further elaborated in this paper, as it is a promising way for future control of the distribution grid. Since the DERs are typically highly distributed, operated by many different owners and with different objectives, it is desirable that the microgrid control system operates in a highly distributed way as well. Besides, a robust control system is needed that does not depend on a single point of failure, as most of the more centralized control methods do.

The rest of the paper is organized as follows: section II introduces the most prominent issues with regard to the integration of DERs in the electrical grid, together with an elaboration of the microgrid concept that would be able to overcome these issues. Section III proposes a categorization for the different architectures of microgrid control. Section IV then proposes a new control paradigm for the distribution grid, based on the microgrid concept and the previously identified peer-to-peer architecture. Finally, the paper is concluded in section V.

II. ISSUES WITH THE INTEGRATION OF DERs IN THE ELECTRICAL GRID

This section summarizes the most prominent issues with regard to the integration of DERs in the current electrical grid. Both voltage issues and frequency or stability issues are discussed. Other type of issues, such as harmonics, security issues and power fluctuations are not discussed here. The microgrid concept is presented as a possible solution that is able to overcome these issues.

A. Voltage Issues

A large penetration of DERs may create problems to maintain the voltage quality of all customers connected to the same part of the distribution network. Up till now, voltage

This work is partially supported by H2020-LCE-2014-3 Peer to Peer Smart Energy Distribution Networks (P2PSmartTest) project (European Commission).

quality in the distribution grid is achieved based on the layout of grid infrastructure that is capable of operating within limits even in worst case scenarios, with the assumption of unidirectional power flows. The planning of the infrastructure is quite straightforward: minimum and maximum load conditions are considered and minimum and maximum voltages in the grid are examined. The network is dimensioned in such a way that the minimum voltage is near the lower limit of the allowed voltage range and the maximum voltage is near the upper limit of the allowed voltage range. When connecting significant amounts of distributed generation to the network, the assumption of unidirectional power flows is not always valid any more and the voltage profile of the network can be quite different than in the case without any generation. With maximum load conditions, distributed generation increases the voltage level in the network and, hence, enhance the voltage quality in the grid. However, when the load on the network is at a minimum, the generated power of the distributed generation can reverse the power flows in the grid, what could lead to a rise of the voltage profile beyond its allowed limits.

Therefore, the hosting capacity for renewable generation of many traditional distribution networks is limited by the voltage variations that occur between maximum and minimum load conditions. The traditional solution to this problem is to reinforce the local distribution grid by installing more cables. However, generally this is quite expensive, as new infrastructure has to be installed in residential neighborhoods. Another approach is by using the already installed infrastructure in a more optimal way, by coordination of the local generation, on-load tap changers or other equipment used to control voltage in distribution networks. This is the purpose of the smart grid [5].

B. Frequency and Stability Issues

The consumption and generation in the electricity system has to be balanced on a second-by-second basis. Traditionally, this balance is maintained by flexible generation units that are standby and are able to regulate their generated amount of electricity as required. However, the intermittent and unpredictable nature of new renewable energy sources creates issues with this traditional approach, as these new sources are usually not dispatchable.

Any deviation from the demand and supply balance results in a deviation of the system frequency from its nominal value, while large frequency deviations will affect the system stability. Therefore, the system operators maintain frequency within strict limits by using ancillary services for balancing of the grid, that are able to respond within various time frames [6]. Up till now these balancing services are exclusively organized by the transmission system operator (TSO). However, with the high penetration of DERs, maintaining the supply and demand balance and thus the system frequency within limits becomes more challenging. Spinning reserves or energy storage can address this problem but with a considerable cost. Therefore, power system operators are increasingly seeking new reserves for frequency response from demand flexibility, instead of

supply. As most of the demand is connected to the distribution grid, this means that the distribution system operators (DSOs) will be involved in this process.

C. Towards a New Control Paradigm for the Distribution Grid

One of the key solutions to overcome the above mentioned challenges of integrating DERs in the distribution grid is the design of a smart grid, containing control systems for the coordination of these DERs, thereby ensuring a reliable, secure and economical operation of the distribution network at all times.

Controlling the distribution network to be able to utilize the emerging diversity of DERs at significant levels of penetration, means that the control system has to be able to manage a wide and dynamic set of resources. Controlling such a complex network is not a trivial task. A potential way to manage this complexity is by breaking the entire grid down into smaller microgrids, containing only a limited amount of DERs. These microgrids should be able to control their local resources as optimal as possible, while being connected to the rest of the grid through a point of common coupling (PCC) [7].

These microgrids can be coordinated on a higher level into a system of multi-microgrids. The main idea is to design the control of the microgrid in such a way that the microgrid is perceived by the main grid as a single element responding to appropriate control signals. There are different possible architectures of operating such a microgrid, for which this paper proposes a classification ranging from fully centralized methods to fully distributed in section III.

A conventional way of controlling such a microgrid, is by a hierarchy of three control levels, each operating on a different timescale and with a different priority: primary, secondary and tertiary [8], [9]. Primary control is focused on keeping the grid stable in all circumstances, thus it needs the largest priority and should act on the smallest time scale. A robust control method is needed, so that in case e.g. the communication network fails, the primary control is still able to maintain stability of the microgrid. Therefore, as little communication as possible is desired. As primary control is often implemented as some kind of proportional controller, a steady state error remains, that shall have to be eliminated with the use of a secondary control method. Secondary control is activated on a slower time scale, e.g. every 15 minutes, and with a lower priority than primary control. Finally, tertiary control is implemented as the slowest level of control, with as purpose the economically optimal operation of the microgrid. Both secondary and tertiary controls usually require at least some kind of communication, as knowledge about the state of the entire system is needed.

These three control levels can be implemented through various organizational architectures of the microgrid. In the following section, this paper proposes a classification for these different architectures.

III. ARCHITECTURES OF MICROGRID CONTROL

The control of the DERs in a single microgrid can be organised according to many different control architectures.

They can range from fully centralized control where all decisions are made by a single central controller, to completely decentralized controls where all decisions are made by the local DERs. The required communication architecture changes accordingly. In most practical cases, a hybrid architecture exists, where e.g. primary control is implemented locally, and secondary control centrally.

This paper identifies five different approaches, shown in figure 1: (a) centralized control, (b) hierarchical control, (c) distributed control, (d) fully decentralized P2P control and (e) local control.

A. Centralized Control Architecture

In an fully centralized design shown in figure 1(a), all available measurements of the considered microgrid are gathered in a central controller that determines the control actions for all units. Reference [10] presents an implementation of a centralized controller based on Wide Area Monitoring and Control system (WAMC) that can be used to implement a centralized secondary and tertiary control. In [11] WAMC has been used to implement a centralized secondary voltage controller.

When looking at a single microgrid, the centralized controller is often referred to as a Microgrid Central Controller (MGCC). The advantage of a centralized control system is that the central system receives all necessary data of the microgrid, and based on all available information the multi-objective controller can achieve globally optimal performance. As there is only one controller, this results in a high controllability of the system. However, this high performance comes at a cost. First of all, the computational burden is heavy, as the optimization is computed based on a large amount of information. Moreover, a centralized controller is a single point of failure and redundancy of the central controller is expensive. The loss of communication with the central controller may cause a shutdown of the overall system. Besides, as all system states and boundary conditions have to be known at the central point, this requires a high quality of communication from all DERs to the central point of control. There is also the concern that the owners of the different DERs are not willing to hand over control of their resources to a third party. Finally, central systems are usually regarded as not being very scalable and system maintenance requires complete shutdown [12]. To overcome these issues, more distributed control architectures are developed, as described in the sections below.

B. Hierarchical Control Architecture

A first step towards a more decentralized control architecture is the introduction of a hierarchical system, as shown in figure 1(b). In this case, there exists some kind of aggregation of the local DERs towards the central controller. Typically, the characteristics of the DERs are represented by a few heuristics or parameters that are combined by an aggregator, who is able to offer these aggregated resources to a central optimizer. The central controller is then able to dispatch the necessary resources, through a hierarchical system of aggregators, who

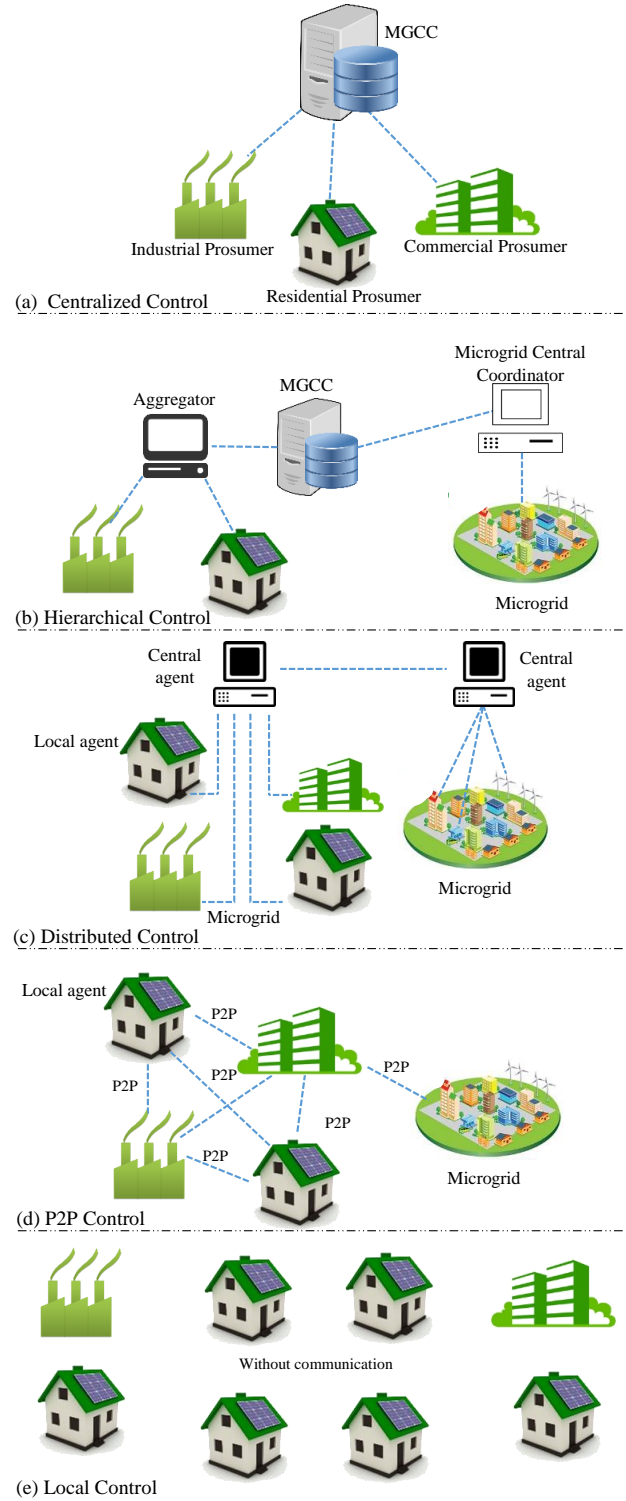


Fig. 1. Architecture of a microgrid control

determine which DERs should be used at which moment. Therefore, these methods are also referred to as *aggregate and dispatch* methods. As the resources are offered to the central optimizer in an aggregated way, there is considerably

less information needed at the central controller, which results in a more scalable system. However, the single point of failure remains, and the points of aggregation might even become new points of failure.

Nowadays, this approach is used for exploiting demand response resources. Examples are the *Intelligator* algorithm [13], or the demand response reserves offered by aggregators to a TSO for e.g. automatic or manual frequency restoration reserves (aFRR or mFRR). The coordination of multiple, centrally controlled microgrids can also be organized in a hierarchical way. In that case, a *central coordinator* coordinates multiple microgrids, each controlled by a local MGCC. The MGCC of a single microgrid tries to reach an optimal operation point using only its local resources. If the internal resources are not sufficient, the MGCC shall ask the microgrid central coordinator for external resources from other microgrids [14].

C. Distributed Control Architecture

In both architectures described above, the DERs are controlled by a third party. However, since the owners of the DERs impose the operational boundary conditions, one can argue that it might be better to keep the control of the DERs locally. Besides, not all DER owners want to exchange all their information with a third party for privacy reasons. However, to reach a (near) optimal operation of the grid, these DERs should be coordinated. It is at this point that distributed control architectures come into play. The idea behind distributed control is to divide the centralized problem into a certain number of local controllers or agents. Therefore, each agent does not have a global vision of the problem [15], but by means of correct coordination they can reach a globally (near) optimal state.

Coordination is organised by a central agent that is able to communicate global constraints, such as the power limit of a transformer, or exceeding voltage limits. This can be done by the communication of Lagrange multipliers. Examples of algorithms that are suited for this approach are dual decomposition methods or the alternating direction method of multipliers (ADMM) [16]. Both are based on the dual ascent method, where price vectors are sent iteratively from the central controller to the DERs. The DERs optimize their consumption towards such a price vector and return demand vectors to the central agent. The central agent then analyses the demand vectors with regard to operational grid constraints, and updates the prices when constraints are being violated. The DERs optimize again according to this new price vector. This iteration goes on until a steady state solution is found. Figure 1(c) represents such a distributed control scheme, consisting of local DERs that optimize and a central agent that controls the global constraints.

Distributed approaches have important advantages that justify their use. As the global optimization problem is divided into several sub-problems, the computational requirements are lower. Besides, the information exchange between local and central agents is limited, which relaxes the requirements of

the communication system. This approach results in a very scalable method. As the local DERs perform an optimization by themselves, they do not need to hand over private information to a third party that controls their resources. However, a central agent still exists, inherently resulting in a single point of failure.

D. Peer-to-Peer Control Architecture

To eliminate the problems that a more centralized control method possesses, having a single point of failure, the idea of peer-to-peer microgrids has been developed. This type of architecture, inspired by P2P computer networking [17], is characterized by the complete absence of a central controller. All local DERs or agents, are equally important and can communicate to other agents [18], in a peer-to-peer fashion, as shown in figure 1(d). The absence of a central controller leads to the term of autonomous control. Peer-to-peer communication is used for dissemination of the grid state to all required agents in the microgrid. The grid-supporting agents can then act according to the received information, in cooperation with each other. In this way they should be able to reach a (near) optimal operation of the considered microgrid. Examples of algorithms that could be used for such P2P communication are gossiping [19] and consensus algorithms [20]. This architecture will be elaborated further in section IV.

In this architecture, there is a clear absence of a single point of failure. In the case a single agent fails, the other agents can still operate the grid in a stable way. Also when a single communication channel fails, the required information can still reach all necessary participants, via other agents. These properties makes this architecture a robust way of controlling a microgrid. Besides, all information is kept local, eliminating possible privacy concerns. On the other hand, all agents need a considerable amount of local intelligence, as they need to be able to execute the necessary optimizations.

E. Local Control Architecture

Finally, there also exist control architectures without any form of communication, as shown in figure 1(e). This paper classifies them as *local* control architectures. In this case, optimal operation of the microgrid is rather difficult, as it is impossible to know the complete state of the grid and all operational boundary conditions of the DERs. However, this method is robust against all communication failures, as the absence of any communication will ensure that the grid is still controlled when all communication channels fail. As primary frequency control should be able to operate even when communication fails, this is often implemented as a local control architecture. Thereby it uses droop characteristics that vary active power with variations in locally measured frequency. Another example is local voltage control, implemented by a voltage-reactive power droop [21].

IV. PROPOSED PEER-TO-PEER BASED CONTROL PARADIGM FOR THE DISTRIBUTION GRID

As the new DERs are typically highly distributed in the grid, operated by a lot of different owners and with different

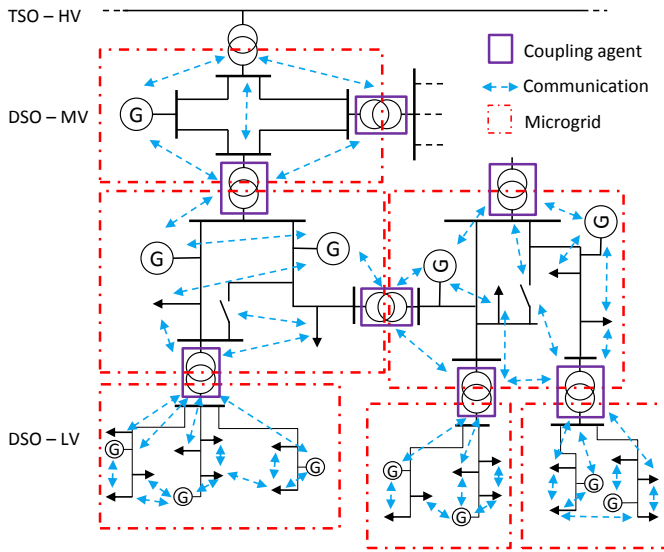


Fig. 2. P2P based control paradigm

objectives, it is desirable that the microgrid control system operates in a highly decentralized way as well. Plug and play of new resources in this microgrid is a crucial to allow for seamless integration over time. In this perspective, a peer-to-peer control architecture, as introduced in section III-D, seems to be a good method for controlling DERs in the distribution grid. It is a robust method and is able to work in a distributed way, without the need for a central controller, having inherent plug and play characteristics. Each agent communicates directly with other agents in the microgrid, without having to go through a central server [22].

It is impossible to impose this architecture on the whole distribution grid, as it incorporates thousands of DERs that are geographically very dispersed. To deal with this, breaking the complete grid down into a smaller microgrids, containing only a limited amount of DERs, can be a solution. These microgrids operate then according to the presented peer-to-peer control architecture. Points of common coupling are used to connect the different microgrids.

The proposed scheme is shown in figure 2. The distribution network is divided into several microgrids, hierarchically organized on different voltage levels. A microgrid can consist of a couple of low voltage feeders, physically connected to the same transformer, or a part of the medium voltage network on the same voltage level, for example. Each microgrid consists of several autonomous agents. Such an agent could be a renewable generation unit, a group of intelligent controllable loads, a substation, or any other form of DERs. On the connection points of two microgrids there is a coupling agent which serves as gateway of one microgrid to the other microgrid, the point of common coupling. As the microgrids represented in this figure are separated by transformers or substations, these would be good candidates for such a coupling agent. Such a coupling agent represents the characteristics of the whole

lower level microgrid (e.g. a low voltage feeder) on the higher level microgrid (e.g. a medium voltage distribution grid).

The agents are each able to communicate with some other neighbouring agents in a peer-to-peer way, creating possibilities to disseminate data about the state of the grid without the need for one central point of information. Certain algorithms from the field of distributed computing, epidemic [23], gossiping [24] and consensus [20] algorithms seem to be particularly appropriate for this goal. These algorithms are designed to disseminate and aggregate data in distributed networks in a quick and robust way, making them good candidates for P2P microgrid control.

Each agent should have some local intelligence that determines the action of the agent based on the perceived state of the grid. The agents decide their own actions, that will result in a new state of the grid. The agents obtain new information about the new state of the grid through the peer-to-peer communication, and decide on a new action based on this new state. The successive grid states should converge to a desired steady state of the grid. Appropriate control algorithms are needed to achieve this.

A. Epidemic Algorithms Suited for Peer-to-Peer Control

Epidemic or gossiping algorithms are used for scalable and efficient data dissemination in distributed P2P networks, without a central controller [25]. They mimic the spread of a contagious disease. Each agent in the distributed system sends new information it has received to other agents rather than to a server or cluster of servers in charge of forwarding it. In turn, each of these agents forwards the information to other selected agents, and so on [23]. Gossiping [19] is often used as a synonym for epidemic algorithms. In [26], a gossip-like distributed P2P optimization algorithm is presented for optimal reactive power flow control in a microgrid. In this method, the agents iteratively take actions that minimize the power losses in the grid, when communicating only with their neighbours. In [27], a P2P gossiping algorithm is presented for active and reactive power sharing in a microgrid, based on frequency and voltage droop control.

Consensus algorithms can be seen as a specific type of epidemic algorithms, where the goal is for all agents to reach an *agreement* on a certain quantity that depends on the states of all agents [20]. In practice, many consensus algorithms are used to calculate an average value of the states of all agents in a distributed way. This can easily be used for P2P economic dispatch of the DERs in a microgrid, where all agents have to agree on the same marginal cost [28], [29]. In [30], a consensus algorithm is used for global information discovery for peer-to-peer based load restoration to isolate faults. Consensus algorithms are applied for peer-to-peer control of DC microgrids in [31], [32].

V. CONCLUSION

This paper discussed the major issues with regard to the integration of DERs in the electrical grid and the concept of microgrids as a possible solution to these problems. As

there are different methods for organizing the control of these microgrids found in literature, this paper presented a classification of these methods, from highly centralized to fully decentralized architectures. The drawbacks of the centralized control and the advantages of the distributed control architecture have been discussed as a motivation to propose a new control paradigm for the distributed grid, based on peer-to-peer controlled microgrids. Coupling agents are introduced to establish a connection between two microgrids.

The absence of a central point and peer-to-peer communication are found to be key elements in this control method. Epidemic algorithms, such as gossip and consensus are proposed as suited algorithms for peer-to-peer control, as they are able to disseminate data in a distributed way. Finally, a short literature review on peer-to-peer microgrid control based on gossiping and consensus algorithms is presented as an illustration of possible algorithms for peer-to-peer controlled microgrids.

Future work may consist of validation and demonstration of a peer-to-peer controlled microgrid, as well as a comparison of the performance of the different algorithms found in literature.

REFERENCES

- [1] R. O’Gorman and M. A. Redfern, “Enhanced autonomous control of distributed generation to provide local voltage control,” in *Power and Energy Society General Meeting - Conversion and Delivery of Electrical Energy in the 21st Century*, 2008 IEEE, July 2008, pp. 1–8.
- [2] J. P. Lopes, N. Hatziaargyriou, J. Mutale, P. Djapic, and N. Jenkins, “Integrating distributed generation into electric power systems: A review of drivers, challenges and opportunities,” *Electric power systems research*, vol. 77, no. 9, pp. 1189–1203, 2007.
- [3] R. H. Lasseter and P. Paigi, “Microgrid: a conceptual solution,” in *Power Electronics Specialists Conference, PESC*, June 2004, pp. 4285–4290.
- [4] N. Hatziaargyriou, “Microgrid control issues,” in *Microgrids: Architectures and Control*, 1st ed. John Wiley and Sons, 2014, ch. 3, pp. 25–80.
- [5] T. Xu and P. Taylor, “Voltage control techniques for electrical distribution networks including distributed generation,” in *The International Federation of Automatic Control, 17th World Congress Seoul*, 2008.
- [6] I. A. Erinmez, D. O. Bickers, G. F. Wood, and W. W. Hung, “Ngc experience with frequency control in england and wales-provision of frequency response by generators,” in *Power Engineering Society 1999 Winter Meeting, IEEE*, vol. 1, Jan 1999, pp. 590–596 vol.1.
- [7] R. H. Lasseter, “Smart distribution: Coupled microgrids,” *Proceedings of the IEEE*, vol. 99, no. 6, pp. 1074–1082, June 2011.
- [8] A. Bidram and A. Davoudi, “Hierarchical structure of microgrids control system,” *IEEE Transactions on Smart Grid*, vol. 3, no. 4, pp. 1963–1976, Dec 2012.
- [9] D. E. Olivares, A. Mehrizi-Sani, A. H. Etemadi, C. A. Caizares, R. Irvani, M. Kazerani, A. H. Hajimiragha, O. Gomis-Bellmunt, M. Saeedifard, R. Palma-Behnke, G. A. Jimnez-Estvez, and N. D. Hatziaargyriou, “Trends in microgrid control,” *IEEE Transactions on Smart Grid*, vol. 5, no. 4, pp. 1905–1919, July 2014.
- [10] M. Chenine, E. Karam, and L. Nordstrom, “Modeling and simulation of wide area monitoring and control systems in ip-based networks,” in *2009 IEEE Power Energy Society General Meeting*, July 2009, pp. 1–8.
- [11] A. Mohamed, A. Ghareeb, T. Youssef, and O. A. Mohammed, “Wide area monitoring and control for voltage assessment in smart grids with distributed generation,” in *Innovative Smart Grid Technologies (ISGT), 2013 IEEE PES*, Feb 2013, pp. 1–6.
- [12] S. Sojoudi, J. Lavaei, and A. G. Aghdam, *Structurally Constrained Controllers: Analysis and Synthesis*. Springer Science and Business Media, 2011, ch. 1, pp. 1–8.
- [13] S. Vandael, B. Claessens, M. Hommelberg, T. Holvoet, and G. Deconinck, “A scalable three-step approach for demand side management of plug-in hybrid vehicles,” *IEEE Transactions on Smart Grid*, vol. 4, no. 2, pp. 720–728, June 2013.
- [14] L. Che, M. Shahidehpour, A. Alabdulwahab, and Y. Al-Turki, “Hierarchical coordination of a community microgrid with ac and dc microgrids,” *IEEE Transactions on Smart Grid*, vol. 6, no. 6, pp. 3042–3051, Nov 2015.
- [15] M. Yazdani and A. Mehrizi-Sani, “Distributed control techniques in microgrids,” *IEEE Transactions on Smart Grid*, vol. 5, no. 6, pp. 2901–2909, Nov 2014.
- [16] D. Alaerts and J. De Turck, “Investigation and comparison of distributed algorithms for demand-side management,” Master’s thesis, ESAT-ELECTA, KU Leuven, 2013.
- [17] R. Schollmeier, “A definition of peer-to-peer networking for the classification of peer-to-peer architectures and applications,” in *Peer-to-Peer Computing, 2001. Proceedings. First International Conference on*, Aug 2001, pp. 101–102.
- [18] S. D. J. McArthur, E. M. Davidson, V. M. Catterson, A. L. Dimeas, N. D. Hatziaargyriou, F. Ponci, and T. Funabashi, “Multi-agent systems for power engineering applications—part i: Concepts, approaches, and technical challenges,” *IEEE Transactions on Power Systems*, vol. 22, no. 4, pp. 1743–1752, Nov 2007.
- [19] D. Kempe, A. Dobra, and J. Gehrke, “Gossip-based computation of aggregate information,” in *Foundations of Computer Science, 2003. Proceedings. 44th Annual IEEE Symposium on*, Oct 2003, pp. 482–491.
- [20] R. Olfati-Saber, J. A. Fax, and R. M. Murray, “Consensus and cooperation in networked multi-agent systems,” *Proceedings of the IEEE*, vol. 95, no. 1, pp. 215–233, Jan 2007.
- [21] E. Demirok, P. C. Gonzalez, K. H. B. Frederiksen, D. Sera, P. Rodriguez, and R. Teodorescu, “Local reactive power control methods for overvoltage prevention of distributed solar inverters in low-voltage grids,” *IEEE Journal of Photovoltaics*, vol. 1, no. 2, pp. 174–182, Oct 2011.
- [22] K. Eger, C. Gerdes, and S. Ztunali, “Towards p2p technologies for the control of electrical power systems,” in *2008 Eighth International Conference on Peer-to-Peer Computing*, Sept 2008, pp. 180–181.
- [23] P. T. Eugster, R. Guerraoui, A. M. Kermarrec, and L. Massoulié, “Epidemic information dissemination in distributed systems,” *Computer*, vol. 37, no. 5, pp. 60–67, May 2004.
- [24] A. G. Dimakis, S. Kar, J. M. F. Moura, M. G. Rabbat, and A. Scaglione, “Gossip algorithms for distributed signal processing,” *Proceedings of the IEEE*, vol. 98, no. 11, pp. 1847–1864, Nov 2010.
- [25] A. Demers et al., “Epidemic algorithms for replicated database maintenance,” in *Proceedings of the Sixth Annual ACM Symposium on Principles of Distributed Computing*, ser. PODC ’87. New York, NY, USA: ACM, 1987, pp. 1–12.
- [26] S. Bolognani and S. Zampieri, “A gossip-like distributed optimization algorithm for reactive power flow control,” in *Proc. IFAC World Congress*, 2011, pp. 1–14.
- [27] K. De Brabandere, “Voltage and frequency droop control in low voltage grids by distributed generators with inverter front-end,” Ph.D. dissertation, KU Leuven, 2006.
- [28] J. Cao, “Consensus-based distributed control for economic dispatch problem with comprehensive constraints in a smart grid,” Ph.D. dissertation, The Florida State University, 2014.
- [29] Z. Zhang and M. Y. Chow, “Incremental cost consensus algorithm in a smart grid environment,” in *2011 IEEE Power and Energy Society General Meeting*, July 2011, pp. 1–6.
- [30] Y. Xu and W. Liu, “Novel multiagent based load restoration algorithm for microgrids,” *IEEE Transactions on Smart Grid*, vol. 2, no. 1, pp. 152–161, March 2011.
- [31] L. Meng, T. Dragicevic, J. Roldn-Prez, J. C. Vasquez, and J. M. Guerrero, “Modeling and sensitivity study of consensus algorithm-based distributed hierarchical control for dc microgrids,” *IEEE Transactions on Smart Grid*, vol. PP, no. 99, pp. 1–1, 2015.
- [32] L. Meng, T. Dragicevic, J. M. Guerrero, and J. C. Vasquez, “Dynamic consensus algorithm based distributed global efficiency optimization of a droop controlled dc microgrid,” in *Energy Conference (ENERGYCON), 2014 IEEE International*, May 2014, pp. 1276–1283.

Modelling and Emulation of an Unbalanced LV Feeder with Photovoltaic Inverters

Ramón López-Erauskin

Johan Gyselinck, *IEEE Member*

Bio-, Electro- and Mechanical Systems department
Université Libre de Bruxelles
rlopezer@ulb.ac.be, johan.gyselinck@ulb.ac.be

Frédéric Olivier, *IEEE Student Member*

Damien Ernst, *IEEE Member*

Department of Electrical Engineering and Computer Science
Université de Liège
frederic.olivier@ulg.ac.be, dernst@ulg.ac.be

María Emilia Hervás, Alexis Fabre

GreenWatch SA

Wavre, Belgium

premasol@greenwatch.be

Abstract—In this paper, the penetration of grid-connected photovoltaic systems is studied, experimentally tested and compared to simulation results. In particular, how the inverse current flow and unbalance situations affect the voltage in the low-voltage grid. Thus, a test platform has been developed for obtaining experimental results with grid-tied commercial inverters. Photovoltaic arrays are emulated and subjected to different irradiance profiles and the inverters are controlled to produce at different power conditions. A model has been developed in order to reproduce the same operating conditions and working environment. Simulations are performed with the software PowerFactory and the results compared to the experimental ones.

Index Terms—distributed power generation, photovoltaic systems, power distribution, reactive power.

I. INTRODUCTION

The operation of grid-tied photovoltaic (PV) units is characterized by several uncertainties due to the number of currently operating units, the points where they are connected, and the delivered power. Due to the historical design of low-voltage (LV) feeders, PV generation (PVG) can have adverse effects and cause voltage deviations due to reversed power flow [1]. Some authors have also studied the overvoltage in low-voltage grids based in probabilistic models [2], [3]. In this context, a scheme that controls the active and reactive power of inverters was previously designed and numerically tested [4]. The first step toward the validation of the control scheme in a real setting is to reproduce in a laboratory the behavior of a LV feeder under different voltage and unbalance conditions.

In previous research, the impact of the penetration of PV units in the low-voltage network with dispersed loads was investigated [5], [6]. The former presents modeling and field measurements and addresses the problems of increasing PV installations in these networks. In the latter, a benchmark LV microgrid network is presented, which is suitable for steady state and transient simulations. In validation, laboratory reproduction allows time-, cost- effective and repeatable tests

of overvoltage conditions of the grid without need of deploying expensive equipment close to large concentrations of PV systems.

In this paper, we present the test platform (Fig. 1) emulating a LV feeder, and the voltage and power variations for several operation scenarios. The effect of active and reactive power variations on the voltage profile is studied. The lab feeder is modeled numerically and simulations are performed for each operation scenarios. The results from the measurements and the simulations are then compared.

II. TEST PLATFORM AND MODEL IN POWERFACTORY

A LV feeder is composed of several elements: the main ones are the external grid, the distribution transformer, the cables, the PV systems and the loads which represent houses consumptions. In our study, loads are not considered. Since they would be connected at the same point as the PV systems, they would reduce the power injected into the network and thus decrease the voltage variations, a behavior that we specifically want to exhibit in our simulations. In this section, every part of the test platform in Fig. 1 is described and its lab implementation explained. The network reproduced in the lab is modeled in PowerFactory, a power system analysis software, with the electrical and hardware characteristics of the external grid, cables and inverters to allow a meaningful comparison.

A. External grid

In a typical setting, the external grid would be the medium voltage network at a voltage close to 15 kV and the distribution transformer would bring this voltage down to 400 V. In the lab setting, the external grid is the low voltage network. In PowerFactory, it is modeled as a slack bus with a constant voltage.

B. Distribution transformer

The transformer that feeds the reproduced LV-grid has the following characteristics: Δ -Y configuration, $S_{trafo} = 100$

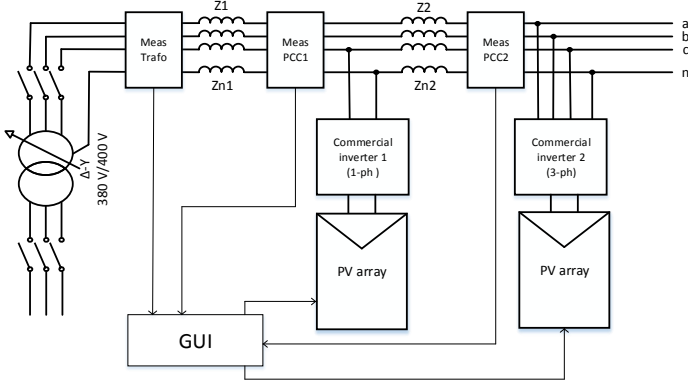


Fig. 1. Laboratory test bench for the study of voltage fluctuations and unbalanced conditions

kVA, the Primary (380 V, three-phase, delta) and the Secondary (400 V, three-phase, four-wire). In particular, abnormal grid conditions can be emulated with e.g. undervoltage or overvoltage in order to test the behaviour and the compensation features of the inverters. The impedance is estimated considering the standardized short-circuit voltage for distribution transformers (where $\omega = 2 \cdot \pi \cdot f$ is the angular frequency and $f = 50$ Hz) [10], as follows:

$$V_{CC} = 4\% V_{ph-n} = 0.04 \cdot 230V = 9.2V \quad (1)$$

Where the short-circuit current is

$$I_{CC} = \frac{S_{trafo}}{\sqrt{3} V_{Nom}} = \frac{100kVA}{\sqrt{3} 400} = 144A, \quad (2)$$

and the value of the reactance and inductance is calculated:

$$X_{L,trafo} = \frac{V_{CC}}{I_{CC}} = 64m\Omega \quad (3)$$

$$L_{trafo} = \frac{X_{L,trafo}}{\omega} = 204\mu H \quad (4)$$

In PowerFactory, the transformer is modeled considering its short-circuit voltage, copper losses, iron losses and magnetizing impedance.

C. Cables

The impedance characteristics of the feeder are important as they will determine the actual voltage variations inside the feeder (see section III). The cables are reproduced in the test bench placing impedances between the transformer and the points of connections of the inverters (PCC) as in Fig. 1. The values of the impedances are gathered in Table I.

D. PV systems

1) *PV array emulator*: The PV array emulator allows the reproduction of the characteristics of a standard PV installation in a flexible manner [7]. It uses the single-exponential model of the solar cells [8] with an adjustable number of panels in parallel and series in function of the output characteristics

TABLE I
CABLE PARAMETERS

Symbol	Description	Value	Units
R	Phase line resistance	0.1	Ω
X	Phase line reactance	65.97	$m\Omega$
R_N	Neutral line resistance	0.165	Ω
X_N	Neutral line reactance	370.7	$m\Omega$

required and takes into account the influence of the in-plane irradiance and the PV cell temperature. The characteristic parameters of the PV panels used for the PV array emulation are grouped in Table II. The emulator is able to reproduce realistic atmospheric conditions either with the clear-sky model or actual recorded data. In addition, shading can be easily set in the Graphical User Interface (GUI) of the emulator in order to test the Maximum Power Point Tracking (MPPT) capabilities of the PV inverters under these conditions [7], [9]. In particular, shading results in several local maxima on the instantaneous Power-Voltage (P-V) curve of the PV array, which requires an appropriate algorithm for proper MPPT.

TABLE II
PARAMETERS OF ONE PV PANEL

Symbol	Description	Value	Units
V_{OC}	Open-circuit voltage	37.3	V
I_{SC}	Short-circuit current	8.52	A
V_{MPP}	MPP voltage	30.5	V
I_{MPP}	MPP current	8.04	A
P_{MPP}	MPP power	245.22	W

TABLE III
CONFIGURATION OF THE PV ARRAYS

Array	N. of panels	Vmax (V)	Peak power (W)
Array 1	11	410.3	2697.42
Array 2	20	746	4904.4

2) *Commercial inverter*: The inverter, through which the PV array is connected to the LV grid, is commonly designed to comply with the latest grid standards. For this reason, compensation features to help support the grid are more and more often implemented by the manufacturers. In commercial inverters, this includes mainly power regulation through active power reduction (w.r.t. the default maximum power production) and reactive power compensation. The former is introduced in order to limit the power delivered for a specific section of the grid and the latter to correct locally some power quality issues such as voltage fluctuations. Depending on the inverter, the reactive power compensation

can be set in different ways; it can be adapted to the needs of the system (so-called static or dynamic $\cos\varphi$ setpoint) or to the country grid codes. For example, the German grid codes require the reactive power setpoint to be either fixed or adjustable by a signal from the network operator. The setpoint value is either a fixed displacement factor (static $\cos\varphi$), a variable displacement factor depending on the active power ($\cos\varphi(P)$), a fixed reactive power value in VAR (dynamic $\cos\varphi$) or a variable reactive power depending on the voltage $Q(U)$ [11]. These features have been previously tested and the voltage compensation capabilities of the inverters assessed [12]. In order to adjust the power setpoints, it is necessary to allow the communication between the user (e.g. network operator) and the inverter. This is done using the RS485 communication protocol, setting absolute values of the active and reactive powers or the $\cos\varphi$ parameter.

TABLE IV
PARAMETERS OF THE SINGLE-PHASE INVERTER

Symbol	Description	Value	Units
V_{DC-MPP}	DC-voltage MPPT range	350 - 600	V
P_{DC-Max}	Maximum DC input power	3200	W
V_{AC}	AC rms voltage (ph-N)	230	V
P_{AC}	Nominal AC power	2600	VA
$\cos\varphi$	Power factor	-0.8..1..0.8	-

TABLE V
PARAMETERS OF THE THREE-PHASE INVERTER

Symbol	Description	Value	Units
V_{DC-MPP}	DC-voltage MPPT range	245 - 800	V
P_{DC-Max}	Maximum DC input power	5150	W
V_{AC}	AC rms voltage (ph-ph)	400	V
P_{AC}	Nominal AC power	5000	VA
$\cos\varphi$	Power factor	-0.8..1..0.8	-

The characteristics such as the configuration of the PV arrays and the peak power for the single- and three-phase inverters are specified in Table III, IV and V.

E. The Graphical User Interface

ControlDesk software is used together with the dSPACE ds1104 platform for the GUI. The user can observe the relevant system variables, such as the grid voltages and currents, and the DC-side voltage and current. Also, the instantaneous characteristic curves of the PV array for the adjustable meteorological conditions set are displayed, so that the evolution of the working point can be observed. This is especially useful for evaluating the MPPT capability of the inverter.

III. VOLTAGE FLUCTUATION

The validation of the results obtained in the simulation are of relevant importance in order to ensure the reliability of a simulation model. For that purpose, the power exchange between the PVGs and the LV feeder will be tested here to see how it affects to the grid voltage. The relation between power exchange and voltage fluctuation is discussed hereafter [13].

As shown in Fig. 1, any current flow will generate a voltage drop and a phase shift between two arbitrary points on the feeder. In LV feeders, to which distributed generation units are commonly connected, the inductive and resistive components have to be considered [13]. Considering no load connected at any PCC, the complex power flowing through that section is the one coming from the PV inverters: $S_{inv} = P_{inv} + jQ_{inv}$. The voltage at the PCC1 is here considered as reference with $V_1 = V_1 \angle 0^\circ$ while the one at the transformer $V_{tr} = V_{tr} \angle \delta$ and the grid current $I = I \angle \varphi$ are phase-shifted by angles δ and φ , respectively. The complex power at the PCC1 is, therefore, the sum of the powers delivered by the inverters and expressed as $S_{PCC-1} = P_{PCC-1} + jQ_{PCC-1}$.

In unbalanced condition for this LV feeder configuration, the existing neutral impedance displaces the neutral voltage V_{N1} from the one at the transformer (V_N). Represented in Fig. 2, V_A , V_B and V_C (in dark blue) are the line voltages at PCC1. The single-phase inverter is connected between phase C and the neutral point, where the inverter voltage is in phase with V_C (Fig. 3).

The voltage drop at the impedance between the transformer and the PCC1 is:

$$\underline{\Delta V}_1 = \underline{Z}_1 \cdot \underline{I} \quad (5)$$

considering the feeder impedance $\underline{Z}_1 = R_1 + jX_1$. The phase A voltage at the transformer is, therefore:

$$\underline{V}_{AN} = \underline{V}_A - \underline{\Delta V}_1 \quad (6)$$

and its neutral point voltage:

$$\underline{V}_N = \underline{V}_{N1} + \underline{\Delta V}_{LN} \quad (7)$$

where \underline{V}_{N1} is the neutral voltage at PCC1 and $\underline{\Delta V}_{LN}$ is the voltage drop at the neutral impedance \underline{Z}_{N1} , caused by the current \underline{I}_N flowing through the neutral line:

$$\underline{\Delta V}_{LN} = \underline{I}_N \cdot \underline{Z}_{N1} \quad (8)$$

considering the neutral impedance $\underline{Z}_{N1} = R_{N1} + jX_{N1}$. The neutral voltage at PCC-1 satisfies the following expression:

$$\underline{V}_{N1} = \underline{V}_N - \underline{\Delta V}_{LN} \quad (9)$$

and the phase A to neutral voltage at PCC-1 is:

$$\underline{V}_{AN1} = \underline{V}_A - \underline{V}_{N1} \quad (10)$$

The displacement of \underline{V}_{N1} from the neutral point of the transformer \underline{V}_N causes a decrease in the magnitude of the vector in phase A and the resulting effect on the voltages (in light blue) at PCC1.

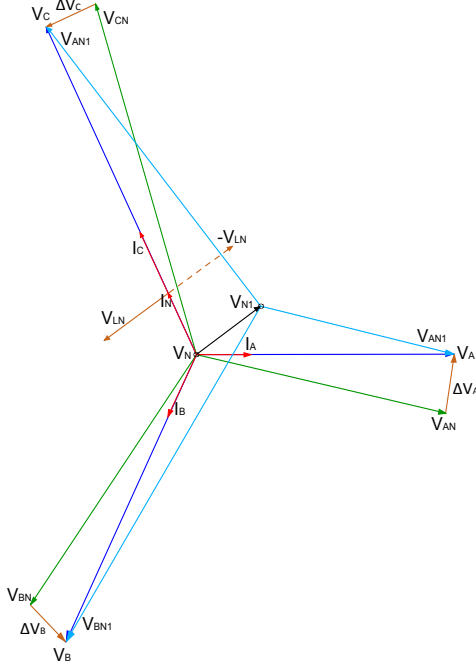


Fig. 2. Voltage phasors of the LV feeder at PCC-1

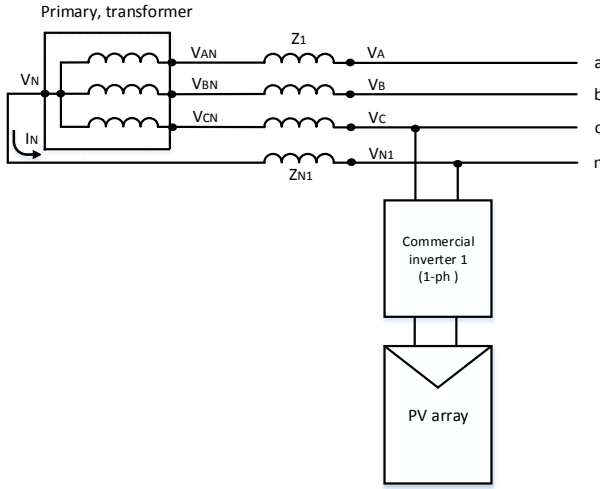


Fig. 3. Part of the laboratory test platform and the neutral current flow direction

IV. RESULTS AND COMPARISON

The testing is done for single- and three-phase inverters, focusing on their power regulation functionality and the resulting voltage compensation capability. The general parameters of the platform are shown in Table I.

The simulations are performed in two different phases:

A. Static production values

The different operating scenarios are:

- 1) Operating scenario 1 (OP1): all PV inverters produces their maximum active power.
- 2) Operating scenario 2 (OP2): all PV inverters produce half their maximum power.
- 3) Operating scenario 3 (OP3): all PV inverters produce half their maximum active power and absorb the maximum reactive power. This last operating scenario allows us to observe the influence of reactive power on the voltages at the LV level.

TABLE VI
ACTIVE AND REACTIVE POWER PRODUCED BY THE INVERTERS IN EACH SCENARIO

	Single-phase inverter		Three-phase inverter	
	P (W)	Q (var)	P (W)	Q (var)
OP1	2317	0	4810	0
OP2	1200	0	2460	0
OP3	1200	-1700	2460	-2500

The three OPs show the voltage fluctuation in a LV feeder in presence of dispersed generation, where the consumption is null. The goal of these simulations is to put in evidence the phenomenon by which a overvoltage can occur. In that regard, power consumption was not considered as it would reduce the power injected in the different PCCs and diminish the effect of power on voltage.

Figs. 4-6 show the voltage profile evolution for simulation (dashed lines) and experimental (solid lines) results for the different scenarios and the impact of PVG and reactive power on voltage.

1) *OP1*: In Fig. 4, all the inverters are producing at their maximum power, without reactive power compensation. The figure shows the influence of the injected power on the grid voltage for each PCC. The furthest the PVG is from the LV feeder transformer, the highest is the voltage level at the PCC for V_{bn} and V_{cn} . In this situation, the generators linked to it are the first to disconnect from the grid if an overvoltage occurs. However, the same does not apply to V_{an} , affected by the displacement of the neutral voltage V_{N1} from the neutral point of the transformer V_N , as explained in section III.

2) *OP2*: In Fig. 5 the inverters are working at half their maximum active power with a lower influence in the voltage increment.

3) *OP3*: For this scenario, the voltage at phase C decreases more notably than at the others due to the two inverters' reactive power consumption.

According to (5)-(10), the voltage drop (ΔV) at the line impedance depends on the feeder characteristics, the direction of the current and the amount of this current. The behavior of the voltage profile along the different points of the feeder is, in most of the cases, the same for both simulation and experimental results. The differences between the numerical

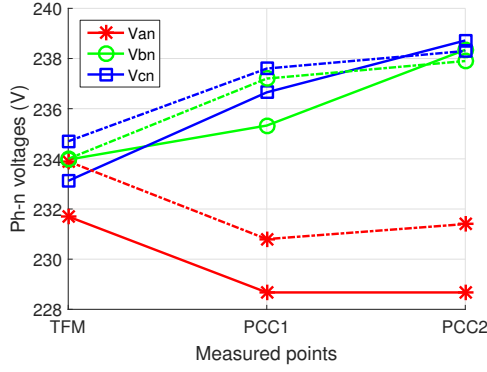


Fig. 4. Voltage profile of the LV feeder, PV inverters producing at full power. Simulation (dashed lines) and experimental (solid lines) results.

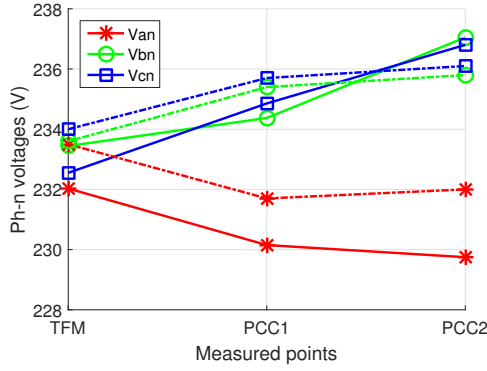


Fig. 5. Voltage profile of the LV feeder, PV inverters producing at half maximum power. Simulation (dashed lines) and experimental (solid lines) results.

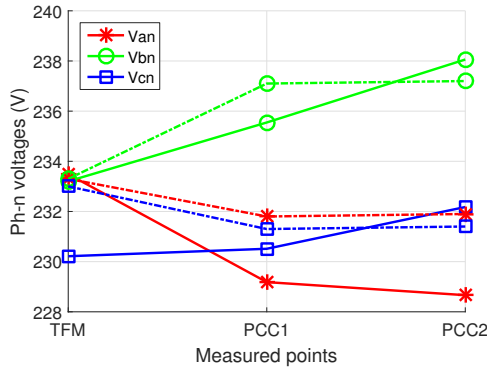


Fig. 6. Voltage profile of the LV feeder, PV inverters producing at half maximum power and absorbing maximum reactive power. Simulation (dashed lines) and experimental (solid lines) results.

results and the measured ones (e.g. measured $V_{an} = 231.7$ V and simulated $V_{an} = 233.9$ V in Fig. 4) are due to the voltage differences in the real transformer, not reproducible in software reliably. However, these divergences need to be studied more deeply to bring the simulations and the real environment measurements closer.

Table VII gathers the values of Figs. 4-6 for the three different operation scenarios: OP1, OP2, and OP3, where the added letter "L" means "Laboratory" and "S" "Simulation".

TABLE VII
VOLTAGES MEASURED AT THE LV FEEDER

Operation scenario	OP1L	OP1S	OP2L	OP2S	OP3L	OP3S
$V_{an,Tr}$ (V)	231.7	233.9	232	233.5	233.5	233.3
$V_{bn,Tr}$ (V)	233.9	234	233.4	233.6	233.2	233.3
$V_{cn,Tr}$ (V)	233.1	234.7	232.5	234	230.2	233
$V_{an,PCC1}$ (V)	228.7	230.8	230	231.7	229	231.8
$V_{bn,PCC1}$ (V)	235.3	237.2	234.4	235.4	235.5	237.1
$V_{cn,PCC1}$ (V)	236.7	237.6	234.9	235.7	230.5	231.3
$V_{an,PCC2}$ (V)	228.7	231	229.8	232	228.7	231.8
$V_{bn,PCC2}$ (V)	238.4	237.9	237	235.8	238.1	237.2
$V_{cn,PCC2}$ (V)	238.7	238.3	236.8	236.1	232.2	231.4

B. Dynamic production values

The PV array emulators follow predefined irradiance profiles to simulate realistic behavior of the inverters during a day. The irradiance profile used for the simulations is the one of a sunny day in Belgium and its acquisition time is 1 minute. The variation of the irradiance is reproduced in the laboratory every 2 seconds, accelerating the execution 30 times. This way, faster experimental results than in field measurements can be obtained, as can be seen in Fig. 8. The variation of voltages, active and reactive power flows are studied and compared to the numerical results to validate them thanks to the real hardware emulation.

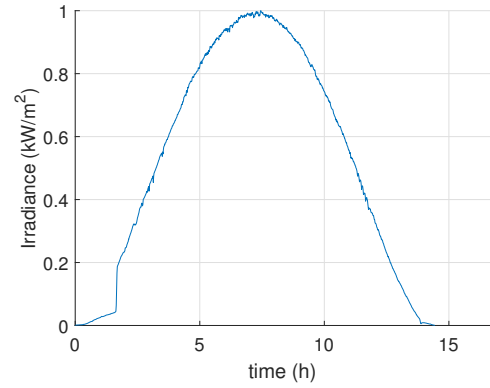


Fig. 7. Irradiance profile during a sunny day

Fig. 9 shows the evolution of the output voltages of the inverters, as well as the active and reactive power flows that corresponds to the irradiance profile for a sunny day (Fig. 7). The output behavior of the inverters is analyzed in the PowerFactory model, as for the static production values, with the same predefined parameters as in the test platform. The results obtained also present a similar evolution, although the voltage differences between phases cannot be reproduced with PowerFactory due to an small initial unbalance in the test platform.

V. CONCLUSIONS

In this manuscript, an unbalanced LV feeder caused by the grid-tied inverters has been studied for different values

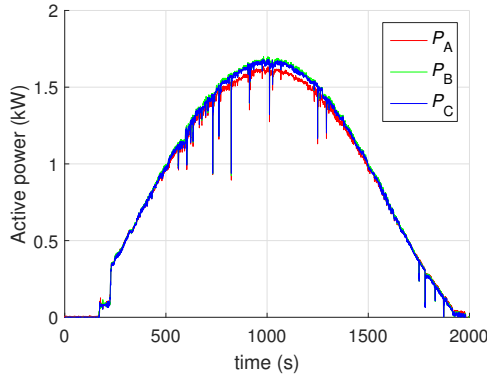


Fig. 8. Time variation of the active power at PCC2 during a sunny day

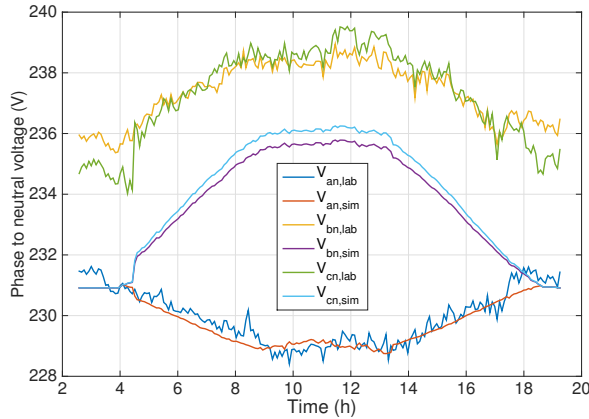


Fig. 9. Time variation of the phase-to-neutral voltages at PCC2 during a sunny day

of active and reactive power production. A test bench that reproduces an specific LV feeder has been designed for this study and its behavior compared to its numerical model. This comparison has illustrated the reproduction of a similar behavior between the experimental work and the simulated model but also the difficulties of obtaining reliable results in simulations, due to the lack of information for some of the parameters of the system. In addition, the effect of local neutral point displacement has been exhibited and explained. It changes the shape of the phase-to-neutral voltages in magnitude and phase and can aggravate the unbalance situation.

ACKNOWLEDGEMENT

This research is financed by the Walloon region in the framework of the PREMASOL project (C-6829).

REFERENCES

- [1] P. P. Barker and R. W. De Mello, "Determining the impact of distributed generation on power systems. I. Radial distribution systems," *Power Eng. Soc. Summer Meet.*, vol. 3, pp. 1645-1656, 2000.
- [2] V. Klonari, F. Vallee, O. Durieux, J. Lobry, "Probabilistic tool based on smart meters data to evaluate the impact of distributed photovoltaic generation on voltage profiles in low voltage grids," *Solar Integraton Workshop*, 2013.

- [3] V. Klonari, F. Vallee, O. Durieux, Z. De Greve, J. Lobry, "Probabilistic Modeling of Short Term Fluctuations of Photovoltaic Power Injection for the Evaluation of Overvoltage Risk in Low Voltage Grids," *IEEE International Energy Conference (ENERGYCON)*, pp. 897-903, 2014.
- [4] F. Olivier, P. Aristidou, D. Ernst, and T. Van Cutsem, "Active Management of Low-Voltage Networks for Mitigating Overvoltages Due to Photovoltaic Units," *IEEE Trans. Smart Grid*, pp. 1-9, 2015.
- [5] Ioulia T. Papaioannou, Minas C. Alexiadis, Charis S. Demoulias, Dimitris P. Labridis, and Petros S. Dokopoulos, "Modeling and Field Measurements of Photovoltaic Units Connected to LV Grid. Study of Penetration Scenarios," *IEEE Trans. Power Delivery*, vol. 26, no. 2, pp. 979-987, April 2011.
- [6] S. Papathanassiou, N. Hatziaargyriou, K. Strunz, "A Benchmark Low Voltage Microgrid Network," *CIGRE Symposium*, 2005.
- [7] T. Geury, and J. Gyselinck, "Emulation of photovoltaic arrays with shading effect for testing of grid- connected inverters," *Proc. 2013 EPE European Conference on Power Electronics and Applications*, pp. 1-9.
- [8] M. G. Villalva, J. R. Gazoli, and E. R. Filho, "Comprehensive approach to modeling and simulation of photovoltaic arrays," *IEEE Trans. Power Electron.*, vol. 24, no. 5, pp. 1198-1208, May 2009.
- [9] I. R. Balasubramanian, S. Ilango Ganesan, and N. Chilakapati, "Impact of partial shading on the output power of pv systems under partial shading conditions," *IET Power Electron.*, vol. 7, no. 3, pp. 657-666, 2014.
- [10] B. Metz-Noblat, F. Dumas, and C. Poulain, "Calculation of short-circuit currents," *Schneider Electric, Grenoble, France, Tech. Rep. TR-0158*, p. 13, 2005.
- [11] E. Troester, "New german grid codes for connecting pv systems to the medium voltage power grid," *2nd Int. Work. Conc. Photovolt. Power Plants Opt. Des. Prod. Grid Connect.*, pp. 1-4, 2009.
- [12] R. Lopez-Erauskin, T. Geury, A. Gonzalez, J. Gyselinck, M.E. Hervas, A. Fabre, "Testing the Enhanced Functionalities of Commercial PV Inverters Under Realistic Atmospheric and Abnormal Grid Conditions," *Solar Integraton Workshop*, 2015.
- [13] R. A. Mastromauro, M. Liserre, and A. D. Aquila, "Single-phase grid-connected photovoltaic systems with power quality conditioner functionality," *European Conference on Power Electronics and Applications*, pp. 1-11, 2007.
- [14] R. Kabiri, D. G. Holmes, and B. P. McGrath, "The influence of pv inverter reactive power injection on grid voltage regulation," *IEEE 5th Int. Symp. Power Electron. Distrib. Gener. Syst.*, pp. 1-8, Jun. 2014.

On the Modelling of LV and MV Electrical Networks in the PLC Frequency Range

Christopher Wawrzyniak

University of Mons

Faculty of Engineering

Electromagnetism and Telecom Unit

Bvd Dolez 31, 7000 Mons

Belgium

Véronique Moeyaert

University of Mons

Faculty of Engineering

Electromagnetism and Telecom Unit

Bvd Dolez 31, 7000 Mons

Belgium

François Vallée

University of Mons

Faculty of Engineering

Power Electrical Engineering Unit

Bvd Dolez 31, 7000 Mons

Belgium

Email: christopher.wawrzyniak@umons.ac.be Email: veronique.moeyaert@umons.ac.be Email: francois.vallee@umons.ac.be

Abstract—This paper presents the modelling approaches used to simulate the transfer function of a typical electrical network composed with cables, transformers and photovoltaic panels. More specifically, it takes place in the context of evaluating the capacity of the power network infrastructure to support PLC technologies. In this way, cables and transformers are modelled based on the two-port network approach. In order to simulate the behavior of the photovoltaic panel and the associated converter, a single diode model is proposed. A comparison between model results and measurement is performed to show the coherence of the results. Finally, in order to evaluate the impact of the network devices on the transfer function, a classical distribution system topology is studied.

I. INTRODUCTION

Concerns about the worldwide energy crisis are obvious. In this context, the use of green energies stands out as a possible alternative to fossil fuels whose resources are dwindling. As part of electrical networks, these so-called renewable energies are characterized by a fluctuating voltage-delivery behaviour difficult to predict. Therefore, in order to maintain the efficiency of these networks (voltage support within the limits recommended by the European standard EN-50160, limitation of network congestions...), power line communications (PLC) are a means to make the electrical system smarter by improving its observability and ensuring a communication between control devices [1]. Within these networks, many voltage and current control equipment exist such as capacitor banks, tap-changer transformers or reactive power compensation equipment based on power electronics. Their presence can have a non-negligible impact on the operation of PLC technologies due to specific transient operations that those control devices can generate. In this context, we propose to study the impact of some specific devices (transformers, photovoltaic panel, cables...) on the powerline transmission channel transfer function in the case of LV and MV networks [2]. Indeed, the transfer function of a transmission channel is highly dependent on the impedances encountered on the whole line which tends to induce a frequency-dependent attenuation of the network. In addition, power fluctuations generated by the PV panels lead to potentially large variations of the impedances within the network, involving constant changes in the transmission

channel transfer function. Therefore, it seems essential to consider the frequency dependence of generation and control equipment in order to estimate and to ensure a given reliability of data communications. In particular, the injection of power from PV panels, wind turbines, micro-cogeneration units, etc. on the distribution network tends to intensify this phenomenon. Let us insist on the industrial purpose of this project, which is to allow the network operator to have an estimate of the PLC communication robustness in the current operating environment of distribution networks. This information is vital to ensure reliable "real-time" coordination of control devices and modern network monitoring. In this contribution, the focus is set to the study and the modelling of photovoltaic panels, transformers and cables.

Power Line Communications are grouped into two families: Narrowband and Broadband PLC. Narrowband PLC is practically used for low bandwidth communication applications as control, command and monitoring. The frequency range is between 9 - 148.5 kHz in Europe (CENELEC standard) and 150 - 450 kHz in the USA. Broadband PLC uses a much wider frequency band (between 1.6 MHz to 100 MHz [3]) and is mainly employed for in-home high-speed data transfer applications.

In this paper, the modelling approaches used to model a typical electrical network are firstly introduced. In the case of cables and transformers, it is usually based on the two-port network model from which any device can be described by its transmission matrix parameters, which are frequency dependent. These parameters can be obtained by performing some specific measurements. The photovoltaic panel and the associated converter are represented using a model based on their physical characteristics. In fact, each photovoltaic cell can be modeled using a single diode model. Hence, a PV conversion chain is modelled as a current source in parallel with a diode. The PV parameters are extracted from a manufacturer datasheet. The converter and the LCL filter are both simulated using MatLab/Simulink. Secondly, the measurement equipment and a methodology to obtain the modelling parameters of the transmission matrix (for transformers and cables) are presented. A method based on the measurement of the

reflection coefficient at the input of the device when the output is successively open and short-circuited is used. Another measurement equipment and a methodology to measure the performance of the PV unit are also proposed. For each equipment, a comparison between each model and measurements is performed in order to conclude about the efficiency of the modelling approaches. Finally, a representative topology of LV systems is simulated and a time dependant transfer function is evaluated in the PLC frequency range.

II. MODELLING APPROACHES OF ELECTRICAL NETWORK DEVICES

A. Power cables modelling

1) *Transmission Line Theory*: In the literature, most of the methods proposed to study a transmission line are based on the transmission line theory ([4]-[10]). Following this theory, an elementary line transmission cell can be represented as in Fig.1 and the time dependent telegraphers equations can be applied as follows:

$$-\frac{\partial u(z,t)}{\partial z} = ri + l \frac{\partial i(z,t)}{\partial t}, \quad -\frac{\partial i(z,t)}{\partial z} = gu + c \frac{\partial u(z,t)}{\partial t} \quad (1)$$

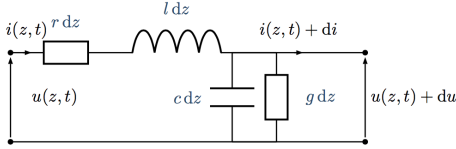


Fig. 1. Elementary line transmission cell

In these equations z represents the position on the line, t the time and the linear resistance r (Ω/m), inductance l (H/m), capacitance c (F/m) and conductance g (S/m) are the primary line parameters.

A transmission line can also be described by its secondary parameters, the characteristic impedance \underline{Z}_c and the propagation constant $\underline{\gamma}$, which depend on the primary parameters and are given by:

$$\underline{Z}_c = \sqrt{\frac{r + j\omega l}{g + j\omega c}}, \quad \underline{\gamma} = \sqrt{(r + j\omega l)(g + j\omega c)} \quad (2)$$

where ω represents the angular frequency.

2) *ABCD matrix*: The knowledge of the secondary parameters allows to describe the relationship between the input voltage U_1 and current I_1 , and output voltage U_2 and current I_2 of a two-port network using the frequency dependent chain parameters matrix A , B , C and D as represented in Fig. 2:

$$\begin{bmatrix} U_1 \\ I_1 \end{bmatrix} = \begin{bmatrix} A(f) & B(f) \\ C(f) & D(f) \end{bmatrix} \begin{bmatrix} U_2 \\ I_2 \end{bmatrix} \quad (3)$$

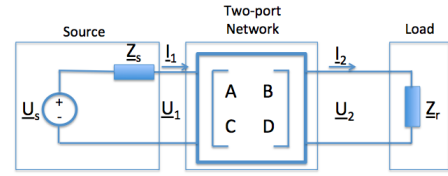


Fig. 2. Two-port network connected to a source and a load

The transfer function of the two-port network can then be given by:

$$\underline{H} = \frac{U_2}{U_s} = \frac{\underline{Z}_r}{A\underline{Z}_r + B + C\underline{Z}_r\underline{Z}_s + D\underline{Z}_s} \quad (4)$$

where \underline{Z}_s is the source impedance, \underline{Z}_r the load impedance and A , B , C and D are calculated as follows, x being the length of the line:

$$T_j = \begin{bmatrix} A & B \\ C & D \end{bmatrix} = \begin{bmatrix} \cosh(\underline{\gamma}x) & \underline{Z}_c \sinh(\underline{\gamma}x) \\ \frac{1}{\underline{Z}_c} \sinh(\underline{\gamma}x) & \cosh(\underline{\gamma}x) \end{bmatrix} \quad (5)$$

3) *Derivations on the line*: The chain matrix that we have considered previously does not take into account the eventual presence of derivation branches on the line. Fig. 3 shows a branch of length x_{branch} located at a distance x_1 of the source and x_2 of the load and terminated by load impedance \underline{Z}_{branch} .

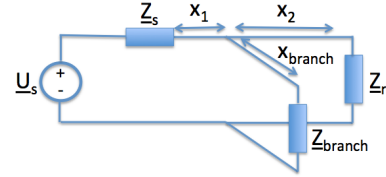


Fig. 3. Transmission line with one branch

In this context, this branch can be replaced by an equivalent impedance \underline{Z}_{eq} placed on the main line (Fig. 4) and given by the following expression:

$$\underline{Z}_{eq} = \frac{A_{branch}\underline{Z}_{branch} + B_{branch}}{C_{branch}\underline{Z}_{branch} + D_{branch}} \quad (6)$$

where A_{branch} , B_{branch} , C_{branch} and D_{branch} are the transmission matrix parameters of the branch and \underline{Z}_{branch} is the load at the end of the branch.

Once this step is done, we can split the transmission line into four areas when dealing with the representation given in Fig. 4, each zone being characterized by its own chain matrix (x_1 and x_2 inside T_j matrices are related to Fig. 3):

$$T_1 = \begin{bmatrix} 1 & \underline{Z}_s \\ 0 & 1 \end{bmatrix} T_2 = \begin{bmatrix} \cosh(\underline{\gamma}_1 x_1) & \underline{Z}_{c1} \sinh(\underline{\gamma}_1 x_1) \\ \frac{1}{\underline{Z}_{c1}} \sinh(\underline{\gamma}_1 x_1) & \cosh(\underline{\gamma}_1 x_1) \end{bmatrix} \\ T_3 = \begin{bmatrix} 1 & 0 \\ \frac{1}{\underline{Z}_{cq}} & 1 \end{bmatrix} T_4 = \begin{bmatrix} \cosh(\underline{\gamma}_2 x_2) & \underline{Z}_{c2} \sinh(\underline{\gamma}_2 x_2) \\ \frac{1}{\underline{Z}_{c2}} \sinh(\underline{\gamma}_2 x_2) & \cosh(\underline{\gamma}_2 x_2) \end{bmatrix} \quad (7)$$

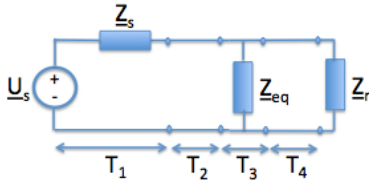


Fig. 4. Equivalent representation of a transmission line with one branch

The transmission matrix T from the source to the load is then simply the product of the transmission matrices of each zone, n being the total number of zones:

$$T = \prod_{j=1}^n T_j \quad (8)$$

4) *Equipment and methodology*: In order to carry out the measurements of the parameters needed for the modelling procedure an HP 4195A Network Analyzer was operated in the frequency range 20 Hz to 10 MHz. The accuracy of the Network Analyzer is ± 1 dB for frequencies under 200 MHz. The number of points taken by the Network Analyzer is 401 which means that the frequency step between two points is 24.94 kHz. Post processing is performed by MatLab.

In the literature, a couple of methods for measuring secondary parameters of a cable exist [2]. Most of them are based on the determination of the cable impedance with load in open circuit Z_{open} and short-circuit Z_{short} :

$$Z_c = \sqrt{Z_{open} Z_{short}}, \quad \gamma = \frac{1}{l} \tanh^{-1} \sqrt{\frac{Z_{short}}{Z_{open}}} \quad (9)$$

The determination of Z_{open} and Z_{short} can be realized by two different methods. The first one is based on a direct measurement of each impedance thanks to an impedance measurement kit. The second one uses the measurement of the reflection coefficient at the input of the cable when the output is opened and short-circuited, S_{11open} and $S_{11short}$ respectively. Indeed, it can be shown that Z_{open} and Z_{short} can be obtained in that case as follows:

$$Z_{short} = Z_{VNA} \frac{1 + S_{11short}}{1 - S_{11short}} \quad (10)$$

$$Z_{open} = Z_{VNA} \frac{1 + S_{11open}}{1 - S_{11open}} \quad (11)$$

where,

- S_{11open} is the reflection coefficient at the input of the two-port network when its output is opened;
- $S_{11short}$ is the reflection coefficient at the input of the two-port network when its output is short-circuited;
- Z_{VNA} is the access impedance of the network analyzer considered to be equal to 50 Ω ;

B. Transformers modelling

The transformer is one of the most important device used in the power network infrastructure. It is employed to increase or decrease the voltage and do the interface between medium voltage (10 or 15kV) and low voltage (230/400V) distribution systems or between two low voltage networks. In order to simulate the behavior of transformers, the same approach as for cables is considered. Indeed, in the literature, this approach has already been established up to 50 Hz [11]. In [12], the validity of the model has even been validated up to 10 MHz for LV(400V)/LV(230V) transformers. Thereby, it is possible to show that a transformer can be modelled, with a good approximation, by an equivalent circuit that has a similar form compared to the one of a transmission line model (Fig. 1).

C. Photovoltaic unit modelling

Since a decade, the installation of photovoltaic units, that are characterized by a fluctuating generation difficult to predict, is increasing especially to ensure the recommendations of the Horizon 2020 programme. Practically, the associated conversion unit generates harmonics that can disturb the network and, in the context of data transmission, induces variations in the impedance spectral content. As a consequence, it can add some changes in the transfer function of the PLC channel. Thereby, it is crucial to give a particular interest to this device in order to study its impact on the PLC channel. Figure 5 shows a typical PV unit scheme which is composed of a photovoltaic panel followed by a buck-boost converter in order to adapt the voltage at the input of the DC/AC converter followed by a LCL filter. A Maximum Power Point Tracking (MPPT) algorithm is used to generate the maximum power from the PV chain. In this section, a single diode model is firstly proposed

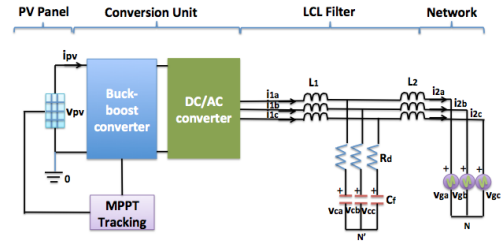


Fig. 5. PV unit scheme

to simulate the photovoltaic panel. Secondly, the associated conversion unit is simulated using MatLab/Simulink.

1) *Single diode model*: A photovoltaic panel is composed of photovoltaic cells connected in parallel and in series. In the literature, some models exist in order to simulate the behavior of a photovoltaic cell ([13]-[17]). In this paper, the focus has been set on the single diode model [13]. This model is based on the statement that a photovoltaic cell is composed of a single p-n junction and can thus be modelled as a current source in parallel with a diode (Fig. 6).

The current at the output of the PV cell is given by [14]:

$$I_{pv} = I_{ph} - \exp((V_{pv} + I_{pv} \cdot R_s) \cdot K_1 + K_2) \quad (12)$$

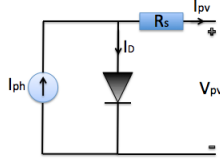


Fig. 6. Single diode model

considering that the thermal voltage V_T is very small compared to the voltage across the diode. In this equation, $K_1 = \frac{q}{nk_B T}$ and $\exp(K_2) = I_o$. n is the diode factor, k_B the Boltzmann constant [J/K], T the temperature [K] and q the electron charge [C]. I_{ph} is the photocurrent [A], I_o the diode saturation current [A], I_D the current through the diode [A], V_{pv} the PV cell voltage [V], I_{pv} the PV cell current [A] and R_s the series resistance which represents the resistive losses [Ω]. There are four unknowns in these equations: K_1 , K_2 , R_s and I_{ph} that can be obtained by the knowledge of the short-circuit current (I_{sc}), the open circuit voltage (V_{oc}) and the PV current and voltage at the Maximum Power Point (I_m and V_m) ([14][15]):

$$\begin{cases} K_1 = -\frac{I_m}{V_m(I_m - I_{ph})} \\ R_s = \frac{\log(\frac{I_{ph} - I_m}{I_{ph}}) - V_m K_1 + V_{oc} K_1}{I_{ph}} \\ K_2 = \frac{I_m K_1}{\log(I_{ph}) - V_{oc} K_1} \\ I_{ph} = I_{sc} + \exp((I_{sc} R_s) K_1 + K_2) \end{cases} \quad (13)$$

In these equations, V_{oc} and I_{sc} are dependent on the irradiance E_i (W/m^2) and the temperature T_i ($^{\circ}C$):

$$V_{oc} = V_{oc(stc)} + TC_v(T_i - T_N) \quad (14)$$

$$I_{sc} = \frac{E_i}{E_{iN}} I_{sc(stc)} (1 + \frac{TC_i}{100} (T_i - T_N)) \quad (15)$$

where E_{iN} and T_N represent respectively the irradiance and the temperature in the standard test conditions stc ($E_{iN} = 1000 W/m^2$, $T_N = 25^{\circ}C$). TC_i is the temperature coefficient of I_{sc} ($\%/^{\circ}C$) and TC_v is the temperature coefficient of V_{oc} ($V/^{\circ}C$).

2) *PV Conversion unit and MPPT algorithm*: Once the photovoltaic panel has been modeled, the associated conversion unit has to be defined. Fig.7 shows the complete chain composed of the photovoltaic panel, the buck-boost converter, the DC/AC converter, the LCL filter and the electrical network (modeled here as an ideal 230V voltage source). In order to generate the maximum power from the photovoltaic panel, a MPPT algorithm has been implemented in MatLab/Simulink [18].

III. EXPERIMENTAL RESULTS

A. Comparison between measurements and model for the cables and transformers

The power cables and transformers are both modelled using the transmission line theory and, more specifically, the

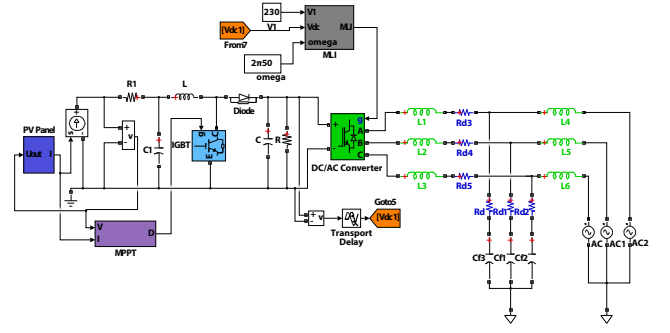


Fig. 7. Complete chain of a photovoltaic unit

transmission matrix. As we have shown in section II-A1, the advantage of modelling these elements by using the same approach allows to simulate complex topologies by a cascade of transmission matrices. In order to conclude about the efficiency of the method, a validation topology composed of a 100 m XFVB-F2 3x1.5 mm^2 cable, a 80 m XVB-F2 3x1.5 mm^2 cable and a 100 kVA Belgian transformer is proposed (Fig.9). The 100 kVA transformer shown in Fig.8 is connected from two phases of the three phase 400 V LV side (phase b_1 and neutral) to a 100 m XFVB-F2 3x1.5 mm^2 cable. Two phases of the three phase 230 V LV side (phases b_2 and c_2) are also connected to a 80 m XVB-F2 3x1.5 mm^2 cable.

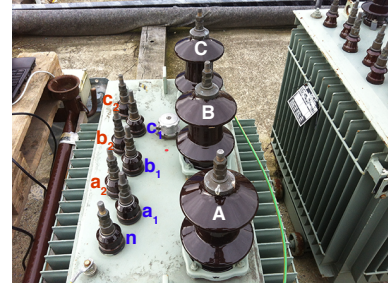


Fig. 8. Typical 100 kVA Belgian transformer with the two LV sides (three phase 230 V (a2-b2-c2) and 400 V (a1-b1-c1-n) respectively) and the MV side

Fig. 10 shows the comparison between the directly measured and the modelled transfer functions of the complete chain. Note that the model of the global chain is obtained by the product of the three transmission matrices ($T_1 \times T_2 \times T_3$). The transmission matrices parameters have been obtained thanks to S parameters measurements.

We can see a fairly good agreement between the simulations and measurements in our frequency range of interest (10 MHz max due to the baluns of the measurement setup), particularly in the NB PLC range. Consequently, it can be concluded on the efficiency of the two-port network model. Indeed, the modeled transfer function appears to be very good up to 1 MHz which includes the narrowband frequency range (between 30 kHz and 500 kHz) and in the frequency range 3 MHz - 7 MHz. In

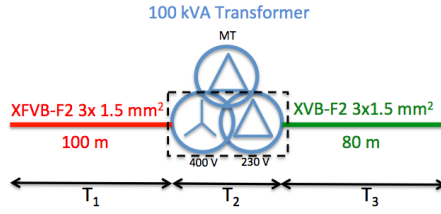


Fig. 9. Topology proposed to validate the two-port network model for a global LV chain

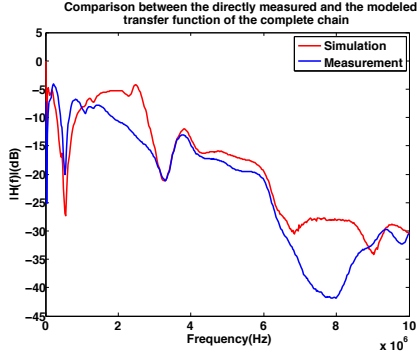


Fig. 10. Comparison between the directly measured and the modeled transfer function of the complete chain

the other frequency ranges, some differences appear and can be due to the limits of the 50 Hz transformer model when working in the narrowband PLC frequency range.

B. Comparison between measurements and model for the PV module

The measurement setup used to validate the single diode model is illustrated in Fig.11. It is composed of four PV units connected in series from the DROBen Energy company. The entire structure charges a variable load. A multimeter (Agilent 34401A) is used to measure the current and voltage at the load position. By varying the load value, the evolutions of current, impedance and power versus voltage are obtained. The characteristics of a PV module are given in [19]. An irradiance

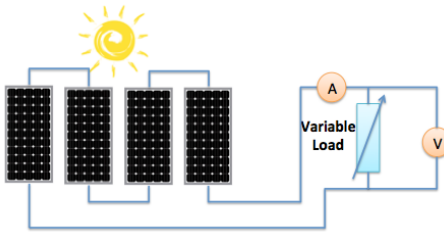


Fig. 11. Measurement setup

of $750W/m^2$ and a temperature of $40^\circ C$ were measured via a probe. Fig. 12 a, b and c show a comparison between the measured evolution of current, power and impedance versus voltage respectively and the simulated ones. The simulations

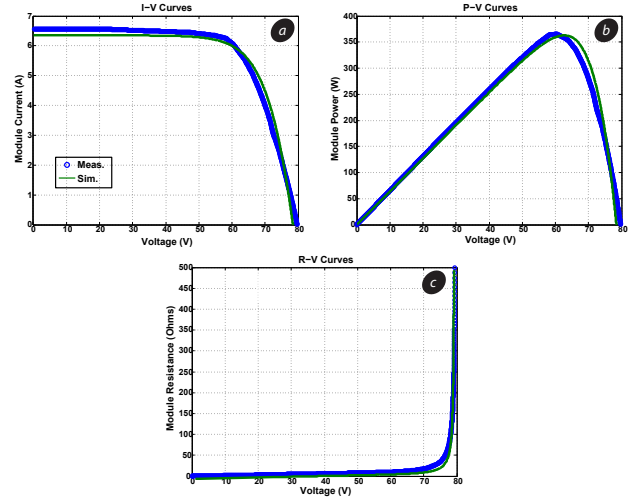


Fig. 12. Comparison between the simulated performance of the PV unit and the measurements

and measurements are very close to each other. In the studied configuration, the installation provides a power of around 360 W at the Maximum Power Point. The model has then been implemented in MatLab/Simulink and completed by its conversion stage (Fig.5) in order to obtain the access impedance of the global unit. The parameters values used for the simulation are given in table I [20][21].

Component	Value	Component	Value
f_{fund}	50Hz	L_1, L_2, L_3	500 μH
$f_{DC/ACconv}$	10kHz	L_4, L_5, L_6	130 μH
R_1	1 Ω	R_d, R_{d1}, R_{d2}	0.3 Ω
L	100mH	R_{d3}, R_{d4}, R_{d5}	0.1 Ω
C_1	500 μF	C_{f1}, C_{f2}, C_{f3}	99 μF
C	10mF	AC voltage sources	230V
R	500 Ω		

TABLE I

COMPONENTS VALUES OF THE PV CONVERSION UNIT (CF. FIG.7)

C. Simulation of complex topology

Now that we have validated a model for transformers, cables and PV units it is possible to simulate the behavior of a complex topology including each element. An example of topology that takes into account the presence of a photovoltaic unit is proposed (Fig.13) and its transfer function is simulated (Fig.14) in the Narrowband PLC frequency range (between 0 Hz and 500kHz) for a constant irradiance of $750W/m^2$ and a constant temperature of $40^\circ C$. Note that each house is taken into account by the way of an impedance of 100 Ω in the proposed simulation. It can be seen in Fig. 14 that the presence of the PV unit in the network leads to variations in the transfer function evolution. Some important variations are observed at the time corresponding to the end of the transient due to the MPPT algorithm ($t = 0.22s$). Consequently, the higher the PV units number in the topology, the higher the attenuation. It is an important observation for the study of the

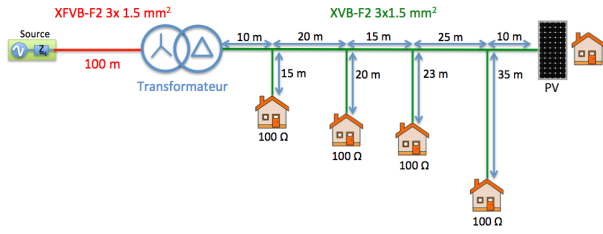


Fig. 13. Example of a topology with 4 branches

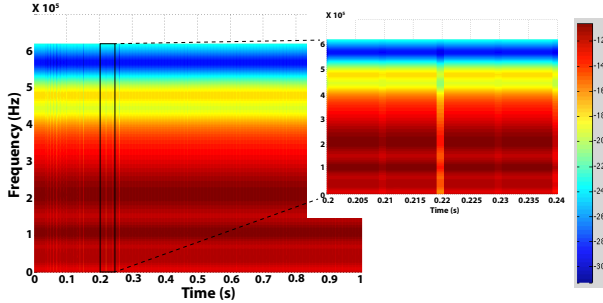


Fig. 14. Transfer function for a topology with 4 branches and terminated with a PV unit

PLC communication performance which can change according to these variations.

IV. CONCLUSION

In this paper, a method for transfer function modelling of power cables based on the two-port network model is applied. The estimation of parameters needed for the model has been realized by determining secondary parameters of XVB-F2 and XFVB-F2 $3 \times 1.5 \text{ mm}^2$ power cables. A method based on the reflection coefficient measurement at the input of the cable has been proposed to obtain these parameters. The application of the modelling method to transformers has shown a good agreement between the measurements and the model and seems to be a good method to be investigated for transformers modelling. Consequently, a simulation tool using the two-port network model can be easily developed to simulate an elaborate power network topology including transformers. Also, a method for modelling the performance of a PV module based on a single diode model was applied. The parameters needed for the model have been extracted by the way of the manufacturer datasheet. The model has shown a good agreement between the measurements and the simulation. Then, the PV model has been implemented in a MatLab/Simulink simulator taking into account a buck-boost converter, a DC/AC converter and a LCL filter in order to simulate the global chain impedance of a PV unit. The component values of the model have been taken according to some references in the domain. Finally, the resulting impedance has been used in the transfer function model based on a two-port network model in order to simulate the impact of this impedance versus time and frequency on a simple topology composed with 4 branches. It

has been concluded that the higher the PV units number in the topology, the higher the attenuation.

ACKNOWLEDGMENT

The research leading to these results has received the financial support of the F.R.S.-FNRS (F.R.I.A.). The Electromagnetism and Telecommunication Unit and the Power Electrical Engineering Unit are part of the Chaire ORES at FPMs-UMONS.

REFERENCES

- [1] H. Ferreira et al., *Power line communications - Theory and applications for narrowband and broadband communications over power lines*, Wiley, 2010.
- [2] L. Wang et al., *Performance analysis of Broadband Power line Communications under impulsive noise and crosstalk*, September 2012.
- [3] L. Lampe et al., *Power Line Communications - Principles, Standards and Applications from Multimedia to Smart Grid*, Wiley, Second Edition, 2016.
- [4] H. Meng et al., *Modeling of transfer characteristics for the broadband power line communication channel*, IEEE Transactions on power delivery, vol. 19, n 13, pp. 1057 - 1064, 2004.
- [5] P. Mlynek et al., *Power line cable transfer function for modelling power line communication system*, Journal of electrical engineering, vol. 62, n 2, pp. 104 - 108, 2011.
- [6] R.M. Rodrigues et al., *Transfer function estimation of telephone lines from input impedance measurements*, IEEE Transactions on instrumentation and measurement, vol. 61, n 1, pp. 43 - 54, 2011.
- [7] S. Khan et al., *Characterization of indoor power lines as data communication channels experimental details and results*, International journal of electrical and computer engineering, vol. 4, pp. 647 - 652, 2009.
- [8] S. Galli et al., *A novel approach to the modeling of the indoor power line channel - Part II: Transfer function and its properties*, IEEE Transactions on power delivery, vol. 20, n 13, pp. 1869 - 1878, 2005.
- [9] T. Esmailian et al., *In-building power lines as high-speed communication channels: channel characterization and a test channel ensemble*, International journal of communication systems, vol. 16, n 5, pp. 381 - 400, 2003.
- [10] A. Vinck et al., *Cooperative multihop power line communications*, 16th IEEE International symposium on power line communications and its applications, pp. 1 - 6, 2012.
- [11] Teshmont Consultants LP, *Transformer modelling guide*, Report, 2014.
- [12] C. Wawrzyniak et al., *Power transformer modeled as a transmission line for simple simulation of complex topologies in the PLC frequency range*, IEEE International symposium on power line communications and its applications, March 2016.
- [13] S. Vijayakumar, *Behaviour of Photovoltaic Systems During Grid Disturbances*. Department of Electrical Engineering, Indian Institute of Science, India, June 2012.
- [14] M. C. Di Piazza, *Identification of photovoltaic array model parameters by robust linear regression methods*. International Conference on Renewable Energies and Power Quality, Valencia (Spain), 15th to 17th April, 2009.
- [15] C. Wawrzyniak et al., *Modeling approach of a photovoltaic conversion in the PLC frequency range*, International Conference and Exhibition on Electricity Distribution (CIRED), June 2016.
- [16] A.J. Anderson, *Photovoltaic Translation Equations: A New Approach*. Final Subcontract Report, Sunset Technology, Janvier, 1996.
- [17] E. I. Ortiz-Rivera, *Analytical Model for a Photovoltaic Module using the Electrical Characteristics provided by the Manufacturer Data Sheet*. Power Electronics Specialists Conference, IEEE 36th, 2005.
- [18] C. Bernard et al., *Panneau photovoltaïque et algorithme MPPT base de logique floue*. Report, Automn 2009.
- [19] DROBen Energy. "Modulos Fotovoltaicos - Droben CM 130 Wp 15 Wp", <http://www.drobenenergy.com/producto130.php>, (2016).
- [20] E. Jimenez et al. "A Dynamic Maximum Power Point Tracker using Sliding Mode Control", 11th Workshop on Control and Modeling for Power Electronics, pp. 1 - 5, (2008).
- [21] E. Figueres et al. "Sensitivity Study of the Dynamics of Three-Phase Photovoltaic Inverters With an LCL Grid Filter", IEEE Transactions on Industrial Electronics, vol. 56, No. 3, pp. 706 - 717, (2009).

Modelling of DC-DC Converter for System Level Studies

Abel A. Taffese^{*1}, Erik C. W. de Jong ^{**2} and Elisabetta Tedeschi^{*3}

^{*}Norwegian University of Science and Technology, Department of Electric Power Engineering, NO-7491 Trondheim, Norway

^{**}Eindhoven University of Technology, Department of Electrical Engineering, P.O. Box 513, 5600MB, Eindhoven, The Netherlands

¹abel.taffese@ntnu.no, ²e.c.w.de.jong@tue.nl, ³elisabetta.tedeschi@ntnu.no

Abstract—With the shift in renewable energy production to far offshore locations, the need for HVDC solution is inevitable. A number of point-to-point links are being commissioned or planned for the near future. Interconnection of such point-to-point links offers additional economic and security incentives. However, the links in operation today are not all compatible, due to differences in voltage levels, grounding schemes, etc. DC-DC converter offers the possibility of interconnecting these incompatible links to create a multi-terminal/meshed system. With this drive, DC-DC converters are gaining more and more attention. This paper presents a review of research on DC-DC converters considering aspects like requirements, topologies, and modeling in system level studies.

Keywords—DC-DC Topology; Model; HVDC

I. INTRODUCTION

In December 2015, The United Nations Climate Change Conference was held in Paris where 195 countries *unanimously* adopted the Paris Agreement [1]. This will likely fuel the already blooming renewable energy industry. To meet this new target, the boundaries of renewable energy production will expand to remote areas where the resources are abundant. An enabling technology for remote renewable integration is HVDC transmission, which is expected to evolve the traditional power system into a hybrid AC/DC grid [2]. However, each HVDC link is individually optimized. There are a number of technical

choices in the implementation of an HVDC link. Among the choices are the converter technology, grounding scheme, and operating voltage. Converter technology is, currently, either Line Commutated Converter (LCC) or Voltage Source Converter (VSC) in its broadest sense. Grounding schemes include monopole, symmetric monopole, and bi-pole, which are further classified based on whether ground or metallic return is used. To date, there is no regulation on the operating voltage, although research groups like the Cigre-B4/C1.65 are working to develop recommended voltage levels. The combination aforementioned choices lead to many possible end designs for the Point-to-Point (P2P) links limited, currently, by the number of major players in the industry. The first multi-terminal grid is expected to be offshore, particularly in the North Sea [3]. A recent study showed that there is a possibility to connect the P2P links in the North Sea [4]. Table 1, taken from [4] and adapted to include the grounding schemes, shows the existing HVDC links in southern part of the North Sea. The table shows that there are five different voltage levels in the area. This case is a good example of the challenges of interconnecting P2P links because it exhibits most of the possible combinations; it has converter technology incompatibility, DC voltage difference, and different grounding schemes. There is a possibility to connect the ones operating at ± 320 kV given other technical challenges are overcome. In [4], a topology utilizing hubs is proposed with the aim of benefiting from the

Table 1 HVDC Links in the North Sea [4]

Name	Country	Length (km)	Power (MW)	Voltage (kV)	Year	Converter Type	Pole Configuration
NorNed	NL-NO	580	700	± 450	2009	LCC	Sym. Mono
BorWin1	DE	200	400	± 150	2012	VSC	Sym. Mono
DolWin1	DE	165	800	± 320	2015	VSC	Sym. Mono
BorWin2	DE	200	800	± 300	2015	VSC	Sym. Mono
SylWin1	DE	205	864	± 320	2015	VSC	Sym. Mono
HelWin1	DE	130	576	± 250	2015	VSC	Sym. Mono
HelWin2	DE	130	690	± 320	2015	VSC	Sym. Mono
DolWin2	DE	135	900	± 320	2016	VSC	Sym. Mono
DolWin3	DE	160	900	± 320	2017	VSC	Sym. Mono
BorWin3	DE	200	900	± 320	2019	VSC	Sym. Mono
COBRACable	DK-NL	350	700	± 320	2019	VSC	Sym. Mono
NordLink	DE-NO	623	1400	± 525	2020	VSC	Bi-pole

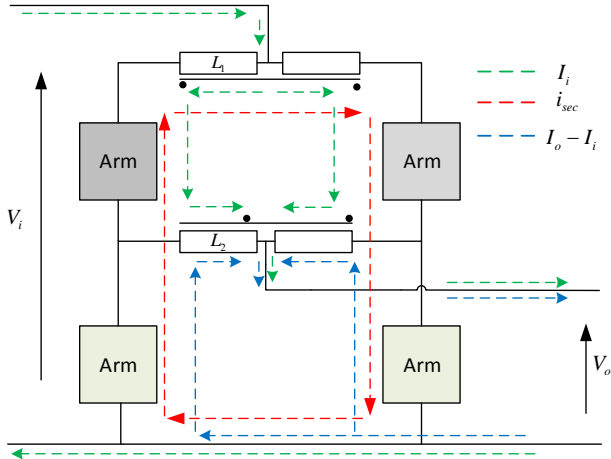


Fig. 1 Modular Multilevel DC Converter

geographical proximity of the farms. Although the final decision will be based on economic benefits, DC-DC converters provide the technical solution for interconnecting the remaining links. However, such converters are not well established for high voltage, high power applications. Moreover, limited research effort is put into the development of correct models for system level studies. This paper presents a review of the DC-DC converter for HVDC application. The rest of this paper is organized as follows. The next section outlines requirements for DC-DC converters followed by a review of selected few topologies that are considered suitable for high power HVDC applications. Section IV discusses the models for DC-DC converters for system level studies.

II. REQUIREMENTS FOR DC-DC CONVERTERS

There are different sets of requirements placed on DC-DC converters for solving each of the challenges mentioned in the previous section. Ref. [5] addresses requirements for DC-DC converters under different applications. The major requirements, which vary with the type of application, are input-output voltage ratio or stepping ratio, need of galvanic isolation, and bi-directional power flow capability. In the remainder of this paper, stepping ratio is defined as low when it is below 1.5 and high when it is above 5 [5]. In order for the DC-DC converter to become economically sound, it also has to offer additional features such as fault blocking and isolation. This is very important since the current difficulty in the implementation of MTDC is partly due to absence of DC circuit breakers at acceptable ratings and price. High-level requirements for selected application are presented in subsequent sections.

A. Power Flow Control

Power flow controller is required in a DC system with more lines than converters [6]. For this application, the primary role of the DC-DC converter is to adjust the DC voltage on the two sides in order to achieve the desired power flow on the link. The converter plays the role of phase angle regulator in AC system. The stepping ratio is normally close to one unless the converter is also used for voltage matching. Therefore, a low ratio

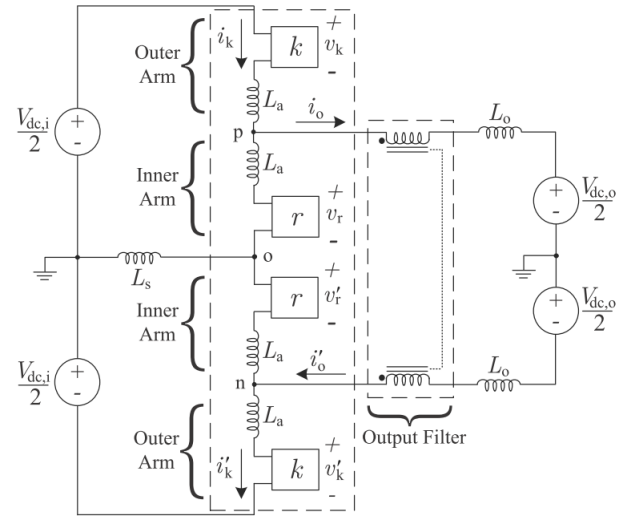


Fig. 2 Single String DC-MMC [9]

converter with bi-direction power flow capability is required in this application.

B. Voltage Level Matching

If the sole purpose of the converter is to match the voltage on the two sides, the main requirements are to produce the proper voltage ratio and meet the isolation needs of the application. Bi-directional power flow might be required depending on application.

C. Interconnection of Different Converter Technologies

Interconnection of LCC and VSC technologies poses a special set of challenges because the converter on one side is a current source and on the other side is a voltage source [5]. The most important difficulty is handling power reversal. For LCC, power is reversed by reversing the voltage; while for the VSC, it is done by reversing the current. Therefore, the DC-DC converter should be able to emulate an LCC behavior with bipolar voltage on the LCC side while maintaining VSC behavior with bipolar current in the VSC side.

III. CONVERTER TOPOLOGIES

Over the past couple of years, a number of DC-DC converter topologies have been proposed for high voltage DC-DC converter. A comprehensive review of these topologies is given in [7]. They can be broadly grouped into two categories: those with single stage conversion and those with double stage conversion. These groups are described in the next sections. This section also discusses the double-II and the diode rectifier dual active bridge converter which are not included in [7].

A. Single Stage DC-DC Topologies

Single stage topologies convert a DC input to a DC output without an intermediate AC stage [8–10]. Although these topologies do not involve an AC stage, balancing of arm and sub-module energies is facilitated by an AC circulating current commonly known as the secondary current. The main advantage of these topologies is reduced component count, and hence footprint. These advantages, however, come at the cost

of being limited low ratio applications for efficient, cost effective operation. Some of the most promising topologies in this class are briefly described below.

1) The Modular Multilevel DC (M2DC)

The M2DC, proposed by Ferreira [8], is a topology based on push-pull configuration [11], (Fig. 1). It introduced the concept of a secondary current which opened the door for a new class of non-isolated DC-DC converter topologies [9,10]. This topology has four arms for single pole operation. For bi-polar configuration, four more arms are needed. In Fig. 1, the current directions indicate a step down operation. In order to achieve power balance between the input and output sides, the output current has to be greater than the input current. The two upper arms carry the input current to the output while, the two lower arms supply the current difference between the input and output. This upsets the power balance in each arm causing the arm energy to drift. The secondary current transfers power in the opposite direction establishing average power balance in each arm. This principle is common to all the topologies in this class. The difference is on how secondary current is established and circulated in the circuit. For this purpose, the M2DC has two coupled inductors, per pole, used to direct the different current components in the system. The secondary current is forced to stay within the loop formed by the four arms as indicated in Fig. 1. The lower arms are rated for the output voltage (half in the case of bi-polar) if the secondary voltage is neglected. The remaining arms are on average rated for more than half the difference between the input and output voltages. Fault blocking capability can be included in this topology by using full bridge modules.

2) The DC Modular Multilevel Converter (DC-MMC)

A single stage converter that uses less number of arms, only two per pole, is the DC-MMC [9]. It has a similar structure to the M2DC with one of the legs removed. The operation principle is also similar to the M2DC. The two outer arms, labeled k in Fig. , have full bridge sub-modules. This choice enables step-up operation and fault blocking capability. Step-up operation is implemented by reversing the polarity of the outer arm voltage in effect causing a negative voltage drop. The secondary

current serves the same purpose as for M2DC. The secondary current is blocked from the output side by a coupled inductor filter. However, this current component is allowed to flow through the input side. Additional filtering on the input side is, therefore, required in order to avoid possible issues in the circuit upstream. Multi-string versions have also been proposed in [12] with added benefit of increased power capacity. Similar to the M2DC, the two inner arms are approximately rated for half the output voltage while the two inner arms are rated for half the difference between input and output voltages.

3) The Double-Π Topology

The last topology in this class, (Fig. 3), is the double- π configuration [10]. This topology does not require the coupled output filter as the previous ones. It has three arms per pole, input shunt, output shunt, and series arms. The input, and output shunt arms are rated for half the input and output voltages, respectively. The series arms are rated for half the difference between the input and output voltages. Fault blocking capability can be incorporated in to this topology by making the sub-modules full bridge type. The main shortcoming of this topology is the fact that the secondary voltage appears as voltage ripple in the pole to ground voltage.

4) Summary of Single Stage Topologies

The M2DC has the highest arm count among the topologies presented above. However, the current shared by each arm is half of the one taken by a corresponding arm in the DC-MMC topology. Both of these topologies have coupled inductor to block the secondary current from reaching the output. The DC-MMC allows the secondary current to flow in the input side. Additional filtering might be required to cope with this challenge. The double- π , on the other hand, contains the secondary current within the converter without the need for coupled inductor filter. However, the ripple in the pole to ground voltage is the major limitation of this topology.

B. Double Stage DC-DC Topologies

This group of topologies has an AC intermediate stage linking the two DC sides. These can be with or without coupling transformer, (Fig. 4). The transformer's purpose is twofold, to provide additional voltage stepping, and galvanic isolation. The additional stepping makes these topologies suitable for high ratio applications. Galvanic isolation helps stop DC fault from propagating to the healthy side [5]. Additionally, having a

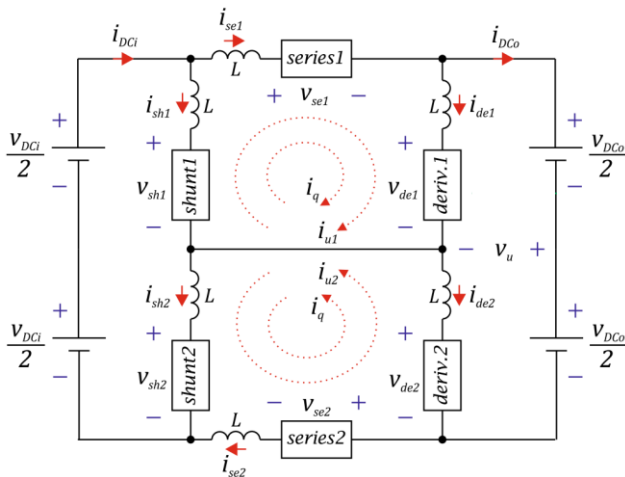


Fig. 3 Double-Π Topology [10]

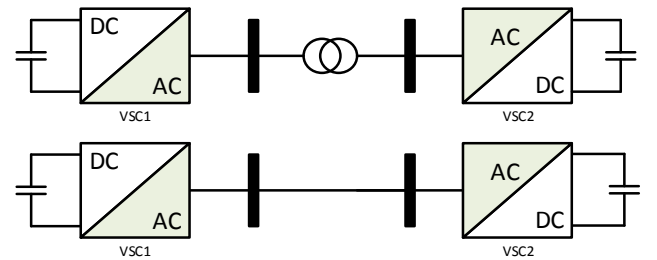


Fig. 4 Font to Front Connected Topologies

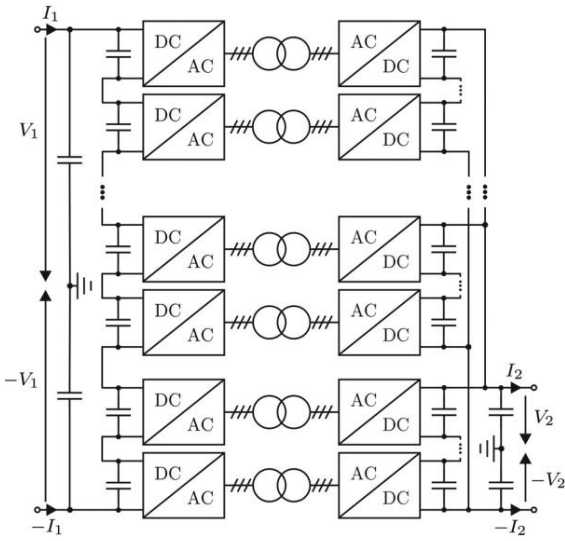


Fig. 5 Dual Active Converter System [16]

transformer isolated topology offers the possibility of extension to multiport operation with a modification to the transformer design. A few isolated topologies were presented in [5,13,14]. Among these, the Front-to-Front (F2F) converter, the Dual Active Bridge (DAB) system, the Autotransformer, and DAB with thyristor rectifier are found to be promising and hence, described briefly in this section.

1) The F2F Topology

The F2F is the interconnection of two full power AC-DC converters on their AC sides. The major difference from back-to-back arrangement is that the AC side is internal and its quantities can be optimized for cost, size, and efficiency. Operation frequency of 350Hz was suggested in [13] as a result of a tradeoff between size and efficiency. Different technologies can be used for each AC-DC converter depending the application and voltage level. Candidate topologies include Modular Multilevel Converter (MMC), Alternate Arm Converter (AAC), and even passive rectifiers when bidirectional power flow is not required. The F2F is well suited for bulk power applications and DC hubs [15].

2) The Dual Active Bridge Topology

The DAB is modular converter with a leg formed by series connection of F2F building blocks, Fig. 5. It offers a very compact and modular design since the transformer is also distributed. The submodules can be connected in series on the high voltage side and in series and parallel on the low voltage side in order to increase the power capacity. The DAB submodule is normally operated in soft-switched mode for improved efficiency [16]. In [16], the DAB is extensively compared with the M2DC under different operational scenarios. The results show that the DAB performs better under most scenarios in terms of size, efficiency, and cost. On the contrary, the M2DC was found to be more efficient in the scenario where the ratio is unity and the converter was used for power flow control.

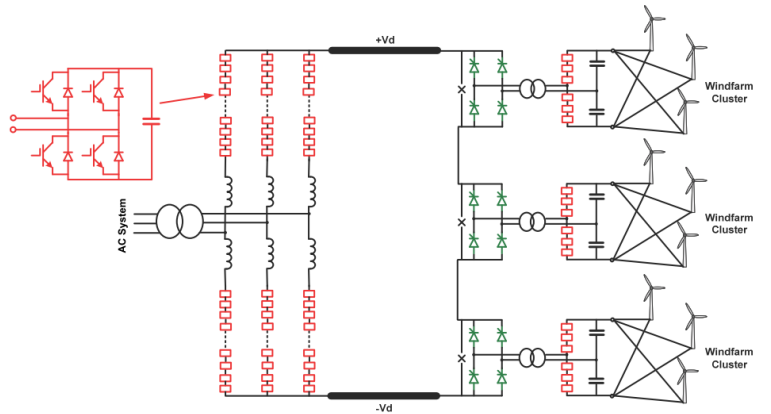


Fig. 6 DC-DC Converter Topology for Wind Farm Integration [5]

3) The DC Auto-transformer

The DC autotransformer, proposed in [17], is a special case of F2F converter based on MMC. It is made up of full bridge submodules. Its operation is equivalent to an AC autotransformer where the output is adjusted in discrete levels. This topology offers high efficiency operation. However, it results in poor utilization factor when comparing the number of components with the functionality gained.

4) DAB with Thyristor Rectifier

The thyristor rectifier DAB [5] is an adaptation of the DAB where the one side of the AC-DC stages is replaced by the thyristor bridge and the other side is a full bridge MMC, Fig. 6. Each thyristor bridge can be bypassed by the parallel switch in case of failure. This type of converter is particularly suited for wind farm interconnection where the power flow is predominantly unidirectional. When wind power is not available, active parts of the farm should be supplied from the connected AC grid to keep functioning properly [5]. The thyristor rectifier can reverse the power flow direction, by reversing the DC voltage, and supply the auxiliary demand. This solution might not be optimal from cost perspective considering the fact that the auxiliary demand is very low compared the rating the rectifier.

Siemens AG recently released a new solution, based on a similar topology, using diode rectifier instead of the thyristor [18]. Since the diode bridge is unidirectional, other means of supplying this auxiliary power is needed. Siemens has proposed the use of umbilical cable to supply the auxiliary demand from shore. As per the press release, the solution can potentially reduce the total topside volume by up to 80% compared to the traditional AC collection grids.

In summary, the double stage converter topologies provide better flexibility with the penalty of added cost. Therefore, selection of the best topology for a given application is a tradeoff between cost and functionality.

IV. MODELS OF DC-DC CONVERTERS

The DC-DC converters are going to be part of a larger system, the multi-terminal DC grid. Therefore, it is of high importance that the whole system, the grid, be studied in detail. System level studies are performed to investigate interactions between components or sub-systems that are individually designed and optimized. With emergence of new DC-DC converter topologies, new tools are needed for analyzing, and studying these topologies at the system level. For such studies, models with varying level of detail are required. For instance, transient studies require high level of detail compared to small signal interaction studies, which normally utilize simplified models [19]. With these applications in mind, models for other components of the DC grid have been developed [19,20]. However, DC-DC converter models have not been developed at the same level. A simplified model proposed by Cigre is shown in Fig. 7 [21]. This kind of models can accurately describe the high-level features but do not correctly capture the internal dynamics of most of the topologies presented in this paper. Therefore, there is a need for development of dynamic models of these emerging topologies. The following section discusses the requirements placed on such models.

A. Model Requirements

There are two major requirements for models to be used in system level studies.

- *Accuracy/Detail:* The models should be accurate enough for the type of study under consideration. Accuracy, in this context, is defined as the ability of the model to predict the system behavior of interest. The level of detail is also dependent on the available degree of detail in the models of other components.
- *Simplicity:* The models should be simple enough for the system to be simulated as fast as possible.

These two requirements are contradictory leading to a tradeoff between speed and accuracy. For small systems, accuracy is given priority since the difference in simulation speed achieved by using simplified models is not significant. On the other hand, in large systems, these requirements are equally important. Therefore, specific applications should be considered for selection of model detail. The following three example cases emphasize this point.

1) Electromechanical Interaction Study Over DC Grid

Electromechanical interaction between AC generators over a DC grid are normally studied using simplified models [22]. These type of interactions typically range in time from few milliseconds to tens of seconds [23]. In this time range, the dynamics of different elements such as AC lines and other elements with similar or faster time constants are normally ignored without significant loss of accuracy. The DC grid is represented by the DC link capacitance and cable resistances.

2) DC Grid Interaction Study

In contrast to the previous case, DC grid interaction studies require detailed models [24]. These interactions normally span the range from few microseconds to hundreds of milliseconds.

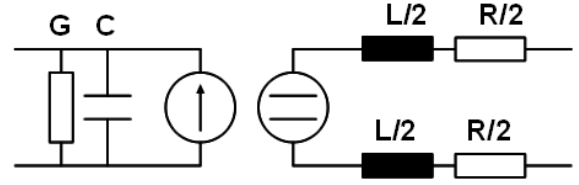


Fig. 7 Simplified DC-DC Converter Model [21]

Therefore, simplification adopted in the electromechanical case lead to loss of accuracy possibly resulting in wrong conclusions about system stability [24].

3) DC Grid Transient Study

Transient studies investigate response of the system to fast changes in the system, such as faults. These phenomena usually span a few microseconds, which is typically in the same range or faster than the time constants of almost all the system components. In the previous two cases, AC signals are represented by phasors; this is commonly known as RMS simulation. Transient studies, on the other hand, are performed in time domain using instantaneous values. Therefore, the models used in such studies should be more detailed than the other two cases. In general, the choice of model detail should be based on: objective of the study, size of the system, and desired level of accuracy.

The other difficulty with these requirements is that they are subjective. The terms accurate and simple may mean different things for different persons. Ref. [19] is an effort to objectify these definitions based on experience of experts in the field. Guides like this should be continuously updated to accommodate new components and types of study.

B. Modeling Approaches

There are two categories of modelling approaches, analytic and black-box [25]. There are also approaches that lie between the two extremes, called gray-box modelling. Analytic modelling requires knowledge of the system dynamics. Although, the development of analytic models is difficult for large system, once developed, they give powerful insight into the system. Black and gray-box models come in handy when there is little or no knowledge about the system. For the case of DC-DC converters, analytic models are easy to develop with the level of detail required by most system level studies. Analytic models are also easy to simplify since they are based on equations. Once models are developed, they should be validated against a reference system. The reference system can be an experimental setup or a more detailed model.

C. Available Models

There is a very limited number of models developed for the topologies presented in this paper. The first one is dynamic model for the DC-MMC [9] which gives average and small signal models based on phasor modelling of the AC quantities. The model was validated against the full detailed model. While this model is accurate enough for different studies, it has to be

simplified in order for it to be better suited for large system studies. Other available models are for the double stage converters which can utilize existing MMC models [26–28]. Once again, these models should also be simplified. As can be seen, all of the converters, except the DC-MMC, do not have accurate dynamic model so far.

V. CONCLUSION

A review of ongoing research around the DC-DC converter was presented in this paper. The need and requirements of DC-DC converter in HVDC transmission was presented with focus on a potential DC grid in the North Sea. DC-DC converters can make it possible to connect existing HVDC point-to-point schemes that are already in service to create a multi-terminal/meshed HVDC grid. A number of different topologies have been proposed recently. Although, isolated topologies are attractive in high ratio application, the single stage converters might be economically attractive in low ratio application such as power flow control. Despite the emergence of a number of DC-DC converter topologies, development of their dynamic models is yet to be undertaken for system level studies; such studies are needed for the design and performance assessment of the complete system.

REFERENCES

- [1] “The Paris Agreement,” Dec. 2015, <http://newsroom.unfccc.int/paris-agreement/>
- [2] Y. Yang, M. Jafar, P. Vaessen, A. Yanushevich, Y. Fu, R. Marshall, T. Bosma, and M. Irvine, *Hybrid Grid: Towards a Hybrid AC/DC Transmission Grid*, DNV GL Strategic Research & Innovation, Position Paper, 2015.
- [3] T.K. Vrana, J. Beerten, R. Belmans, and O.B. Fosfo, “A Classification of DC node voltage control methods for HVDC grids,” *Electric power systems research*, vol. 103, 2013, pp. 137–144.
- [4] R. Irnawan, F.M.F. da Silva, C.L. Bak, and T.C. Bregnhøj, “An Initial Topology of Multi-terminal HVDC Transmission System in Europe: A Case Study of the North-Sea Region,” *Ieee International Energy Conference (enrgycon) 2016*, 2016.
- [5] C. Barker, C. Davidson, D. Trainer, and R. Whitehouse, “Requirements of DC-DC Converters to facilitate large DC Grids,” *Cigre Session 2012*, 2012.
- [6] D. Jovicic, M. Hajian, H. Zhang, and G. Asplund, “Power flow control in DC transmission grids using mechanical and semiconductor based DC/DC devices,” *AC and DC Power Transmission (ACDC 2012)*, 10th IET International Conference on, 2012, pp. 1–6.
- [7] G.P. Adam, I.A. Gowaid, S.J. Finney, D. Holliday, and B.W. Williams, “Review of dc-dc converters for multi-terminal HVDC transmission networks,” *IET Power Electronics*, vol. 9, 2016, pp. 281–296.
- [8] J.A. Ferreira, “The multilevel modular DC converter,” *IEEE Transactions on Power Electronics*, vol. 28, 2013, pp. 4460–4465.
- [9] G. Kish and P. Lehn, “Modeling Techniques for Dynamic and Steady-State Analysis of Modular Multilevel DC/DC Converters,” 2015.
- [10] R. Vidal, D. Soto, I. Andrade, J. Riedemann, C. Pesce, E. Belenguer, R. Pena, and R. Blasco-Gimenez, “A multilevel modular DC–DC converter topology,” *Mathematics and Computers in Simulation*, 2015.
- [11] N. Mohan and T.M. Undeland, *Power electronics: converters, applications, and design*, John Wiley & Sons, 2007.
- [12] G.J. Kish and P.W. Lehn, “A modular bidirectional DC power flow controller with fault blocking capability for DC networks,” *Control and Modeling for Power Electronics (COMPEL)*, 2013 IEEE 14th Workshop on, 2013, pp. 1–7.
- [13] T. Luth, M.M.C. Merlin, T.C. Green, F. Hassan, and C.D. Barker, “High-Frequency Operation of a DC/AC/DC System for HVDC Applications,” *IEEE Transaction on Power Electronics*, vol. 29, 2014, pp. 4107–4115.
- [14] N. Soltan, R.U. Lenke, and R.W. De Doncker, *High-Power DC-DC Converter*, E.ON Energy Research Center, 2013.
- [15] I.A. Gowaid, G.P. Adam, A.M. Massoud, S. Ahmed, D. Holliday, and B.W. Williams, “Modular multilevel structure of a high power dual active bridge DC transformer with stepped two-level output,” *Power Electronics and Applications (EPE'14-ECCE Europe)*, 2014 16th European Conference on, IEEE, 2014, pp. 1–10.
- [16] S.P. Engel, M. Stieneker, N. Soltan, S. Rabiee, H. Stagge, and R.W. De Doncker, “Comparison of the Modular Multilevel DC Converter and the Dual-Active Bridge Converter for Power Conversion in HVDC and MVDC Grids,” *IEEE Transaction on Power Electronics*, vol. 30, 2015, pp. 124–137.
- [17] S. Kenzelmann, A. Rufer, D. Dujic, F. Canales, and Y.R. De Novaes, “Isolated DC/DC Structure Based on Modular Multilevel Converter,” *IEEE Transaction on Power Electronics*, vol. 30, 2015, pp. 89–98.
- [18] “Mighty Efficient: Offshore Grid Access,” <https://www.siemens.com>
- [19] R. Wachtal, A. Jindal, and others, *Guide for the Development of Models for HVDC Converters in a HVDC Grid*, CIGRE B4.57, 2014.
- [20] J. Beerten, S. D Arco, and J. Suul, “Identification and Small-Signal Analysis of Interaction Modes in VSC MTDC Systems,” 2015.
- [21] T.K. Vrana, Y. Yang, D. Jovicic, S. Dennetière, J. Jardini, and H. Saad, “The CIGRE B4 DC grid test system,” *Electra*, vol. 270, 2013, pp. 10–19.
- [22] A.G. Endegnanew, J. Beerten, and K. Uhlen, “Dynamic interactions between asynchronous grids interconnected through an MTDC system,” *Proc. CIGRE International Symposium Lund*, 2015, pp. 1–7.
- [23] J. Machowski, J. Bialek, and J. Bumby, *Power system dynamics: stability and control*, John Wiley & Sons, 2011.
- [24] M. Amin, J.A. Suul, S. D’Arco, E. Tedeschi, and M. Molinas, “Impact of state-space modelling fidelity on the small-signal dynamics of VSC-HVDC systems,” *AC and DC Power Transmission, 11th IET International Conference on*, 2015, pp. 1–11.
- [25] L. Arnedo, R. Burgos, D. Boroyevich, and F. Wang, “System-level black-box DC-to-DC converter models,” *Applied Power Electronics Conference and Exposition, 2009. APEC 2009. Twenty-Fourth Annual IEEE*, IEEE, 2009, pp. 1476–1481.
- [26] G. Bergna Diaz, J.A. Suul, and S. D’Arco, “Small-signal state-space modeling of modular multilevel converters for system stability analysis,” *Energy Conversion Congress and Exposition (ECCE)*, 2015 IEEE, IEEE, 2015, pp. 5822–5829.
- [27] W. Lin and D. Jovicic, “Average Modelling of Medium Frequency DC–DC Converters in Dynamic Studies,” *Power Delivery, IEEE Transactions on*, vol. 30, 2015, pp. 281–289.
- [28] N.-T. Trinh, M. Zeller, K. Wuerflinger, and I. Erlich, “Generic Model of MMC-VSC-HVDC for Interaction Study With AC Power System,” *Power Systems, IEEE Transactions on*, vol. 31, 2016, pp. 27–34.

Centralized Model Predictive Control of Multi-Terminal Direct Current Grids

Lampros Papangelis
Dept. of Elec. Eng. and Comp. Science
University of Liège, Belgium
l.papangelis@ulg.ac.be

Abstract—This work describes a centralized control for Multi-Terminal Direct Current (MTDC) grids. It is based on Model Predictive Control (MPC) whose aim is to satisfy a desired schedule, while avoiding or correcting any system limit violation. The central controller collects voltage and power measurements from the converters of the system in regular intervals and sends back converter power setpoints. The latter are calculated by solving a quadratic programming problem subject to linear constraints and using a simplified model for the DC system. In addition, the overall MTDC grid control structure including the local and the centralized controllers is described.

Index Terms—Model Predictive control, Multi-terminal DC grids, Voltage Source Converter.

I. INTRODUCTION

The increasing need for bulk power transfer over long distances driven by the shift to renewable energy production and the gradual replacement of conventional power plants has led to the development of HVDC systems, whereas MTDC grids are the next step envisaged [1]. One of the biggest challenges that have to be addressed is the secure and robust operation of such grids. To achieve this, a control structure has to be devised, which will ensure system stability without relying on extensive communications, smoothly drive the system between two operating points, respect the operating limits of the MTDC system and the constraints imposed by the surrounding AC areas, and correct or prevent any possible limit violation.

The control of MTDC grids has recently received significant attention. Various methods have been proposed in order to control the DC grid power flows and the DC voltages. In [2] the authors are proposing a control structure based on the DC voltage droop control at the lower level and an Optimal Power Flow (OPF) at a higher level. The droop control ensures the robust operation of the MTDC grid while the higher level sends new DC voltage setpoints to the Voltage Source Converters (VSC) in regular intervals, aiming to minimize the losses of the MTDC grid and the VSCs.

The work in [3] proposes a three-level control structure inspired from the AC frequency control practice, i.e. primary, secondary and tertiary control. The primary control includes a simple current-based droop scheme. The secondary control consists of a slow PI controller, which aims at restoring the powers of all VSCs to their reference values, and a central power redispatch scheme which sends new power references in regular intervals. The tertiary controller is not detailed, but it is noted that it will be based on an OPF. In [4] a coordinated

control is proposed for a droop controlled MTDC grid. The method calculates new voltage and power setpoints using a DC load flow algorithm and sends them to the converters in regular intervals. Similarly, in [5] and [6] the authors propose a method to estimate the changes in the setpoints that have to be sent to the VSCs so that the power flows of selected terminals are restored.

In [7] an analysis and comparison of various redispatch schemes is reported. The aim was to define new DC voltage setpoints that will be sent to the converters in order to cancel the voltage offset caused after a disturbance due to the droop effect. Moreover, the ability of the various schemes to track the desired power setpoints is evaluated.

Reference [8] introduces the concept of the pilot voltage droop for DC grid control. In this case, a common DC voltage is communicated to all converters of an MTDC grid to make the power sharing between the converters more efficient. In addition, two methods were employed to achieve power setpoint tracking, one based on using a simple PI controller and the other by redispatching setpoints calculated by a centralized entity.

A different approach is described in [9]. The authors propose the direct current matching control which uses fast communication in order to match at each time the sum of the DC currents injected by the WFs to the sum of the DC currents of the grid side converters. However, it is noted that this method requires fast communications in order to work properly.

This paper focuses on a hierarchical control structure for an MTDC grid inspired of MPC [10]. MPC has been also proposed as a secondary control in [11]. However, the focus was on minimizing the losses in the MTDC grid while satisfying some operational constraints and the performance of the controller after a contingency or in alleviating violations was not reported.

The rest of the paper is organized as follows. Section II describes the first level, acting locally on the converters. Section III describes the centralized control. Illustrative simulation results are provided in Section IV. Finally, concluding remarks are offered in Section V.

II. FIRST LEVEL: LOCAL CONTROL

Proper operation of an MTDC grid requires keeping the voltages at all its nodes stable and in acceptable ranges. This

is achieved by balancing the active powers injected in and extracted from the MTDC grid. As shown in [4], a power deficit/surplus in a DC system leads to a DC voltage drop/rise in the same way a power deficit/surplus leads to a frequency drop/rise in an AC system.

The rate of change of AC frequency is inversely proportional to the total inertia of the synchronous machines connected to the system, and is usually in the order of several seconds. On the contrary, the DC voltage response is much faster because it depends only on the electrostatic constant of the DC grid, which is proportional to the total DC capacitance connected to it and is usually in the order of some hundreds milliseconds. This renders the DC voltage control a very challenging task, for which various methods have been proposed (e.g. [5], [12] and [13]).

The DC voltage droop method is generally considered the most appropriate for multi-terminal MTDC operation due to its redundancy, good dynamic performance and its direct analogy with the AC frequency control practice. It allows multiple converters to share any power imbalance in the MTDC grid. In a droop-controlled MTDC grid, some of the VSCs are given a $P - V$ characteristic defined by a power setpoint (P^{set}), a voltage setpoint (V^{set}) and a droop gain (K_V). The power (P) of the VSC then follows the variation of the DC voltage (V) according to the relation:

$$P = P^{set} - K_V(V - V^{set}) \quad (1)$$

where positive power corresponds to rectifier operation.

The DC voltage droop control results in a voltage offset after an imbalance in the MTDC grid, as is the case for primary frequency control in an AC system.

III. SECOND LEVEL: CENTRALIZED CONTROL

A. Principle

The primary objective of the centralized control is to smoothly drive the system between different operating points in a coordinated way. Meanwhile, it corrects any DC voltage violation to ensure the reliable operation of the grid and alleviates any DC branch current violation. In addition, a closed-loop control system is needed to account for model inaccuracies and react to unscheduled events.

The controller proposed in this work is based on MPC. MPC is a multi-step, optimization-based, closed-loop control scheme. It relies on the determination of an optimal sequence of control actions using a (simplified) model of the system under concern, in order to satisfy an objective in the future. Its basic principle is recalled in Fig. 1. At the current time instant k , the controller receives the latest available measurements and calculates the optimal N_c control changes from k up to the end of the control horizon $k + N_c - 1$, so that the system meets a desired target at the end of the prediction horizon $k + N_p$. After the calculation, only the first control action $\Delta \mathbf{u}(k)$ is applied. Then, at the next time instant $k + 1$, the procedure is repeated for the updated control and prediction horizon based on the new measurements received.

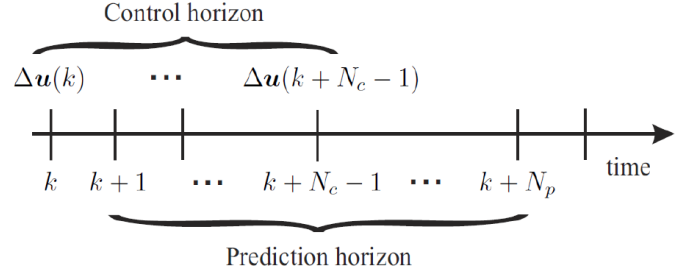


Fig. 1. Definition of MPC control and prediction horizons

B. MPC Formulation

This work focuses on MTDC grids consisting of dispatchable and non-dispatchable VSCs. The former correspond to VSCs that have been assigned a $P - V$ droop characteristic as discussed in Section II. These VSCs are either participating in DC voltage control (if assigned a positive K_V) or keep their power to a constant value as specified e.g. by market agreements. It generally includes VSCs connected to strong AC areas. The non-dispatchable VSCs, on the other hand, have their power determined by external factors. For instance, a VSC connecting an offshore wind farm to the MTDC grid is considered a non-dispatchable terminal, since its power injection will match the power produced by the WF, usually operating in Maximum Power Point Tracking (MPPT) mode.

The centralized controller should mainly act on the dispatchable terminals. Control actions can also be sent to non-dispatchable terminals (e.g. decrease of WF power), although they should be reserved for emergency cases.

The proposed control structure is shown in Fig. 2. The lower level includes a total of N_{term} terminals, out of which N_D are dispatchable and the rest non-dispatchable. The upper level consists of the centralized (or supervisory) controller and the Power Rescheduler, whose function is described in the following.

The MPC objective is to satisfy a specific schedule at each time instant, given by the Power Rescheduler. Meanwhile, it should ensure that the wind farm power is directed to specific AC areas or shared between the areas according to a pre-specified ratio. This should be done in a smooth manner avoiding any constraint violations. These constraints include:

- DC voltage limits,
- limits on the rate of change of VSC power because large changes of power injection into an AC area could cause unacceptable frequency excursions,
- maximum and minimum power of each VSC,
- HVDC branch current limits, etc.

Based on the aforementioned, the optimization problem at the heart of the MPC is formulated as follows:

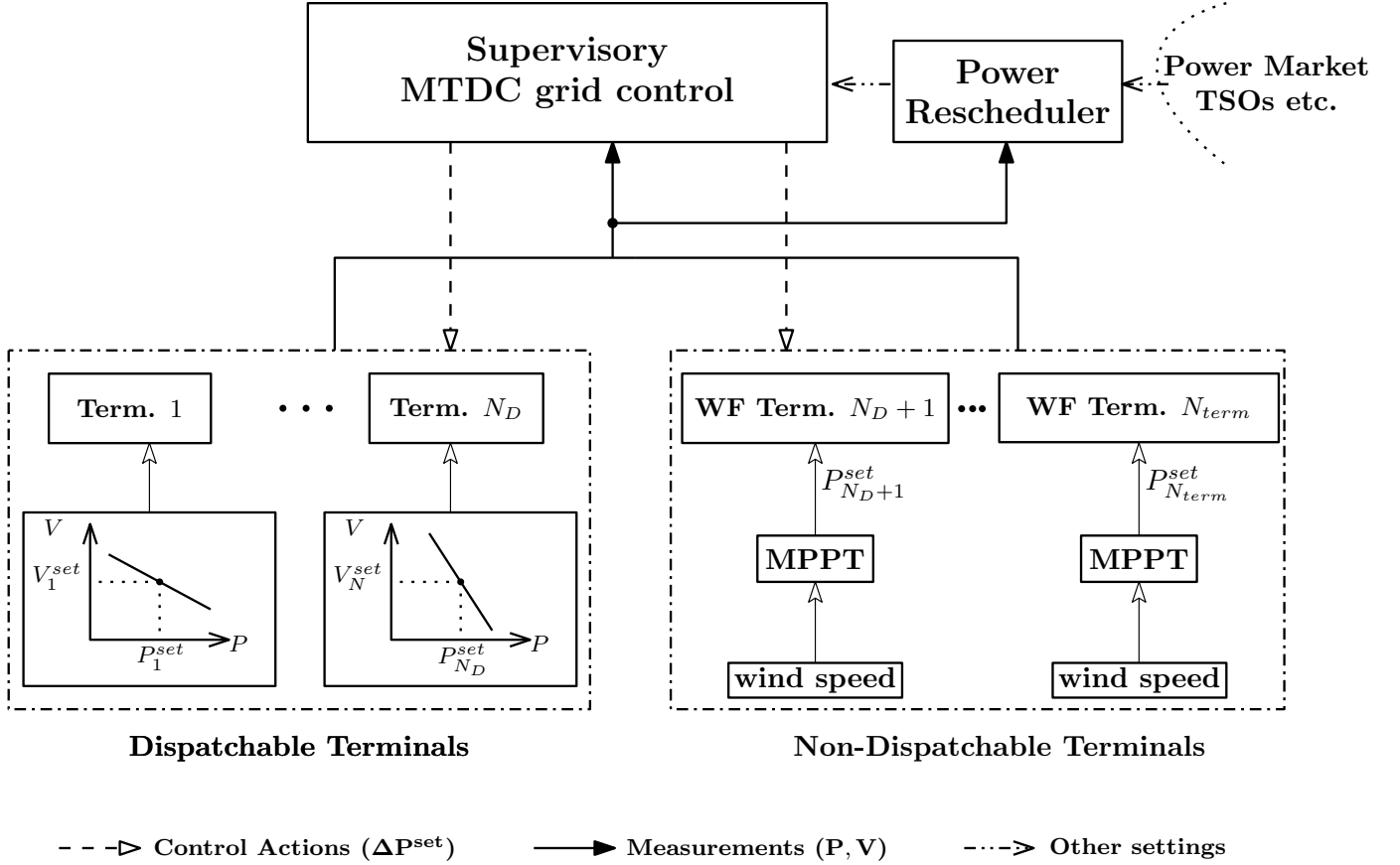


Fig. 2. Proposed hierarchical control structure

$$\begin{aligned}
 \min \sum_{j=0}^{N_c-1} & \left(r_D(k+j) \sum_{i=1}^{N_D} (\Delta P_i^{set}(k+j))^2 \right) \\
 & + \sum_{j=0}^{N_c-1} \left(r_{ND}(k+j) \sum_{i=N_D+1}^{N_{term}} (\Delta P_i^{set}(k+j))^2 \right) \\
 & + w \sum_{i=1}^{N_{term}} \zeta_i^2 + v \sum_{j=1}^{N_c} \sum_{i=1}^{N_{term}} \epsilon_i^2(k+j) \\
 & + q \sum_{j=1}^{N_c} \sum_{i=1}^{N_{term}} \eta_i^2(k+j)
 \end{aligned} \quad (2)$$

where N_c is the control horizon (taken equal to the prediction horizon N_p), $\Delta P_i^{set}(k+j)$ is the change of the power setpoint of converter i at time $k+j$, ϵ_i and ζ_i are relaxation variables to prevent infeasibility, r_D is the weighting factor of control actions on the dispatchable VSCs, r_{ND} is the weighting factor of control actions on the non-dispatchable VSCs, and v, w, q are weighting factors for the relaxation variables.

By choosing to minimize the L_2 norm the total control effort is distributed throughout the whole control horizon and a smooth response is achieved.

The optimization is subject to the following constraints:

For $i = 1, \dots, N_{term}$, $j = 1, \dots, N_c$, $m = 1, \dots, N_{term}$

$$-\delta P - \zeta_i \leq P_i^{ref} - P_i(k + N_c) \leq \delta P + \zeta_i \quad (3)$$

$$V_i^{min}(k+j) - \epsilon_i(k+j) \leq V_i(k+j) \leq V_i^{max}(k+j) + \epsilon_i(k+j) \quad (4)$$

$$P_i^{min} \leq P_i(k+j) \leq P_i^{max} \quad (5)$$

$$\Delta P_i^{min} - \eta_i(k+j) \leq P_i(k+j) - P_i(k+j-1) \leq \Delta P_i^{max} + \eta_i(k+j) \quad (6)$$

$$I_{i,m}^{min}(k+j) \leq \frac{V_i(k+j) - V_m(k+j)}{R_{i,m}} \leq I_{i,m}^{max}(k+j) \quad (7)$$

$$\epsilon_i(k+j) \geq 0, \zeta_i \geq 0, \eta_i(k+j) \geq 0 \quad (8)$$

Constraint (3) is the schedule constraint which states that the power of VSC i at the end of the control horizon $P_i(k + N_c)$ should be equal (inside a tolerance δP) to its reference power P_i^{ref} . Non-satisfaction of this constraint is heavily penalized in the objective function through the relaxation variable ζ_i .

Constraint (4) sets the normal operating range of the DC voltage V_i at each converter bus i . At each time step the (predicted) DC voltage must remain between the minimum and maximum limits (V_i^{min} and V_i^{max} , respectively). In order to prevent infeasibility the relaxation variable ϵ_i is introduced, which is also heavily penalized in the objective function.

Constraint (5) relates to the maximum capacity of each VSC, which cannot be exceeded.

Constraint (6) stems from the AC networks. Too fast changes in the power injections into or from the AC areas could cause unacceptable frequency deviations. Therefore, this constraint limits the power change of each VSC i between two discrete time steps to ΔP_i^{min} and ΔP_i^{max} . The relaxation variable η_i is introduced for the same reason as ϵ_i .

Finally, constraint (7) keeps the current in the DC branch between nodes i and m between $I_{i,m}^{max}$ and $I_{i,m}^{min}$ (normally equal to $-I_{i,m}^{max}$). $R_{i,m}$ is the DC branch resistance.

The measurements received at each time step are the powers and DC voltages of all the converters ($i = 1, \dots, N_{term}$):

$$P_i^{meas} = P_i(k) \quad (9)$$

$$V_i^{meas} = V_i(k) \quad (10)$$

The predicted DC voltage evolution due to the changes in the power setpoints is found from the following equality constraints:

$$\Delta P_i^{set}(k+j-1) = \sum_{l=1}^{N_{term}} [\mathbf{S}_p]_{i,l} [V_l(k+j) - V_l(k+j-1)] \quad (11)$$

where \mathbf{S}_p is the sensitivity matrix that relates the DC voltage changes to power setpoint changes:

$$\mathbf{S}_p = \mathbf{J}_{dc} + \text{diag}(\mathbf{K}_v) \quad (12)$$

where \mathbf{J}_{dc} is the Jacobian matrix of the DC grid power flows and $\text{diag}(\mathbf{K}_v)$ is a diagonal matrix with the (i, i) term equal to the droop gain $K_{v,i}$ of VSC i . Obviously, for non-dispatchable terminals the corresponding droop gain is equal to zero. The analytical derivation of (12) has been detailed in [5].

Following the DC voltage predictions, the power prediction of each VSC is given by

$$P_i(k+j) = P_i(k+j-1) + \Delta P_i^{set}(k+j-1) - K_{v,i} [V_i(k+j) - V_i(k+j-1)]. \quad (13)$$

C. Power Rescheduler - Determination of reference power

The Power Rescheduler is provided with a power schedule P_i^{sch} for each VSC i . This schedule corresponds to a specific non-dispatchable VSC power and may satisfy various criteria. Due to the non-dispatchable VSC power variability, it is necessary to make the power references of the dispatchable VSCs to also vary. This can be made by following specific rules, indicating how the deviation of the non-dispatchable VSC power should be distributed over the dispatchable VSCs. One simple option is to introduce a participation factor ρ_i for each VSC, as discussed in the following.

First, for non-dispatchable VSCs (e.g. WFs), the reference power is taken equal to the last available measurement, i.e.

$$P_i^{ref} = P_i^{meas}. \quad (14)$$

A better prediction could be used (e.g. based on wind speed forecast), if available. However, due to the short-term horizon considered here, this is not obvious.

Then, the power references of the dispatchable VSCs are adjusted as follows ($i = 1, \dots, N_D$):

$$P_i^{ref} = P_i^{sch} - \rho_i \left(\underbrace{\sum_{m=1}^{N_D} P_m^{sch}}_{\text{disp. schedules}} + \underbrace{\sum_{l=N_D+1}^{N_{term}} P_l^{ref}}_{\text{non-disp. references}} \right) \quad (15)$$

where N_D the number of the dispatchable VSCs, $\sum_{i=1}^{N_D} \rho_i = 1$ and $\rho_i \geq 0$.

If the losses are neglected, the first term in the brackets in (15) is constant and opposite of the total non-dispatchable VSC power at the schedule, i.e.:

$$\sum_{l=1}^{N_D} P_m^{sch} = - \sum_{l=N_D+1}^{N_{term}} P_m^{sch} \quad (16)$$

As a result, the total sum in the parentheses in (15) accounts for the deviation of the non-dispatchable VSCs from the P^{sch} values. In addition, (15) also accounts for the case the power schedule of a VSC has been updated, e.g. after the tripping of another VSC. An example will be given in the simulation results of Section IV.

Equation (15) is used to correct the power references of the dispatchable VSCs. If the setpoints of the VSCs were not varied according to the change of the wind power, the MPC would try to track an infeasible operating point, leading to a steady-state which would be decided by the relative values of the weighting factors r_D, r_{ND}, v, w in the objective function (2), which is not desirable.

D. Treatment of limit violations

It is possible that after a disturbance the DC voltage and/or branch current limits are temporarily violated. The MPC should alleviate this violation before it leads to equipment tripping or damage. On the other hand, abrupt corrections should be avoided. To this purpose, a progressive constraint tightening has been chosen in order to remove the violation. Therefore, if the DC voltage of terminal i violates one of the limits V_i^{min}, V_i^{max} the latter is progressively enforced by specifying for $j = 1, \dots, N_c$:

$$V_i^{min}(k+j) = V_i^{meas} + (V_i^{min} - V_i^{meas}) \frac{j}{N_c} \quad (17)$$

$$V_i^{max}(k+j) = V_i^{meas} + (V_i^{max} - V_i^{meas}) \frac{j}{N_c} \quad (18)$$

Similarly, for the DC current of branch i :

$$I_{i,m}^{min}(k+j) = I_{i,m}(k) + (-I_{i,m}^{max} - I_{i,m}(k)) \frac{j}{N_c} \quad (19)$$

$$I_{i,m}^{max}(k+j) = I_{i,m}(k) + (I_{i,m}^{max} - I_{i,m}(k)) \frac{j}{N_c} \quad (20)$$

This is also illustrated in Fig. 3, where the dash-dotted line shows the progressive tightening of the V_i^{min} constraint at time instant k . After the new measurements are collected at

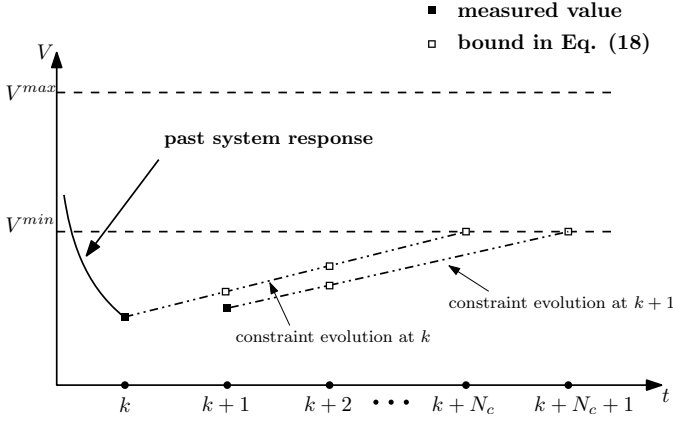


Fig. 3. DC Voltage progressive constraint tightening

time instant $k+1$, a new dash-dotted line is calculated, which brings the DC voltage above the limit at the end of the updated control horizon $k+N_c+1$.

This way of alleviating the violations is inherited from AC system practice, where limit violations can usually be tolerated for a brief period. However, in HVDC systems the violations may not be tolerated at all. For example, as far as the DC voltage limits are concerned, they have to be chosen with a sufficient security margin from their real technical limits because too low a DC voltage may immediately lead to converter tripping, while a high voltage can damage the insulation materials. In any case, the soonest the MPC can alleviate a violation is after a delay of one step. If it is required to act faster, other methods (i.e. depending only on local information, or event-based schemes) should be considered.

IV. SIMULATION RESULTS

The proposed control has been tested on the simple system shown in Fig. 4. It consists of five VSCs (T1-T5); four (T1-T4) are connected each to an AC area and T5 connects a wind farm to the HVDC grid. The four AC areas are modeled as Thevenin equivalents, while the wind farm is modeled as a constant power injection. The four VSCs connected to the AC areas are modeled in detail including their phase reactor dynamics, the VSC capacitor and the inner and outer control loops [4], [14]. The DC lines are represented by their series resistance, ignoring the series inductance and accounting for their capacitance in the DC capacitors of the VSCs at their neighboring buses, as also described in [15]. T5 imposes constant voltage and frequency on its AC side, thus acting as a slack bus for the wind farm [16]. T1-T4 are operating in DC voltage droop mode with droop gains K_v and participation factors ρ as defined in Fig. 4. The remaining parameters (controller gains, phase reactor, etc.) are the same for all VSCs.

A control horizon of $N_c = 3$ steps has been considered for the MPC with a sampling time $T = 5$ s. The measurements are collected 1 s before each control action, to account for the time needed to process them, solve the optimization problem and send the control actions. The weighting factors

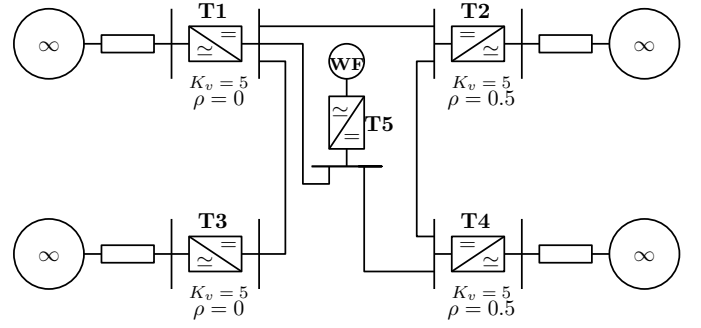


Fig. 4. Five terminal HVDC test system

r_D , r_{ND} , v , q and w are taken equal to 1 , 10^7 , 10^9 , 10^3 and 10^7 , respectively.

The limits involved in constraints (4)-(7) are listed in Table I. The base power is $P_b = 100$ MW.

TABLE I
MPC LIMITS VALUES

Limit	Value (pu)	Limit	Value (pu)
P^{min}	-10	ΔP^{min}	-10
P^{max}	10	ΔP^{max}	10
V^{min}	0.95	I^{min}	-10
V^{max}	1.05	I^{max}	10

Initially there is no power flowing in the system and all the DC voltages are equal to 1 pu. The test scenario includes the following events:

- From $t = 1$ s until $t = 11$ s gradual (although accelerated) increase of the WF power by 300 MW.
- At $t = 71$ s update of the scheduled powers P_i^{sch} for the dispatchable VSCs. The new schedule corresponds to the WF production of 300 MW and is shown in Table II.
- At $t = 141$ s, T4 is suddenly tripped.

TABLE II
SCHEDULE CHANGE AT $t = 71$ s

Terminal	Initial schedule	Final schedule
T1	0	500
T2	0	400
T3	0	-500
T4	0	-700

Figure 5 shows the DC powers of the VSCs. Immediately after the WF power increase all converters share its power. The sharing depends on the droop gains of the VSCs and the topology of the system. When the MPC starts acting (after $t = 5$ s), the power of T1 and T3 gradually return back to 0, while T2 and T4 share the WF power equally, in accordance with the selected participation factors (see Fig. 4).

Following the schedule change at $t = 71$ s, the powers of the VSCs are smoothly adjusted in order to satisfy the new schedule. The MPC settling time is approximately 40 s.

Following the tripping of T4, the parameters of the Power Scheduler have to be updated. Specifically, the schedule P_4^{sch} and the participation factor ρ_4 of T4 become equal to zero, and

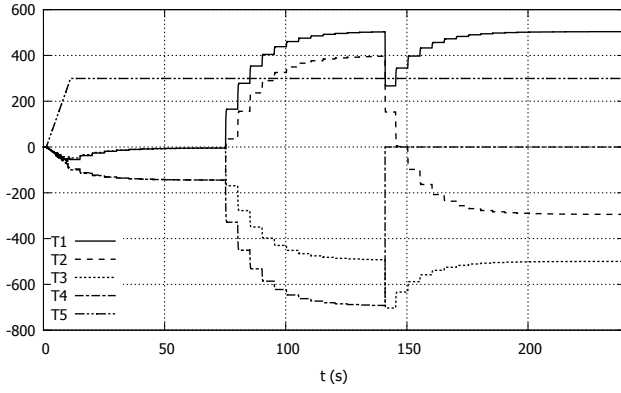


Fig. 5. VSC DC powers (MW)

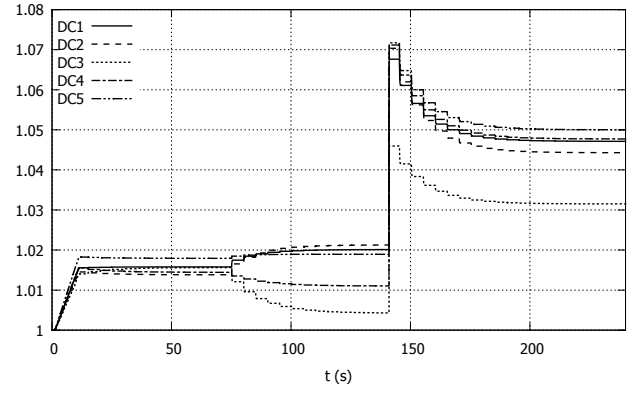


Fig. 6. HVDC grid voltages (pu)

so does P_4^{ref} . Meanwhile, it is chosen to direct the whole lost power of T4 to T2 by specifying $\rho_2 = 1$ ($\rho_i = 0$ for the other VSCs). The P^{ref} values of the remaining dispatchable VSCs remain unchanged. As can be seen in Fig. 5, immediately after the tripping of T4 all the VSCs react according to their droop gains in order to stabilize the DC voltage. Then, the MPC restores the powers of T1 and T3 to their schedule and redirects the lost power to T2.

The HVDC grid voltages are presented in Fig. 6. At the beginning, the voltages rise due to the increased injection by the WF. At $t = 71$ s, the difference between the DC voltages increases to accommodate the larger power flow in the HVDC grid. Finally, following the tripping of T4, there is a sudden increase of all voltages stabilized by the local droop control of the remaining VSCs. This increase causes a violation of the upper DC voltage limit which is corrected by the MPC.

V. CONCLUSION

This paper has presented a novel centralized control scheme for MTDC grids. The control scheme relies on the concept of MPC and is intended to act on MTDC grids including VSCs operating in DC voltage droop control and non-dispatchable VSCs, such as those of offshore WFs.

Simulation results on a simple test system have shown the efficiency of this formulation to track the desired power reference while maintaining the system between security limits.

Ongoing research investigates the coordination of the centralized controller with other local control schemes that change the behavior of the DC grid, such as the activation of frequency support by one terminal. Furthermore, the implementation of a third level is considered, to adapt the parameters of the lower levels and refine the rules defining how to distribute the power after a disturbance.

ACKNOWLEDGMENT

Research supported by the R&D department of RTE, the French Transmission System Operator. The author especially thanks Mrs. Marie-Sophie Debry and Mr. Patrick Panciatici for their valuable comments and suggestions. This research is performed under the supervision of Dr. Thierry Van Cutsem at University of Liège.

REFERENCES

- [1] D. Van Hertem and M. Ghandhari, "Multi-terminal VSC HVDC for the European supergrid: Obstacles," *Renewable and Sustainable Energy Reviews*, vol. 14, pp. 3156–3163, dec 2010.
- [2] M. Aragüés-Peñalba, A. Egea-Álvarez, S. G. Arellano, and O. Gomis-Bellmunt, "Droop control for loss minimization in HVDC multi-terminal transmission systems for large offshore wind farms," *Electric Power Systems Research*, vol. 112, pp. 48–55, 2014.
- [3] A. Egea-Álvarez, J. Beerten, D. V. Hertem, and O. Gomis-Bellmunt, "Hierarchical power control of multiterminal HVDC grids," *Electric Power Systems Research*, vol. 121, pp. 1–7, apr 2015.
- [4] P. Rault, *Dynamic Modeling and Control of Multi-Terminal HVDC Grids*. PhD thesis, Ecole Centrale de Lille, L2EP, 2014.
- [5] T. Haileselassie, *Control, Dynamics and Operation of Multi-terminal VSC-HVDC Transmission Systems*. PhD thesis, 2012.
- [6] T. M. Haileselassie, A. G. Endegnanew, and K. Uhlen, "Secondary control in multi-terminal VSC-HVDC transmission system," in *2015 IEEE Power & Energy Society General Meeting*, pp. 1–5, IEEE, jul 2015.
- [7] J. Beerten and D. Van Hertem, "Analysis of power redispatch schemes for HVDC grid secondary voltage control," in *IEEE Power & Energy Society General Meeting*, no. 3, pp. 1–5, IEEE, jul 2015.
- [8] B. Berggren, K. Linden, and R. Majumder, "DC Grid Control Through the Pilot Voltage Droop Concept - Methods for Establishing Set-Point Tracking," *IEEE International Energy Conference (Energycon)*, pp. 1562–1569, 2014.
- [9] J. Zhu, C. D. Booth, G. P. Adam, and A. J. Roscoe, "Coordinated direct current matching control strategy for multi-terminal DC transmission systems with integrated wind farms," *Electric Power Systems Research*, vol. 124, pp. 55–64, 2015.
- [10] J. M. Maciejowski, *Predictive control: with constraints*. Pearson education, 2002.
- [11] M. J. Carrizosa, *Hierarchical control scheme for multi-terminal high voltage direct current power networks*. PhD thesis, Université Paris Sud, 2015.
- [12] R. T. Pinto, *Multi-terminal DC networks - System integration, control etc.* PhD thesis, Technical University of Delft, 2014.
- [13] T. K. Vranaa, L. Zenib, and O. B. Fosso, "Active Power Control with Undead-Band Voltage & Frequency Droop for HVDC Converters in Large Meshed DC Grids," *EWEA2012presentation*, 2012.
- [14] M. Imhof and G. Andersson, "Dynamic modeling of a VSC-HVDC converter," in *Proceedings of the Universities Power Engineering Conference*, 2013.
- [15] X. Guillaud, L. Papangelis, and T. Van Cutsem, "Frequency support among asynchronous AC systems through VSCs emulating power plants," in *11th IET International Conference on AC and DC Power Transmission*, Institution of Engineering and Technology, 2015.
- [16] L. Xu, L. Yao, and C. Sasse, "Grid Integration of Large DFIG-Based Wind Farms Using VSC Transmission," *IEEE Transactions on Power Systems*, vol. 22, pp. 976–984, aug 2007.

Combined Centralized and Local Voltage correction in Active Distribution Network

Hamid Soleimani Bidgoli

Dept. of Elec. Eng. and Comp. Science University of Liège, Belgium

h.soleimani@ulg.ac.be

Abstract—This paper presents a two-level real-time voltage control scheme to address the voltage violations in distribution grids hosting a significant number of Dispersed Generation Units (DGUs). The proposed scheme consists of a centralized and a local reactive power control. The local control provides fast response after a disturbance, reducing its impact and enhancing voltage quality. The centralized control relies on Model Predictive Control (MPC). It uses measurements collected throughout the network to bring the voltages inside desired limits. To do so, it adjusts in a coordinated way the reactive power set-points of the DGUs taking into account the local controls. The control method effectiveness has been evaluated on a 75-bus 11-kV test system hosting 22 DGUs.

Index Terms—distribution network, model predictive control, real-time control, voltage correction.

I. INTRODUCTION

The progressive growth of renewable energy sources connected to medium-voltage distribution systems is expected to create new operational problems. Over- or under-voltages are some of the main issues caused by intermittent production of Distributed Generation Units (DGUs). Although excessive voltages can be tolerated for a short period of time, it is required to alleviate the violations fast enough. In the context of active distribution networks, the network equipment and the DGUs must be controlled in real time to obey the operational constraints.

Over the last decade, a lot of efforts have been devoted to real-time voltage control of distribution network with different control architectures. For example, in [1] a local approach was proposed for the correction of voltage violations and thermal overloads, using voltage and apparent power flow sensitivities to identify the most effective control actions. Using an Optimal Power Flow, Ref. [2] discussed the impact of centralized and distributed voltage control schemes on potential penetration of dispersed generation, while the authors in [3] developed an agent-based system to control the DGUs of a low voltage test grid in a decentralized manner. The work has been complemented by considering different local reactive power characteristics and comparing the corresponding system behaviours. References [4], [5] proposed a centralized voltage control scheme inspired by MPC relying on appropriate measurements and communication infrastructures. The problem was formulated as a receding-horizon multi-step optimization using a simple sensitivity model (justified by the speed of actions of the power-electronics interfaces

of DGUs). The controller coordinates the power output of DGUs and the voltage set-point of the transformer Load Tap Changer (LTC) to smoothly bring the unacceptable voltages back within their limits. A combined centralized and local control scheme was proposed in [6] where the local controllers provide a fast reaction. The centralized controller, using power injection prediction for the following hours, updates the droop parameters of the local controllers to ensure the voltages are kept within the admissible limits in the forecasted range. Although it is achieved at different operating points, the local controller tuning is highly dependent on the accuracy of the forecasts. The latter can cause the network operates not close to the optimum.

In this paper a real-time two-level control scheme is proposed in which both local and centralized controllers exist and interact with each other. With the purpose of exploiting the benefits of both control schemes, the two-level controller is able:

- at the local level, to provide a first, fast response after any limit violation;
- at the central level, to coordinate the DGUs in order to adjust and complement the actions taken locally;
- globally, to improve network reliability, since the local controllers still act in case of communication problems between the DGUs and the centralized controller.

The paper is organized as follows. Section II introduces different control architectures for voltage correction while Section III details the proposed two-level control scheme. Simulation results are reported in Section IV, and concluding are offered in Section V.

II. VOLTAGE CONTROL ARCHITECTURES

Different control schemes can be considered in a distribution system taking into account the practical needs, the technical limitations of the controllable devices (mainly DGUs and LTCs) and the regulatory policies. Two broad categories are the centralized and the local architectures. The local control is implemented inside the equipment and adjusts the reactive power of each DGU based on the local measurements, essentially equipment terminal voltage. Unlike the centralized controller, the measurements are collected instantaneously. Thus, a fast reaction is obtained while communication infrastructure is not required. The centralized control detects the voltage violations by periodically collecting measurements and smoothly

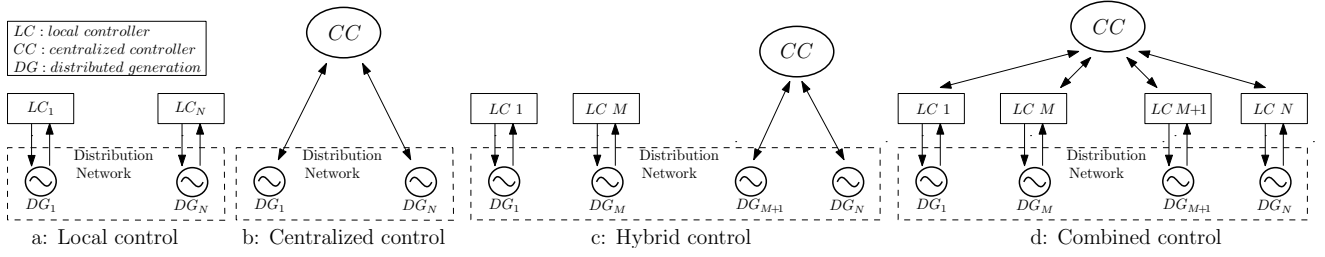


Fig. 1. Voltage control architectures

driving the system inside the prescribed limits. Having a wide-area view of the system, this controller is able to share the corrective efforts between DGUs based on market objectives and technical limits. The two aforementioned schemes are depicted in Figs. 1.a and 1.b, respectively.

As a variant or due to practical constraints, a control architecture could be implemented where the centralized controller and the local controllers are acting on separate DGUs in the same distribution network. This leads to the hybrid control shown in Fig. 1.c. The challenge in this case is to enable the centralized controller to take into account the action of local controllers on network voltages.

A more attractive scheme consists of appropriately combining the local and centralized controllers, which yields a larger flexibility. This approach, shown in Fig. 1.d, will be the main focus of this paper, and is explained in detail in the following section.

III. TWO-LEVEL CONTROL SCHEME

In this section a two-level control architecture is presented which relies on DGUs equipped with local controllers at the lower level, and a centralized controller at the upper level. The latter observes the voltage evolution and interacts with the local level in order to improve the overall system behaviour. To do so, some parameters of the local controllers are adjusted in discrete steps by the upper level, if needed.

A. Lower level: local controller

The output reactive power of each DGU is locally controlled according to a piecewise linear $Q(V)$ characteristic [7], as depicted in Fig. 2. As long as the measured terminal voltage is within the dead-band $[V_{min1}^{loc}, V_{max1}^{loc}]$, the produced reactive power is kept at zero aiming at minimizing the DGU internal losses. Outside the above mentioned dead-band, the DGU reacts to over or under-voltage by consuming or producing reactive power, respectively. The DGU remains at its highest level of reactive power production (consumption), if the terminal voltage is lower (higher) than V_{min2}^{loc} (V_{max2}^{loc}). Furthermore, we assume that there is a possibility for the centralized controller to communicate its desired reactive power correction Q_{cor} to the local controller. Then, the $Q(V)$ characteristic is adjusted accordingly to satisfy the received command. Further detail on this adjustment is provided in Section III-B.

Figure 3 presents the reactive power control loop in each DGU. The DGU measured reactive power, Q_{meas} , is driven

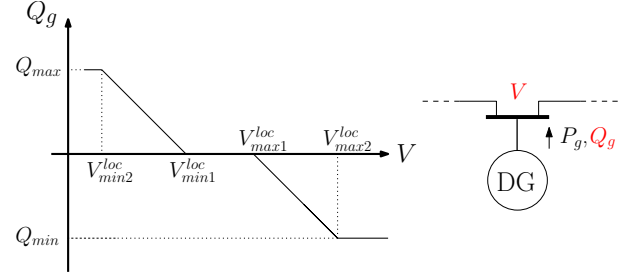


Fig. 2. Local $Q(V)$ control characteristics

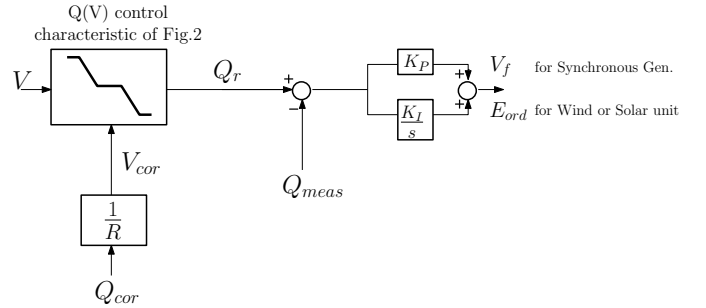


Fig. 3. Reactive power control loop with local $Q(V)$ characteristic

towards the desired reactive power Q_r , using a PI controller. The output of the control loop can be used as reference field voltage V_f , for synchronous generators, or as reference terminal voltage E_{ord} , for power-electronics based DGUs.

The change of reactive power output of one DGU affects the voltages at other buses, including DGU buses. Assuming that these DGUs are not operating in the dead-band of their $Q(V)$ characteristics, they will react to the voltage change by also adjusting their reactive powers. The interactions between locally controlled DGUs is such that the reactive power increase of one DGU causes reactive power decrease of other DGUs. Due to the fast response of local controllers they reach their final values in the order of a few seconds.

B. Upper level: centralized controller

The correction Q_{cor} received from the centralized controller is aimed to adjust the $Q(V)$ characteristic, as depicted in Fig. 3. Namely, the piecewise linear characteristic of Fig. 2 is shifted horizontally until the desired reactive power output is obtained. This is better explained with an example. Figure 4

shows an over-voltage situation and consecutive actions of both levels to clear the violation. The initial operating point of the DGU, shown with the black disk, is at the intersection of the network and the local control $Q(V)$ characteristics. In the example shown, the voltage falls in the dead-band (Fig. 4.a). Therefore, initially the DGU is operating at unity power factor. Under the effect of a disturbance, the network characteristic changes and the voltage at the DGU terminal exceeds the upper local limit V_{max1}^{loc} . The gray disk in Fig. 4.b corresponds to the terminal voltage if there was no control. Although the violation is partly alleviated by a first and fast reaction of the local controller (black disk in Fig. 4.b), the voltage is still above the network admissible upper voltage V_{max}^{cnt} monitored by the centralized controller. In the coming control steps, the latter collects measurements and observes the violation. It computes the required correction Q_{cor} and communicates the latter to the local controller. At the lower level, V_{cor} , which is linearly related to Q_{cor} is used to shift the piecewise linear characteristic $Q(V)$ to the left. The new operating point, shown by the black disk in Fig. 4.c, is back below the centralized controller limit V_{max}^{cnt} .

As shown in Fig.3, V_{cor} and Q_{cor} are related through:

$$V_{cor} = \frac{Q_{cor}}{R} \quad (1)$$

where R is the droop coefficient of the $Q(V)$ characteristic. In this work the same value is considered for both high and low voltage conditions in Fig. 2.

As seen in Fig. 4.c, the DGU effective reactive power change, i.e. the difference of Q_g between the black and the gray disk, is different from the correction Q_{cor} received from the centralized controller. There is a linear relation between both of them though. This relation will be detailed in subsection III-D.

It should be noted that two different voltage limits can be specified for the local and centralized controllers. Since in this scheme the objective of the local controller is to mitigate, but not fully remove the violation in the very first moments, a relaxed range of voltage is considered ($V_{max1}^{loc} > V_{max}^{cnt}$) in the above example. This range is further modified by the centralized controller to smoothly adjust the operating point. A similar response can be illustrated for an under voltage problem.

Coming back the reactive power control loop of Fig.3, the expression of Q_r as a function of V and V_{cor} can be detailed as follows:

$$Q_r = \begin{cases} Q_{max} & \text{if } V - V_{cor} \leq V_{min2}^{loc} \\ R(V_{min1}^{loc} + V_{cor} - V) & \text{if } V_{min2}^{loc} < V - V_{cor} < V_{min1}^{loc} \\ 0 & \text{if } V_{min1}^{loc} \leq V - V_{cor} \leq V_{max1}^{loc} \\ -R(V - V_{max1}^{loc} - V_{cor}) & \text{if } V_{max1}^{loc} < V - V_{cor} < V_{max2}^{loc} \\ Q_{min} & \text{if } V - V_{cor} \geq V_{max2}^{loc} \end{cases} \quad (2)$$

For very high (resp. very low) voltage the desired value of reactive power is saturated at its maximum (resp. minimum)

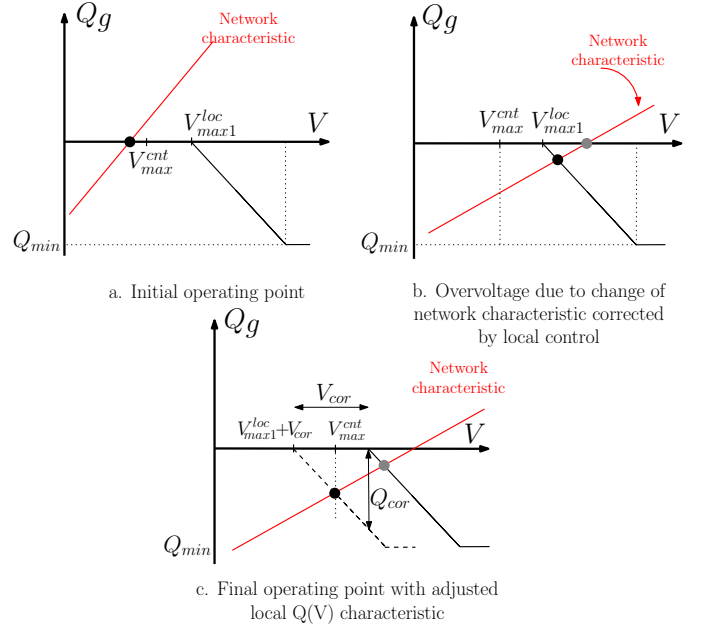


Fig. 4. Over voltage correction with combined control

value, while it is kept at zero if the measured voltage is within the dead-band. And, in the remaining two voltage intervals, the variation is linear according to the droop R . Having V_{cor} in the right-hand side of the Eq. (2) causes the shift of voltage intervals when needed.

C. Formulation of upper-level Model Predictive Control

As mentioned before, a multi-time step optimization is at the heart of the MPC used at the centralized level. The control variables are the corrections Q_{cor} to be communicated to the lower level, and the controlled variables are DGU reactive power outputs Q_g .

The objective of the centralized control is similar to the one used in [5]. However, some modifications to account for the local controller impacts are required.

Since the focus is only on reactive power of the DGUs, the objective is:

$$\min_{Q_{cor}, \epsilon} \sum_{i=0}^{N_c-1} \|Q_g(k+i) - Q_{meas}(k)\|_R^2 + \|\epsilon\|_S^2 \quad (3)$$

The first term in (3) aims at minimizing the deviations of DGUs reactive powers from their measured values $Q_{meas}(k)$. The diagonal matrix R is the weight assigned to those deviations. The second term involves the slack variables ϵ aimed at relaxing the inequality constraints in case of infeasibility; the entries of the diagonal matrix S are given very high values. k is the given time step and N_c is the control horizon in which the objective function is minimized.

The above objective is satisfied subject to the linearized system evolution at the future N_p discrete steps:

for $i = 1, \dots, N_p$:

$$\mathbf{V}(k+i|k) = \mathbf{V}(k+i-1|k) + \mathbf{S}_V [\mathbf{Q}_g(k+i-1) - \mathbf{Q}_g(k+i-2)] \quad (4)$$

where $\mathbf{V}(k+i|k)$ are the predicted bus voltages, and \mathbf{S}_V is sensitivity matrix of those voltages with respect to DGU reactive powers. The prediction is initialized with $\mathbf{V}(k|k)$ set to the last received measurements.

Next, the following inequality constraints are imposed:

for $i = 1, \dots, N_p$:

$$-\varepsilon_1 \mathbf{1} + V_{min}^{cnt} \mathbf{1} \leq \mathbf{V}(k+i|k) \leq V_{max}^{cnt} \mathbf{1} + \varepsilon_2 \mathbf{1} \quad (5)$$

and for $i = 0, \dots, N_c - 1$:

$$\mathbf{Q}_g^{min} \leq \mathbf{Q}_g(k+i|k) \leq \mathbf{Q}_g^{max} \quad (6)$$

$$\Delta \mathbf{Q}_g^{min} \leq \mathbf{Q}_g(k+i|k) - \mathbf{Q}_g(k+i-1|k) \leq \Delta \mathbf{Q}_g^{max} \quad (7)$$

where \mathbf{Q}_g^{min} , \mathbf{Q}_g^{max} , $\Delta \mathbf{Q}_g^{min}$ and $\Delta \mathbf{Q}_g^{max}$ are the lower and upper limits on DGU outputs and on their rate of change. ε_1 , ε_2 and ε_3 are the components of ε , and $\mathbf{1}$ denotes a unit vector. Constraint (6) includes the limits on reactive powers of DGUs, which are updated at each time step based on the measured active power and terminal voltage.

The main difference with respect to formulation shown in [5] is that $\mathbf{Q}_g(k)$ is linearly related to the control variable optimized by the centralized controller $\mathbf{Q}_{cor}(k)$. The sensitivity of DGU reactive power changes $\Delta \mathbf{Q}_g(k)$ with respect to the control variable changes $\Delta \mathbf{Q}_{cor}(k)$ is derived in the following subsection.

D. Sensitivity matrices

Figure 4.c is redrawn with additional information in Fig.5 showing the effective change of reactive power, $\Delta \mathbf{Q}_g$, and the correction sent by the centralized controller, \mathbf{Q}_{cor} . Hereafter, the relation between these two variables is derived.

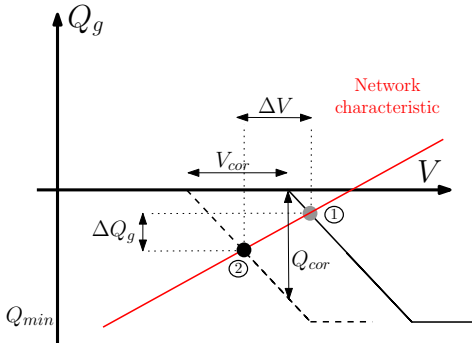


Fig. 5. Comparison of requested and effective reactive power adjustments

Assuming R_i is the already defined droop of the i -th DGU $Q(V)$ characteristic, the equation of the dashed line in Fig. 5 is:

$$Q_{gi} - Q_{cor,i} = -R_i(V_i - V_{max}^{loc}) \quad (8)$$

Considering small deviations denoted with Δ , Eq. (8) gives:

$$\Delta Q_{gi} - \Delta Q_{cor,i} = -R_i \Delta V_i \quad (9)$$

In matrix form, this equation can be rewritten as:

$$\Delta \mathbf{Q}_g = \Delta \mathbf{Q}_{cor} - \mathbf{R} \Delta \mathbf{V} \quad (10)$$

where \mathbf{R} is a diagonal matrix whose entries are the droop coefficients R_i .

The variation of the bus voltages with the DGU reactive power is given by:

$$\Delta \mathbf{V} = \mathbf{S}_V \Delta \mathbf{Q}_g \quad (11)$$

The sensitivity matrix \mathbf{S}_V can be obtained from the transposed inverse of the power flow jacobian matrix. As an alternative, each column of the sensitivity matrix can be computed by running a power flow calculation with one DGU reactive power slightly modified, and simply dividing the variation of the monitored bus voltages by the reactive power variation. Interested readers are referred to [5] for more detail.

By substituting (11) in (10), one easily obtains:

$$\Delta \mathbf{Q}_g = (\mathbf{1} + \mathbf{R} \mathbf{S}_V)^{-1} \Delta \mathbf{Q}_{cor} = \mathbf{S}_Q \Delta \mathbf{Q}_{cor} \quad (12)$$

where $\mathbf{1}$ is a unit matrix. $\mathbf{S}_Q = (\mathbf{1} + \mathbf{R} \mathbf{S}_V)^{-1}$ is the sensitivity matrix of the DGU reactive powers to the reactive power controls.

Equation (12) can be rewritten at time $k+i$ as:

$$\begin{aligned} \Delta \mathbf{Q}_g(k+i) &= (\mathbf{1} + \mathbf{R} \mathbf{S}_V)^{-1} \Delta \mathbf{Q}_{cor}(k+i) \\ &= \mathbf{S}_Q \Delta \mathbf{Q}_{cor}(k+i) \end{aligned} \quad (13)$$

Finally by substituting $\Delta \mathbf{Q}_g(k+i)$ as $\mathbf{Q}_g(k+i) - \mathbf{Q}_{meas}(k)$ and $\Delta \mathbf{Q}_{cor}(k+i)$ as $\mathbf{Q}_{cor}(k+i) - \mathbf{Q}_{cor}(k)$, the sought linear relation is:

$$\mathbf{Q}_g(k+i) - \mathbf{Q}_{meas}(k) = \mathbf{S}_Q \mathbf{Q}_{cor}(k+i) - \mathbf{S}_Q \mathbf{Q}_{cor}(k) \quad (14)$$

This relation is added to the set of constraints (4 -7) treated in the optimization problem.

IV. SIMULATION RESULTS

A. Test system

In this section the performance of the combined control architecture, is illustrated on a 75-bus, 11-kV distribution network whose one-line diagram is shown in Fig.6 [8]. It is connected to the upper voltage level (referred to as external grid) through a 33/11 kV transformer.

The network hosts 22 DGUs, consisting of 3.33-MVA doubly fed induction generators driven by 3-MW wind-turbines, and 3-MVA synchronous generators driven by 2.55-MW turbines, respectively. The DGU models and parameters were taken from [9], [10], and simplified in accordance with the type of dynamics considered in this work.

The network feeds 52 loads, of which 38 are modelled as constant current for active power and constant impedance for reactive power, and 14 with induction motors.

It is assumed that the terminal voltage and the active/reactive power outputs of the 22 DGUs are measured, as well as the

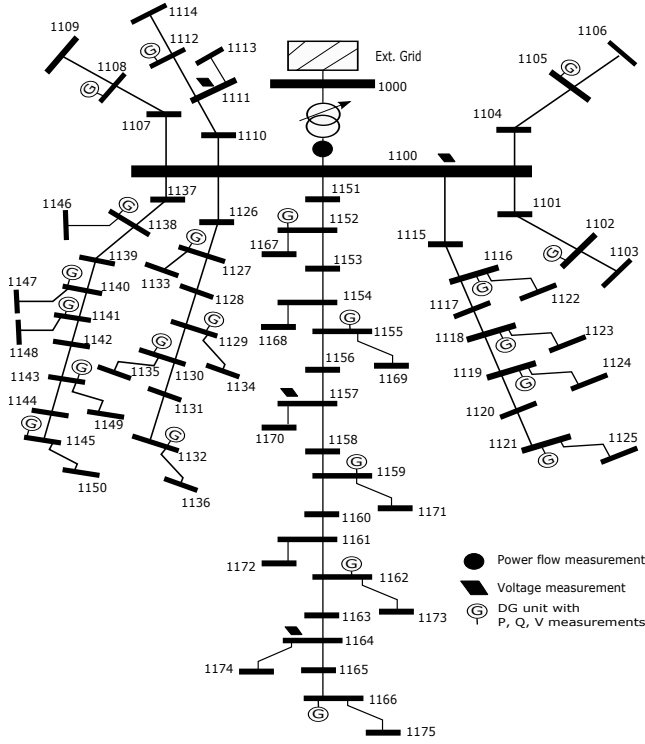


Fig. 6. 75-bus test system

terminal voltage of the transformer on its 11-kV side. These measurements are sent to the centralized controller every 10 s. The DGUs respond to the corrections Q_{cor} with time constants in the order of a few seconds, due to their internal dynamics.

In all simulation results, the following limits on voltages were considered $V_{max}^{cnt} = V_{max1}^{loc} = 1.03 pu$, $V_{min}^{cnt} = V_{min1}^{loc} = 0.97 pu$, $V_{min2}^{loc} = 0.92 pu$ and $V_{max2}^{loc} = 1.08 pu$. Furthermore, the DGUs are assumed to operate between the power factor of 0.9 when consuming and 0.9 when producing reactive power.

The simulations were carried out with RAMSES, a detailed time simulation program developed at the University of Liège [11].

B. Scenario 1: Local control only

In this first scenario, the voltages are initially within the dead-band (0.97-1.03 pu) defined for the controller. As it is shown in Fig. 7, the network voltages drop at $t = 30 s$, under the impact of 4% voltage drop on the HV side of the transformer. The value was chosen to push the operating point outside the dead-band. Therefore, as clearly seen in Fig. 8, those DGUs whose measured terminal voltage is lower than $V_{min1}^{loc} = 0.97 pu$ begin to produce reactive power immediately after the voltage disturbance. The remaining DGUs keep operating at unity power factor. The light gray rectangle at the bottom of Fig. 7 indicates the bus voltage range if there were no local controllers. The voltages are partly but rapidly corrected, leading to fewer buses in under-voltage situation.

Depending on the DGU active power productions, shown in Fig. 9, and constraints on their power factor, different values of

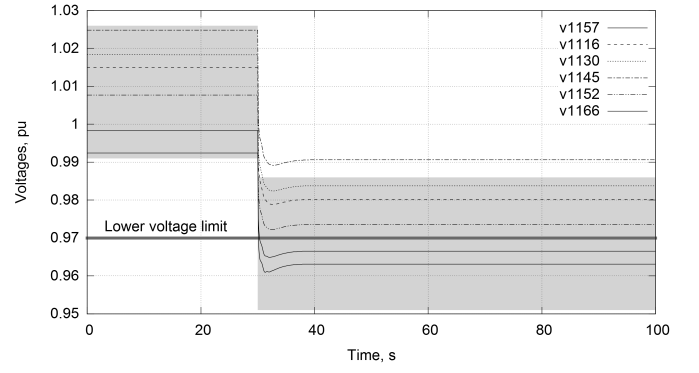


Fig. 7. Scenario 1: Bus voltages

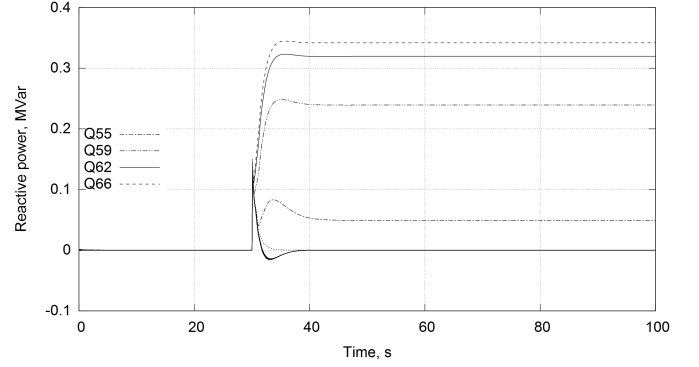


Fig. 8. Scenario 1: Reactive power produced by the units

Q_g^{min} and Q_g^{max} are imposed to the DGUs. However, in this scenario none of the units is limited by its maximum reactive power.

It is worth mentioning that the steady state values of voltages are highly dependent on the choice of the parameters V_{min1}^{loc} , V_{min2}^{loc} , V_{max1}^{loc} and V_{max2}^{loc} as well as limits on DGU reactive powers.

C. Scenario 2: Both control levels acting

It is now assumed that the centralized controller detailed in Section III-C sends the Q_{cor} corrections to the local

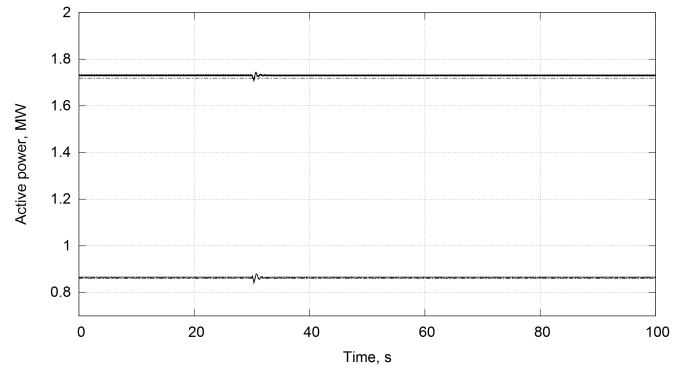


Fig. 9. Scenario 1: Active power produced by the units

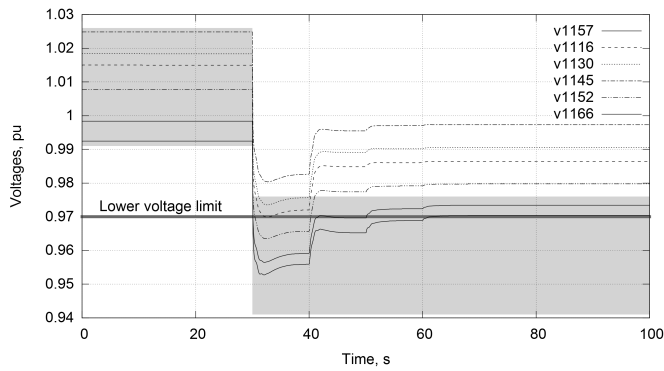


Fig. 10. Scenario 2: Bus voltages

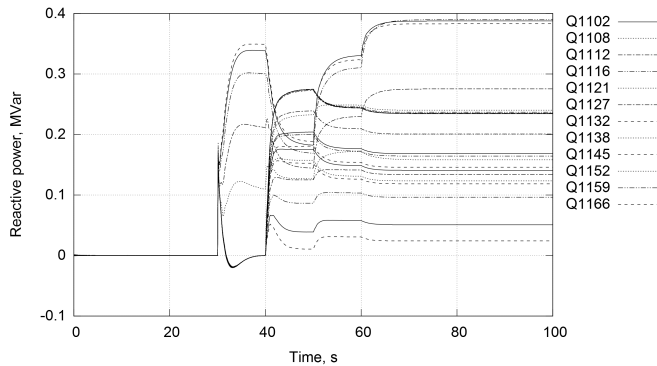


Fig. 11. Scenario 2: Reactive power produced by the units

controllers every 10 seconds. Moreover, the voltage drop on the HV side of the transformer is increased to 5%. By comparing the light gray rectangle at the bottom of Fig. 10 with the voltages in the time interval from $t = 30$ to $t = 40$ s, the fast corrective action of the local controllers can be verified. However, the voltages at some buses are still below the lower admissible limit. Thus, at the next discrete time step, the centralized controller senses the unsatisfactory voltages and, consequently, applies the necessary corrective actions. It adjusts the local controller $Q(V)$ characteristics, steering them to produce the desired reactive powers. The goal is achieved after three successive discrete steps.

Figure 11 shows the variations reactive power generations of various DGUs. The evolution between $t = 30$ and $t = 40$ s is produced by the local controllers, while the response after $t = 40$ s is due to the higher level sending the Q_{cor} corrections. Similar to the Scenario 1, in the time interval from $t = 30$ to $t = 40$ s, the DGU reactive powers are either increased or kept at zero. While from $t = 40$ to $t = 50$ s, the centralized controller increases some and decreases other DGU reactive powers in order to control the voltages in a coordinated way.

V. CONCLUSION

In this paper four control schemes have been briefly introduced aiming at voltage control of medium-voltage distribution networks by DGUs. Out of these four configurations, the

combined control scheme has been considered in detail in the rest of the paper.

At the lower level, DGU output reactive powers are locally controlled according to a piecewise linear $Q(V)$ characteristic. This local control provides a fast response to disturbances. A dead-band has been considered in the latter to keep DGUs operating at unity power factor as far as possible.

At the higher (centralized) control level, model predictive control is used to compute and send reactive power corrections to the local controllers, with the effect of shifting their $Q(V)$ characteristics. This multi-step optimization uses linearized models in which the sensitivity matrices take into account the slope of the local $Q(V)$ characteristics.

The reported simulation results clearly show the combination of a fast but partial correction by the local controllers, followed by the smooth, coordinated control of the DGU reactive powers by the upper-level control.

ACKNOWLEDGMENT

Work supported by Public Service of Wallonia, Dept. of Energy and Sustainable Building, within the framework of the GREDOR project. This research is performed under the supervision of Professor Thierry Van Cutsem at University of Liège.

REFERENCES

- [1] T. Sansawatt, L. F. Ochoa, and G. P. Harrison, "Smart Decentralized Control of DG for Voltage and Thermal Constraint Management," *IEEE Transactions on Power Systems*, vol. 27, pp. 1637–1645, aug 2012.
- [2] P. N. Vovos, A. E. Kiprakis, A. R. Wallace, and G. P. Harrison, "Centralized and Distributed Voltage Control: Impact on Distributed Generation Penetration," *IEEE Transactions on Power Systems*, vol. 22, pp. 476–483, feb 2007.
- [3] A. Seack, J. Kays, and C. Rehtanz, "Time series based distribution grid planning approach with decentralised voltage regulation," in *2014 Power Systems Computation Conference*, pp. 1–7, IEEE, aug 2014.
- [4] H. Soleimani Bidgoli, M. Glavic, and T. Van Cutsem, "Model predictive control of congestion and voltages problems in active distribution networks," *Proc. of CIRED Workshop 2014*, no. June, 2014.
- [5] H. Soleimani Bidgoli, M. Glavic, and T. Van Cutsem, "Receding-Horizon Control of Distributed Generation to Correct Voltage or Thermal Violations and Track Desired Schedules," *paper accepted for presentation at the 2016 Power System Computation Conference (PSCC), Genoa, Italy*, June 2016.
- [6] Y. Chistyakov, E. Kholodova, K. Netreba, A. Szabo, and M. Metzger, "Combined central and local control of reactive power in electrical grids with distributed generation," *2012 IEEE International Energy Conference and Exhibition, ENERGYCON 2012*, pp. 325–330, 2012.
- [7] S. Weckx, C. Gonzalez, and J. Driesen, "Combined central and local active and reactive power control of PV inverters," *IEEE Transactions on Sustainable Energy*, vol. 5, no. 3, pp. 776–784, 2014.
- [8] "United Kingdom Generic Distribution Network (UKGDS)," Available: <http://sedg.ac.uk>.
- [9] J. D. Hurley, L. N. Bize, and C. R. Mummert, "The adverse effects of excitation system var and power factor controllers," *IEEE Transactions on Energy Conversion*, vol. 14, no. 4, pp. 1636–1645, 1999.
- [10] G. Tsourakis, B. M. Nomikos, and C. D. Vournas, "Effect of wind parks with doubly fed asynchronous generators on small-signal stability," *Electric Power Systems Research*, vol. 79, no. 1, pp. 190–200, 2009.
- [11] P. Aristidou, S. Lebeau, and T. Van Cutsem, "Power System Dynamic Simulations Using a Parallel Two-Level Schur-Complement Decomposition," *IEEE Transactions on Power Systems*, pp. 1–12, 2016.

Impact of Amplifier Errors on Position Loop Accuracy of High Precision Moving Stages

S. J. Settels, J. van Duivenbode, J. Everts

Electromechanics and Power Electronics (EPE) group, Eindhoven University of Technology, The Netherlands

Email: s.settels@tue.nl

Abstract—A generic approach to model the position control of an electromechanical system is described that includes several potential error mechanisms originating from the power amplifier, independent of the actual amplifier implementation. The simplified outline of a mechatronic system is given to which models of the power amplifier are added in order to emulate the error mechanisms. Analysis of the impact of each error mechanism on the position accuracy of the mechatronic system is given from which boundary specifications for the power amplifier can be obtained for a certain required position accuracy.

I. INTRODUCTION

Industrial applications using fast-moving high precision stages require power amplifiers with high precision output current generation. The errors produced by the amplifier with respect to the current setpoint input can have a significant influence on the positioning accuracy of a high precision mechatronic system [1].

Combining (simplified) models of the mechanical, electrical and control systems can provide insight in the significance of each error mechanism incorporated in the amplifier. For a given required maximum allowed position error for the complete system, boundary specifications for the amplifier can be deduced, resulting in a more efficient design process of the power electronics.

This paper describes a generic approach to model the position control of an electromechanical system [2], to which models for the amplifier are added in order to emulate the corresponding error mechanisms. The starting point is the ideal amplifier represented by a gain of 1, to which the respective error mechanisms are added: offset current, gain error and non-linearity error, of which the latter is modelled using spatial frequencies [3]. Furthermore, a model of a current-controlled current amplifier with load, comprising closed-loop output current control, is used to simulate the bandwidth limitation and corresponding phase-shift of the amplifier [1]. For each error mechanism, the resulting influence on the positioning accuracy of the mechatronic system is evaluated. Boundary specifications for the performance of the power amplifier can then be deduced for a given required position accuracy.

Model definitions of the mechanical, electrical and control systems are given in section II and section III, together with the respective error mechanism definitions. The resulting simulation results are discussed in section IV, and finally the conclusions are drawn in section V.

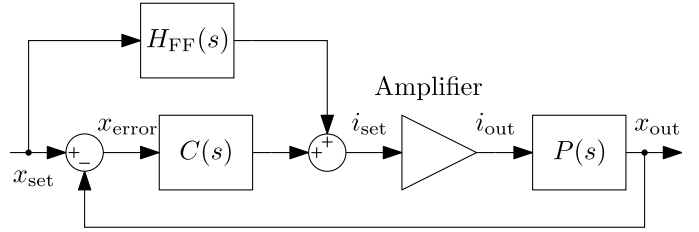


Fig. 1. Global outline of the position control of the analysed electromechanical system.

II. POSITION CONTROL OF ELECTROMECHANICAL SYSTEM

The global outline of the position control system of the electromechanical system analysed in this paper is shown in Fig. 1. The electromechanical plant $P(s)$ consists of a (simplified) linear motor model with a motor constant k_m to calculate the force from the current generated by the amplifier, and a mass m and damping c to which the force is applied (see (1)) [4].

The actual position x_{out} of the moving mass, obtained from the transfer function of $P(s)$, is fed back to the position controller $C(s)$ that, together with a feed forward transfer function $H_{FF}(s)$ (see (2)) consisting of estimates of the actual electromechanical plant, generates the current setpoint i_{set} for the amplifier [2]. The position controller $C(s)$ is a standard PID controller of which the transfer function (including the inverse of \hat{k}_m) is given by (3), which is designed for a closed-loop bandwidth $f_{bw,pos}$.

$$P(s) = \frac{k_m}{ms^2 + cs} \quad (1)$$

$$H_{FF}(s) = \frac{1}{\hat{P}(s)} = \frac{\hat{m}s^2 + \hat{c}s}{\hat{k}_m} \quad (2)$$

$$C(s) = \frac{K_D s^2 + K_P s + K_I}{\hat{k}_m s} \quad (3)$$

The values of the estimated parameters \hat{m} , \hat{c} and \hat{k}_m , are taken equal to the actual parameter values as the aim is to assess amplifier error impact only.

To obtain very high positioning accuracy, it is essential that the input position setpoint x_{set} is delayed with the same amount as the total time delay in the feed forward path, comprising of $H_{FF}(s)$, the amplifier and $P(s)$ [5]. In order to achieve this when the system is transformed to the discrete

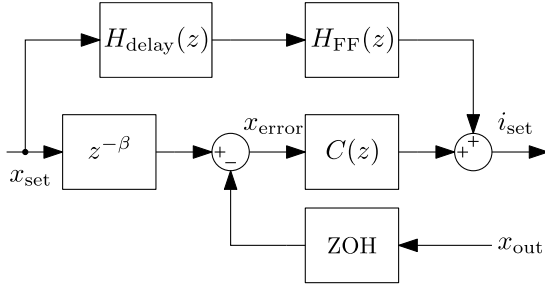


Fig. 2. Outline of the discrete position control model including delays $H_{\text{delay}}(z)$ and $z^{-\beta}$.

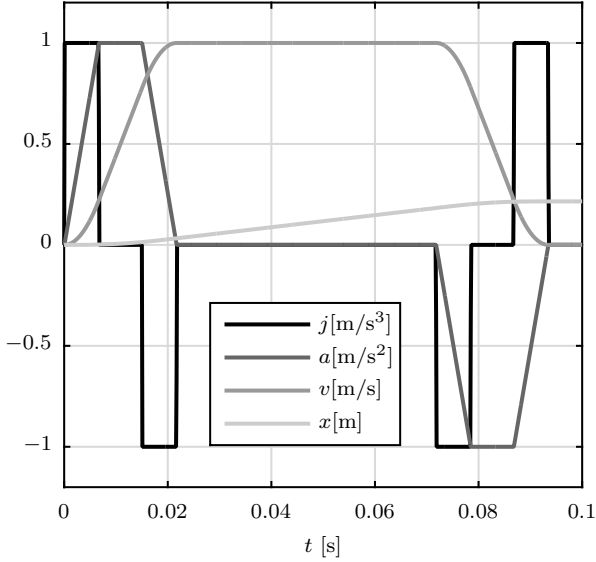


Fig. 3. Normalized representation of the 3rd order motion profile used as position input.

domain with a sample frequency of $f_{s,\text{pos}}$, the input of the feedback subtractor is delayed with a fixed integer number of samples β and the input of $H_{\text{FF}}(s)$ is delayed with a tunable natural number of samples α using an interpolating delay function, see (4). Fig. 2 shows the resulting discrete position control model with the added delays $H_{\text{delay}}(z)$ and $z^{-\beta}$, and a Zero-Order Hold (ZOH) block to convert the actual position from the continuous domain to the discrete domain with sample frequency $f_{s,\text{pos}}$.

$$H_{\text{delay}}(z) = \alpha + (1 - \alpha)z^{-1} \quad (4)$$

A 3rd order motion profile is used for the position input setpoint x_{set} of which a normalized representation is shown in Fig. 3. The parameters of the position control system used in this paper for a generic high-speed high precision moving stage are given in Table I.

III. AMPLIFIER ERROR MODELLING

A model for implementing additive current errors (offset, gain error and non-linearity) is described in subsection III-A,

TABLE I
POSITION CONTROL PARAMETERS

Parameter	Value	Unit
k_m	200	N/A
m	75	kg
c	200	Ns/m
v^*	3	m/s
a^*	200	m/s ²
j^*	$3 \cdot 10^4$	m/s ³
$f_{s,\text{pos}}$	20	kHz
$f_{\text{bw,pos}}$	500	Hz

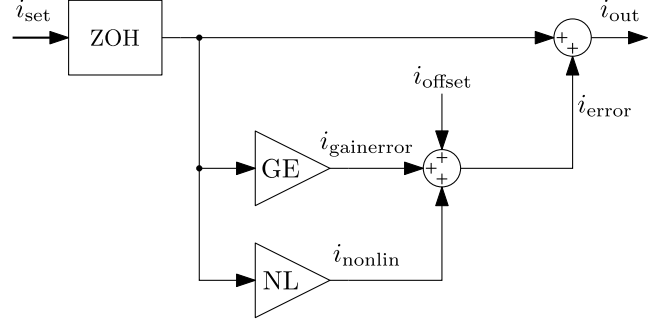


Fig. 4. Schematic representation of additive current errors.

and an implementation of a current-controlled current amplifier with closed-loop current control for modelling bandwidth limitation is given in subsection III-B.

A. Additive current errors

The potential current generation errors discussed in this paper that give an error current i_{error} that can be added to obtain the modelled output current i_{out} of the amplifier, are offset current, gain error and non-linearity error [3]. A schematic outline of the amplifier error model is drawn in Fig. 4 which does not contain any details concerning the actual implementation of the amplifier. The respective error currents i_{offset} , $i_{\text{gainerror}}$ and i_{nonlin} are added, resulting in i_{error} which is added to i_{set} . A ZOH block is added at the input to convert the sample rate of i_{set} from $f_{s,\text{pos}}$ to $f_{s,\text{cur}} = 1$ MHz, which corresponds with the fixed-step size at which the discrete amplifier and mechanical plant models are simulated.

While the implementation of the offset current and gain error is straightforward, for the generation of i_{nonlin} a dimensionless spatial frequency f_{spat} [A/A] is used to obtain non-linear components as a function of i_{set} . The equations for even and odd functions respectively are given in (5) and (6), where i_{NL} is the non-linearity current amplitude and i_{max} defines the applicable current range.

$$i_{\text{nonlin,even}} = i_{\text{NL}} \cdot \cos\left(2\pi f_{\text{spat}} \frac{i_{\text{set}}}{i_{\text{max}}}\right) \quad (5)$$

$$i_{\text{nonlin,odd}} = i_{\text{NL}} \cdot \sin\left(2\pi f_{\text{spat}} \frac{i_{\text{set}}}{i_{\text{max}}}\right) \quad (6)$$

Example plots of both equations for $f_{\text{spat}} = 0.5$ A/A and $f_{\text{spat}} = 3$ A/A are shown in Fig. 5 and Fig. 6 for the even and

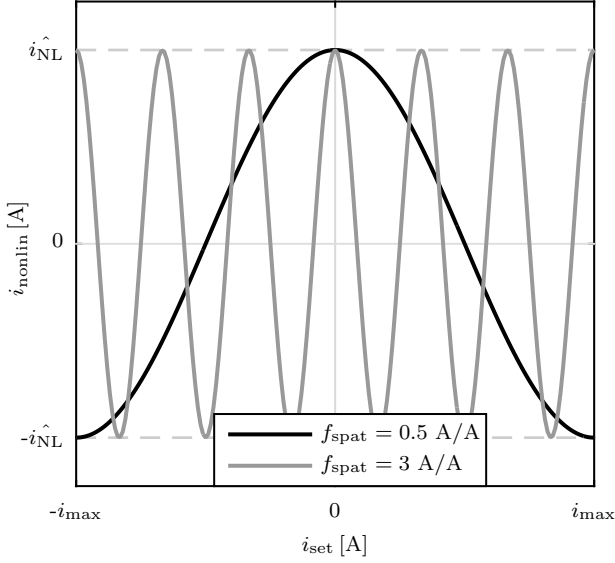


Fig. 5. Example plot of i_{nonlin} as a function of i_{set} for $f_{\text{spat}} = 0.5 \text{ A/A}$ and $f_{\text{spat}} = 3 \text{ A/A}$, regarding even non-linearity.

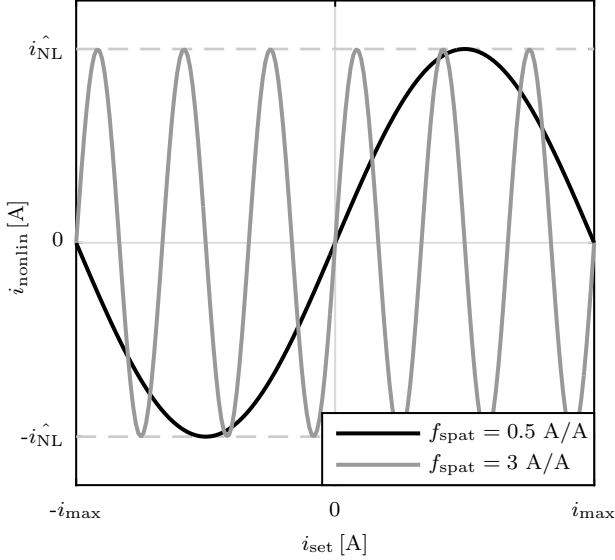


Fig. 6. Example plot of i_{nonlin} as a function of i_{set} for $f_{\text{spat}} = 0.5 \text{ A/A}$ and $f_{\text{spat}} = 3 \text{ A/A}$, regarding odd non-linearity.

TABLE II
NON-LINEARITY PARAMETERS

Parameter	Value	Unit
\hat{i}_{NL}	0.04	A
i_{max}	100	A

odd functions respectively. The parameters of the non-linearity error description used in this paper are given in Table II.

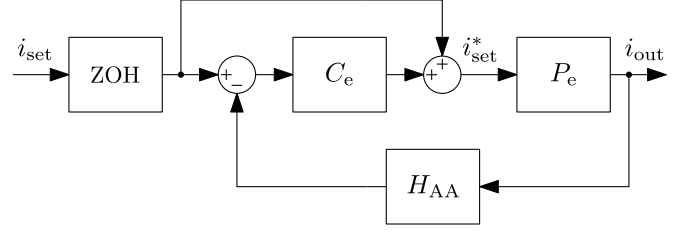


Fig. 7. Outline of the amplifier current control model.

B. Bandwidth limitation

The generic control outline of a current-controlled current amplifier is shown in Fig. 7 with an electrical plant P_e , an output current controller C_e with a direct feed forward path, and an anti-aliasing filter H_{AA} [1]. The anti-aliasing filter is required in a practical implementation, and since it influences the closed-loop control characteristics of the system, it is therefore included in the model. Furthermore, a ZOH block is added at the input to convert the sample rate of i_{set} from $f_{s,\text{pos}}$ to $f_{s,\text{cur}}$, the fixed-step size at which the model is simulated.

An equivalent electrical circuit schematic of P_e is shown in Fig. 8 with output capacitor C_f , load characteristics R_o , L_o and a voltage source emulated EMF . The resonance of C_f and L_o is actively damped to a Butterworth characteristic by subtracting the measured capacitor voltage v_{Cf} , multiplied with damping factor K , from i_{set}^* :

$$i_{\text{amp}} = i_{\text{set}}^* - K \cdot v_{Cf} \quad (7)$$

$$K = \sqrt{2 \cdot \frac{C_f}{L_o}}. \quad (8)$$

A state-space model is derived from the differential equations of the actively damped circuit in Fig. 8 (see (9)). The current controller C_e is of the PID type, see (10), which is tuned such that the open-loop bandwidth $f_{\text{bw},\text{cur}}$ is 10 kHz for the example in this section. The Bode diagrams of the discrete-time models with sample frequency $f_{s,\text{cur}} = 1 \text{ MHz}$ for the electrical plant P_e , current controller C_e , anti-aliasing filter H_{AA} , and resulting open-loop gain $H_{AA}P_eC_e$ are shown in Fig. 9. The anti-aliasing filter is a 2nd order Butterworth low-pass filter with a cut-off frequency of $4 \cdot f_{\text{bw},\text{cur}}$.

$$\begin{bmatrix} \dot{i}_{Lf} \\ \dot{v}_{Cf} \end{bmatrix} = \begin{bmatrix} -\frac{R_o}{L_o} & \frac{1}{L_o} \\ -\frac{1}{C_f} & -\frac{K}{C_f} \end{bmatrix} \begin{bmatrix} i_{Lf} \\ v_{Cf} \end{bmatrix} + \begin{bmatrix} 0 \\ \frac{1}{C_f} \end{bmatrix} i_{\text{set}}^* \quad (9)$$

$$C_e(s) = \frac{K_D s^2 + K_P s + K_I}{s} \quad (10)$$

IV. SIMULATION RESULTS

To obtain insight in the influence of amplifier errors on positioning accuracy, the mechanical, electrical and control system models are combined into a single simulation platform. The resulting position error x_{error} is determined after a settling time of $t_{\text{settling}} = 3 \text{ ms}$ when acceleration $a = 0 \text{ m/s}^2$ and

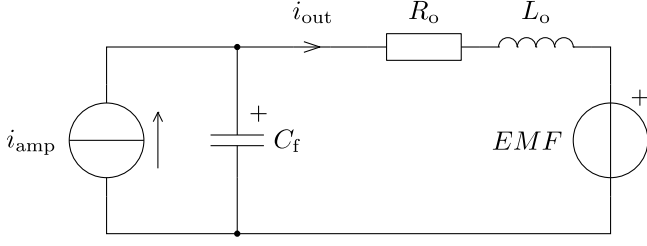


Fig. 8. Schematic representation of electrical plant P_e .

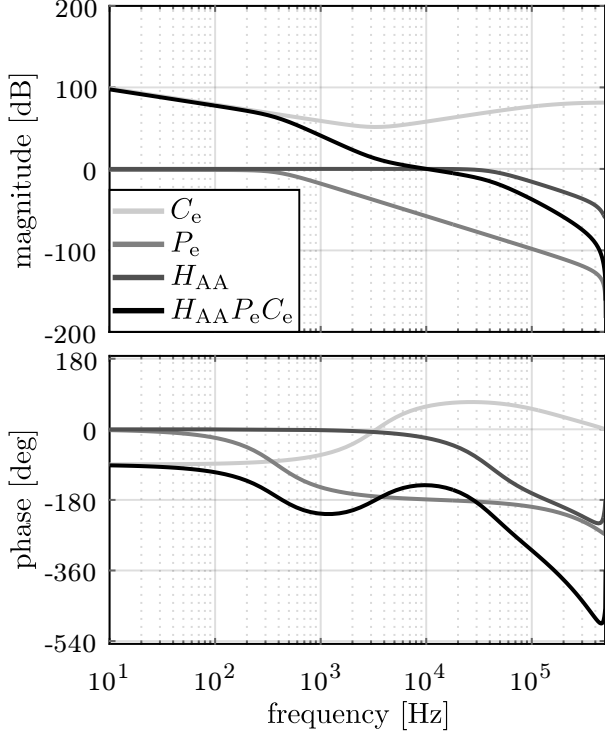


Fig. 9. Bode diagram of the discrete-time models with sample frequency $f_{s,cur} = 1$ MHz for the electrical plant P_e , current controller C_e , anti-aliasing filter H_{AA} , and resulting open-loop gain $H_{AA} P_e C_e$.

TABLE III
PARAMETERS FOR OUTPUT CURRENT CONTROL

Parameter	Value	Unit
R_o	5	Ω
L_o	20	mH
C_f	10	μF

jerk $j = 0$ m/s³ after accelerating from standstill to constant speed. For imaging applications, two aspects of the position error of the moving stage are critical to its performance: low frequency position error defined by MA (Moving Average) determining the absolute error, and a high frequency part defined by MSD (Moving Standard Deviation) determining image contrast loss. The respective position errors $MA(t)$ and

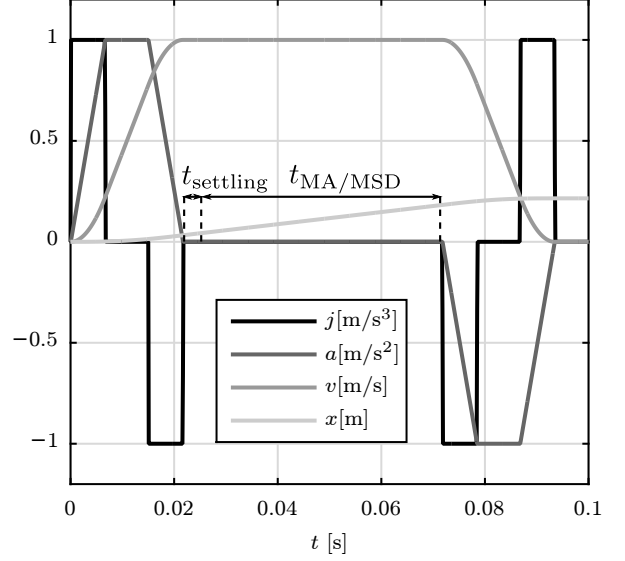


Fig. 10. Motion profile with designated $t_{settling}$ and $t_{MA/MSD}$.

$MSD(t)$ are defined as follows:

$$MA(t) = \frac{1}{T} \int_{t-T/2}^{t+T/2} e(\tau) d\tau \quad (11)$$

$$MSD(t) = \sqrt{\frac{1}{T} \int_{t-T/2}^{t+T/2} (e(\tau) - MA(t))^2 d\tau}, \quad (12)$$

where T represents the imaging expose time window, and $e(t)$ the stage position error x_{error} as function of t [4]. When determining the MA and MSD positioning error, the peak value of the respective definition is taken after the settling time $t_{settling}$ until deceleration, designated with $t_{MA/MSD}$ (see Fig. 10).

When an ideal amplifier is used in the simulation platform with no additional errors introduced and the feedforward delay factor α is properly tuned, the MA and MSD position errors are determined by the numerical accuracy of the simulation run in MATLAB Simulink: $MA = 0.968$ fm and $MSD = 0.691$ fm.

For each individual error mechanism discussed in section III, a diagram is made of maximum MA and MSD position errors as a function of the corresponding error, and the results are discussed in the next paragraphs.

A. Offset error

The current offset error range for which the simulation is run, is set from -1 A to $+1$ A, corresponding with 1% of a ± 100 A output current range, for which the results are shown in Fig. 11. It can be seen that for even relatively large offset currents, the position controller is able to compensate and the maximum MA and MSD position errors remain in the femtometer range.

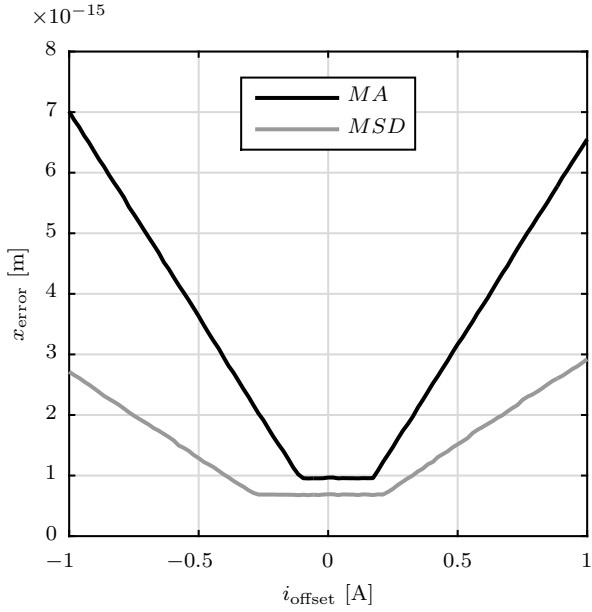


Fig. 11. Maximum MA and MSD position error vs. offset current error.

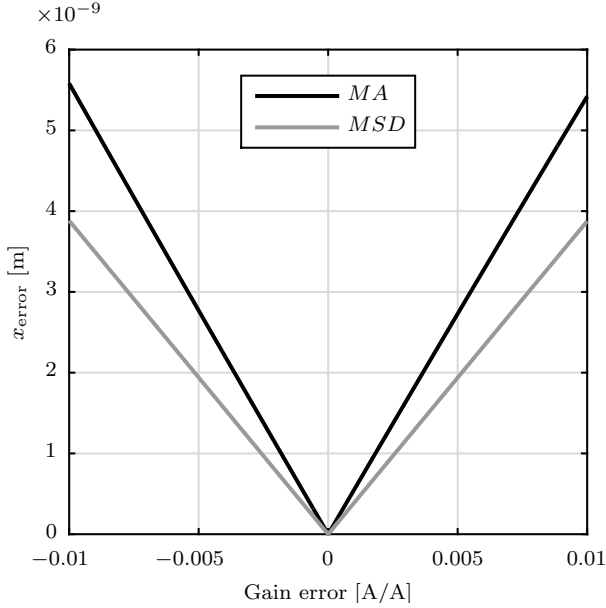


Fig. 12. Maximum MA and MSD position error vs. gain error.

B. Gain error

Fig. 12 shows the maximum MA and MSD position errors for a modelled gain error ranging from -0.01 A/A to $+0.01$ A/A. As can be seen from the graph, gain error originating from the amplifier has a significant influence on the position accuracy of the mechatronic system, increasing to the nanometer range for even relatively small gain errors.

C. Non-linearity error

Both even and odd non-linearity error functions are simulated for a spatial frequency f_{spat} range from 0 A/A to 50 A/A,

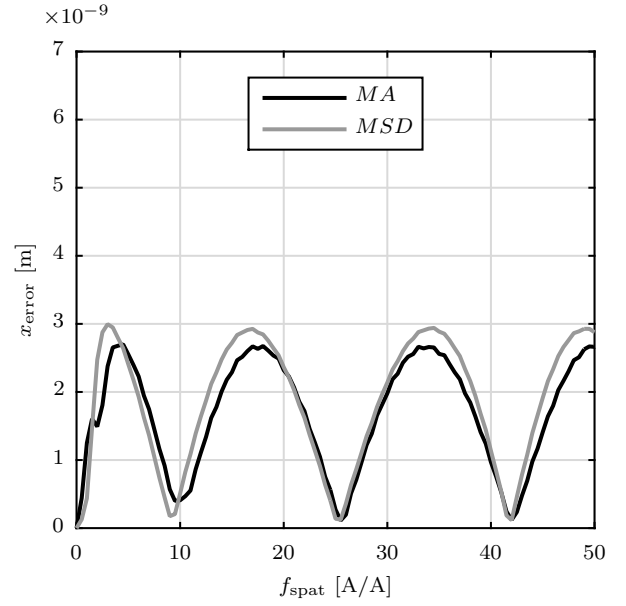


Fig. 13. Maximum MA and MSD position error for even non-linearity as a function of f_{spat} .

and the respective graphs are shown in Fig. 13 and Fig. 14. The resulting maximum MA and MSD position errors are again in the nanometer range. From the waveforms in both graphs can be concluded that distinct spatial frequencies are dominant and determine the potential position error, and thereby the acceptable upper limit for i_{NL} . A correlation exists between f_{spat} and the spectral content of i_{set} depending on the specific system that is analysed. Extensive application-specific analysis might be required to obtain a proper value for the upper limit for amplifier non-linearity.

D. Bandwidth limitation

In order to obtain the bandwidth limitation of the current-controlled amplifier in the positioning system, the model for the current-controlled current amplifier as described in subsection III-B is simulated for an open-loop bandwidth $f_{\text{bw,cur}}$ ranging from 5 kHz to 20 kHz. The resulting maximum MA and MSD position errors for each simulated $f_{\text{bw,cur}}$ are shown in Fig. 15, and the values increase significantly for a decreasing bandwidth from 8 kHz and lower. The minimum at around 7.75 kHz was not expected and is probably around a frequency for which most error frequency components cancel out and are compensated by the current controller. For a bandwidth of 7 kHz or higher, the resulting maximum MA and MSD position errors remain in the order of 10 pm – 50 pm, which is relatively small.

V. CONCLUSION

In order to obtain specifications for the performance of a power amplifier in a mechatronic system with position accuracy requirements, a model containing electrical, mechanical and control systems is presented. An amplifier error model is incorporated to simulate potential error mechanisms

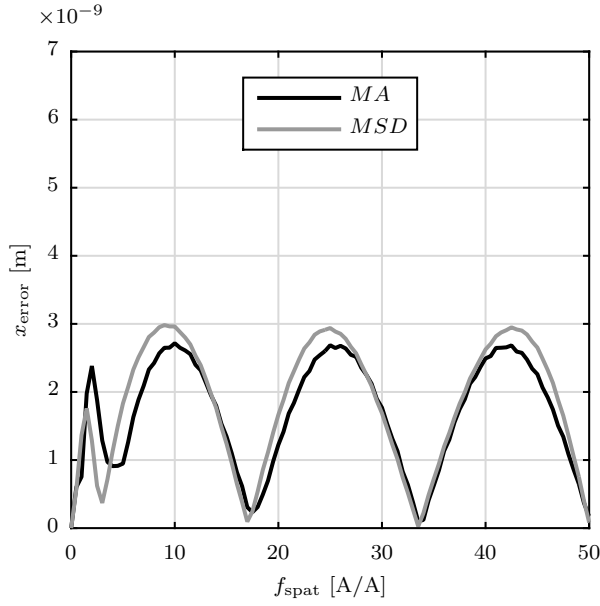


Fig. 14. Maximum MA and MSD position error for odd non-linearity as a function of f_{spat} .

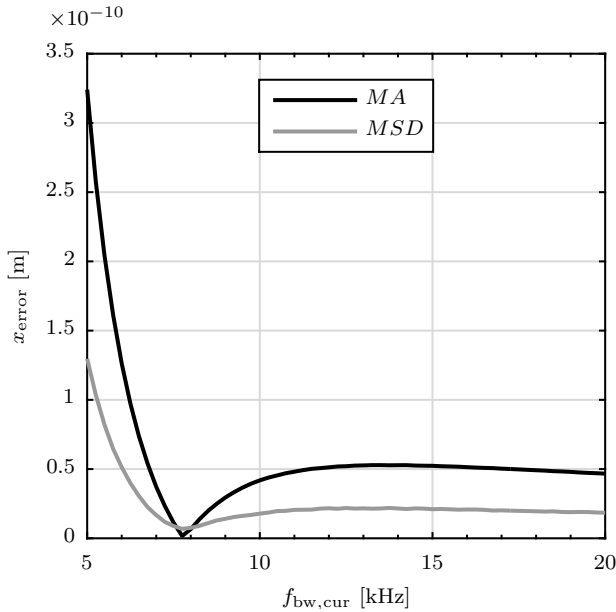


Fig. 15. Maximum MA and MSD position error vs. bandwidth of the current-controlled current amplifier.

originating from the amplifier. A model for additive error components, i.e. current offset, gain error and non-linearity of the output current, is presented together with a generic model for a current-controlled current amplifier to emulate bandwidth limitation. For a 3rd order motion profile, the maximum MA and MSD position error is determined for a range of values of each individual error mechanism in order to determine its significance.

The added offset current has no significant influence on the resulting position error for a mechatronic system actuated by

a linear motor, as it is compensated by the position controller. On the contrary, even a slight gain error results in a significant position error. The same holds for introduced non-linearity errors, though from the simulation results can be concluded that it might differ per specific mechatronic system. Regarding bandwidth limitation, an optimal bandwidth for the current controller seems to exist for the analysed system. Decreasing the bandwidth below the optimum results in a significant increase in position error.

A generic platform has been presented on which extended amplifier error analysis can be conducted and from which boundary specifications can be derived when the required position accuracy of the complete mechatronic system is known. The platform can be extended with increased level of detail in e.g. mechanical model and amplifier electrical model to obtain results that are more correlated to practical applications.

REFERENCES

- [1] J. M. Schellekens, *A Class of Robust Switched-Mode Power Amplifiers with High Linear Transfer Characteristics*. PhD Thesis, Eindhoven University of Technology, 2014.
- [2] M. Boerlage, M. Steinbuch, P. Lambrechts, and M. van de Wal, "Model-based feedforward for motion systems," in *Proceedings of 2003 IEEE Conference on Control Applications*, 2003. CCA 2003., vol. 2. IEEE, 2003, pp. 1158–1163.
- [3] M. Mauerer, A. Tuysuz, and J. W. Kolar, "Distortion Analysis of Low-THD / High-Bandwidth GaN / SiC Class-D Amplifier Power Stages," *2015 IEEE Energy Conversion Congress and Exposition (ECCE)*, pp. 2563–2571, sep 2015.
- [4] H. Butler and W. Simons, "Position Control in Lithographic Equipment," in *ASPE 2013 Spring Topical Meeting MIT Laboratory for Manufacturing and Productivity Annual Summit*, 2013, pp. 7–12.
- [5] H. Butler, "Feedforward signal prediction for accurate motion systems using digital filters," *Mechatronics*, vol. 22, no. 6, pp. 827–835, 2012.

Optimizing state trajectories using surrogate models with application on a mechatronic example

T.J.P. Lefebvre, F. De Belie, G. Crevecoeur

Department of Electrical Energy, Systems and Automation (EESA)

Ghent University (UGent), Technologiepark 913, B-9052 Zwijnaarde, Belgium

e-mail: Tom.Lefebvre@UGent.be

Abstract—The classic design- and simulation methodologies, that are constituting today’s engineer main tools, fall behind with industry’s ever increasing complexity. The strive for technological advancement heralds new performance requirements and optimality remains no longer a concern limited to regime operation. Since the corresponding dynamic optimization problems incorporate accurate system models, the current techniques are plagued by the high computational weight these multi-disciplinary and highly dimensional system models bear with them. This imbalance advocates for the need to adapt the existing approaches. In this study we propose an algorithmic framework as an extension of the direct transcription method, which has already proven its usefulness concerning this matter. It is suggested to construct a surrogate model of the derivative function that is iteratively refined in a region of interest. Thereafter the method will be illustrated on an academic yet nonlinear example.

Index Terms—Direct transcription, Dynamic optimization, Nonlinear mechatronic systems, Surrogate models

I. INTRODUCTION

Optimality of regime operation no longer suffices and transient phenomena are gaining fast importance in nowadays industry, even more for those applications where regime operation loses all meaning and operation merely entails transient behaviour. Optimality has now direct bearing to the realised state trajectory and therefore they should be addressed within the corresponding optimality formulation. Techniques that cope with such problem formulations require the availability of a dynamic model. Whilst dynamical accuracy benefits from increased model complexity - by including multiple modelling disciplines, and considering high dimensionality and nonlinearity - the solution techniques do not and the designated influence can no longer be evaluated analytically; especially when no analytical expression is available and evaluations correspond with numerical computer experiments [1], [2].

For the purpose of fast and reliable dynamic optimization of yet complex and accurate systems, it is necessary to accommodate this computational burden without affecting optimality. From the successful and repeated application within several engineering disciplines, the computational strength of surrogates already appeared [3]. To that end, we will try to incorporate these surrogate modelling techniques within the framework and methods addressing dynamic optimization.

This article provides a brief introduction to these separate research areas and proposes an algorithm to bridge the gap.

II. TRAJECTORY OPTIMIZATION

Whenever it is one’s desire to optimize a system in such manner that the time evolution of states - governed by the system dynamics - is of significance to the interpretation of optimality, it is classified as a dynamic optimization problem [4], [5]. A special class of dynamic optimization problems is referred to as trajectory optimization [6]. Whilst closely related to optimal control problems, trajectory optimization is most often practiced offline and before actual system operation, as part of the design process. The online problem addressing the realisation of the optimized trajectory, as in a tracking problem, is then referred to as the corresponding optimal control problem. So while the input sequence will be considered within trajectory optimization in general, it does not embody its main result.

A. General formulation

A general formulation is presented in (1), where $\mathbf{x} \in \mathbb{R}^{n_x}$ and $\mathbf{u} \in \mathbb{R}^{n_u}$, represent state- and input variables respectively. Each state- and input combination is related to an instantaneous cost $\mathcal{L}(\cdot)$, the term $E(\cdot)$ expresses a possible additional cost related to the end state of the system. The total cost related to a specific time evolution of $\mathbf{u}(t)$ over the time interval $[t_0, t_f]$ is denoted by J . Moreover, the state- and input variables can be subject to constraint functions $\mathbf{g}(\cdot)$ and $\mathbf{h}(\cdot)$. It is assumed that dynamics are governed by the derivative nonlinear function $\mathbf{f}(\cdot)$ and matrix $\mathbf{B}(\cdot)$.

$$\begin{aligned} \min_{\mathbf{u}(\cdot)} J &= \int_{t_0}^{t_f} \mathcal{L}(\mathbf{x}(\tau), \mathbf{u}(\tau)) d\tau + E(\mathbf{x}(t_f)) \\ \text{s.t. } &\begin{cases} \dot{\mathbf{x}} = \mathbf{f}(\mathbf{x}) + \mathbf{B}(\mathbf{x})\mathbf{u} \\ \mathbf{g}(\mathbf{x}, \mathbf{u}) = 0 \\ \mathbf{h}(\mathbf{x}, \mathbf{u}) < 0 \end{cases} \end{aligned} \quad (1)$$

This mathematical formulation can be moulded to fit a vast amount of existing and powerful optimization algorithms; yet, dynamic optimization of physical plant and control system of today’s mechatronic applications remains a challenging problem for which the availability of an assessable dynamic system model, and thus function $\mathbf{f}(\cdot)$ and $\mathbf{B}(\cdot)$, is of vital essence.

B. Direct Transcription

Direct transcription (DT) has proven to be a helpful instrument for solving nonlinear dynamic optimization problems. Its principle is founded on the idea of transcribing the infinite into a finite dimensional problem, resulting into a discretised problem that can be approached as a Nonlinear Program (NLP). The NLP is solved thereafter by practice of an effective nonlinear programming technique.

Transcription is achieved by partitioning and successively parameterizing the continuous problem, leading to the desired discrete equivalent representation. Agreement with dynamics is governed by a set of nonlinear constraints that wards continuity of the time evolution of states.

The technique sets off by partitioning the time interval into n_t time segments, \mathcal{I}_k , for which the boundaries are denoted by t_k and t_{k+1} , respectively:

$$\mathcal{I}_k = [t_k, t_{k+1}], \quad k \in \chi = \{0, \dots, n_t - 1\}$$

For each time interval we introduce a parameterized zero-order hold representation of the control variables, $\mathbf{u}_k(t)$, $t \in \mathcal{I}_k$, that is uniquely defined by the parameters, \mathbf{q}_k . Such is an accurate approximation of realistic control scenarios. More elaborate representations exist yet would distract more than they would contribute.

$$\mathbf{u}_k(t) = \mathbf{q}_k$$

The major trick entails the parameterisation of the state trajectory by introducing $n_t + 1$ state node values, \mathbf{s}_k , as additional function handles and considering an initial value problem for each time segment. Numerical solution yields the trajectory pieces, $\mathbf{x}_k(t|\mathbf{s}_k, \mathbf{q}_k)$:

$$\begin{cases} \dot{\mathbf{x}}_k = \mathbf{f}(\mathbf{x}_k) + \mathbf{B}(\mathbf{x}_k)\mathbf{q}_k, & t \in \mathcal{I}_k \\ \mathbf{x}_k(t_k) = \mathbf{s}_k \end{cases}$$

Continuity of the state trajectory is enforced by introducing n_t constraints, ζ_k , demanding that the propagation of the state trajectory starting at time instant t_k is equal to the state value at time instant t_{k+1} :

$$\zeta_k(\mathbf{s}_{k+1}, \mathbf{s}_k, \mathbf{q}_k) \equiv \mathbf{s}_{k+1} - \mathbf{x}_k(t_{k+1}|\mathbf{s}_k, \mathbf{q}_k) = 0$$

Arranging these ingredients to our liking allows to cook up a formulation of the problem, that can be approached as a NLP. For a more extensive elaboration of the family of direct dynamic optimization methods, we refer to [7].

$$\begin{aligned} & \min_{\mathbf{s}_k, \mathbf{q}_k} \sum_{j=1}^{n_t} \int_{t_j}^{t_{j+1}} \mathcal{L}(\mathbf{x}_j(\tau), \mathbf{u}_j(\tau)) d\tau + E(\mathbf{s}_{n_t}) \\ &= \min_{\mathbf{s}_k, \mathbf{q}_k} \sum_{j=1}^{n_t} \mathcal{L}_j(\mathbf{s}_j, \mathbf{q}_j) + E(\mathbf{s}_{n_t}) \\ & \text{s.t.} \begin{cases} \zeta_k(\mathbf{s}_{k+1}, \mathbf{s}_k, \mathbf{q}_k) = 0 \\ \mathbf{g}(\mathbf{s}_k, \mathbf{q}_k) = 0 \\ \mathbf{h}(\mathbf{s}_k, \mathbf{q}_k) < 0 \end{cases} \end{aligned} \quad (2)$$

We end this section by noting that the numerical propagation can be as simple as trapezoidal quadrature, simplifying the computation of constraints yet at the cost of an increased discretization error [8].

III. SURROGATE APPROXIMATIONS IN DIRECT TRANSCRIPTION

The direct transcription methodology offers a powerful instrument to handle challenging optimization problems and opens the door to dynamic optimization of systems that exhibit strong nonlinearity. Nonetheless, it does not omit evaluation of the derivative function which is often found to be computationally cumbersome; when for example function evaluations correspond with a finite element analysis. Moreover, algorithms that deal with the resulting NLP, such as Sequential Quadratic Programming (SQP), depend inherently on reliable gradient evaluations of the nonlinear constraints; and thus by action of the chain rule, the gradient of the derivative function.

To accommodate both of these challenges we suggest to replace the functions $\mathbf{f}(\cdot)$ and $\mathbf{B}(\cdot)$ by means of the approximated but computationally beneficial models $\hat{\mathbf{f}}(\cdot)$ and $\hat{\mathbf{B}}(\cdot)$:

$$\dot{\mathbf{x}}(\mathbf{x}, \mathbf{u}) = \mathbf{f}(\mathbf{x}) + \mathbf{B}(\mathbf{x})\mathbf{u} \rightarrow \hat{\mathbf{x}}(\mathbf{x}, \mathbf{u}) = \hat{\mathbf{f}}(\mathbf{x}) + \hat{\mathbf{B}}(\mathbf{x})\mathbf{u} \quad (3)$$

In this way evaluations of the derivative function and its gradient are computationally effortless albeit with a loss of accuracy. Subsequently, the NLP can be solved at lower computational cost, thus resulting in shorter computation times, therewith making the direct transcription methodology applicable for computationally burdened problems.

A. Surrogate modelling

Surrogate modelling techniques address the approximation of computationally cumbersome computer models that effectuate a deterministic input-output relation, $\omega \rightarrow \phi$; based on a limited number of known input-output couples. The techniques aim to construct an elementary model that mimics the generic relation whilst omitting its complex underlying structure, such that the complex model can be evaluated at untried parameters sites with less extensive computational force.

$$\phi = \phi(\omega) \rightarrow \hat{\phi} = \hat{\phi}(\omega)$$

The overarching principle originates from the notion that the distance between input sites is a measure for the correlation between the resulting output values. This dissertation considers the Kriging predictor and it is assumed that we have a set of m training sites $\Omega = [\omega_1 \dots \omega_m]'$, $\omega_i \in \mathbb{R}^n$, and responses $\Phi = [\phi_1 \dots \phi_m]'$, $\phi_i \in \mathbb{R}^q$, to our disposal.

The predictor is premised on a model that expresses the deterministic response, $\phi(\omega)$, as the superposition of a regression model, $\mathcal{F}(\omega)$, and stochastic process, $\mathbf{z}(\omega)$. The regression model embodies a linear combination of base functions, $\psi(\omega)$, whilst the stochastic process is characterised by a mean value equal to zero and the following covariance expression:

$$\mathcal{F}(\omega) = \psi(\omega)' \beta \text{ and } E(z_i(\mathbf{v})z_i(\mathbf{w})) = \sigma_i^2 \mathcal{R}_\theta(\mathbf{v} - \mathbf{w})$$

Where σ_i^2 expresses the process covariance for the i^{th} component of the response and $\mathcal{R}_\theta(\mathbf{v} - \mathbf{w})$, defines a parameterized correlation model. As was noted the correlation model depends explicitly on the distance between parameter sites. Further, we

introduce following notations for the design matrix, Ψ , the correlation matrix, Π , and correlation function, $\pi(s)$:

$$\begin{aligned}\Psi &= [\psi(\omega_1) \quad \dots \quad \psi(\omega_m)], \\ \Pi_{ij} &= \mathcal{R}_\theta(\omega_i - \omega_j) \text{ and} \\ \pi(s) &= [\mathcal{R}_\theta(\omega_1 - \omega) \quad \dots \quad \mathcal{R}_\theta(\omega_m - \omega)]\end{aligned}$$

Kriging considers the linear predictor:

$$\hat{\phi}(\omega) = \alpha(\omega)' \Phi$$

A definition for the function, $\alpha(\omega)$, can be obtained by expressing the error $\epsilon(\omega) = \hat{\phi}(\omega) - \phi(\omega)$. Given the stochastic interpretation of $\phi(\omega)$, we can define the mean squared error (MSE): $E(\epsilon(\omega)^2)$. Minimization of this expression to the designated model parameters, yields the desired expression for $\alpha(s)$, and thus $\hat{\phi}(s)$:

$$\hat{\phi}(\omega) = \psi(\omega)' \tilde{\beta} + \pi(s)' \Pi^{-1} (\Phi - \Psi \tilde{\beta})$$

Where $\tilde{\beta}$, $\tilde{\sigma}^2$ and θ are determined by means of a maximum likelihood estimation. It is easily seen that the predictor entails the superposition of the regression model, and a distance based weighing of the observed deviation between output values and the regression model at training sites. For a more extensive elaboration of the methodology and an exposition of typical regression and correlation models, we refer to [9].

B. Sketch of an algorithmic architecture

Since the surrogate model has to be initiated with no prior knowledge available about the solution nor the generic dynamical behaviour, a space filling approach ought to be preferred. Amongst these space filling methods Latin Hypercube Sampling (LHS) is most common practice [10].

The resulting *surrogate* solution, $\{\hat{x}^*\}$, will in general, however optimal under the surrogate dynamics, not be in agreement with the simulated trajectory, $x_{\hat{u}^*}^{sim}$, - that is the trajectory resulting from simulation of the optimized control sequence with real dynamics - since the surrogate dynamic model is only an approximation, and as such only reliable close to sampled sites. This clearly indicates that the sampling strategy is of crucial importance when surrogate models are included within the trajectory optimization framework.

An iterative solution approach (Fig. 1) is proposed that assesses the surrogate performance along the momentary trajectory. Whenever it is found necessary, the surrogate model shall be refined in the neighbourhood of the optimal trajectory resulting from the optimization with the current surrogate model. A similar approach has been suggested by Allison and Deshmukh [11] but has not yet been elaborated.

IV. THE ADAPTIVE SURROGATE REFINEMENT ALGORITHM

The proposed algorithm starts by initialising n_s training sites - by application of the LHS strategy - in the training set, D_{ini} , where we evaluate the functions $\{f, B\}$. These evaluations are used to construct initial surrogate models $\{\hat{f}_0, \hat{B}_0\}$ by use of Kriging. Each step is illustrated unambiguously hereafter:

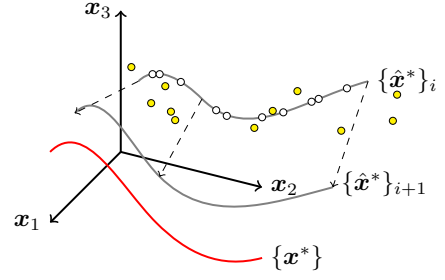


Fig. 1: Illustration of the iterative solution approach through the feasible solution space. The white dots denote the evaluation sites whilst the yellow present a possible refinement sampling plan.

- 1) *Acquire momentary solution*: Solve the NLP of (2) with the current surrogate dynamics using a standard NLP solver, resulting in a momentary optimum $\{\hat{x}^*, \hat{u}^*\}_i$.
- 2) *Generation of validation sites*: We generate n_v time instants t_j , $j \in \vartheta_i = \{1, \dots, n_v\}$ by sampling from a piece wise linear distribution $p_{\hat{x}^*}(t_k)$ that relates to the surrogate's accuracy along the current solution, and such that samples are more likely to be drawn at sites where accuracy is lowest. The authors propose:

$$\{t_j\}_{j \in \vartheta_i} \sim p_{\hat{x}^*}(t_k) = \frac{1}{\max(\text{MSE}_f(\hat{x}^*(t_k)), \text{MSE}_B(\hat{x}^*(t_k)))}$$

The accuracy of the matrix B is assessed by considering each column individually.

- 3) *Error estimation*: Evaluate the surrogate dynamics along the solution by defining an error estimate that compares real derivative function evaluations with surrogate evaluations at the time instants t_j . The authors propose:

$$\max \left(\frac{t_f - t_0}{n_v} \sum_{j=1}^{n_v} \left| \dot{x}(\hat{x}^*(t_j), \hat{u}^*(t_j)) - \hat{\dot{x}}(\hat{x}^*(t_j), \hat{u}^*(t_j)) \right| \right)$$

With $\dot{x}(\cdot)$ and $\hat{\dot{x}}(\cdot)$ defined as in in (3), $\hat{x}^*(t_j)$ a spline interpolation of the discrete vector function $\hat{x}^*(t_k)$, since generally the sampled time instants t_j will not coincide with the time nodes t_k , $\exists j \in \vartheta_i : t_j \notin \{t_k\}_{k \in \chi}$; and $\hat{u}^*(t_j)$ an evaluation of the parameterized input.

The corresponding value can be interpreted as the maximum integrated mean derivative error over the considered time interval, which functions as an estimate for the expected absolute surrogate induced error between the optimal end state, $\hat{x}^*(t_{n_i})$, and $x_{\hat{u}^*}^{sim}(t_f)$. As such we will be able to define an intuitive and generic value for the convergence threshold.

- 4) *Surrogate refinement*: As long as the convergence condition has not been met, construct $\{\hat{f}_{i+1}, \hat{B}_{i+1}\}$ by adding the function evaluations from the previous step, to the training set $D_{i+1} = D_i \cup \{\hat{x}^*(t_j)\}_{j \in \vartheta_i}$ and repeat steps 1:4. As such dynamics will become more accurately from iteration to iteration, in that region seems to contain the true optimum. Crucial is to initialize the next iteration with the solution of the prior.

The algorithm will generate a solution whose proposed trajectory will be in agreement with simulation of the suggested control sequence. That is, the trajectory resulting from the optimization will be in a vicinity of the trajectory resulting from simulation of the optimized control sequence and the real dynamics, assuring practical feasibility of the optimum.

However, the solution will be optimal under the final surrogate dynamics; which only approximate the real dynamics accurately in the vicinity of the surrogate optimum. This self-referencing property will result in an optimum that may deviate from the real optimum. For the time being no measures are taken to drive the surrogate optimum to the real optimum and it is assumed that the initial sampling delivers a sufficient approximation of the global dynamics to assure correspondence with the real optimum.

V. ILLUSTRATIVE EXAMPLES

In this section we will address a mechatronic problem to illustrate the applicability and performance of the proposed algorithm. For this problem an analytical expressions is available and therefore no real urge is present to apply the algorithm. Yet the example has the specific property that it exhibits heavily nonlinear dynamics, and is as such an ideal candidate to demonstrate the potential benefits of the algorithm. It should be noted that for this problem no reduction of computation time shall be observed and performance will be quantified by examining the total number of derivative function evaluations.

The problem considers a trajectory optimization of a whirling pendulum, to demonstrate the working principle and iterative character of the algorithm and its handling of nonlinear dynamics. We assumed a piecewise constant control scenario. The resulting NLP was solved by use of *fmincon*, a standard function provided by the software package MATLAB (R2013a; Mathworks, Natick, MA, USA).

A. Dynamical model

The whirling pendulum can be represented by a nonlinear 4-dimensional state space model. Rotation about the z -axis of the observers frame is denoted by ϕ . A coordinate frame was fixed to the pendulum's point of suspension and rotation about the pendulum's x -axis is denoted by θ , consequently the pendulum's state can be represented by $\mathbf{x} = [\theta \ \dot{\theta} \ \phi \ \dot{\phi}]'$. The state space model has been derived through application of the Euler-Lagrange principle.

$$L(q, \dot{q}) = T + D - V \quad (4a)$$

$$\frac{\partial L(q, \dot{q})}{\partial q} - \frac{d}{dt} \frac{\partial L(q, \dot{q})}{\partial \dot{q}} = \Upsilon = \begin{bmatrix} u_\theta \\ u_\phi \end{bmatrix} \quad (4b)$$

Expressions for kinetic, potential and dissipative energy, are given respectively by T, V and D:

$$T = \frac{1}{2} [\dot{\theta} \ \dot{\phi}] \text{diag}(I_x, I_y \sin^2 \theta + I_z \cos^2 \theta) [\dot{\theta} \ \dot{\phi}]',$$

$$V = -\frac{mg}{2} r \cos \theta \text{ and } D = \frac{1}{2} [\dot{\theta} \ \dot{\phi}] \text{diag}(b_\theta, b_\phi) [\dot{\theta} \ \dot{\phi}]'$$

The moments of inertia are defined in the coordinate system fixed to the pendulum and located at the suspension point

parameter	m	r	$I_x = I_y = 2I_z$	$b_\theta = b_\phi$
value	10 [kg]	1 [m]	4.44 [kgm ²]	0.5 $\left[\frac{\text{kg}\cdot\text{m}}{\text{s}}\right]$

TABLE I: Parameter values of the whirling pendulum model.

with the z -axis according to the longitudinal dimension of the cylindrical pendulum. The length of the cylindrical pendulum is denoted by r , the mass of the system by m and the gravitational constant by g . Values are noted in table I.

B. Optimization problem

We defined an illustrative minimal input cost problem for which the optimal control sequence had to be determined over a predefined time span of 1.5 seconds. Optimality had to be achieved for the quadratic cost, $\mathcal{L}_j(\mathbf{q}_j)$, and was subject to the following boundary states:

$$\mathcal{L}_j(\mathbf{q}_j) = \mathbf{q}_j' \mathbf{q}_j,$$

$$\mathbf{x}_0 = \left[\frac{\pi}{2} \ 0 \ 0 \ 0\right]' \text{ and } \mathbf{x}_{n_t} = \left[\frac{\pi}{4} \ 0 \ \frac{\pi}{2} \ 0\right]'$$

Dynamics were discretised using trapezoidal quadrature with $n_t = 80$ steps, resulting in a step size of about 19 ms.

C. Results

The iterative character of the algorithm is illustrated in Fig. 2. As anticipated, the algorithm gradually forces the optimal trajectory towards the true optimum. Despite the considerable increase of necessary iterations before a feasible solution was attained, the overall number of derivative function evaluations is drastically diminished. A reduction of 97.57% was achieved, having evaluated the derivative function 2880 times to obtain the real optimum compared to 70 evaluations using ASR. Included are 30 evaluations to initialize the surrogate models and 5×8 additional refinement evaluations.

The final control sequence has been simulated with the real dynamics as a visual validation of the measure that was taken to guarantee practical feasibility.

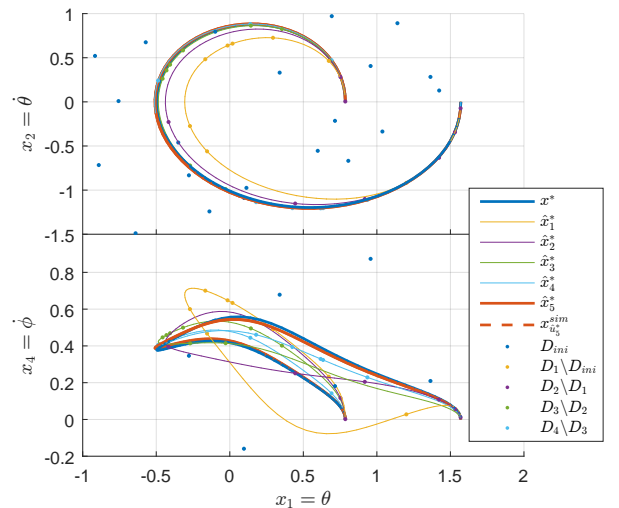


Fig. 2: The true optimal trajectory, \mathbf{x}^* , the iterative trajectories, $\hat{\mathbf{x}}_i^*$, and the simulated trajectory for the final control sequence, $\mathbf{x}_{u^*}^{sim}$, which coincides with $\hat{\mathbf{x}}_5^*$. ($n_t = 80, n_s = 90, n_v = 8$).

VI. CONCLUSIONS AND FUTURE DEVELOPMENT

In this treatise we proposed to tackle computational unwieldiness, introduced by derivative function evaluations in a dynamic optimization context, by exploitation of the computational grace of surrogate models. The proposed algorithmic framework managed to enforce reductions in evaluations up to 97.57%, when applied on a highly nonlinear mechatronic problem, and thus exhibits large potential for future applications where derivative function evaluations correspond with extensive computation time and as such offer a lever to extend the applicability of trajectory optimization to highly accurate models. For the time being a self-referencing mechanism is still inherent to the algorithm and partially subverts the global optimization, moreover due to its stochastic nature the solution may differ for each run. Therefore further sculpting of the algorithm shall be required before a robust and wide applicability will be possible. Yet the authors are confident that within a reasonable timespan such improvements can be obtained.

ACKNOWLEDGEMENTS

The authors acknowledge the support of the Strategic basic research project EMODO of the Flanders Make Strategic Research Centre for the Manufacturing Industry, and the FWO Research project G.0D93.16N.

REFERENCES

- [1] P. J. Moriarty and A. C. Hansen. *AeroDyn Theory Manual*. National Renewable Energy Laborator, 1617 Cole Blvd., Golden, CO 80401-339, August 2005.
- [2] Jason P Halloran, Ahmet Erdemir, and Antonie J van den Bogert. Adaptive surrogate modeling for efficient coupling of musculoskeletal control and tissue deformation models. *Journal of biomechanical engineering*, 131(1):011014, 2009.
- [3] Alexander Forrester, Andras Sobester, and Andy Keane. *Engineering design via surrogate modelling: a practical guide*. John Wiley & Sons, 2008.
- [4] Rush D Robinett III, David G Wilson, G Richard Eisler, and John E Hurtado. *Applied dynamic programming for optimization of dynamical systems*, volume 9. SIAM, 2005.
- [5] Lorenz T. Biegler. An overview of simultaneous strategies for dynamic optimization. *Chemical Engineering and Processing: Process Intensification*, 46(11):1043 – 1053, 2007. Special Issue on Process Optimization and Control in Chemical Engineering and Processing.
- [6] P. Fiorini and Z. Shiller. Time optimal trajectory planning in dynamic environments. In *Robotics and Automation, 1996. Proceedings., 1996 IEEE International Conference on*, volume 2, pages 1553–1558 vol.2, Apr 1996.
- [7] Moritz Diehl, Hans Georg Bock, Holger Diedam, and Pierre-Brice Wieber. Fast direct multiple shooting algorithms for optimal robot control. *Fast Motions in Biomechanics and Robotics*, 2005.
- [8] Oskar Stryk. *Optimal Control: Calculus of Variations, Optimal Control Theory and Numerical Methods*, chapter Numerical Solution of Optimal Control Problems by Direct Collocation, pages 129–143. Birkhäuser Basel, Basel, 1993.
- [9] H. B. Nielsen, S. N. Lophaven, and J. Søndergaard. *DACE - A Matlab Kriging Toolbox*. Informatics and Mathematical Modelling, Technical University of Denmark, DTU, 2002.
- [10] Michael D McKay, Richard J Beckman, and William J Conover. A comparison of three methods for selecting values of input variables in the analysis of output from a computer code. *Technometrics*, 42(1):55–61, 2000.
- [11] Anand P Deshmukh and James T Allison. Design of nonlinear dynamic systems using surrogate models of derivative functions. pages V03BT03A011–V03BT03A011, 2013.

2D Harmonic Modeling of Eddy Currents in Segmented Rectangular Conductors

C.H.H.M. Custers, J.W. Jansen, and E.A. Lomonova

Department of Electrical Engineering, Eindhoven University of Technology, Eindhoven, The Netherlands

Abstract—The paper concerns the semi-analytical modeling of eddy currents in segmented structures of electromagnetic devices. A Fourier series is used to describe the spatial distribution of the conductivity and included in the magnetic field solutions. By incorporating multiple time harmonics in the solution, transient behavior of forces due to eddy currents can be obtained. To validate the developed method, it is applied to a coreless linear motor and compared to finite element results. The eddy currents in segmented conducting structures of motors, such as permanent magnet arrays, can be accurately determined with this method.

I. INTRODUCTION

In synchronous permanent magnet (PM) machines, the static field of the magnets interacts with a time varying field caused by a set of coils. Besides the intended force, also parasitic forces are produced, for instance due to eddy currents induced in non-laminated conducting parts of the machine, such as the magnets. These currents and their associated force and losses depend on the structure of the magnets and can be reduced by segmentation [1]. Hence, to accurately predict the eddy current behavior in the magnets, their finite dimensions and segmentation has to be taken into account.

The 2D Fourier analysis technique [2], [3], is a fast alternative for finite element analysis for the design and analysis of electromagnetic devices. With this semi-analytical technique, eddy currents and their reaction field can be modeled. A limitation of this method as described in [2], [4] is that the eddy currents are only calculated in a infinitely long electrically conducting slab with homogeneous material properties, and as a result, segmentation is not taken into account. To overcome this limitation, in [5] the eddy currents in a conducting plate with finite length are approximated with the method of images. However, for problems in which the conducting part is smaller than the source of the magnetic field the results are inaccurate.

In this paper, the Rigorous Coupled Wave Analysis (RCWA) technique [6] is applied to 2D quasi-static magnetic field modeling of motor topologies with a variable conductivity in the Cartesian domain. In [6], the diffraction of a high-frequent electromagnetic wave by a planar grating with a position dependent permittivity and permeability is modeled. With this technique, inhomogeneous material properties are included in the solution of electromagnetic field quantities. By incorporating a position dependent conductivity function in the Fourier based field analysis, eddy currents in segmented parts are modeled. The developed method is applied to a coreless motor model of which the top half of a periodic section is

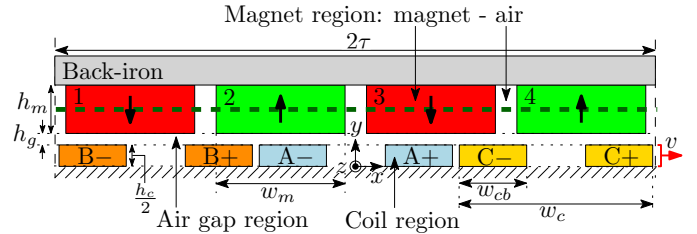


Fig. 1. Top half geometric model of a periodic section of a linear coreless motor.

shown in Fig. 1. The back-iron is assumed to be infinitely permeable and nonconductive because the focus of the paper is on the eddy currents induced in the segmented region.

II. MAGNETIC FIELD MODELING

The model of the coreless motor of Fig. 1 is divided into three horizontal regions, respectively the magnet region, air gap region and coil region. To obtain the solutions of the magnetic field quantities, the vector potential formulation is used. The magnetic vector potential \vec{A} is defined as $\vec{B} = \nabla \times \vec{A}$, where \vec{B} is the magnetic flux density. Because a two-dimensional problem is treated, the vector potential is reduced to the z -component. Based on Maxwell's equations and the constitutive relations, the Poisson equation is derived for nonconducting regions

$$\frac{\partial^2 A_z}{\partial x^2} + \frac{\partial^2 A_z}{\partial y^2} = -\mu_0 \frac{\partial M_y}{\partial x} - \mu_0 \mu_r J_z^{ext}, \quad (1)$$

where μ_0 is the permeability of vacuum and μ_r is the relative permeability. M_y is the remanent magnetization and J_z^{ext} is an externally imposed current density.

In the magnet region, eddy currents are induced, which can be obtained from the vector potential by

$$J_z^{eddy} = -\sigma(x) \frac{\partial A_z}{\partial t}, \quad (2)$$

where $\sigma(x)$ describes the position dependent conductivity of the magnet array. Generally, the vector potential of a conducting region has to satisfy the diffusion equation

$$\frac{\partial^2 A_z}{\partial x^2} + \frac{\partial^2 A_z}{\partial y^2} = -\mu_0 \frac{\partial M_y}{\partial x} + \mu_0 \mu_r \sigma(x) \frac{\partial A_z}{\partial t}. \quad (3)$$

III. SEMI-ANALYTICAL SOLUTION

The magnetic field solutions are expressed in terms of Fourier series. The model is assumed to be periodical in the x -direction. As a result, the x -dependent solution is described

by a complex Fourier series. To model the movement of the coil array, also the time dependent solution is described by a Fourier series. Because there is no correlation between the different time harmonics the principle of superposition is applicable. As a consequence, the vector potential solution can be determined for each time harmonic separately and the results can be superimposed. The solution to the vector potential is found by applying the method of separation of variables and has the following general form with a homogeneous and particular solution respectively

$$A_z(x, y, t) = \sum_{m=-\infty}^{\infty} \sum_{n=-\infty}^{\infty} \left(P_{m,n}(x, y, t) + Y_{m,n}(y) e^{j(k_n x + \omega_m t)} \right). \quad (4)$$

The spatial frequency, k_n , is defined as $k_n = \frac{n\pi}{\tau}$, where τ is half of the periodic width of the model and $\omega_m = \frac{m2\pi}{T}$, where T is the time period. The y -dependent solution $Y_{m,n}(y)$ is equal to

$$Y_{m,n}(y) = a_{m,n} e^{\sqrt{\lambda_{m,n}} y} + b_{m,n} e^{-\sqrt{\lambda_{m,n}} y}, \quad (5)$$

where $a_{m,n}$ and $b_{m,n}$ are unknown coefficients for each harmonic which will be determined by applying boundary conditions between the regions. The eigenvalues $\lambda_{m,n}$ of the y -dependent solution are derived in section III-B and III-C. $P_{m,n}(x, y, t)$ in (4) is the particular solution that is related to the source terms and will be derived in the following section.

A. Particular solution

For the magnet region the following holds for the particular solution

$$P_{0,n}(x) = \begin{cases} \mu_0 \frac{1}{k_n} M_{y_{0,n}} e^{j k_n x} & \text{for } |n| > 0, \\ 0 & \text{for } n = 0, \end{cases} \quad (6)$$

where $M_{y_{0,n}}$ are the Fourier coefficients describing the spatial distribution of the magnetization which does not depend on time. For the coil region with the source current density the following holds

$$P_{m,n}(x, y, t) = \begin{cases} \mu_0 \mu_r \frac{1}{k_n^2} J_{z_{m,n}}^{ext} e^{j(k_n x + \omega_m t)} & \text{for } |n| > 0, \\ -\mu_0 \mu_r \frac{1}{2} J_{z_{m,n}}^{ext} y^2 e^{j(k_n x + \omega_m t)} & \text{for } n = 0. \end{cases} \quad (7)$$

where $J_{z_{m,n}}^{ext}$ are the Fourier coefficients that describe the spatial and time distribution of the externally imposed current density. The three-phase current density in the coil array, described by $J_{z_{m,n}}^{ext}$, is sinusoidal and synchronously commutated for maximum propulsion force. This means that the frequency of the current is equal to $f = \frac{v}{\tau}$, where v is the speed of the coil array. The time varying behavior of the current density is written as the complex form of a cosine function

$$J_{ph}(t) = \hat{J} \frac{1}{2} \left(e^{j(2\pi \frac{v}{\tau} t + \theta_{ph})} + e^{-j(2\pi \frac{v}{\tau} t + \theta_{ph})} \right), \quad (8)$$

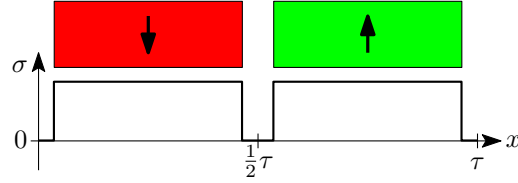


Fig. 2. Varying conductivity as a function of position in the magnet region.

where \hat{J} is the peak current density, ph denotes the phase and $\theta_A = 0$, $\theta_B = -\frac{2\pi}{3}$ and $\theta_C = \frac{2\pi}{3}$. The coefficients $J_{z,ph_{m,n}}$ of phase ph are calculated by performing the integral

$$J_{z,ph_{m,n}} = \hat{J} K_{ph_n} \frac{1}{2T} \int_0^T \left(e^{j(2\pi \frac{v}{\tau} t + \theta_{ph})} + e^{-j(2\pi \frac{v}{\tau} t + \theta_{ph})} \right) e^{-j k_n v t} e^{-j \omega_m t} dt, \quad (9)$$

where K_{ph_n} are the coefficients of the spatial distribution of the current density of phase ph . The coefficients $J_{z_{m,n}}^{ext}$ are obtained by $J_{z_{m,n}}^{ext} = J_{z,A_{m,n}} + J_{z,B_{m,n}} + J_{z,C_{m,n}}$.

B. Homogeneous solution for nonconducting regions

For the nonconducting regions the eigenvalues $\lambda_{m,n}$ are determined by

$$\lambda_{m,n} = k_n^2. \quad (10)$$

In the nonconducting region, the eigenvalue of harmonic number n depends only on spatial frequency k_n . This means that the spatial harmonics are uncorrelated. The matrix representation of (10) is given by

$$\Lambda_m = K^2, \quad (11)$$

where K is a diagonal matrix containing the spatial frequencies k . The matrix Λ_m is also diagonal and contains the eigenvalues λ_m of time harmonic m .

C. Homogeneous solution for conducting regions

The conductivity σ in the magnet region varies as function of position. A Fourier series is introduced that represents the spatial distribution of σ inside the region

$$\sigma(x) = \sum_{n=-\infty}^{\infty} \psi_n e^{j k_n x}. \quad (12)$$

The coefficients ψ_n in (12) are obtained by calculating the Fourier transform of the function shown in Fig. 2. For this function it holds that $\sigma > 0$ for positions where conductive material is present and $\sigma = 0$ for positions where air is located. Up on substituting (12) and homogeneous solution of (4) in the diffusion equation of (3) and performing the derivatives, the following is obtained

$$\sum_{n=-\infty}^{\infty} \lambda_{m,n} Y_{m,n}(y) e^{j k_n x} = \sum_{n=-\infty}^{\infty} k_n^2 Y_{m,n}(y) e^{j k_n x} + j \omega_m \mu_0 \mu_r \left(\sum_{n=-\infty}^{\infty} \psi_n e^{j k_n x} \right) \left(\sum_{n=-\infty}^{\infty} Y_{m,n}(y) e^{j k_n x} \right). \quad (13)$$

This equation contains the product of two series with the same spatial frequencies. A new series with the same spatial

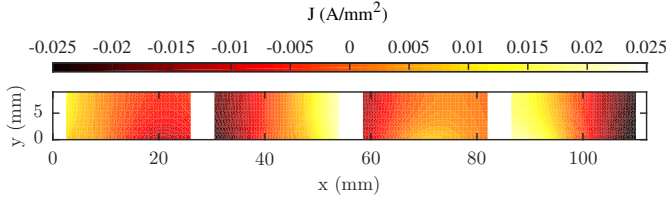


Fig. 3. Eddy current density in the magnets calculated by FEA.

frequencies can be calculated, according to Laurent's multiplication rule [7]

$$j\omega_m \mu_0 \mu_r \left(\sum_{n=-\infty}^{\infty} \psi_n e^{jk_n x} \right) \left(\sum_{n=-\infty}^{\infty} Y_{m,n} e^{jk_n x} \right) = j\omega_m \mu_0 \mu_r \sum_{n=-\infty}^{\infty} \sum_{q=-\infty}^{\infty} \psi_q Y_{m,n-q} e^{jk_n x}. \quad (14)$$

This multiplication can be written in matrix form

$$\Psi \mathbf{y}_m, \quad (15)$$

where \mathbf{y}_m is a vector containing the coefficients of the y -dependent solution. The matrix Ψ is a Toeplitz matrix containing the coefficients of $\sigma(x)$. Using Laurent's multiplication rule, the solution of Λ_m is given by

$$\Lambda_m = \mathbf{K}^2 + \mu_0 \mu_r j\omega_m \Psi. \quad (16)$$

Contrary to Section III-B, the eigenvalue $\lambda_{m,n}$ of harmonic number n depends on multiple spatial frequencies and a coupling of different spatial harmonics occurs. As a result, the matrix Λ_m is not diagonal and the eigenvalues of the y -dependent solution are not directly obtained. To determine the eigenvalues, an eigenvalue decomposition is performed on Λ_m

$$\Lambda_m = \mathbf{Q}_m \Lambda'_m \mathbf{Q}_m^{-1}, \quad (17)$$

where Λ'_m is a diagonal matrix containing the eigenvalues and \mathbf{Q}_m is the matrix containing the corresponding eigenvectors. After performing the decomposition, the solution of A_z is equal to

$$A_z(x, y, t) = \sum_{m=-\infty}^{\infty} \left(\sum_{n=-\infty}^{\infty} P_{m,n}(x, y, t) \right) + (e^{j\omega_m t} \mathbf{Q}_m (\mathbf{E}_{\mathbf{y}_m}(y) \mathbf{a}_m + \mathbf{E}_{\mathbf{y}_m}(-y) \mathbf{b}_m))^{\top} e^{jkx}, \quad (18)$$

where

$$\mathbf{E}_{\mathbf{y}_m}(y) = \text{diag} \left(e^{\sqrt{\Lambda'_m} y} \right). \quad (19)$$

The unknown coefficients, which are determined by applying boundary conditions between regions, are collected in vectors denoted by \mathbf{a}_m , \mathbf{b}_m . The vectors Λ'_m and \mathbf{k} contain the diagonal entries of Λ'_m and \mathbf{K} respectively.

IV. MODEL VERIFICATION

The coreless motor of Fig. 1 is modeled to verify the developed method. Because the model is symmetric with respect to the x -axis a Neumann boundary condition is applied in the center of the coils and no forces in the y -direction

TABLE I
DIMENSIONS OF THE CORELESS MOTOR

Dimension	Symbol	Value	Unit
Half periodic width	τ	56.0	mm
Air gap height	h_g	1.0	mm
Magnet width	w_m	24.0	mm
Magnet height	h_m	9.0	mm
Coil width	w_c	36.0	mm
Conductor bundle width	w_{cb}	12.5	mm
Coil height	h_c	8.0	mm

are considered. The dimension of the simulated motor are listed in Table I. The force exerted on the segmented magnet array are calculated using the Maxwell Stress tensor. To only model the eddy current force acting on the magnet array, the magnetization of the magnets is set to 0 A/m and their relative permeability μ_r is set to 1. The back-iron is assumed to be infinitely permeable and nonconductive, and therefore, it is replaced by a Neumann boundary condition.

The results of the developed semi-analytical method are compared to results obtained from a transient FE analysis performed with Cedrat Flux 2D [8]. The back-iron is also replaced by a Neumann boundary. The current density in the coils is commutated on the q -axis and has a peak value of $\hat{J} = 5$ A/mm². A second order triangular mesh is applied to the model. The mesh size throughout the entire model is equal to 0.5 mm, which results in a total number of 15826 mesh elements. Assuming that at least three mesh elements per skin depth are required for simulation of eddy currents, results of the FE analysis are accurate up to a frequency of 5.6 kHz for $\sigma = 2 \cdot 10^7$ S/m. Fig. 3 shows the eddy current distribution in the magnets at one time instant, calculated by FEA.

A. Modeling multiple conducting segments

In the model, eddy currents are induced in four separate magnets. When the conductivity function describes the conductivity of multiple segments as shown in Fig. 2, the obtained results are incorrect because the segments are modeled as if they are connected while they are in fact electrically isolated. This is illustrated by the solid line in Fig. 4, where the calculated eddy currents are shown in the center of the magnets (dashed line in Fig. 1) as a function of the position. In this steady-state simulation, the coils are stationary and excited with a frequency of 50 Hz. The sum of currents inside one magnet is not equal to 0 A. To approach the correct result, the conductivity function has to describe the conductivity of one segment only and the eddy currents are calculated for each segment separately. Afterwards the results are superimposed. This result is shown in Fig. 4 by the dashed line, which is in good agreement with the FE simulation. The error with respect to the FE analysis result is less than 1 %. The method of calculating the eddy currents in each segment separately is used in the remainder of the paper. The disadvantage of this method is that the effects of the eddy currents in the individual segments on each other are not modeled.

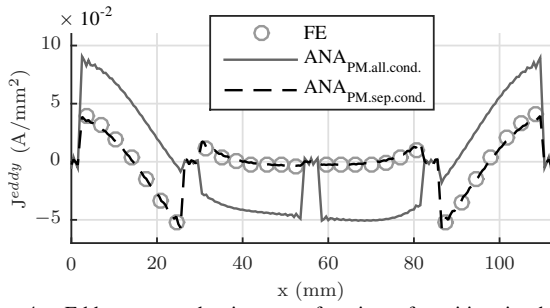


Fig. 4. Eddy current density as a function of position in the center of the magnets compared to FE results. $ANA_{PM.all.cond.}$ is the result of using a conductivity function that describes the conductivity of all magnets. $ANA_{PM.sep.cond.}$ is the result of using a conductivity function that describes the magnets separately. The conductivity of the magnets is $1 \cdot 10^6$ S/m.

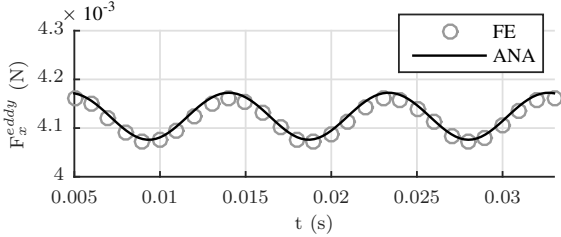


Fig. 5. Verification of obtained transient eddy current force in the x -direction.

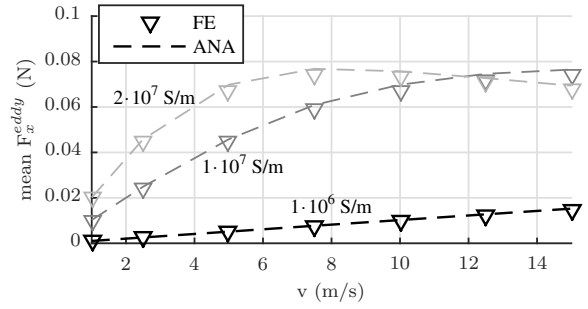
B. Modeling transient behavior

To verify the transient forces during movement obtained with the developed semi-analytical model, a simulation is performed in which the coil array moves in the positive x -direction with a constant speed of $v = 1$ m/s. The conductivity of the magnets is set to $1 \cdot 10^6$ S/m, which is a typical conductivity value for sintered NdFeB magnets. The results are obtained using 61 spatial harmonics and 61 time harmonics. The eddy current force is shown in Fig. 5. The error at the peak values of the force is less than 3 % with respect to the FE result.

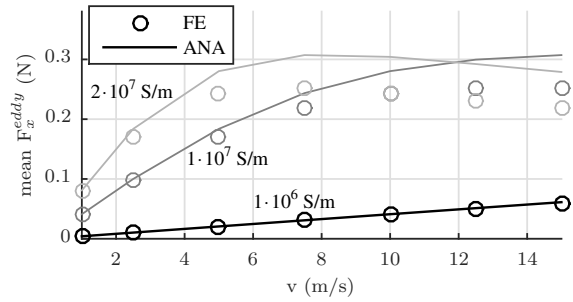
To analyze the accuracy of the method of calculating eddy currents in individual segments and superimposing the resulting force, a transient simulation is performed at several speeds and for three values of the conductivity. Two different cases are studied. Firstly, a simulation is performed in which magnet 1 of Fig. 1 is conducting, while the other magnets are not. The mean force due to the eddy currents of both the developed semi-analytical method and FE analysis is shown in Fig. 6a. The figure shows that for all conductivity values the results are in good agreement and the maximum error with respect to the FE result is less than 4 %. Secondly, a simulation is performed in which all four magnets are conducting (Fig. 6b). For a conductivity value of $1 \cdot 10^6$ S/m, the maximum error is 2 %. However, for conductivity values higher than $1 \cdot 10^7$ S/m the error significantly increases, especially at high speeds. This is caused by the influence of the eddy current distribution in one magnet on another magnet, which is larger at high conductivity values.

V. CONCLUSION

In this paper a 2D magnetic field modeling technique has been presented that is capable of modeling the spatial



(a)



(b)

Fig. 6. Mean eddy current force versus speed for 3 different values of the conductivity. (a) Resulting force when only magnet 1 is conducting. (b) Resulting force when all magnets are conducting.

distribution of the conductivity. The conductivity has been described by a Fourier series and incorporated in the solution of magnetic field quantities. With this method the eddy currents in segmented structures are modeled. The inclusion of multiple time harmonics to the solution makes it possible to model transient eddy current forces.

With the presented method it is not possible to model the spatial conductivity distribution of multiple conducting segments at once. When multiple conducting segments are considered inside a region, the conductivity of each segment has to be separately modeled and the results have to be summed. As a consequence, the effects of the eddy currents in the individual segments on each other is not modeled. However, for typical conductivity values of NdFeB magnets, accurate results (less than 3 % error with respect to FE) have been obtained with superposition.

REFERENCES

- [1] K. Yamazaki, M. Shina, Y. Kanou, M. Miwa, and J. Hagiwara, "Effect of eddy current loss reduction by segmentation of magnets in synchronous motors: Difference between interior and surface types," *Magnetics, IEEE Transactions on*, vol. 45, no. 10, pp. 4756–4759, Oct 2009.
- [2] K. Binns, P. Lawrenson, and C. Trowbridge, *The Analytical and Numerical Solution of Electric and Magnetic Fields*. Wiley, 1992.
- [3] L. Wu, Z. Zhu, D. Staton, M. Popescu, and D. Hawkins, "Analytical model for predicting magnet loss of surface-mounted permanent magnet machines accounting for slotting effect and load," *Magnetics, IEEE Transactions on*, vol. 48, no. 1, pp. 107–117, Jan 2012.
- [4] J. W. Jansen, E. A. Lomonova, and J. M. M. Rovers, "Effects of eddy currents due to a vacuum chamber wall in the airgap of a moving-magnet linear actuator," *Journal of Applied Physics*, vol. 105, no. 7, 2009.
- [5] K. Pluk, T. van Beek, J. Jansen, and E. Lomonova, "Modeling and measurements on a finite rectangular conducting plate in an eddy current damper," *Industrial Electronics, IEEE Transactions on*, vol. 61, no. 8, pp. 4061–4072, Aug 2014.

- [6] M. G. Moharam and T. K. Gaylord, "Rigorous coupled-wave analysis of planar-grating diffraction," *J. Opt. Soc. Am.*, vol. 71, no. 7, pp. 811–818, Jul 1981.
- [7] L. Li, "Use of fourier series in the analysis of discontinuous periodic structures," *J. Opt. Soc. Am. A*, vol. 13, no. 9, pp. 1870–1876, Sep 1996.
- [8] *Flux 11 User's guide*, release 11.2 ed., Cedrat Corporation, Grenoble, 2012.

Developing for Developing Nations: Exploring a Low-cost PV System Design Methodology

Nishant Narayan*, Jelena Popovic*, Pavol Bauer*, and Miro Zeman*

*Delft University of Technology, Department of Electrical Sustainable Engineering, P.O. Box 5031, 2600GA, Delft, The Netherlands
Email: N.S.Narayan@tudelft.nl

Abstract—Developing technological solutions for the developing nations is more than simply re-sizing a prevalent solution from the developed world. Not only the environmental conditions, but also the technology usage varies greatly between the developing nations in sunnier latitudes around the world and the developed nations of north-western Europe. This paper sheds light on the various technical and non-technical factors to be considered for designing a standalone PV system for low-income households in developing nations. The importance of battery in a low-cost PV system is examined and the role of power electronics in such a system design is highlighted. Finally, the paper proposes a system design methodology.

I. INTRODUCTION

Nearly one-fifths of the global population still lacks access to electricity, with around 85% of them living in the rural areas [1]. Figure 1 shows the distribution of the electricity-starved population around the world.

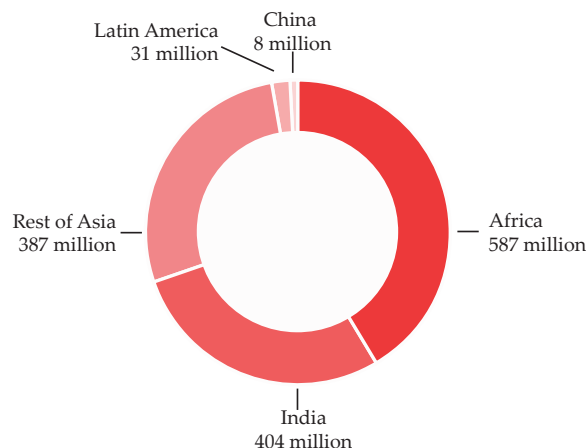


Fig. 1. Global population lacking electricity [2]

Due to the remote location of the unelectrified villages and unstable electricity-grid in many of these developing nations, grid-based electrification is certainly not an immediate solution to eradicate energy poverty. Therefore, the attention of this work was focused on off-grid energy solutions. Since most of these locations also happen to lie in the latitude-belts blessed with abundant sun (refer to Figure 2), the choice of standalone PV-battery energy system is quite obvious.

In an effort to technically contribute towards mitigating the growing problem of energy poverty, this work was formulated

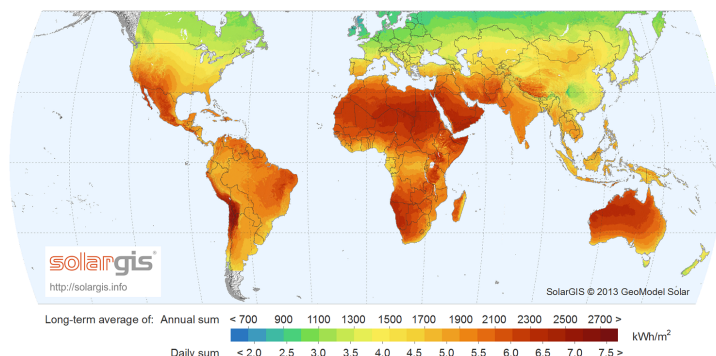


Fig. 2. Global solar irradiation [SolarGIS ©2014 GeoModel Solar]

as a low-cost PV system design project tailored for developing nations, with an emphasis on the power electronics development in the system. Due to the social impact-based nature of this project, it is essential to first get a good grip on the technical requirements from the energy system, understand the user needs and usage environment, and envisage the relation between the two. It is also necessary to identify the scientific contribution in this project that can not only optimize the primary metric of cost, but also serve as a significant addition to the field of photovoltaic based energy storage systems.

II. LOW-COST PV SYSTEM DESIGN

Since this project is aimed at helping the unelectrified communities in developing nations, care should be taken that it does not fall under some of the typical traps, like [3] [4]:

- ‘Designs for developing world’ being no better than quick resizing of prevalent western technology solutions.
- Not understanding the needs of the people who are eventually going to be using the technology.
- Lack of correlation between income of the target groups and the cost of the system or electricity.
- System designed such that intensive maintenance being needed by users who lack even the most basic of technical skills.

Therefore the first steps taken were to understand the current state of rural electrification initiatives with respect to PV-storage systems.

A. Understanding the rural off-grid solar market space

As part of this project, a 2-month extensive literature survey was carried out to understand the progress of various solar powered electrification initiatives in developing nations [4]. Several present day rural lighting/electrification projects were studied, mainly in Africa and South-Asia. Figure 3 shows some of the projects that were looked into.

It was observed that the low power (sub 100 W) space is quite crowded, with scores of products and initiatives, especially in the portable solar (sub 10 W) segment. This is illustrated in Figure 4. The portable solar products seem to outnumber the Solar Home Systems (SHS), like the ones from Rural Sparks, Onergy and SolarNow. There are relatively fewer community level initiatives in comparison that look at higher power levels (0.5 kW to 1.5 kW). For example, the IEEE SunBlazer from the IEEE Smart Village initiative. For various socio-economic as well as technical reasons, there is no one single solution ubiquitous enough to cause a significant impact to the energy poverty problem as discussed in section I.

Between the portable products and the community level initiatives, there is a dearth of dedicated household level low-cost solutions, and this is where (around 200 W) the project discussed in this paper aims to fill the gap.

B. Impact of user-environment on system development

Developing a system to be used in emerging economies in Africa and the Indian subcontinent, for example, requires taking into account factors that are beyond the electrical realm. For instance, understanding the socio-economic needs of the target user groups not only gives the expected electrical load profile to be satisfied by the proposed energy system, but also highlights the cost-constraints that the system has to eventually satisfy. While some of these factors have a direct bearing on system design, some of the factors affect system choices indirectly.

Examples of social/environmental factors that may have a direct impact on system design include: social needs of the people as translated to an electrical load profile, climate endemic to the target region, façade /roofing infrastructure or community space available for PV system implementation, etc. Examples of socio-environmental factors that may have an indirect impact on the system choices include: need for tamper-proof robustness, modularity requirement for future-needs, preferred way of implementation in the community, need for aesthetics, etc.

There are interesting anecdotes from the field that remind us that it is the user that ultimately decides how to use a product, while the designers, engineers and scientists have to tailor their specs and solutions accordingly. One such anecdote tells of men using solar based lighting (initially given to their homes) not for their homes but for their shops - the justification being longer illumination after dusk would ensure a bustling business for their shops over their competitors'. In another incident, households in a part of rural India felt more secure to have the solar panels on the ground in front of their houses

where they can always see them, instead of mounting on the roof where one can't always have a watchful eye. This is imperceptible to the regular PV system architect, who would only want the panels to be mounted in the highest, shade-free area of a building. These anecdotes were recalled in a personal interview (December 2015) of a student who interned with a solar-based startup in India in 2014.

These incidents from the field go to show that the socio-environmental factors are inseparably linked with the system design conundrum.

III. ROLE OF TECHNOLOGY

Technology of course has the primary role to play in such a project, but its development is a complex mix of several factors.

Figure 5 shows a basic block diagram schematic of a standalone PV system. Each block additionally lists various parameters needed for the electrical design of the PV system. Most of these parameters have a direct or indirect dependency on the socio-environmental factors as discussed above. For instance, the local climate will have an impact on the thermal behaviour of PV modules, battery and power electronics, which would need to be designed accordingly. Similarly, the load profile of the communities will have a direct impact on the required system and components sizing. An accurate knowledge of the load demand and the load priority may yield extra room in incorporating features like Demand Side Management (DSM).

A. Battery in a low-cost PV system

A battery is by-far the most expensive part of a standalone PV system. Although indispensable, it can account for more than 50% of the total system costs while having the least lifetime among all PV system components [5]. Therefore the challenge would lie in minimizing the costs associated with the battery while increasing its lifetime. There are two kinds of battery costs incurred in an off-grid PV system: upfront costs and running costs.

Upfront costs are directly related to the size of the battery used. Larger the battery, higher the upfront costs. Therefore, if the battery size can be reduced for a given load profile, there can be considerable costs savings. Running costs are associated with the battery having a limited lifetime, and generally far shorter than the other components. Some of the more efficient batteries may last 8 to 10 years in comparison to the 25-30 years of a PV module. Therefore the battery would need occasional replacement [5] [6].

Ensuring a longer battery life is technically quite demanding. Battery performance is a complex interplay of various battery parameters, like Depth of Discharge (DOD), C-rate, temperature, and cycle life, amongst others. For example, the energy capacity of a typical Valve Regulated Lead Acid (VRLA) battery is enhanced with temperature due to increased chemical activity [7]. However, increase of temperature has a detrimental effect on the battery lifetime. This effect is shown in Figure 6, where the high temperature seems to take

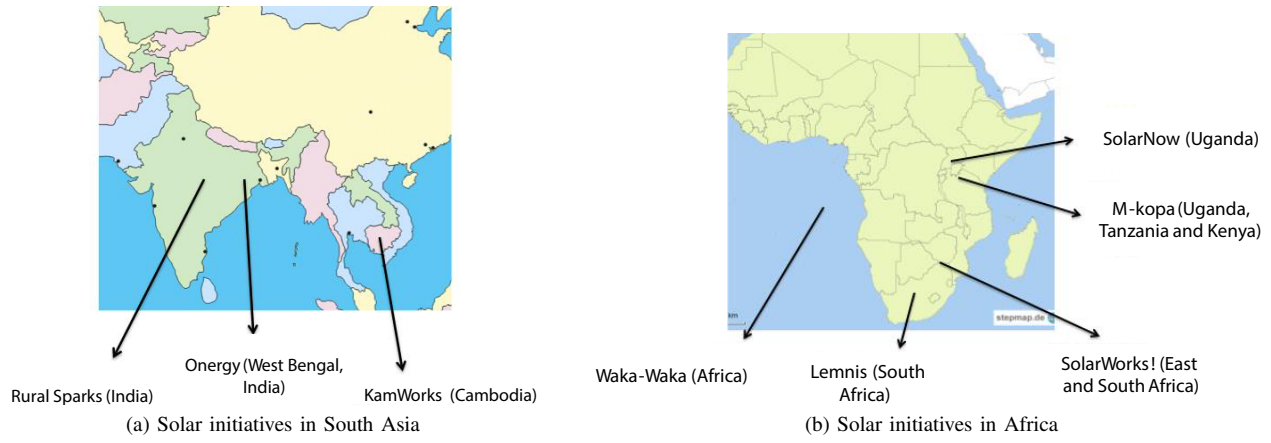


Fig. 3. Some of the projects covered in the survey.

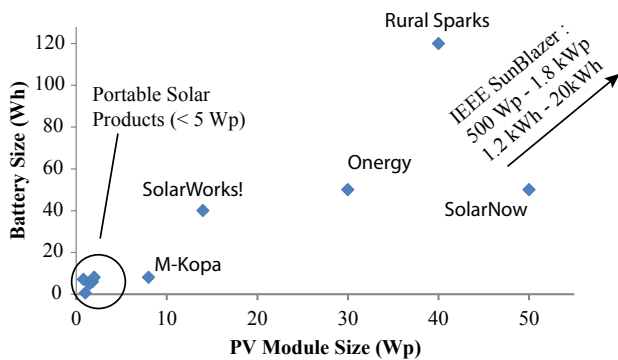


Fig. 4. Various off-grid solar products based on their PV-Storage size.

the apparent capacity beyond 100%. However, this is only temporary, and severely damaging to the battery life.

Similarly, the energy generation and consumption mismatch along with the particular battery size can lead to a range of DOD values encountered during the battery operation. For the same VRLA battery mentioned above, high DOD values lead to a reduced cycle life. This effect can be worse for higher temperatures. This can be seen in Figure 7.

Additionally, although a certain load might demand a higher C-rate from the battery, it may be very bad for the battery lifetime to go exceed certain C-rates [6] [7]. In general, a battery lasts the longest if it is operated in the ‘sweet spots’ of these parameter curves. However, given the intermittent nature of solar energy and priority of load demand, it is tough to maintain the battery operations always limited to the optimal regions.

B. Role of power electronics

Power electronics forms the backbone of the PV system. In a PV system design such as this one, the role of power electronics is even more accentuated. The additional challenge in this project lies in optimal battery management, which needs to be ensured through efficient power electronics implementation.

The power converter for such an application would serve multiple purposes: Firstly, it will serve as a regular solar power converter with Maximum Power Point Tracking (MPPT). Secondly, and more importantly for the low-cost PV system, it will maximize battery life and performance so as to minimize running battery costs. Thirdly, it will optimize power flows so that as often as possible, the PV can directly power the load instead of the PV charging the battery and the battery powering the load.

The battery upfront and running costs are intrinsically linked. For a given application, an over-sized battery will lead to lesser DOD states in operation, thereby increasing its lifetime. On the other hand, a smaller battery would have lesser upfront costs, but the larger DOD states would cost the cycle life dearly, as was seen in Figure 7. *Ceteris paribus*, the battery size in itself forms an interesting trade-off between the upfront and running costs. The power electronics in such a case will play a vital role in determining how much it can help with reducing the running costs, so that it gives more room to reduce the upfront costs by choosing a lower battery size than what would have otherwise been possible.

C. Need for Modularity

Most rural off-grid initiatives fail to take into account the future needs of the people. Electricity access raises the standard of life of people by directly and indirectly affecting socio-economic factors like education, employment, health and women empowerment [9] [10] [11]. This in turn leads to greater number of electric loads a household enjoys.

This begs the system architecture to be modular in nature. While this leaves an important option of scaling up of the system if needed later, it also adds an extra constraint on the system design. Additionally, the authors envisage that the houses of the future, 20 years from now, no matter how remote and decentralized in terms of power generation, will still be connected to other houses. This may not even be in the strict definitions of mini- and micro-grids as being talked about now, but could be more asymmetric and organically evolving in time. Thus the system needs to have the added capability of inter-connectivity if needed.

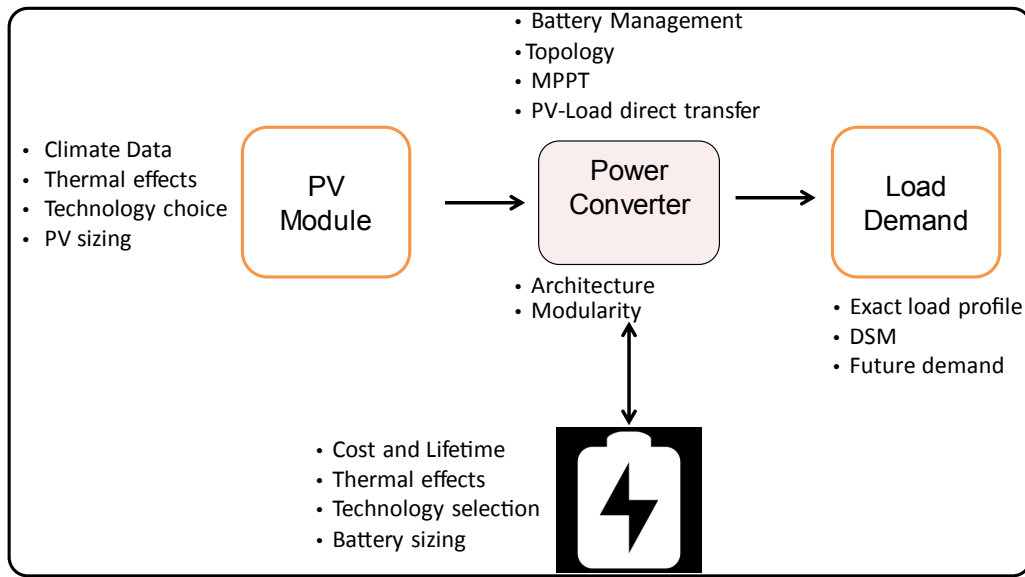


Fig. 5. Block diagram of a standalone PV system, showing various design parameters

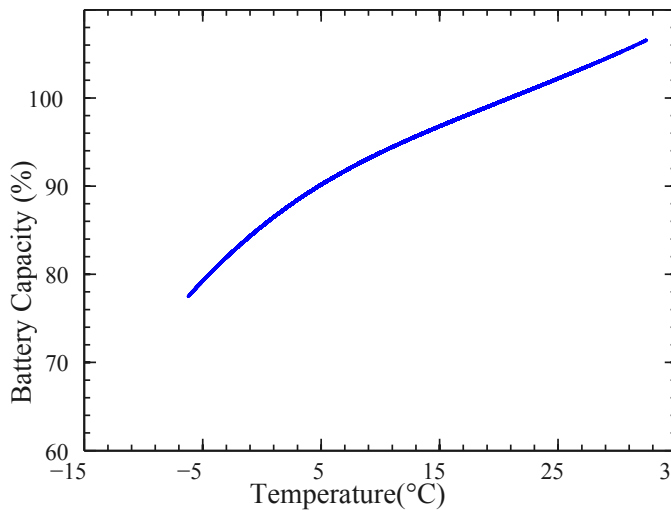


Fig. 6. Effect of temperature on battery capacity of a VRLA battery [8].

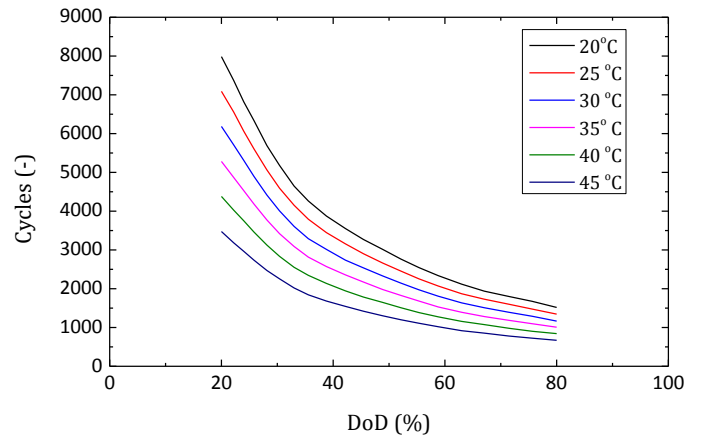


Fig. 7. Effect of temperature and DOD on a VRLA Battery life. [Data sourced from [7]]

IV. METHODOLOGY

As shown in Figure 5, the standalone PV system design for this project has to account for myriads of parameters. Each component of the system needs to be design individually to the best performance-to-cost ratio, while taking into account the overall system constraints.

The methodology for approaching such a complex project cannot efficiently work with a linearly planned system design or even a simple pipelined approach. Figure 8 shows a linear system design cycle, which would involve the following phases in serial occurrence:

1) Understanding user needs.

- 2) Drawing system constraints and system-level design (system architecture).
- 3) PV-Battery sizing.
- 4) Power electronics design.

A linear methodology is inadequate to handle the intricacies linked to a multi-faceted project like this one. The simple pipelined approach also falls short because each phase and aspect of the design may need to be revisited, based on the influx of user input or field data.

The Spiral Design Approach

A spiral system design cycle is proposed for this project. Spiral design incorporates the added benefits of iteration and feedback from different phases. This concept is already in use in software design as well as human interaction based system

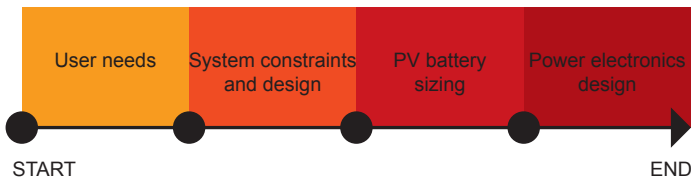


Fig. 8. Linear system design cycle concept.

developments [12]. Figure 9 illustrates this concept as applied to this project.

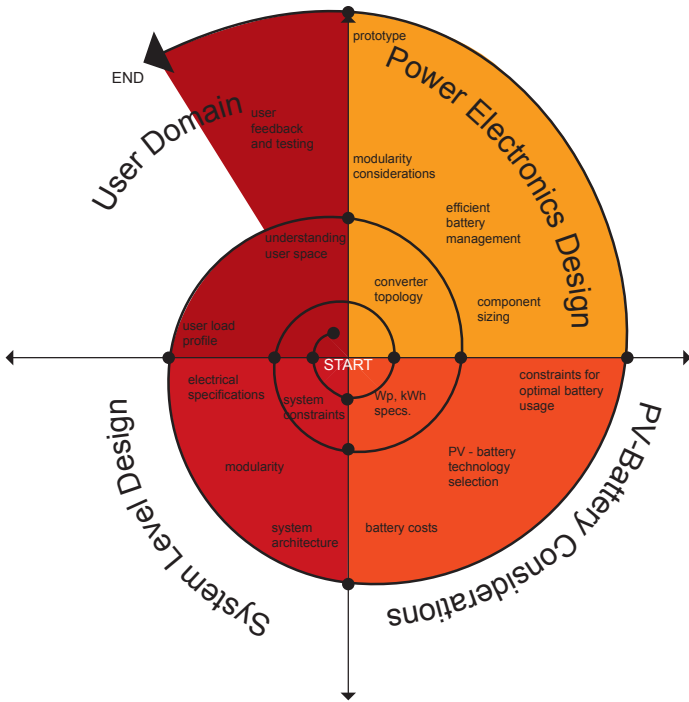


Fig. 9. Spiral system design cycle concept.

The spiral shows 4 main phases:

- 1) User domain.
- 2) System level constraints and architecture.
- 3) PV-Battery sizing.
- 4) Power electronic design.

These phases would be iteratively visited, while feedback from each phase would interact with and impact every other phase.

In reality, not all phases would last the same duration as shown in the concept illustration (Figure 9). Also, based on the maturity of the project and other constraints, some phase may have to be revisited 'out of turn'. Therefore, robust design-flows need to be ensured so that the design cycle can take in more data in its different phases.

V. CONCLUSION

A dedicated PV-storage energy system design for communities in developing nations can be a complex task, especially if the emphasis is on a low-cost, affordable solution that takes current and (foreseeable) future needs of the people

into account. Both technical as well as non-technical or socio-economic factors have a huge bearing on the way the system should be designed and developed.

From a technical design perspective, much of the challenge in optimizing costs in a low power PV system revolves around the successful optimization of battery. In this respect, the power electronics in such a standalone PV system needs to be more than just a charge-controller with MPPT. The power converter needs to also efficiently manage the battery operation so as to maximise its lifetime while requiring the least possible battery size for a given system power rating.

A spiral design methodology is suggested that is flexible to evolve as more data comes in at various stages of the project. Lastly, developing technological solutions for the developing world calls for a different mindset from the researcher than what maybe usually seen in his or her field of expertise. The authors are confident that as more socially inclined scientists endeavor down this path, technology can indeed become *the* solution that transcends socio-economical, geopolitical and other man-made boundaries prevalent today.

Future recommendations

In the future it is important to be able to quantify the social impact of this project. Even though the system development may be successful purely based on the project deliverables, i.e., a low-cost, robust PV system built taking into account the current and future needs of the target communities, it has to have a measurable social impact. The sooner this 'impact assessment tool' is developed, the more *useful* this and other socially driven technical projects can become.

ACKNOWLEDGMENT

The authors would like to thank Natalie Kretzschmar, Thomas den Heeten and Vasilis Marioleas for their contributions. This work is supported by a fellowship from the Delft Global Initiative of Delft University of Technology.

REFERENCES

- [1] I. E. Agency, *Energy Poverty: How to make modern energy access universal*, ser. World Energy Outlook 2010, 2010. [Online]. Available: http://www.worldenergyoutlook.org/media/weowebsite/energydevelopment/weo2010_poverty.pdf
- [2] C. Gradl and C. Knobloch, *Energize the BoP! A Practitioner's Guide*, 2011.
- [3] S. Ofordile ANI, "Low cost small wind turbine generators for developing countries," Ph.D. dissertation, Delft University of Technology, 2013.
- [4] N. Kretzschmar, *Studying the success, failure and progress of various (solar-powered) rural electrification initiatives in developing nations*, 2016.
- [5] J. Hoppmann, J. Volland, T. S. Schmidt, and V. H. Hoffmann, "The economic viability of battery storage for residential solar photovoltaic systems: a review and a simulation model," *Renewable and Sustainable Energy Reviews*, vol. 39, pp. 1101 – 1118, 2014. [Online]. Available: <http://www.sciencedirect.com/science/article/pii/S1364032114005206>
- [6] D. G. für Sonnenenergie, *Planning and Installing Photovoltaic Systems: A Guide for Installers, Architects and Engineers*, ser. Planning and Installing. Taylor & Francis, 2008. [Online]. Available: <http://books.google.nl/books?id=fMo3jJZDkpUC>
- [7] "Installation , commissioning and operating instructions for vented stationary lead-acid batteries - solar battery data sheet," Hoppecke 2013, Germany.

- [8] N. Narayan, "Solar charging station for light electric vehicles: A design and feasibility study," Master's thesis, Delft University of Technology, 2013.
- [9] S. Ray, B. Ghosh, S. Bardhan, and B. Bhattacharyya, "Studies on the impact of energy quality on human development index," *Renewable Energy*, vol. 92, pp. 117–126, 2016.
- [10] T. Dinkelman, "The effects of rural electrification on employment: New evidence from south africa," *The American Economic Review*, pp. 3078–3108, 2011.
- [11] S. Aid, *Impact Report*, 2015. [Online]. Available: <http://www.solar-aid.org/assets/Uploads/Impact-week-2015/SolarAid-IMPACT-REPORT-2015.pdf>
- [12] A. S. Mavor, R. W. Pew *et al.*, *Human-System Integration in the System Development Process:: A New Look*. National Academies Press, 2007.

Analytical Surface Charge Method for Rotated Permanent Magnets: Boundary Element Method Comparison and Experimental Validation

J. R. M. van Dam¹, J. J. H. Paulides¹, W. S. P. Robertson², M. Dhaens³, and E. A. Lomonova¹

¹Department of Electrical Engineering, Eindhoven University of Technology, Eindhoven 5612 AP, The Netherlands

²School of Mechanical Engineering, The University of Adelaide, SA 5005, Australia

³Advanced Chassis Research, Tenneco Automotive Europe BVBA, B 3800 Sint-Truiden, Belgium

This paper is concerned with the analytical calculation of the interaction force between two permanent magnets (PMs) under relative rotation by means of the surface charge method, taking into account the non-unity relative permeability of the PMs. This model combines high accuracy and a short calculation time. As the considered PM configuration is a free-space, unbounded problem, the results from the surface charge method are compared to its numerical counterpart, the boundary element method. The analytical expressions were validated by means of the measurement results obtained from a 3-D printed test setup.

Index Terms—Analytical models, electromagnetic fields, electromagnetic forces, permanent magnets.

I. INTRODUCTION

THE increasing interest in wireless sensors and wearable electronics has encouraged the research into renewable battery-replacement technologies, as to reduce the maintenance and resource cost inseparably related to batteries. An attractive alternative is to harvest energy from natural vibration sources, as they are widely available, and potentially contain a high power density. The conversion of the kinetic energy in vibrations into electrical energy has been achieved using many different types of transducers, such as mechanical [1], magnetoelectric [2], electrostatic [3], electromagnetic [4], and piezoelectric [5]–[7].

In piezoelectric cantilever beam energy harvesters [6], [7], the beam fundamental resonance frequency is usually matched with the system excitation frequency, as to yield the largest harvested energy. However, to allow for a range of excitation frequencies, the interaction forces between permanent magnets (PMs) are applied to tune the beam resonance frequency. In [7], the PM interaction forces result from an approximation function. The optimization of the energy-harvesting capabilities requires an improved accuracy with respect to the determined interaction forces. Hence, a PM modeling method is desired which provides a 3-D magnetic field solution, works well in free-space unbounded problems, handles relative rotations between PMs, and does not require periodicity of the considered magnetic structure. Moreover, to allow for fast optimization and geometry selection, an analytical model is preferred over numerical alternatives. Both the surface charge method [8]–[13] and the Boundary Element Method (BEM) [14] satisfy the above conditions.

This paper provides an improved calculation of the interaction force between two PMs under relative rotation with respect to existing cantilever beam vibration energy harvesters. The analytical surface charge method and the BEM simulation results are compared to the results from the Finite Element Method (FEM). Additionally, an experimental setup is designed to validate the simulation results.

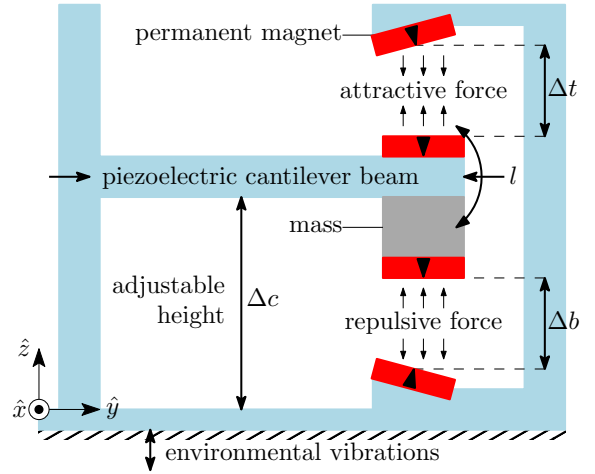


Fig. 1. Energy-harvesting piezoelectric cantilever beam.

II. CONSIDERED GEOMETRY

An implementation of the considered energy harvesting cantilever beam is shown in Fig. 1. Environmental vibrations are transferred to the beam structure, where minor vibrations of the tip mass are amplified by the forces between the PMs. The beam oscillates at its resonance frequency, f_r , which is partially determined by the height and length of the beam, Δc and l , respectively, and the distances between the PMs, Δt and Δb . Energy is generated by the deformation of the piezoelectric elements in the beam. This is illustrated on an energy-harvesting cantilever beam in Fig. 1, where the energy harvester consists of a non-magnetic beam to which piezoelectric elements, PMs, and a non-magnetic free end tip mass are attached. A simplified representation of the cantilever beam PMs is shown in Fig. 2, where only two PMs are considered. The PM dimensions are summarized in Table I.

III. SURFACE CHARGE METHOD FOR ROTATED PMs

Simplified two-dimensional (2-D) analytical models to obtain the interaction force between magnets in radial bearings

TABLE I
PERMANENT MAGNET DIMENSIONS

$2a_1$	17 mm	$2a_2$	17 mm	α	0 mm
$2b_1$	11.5 mm	$2b_2$	11.5 mm	β	$60 (\cos \theta - 1)$ mm
$2c_1$	3.5 mm	$2c_2$	3.5 mm	γ	$60 \sin \theta$ mm
B_r	1.18 T	μ_r	1.02		

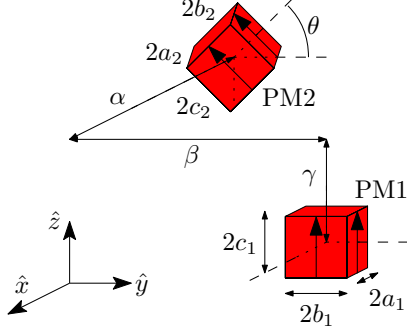


Fig. 2. Two permanent magnets under relative rotation. In the system under investigation, the center of rotation lies at a distance to the magnet center, leading to changes in displacement with changes in rotation.

and couplings were initially proposed using superposition of the interaction force [15]–[19]. Using the magnetic imaging technique [20], a soft-magnetic slotless back-iron was incorporated in the models of the PM coupling [18]. Investigation into 3-D solutions performed in [21] resulted in semi-analytical equations requiring a numerical integration of the logarithmic terms. The current sheet model used in [21] and [22] employed the Lorentz force calculation for a simple topology.

The surface charge method has been a research topic since 1984, when Akoun and Yonnet [8] analytically expressed the magnetic field and the interaction force between two axially displaced PMs with parallel magnetization. Several researchers have contributed to the model advancement, for instance, by developing equations for interactions between perpendicularly magnetized PMs for multi-axial displacements [11]. More recently, a comprehensive overview of the surface charge method was composed [13], in which the force equations for rotated permanent magnets were stated, based on [9].

A short derivation of the surface charge method, resulting in expressions for the interaction force between relatively rotated permanent magnets, will be presented now [10]. Starting with the magnetostatic Maxwell equations for current-free regions,

$$\nabla \times \vec{H} = 0, \quad \text{and} \quad \nabla \cdot \vec{B} = 0,$$

the magnetic scalar potential, φ_m , is introduced by means of the vector identity $\nabla \times (\nabla \varphi_m) = 0$,

$$\vec{H} = -\nabla \varphi_m. \quad (1)$$

To relate the magnetic scalar potential to the PM magnetization vector, \vec{M} , substitute the constitutive relation $\vec{B} = \mu_0(\vec{H} + \vec{M})$ and (1) into $\nabla \cdot \vec{B} = 0$ to obtain

$$\nabla^2 \varphi_m = \nabla \cdot \vec{M}.$$

If \vec{M} only exists inside a volume \mathcal{V} , bounded by \mathcal{S} , then the solution to this equation is represented by means of the free-space Green's function as

$$\varphi_m(\vec{x}) = -\frac{1}{4\pi} \int_{\mathcal{V}} \frac{\nabla' \cdot \vec{M}(\vec{x}')}{|\vec{x} - \vec{x}'|} dv' + \frac{1}{4\pi} \oint_{\mathcal{S}} \frac{\vec{M}(\vec{x}') \cdot \hat{n}}{|\vec{x} - \vec{x}'|} ds',$$

in which the volume charge density, $\rho_m = -\nabla \cdot \vec{M}$ (A/m²), and the surface charge density, $\sigma_m = \vec{M} \cdot \hat{n}$ (A/m). The magnetic flux density for a uniformly magnetized PM, i.e., where $\rho_m = -\nabla \cdot \vec{M} = 0$, is calculated with

$$\vec{B}(\vec{x}) = \frac{\mu_0}{4\pi} \oint_{\mathcal{S}} \frac{\sigma_m(\vec{x}')(\vec{x} - \vec{x}')}{|\vec{x} - \vec{x}'|^3} ds'.$$

Usually, the relative magnetic permeability, μ_r , is assumed unity in the charge method. This introduces a deviation between the analytical results, and the results from FE simulations. The correct value for μ_r is taken into account by adjusting the remanent magnetization, B_r , using [23]

$$\sigma = \frac{B_r/\mu_0}{\mu_r \left(\frac{3}{2} - \frac{\mu_r}{2} \right)}, \quad \text{and} \quad B_r = \sigma \mu_0.$$

Consider the magnets PM1 and PM2 in Fig. 2 of dimensions $[a_1, b_1, c_1]^T$ and $[a_2, b_2, c_2]^T$, respectively. Their centers are displaced by $[\alpha, \beta, \gamma]^T$, and PM2 is rotated with respect to the x -axis by an angle θ . As α is zero, and only a rotation around the x -axis is considered, F_x is zero. If θ is an integer multiple of π rad, the magnetization directions of the PMs are (anti-)parallel and F_z is calculated according to [8], [11], [13]

$$F_z|_{\theta=k\pi} = \frac{B_{r1}B_{r2}\cos(\theta)}{4\pi\mu_0} \times \sum_{i,j,k,l,m,n=0}^1 [-1]^{i+j+k+l+m+n} f_{3z}(x', y', z'), \quad (2)$$

where

$$\begin{aligned} x' &= \alpha + (1-i)a_1 - (1-j)a_2, \\ y' &= \beta + (1-k)b_1 - (1-l)b_2 + \frac{1}{2}c_2 \sin(\theta), \\ z' &= \gamma + (1-m)c_1 - (1-n - \cos(\theta))c_2 - \frac{1}{2}b_2 \sin(\theta), \end{aligned}$$

and, using $r = \sqrt{u^2 + v^2 + w^2}$,

$$\begin{aligned} f_{3z}(u, v, w) &= uv \arctan\left(\frac{uv}{wr}\right) - wr \\ &\quad - \frac{1}{2}uw \ln\left(\frac{r-u}{r+u}\right) - \frac{1}{2}vw \ln\left(\frac{r-v}{r+v}\right). \end{aligned} \quad (3)$$

The limit cases for these expressions have been derived in [24]. Complementary, for $\theta \neq k\pi$, F_z follows from [9], [13]

$$\begin{aligned} F_z|_{\theta \neq k\pi} &= -\frac{B_{r1}B_{r2}}{4\pi\mu_0} \sum_{i,j,k,l,m,n=0}^1 [-1]^{i+j+k+l+m+n} \times \\ &\quad \left(\frac{f_3(U, V, W, \theta, b_1k, 0, b_2l, 0)}{\tan \theta} \right. \\ &\quad \left. + \frac{f_3(UU, VV, WW, -\theta, b_1k, 0, b_2l, 0)}{\sin \theta} \right), \end{aligned} \quad (4)$$

where

$$\begin{aligned}
 U &= \alpha - (i-1)a_1 + (j-1)a_2, \\
 V &= \beta + b_1 - b_2 \cos \theta + (1-n)c_2 \sin \theta, \\
 W &= \gamma - (m-1)c_1 + (n-1)c_2 \cos \theta - b_2 \sin \theta, \\
 UU &= -\alpha - (i+1)a_1 + (j+1)a_2, \\
 VV &= -V \cos \theta - W \sin \theta, \\
 WW &= V \sin \theta - W \cos \theta,
 \end{aligned}$$

and

$$\begin{aligned}
 f_3(u, v, w, \theta, b, c, y, z) &= uf_5 [\ln(f_4 - u) - 1] + \\
 &uf_6 \arctan\left(\frac{uf_4 - f_6^2 - u^2}{f_5 f_6}\right) + \frac{1}{2}\pi u \operatorname{sgn} f_5 |f_6| + \\
 &\frac{1}{2}f_4 f_5 + \frac{1}{2}(f_6^2 - u^2) \ln(f_4 + f_5), \quad (5)
 \end{aligned}$$

where

$$\begin{aligned}
 f_4 &= \sqrt{u^2 + f_5^2 + f_6^2}, \\
 f_5 &= y + (v-b) \cos \theta + (w-c) \sin \theta, \\
 f_6 &= z - (v-b) \sin \theta + (w-c) \cos \theta.
 \end{aligned}$$

For both considered cases, the y -component of the force, F_y , is calculated according to

$$\begin{aligned}
 F_y &= \frac{B_{r1} B_{r2}}{4\pi\mu_0} \sum_{i,j,k,l,m,n=0}^1 [-1]^{i+j+k+l+m+n} \times \\
 &f_3(U, \beta + b_1 - b_2 \cos \theta + c_2 \sin \theta, \\
 &\gamma + (1-m)c_1 - b_2 \sin \theta + c_2(\cos \theta - 1 + n), \\
 &\theta, b_1 k, c_1 m, b_2 l, c_2 n). \quad (6)
 \end{aligned}$$

IV. SIMULATION SETUP

Contrary to the analytical surface charge method, a numerical approach to model the PM configuration in Fig. 2 is the BEM. The BEM is well suited for the problem, as the considered configuration is a free-space, unbounded problem, in which the material properties are assumed linear and homogeneous. In the following, the results from the analytical surface charge method and the BEM will be compared with each other as well as with FE simulation and experimental results. The applied BEM is the software package Faraday 3-D Eddy Current Solver Version 8.0, 2009 by Integrated Engineering Software. In the simulation, 972 2-D quadrilateral elements have been taken into account. The solving process of a single step takes less than a second. The applied electromagnetic 3-D FEM is Flux Version 12 Service Pack 2, 2015 by Cedrat. In the simulation, 3 621 184 volume elements have been taken into account. The solving process takes approximately 24 hours.

V. COMPARISON AND VALIDATION

The measurement results that were obtained on the 3-D printed test setup shown in Fig. 3 are used to validate the results from the charge method. The PMs were in a repulsive configuration; hence, PM1 was pushed to the load cell, whereas PM2 retained its position because of the slotted construction. A six degree-of-freedom (6-DoF) ATI F/T Mini40

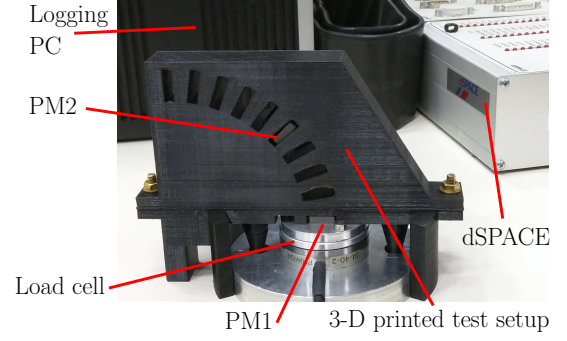


Fig. 3. Experimental setup.

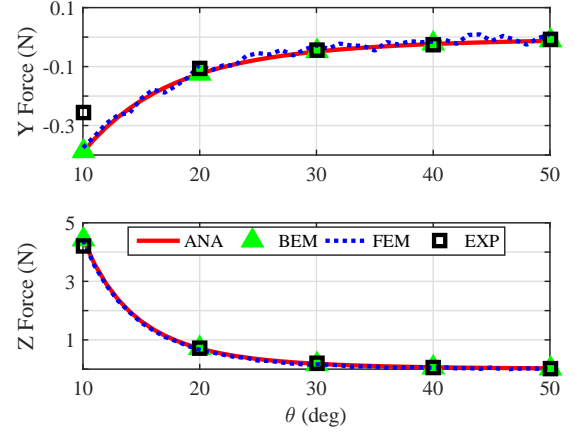


Fig. 4. Comparison of the simulation and measurement results, where ANA is the analytical surface charge method, BEM is the Boundary Element Method, FEM is the Finite Element Method, and EXP is the experimental result.

load cell was used, whose output was logged by means of a dSPACE module and a logging computer. Multiple runs were performed, and the filtered average results are displayed in Fig. 4 together with the simulation results.

Very close agreement between the charge method and the BEM is found, as the results deviate on average 0.63 %, as shown in Fig. 5. This deviation is attributed to numerical inaccuracies in the assignment of the PM dimensions. The results from the FEM are less accurate, which is attributed to numerical noise resulting from an insufficiently dense mesh. The requirement of the FEM for such a dense mesh for this type of free-space unbounded problem makes the FEM less suitable than both the BEM and the charge model.

The measurement results confirm the simulated force development in both the y - and z -directions. However, for the smallest θ -value, the measurement results deviate, and especially the y -component deviates largely, as shown in Fig. 5. This is attributed to inaccuracies in the test setup, which are composed of deviations in the remanent magnetization and magnetization angle of the PMs, 3-D printer manufacturing tolerances, and deviations in the alignment of the test setup with respect to the xy -plane of the load cell.

VI. DISCUSSION

A close agreement between the results from the surface charge method and the BEM was found, despite the distinct differences between the methods. The BEM employs a densely

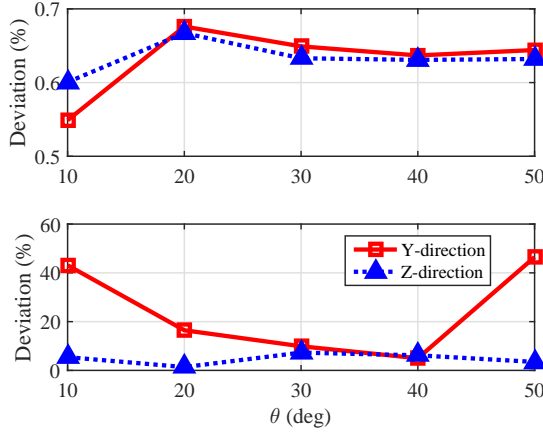


Fig. 5. Percentage deviation between the analytical surface charge method and the BEM (top), and the experimental results (bottom).

populated, non-symmetric system matrix that elevates memory usage and could, potentially, increase computer times to the level of the FEM. Additionally, material properties are assumed linear and homogeneous, which renders the BEM unsuitable for configurations involving soft-magnetic material. A major asset of the BEM surfaces when considering free-space, unbounded problems, as it only requires field source boundaries to be discretized, resulting in faster solutions than the FEM. Contrary to the BEM, the surface charge method is analytically formulated, resulting in faster solutions. As a result of recent developments, the applicability of the surface charge method has improved with the introduction of (semi-)analytical solutions to include the relative permeability of soft-magnetic materials [25].

For now, the applicability of the surface charge method is limited to rotations around the non-magnetized axis, in combination with a translation with respect to the magnetized axes. Therefore, the method does not serve as a FEM-replacement yet [13]. Model extensions include the forces between cylindrical PMs with single-axis rotation. Subsequently, the forces and torques between pairs of cuboidal and pairs of cylindrical PMs with arbitrary rotation should be considered. Then, force and torque expressions between pairs of spherical, triangular, and differently-shaped permanent magnets should be developed.

VII. CONCLUSION

In this paper, the analytical surface charge method is applied to two relatively rotated permanent magnets (PMs). The calculated interaction force is compared with results from the Boundary Element Method (BEM), and validated against experimental results. Although the surface charge method already shows superior applicability and computational time, compared with the BEM, great promise lies in the extension of the method to allow for multi-axial rotations to provide a 6-DoF PM interaction model, which can serve as a fast, analytical replacement to the finite element method.

REFERENCES

- [1] Z. Li, L. Zuo, J. Kuang, and G. Luhrs, "Energy-harvesting shock absorber with a mechanical motion rectifier," *Smart Mater. Struct.*, vol. 22, no. 2, p. 025008, 2013.
- [2] J. Yang, Y. Wen, P. Li, X. Dai, and M. Li, "A Broadband Vibration Energy Harvester Using Magnetolectric Transducer," in *IEEE Sensors*, Nov. 2010, pp. 1905–1909.
- [3] A. Fowler, S. Moheimani, and S. Behrens, "An Omnidirectional MEMS Ultrasonic Energy Harvester for Implanted Devices," *J. Microelectromech. S.*, vol. 23, no. 6, pp. 1454–1462, Dec. 2014.
- [4] Q. Zhang and E. S. Kim, "Vibration Energy Harvesting Based on Magnet and Coil Arrays for Watt-Level Handheld Power Source," *Proc. IEEE*, vol. 102, no. 11, pp. 1747–1761, Nov. 2014.
- [5] J. Jung, P. Kim, J.-I. Lee, and J. Seok, "Nonlinear dynamic and energetic characteristics of piezoelectric energy harvester with two rotatable external magnets," *Int. J. Mech. Sci.*, vol. 92, pp. 206–222, Sep. 2015.
- [6] S. R. Anton and H. A. Sodano, "A review of power harvesting using piezoelectric materials (2003-2006)," *Smart Mater. Struct.*, vol. 16, no. 3, pp. R1–R21, 2007.
- [7] V. R. Challa, M. G. Prasad, Y. Shi, and F. T. Fisher, "A vibration energy harvesting device with bidirectional resonance frequency tunability," *Smart Mater. Struct.*, vol. 17, no. 1, p. 015035, 2008.
- [8] G. Akoun and J.-P. Yonnet, "3D analytical calculation of the forces exerted between two cuboidal magnets," *IEEE Trans. Magn.*, vol. 20, no. 5, pp. 1962–1964, Sep. 1984.
- [9] J. F. Charpentier and G. Lemarquand, "Study of Permanent-Magnet Couplings with Progressive Magnetization Using an Analytical Formulation," *IEEE Trans. Magn.*, vol. 35, no. 5, pp. 4206–4217, Sep. 1999.
- [10] E. P. Furlani, *Permanent Magnet and Electromechanical Devices: Materials, Analysis, and Applications*, ser. Academic Press Series in Electromagnetism. Academic, 2001.
- [11] J. L. G. Janssen, J. J. H. Paulides, E. Lomonova, F. Bölöni, A. Tounzi, and F. Piriou, "Analytical Calculation of Interaction Force Between Orthogonally Magnetized Permanent Magnets," *Sensor Letters*, vol. 7, no. 3, pp. 442–445, 2009.
- [12] H. Allag, "Models and Calculation of Passive Magnetic Suspension – 2D and 3D Analytical Calculation of Interactions Between Permanent Magnets," Ph.D. dissertation, Université de Grenoble, Jun. 2010.
- [13] W. S. P. Robertson, "Modelling and design of magnetic levitation systems for vibration isolation," Ph.D. dissertation, The University of Adelaide, SA, Australia, Nov. 2013.
- [14] L. Gaul, M. Kögl, and M. Wagner, *Boundary Element Methods for Engineers and Scientists – An Introductory Course with Advanced Topics*, 1st ed. Springer-Verlag Berlin Heidelberg, 2003.
- [15] J.-P. Yonnet, "Passive magnetic bearings with permanent magnets," *IEEE Trans. Magn.*, vol. 14, no. 5, pp. 803–805, Sep. 1978.
- [16] R. Hornreich and S. Shtrikman, "Optimal design of synchronous torque couplers," *IEEE Trans. Magn.*, vol. 14, no. 5, pp. 800–802, Sep. 1978.
- [17] J.-P. Yonnet, "Permanent magnet bearings and couplings," *IEEE Trans. Magn.*, vol. 17, no. 1, pp. 1169–1173, Jan. 1981.
- [18] J.-P. Yonnet, S. Hemmerlin, E. Rulliere, and G. Lemarquand, "Analytical calculation of permanent magnet couplings," *IEEE Trans. Magn.*, vol. 29, no. 6, pp. 2932–2934, Nov. 1993.
- [19] J. M. D. Coey, *Rare-Earth Iron Permanent Magnets*, 1st ed., ser. Monographs on the Physics and Chemistry of Materials. Oxford, U.K.: Oxford University Press, 1996, vol. 54.
- [20] B. Hague, *The principles of electromagnetism applied to electrical machines*, 1st ed. New York: Dover Publications, 1962.
- [21] J. Tsui, D. Iden, K. Strnat, and A. Evers, "The effect of intrinsic magnetic properties on permanent magnet repulsion," *IEEE Trans. Magn.*, vol. 8, no. 2, pp. 188–194, Jun. 1972.
- [22] H. S. Nagaraj, "Investigation of Magnetic Fields and Forces Arising in Open-Circuit-Type Magnetic Bearings," *Tribology Transactions*, vol. 31, no. 2, pp. 192–201, 1988.
- [23] M. F. J. Kremers, J. J. H. Paulides, E. Ilhan, J. L. G. Janssen, and E. A. Lomonova, "Relative Permeability in a 3D Analytical Surface Charge Model of Permanent Magnets," *IEEE Trans. Magn.*, vol. 49, no. 5, pp. 2299–2302, May 2013.
- [24] J. L. G. Janssen, J. J. H. Paulides, and E. A. Lomonova, *Computer field models of electromagnetic devices - Studies in applied electromagnetics series*. Amsterdam: IOS Press, 2010, ch. Analytical Force and Stiffness Calculations for Magnetic Bearings and Vibration Isolation, pp. 502–511.
- [25] D. van Casteren, J. Paulides, and E. Lomonova, "Modeling the Field Inside a Soft-Magnetic Boundary using Surface Charge Modeling," *IEEE Trans. Magn.*, vol. PP, no. 99, pp. 1–1, 2015.

Grid Hybridization using AC-DC Reconfigurable Underground Cable links in Distribution Networks

Aditya Shekhar, Laura Ramírez-Elizondo and Pavol Bauer
DC Systems & Storage, Delft University of Technology, The Netherlands
a.shekhar@tudelft.nl

Abstract—This work represents the progressing efforts towards grid hybridization and provides an overview of the evolving concept of reconfigurable ac-dc links. The motivation for refurbishing ac infrastructure to operate under dc conditions is also offered. The possibility of power transmission capacity enhancement with dc links is highlighted. Finally, the objective of dc link control and grid integration is presented.

Index Terms—ac, cables, capacity, converter, control, dc, dc link, electric fields, flexibility, grid integration, hybrid, modularity, redundancy, reconfigurable, refurbishing.

I. INTRODUCTION

Increasing integration of dispersed renewable energy sources in existing electricity supply systems have enabled bidirectional power flows in the distribution networks [1]. Looking at the current grid structure, it is possible that dc distribution has some operation advantages over ac [2]. New energy consumers like electric vehicles have changed the localized energy consumption patterns, introducing more complexity to the grid operability [3].

Infrastructural complexity and investment costs are required for maintaining sufficient and optimized power flow to cope with localized demand deficits and quality of supply at acceptable voltage deviations [4]. Distribution network operators (DNOs) should have adequate flexibility and control on grid operation^{*}.

A. Research Objectives

It is anticipated that reconfigurable dc links employing power electronic devices with advanced controls and protection algorithms can serve as a flexible backbone to existing distribution systems.

Possible research directions to be explored in using reconfigurable dc links are as follows:

- Economical interconnectivity between grid sections ensuring efficient power balancing using interactive power flow optimization algorithms.
- Maintaining voltage parity at desired level between interconnected sections using advanced control algorithms.
- Enabling smart integration of renewable energy sources operating at different output voltage levels.
- Protection algorithms to improve safety of operation and isolation in case of fault conditions.

- Exploring different architectures and constraints involved in utility interactive power balancing, voltage control and protection algorithms employed in proposed system.

B. Impact Overview

Current solutions like demand response at end users or electrical storage offer limited flexibility to the distribution network operators. The proposed reconfigurable dc links as utility interactive power electronics offer a possibility to independently control the power and voltage profiles within the network. The concept of reconfigurability is highlighted in Section II.

In Section III, aspects associated with refurbishing ac cables to operate under dc conditions are explored.

Reconfigurable dc links can increase the existing capacity, without which the network operators will be forced to expand, incurring additional costs. This thought is further expanded in Section IV.

Furthermore, undesired smart grid phenomena like increased dynamic behaviour due to greater fluctuations in load and generation, decreased power quality, increased harmonic distortion, reactive power demand and decrease of system inertia may be mitigated. Section V explores the control and integration of the dc link with the existing ac distribution network in order to achieve the final goal of grid hybridization.

Finally, Section VI concludes the ideas and research study presented in this paper.

II. RECONFIGURABLE AC-DC MODULAR OPERATION

Reconfigurability of the underground medium voltage cable link is considered as central concept around which this project revolves. By this way, not only can the operational and technical benefits of the dc transmission be exploited, but the utility operators have the option of reverting back to ac operation, if need be, in case of contingencies. The concept of hardware and software reconfigurability of the ac-dc underground cable link in order to achieve adequate redundancies, modularity and flexibility in the distribution grid is expanded in [5]. In [5], the authors have described the concept of reconfigurable dc links and discussed the different control functionalities that can be incorporated in the dc link in order to obtain a flexible operation.

Fig. 1. depicts one of the hardware system reconfiguration that can work as a bipolar dc link as well as revert back to 3

phase ac operation during converter faults by modular repair scheme.

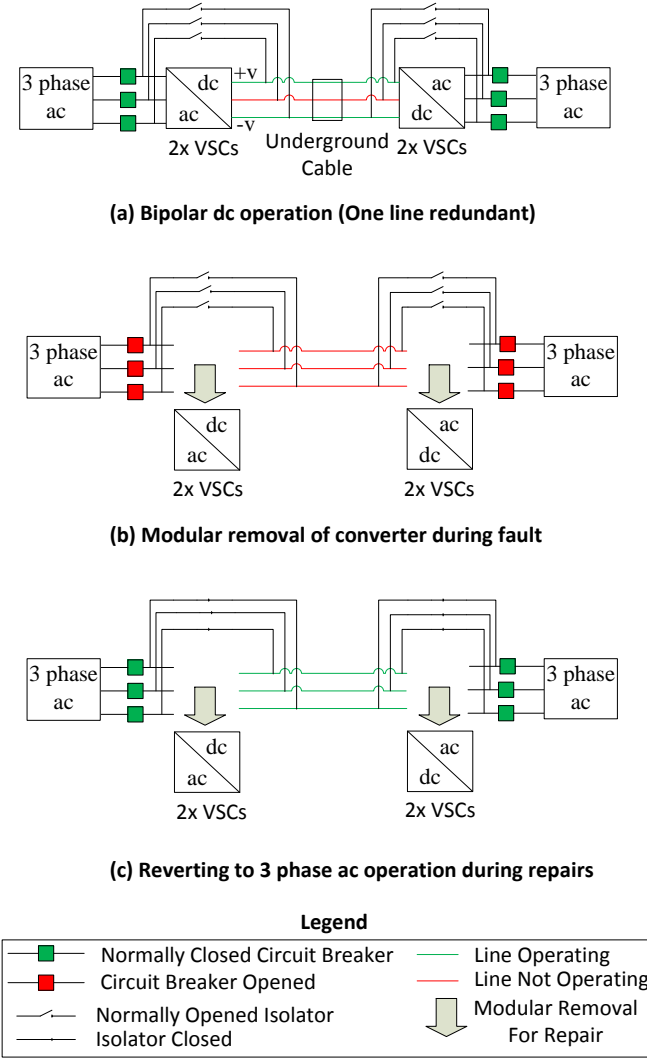


Fig. 1. Hardware reconfiguration for modular and flexible ac-dc operation of underground cables.

In this scheme, the 3 core cable operates as a bipolar dc link under normal operational conditions. Two of the cables can be fully loaded while one is either redundant or acts as a return path as shown in Fig. 1. (a). During converter faults, which are the least reliable part of the system, the circuit breakers on the ac side open and the faulted components can be modularly removed as shown in Fig. 1. (b). The system can revert back to 3 phase 3 line ac operation as shown in Fig. 1. (c), by closing the isolator and reclosing the circuit breakers at both sides.

In this way, we not only achieve a flexible and modular ac-dc operation by re-using the same underground cable infrastructure, but also, save costs by common use of the circuit breakers for both operating modes. The isolators are cheaper and used only for ac connection, and remain normally open during dc operation. These isolators are not operated to

make or break cable current, which is done using the common connected circuit breakers.

III. REFURBISHING AC TO DC CABLES

In the previous section, reusing the same underground cable for ac as well as dc operation is offered as a solution to achieve greater modularity, flexibility and redundancy. In practical sense, such an operational requirement has technical implications for the underground cable. Therefore, the subject of refurbishing ac medium voltage underground cables to operate under dc conditions in terms of aspects such as component lifetime, electric fields, temperature dependence, protection, capacity and efficiency enhancement is discussed extensively in [6].

For example, the electric fields imposed on the cable insulation are very different in ac and dc conditions. The approximated expression for temperature dependent electric field stress $E(x)$ on the cable insulation under dc operating conditions is given by (1) [7], [8].

$$E(x) = \frac{\delta U_0 \left(\frac{x}{r_o} \right)^{(\delta-1)}}{r_o \left(1 - \left(\frac{r_i}{r_o} \right)^\delta \right)} \quad (1)$$

U_0 is the nominal operating voltage imposed on the cable, r_i and r_o are the inner and outer radius of the insulation respectively and δ is a dimensionless quantity given by (2).

$$\delta = \frac{\frac{\alpha \Delta T}{\ln(r_o/r_i)} + \frac{b U_0}{r_o - r_i}}{1 + \frac{b U_0}{r_o - r_i}} \quad (2)$$

Herein, b is the stress coefficient in mm/kV, α is the temperature coefficient in $^{\circ}\text{C}^{-1}$ and ΔT is the temperature difference between outer and inner surfaces of the insulation.

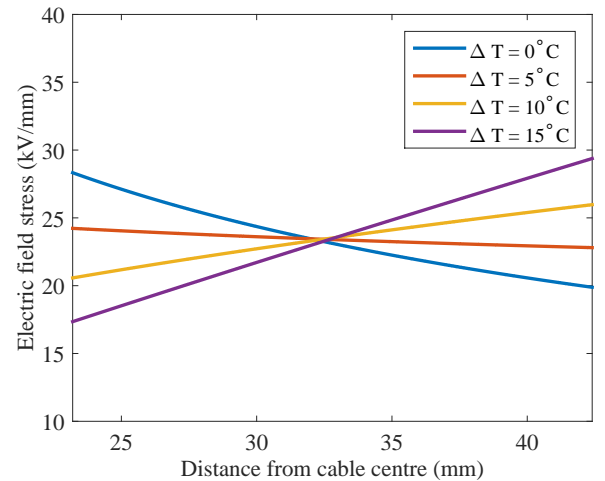


Fig. 2. Temperature dependence of electric field stress on insulation of the standard cable.

Fig. 2 shows the resistive electric field distribution in the cable insulation for different ΔT for standard impregnated paper type cable with 450 kV rated voltage, $\alpha = 0.1^{\circ}\text{C}$,

$b=0.03 \text{ mm/kV}$, $r_i = 23.2 \text{ mm}$ and $r_o = 42.4 \text{ mm}$ [8].

As the temperature difference increases, the electric field starts reducing at the inner insulation surface and increasing at the outer until it is completely inverted. It can be observed that for $\Delta T = 10^\circ\text{C}$ the electric field distribution in the insulation is almost flat. It follows that at specific temperature distributions, it is possible to increase the operating voltage of the cable to obtain the same maximum field.

The electric field distribution for cables operating under dc voltage illustrated here are for a high voltage XLPE standard cable used in [8]. However, the same principles apply for medium voltage XLPE cables. In [6], the novel idea of temperature dependent dynamic voltage rating is established that takes into account the varying electric field distribution for a medium voltage 11 kV XLPE cable.

IV. CAPACITY ENHANCEMENT

Higher power transfer capacity can be achieved with a dc link as compared to ac due to enhanced voltage rating [9], [10], atleast by $\sqrt{2}$. In [9], it is offered that the dc cable transmission capacity enhancement is 294% as against the existing three phase double circuit ac system. The current rating enhancement due to thermal proximity is also taken into account to reach this number.

While it can be recognized that some capacity gains can realistically be achieved, a more comprehensive study may be required [6]. For example, different system configurations can lead to different capacity gains, and sometimes even reduction.

Table I highlights the impact of system topology on capacity enhancement. In this only voltage rating enhancement is taken into account.

TABLE I
TOPOLOGY DEPENDENT CAPACITY ENHANCEMENT AT UPF

AC Circuit	DC Topology	Ground Return	Enhancement	%
Single, 3 line	Monopolar	Yes	$\sqrt{2}$	41
Double, 3 line	Monopolar	Yes	$\sqrt{2}$	41
Single, 3 line	Bipolar	No	$(2\sqrt{2})/3$	-7
Double, 3 line	Bipolar	No	$\sqrt{2}$	41

Therefore, for DNOs to ascertain the gains of shifting to dc using the existing ac infrastructure, influence of initial and final system topology, the consequences of the choice such as ground return and voltage enhancement and the associated trade-offs such as component lifetime reduction must be known [11]. The subject of this discussion is explored in [6].

Furthermore, an accurate representation of the realistic capacity gains must also include factors other than voltage rating enhancement and topology, such as:

- Current rating enhancement: skin effect, dielectric losses, thermal proximity effect and capacitive current.

- Voltage regulation with varying line lengths and cable cross-sectional area.
- Power Factor at load side

Equations meticulously taking into account all the associated factors while imposing the rated cable current at the sending end of the transmission link have been derived in [12]. The results describing the capacity enhancement taking into account all the listed factors with different system topologies, varying cable lengths and cross-sectional areas are presented in [13].

V. DC LINK CONTROL AND GRID INTEGRATION

Since the objective of this project is to finally benefit from grid hybridization using reconfigurable dc links at medium voltage level in existing ac distribution networks, interfacing infrastructure, converter topologies, control functionalities and ancillary services are an integral part of the research study. The following research aspects are important from this context:

- Interfacing options for dc link integration with predominantly ac distribution grid based on converter topology, efficiency, costs, protection and reliability of the system.
- Point to point dc link connection feasibility and whether opportunities exist to extend the infrastructure to a meshed dc grid with integrated renewable energy sources.
- Power balance, bi-directionality and voltage support using the dc link during normal operation and its subsequent impact on the stable ac grid operation.
- Protection mechanism during a short circuit at different grid locations, both at ac and dc side.

The converter topology itself can be voltage source converters (VSC) of two level, three level neutral clamped or multilevel converters, controlled using dq transformation of the measured grid voltage, output converter current and the dc link voltage [14].

VI. CONCLUSIONS

In this document, the concept of reconfigurable dc links is described. The benefits corresponding to flexibility, modularity and redundancies is highlighted. The aspects associated with refurbishing ac cables to operate under dc conditions are also mentioned. The idea of capacity enhancement as a possible advantage of employing dc links in distribution networks is put forth. Finally, control functionalities and grid integration of the dc links is expressed as an important research direction towards realizing a working reconfigurable dc link technology in the existing ac distribution grid in order to achieve hybrid operation.

ACKNOWLEDGEMENTS

The authors would like to acknowledge Mr. Epameinondas Kontos and Dr. Armando Rodrigo Mor for their inputs, with which the framework of the cited publications ([5]-[13]) was established. We are thankful to dutch distribution network operator (DNO) representatives from Alliander (Dr. Maarten Van Riet, Dr. Frans Provoost and Dr. Irina Melnik) and Enexis (Dr. Johan Morren) for workshop feedback.

Authors would also like to thank all the partners of the FLINK project funded by TKI switch2smartgrids, including TU Eindhoven and DNV-GL under the supervision of Dr. Erik C.W. de Jong.

APPENDIX

Based on the author's research, the following handout with discussion points for the workshop feedback with utility operators was prepared:

- 1) What can reconfigurable dc links offer in terms of operability and flexibility to the DNOs? The impact of installing such links on conventional grids must also be explored.
 - What are the benefits associated with research purposes?
 - How and what kind of flexibility and redundancies be incorporated using reconfigurability?
 - What are the possibilities of grid voltage support, active and reactive power injection?
 - What are the protection and integration aspects to be looked into?
- 2) What kind of dc link configurations can be employed (monopolar/bipolar/homopolar) according to the existing systems?
- 3) What specific situations DNOs may have encountered in which reconfigurable dc links can be advantageous, for example, in terms of network de-congestion and addressing local power deficits?
- 4) Is refurbishing ac to dc lines relevant in context of capacity enhancement?
- 5) What control functionalities should the dc link converter have?

REFERENCES

- [1] D. E. Olivares, A. Mehrizi-Sani, A. H. Etemadi, C. a. Canizares, R. Iravani, M. Kazerani, A. H. Hajimiragha, O. Gomis-Bellmunt, M. Saeedifard, R. Palma-Behnke, G. a. Jimenez-Estevez, N. D. Hatziargyriou, "Trends in Microgrid Control," *IEEE Transactions on Smart Grid*, 2014.
- [2] J. J. Justo, F. Mwasilu, J. Lee, J.-W. Jung, "Ac-microgrids versus dc-microgrids with distributed energy resources: A review," *Renewable and Sustainable Energy Reviews*, 2013.
- [3] G.R. Chandra Mouli, P. Bauer, M. Zeman, "System design for a solar powered electric vehicle charging station for workplaces," in *Applied Energy*, Volume 168, 15 April 2016, Pages 434-443.
- [4] A. Werth, N. Kitamura, K. Tanaka, "Conceptual Study for Open Energy Systems: Distributed Energy Network Using Interconnected DC Nanogrids," *IEEE Transactions on Smart Grid*, 2015.
- [5] A. Shekhar, L. Ramírez-Elizondo, E. Kontos, A. Rodrigo Mor and P. Bauer, "Flexible and Hybrid MV and LV Distribution Grids with Reconfigurable DC Links," *Energy Congress and Expo, IEEE*, Milwaukee, WI, Submitted, 2016.
- [6] A. Shekhar, A. Rodrigo Mor, E. Kontos, L. Ramírez-Elizondo and P. Bauer, "Refurbishing Existing MVAC Distribution Cables to Operate Under DC Conditions," *Power Electronics and Motion Control Conference and Exposition (PEMC) 17th International*, Varna, Submitted, 2016.
- [7] M. M. Mazzanti, G., *Extruded Cables for High-Voltage Direct-Current Transmission: Advances in Research and Development*. 2013.
- [8] M. Jeroense and P. Morshuis, "Electric fields in hvdc paper-insulated cables," *Dielectrics and Electrical Insulation, IEEE Transactions on*, vol. 5, pp. 225-236, Apr 1998.
- [9] J. Arrillaga, "High Voltage Direct Current Transmission", vol. Second Edition, 2008.
- [10] D.M. Larruskain, I. Zamora, A.J. Mazon, O. Abarregui, J. Monasterio, "Transmission and Distribution Networks: AC versus DC,"
- [11] F. Krueger, *Industrial High Voltage*. Delft University Press, 1992.
- [12] A. Shekhar, L. Ramírez-Elizondo, E. Kontos, A. Rodrigo Mor and P. Bauer, "Power Transfer Computations for Medium Voltage AC Link by Imposing Rated Current at Sending End," *Power Electronics and Motion Control Conference and Exposition (PEMC) 17th International*, Varna, Submitted, 2016.
- [13] A. Shekhar, E. Kontos, L. Ramírez-Elizondo, A. Rodrigo Mor and P. Bauer, "Capacity Enhancement in Transmitted Power Using DC Links in MVAC Distribution Grids," *Energy Congress and Expo, IEEE*, Milwaukee, WI, Submitted, 2016.
- [14] Amirnaser Yazdani, Reza Iravani, "Voltage-sourced Converters In Power Systems - Modeling, Control, and Applications," *Wiley, IEEE Press*, 2010.

Long-Term Planning of Industrial Microgrids

Charline Stevanoni, François Vallée,
Zacharie De Grève and Olivier Deblecker
University of Mons, Faculty of Engineering
Electrical Power Engineering Unit
Boulevard Dolez 31, 7000 Mons, Belgium
Email: charline.stevanoni@umons.ac.be

Pascal Couneson
Decube Consult
Quai du Pont Canal 3,
7110 Strépy-Bracquegnies, Belgium
Email: p.couneson@decube.be

Abstract—This paper deals with the context and objectives of the long-term planning of industrial microgrids. A first flowchart for the development of a tool helping to the setting up of industrial microgrids is presented. The imagined methodology allows taking into account the different (possibly conflicting) objectives of the microgrid stakeholders, by seeking an equilibrium from a game theoretical perspective. Beforehand, the role of each stakeholder as well as the decisions they can take have to be well-defined through an interaction model. The description of such an interaction model is developed in this paper.

I. INTRODUCTION

In order to respond to the plan "20-20-20" decided by the European Union and to the current society willingness of moving towards a greener environment thanks to the reduction of nuclear electricity production, recent years have witnessed a large deployment of Renewable Energy Systems (RESs). The network has therefore undergone a change of paradigm in which the electricity production is not centralized anymore but distributed in the network. However, the proliferation of RESs is limited because of the intermittent operation of some of them, such as solar photovoltaic (PV) and wind generation units. Those fluctuating energies may cause troubles in transmission and distribution networks. Moreover, the fixed loads of the network have to be fed continually and may not face a lack of supply. Those reasons involve that the proliferation of RESs is not possible without a smart management [1] and the use of Energy Storage Systems (ESSs) to allow flexibility. In order to integrate new productions and load management in the network, the notion of microgrid is more and more widespread. According to [2], a microgrid is "a group of interconnected loads and distributed energy resources (DERs) with clearly defined electrical boundaries that acts as a single controllable entity with respect to the grid and can connect and disconnect from the grid to enable it to operate in both grid-connected or island modes". In this definition, DERs include distributed generations (DGs), RESs and ESSs. Microgrids are more than simple backup generation because they can provide a wide range of benefits at a larger scale and they are more flexible [2]. Indeed, microgrids can be used as a support for the distribution network performance such as reliability, resiliency and power quality. The installed microgrid world's capacity was about 1.1 GW in 2012 and is estimated to

be 4.7 GW in 2017 [2]. In Europe, microgrids that are often developed in existing networks must be adapted to the existing configuration and are connected to the general network. However, the microgrid development is also more and more intended in emerging countries without initial infrastructure such as in Africa. In this case, they are built from nothing and operated in island mode [3].

In this work, grid-connected microgrids are considered at a Medium Voltage (MV) industrial level and not at a residential one. A motivation for industrial microgrids development is to decrease the electricity bill for companies which take part to the microgrid. Indeed, the MV electricity purchase price is more and more expensive for industries, especially in Belgium. A survey conducted in 2016 showed that, for belgian industrial companies, their electricity bill is 16 to 40 % more expensive than the mean one of the neighbour countries (France, Holland and Germany) taking into account taxes and network costs which are also consequent in Belgium, as shown in Fig. 1 [4].

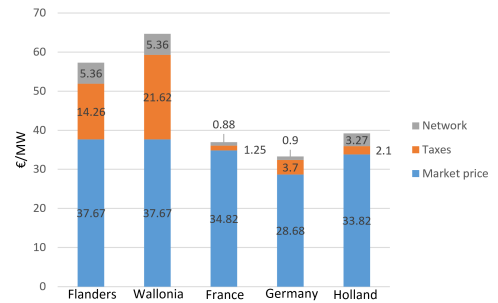


Fig. 1. Electricity Price in 2016 (€/MWh) (profil baseload 100 GWh) [4].

Therefore, investing in decentralized generation such as wind or PV may become interesting for industrial companies. The industries which install those kinds of productions want to improve their self-consumption, *i.e.* to make profitable their investment by trying to consume locally all their generated electricity and, consequently, to avoid selling it at a cheaper price than the one paid for direct consumption from the grid. Indeed, the excess of generation is sold to the distribution network at a very low price (market price) compared with the purchase price (market price + taxes + network price).

As an example, the company partially funding this work previously invested in a PV installation of 250 kWp. However, after a few years of operation, the objective of 100% self-consumption has not yet been achieved due to the high variability of sunshine in Belgium. Indeed, PV generation was sometimes not sufficient to fully supply the consumption, whereas reverse power flows occurred at other times. For such an installation, the residual produced electricity has to be sold to the distribution network, but the selling price is very low compared to the purchasing one. Such a difference represents a shortfall for the company. One way to reduce it is to consider electricity storage facilities. However, a first study has shown that storage batteries are still too expensive to be cost-effective for a single company [5].

At a larger scale, in an industrial estate, the consumption profiles of the companies can be complementary. The installation of a single storage unit shared among several companies could therefore be more profitable. In such an industrial estate, in which several companies would massively invest in RESs, a pooling of the production units could be considered in a microgrid framework. However, the companies would like to know if such a microgrid could be profitable over the years considering their wish to keep a connection with the distribution network and the costs that this involves. In order to meet this demand, it is necessary to plan at a long-term horizon (typically up to 20 years) the evolution of the microgrid. In this context, the present work aims at providing a tool for the setting up of industrial MV microgrids with a minimization of the electricity costs while taking into account the individual (possibly conflicting) objectives of the microgrid stakeholders.

This paper is organized as follows. In section II, the methodology of the long-term planning tool is described, including the management of the microgrid and the costs objective functions formulation. Section III then presents a first model of interaction in detail *i.e.* the role of each stakeholder and the decisions they can take. Finally, conclusions are drawn and perspectives for future work are given.

II. METHODOLOGY OF THE LONG-TERM PLANNING TOOL

In an industrial microgrid, several parties have to be considered. These are the individual prosumers (which are the consumers who possibly own their local RESs), the Distribution System Operator (DSO) and the Industrial Estate Operator (IEO). In this contribution, the microgrid is managed by an aggregator. One of the goals of this work, which is also one of its originalities, is to put as aggregator each stakeholder of the microgrid alternately. Depending on the aggregator, the management strategy of the microgrid will be different. In addition, two additional strategies are considered in which the aggregator is, respectively, an independent entity or a state organization. Those strategies are detailed in this paper. Moreover, for each stakeholder of each strategy, an

annual objective function Va_N is written and a global objective function NPV for Net Present Value is written over N_{tot} years.

A. Costs objective function formulation

The annual objective function Va_N for each stakeholder is the net Value for year N , which is defined by Eq. (1) as the difference between the revenues and the expenses during the year N . This expression (inspired from [6]) has two parts: an hourly part (terms in parentheses) and an annual part.

$$Va_N = \left(\sum_{h=1}^{h=8760} (R_{h,N} - C_{h,N}) \right) - Cm_N - Cs_N - Ci_N \quad (1)$$

where $R_{h,N}$ and $C_{h,N}$ are, respectively, the revenue and cost per hour, Cm_N is the annual maintenance cost, Cs_N is the annual additional cost and Ci_N is the annual investment cost.

In order to analyze the profitability of the microgrid over N_{tot} years, the NPV is used because costs and revenues in year 1 are not equivalent to those of the future, as time has an impact on the value of cash flows. After computing Va_N for year N , the Present Value (PV_N) is computed taking into account the discounting of future cash flows through the discount rate i and they are cumulated over the planning time horizon of N_{tot} years to obtain the NPV (2):

$$NPV = \sum_{N=1}^{N_{tot}} PV_N = \sum_{N=1}^{N_{tot}} \frac{1}{(1+i)^N} Va_N \quad (2)$$

Thus, a positive NPV indicates that the project is making benefits over the planning period.

B. Strategies

The goals pursued by each aggregator are described in this part. They differ by the direct benefits they expect from the microgrid (sign of the NPV).

Strategy I (aggregator = DSO): The DSO intends to make benefits by decreasing transmission costs, even if the microgrid client electricity bill is expected to decrease. Its role is also to maintain or improve the quality of the electricity in the distribution system and in the microgrid and to ensure their stability $\Rightarrow NPV > 0$;

Strategy II (aggregator = a single or a group of prosumers): They want to make benefits thanks to a reduction of the difference between the actual purchasing price of electricity to supply their needs and the actual selling price of the excess of electricity produced by their RESs. In that way, an improvement of their self-consumption, *i.e.* a decrease of the electricity amount exchanged with the distribution network, is pursued. They can also provide services to the DSO to obtain an extra revenue $\Rightarrow NPV > 0$;

Strategy III (aggregator = IEO): IEO wants to optimize the proper operation of the microgrid by promoting the RESs of the prosumers. Its first interest is not to make direct

benefits but to provide a social global welfare and to develop its industrial estate by attracting new companies in the area thanks to an attractive price of electricity (socio-economic dimension) $\Rightarrow NPV <, = \text{ or } > 0$;

Strategy IV (aggregator = an independant entity): Its objective is to make pure benefits thanks to a maximization of the revenues coming from the microgrid and the optimization of its proper operation $\Rightarrow NPV > 0$;

Strategy V (aggregator = a state organization): Its objective is to manage the microgrid with the goal of optimizing its proper operation and keeping a social global welfare between all the stakeholders without making any benefits $\Rightarrow NPV = 0$.

In conclusion to this point, it is obvious that the choice of the aggregator will influence the decisions to be undertaken in the management process of the microgrid.

C. General organization of the decision-making tool

Each management strategy described above is studied under a large number of scenarios [7] which represent possible evolutions of the microgrid in terms of consumption and production profiles, as well as in terms of new RESs by the prosumers (note that RESs are supposed to be only placed by the prosumers and not by the DSO). Each scenario is created on a planning period of 20 years (which approximately corresponds to the life time of RESs). For each hour of each scenario, a load flow is performed and the state of the microgrid is defined through technical [8] and reliability [9] indicators. At the end of the load flow, the flowchart presented in Fig. 2 is applied. The aggregator and the stakeholders recover all those indicators and analyze them. Each one will have to choose between several decisions among the possibilities arising from the interaction model of the concerned strategy, such as investments or flexibility services. Every decision is associated with a price that has to be taken into account in (1) and, thus, in (2) over 20 years. Following the level of benefit, those decisions are classified in a preference order. Practically, the final decision will be found thanks to the computation of an equilibrium between all the stakeholders using a game extracted from the Game Theory [10].

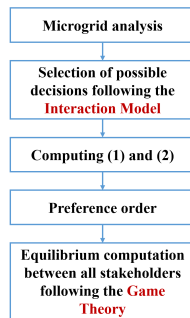


Fig. 2. Flowchart for each microgrid stakeholder (including the aggregator).

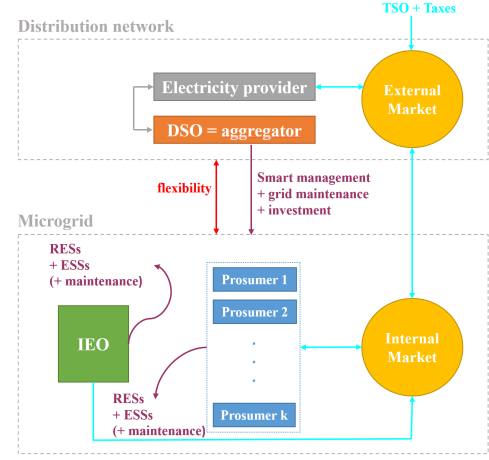


Fig. 3. Interaction model for strategy I.

III. A FIRST INTERACTION MODEL

For each strategy, it is necessary to define the interaction model between all the stakeholders (with their roles and decisions), as well as to establish the cost terms in detail. In this paper, an interaction model for the first strategy (aggregator = DSO) is presented (Fig. 3). There are three kinds of interactions: cyan arrows represent interactions related to the cost of electricity exchanged through the External Market (EM) and the Internal Market (IM), the red double arrow represents flexibility services and the purple arrows depict the microgrid development.

A. Electricity exchanges

The privileged electricity exchanges are those inside the microgrid. The prosumers who own a RES use their own generation in the first instance. Three cases can then appear for each prosumer. In the first situation, the production and the consumption are equal and the balance is respected. In the second case, there is more generation than consumption and, consequently, the prosumer needs to sell its electricity surplus (*prosumer = seller*). In the last configuration, generation is lower than consumption and the prosumer has to buy electricity through the aggregator (*prosumer = buyer*). For the first case, there are no exchanges but, in the two other cases, exchanges have to be managed by the aggregator in the IM. As shown in Fig. 4, each seller gives a minimal price at which he accepts to sell its electricity surplus and each buyer gives a maximal purchase price at which he accepts to purchase the electricity to fully provide its own consumption. Those bounds are then centralised by the aggregator. In this work, the optimization part done in the IM is not handled and will be considered as a "black box". The outputs of this black box are purchase ($Pr_{purchase,\mu}$) and sale ($Pr_{sale,\mu}$) prices at which prosumers can buy and sell electricity inside the microgrid. Those prices are computed in such a way that the aggregator is paid for its operator role by a fee $Pr_{fee,IM}$, which is a percentage of the difference between $Pr_{purchase,\mu}$ and $Pr_{sale,\mu}$.

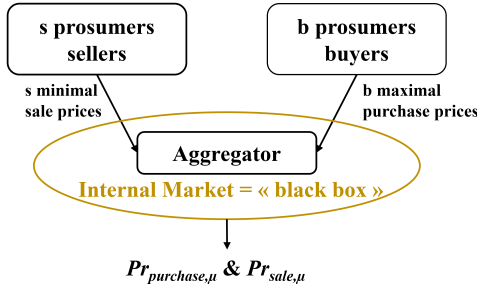


Fig. 4. Electricity exchanges inside the microgrid.

When the exchanges inside the microgrid are done, there are three possibilities: either there is a balance (all the generation is used and all the consumption is provided inside the microgrid), or there is still an electricity surplus (more global generation than the global consumption) or there is a lack of electricity (the global consumption is higher than the global generation). In the two last cases, it will be necessary to have exchanges between the microgrid and the distribution network. Fig. 5 shows how the costs of those exchanges are defined.

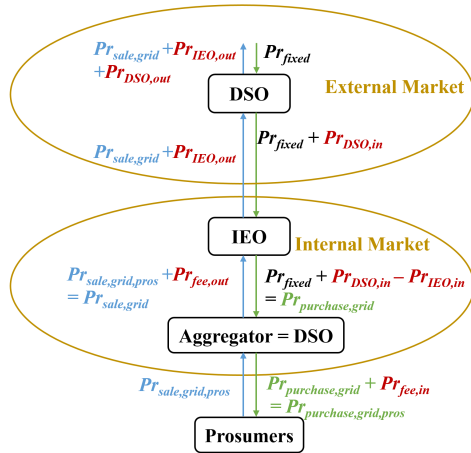


Fig. 5. Electricity exchanges between the distribution network and the microgrid.

The case with a lack of electricity in the microgrid is presented using the green arrows (on the right part of Fig. 5). In the EM, Pr_{fixed} is the base price of electricity with the transmission costs and state taxes. To that price, the DSO adds the distribution cost ($Pr_{DSO,in}$), but since the aggregator is the DSO here, it can be imagined that this price will be flexible (the DSO can decide to put it equal, higher or lower than the classical actual price). Then, in the IM, as one objective of the IEO is to make electricity price more interesting for the prosumers, IEO could help to reduce the electricity purchase price thanks to a contribution $Pr_{IEO,in}$. As a result, the electricity purchase price $Pr_{purchase,grid}$ is paid by the aggregator. The aggregator then grants himself with a fee $Pr_{fee,in}$ and sells the electricity to the prosumers according to their needs ($Pr_{purchase,grid,pros}$).

Consider now the case in which there is an electricity surplus from the microgrid. This exchange is presented by the blue arrows in Fig. 5. First, the prosumers give to the aggregator their selling price ($Pr_{sale,grid,pros}$). Then the aggregator puts its fee ($Pr_{fee,out}$) and the selling price of electricity is defined ($Pr_{sale,grid}$). Afterwards, the IEO takes back a flexible part of its contribution through the increasing of the selling price with the value $Pr_{IEO,out}$. Finally, in this particular strategy with the DSO as aggregator, the DSO adds its distribution cost $Pr_{DSO,out}$ in the EM. Note that the prices in red on Fig. 5 are flexible, *i.e.* their values depend on the decision of the concerned stakeholder.

B. Flexibility services

In reference [11], the flexibility is defined as a "modification of injection or consumption in reaction to an external price (from the DSO) or to the activation of a signal in order to provide services". The red double arrow in Fig. 3 represents the flexibility services exchanges between all the stakeholders from the distribution network and from the microgrid. For an easier understanding of those services, they are summarized in tables inspired from [12] and are divided between the microgrid needs (Table I) and the distribution network needs (Table II). In those tables, the second column indicates which service(s) can be done to cater the needs. The third column indicates how the service is managed and the last two columns specify the provider and user of the service, respectively. Note that when the provider or the user is the aggregator, it can be either on its behalf or on behalf of prosumers. In the second case, the aggregator charges a fee as operator of flexibility service and the costs or the revenues are shared between the concerned prosumers. In the economical record, the costs linked to flexibility services have to be compared with investment costs to make the more profitable choice.

From the microgrid point of view (Table I), the first need is obviously the electricity which can be provided either by the distribution network or by other prosumers inside the microgrid. The exchange mechanisms are those explained in section III. A. The second need is to avoid congestion and an oversize of the microgrid. There are several ways to supply this need such as the adjustment of the RES generation and the load shifting of some prosumers. The goal of this service is to allow the aggregator to avoid investments inside the microgrid such as line reinforcement or reconfiguration. A special contract is done between the prosumers and the aggregator in order to fix the cost and the conditions of that service. Another service is the voltage control inside the microgrid. Indeed, overvoltage can damage prosumer's equipments. This voltage control is done locally by prosumers thanks to the management of active and reactive powers. Again, this service is managed by the aggregator who will take a fee. The penultimate service is the management of the RESs and ESSs by the aggregator. When the aggregator is the DSO, it knows the production and consumption previsions and thus he has to manage the RESs and ESSs integration in order to maximize it. Another way to

maximize prosumer's RESs and ESSs could be investment aids from the IEO. Finally, the IEO profits are the development of the IEO's industrial estate thanks to attractive electricity prices from the aggregator which will allow a cheaper electricity bill to the companies. In that way, the IEO has interest in providing a budget for the growth (new jobs) or the attraction of new businesses.

TABLE I
FLEXIBILITY SERVICES - MICROGRID NEEDS

Microgrid needs	Service(s)	Procurement mechanism	Provider	User
Electricity	Supply electricity from general network	Contract (markets)	Electricity provider	Aggregator (=DSO) on behalf of prosumers
	Supply electricity from RESs and ESSs	IM	IEO or some prosumers	
Congestion management and avoid oversizing	Generation adjustment, load management and peak shifting	Contract	Prosumers	Aggregator (=DSO)
Local voltage control	Active and reactive power provision	Contract	Aggregator (=DSO) on behalf of prosumers	Aggregator (=DSO) on behalf of prosumers
Maximizing RESs and ESSs integration	Prevision production	Aggregator's role	Aggregator (=DSO)	Prosumers
	Investment aids	Contract	IEO	
Industrial development	Attractive electricity prices	Contract (markets)	Aggregator (=DSO)	IEO

From the distribution network point of view (Table II), note that the provider is always the aggregator who charges a fee as flexibility operator and divides the remaining benefits to some prosumers according to their participation in the provided service. The user is always the DSO, not in its aggregator's role but in its classical role. The first service is the supply of electricity by the microgrid if there is a surplus of RESs generation or some electricity from ESSs. The second service is the congestion management in the distribution network which is possible thanks to a management of the microgrid injection and its global consumption regulation. The last service is the voltage control at a larger scale which is possible thanks to the management of active and reactive powers exchanged by the microgrid with the main electrical network.

C. Economical record

This part summarizes in detail all the terms of Eq. (1) for each stakeholder in this investigated strategy (with the

TABLE II
FLEXIBILITY SERVICES - DISTRIBUTION NETWORK NEEDS

Distribution network needs	Service(s)	Procurement mechanism	Provider	User
Electricity	Surplus from RESs and ESSs	Contract (markets)	Aggregator (=DSO) on behalf of prosumers	DSO
Congestion management and avoid oversizing	Adjust injection from microgrid, microgrid global consumption regulation	Contract	Aggregator (=DSO) on behalf of prosumers	DSO
Voltage control	Active and reactive power provision	Contract	Aggregator (=DSO) on behalf of prosumers	DSO

DSO as aggregator). Eq. (1), and thus Eq. (2) after N_{tot} years, has to be written and computed for the aggregator, for all the prosumers and for the IEO. Note that, in this particular strategy, all the expenses and revenues linked to the DSO's aggregator role and its classical role have to be taken into account separately (even if there will probably be some balances). The terms for the aggregator are described in Table III and those for all the prosumers and the IEO are presented in Table IV.

For the aggregator (Table III), the revenue term takes into account all the contributions described above, *i.e.* the revenues linked to the classical role of the DSO through the billing of distribution services which is variable following its decision ($Pr_{DSO,in}$ and $Pr_{DSO,out}$), the flexible revenues linked to its role of IM operator ($Pr_{fee,IM}$, $Pr_{fee,in}$ and $Pr_{fee,out}$), the revenues linked to its role of flexibility services operator (services that it manages for the prosumers) and also revenues thanks to provided services. The hourly costs are those for the use of flexibility services. The last three terms take into account the costs linked to the development of the microgrid (smart management and investments) and its maintenance. For the prosumers (Table IV), the revenues are those linked to the sale of electricity outside and inside the microgrid ($Pr_{sale,grid,pros}$ and $Pr_{sale,\mu}$), as described in the electricity exchanges, and the revenues related to the supply of flexibility services described in previous tables. The hourly costs are structured in the same way, *i.e.* the costs linked to the purchase of electricity outside and inside the microgrid ($Pr_{purchase,grid,pros}$ and $Pr_{purchase,\mu}$) added to the costs of the flexibility services that are used. The investment and maintenance costs are those related to the RESs and ESSs. In addition, for the last three costs, it is considered that prosumers participate for a percentage of the aggregator costs to develop

the microgrid (contract between the stakeholders). For the IEO (Table IV), the revenues are, on the one hand, $Pr_{IEO,out}$ defined above as a recovery of money when electricity is sold to the distribution network and, on another hand, the supply of electricity (flexibility service) thanks to their potential RESs and ESSs. Note that in this last case, their selling price is identical to the one of the other prosumers (IEO takes part to the IM on the same level as another producer). The hourly cost is $Pr_{IEO,in}$ which represents its contribution to the reduction of the electricity price inside the IM when the electricity is purchased to the EM. The maintenance costs are related to its own RESs and ESSs, whereas investment costs could also be related to investment aids provided to prosumers. An additional annual revenue is taken into account in the Cs_N 's row thanks to the industrial development. Note that this last revenue is not an hourly revenue and is consequently considered as a negative annual additional cost. Moreover, $Pr_{IEO,in}$ and $Pr_{IEO,out}$ could possibly be equal to zero.

TABLE III
DETAILS OF THE COST TERMS FOR THE AGGREGATOR

Terms	aggregator = DSO
$R_{h,N}$	$Pr_{DSO,in} + Pr_{DSO,out} + Pr_{fee,IM} + Pr_{fee,in} + Pr_{fee,out}$ + flexibility provider + fees as operator of the flexibility services
$C_{h,N}$	Flexibility user
Cm_N	Grid maintenance + ESSs maintenance
Cs_N	Grid intelligence
Ci_N	Shared ESSs + lines reinforcement + microgrid reconfiguration

TABLE IV
DETAILS OF THE COST TERMS FOR THE OTHER STAKEHOLDERS

Terms	Prosumers	IEO
$R_{h,N}$	$Pr_{sale,grid,pros} + Pr_{sale,\mu}$ + Flexibility provider	$Pr_{IEO,out}$ + Flexibility provider
$C_{h,N}$	$Pr_{purchase,grid,pros} + Pr_{purchase,\mu}$ + Flexibility user	$Pr_{IEO,in}$
Cm_N	RESs and ESSs maintenance + % aggregator's Cm_N	RESs and ESSs maintenance
Cs_N	% aggregator's Cs_N	(-%) of industrial development (=revenue)
Ci_N	RESs + ESSs + % aggregator's Ci_N	RESs + ESSs + investment aids

IV. CONCLUSION AND FUTURE WORK

This paper deals with the planning of an MV industrial microgrid connected to the general network. As many stakeholders take part into those kinds of microgrids, it seems important to consider the objectives and the welfare of each one. The presented methodology includes a microgrid manager called aggregator. The originality of this work is to put as aggregator successively each stakeholder in order to see how

the planning of the microgrid is impacted. Indeed, the choice of the aggregator will influence the decisions to be undertaken in the management process. Concerning those decisions, they are defined through an interaction model for each strategy. This paper described only the case in which the aggregator is the DSO. This interaction model summarizes the electricity exchanges, the flexibility services between the microgrid and the distribution network and details the economical record for this strategy. Thanks to this interaction model, possible decisions are defined, attached to a cost and can be compared. The computation of the Net Present Value defined in this paper for each stakeholder, including the aggregator, allows the ranking of those decisions in a preference order and a final equilibrium can be computed following the Game Theory rules. Currently, the imagined tool is deterministic but the objective of the work is to make preventive planning taking into account all the possible uncertainties as the installation of RESs within the microgrid.

ACKNOWLEDGEMENT

The authors would like to thank all the partners of this thesis. This work is realised within the University of Mons in collaboration with IDEA (inter-communal structure which is an industrial estate operator) and the Engineering and Consulting office Decube Consult.

REFERENCES

- [1] M. Liserre, T. Sauter and J. Y. Hung, *Future Energy Systems*, IEEE Industrial Electronics Magazine, March 2010.
- [2] S. Parhizi, H. Lofti, A. Khodaei and S. Bahramirad, *State of the Art in Research on Microgrids: A Review*, IEEE Access, vol 3, 2015.
- [3] B. Martin, E. De Jaeger, F. Glineur and A. Latiers, *A dynamic programming approach to multi-period planning of isolated microgrids*, In proc. IESO International Symposium on Energy System Optimization, 2016.
- [4] Federation of Belgian industrial energy consumers, *Less taxes on electricity for industrial consumers in our neighbouring countries*, Press release, April 2016, <http://www.febeliec.be>
- [5] C. Stevanoni, *Study of interest for the shared storage of photovoltaic electrical energy in an industrial estate (French)*, Internal report, University of Mons, Faculty of Engineering, Power Electrical Department, 2015.
- [6] M.H. Moradi, M. Eskandari and S.M. Hosseini, *Optimal Strategy Optimization in an Optimal Sized Smart Microgrid*, IEEE Trans. on smart grid, vol. 6, no. 3, May 2015.
- [7] H. Dutrieux, *Multi-year planning methods of the distribution networks. Application to the technical-economic analysis for the integration solutions of the intermittent renewables energies (French)*, PhD Thesis, Ecole centrale de Lille, 2015.
- [8] L.F. Ochoa, A. Padilha-Feltrin and G. P. Harrison, *Evaluating Distributed Generation Impacts with a Multiobjective Index*, IEEE Trans. on Power Delivery, vol. 21, no. 3, July 2006.
- [9] S. Wang, Z. Li, L. Wu, M. Shahidehpour and Z. Li, *New Metrics for Assessing the Reliability and Economics of Microgrids in Distribution System*, IEEE Trans. on Power Systems, vol. 28, no. 3, August 2013.
- [10] Martin J. Osborne, *An Introduction to Game Theory*, Departments of Economics, University of Toronto, Oxford University Press, 2003.
- [11] S. Mathieu, *Flexibility services in the electrical system*, PhD Thesis, University of Liege, 2015.
- [12] European Distribution System Operators for Smart Grids, *Flexibility: the role of DSOs in tomorrow's electricity market*, 2014, <http://www.edsoforsmartgrids.eu/wp-content/uploads/public/EDSO-views-on-Flexibility-FINAL-May-5th-2014.pdf>

Linear Representation of Preventive and Corrective Actions in OPF Models

T. Van Acker, and D. Van Hertem

Research Division ELECTA, Department of Electrical Engineering (ESAT), KU Leuven

Leuven, Belgium

tom.vanacker@esat.kuleuven.be

Abstract—Several preventive and corrective actions are available to the system operator enabling reliability management within a power system. The objective of reliability management is trying to exploit a power system with a minimal socio-economic cost while taking into account the possibility of a contingency on one or multiple elements (e.g. branch, generator) and changing operating conditions. The operating cost is minimized by optimally choosing between all available preventive and corrective actions, most commonly facilitated by an optimal power flow algorithm. This paper presents an overview of the most relevant actions for AC power systems and how to efficiently implement them in an OPF environment.

I. INTRODUCTION

Power system reliability management can be defined as a sequence of decisions which are taken under uncertainty in order to meet a certain reliability criterion. A reliability criterion is a principle imposing a basis to determine whether or not the reliability level of a given operating state of the power system is acceptable [1]. This can be expressed as a set of constraints that must be satisfied by the decisions taken by the system operator (SO). An example of such a reliability criterion is the N-1 criterion, which states that the considered power system must be able to withstand any credible single contingency (e.g. the loss of a generator), in such a way that a new operational set point can be reached without violating the security constraints of that power system. The SO makes use of a power systems inherent flexibility options to reach a new operation set point. These flexibility options are also referred to as actions and the distinction can be made between preventive and corrective actions. Preventive actions are those flexibility options preventively activated to adapt the system state, anticipating all possible contingencies and uncertainty the need for corrective operator intervention when a certain contingency occurs. Corrective actions are those flexibility options available to adapt the system state immediately after a contingency has occurred, sufficiently quick to avoid cascading of the event. It is the responsibility of the SO to select the actions, both preventive and corrective, that result in an optimal reliability, which ideally leads to a minimal global socio-economic cost. Most efficiently, this is done by implementing all considered actions in an Optimal Power Flow (OPF) [2], which is adapted to take the possibility of contingencies into account. This type of OPF is generally referred to as a Security Constrained OPF (SCOPF) [3]. The general formulation of a SCOPF is given by (1)-(5):

$$\min_{u_0, u_c} f(u_0, u_c) \quad (1)$$

$$\text{subject to: } G_0(x_0, u_0, y_0) = 0 \quad (2)$$

$$H_0(x_0, u_0, y_0) \geq 0 \quad (3)$$

$$G_c(x_c, u_c, y_c) = 0 \quad \forall c \quad (4)$$

$$H_c(x_c, u_c, y_c) \geq 0 \quad \forall c \quad (5)$$

In this formulation, u , x and y respectively represent the control variables, state variables and parameters. The index 0 and c indicate the preventive base case and the corrective contingent cases. Equation (2)-(3) respectively ensure that the power flow equations and the operating limits are respected for the preventive base case while (4)-(5) does this for the considered corrective contingent cases. This paper presents an overview of available actions for AC power system and the linear implementation of those actions in an SCOPF environment.

II. AVAILABLE ACTIONS IN AC POWER SYSTEMS

In this section, the most common available actions in an AC power system are listed. There are four main type of actions:

- 1) Actions that affect the power balance in the system: generator redispatch, demand side management and load curtailment [4].
- 2) Topological actions influencing power flows through the system: phase shifting transformer control [5], switching actions [6].
- 3) Reactive power and voltage management: generator voltage set point changes, on-load tap changer transformer control.
- 4) Special protection schemes: Specific actions triggered by specific grid related events.

This paper focusses on the first two types of actions.

A. Generator Redispatch

Generator redispatch uses the available upward and downward power reserves in the power system to change the power injection and consequently change the power flows within the grid [7]. Generator redispatch can be used to alleviate congestion or to compensate for a generator outage. The implementation of generator redispatch is very case specific and depends on the market structure as well as

the SO. These power reserves are stipulated in contracts or purchased on the market in a liberalized system. The SO can ask to shut down, start up or change the power output of a generator. These actions need to be financially compensated by either the SO or the generator, depending on the type of redispatch. In a vertically integrated system, these reserves are made available to the SO.

B. Load Shedding and Demand Side Management

As an alternative to generator redispatch, the demand can also be altered in order to keep the power balance within the system. Two methods exist that facilitate a change of the power demand: load shedding and demand side management [8]. Load shedding entails the unannounced interruption of supply. The cost of load shedding corresponds to the value of lost load, which is the estimated amount a customer is willing to pay to avoid a disruption in their electricity service. The value of the loss of electricity can be expressed as a customer damage function (CDF), which is a non-linear function of load type, time and duration of the interruption.

Demand side management is the modification of consumer demand in exchange for financial compensation. Demand side management allows to shift a part of a consumers energy requirements to another point in time. The cost of demand side management is directly linked to the electricity price at a specific point in time.

C. Phase Shifting Transformer

A phase shifting transformer (PST) is able to control the active power flow through a certain transmission line, thus changing the power flows throughout the entire grid.

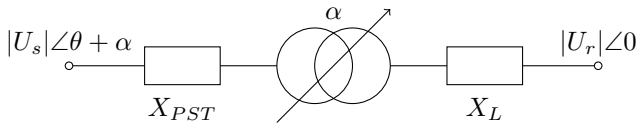


Fig. 1: Representation of transmission line with a PST

A PST can be represented as a reactance X_{PST} in series with a phase shift as depicted in Figure 1 [9]. The power flow through the line is altered by inserting an angle α which changes the phase angle over the line from δ to $\delta + \alpha$. The angle α of the phase shifting transformer is controllable within certain limits, α^{\max} and α^{\min} . A PST operated by the SO can significantly influence the power flows in the system while the cost associated with its control is very low.

D. Switching Actions

Reconfiguration of the grid topology using switching actions allows to alter the power flow in the system, alleviating possible congestion. Switching as a means of control in a power system is described in [10]. This can enable cheaper redispatch or avoid the need for load shedding when balancing the system. Several methods are available to alter the topology of a transmission system. The first method, in literature often

referred to as transmission switching, allows for the switching of the branches within a transmission grid. A second and more complete method, bus bar switching, allows to adapt the topology of a transmission grid on breaker level and thus also includes transmission switching. As switching enables a larger set of possible topology configurations, it also increases the complexity of the problem.

III. LINEAR IMPLEMENTATION OF THE ACTIONS IN AN OPF ENVIRONMENT

In this section, the linear implementation in an OPF environment of all considered actions of section II is discussed. The presented formulation generates a finite set of linear constraints which produces a search space in the form of a convex polytope, entailing a minimal computational burden. Implementation of the preventive and corrective formulation for the same action are fairly similar. In each subsection, the formulation of the preventive implementation of an action is discussed, after which the changes for the corrective implementation are highlighted. The index 0 for the preventive variables introduced in section I in (1)-(3) is omitted as it is redundant.

A. Generator Redispatch

The implementation of preventive generation redispatch within an OPF requires the addition of a cost term (6) to the objective function (1) and the addition of constraints (7) to (9).

$$\sum_g C_g^{\text{prev}} \Delta P_g^{\text{prev}} \quad (6)$$

The total preventive redispatch penalty is the sum of the cost of preventive redispatch $C_g^{\text{prev}} \Delta P_g^{\text{prev}}$ for all generators g . The cost parameter C_g^{prev} changes depending on the type of generator and on the nature of the redispatch. Piece-wise linear formulation [11] of the objective function allows to integrate such a non-constant parameter C_g^{prev} . This formulation is convex as long as the cost parameter $C_g^{\text{prev,up}}$ for upward preventive redispatch of a generator g exceeds that of downward preventive redispatch $C_g^{\text{prev,down}}$. An example of such a piece-wise linear representation of the preventive redispatch cost is depicted Figure 2.

$$P_g^{\min} \leq P_g^{\text{prev}} \leq P_g^{\max} \quad \forall g \quad (7)$$

$$\Delta P_g^{\text{prev}} = P_g^{\text{prev}} - P_g^{\text{market}} \quad \forall g \quad (8)$$

$$R_g^{\text{prev,down}} \leq \Delta P_g^{\text{prev}} \leq R_g^{\text{prev,up}} \quad \forall g \quad (9)$$

Equation (7) ensures that the technical limits of all generators g are respected. Equation (8) determines the preventive generator redispatch ΔP_g^{prev} , which is equal to the difference between the generator set point after preventive generator redispatch P_g^{prev} and the set point provided by the market P_g^{market} . Equation (9) ensures that the preventive generator redispatch ΔP_g^{prev} is within the downward $R_g^{\text{prev,down}}$ and the upwards reserves $R_g^{\text{prev,up}}$.

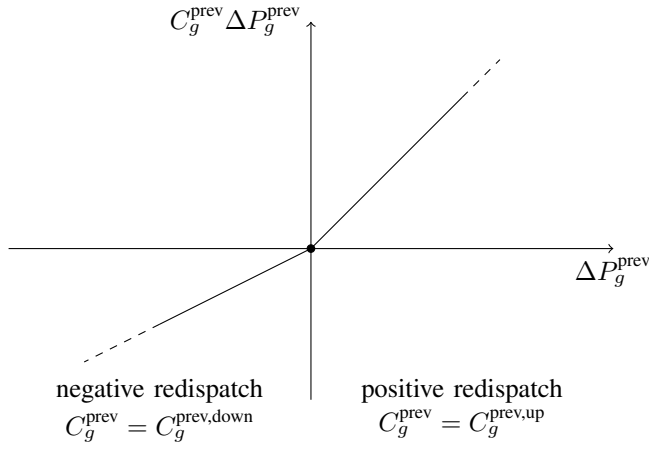


Fig. 2: Piece-wise linear representation of the preventive generator redispatch cost

The implementation of corrective generation redispatch within an OPF requires the addition of a cost (10) to the objective function (1) and the addition of constraints (11) to (13).

$$\sum_g \sum_c \lambda_c \zeta_{g,c} C_g^{\text{cor}} \Delta P_{g,c}^{\text{cor}} \quad (10)$$

The corrective redispatch cost penalty for a generator g is equal the cost of corrective redispatch $C_g^{\text{cor}} \Delta P_{g,c}^{\text{cor}}$, taking into account the probability of the occurrence of a certain contingency λ_c . If an contingency c occurs on a certain generator g , that generator needs to be excluded from the penalty. This is done by multiplying the penalty with a parameter $\zeta_{g,c}$. The constant $\zeta_{g,c}$ is equal to zero when the generator g is unavailable during a contingency c , in all other instances $\zeta_{g,c}$ is equal to one. The integration of different cost parameters for upward and downward redispatch can be done using piece-wise linear constraints, similar to preventive redispatch. The total penalty is the summation of the cost of redispatch for all generators g and contingencies c .

$$\zeta_{g,c} P_g^{\min} \leq P_{g,c}^{\text{cor}} \leq \zeta_{g,c} P_g^{\max} \quad \forall g, c \quad (11)$$

$$\Delta P_{g,c}^{\text{cor}} = P_{g,c}^{\text{cor}} - P_g^{\text{prev}} \quad \forall g, c \quad (12)$$

$$R_g^{\text{cor,down}} - M(1 - \zeta_{g,c}) \leq \Delta P_{g,c}^{\text{cor}} \leq R_g^{\text{cor,up}} \quad \forall g, c \quad (13)$$

Equation (11) makes sure that the technical limits of the generator are respected, the addition of $\zeta_{g,c}$ on both the left and the right hand side of the equation ensures that during a contingency involving the generator g , the power output $P_{g,c}^{\text{cor}}$ of the generator is zero. Equation (12) determines the corrective redispatch ΔP_g^{prev} , which is equal to the differences between the corrective and preventive generator set points. Equation (13) ensures that the corrective redispatch ΔP_g^{prev} is within the contracted downwards $R_g^{\text{cor,down}}$ and the upwards reserves $R_g^{\text{cor,up}}$, which takes the ramping rates of the generators into account. The downward redispatch limit is disabled for a contingent generator using the term $M(1 - \zeta_{g,c})$, where M is a big number [12].

B. Load Shedding

In order to implement load shedding as linear constraints, each load needs to be subdivided in smaller loads with a constant load shedding cost. The implementation of preventive load shedding within an OPF requires the addition of a cost term (14) to the objective function (1) and the addition of constraints (15) to (16).

$$\sum_l C_l^{\text{prev}} \Delta P_l^{\text{prev}} \quad (14)$$

The load shedding penalty for a load l is equal the cost of load shedding $C_l^{\text{prev}} \Delta P_l^{\text{prev}}$. The total penalty is the summation of the cost of load shedding for all loads l .

$$P_l^{\min} \leq P_l^{\text{prev}} \leq P_l^{\max} \quad \forall l \quad (15)$$

$$\Delta P_l^{\text{prev}} = P_l^{\max} - P_l^{\text{prev}} \quad \forall l \quad (16)$$

Equation (15) ensures that the active power consumed by the load l is limited between P_l^{\min} and P_l^{\max} . Equation (16) ensures that the shedded load ΔP_l^{prev} is equal to the difference between the maximum load power P_l^{\max} and the actual preventive load set point P_l^{prev} . The implementation of corrective load shedding uses a similar formulation. The penalty cost of corrective load shedding (17) needs to be calculated for each contingency c taking into account the probability of each contingency λ_c .

$$\sum_l \sum_c \lambda_c C_l^{\text{cor}} \Delta P_{l,c}^{\text{cor}} \quad (17)$$

The constraints are similar but need to be generated for all contingencies c . Constraint (16) needs to be adapted into (18) for corrective load shedding in order to reflect the difference between the preventive set point P_l^{prev} and the corrective set point $P_{l,c}^{\text{prev}}$ instead of the difference between the maximal set point and the preventive set point.

$$\Delta P_{l,c}^{\text{cor}} = P_{l,c}^{\text{prev}} - P_{l,c}^{\text{cor}} \quad \forall l, c \quad (18)$$

Demand side management can be implemented in the same way as load shedding, taking into account that both an increase as a decrease of the load power is possible.

C. Phase Shifting Transformer

A transmission line equipped with a PST can be modeled as depicted in Figure 3. The phase shifting angle α is modelled as two additional active power injections with an opposite sign on both sides of the PST, represented by the impedance X_{PST} . The addition of those power injections $P^+(\alpha)$ and $P^-(\alpha)$ alters the power flow through the transmission line. The sum of the injections of both fictive generators needs to be zero, as they do not exist in reality. Their injections must also be limited, taking into account the technical limits α^{\min} and α^{\max} of the PST.

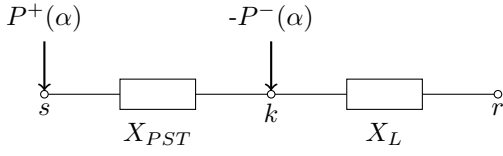


Fig. 3: Model of a PST

The implementation of a PST within an OPF requires the addition of a cost term (19) to the objective function (1) and the addition of constraints (20) to (22).

$$\sum_p C_p^{\text{prev}} \Delta P_p^{\text{prev}} \quad (19)$$

The cost penalty for a PST p is equal to the product of the cost of preventive usage of the phase shifting transformer C_p^{prev} , accounting for the wear of the transformer, and the difference of the phase shifting transformer setting ΔP_p^{prev} . The total penalty is the summation of the cost of phase shifting for all phase shifting transformers p .

$$P_p^{\text{prev},+} - P_p^{\text{prev},-} = 0 \quad \forall p \quad (20)$$

$$\Delta P_p^{\text{prev},+, \min} \leq \Delta P_p^{\text{prev},+} \leq \Delta P_p^{\text{prev},+, \max} \quad \forall p \quad (21)$$

$$|P_p^{\text{ini},+} - P_p^{\text{prev},+}| = \Delta P_p^{\text{prev}} \quad \forall p \quad (22)$$

Equation (20) ensures that the fictive power $P_p^{\text{prev},+}$ injected at node s is equal to the power $P_p^{\text{prev},-}$ extracted at node k (Fig. 3). Equation (21) limits the fictive power injection $P_p^{\text{prev},+}$, and consequently also $P_p^{\text{prev},-}$, taking into account the limits on α . Equation (22) determines ΔP_p^{prev} which is equal to the absolute difference between the initial set point $P_p^{\text{ini},+}$ and the set point $P_p^{\text{prev},+}$ of the phase shifting transformer in the preventive grid state. As it is the objective of the optimization to minimize the cost, the absolute value $|P_p^{\text{ini},+} - P_p^{\text{prev},+}|$ can be implemented in a linear way by replacing equations (21) and (22) with equations (23), (24) and (25).

$$\Delta P_p^{\text{prev}} = \Delta P_p^{\text{prev}, \text{up}} + \Delta P_p^{\text{prev}, \text{down}} \quad \forall p \quad (23)$$

$$\left. \begin{matrix} P_p^{\text{prev},+} - P_p^{\text{ini},+} \\ 0 \end{matrix} \right\} \leq \Delta P_p^{\text{prev}, \text{up}} \leq \Delta P_p^{\text{prev},+, \max} \quad \forall p \quad (24)$$

$$\left. \begin{matrix} 0 \\ P_p^{\text{ini},+} - P_p^{\text{prev},+} \end{matrix} \right\} \leq \Delta P_p^{\text{prev}, \text{down}} \leq |\Delta P_p^{\text{prev},+, \min}| \quad \forall p \quad (25)$$

Either $\Delta P_p^{\text{prev}, \text{up}}$ or $\Delta P_p^{\text{prev}, \text{down}}$ deviates from zero in case the set point of the PST is changed and represent the absolute value $|P_p^{\text{ini},+} - P_p^{\text{prev},+}|$, the other variable is then equal to zero. The implementation of corrective usage of a PST is similar to the preventive formulation. The penalty cost for corrective PST usage (26) needs to be calculated for each contingency c taking into account the probability of each contingency λ_c .

$$\sum_p \sum_c \lambda_c C_p^{\text{cor}} \Delta P_{p,c}^{\text{cor}} \quad (26)$$

The constraints are similar to the preventive formulation but need to be generated for all contingencies c . Constraint (22) needs to be adapted into (27) for the corrective usage of the PST in order to reflect the difference between the preventive set point $P_p^{\text{prev},+}$ and the corrective set point $P_{p,c}^{\text{cor},+}$ instead of the difference between the initial set point and the preventive set point.

$$|P_p^{\text{prev},+} - P_{p,c}^{\text{cor},+}| = \Delta P_{p,c}^{\text{cor}} \quad \forall p, c \quad (27)$$

D. Switching

Breakers can be modeled in an OPF as lossless elements using on/off constraints [13]. An on/off constraint is a constraint that is activated when the corresponding binary variable δ_b of the considered breaker b is equal to one. The implementation of preventive usage of a breaker within an OPF requires the addition of a cost (28) to the objective function (1) and the addition of constraints (29) to (31).

$$\sum_b C_b^{\text{prev}} \Delta \delta_b^{\text{prev}} \quad (28)$$

The penalty for operating a breaker b is equal to the product of the cost of preventive usage of the breaker C_b^{prev} , accounting for the wear of the breaker, and the change of the state of the breaker $\Delta \delta_b$. The total penalty is the summation of the cost of breaker usage for all breakers b .

$$\delta_b^{\text{prev}} P_b^{\min} \leq P_b^{\text{prev}} \leq \delta_b^{\text{prev}} P_b^{\max} \quad \forall b \quad (29)$$

$$-M(1 - \delta_b^{\text{prev}}) \leq \bar{U}_i^{\text{prev}} - \bar{U}_j^{\text{prev}} \leq M(1 - \delta_b^{\text{prev}}) \quad \forall b \quad (30)$$

$$|\delta_b^{\text{ini}} - \delta_b^{\text{prev}}| = \Delta \delta_b^{\text{prev}} \quad \forall b \quad (31)$$

Equation (29) ensures that the power flow P_b^{prev} through a breaker b is equal to zero if the breaker is open ($\delta_b^{\text{prev}} = 0$). In case the breaker is closed ($\delta_b^{\text{prev}} = 1$), equation (29) ensures that the technical limits of the breaker are respected. The actual power flow P_b^{prev} through the breaker is determined by the power balance equations included in the standard OPF formulation. Equation (30) sets the voltage \bar{U} of both end nodes of the breaker equal to each other when the breaker b is closed. A linear implementation of this constraints requires generating this constraint for both the voltage magnitude $|U|$ and the voltage angle θ . In case the breaker is open, equation (30) ensures that the voltages are independent from each other. Equation (31) determines $\Delta \delta_b^{\text{prev}}$ which is the absolute difference between the status of the breakers for their initial state δ_b^{ini} and their preventive state δ_b^{prev} . The absolute value in Equation (31) can be linearized using the same technique as described for the phase shifting transformers.

The implementation of corrective usage of a breaker is similar to the preventive formulation. The penalty cost for breaker usage (32) needs to be calculated for each contingency c taking into account the probability of each contingency λ_c .

$$\sum_b \sum_c \lambda_c C_b^{\text{cor}} \Delta \delta_{b,c}^{\text{cor}} \quad (32)$$

The constraints are similar as well but need to be generated for all contingencies c . Constraint (31) becomes (33) for the corrective usage of the breakers in order to reflect the difference between the preventive set point δ_b^{prev} and the corrective set point $\delta_{b,c}^{\text{cor}}$ instead of the difference between the initial set point and the preventive set point.

$$|\delta_b^{\text{prev}} - \delta_{b,c}^{\text{cor}}| = \Delta\delta_{b,c}^{\text{cor}} \quad \forall b, c \quad (33)$$

IV. CASE STUDY OF PREVENTIVE AND CORRECTIVE ACTIONS

In order to test the different preventive and corrective actions, they are implemented in a DC SCOPF and tested on the Roy Billinton Test System (RBTS), depicted in Figure 4. The RBTS consists of five substations and a load (Table II) is connected to each substation, except for substation S1. The RBTS is interconnected by seven transmission lines (Table III). Eleven generators (Table IV) are located in the grid, of which four are connected to substation S1 and seven to substation S2.

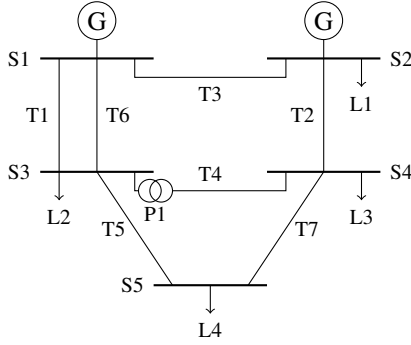


Fig. 4: Roy Billinton Test System

In this section, three case studies are conducted. Each case study is a one-hour Day Ahead Congestion Forecast (DACF) where all possible N-1 contingencies are considered. In order to keep the results clear, it is assumed that the load demand and renewable generation during the considered hour remain constant. During each case study, the SO has different preventive and corrective actions at his disposal. The available actions during each case study are depicted in Table I.

TABLE I: Available actions for each case study

	Preventive Actions			Corrective Actions			
	Redisp.	PST	Switch.	Redisp.	Shed.	PST	Switch.
1	✓	—	—	✓	✓	—	—
2	✓	—	—	✓	✓	✓	—
3	✓	—	✓	✓	✓	—	✓

The preliminary set points of all generators (P_g^{market}) are submitted to the SO. Based on that data, a DACF analysis is conducted by the SO in order to determine the preventive and corrective actions it has to take in order to have a stable system at all times. During this analysis, the considered contingencies are the failure of exactly one element (e.g. generator or

transmission line) with the probability of failure λ_c denoted in their respective tables.

TABLE II: Load Data

Load	Sub.	P_l^{min} [MW]	P_l^{max} [MW]	C_l^{cor} [€/MWh]
L1	S2	10	20	10206
L2	S3	75	85	10206
L3	S4	30	40	10206
L4	S5	10	20	10206

TABLE III: Transmission Line Data

Line	Length [km]	Admittance [p.u.]	P_l^{max} [MW]	λ_c [-]
T1, T6	48	5.555	85	0.001713
T2	160	1.666	50	0.005710
T3	128	2.083	50	0.004568
T4, T5, T7	32	8.333	71	0.001142

A. Case Study 1: Generator Redispatch and Load Shedding

In the first case study, preventive generation redispatch, corrective generation redispatch and corrective load shedding are the only available actions. The preventive redispatch allows to adapt the generation set point compared to those set by the market P_g^{market} . As preventive generation redispatch comes at a cost, it is only activated if the market set points cause congestion in the system or if preventive redispatch is cheaper than corrective redispatch taking into account the probability of the contingencies. The market set points P_g^{market} provided in Table IV cause congestion on the transmission lines T2 and T3 as a result of an excessive generation output on substation S2. Preventive generation redispatch alleviates this congestion by reducing the generation of generator G5 and G10 of substation S2 and increasing the generation of generators G1 and G2 of substation S1.

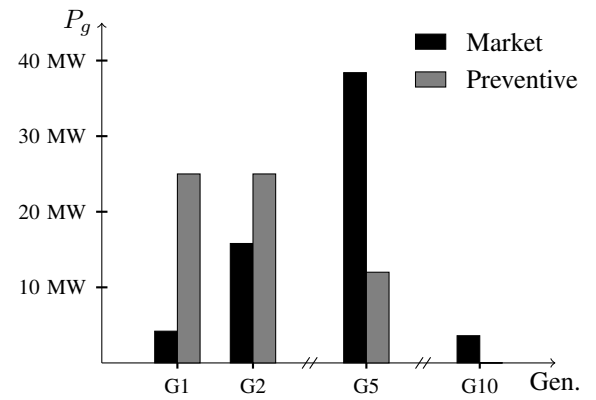


Fig. 5: Case Study 1: Preventive generator redispatch

An unbalance in the generation and load due to a contingency, because of the failure of a generator or because of congestion caused by an outage of a transmission line, can only be corrected by corrective generation redispatch or by shedding load in the first case study. The corrective generation

TABLE IV: Generator Data

Gen.	Sub.	P_g^{\max} [MW]	P_g^{market} [MW]	λ_c [-]	Preventive Generator Data				Corrective Generator Data			
					$C_g^{\text{pre,down}}$ [€/MWh]	$C_g^{\text{pre,up}}$ [€/MWh]	$R_g^{\text{pre,down}}$ [MW]	$R_g^{\text{pre,up}}$ [MW]	$C_g^{\text{cor,down}}$ [€/MWh]	$C_g^{\text{cor,up}}$ [€/MWh]	$R_g^{\text{cor,down}}$ [MW]	$R_g^{\text{cor,up}}$ [MW]
G1	S1	40	4.2	0.015	4.45	12.05	-40	40	44.5	120.5	0	10
G2	S1	40	15.8	0.015	4.35	12.05	-40	40	43.5	120.5	-10	10
G3	S1	10	8.7	0.015	—	—	0	0	-3000.0	—	-10	0
G4	S1	20	16.3	0.015	—	—	0	0	-3000.0	—	-20	0
G5	S2	40	38.4	0.005	5.00	14.00	-40	40	50.0	140.0	-10	10
G6	S2	20	19.7	0.005	4.30	11.90	-20	20	43.0	119.0	-20	0
G7	S2	20	19.2	0.005	—	—	0	0	-3000.0	—	-20	0
G8	S2	20	19.8	0.005	—	—	0	0	-3000.0	—	-20	0
G9	S2	20	19.3	0.005	—	—	0	0	-3000.0	—	-20	0
G10	S2	5	3.6	0.005	5.45	15.35	-5	5	54.5	153.5	0	5
G11	S2	5	0	0.005	4.40	12.20	-5	5	44.0	122.0	0	5

redispatch and shedded load is depicted in Figure 6 for contingencies C1 to C18.

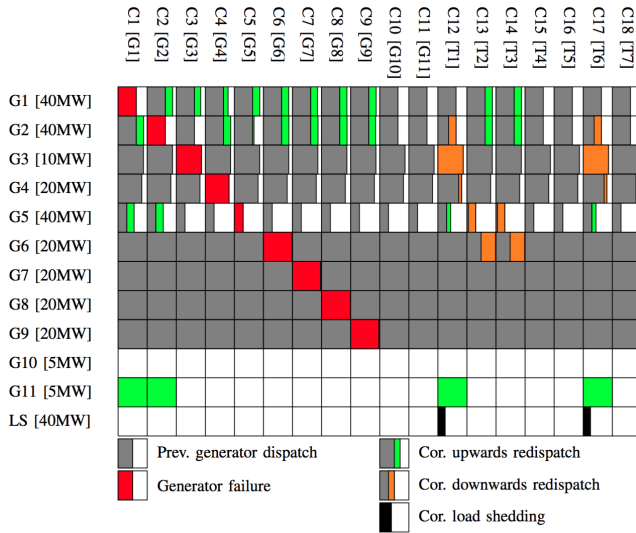


Fig. 6: Case Study 1: Corrective generator redispatch. Each square of the first eleven rows depicts the corrective generator set point $P_{g,c}^{\text{cor}}$ relative to the maximal set point P_g^{\max} of that generator for each contingency. The corrective generator set point consist of the preventive generator set point P_g^{prev} , depicted in gray, adjusted with possible upwards or downwards corrective generation redispatch, respectively depicted in green and orange. Each square in the last row depicts the part of the total shedable load that is shedded during a contingency.

B. Case Study 2: Generator Redispatch, Load Shedding and PST

The implementation of a PST can help to alleviate congestion during certain contingencies and consequently enable cheaper generation redispatch. Case study 2 introduces a PST P1 to transmission line T4 (Figure 4). For the purpose of this case study, the angle limits are set to ± 0.4 (rad). The usage of the PST causes wear of the transformer tap changer and consequently comes at a cost. The cost of using the PST is set equal to 400 €/ (rad). The implementation of the

PST P1 enables cheaper generator redispatch options during contingencies C12 and C17 (Figure 7).

Contingencies C12 and C17 exclude either transmission line T1 or T6, which are equivalent, resulting in the same grid state. This causes congestion on both T6/T1 and T2. The total power that can be transported by T6/T1 (85 MW) and T2 (50 MW) is 135 MW, which is insufficient to supply the loads connected to substations S3, S4 and S5 with a total demand of 145 MW. In order to correct this unbalance, 10 MW of load L2 is shed. To supply the remaining load, the flow through the grid needs to be adapted. In case study 1, this is accomplished by downwards redispatch of the generators G2, G3 and G4 of substation S1 and upwards generator redispatch of G5 and G11 of substation S2. The downwards redispatch of G3 and G4 comes at a high cost as these are renewable generators and their downwards redispatch cost significantly exceeds that of a conventional generator.

$$\begin{aligned} \Delta P_{L2,C12}^{\text{cor}} + \Delta P_{G5,C12}^{\text{cor,up}} + \Delta P_{G11,C12}^{\text{cor,up}} \\ = \\ \Delta P_{G2,C12}^{\text{cor,down}} + \Delta P_{G3,C12}^{\text{cor,down}} + \Delta P_{G4,C12}^{\text{cor,down}} \end{aligned}$$

The redispatch can be avoided by adapting the power flow in the power system using a PST. In case study 2, the set point of the PST for contingencies C12 and C17 is adapted to change the power flow through T4 changes from 0 to 21 MW. This influences the power flow in the system in such a way that the power flow through T3 is reduced to 20 MW compared to 30 MW in the case without a PST, negating the need for redispatch between generators of substations S1 and S2. Load shedding of 10 MW (L2) still takes place as the lines T6/T1 and T2 are incapable of supplying the entire load of substation S3, S4 and S5. The corresponding downward redispatch is provided by generator G2 of substation S1.

$$\Delta P_{L2,C12}^{\text{cor}} = \Delta P_{G2,C12}^{\text{cor,down}}$$

C. Case Study 3: Generator Redispatch, Load Shedding and Switching

An alternative approach to adapting the power flow in a transmission system is changing its topology. The case study

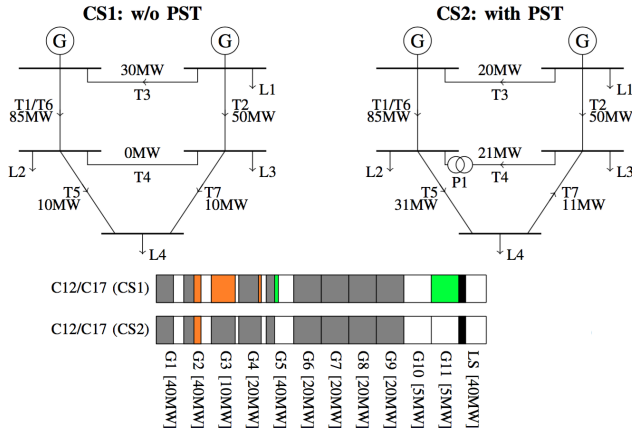


Fig. 7: Case study 2: The difference in corrective generation redispatch and load shedding between CS1 without PST in the grid and CS2 with a PST connected to transmission line T4 for contingencies C12 (T1) and C17 (T7).

3 introduces transmission line switching which allows to eliminate transmission lines by opening their breakers. This causes wear of the breakers and consequently comes at a cost. For the purpose of this case study, the cost of breaker operation is set at 400€. Elimination of transmission lines T4 and T5 influences the power flow in the system in such a way that the power flow through T3 is reduced to 10 MW (Fig. 8). This allows the negative redispatch needed to compensate for the load shedding of 10 MW (L4) to be done by generator G5.

$$\Delta P_{L4,C12}^{cor} = \Delta P_{G5,C12}^{cor,down}$$

A note must be made on the fact that these switching actions reduce the RBTS system to a radial system, which in reality is not an acceptable strategy.

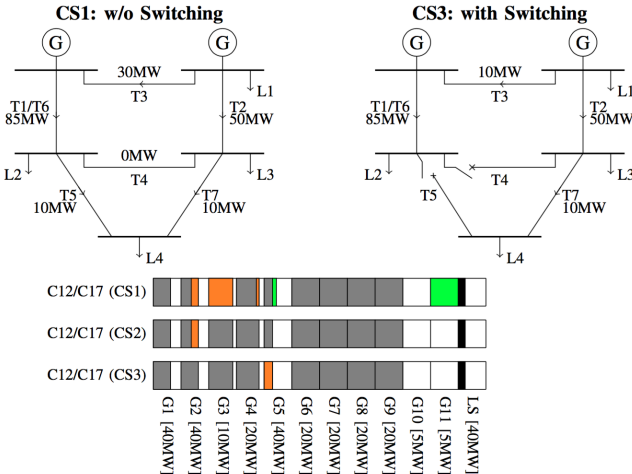


Fig. 8: Case study 3: The difference in corrective generation redispatch and load shedding between CS1 without transmission line switching in the grid and CS3 with transmission line switching for contingencies C12 (T1) and C17 (T7).

V. CONCLUSION

This paper has presented the preventive and corrective actions as well as a linear implementation for generator redispatch, load shedding, demand side management, PST control and switching operations in a SCOPF. The effectiveness of these actions is demonstrated in a test case. Even in a small test network, it can be seen that considering all possible actions can result in reduced need for generator redispatch.

ACKNOWLEDGEMENT

The ELECTA research group is a founding member of EnergyVille.

REFERENCES

- [1] P. Kundur, J. Paserba, V. Ajjarapu, G. Andersson, A. Bose, T. Van Cutsem, C. Canizares, N. Hatziargyriou, D. Hill, V. Vittal, A. Stankovic, and C. Taylor, "Definition and Classification of Power System Stability IEEE/CIGRE Joint Task Force on Stability Terms and Definitions," *IEEE Transactions on Power Systems*, vol. 19, no. 3, pp. 1387–1401, 2004.
- [2] A. J. Wood and B. F. Wollenberg, *Power Generation, Operation and Control, 2nd Edition*. Wiley, 1996.
- [3] F. Capitanescu, J. L. Martinez Ramos, P. Panciatici, D. Kirschen, A. Marano Marcolini, L. Platbrood, and L. Wehenkel, "State-of-the-art, challenges, and future trends in security constrained optimal power flow," *Electric Power Systems Research*, vol. 81, no. 8, pp. 1731–1741, 2011.
- [4] R. D. Christie, B. F. Wollenberg, and I. Wangenstein, "Transmission management in the deregulated environment," *Proceedings of the IEEE*, vol. 88, no. 2, pp. 170–195, 2000.
- [5] Z. X. Han, "Phase shifter and power flow control," *IEEE Transactions on Power Apparatus and Systems*, vol. PAS-101, no. 10, pp. 3790–3795, 1982.
- [6] K. W. Hedman, S. Member, R. P. O. Neill, E. B. Fisher, and S. S. Oren, "With Contingency Analysis," vol. 24, no. 3, pp. 1577–1586, 2009.
- [7] K. Van den Bergh, D. Couckuyt, E. Delarue, and W. D'haeseleer, "Redispatching in an interconnected electricity system with high renewables penetration," *Electric Power Systems Research*, vol. 127, no. January, pp. 64–72, 2015.
- [8] A. Capozza, C. D'Adamo, G. Mauri, and A. Pievatolo, "Load shedding and demand side management enhancements to improve the security of a national electrical system," *2005 IEEE Russia Power Tech, PowerTech*, pp. 1–7, 2005.
- [9] J. Verboomen, D. Van Hertem, P. Schavemaker, W. Kling, and R. Belmans, "Phase shifting transformers: principles and applications," *2005 International Conference on Future Power Systems*, no. February 2016, pp. 6 pp.–6, 2005.
- [10] H. Glavitsch, "Switching as means of control in the power system," *International Journal of Electrical Power & Energy Systems*, vol. 7, no. 2, pp. 92–100, 1985.
- [11] C. B. Somuah and N. Khunaizi, "Application of linear programming redispatch technique to dynamic generation allocation," *IEEE Transactions on Power Systems*, vol. 5, no. 1, pp. 20–26, 1990.
- [12] T. Ding, R. Bo, W. Gu, and H. Sun, "Big-M based MIQP method for economic dispatch with disjoint prohibited zones," *IEEE Transactions on Power Systems*, vol. 29, no. 2, pp. 976–977, 2014.
- [13] C. Liu, J. Wang, and J. Ostrowski, "Static switching security in multi-period transmission switching," *IEEE Transactions on Power Systems*, vol. 27, no. 4, pp. 1850–1858, 2012.

Determining the Theoretical Maximum Capacity Gain of Refurbishing MVAC Cables as Reconfigurable DC-links

Andrew W. Burstein

Electrical Energy Systems
Eindhoven University of Technology
Eindhoven, Netherlands
a.w.burstein@tue.nl

Vladimir Čuk

Electrical Energy Systems
Eindhoven University of Technology
Eindhoven, Netherlands
V.cuk@tue.nl

Erik C.W. de Jong

DNV·GL
Arnhem, Netherlands
Erik.deJong@dnvgl.com

Abstract—By changing the function of an underground cable from transporting power in AC to DC, it is the hope of this study to determine how much capacity can be gained. This paper evaluates the theoretical limitations of switching an existing cable from AC to DC.

Keywords—reconfigurable DC-links; underground cables; MV networks; capacity gain; theoretical maximum limitations

I. INTRODUCTION

The network of today is in a state of great change, largely due to the increased demand for clean and sustainable sources of energy. This demand has led to and will likely continue to experience an increase in the connection of distributed generation (DG) and renewable energy sources (RES) (such as solar and wind) and new consumer loads (such as electric vehicles and heat pumps). This change in demand leads to new challenges in network design. Such challenges include: bidirectional power flow, fast and large load changes, voltage variations, overloading components, and other bottlenecks. These issues are found even more prevalent in the medium and low voltage networks as the amount of control decreases with voltage level.

One approach to alleviate these issues is being researched by the DNV·GL led project: *Flexible and Future Power Links for Smart Grids* (FLINK). By repurposing an existing AC cable as a flexible DC-link, these issues can be mitigated with power electronics with minimal invasiveness for installation, i.e. it can be connected in existing substations with no digging. (The basic principle of connection of the flexible DC-link can be

seen in Fig. 1.) The use of power electronics gives rise to possibilities for power (active and/or reactive) and voltage control among other mitigation mechanisms (e.g. harmonic mitigation). Furthermore, the switch to DC alone gives way to increasing the capacity of the cable. By increasing transport capacity and efficiency, the distribution network operators (DNOs) would not have to take on the expensive task of reinforcing the network via laying extra cables in parallel to alleviate bottlenecks caused by new generation and consumption.

This paper will evaluate the limitations of reusing an AC cable for DC under steady-state conditions. The first section will give a more detailed description of the FLINK project and its goals. Following that, a detailed analysis of theoretical limitations will be conducted. After the theoretical analysis, testing procedures will be described, followed by conclusions.

II. FLINK PROJECT OVERVIEW

One of the major goals of the FLINK project is to explore the possibilities of refurbishing an existing AC cable as a flexible DC-link (FDCL), thus allowing the cable to operate as either AC or DC (as seen in Fig. 1). The placement of the FDCL in the MV network is yet to be determined, however, there are a few promising possibilities depending on the results most appealing to the distribution network operators (DNOs). These locations include: the MV transmission; connection between two distribution networks' main distribution buses; and replacing normally-open points near the end of feeders.

Of these placements, when looking into the issues of capacity, DNOs involved in this project have pointed out the target areas to be within the transmission portion of the network. This area realizes the most overloading of components, and is the most often in need of reinforcement due to feeling the full extent of load growth within the distribution network. This section also has the longest cables laid (based on its function as transmission) and therefore the cost of reinforcement is steeper than for sections of the distribution network.

For the FLINK project, all areas of potential connections are considered; however, for capacity gains, the transmission portion of the MV grid is chosen as a focus for this study.

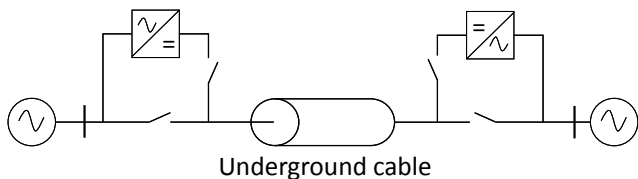


Fig. 1. One-line diagram of a reconfigurable DC-link connecting two neighboring distribution networks

This project is funded by the Rijksdienst voor Ondernemend Nederland project TKI switch2smartgrids.

The research for the FLINK project is performed by the Technical Universities of Eindhoven and Delft; coordinated by DNV·GL.

This project also benefits from a consortium of experts from SMEs: Early Minute and EMForce; and DNOs: Alliander and Stedin.

III. THEORETICAL MAXIMUM CAPACITY GAIN

In the search for capacity gain, switching from AC to DC, we are concerned with the active power capacity of the cables. This is defined for one phase as:

$$P = U_{\phi} I_{\phi} \cos \varphi \quad (1)$$

Where U_{ϕ} and I_{ϕ} are the applied phase voltage and current respectively and φ is the phase angle between the voltage and current. Already, an advantage can be seen for capacity with DC, as the power factor, $\cos \varphi$, is unity for DC.

Equation (1) also shows that in the search for capacity gain, there are only two areas (excluding power factor) which can be enhanced for greater active power transport, i.e. either voltage or current. In most cases, it is more advantageous to increase the voltage rather than the current, one major advantage is lower losses for the same transported power. Other advantages are found decreasing the thermal loading of the cable, limiting expansion and contraction of the insulation and sheath which can create gaps where partial discharges can occur.

In the following sections, ways to enhance the voltage and current limits will be overviewed. Another area that offers change of the power capacity is in the topology of the circuit.

A. Topologies

In the AC system, three conductors are used in one cable. The three phases must be in balance, i.e. equivalent magnitudes separated by 120° phase shift between phases. This allows for cancellation of the currents and no return path is required. For DC, on the other hand, there is just the positive and negative poles. To complete the circuit, either a conductive return path is required, or a return path through the ground may be used (if allowed by regulations).

To connect a DC-link, three main topologies exist: monopolar, bipolar, and homopolar (as seen in Fig. 2). The advantage of the bipolar and homopolar links is that the voltage is effectively doubled. Because of their similar outcomes, further exploration will neglect to mention the homopolar link as the results will be the same as the bipolar link in this paper.

To determine the gains from the topological changes, it is assumed that the current is limited by its thermal rating, and therefore the DC current rating will remain the same as the RMS current rating. Furthermore, it is assumed that the AC cables can withstand continuous operation at its peak phase-to-ground voltage [1],[2],[3]. These assumptions are notated here as:

$$\begin{aligned} I_{DC} &= I_{\phi} \\ U_{DC} &= \sqrt{2} U_{\phi} \end{aligned} \quad (2)$$

Where U_{ϕ} and I_{ϕ} are the RMS: phase-to-ground voltage and phase current respectively.

Assuming only one AC cable is available (three conductors), the monopolar link can create three circuits with ground return, but only one circuit if a conductive return is required. Comparing to the 3-phase active power capacity of the AC

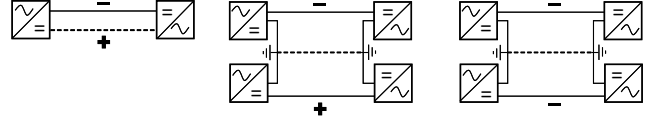


Fig. 2. DC-link topologies (from left to right): monopolar; bipolar; homopolar

network, the ground-return link can supply $\sqrt{2}/\cos \varphi$ times more active power. With the conductive return, however, this value is decreased by one-third.

With a bipolar link, there is also a requirement for a positive and negative pole (two conductors for one circuit), so it is similar to the monopolar with conductive return results, however, the voltage is effectively doubled, doubling its capacity.

If there are two (or a multiple of two) cables running in parallel (which often happens in MV transmission), then the number of circuits that can be made increases. In the case of the ground return, the number of circuits increases for DC at the same rate as for AC, so no change in the capacity ratio $P_{DC} / P_{AC,3\phi}$ occurs. However, for the conductive return monopolar and the bipolar circuits, when there are two cables, three circuits can be made in comparison to just one, tripling its capacity, whereas the capacity for AC only doubles. These results can be seen in Table I.

When these results are plotted against the displacement power factor, it is easier to see when capacity gains are achieved (Fig. 3). It is important to note, that in this figure, the monopolar curves represent the monopolar link with conductive return. The monopolar link with ground return has the same curve as the bipolar curve with two AC cables available.

In the case of the monopolar circuit with conductive return, there is only capacity gain when there are two cables available and the displacement power factor is less than 0.7 (which is an unlikely power factor to be seen in operation). The bipolar circuit, on the other hand, offers capacity gains when one cable is available when the power factor is less than 0.95 (which is often the case in operation); furthermore, when there are two cables available, it will always give capacity gains, even at unity power factor, reaching a 60% gain at $PF = 0.88$ (a likely possible power factor in operation).

TABLE I. POWER CAPACITY GAIN FOR DC-LINK TOPOLOGIES

DC Topology	$P_{DC}/P_{AC,3\phi}$	
	1 AC cable	2 AC cables
Monopolar (w/ ground return)	$\frac{\sqrt{2}}{\cos \varphi}$	$\frac{\sqrt{2}}{\cos \varphi}$
Monopolar (w/ conductive return)	$\frac{1}{3} \frac{\sqrt{2}}{\cos \varphi}$	$\frac{1}{2} \frac{\sqrt{2}}{\cos \varphi}$
Bipolar	$\frac{2}{3} \frac{\sqrt{2}}{\cos \varphi}$	$\frac{\sqrt{2}}{\cos \varphi}$

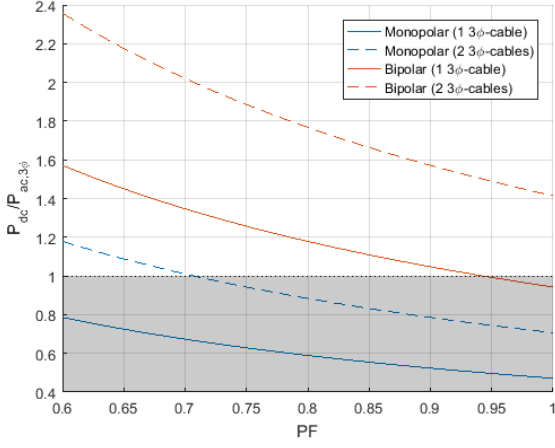


Fig. 3. Capacity gain from AC to DC depending on DC-link topology

B. Conductor Current Limit

In the last section, the assumption was made that the DC current rating would be equal to that of the RMS current rating. This was based on the fact that the current rating is determined by thermal losses of the conductor, W_c . This inherently assumes that the DC and AC conductor resistances are the same, based on the formula for thermal loss of the conductor:

$$W_c = I_\phi^2 R_c \quad (3)$$

Where R_c is the conductor resistance.

However, when operating in AC, there are a couple phenomenon that increase the effective resistance of the conductor, thus increasing the thermal losses at a lower current. These are namely: skin and proximity effect. With the absence of these phenomenon, the current can be raised to match the same thermal losses.

From the standard, IEC 60287-1-1[4], the skin and proximity effects were calculated for three-core cables.

The AC resistance is calculated as:

$$R_{AC} = R_{DC} (1 + y_s + y_p) \quad (4)$$

Where R_{AC} and R_{DC} are the effective AC and DC resistances of a conductor respectively, and y_s and y_p are the skin and proximity effect factors respectively.

To determine the increased capacity gain from the previous gain based on topology, it is assumed that the thermal losses, W_c , still remain constant as defined by (3).

Initially the DC current was assumed equal to the RMS current, i.e.:

$$I_{DC} = I_\phi = \sqrt{W_c / R_{AC}} \quad (5)$$

Now, R_{AC} can be shown to be greater than R_{DC} as determined by (4). One can define the new rated DC current as I'_{DC}

by replacing R_{AC} in (5) with R_{DC} . From the power formula for DC:

$$P_{DC} = U_{DC} I_{DC} \quad (6)$$

it can be determined that the increase of capacity from the previous topological gain to be:

$$\frac{P'_{DC}}{P_{DC}} = \sqrt{\frac{R_{AC}}{R_{DC}}} \quad (7)$$

In the MV network, the most often used cables have a cross-sectional area between 150-400 mm² with either aluminum or copper conductors. What can be seen in Fig. 4, is that for very large cables, like the ones found in HV, the skin and proximity effect greatly hinder the conductance of the conductor. For the MV level, however, the change in resistance is relatively small, with the greatest increase being for a copper 400 mm² cable. Because of the root function in (7), the capacity gain is even smaller, but does enhance the capacity by 1.05 times the capacity gain found by topology alone and initial assumptions ($P'_{DC} / P_{DC} = 1.05$) for a 400 mm² copper cable.

C. Voltage Limit

In section A of this chapter, the topological gain was determined with the assumptions of (2). In section B, the assumption of the current was challenged because of phenomenon that are present in AC but not DC conditions. This section aims to determine if the second assumption (that of voltage) holds true or also needs refining. (Note that this change could be positive or negative for capacity gain.)

Where the current is limited by the thermal losses of the conductor, the voltage is limited by the breakdown strength of the insulation. Breakdown can occur for various reasons. The main breakdown mechanisms are: intrinsic; thermal; partial discharges and treeing; electro- and thermo-chemical deterioration; and human err and unforeseen causes [5].

Except for the last of these breakdown types, they all rely heavily upon the electric stress distribution of the insulation

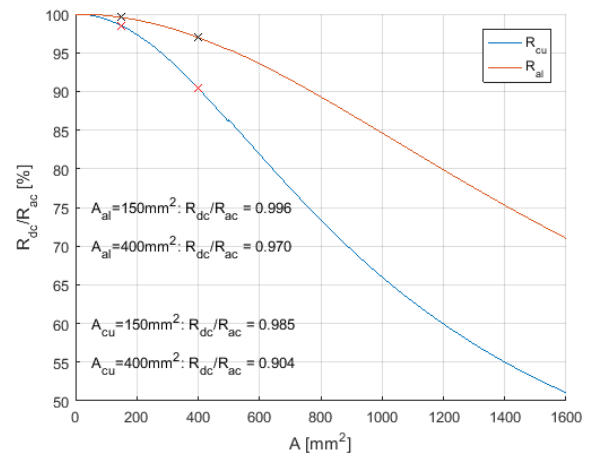


Fig. 4. Effective resistance change from AC to DC based on conductor cross-sectional area

(which is directly related to the applied voltage). Because of this, it is important to know how the electric stress distribution is affected by changing operation from AC to DC.

During AC operation, the electrical stress distribution is dependent on permittivity, ϵ_r , and the insulation conductivity, σ , is considered negligible. This is due to the charging current being far greater than the leakage current. This assumption also means that the electrical stress distribution is not affected by the temperature distribution. With these assumptions, the electrical stress distribution can be estimated with [6]:

$$E(r) = \frac{U}{r \ln\left(\frac{r_i}{r_c}\right)} \quad (8)$$

Where, $E(r)$ is the electrical field strength at position r , U is the applied voltage, and the other variables are defined by Fig. 5.

It can be seen by this formula, the maximum electrical field strength will be at $r = r_c$, and the lowest at $r = r_i$.

When calculating the same distribution for DC, the charging current (in steady-state) drops to zero, leaving the leakage current. This current is defined by the conductivity of the insulation. This makes calculation more difficult as now, more variables are involved, including temperature, and all of the variables depend on each other as such:

$$\begin{aligned} T(r, E, \sigma) \\ \sigma(r, T, E) \\ E(r, T, \sigma) \end{aligned} \quad (9)$$

And this is excluding the effect of space charge, which can either enhance or decrease the electric stress distribution depending on how charges can travel through the medium.

From [7], certain assumptions are made and an estimation of the electrical field strength can be determined with:

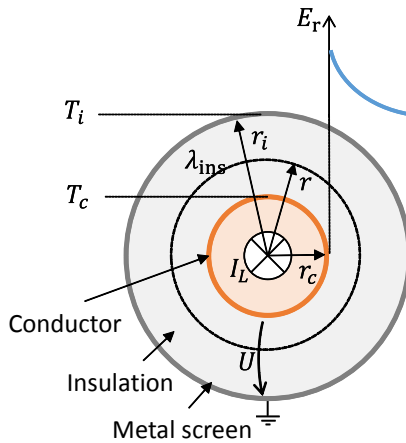


Fig. 5. Cable cross-section with variables labeled for electric stress distribution calculations

$$E(r) = \frac{dU}{dr} = \frac{\delta U \left(\frac{r}{r_i}\right)^{\delta-1}}{r_i \left[1 - \left(\frac{r_c}{r_i}\right)^{\delta}\right]} \quad (10)$$

$$\delta = \frac{\frac{\alpha \Delta T}{\ln(r_i/r_c)} + \frac{\beta U}{r_i - r_c}}{\frac{\beta U}{r_i - r_c} + 1} \quad (11)$$

Where:

$$\Delta T = T_i - T_c$$

β is the electrical stress coefficient of the insulator $[m/V]$

α is the temperature coefficient of electrical resistivity of the insulator $[(^{\circ}C)^{-1}]$

From Fourier's law, the expression in (11) can be determined based on load current with the replacement of ΔT :

$$\Delta T = \frac{I_L^2 R_c \ln(r_i/r_c)}{2\pi\lambda} \quad (12)$$

Where λ is the thermal conductivity of the insulator in $[W/(m \cdot K)]$ and R_c is the electrical resistance of the conductor in $[\Omega]$.

Equations (8) and (10) were then used to determine what happens to the electric stress distribution with different temperatures operating as DC as comparing to AC, as well as a comparison of these results for a typical HV cable vs an MV cable.

The cable parameters used from [6] can be found in Table II, and the resulting distributions in Figs. 6 and 7.

This analysis is performed for a single-core cable to show the electrical stress distribution as affected by temperature. However, for MV AC cables, generally three conductors are in

TABLE II. CABLE PARAMETERS USED FOR HV AND MV CABLES

Variable	HV Cable	MV Cable
Insulation material	PILC	
$\alpha_{ins} [(^{\circ}C)^{-1}]$	0.1	
$\beta_{ins} [m/V]$	0.03×10^{-6}	
$\lambda_{ins} [W/(m \cdot K)]$	1/6	
Conductor material	Aluminum	
$U_{nom,RMS} [kV]$	450	10
$r_c [mm]$	23.2	11.3
$r_i [mm]$	42.4	13.1
$A [mm^2]$	1690	400

one cable, this greatly changes the temperature distribution of the conductors' insulators and creates much more complex scenarios which would require a finite element model to compute. To show how the stress distribution is affected by temperature, however, this simplified model is used.

There are a couple of things to note from this analysis, the first is that as the temperature difference increases, the electrical stress distribution levels, and at a certain point flips the location of highest electrical field strength from r_c to r_i .

The second thing to note about these curves is that, because of the various differences of the HV and MV cable (namely in this case the cross sectional area and nominal voltage), the initial electrical stress distribution (that is on the AC loaded cable, or non-loaded DC cable) the MV cable has a shallower electrical stress distribution than the HV cable. That is, the difference between the electric field strength at the conductor is closer to the electrical field strength at the edge of the insulator than it is for the HV cable. What this causes is for the 'flip' in location of maximum electrical field strength to occur at a much lower temperature difference across the insulator when compared to the HV cable. However, when looking into the current ratings, it may not be much of a problem, as the MV cable is rated up to 450 A, and the flip occurs shortly after reaching 300 A. When loaded at 450 A, the maximum electrical stress (at $r = r_i$) is at 98% of the maximum electric stress found in the AC case (at $r = r_c$).

One can speculate that because the maximum stress in the DC case does not reach the maximum stress of the AC case (98%), the voltage can be rated such that the two maximum stresses are equal (raising the voltage will raise the stress curve in the positive y-direction). However, this assumes that the location of the maximum stress has no effect on breakdown strength of the insulation. So how can this location affect the breakdown strength?

One of the breakdown mechanisms listed earlier was that of partial discharges and treeing. Partial discharges occur when space charges build up across a void or defect. When the charge builds up high enough, a breakdown occurs across the defect, causing damage to the insulator. Further discharges can

then occur in the chasms created by the initial discharge, leading to treeing, which, if the breakdown channel makes its way across the full insulation, total failure of the cable will result.

In DC operation, the electric stress required for partial discharge to occur is higher than in AC, however, after the initial discharge, the breakdown path creation is much faster than in AC, and leads to failure much more quickly [8].

During operation, a cable undergoes dynamic loading. At times of high load, the cable is the most thermally stressed, which leads to the conductor, insulation, and screen expanding. However, after the load decreases, the insulating material will contract much faster than the protective screen, leaving a gap for space charges to build upon, leading to partial discharges.

Other factors that may decrease the breakdown strength when the maximum electric stress is on the outer edge, is that it is much easier for the area between the insulator and screen to become damaged than it is for the interface between the insulator and conductor. Protrusions and corrosion may occur, termites may eat away at the screen, water can enter from the surrounding soil creating water trees in the insulation, etc. [9]. By having the maximum electrical stress in this area, extra strain is placed upon defects that may have not been as affected with the no-load electric stress distribution.

In the past, the theoretical maximum voltage has been determined by the maximum thermal voltage (point of thermal breakdown) [10], [11], [12]. However, it has been speculated that, especially for AC XLPE cables, the breakdown strength, and therefore maximum applied voltage, will be determined primarily by defects and impurities which will cause cable failure well before thermal runaway would occur [8]. (XLPE is considered to be more at risk of failure through partial discharges because, unlike PILC, the insulation is not self-healing. With PILC, when a partial discharge occurs, the gap created can be filled by oil, i.e. self-healing.)

A breakdown strength governed by defects leads to difficulties in estimating an applicable maximum voltage. Cable impurities and amount of defects is not something that can be easily modelled or estimated. Especially for MV AC cables, the quality of the cables are not given in detail more than that they

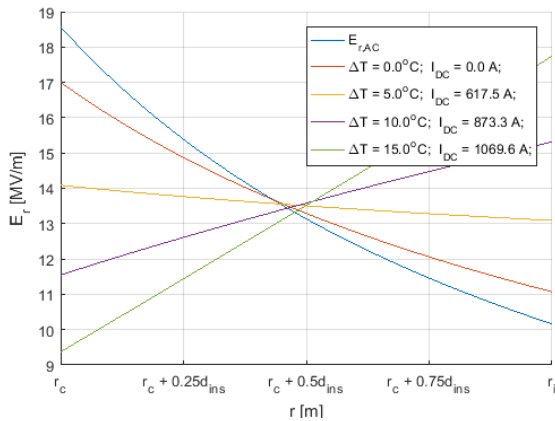


Fig. 6. Electric stress distribution of HV PILC cable with AC and DC of varying temperature differences, with $U_{DC} = U_{nom,RMS}$

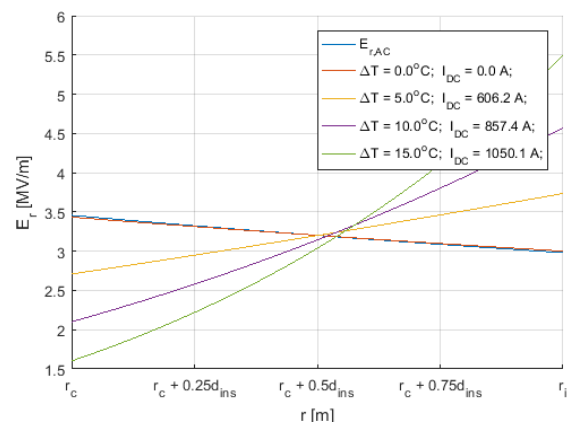


Fig. 7. Electric stress distribution of MV PILC cable with AC and DC of varying temperature differences, with $U_{DC} = U_{nom,RMS}$

have passed a minimum quality benchmark from the manufacturer. However, the level of insulation impurities can change, not per cable type, but per manufacturer, internal manufacturing processes (e.g. machines used, calibration), year of production, etc.

In order to determine the applicable voltage limit on the cables within the scope of this project, it is therefore determined that the best method is to physically test cables that are as similar to the cables currently installed and used in the networks that are chosen as targets for the FDCL implementation.

IV. FUTURE WORK

In order to assess how an installed AC cable will respond to being operated as DC, laboratory and field tests must be carried out. As discussed earlier, modelling would likely yield unrealistic results because of the number of uncontrollable factors that determine a cable's strength.

In the lab, using cables that are similar to the ones in the field, they would need to go through an advanced aging process in order to replicate the degradation that field cables had gone through over the years/decades of use. After that, a sample size will be determined to run tests repeatedly in order to gain enough data for reliable results. This is done because of the variances that can be apparent in material over different sections of insulation. However, the amount of cable that will be available in the lab will likely be far shorter than the length of the cable the FDCL will be applied to, and therefore it is likely that the results in the lab will still fare better than in the field. For this reason, careful consideration needs to be taken to perform a proper statistical analysis of the results.

Furthermore, a decision needs to be made if long-term (upwards of two years) tests will be required to accurately determine the nominal voltage that can be applied to the cable operating as DC. However, these long-term tests may not be necessary for breakdown strength predictions [6].

V. CONCLUSIONS

The power capacity gain of the network is largely dependent on the topology of the DC circuit. Namely by doubling the effective voltage using a bipolar or homopolar connection. However, there are other areas for capacity gain and other aspects to be looked into for the benefits of an FDCL.

The flipping of the point of maximum electrical field strength, is a common phenomenon found in DC cable handbooks and literature, such as [6], and the reference used here of [7] is still seen in papers today and used as a test reference to test new methods of calculating the theoretical field distribution because of its extensive work and thorough experiments [13].

What is new from the research presented here is the exploration of these stress distributions for MV applications, as before most research in DC has been for HV. What is commonly found is that certain assumptions that can be made for HV cannot be directly applied to MV applications, meaning new methods or assumptions may need to be made, and different models may need to be developed.

One of these assumptions that is common to find in papers is that of the inherent capacity gain by switching to DC based on the increased current from loss of skin and proximity effects and increased voltage due to operating at a continuous peak RMS voltage.

A great enhancement of load current capacity should not be taken as a given in all cases. In the case presented here, it is clear that there is a decrease in losses due to the absence of the skin and proximity effects, however, the lower the voltage level being discussed (i.e. the smaller the conductors) the less impact these phenomena play in capacity gains, as seen in Fig. 4 and calculated by (7).

As for the voltage assumption, in this study the voltage limit is yet undetermined, as it is believed by the authors that it cannot be well predicted through models due to its dependence on insulation impurities which vary by too many unpredictable factors. Although some experts claim that an MV AC cable can handle the peak RMS voltage continuously as a DC voltage, other experts are more hesitant to accept this assumption, especially if the cable in question is of type XLPE. It is therefore taken upon this project to test cables that are as close in state and structure to the installed cables that are likely to be used for an FDCL in a lab setting for their breakdown strengths in order to determine the applicable maximum voltage.

REFERENCES

- [1] E. W. Kimbark, *Direct Current Transmission*. John Wiley & Sons, Inc., 1971.
- [2] D. Antoniou, A. Tzimas, and S. M. Rowland, "DC utilization of existing LVAC distribution cables," in *2013 IEEE Electrical Insulation Conference, EIC 2013*, 2013, no. June, pp. 518–522.
- [3] S. Hay, C. Cleary, G. Mcfadzean, J. Mcgray, and N. Kelly, "MVDC Technology Study – Market Opportunities and Economic Impact," Feb. 2015.
- [4] "International Standard IEC 60287-1-1: Electric cables - Calculation of the current rating," 2006.
- [5] E. F. Steennis, Ed., "Ageing," in *Power Cables in General*, Arnhem: DNV KEMA Academy, 2013, p. 40.
- [6] G. F. (BICC C. L. Moore, Ed., *Electric Cables Handbook*, 3rd ed. Wiley-Blackwell, 1997.
- [7] C. K. Eöhl, "Theory of Stress Distribution in Insulation of High-Voltage DC Cables: Part I and II," *IEEE Trans. Electr. Insul.*, vol. EI-10, no. 1, pp. 27–54, 1975.
- [8] F. H. Kreuger, *Industrial High DC Voltage*. Delft: Delft University Press, 1995.
- [9] E. F. Steennis, Ed., *Power Cables in General*. Arnhem: DNV KEMA Academy, 2013.
- [10] C. C. Reddy, "Theoretical maximum limits on power-handling capacity of HVDC cables," *IEEE Trans. Power Deliv.*, vol. 24, no. 3, pp. 980–987, 2009.
- [11] J. J. O'Dwyer, "Theory of Dielectric Breakdown in Solids," *J. Electrochem. Soc.*, vol. 116, no. 2, p. 239, 1969.
- [12] S. Whitehead, *Dielectric Breakdown of Solids*. London: Oxford University Press, 1953.
- [13] C. C. Reddy and T. S. Ramu, "Estimation of thermal breakdown voltage of HVDC cables - A theoretical framework," *IEEE Trans. Dielectr. Electr. Insul.*, vol. 14, no. 2, pp. 400–408, 2007.

DC Fault Analysis in Bipolar HVDC Grids

Mian Wang*, Jef Beerten*, Dirk Van Hertem*

*KU Leuven, ESAT, div. Electa/EnergieVille, Kasteelpark Arenberg 10 - box 2445, 3001 Leuven Belgium

Email: mian.wang@esat.kuleuven.be

Abstract—Bipolar High Voltage Direct Current (HVDC) is expected to form the backbone of future HVDC grids because it offers advantages in terms of redundancy and added flexibility in developing and operating the system. This comes at the cost of introducing unbalances in the system. However, most DC fault studies until now have assumed a monopolar configuration or a balanced operation of a bipole, and thereby not addressing the challenges that comes with the operation of bipolar systems, such as the influence of unbalanced conditions and grounding relocation on the fault behavior and DC protection systems. This paper deals with DC fault analysis in bipolar HVDC grids, particularly taking those unbalances and grounding relocation into consideration. DC fault behavior under unbalanced conditions and different grounding locations is investigated via simulation studies using PSCAD/EMTDC. The influence of unbalances and groundings on the development of protection systems is evaluated.

Index Terms—Bipolar configuration, HVDC grid, DC fault, Unbalances, Grounding.

I. INTRODUCTION

Meshed HVDC Grids are seen as a viable option for the future transmission system in order to allow massive integration of often remotely-located renewable energy sources and to provide increased reliability and flexibility at a lower cost. Although multi-terminal HVDC systems in operation today are based on LCC (Line Commutated Converter) technology, it is considered that VSC (Voltage Source Converter) technology is more suitable to build meshed DC grids [1]. VSC technology provides better capabilities such as increased controllability, power reversal by changing the current direction and common voltage enabling straightforward shunt connection. Moreover recent development of the VSC technology has lead to converter losses which are comparable to those of the LCC technology. VSC-based HVDC systems are considered as a key technology for the European Supergrid, which will connect the AC grids and offshore wind farms through a HVDC grid [2]. In China, two pilot multi-terminal VSC HVDC projects have already been commissioned and are in operation [3], [4].

Existing VSC HVDC links are mainly used with symmetrical monopolar configurations. However, future HVDC grids are expected to develop into systems with a bipolar configuration. The bipolar configuration offers increased flexibility, e.g. for post-fault operation and higher extensibility in developing HVDC grids. Through unbalanced operation, a bipolar link still has half of the capacity in case of an outage of one pole. In addition, a bipolar grid can be extended with bipoles or with monopolar tapplings [5], [6]. The importance of system configuration and grounding has been acknowledged, especially in the area of system protection, since the fault currents largely

depend on the grounding [1], [5] and [6]. In recent years, more and more attention has been paid to the bipolar configuration. Nevertheless, most fault detection and protection studies have either implicitly assumed or explicitly limited to a symmetrical monopolar configuration or a balanced operation of a bipolar configuration, thereby disregarding the effect of the unbalances in bipolar grids. Up to now, the influence of the location of the grounding points on the fault behavior in bipolar systems has never been addressed. In [7] and [8], a solidly grounded bipolar configuration with sea return under balanced operation is used to analyze the fault currents, and possible fault clearing options. In [9], the specific case of a bipolar scheme with a metallic return was considered to calculate fault currents in a MTDC system for different grounding options. The impact of the HVDC topology on network faults is investigated in [10], but only balanced bipolar operation is considered. The situation is very similar in the area of HVDC grid protection studies. For example, the authors proposed a traveling-wave based protection algorithm considering a symmetrical monopolar configuration in [11]. A wavelet energy based differential protection is proposed in [12] for a bipolar system; however, the paper did not consider unbalanced operation.

At this stage, the influence of the unbalances and the grounding location in bipolar HVDC grids on fault behavior and protection systems are not fully understood. This paper especially focuses on selective primary protection algorithms such as [11], which normally use voltages and currents of the first few milliseconds to detect and identify the fault. It is essential to evaluate whether these signals are affected by the unbalances and grounding configuration or not. This paper aims at providing a first indication of the potential influence by analyzing DC fault behavior under unbalanced conditions and different grounding locations in bipolar HVDC grids. The paper is organized as follows. Section II gives brief introduction on system configurations and grounding options. In section III, the test system and case studies are presented, and in section IV the fault behaviors under different conditions are explained using travel wave theory. Section V analyzes the influence of the unbalances and groundings on the protection system. The conclusions are given in section VI.

II. CONFIGURATION AND GROUNDING OF BIPOLAR HVDC GRIDS

Future bipolar DC grids are expected to have intrinsic unbalances, which could be unbalanced power flow or unbalanced configuration due to an outage of a converter, a line or through monopolar tapplings. The influence of such unbalances on the

fault behavior has to be properly studied in order to develop robust protection systems. In addition, the grounding points in a meshed DC grid might change due to system reconfiguration and the protection system needs to be able to detect any type of fault regardless of the fault location and the distance to the grounding point. With a bipolar backbone, the DC grid can have various possible configurations [6]:

- bipolar grid with metallic return
- bipolar grid with metallic return and asymmetric monopolar tapping
- bipolar grid with metallic return and symmetric monopolar tapping
- bipolar grid with metallic return and bipolar tapping with earth return

Configuration b), in particular, is intrinsically unbalanced even during normal operation.

During normal operation, a bipolar system operates the two poles with practically the same DC voltage and current so that the neutral current remains near zero. In a point-to-point bipolar HVDC link, the healthy pole conductor can be used as the return path in case of a single pole outage. However, a low voltage dedicated conductor (metallic return) is required to operate as the return path in meshed HVDC grids. A bipolar grid can be high-impedance or low-impedance grounded. In case of high-impedance grounding, the fault currents are effectively limited at the cost of higher insulation requirements. In low-impedance grounded systems the overvoltages are limited, but the fault currents may reach very large values, which results in more stringent time constraints of the protection system. Due to the limitation of insulation materials and their costs, especially for cable systems, low-impedance or solidly grounded HVDC grid alternatives are seen as more advantageous options in the long run [1]. For the reasons described above, we focus on a solidly grounded bipolar grid with metallic return under three scenarios: balanced operation, unbalanced conditions and different grounding locations.

III. TEST SYSTEM AND CONSIDERED CASE STUDIES

A. Bipolar Test System

A three-terminal bipolar test system was built based on the HVDC grid test system provided in [13], implemented in PSCAD/EMTDC. The three-terminal bipolar test system, shown in Fig. 1, is a bipolar cable-based configuration with metallic return, with a dc voltage of ± 320 KV. For the sake of simplicity, the metallic return is dimensioned the same as the main cables. The bipolar test system is solidly grounded at converter station 3.

The capacity of the converters are reduced to 500 MVA, and the parameters of the converters are scaled accordingly. Main parameters of the DC grid and converters are shown in Table I. The bus filter reactor of 10 mH is removed to fully incorporate the dynamics of the converters, while the series inductor of 100 mH associated with the DC breakers is included in the bipolar test system since it plays an important role in selective protection [11]. The controllers of converter 1 and 2 are

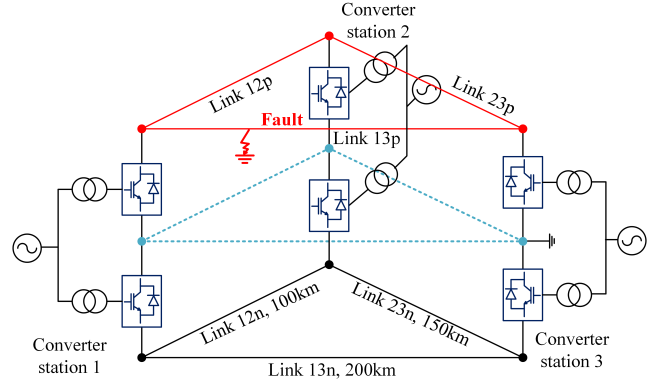


Fig. 1. Three-terminal meshed bipolar HVDC grid test system

TABLE I
CONVERTER AND GRID PARAMETERS

Converters		
Rated Power	500	[MVA]
DC Voltage	320	[kV]
AC grid voltage	400	[kV]
AC converter voltage	185	[kV]
Arm capacitance C_{arm}	65.1	[μF]
Arm inductance L_{arm}	38.2	[mH]
Arm resistance R_{arm}	0.4	[Ohm]

TABLE II
SIMULATION CASES AND CONDITIONS

Case Study		Conditions	
No.	Suffix used in figures	Power Flow (+/-: inverter/rectifier)	Grounding Location
1	B (g3)	Balanced, $P_{1p}=P_{1n}=-200$ MW, $P_{2p}=P_{2n}=-300$ MW, $P_{3p}=P_{3n}=500$ MW	station 3
2	U	Unbalanced, $P_{1p}=-500$ MW, $P_{2p}=0$ MW, $P_{3p}=500$ MW	station 3
	LO	Balanced (same as Case 1) with Link 12p open	station 3
3	g2	Balanced (same as Case 1)	station 2

set to control the DC voltage with the same power-voltage droop ratio, while converter 3 controls the active power. The only protection implemented is overcurrent protection of the converter, which will block the converters once the current exceeds the pre-defined thresholds. The aim is thus to have a first indication of the differences in fault currents when no line protection is applied.

B. Case Study

The DC fault studied in this paper is a pole-to-ground fault, considering that it is the most probable fault in a cable-based system. A solid pole-to-ground fault in the middle of the cable connecting to converter 1 and converter 3 of the positive pole (Link 13p), is inception at time 0 s in the simulation to investigate the natural fault response. Measurements are taken at both ends of the cables, where the protective relays are expected to be located. Three case studies are considered in this paper. Simulation cases and conditions are summarized

in Table II. Case 1 is a reference case, where the pre-fault condition is under balanced operation. Case 2 investigates two unbalanced conditions, unbalanced power flow and unbalanced configuration. Case 3 investigates the influence of different grounding locations.

1) *Case 1: Balanced operation:* As a reference case, the DC fault behavior under balanced operation is studied. In the pre-fault steady-state, converter station 1 and 2 export 400 MW and 600 MW respectively to converter station 3, with power evenly shared between the positive and negative poles.

Fig. 2 shows the currents and voltages at both ends of Link 13p where the pole-to-ground fault is applied and one end of the healthy cables, Link 12p and Link 23p. Currents and voltages of the negative pole and the metallic return are shown in Fig. 3. From the simulation results, the characteristics of a pole-to-ground fault in a bipolar system can be summarized as follows:

- As shown in Fig. 2 (a) and (c), currents in the faulted cable increase very fast, with a maximum derivative of 2 kA/ms. On the contrary, currents in the healthy cables of the same pole increases much slower, with maximum derivative of 1 kA/ms. The voltages of the faulted cable drop to negative values within 1 ms after fault inception as illustrated in Fig. 2 (b). The voltages change much slower in the healthy links of the same pole due to the smoothing effect of the series inductors. The differences of these currents and voltages are normally used to identify the faulted link.
- During the transient, the currents of the negative pole increased. However, they did not exceed the thresholds of the overcurrent protection of the converters. Overvoltages occurred on the negative pole, with a maximum magnitude of 1.22 pu measured at Link 12n near the terminal of converter 1, which need to be properly handled in real operation.
- Fig. 3 (b) shows that the steady-state fault current at the fault location is about -20 kA, which is contributed almost equally from both directions of Link 13p as indicated by I13p and I31p in Fig. 2 (a). Large steady-state currents also flow in the metallic returns. The negative voltages at the ungrounded sides of the metallic return reach very high values, with a maximum overvoltage of -85 kV at converter station 1.

2) *Case 2: Unbalanced conditions:* Two unbalanced conditions, unbalanced power flow and unbalanced configuration, are considered in the second case study. In the unbalanced power flow case, U (see Table II for details), the power set points of the positive converters are changed, while negative converters remain the same as in the reference balanced power flow case. In the unbalanced configuration case, LO, the cable connecting converter 1 and converter 2 of the positive pole, Link 12p is opened while keeping the power set points of all the converters the same as in the reference balanced power flow case.

Simulation results are shown in Fig. 4 and Fig. 5. The suffixes of the signals are in correspondence with the names of

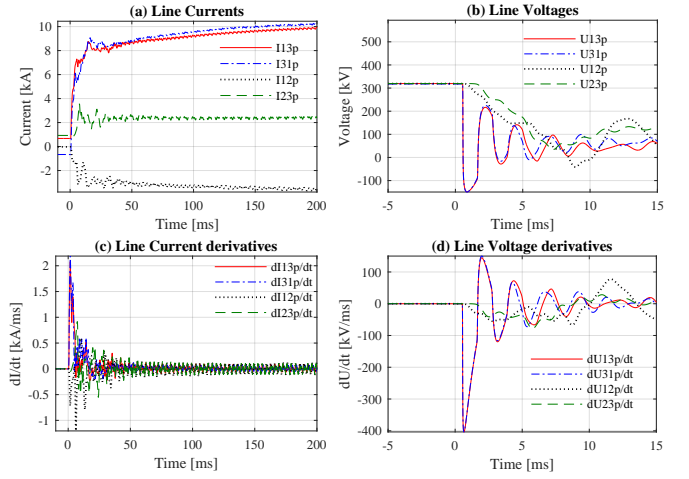


Fig. 2. Currents and voltages of the faulted pole, Case 1 Balanced operation (voltages and their derivatives are only shown up to 15 ms)

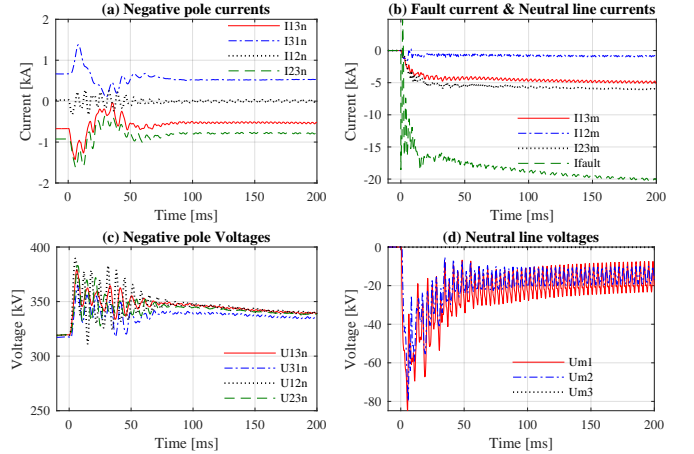


Fig. 3. Currents and voltages of the healthy pole and the metallic return, Case 1 Balanced operation

the simulation cases listed in Table II. Fig. 4 compares voltages and currents of the faulted pole under the three conditions in order to investigate the influence of the unbalances on selective primary protection algorithms. Since only the fault behavior in the first milliseconds is of interest for selective primary protection algorithms, the voltages and currents of the faulted pole are plotted up to 15 ms in Fig. 4. Fault currents at the fault location, currents and voltages of Link 13n of the healthy pole and the metallic return are shown in Fig. 5 in order to investigate the influence both on the transients and the steady-states. From the simulation results we can reach the following conclusions:

- As shown in Fig. 4 (a), in the first 2 milliseconds, the unbalanced conditions have insignificant impact on the voltages of the positive (faulted) pole. The currents of the faulted cable increase at similar rate, with more differences after 2 ms. As long as fast selective primary protection is concerned, unbalanced conditions will not

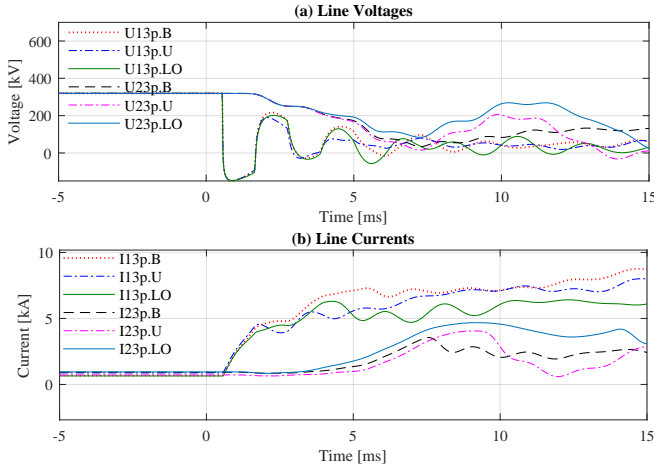


Fig. 4. Currents and voltages of the faulted pole, Case 2 Unbalanced condition (B: Balanced operation, U: Unbalanced power flow, LO: Unbalanced configuration, Link 12p open)

significantly affect the detection algorithms in systems with large series inductors. However, currents and voltages diverge as the fault develops in the grid, which imply influences on backup protection.

- As shown in Fig. 5, current variations and overvoltage levels of the negative (healthy) pole also have similar levels despite the unbalances. In addition, Fig. 5 (d) shows that the negative voltages at the ungrounded sides of the metallic return reach similar values as well.
- Balanced and unbalanced power flow (cases B and U) show same steady-state fault currents because the steady-state fault currents are determined by the grounding location and fault location. In the case with positive Link 12p open (case LO), the steady-state currents are different since routes to the grounding location differ. However, in selective primary protection systems, these steady-state differences are of little importance since it falls out of the time range of the protection system.

3) *Case 3: Different grounding locations:* In a bipolar DC grid with metallic return, the system is normally low-impedance grounded with one or multiple grounding locations. In the course of operation, the groundings of the bipolar grid might change due to possible contingencies or operational requirements. A robust protection system has to be able to detect any faults irrespective of the fault location and the distance to the grounding point. In this study, pole-to-ground faults with different grounding locations are simulated. In the case g2, the system is grounded at converter station 2 instead of converter station 3 (case g3). The fault currents and voltages are compared in Fig. 6 and Fig. 7. The following conclusions can be drawn:

- Fig. 6 shows that in the first few milliseconds after fault inception, voltages and currents of the faulted cable are almost overlapping each other regardless of the grounding locations. Similar to the unbalanced conditions study,

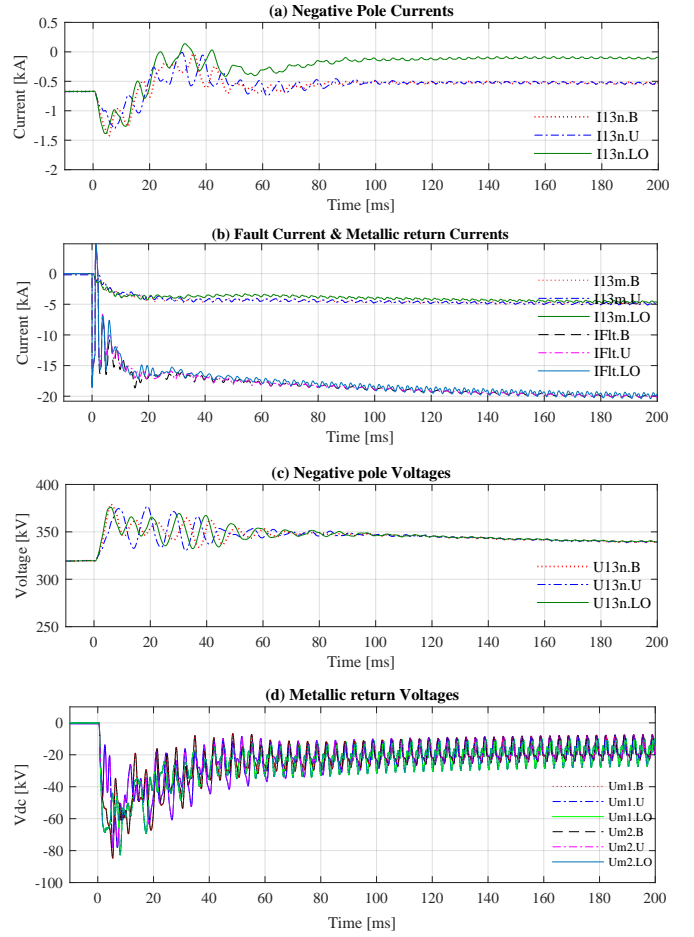


Fig. 5. Currents and voltages of the healthy pole and the metallic return, Case 2 Unbalanced condition (B: Balanced operation, U: Unbalanced power flow, LO: Unbalanced configuration, Link 12p open)

fast selective primary protection algorithms are thus not expected to be significantly influenced by different grounding locations.

- Influences on backup protection are implied since currents and voltages diverge as the fault develops in the grid.
- Current variations and overvoltages of the negative pole and the metallic return are of similar level as shown in Fig. 7. Fig. 7 (d) shows that the maximum overvoltage of the metallic return appeared at station 1 when converter station 3 (case g3) is grounded, while the maximum overvoltage appeared at station 3 when station 2 (case g2) is grounded. The steady-state currents differ as a result of the different grounding locations and the consequently different resistances of the fault paths.

IV. FAULT BEHAVIOR IN BIPOLAR SYSTEMS WITH LARGE SERIES INDUCTORS

According to the simulation studies, in the first few milliseconds after fault inception, the fault behavior in terms of voltages and currents of the faulted pole in cable-based

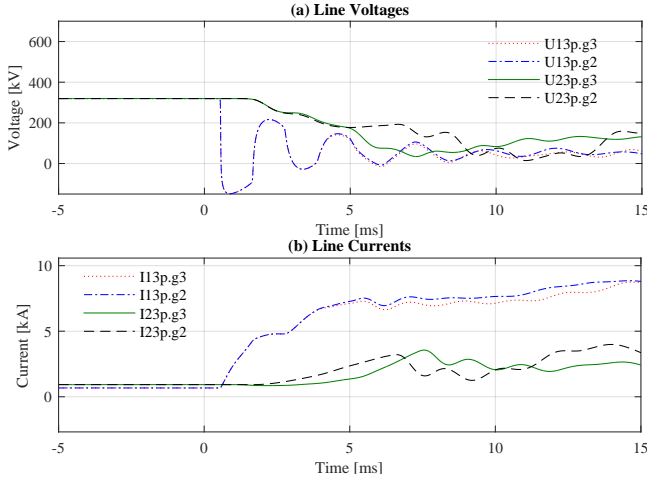


Fig. 6. Currents and voltages of the faulted pole, Case 3 Different grounding location (g3: grounded at station 3, g2: grounded at station 2)

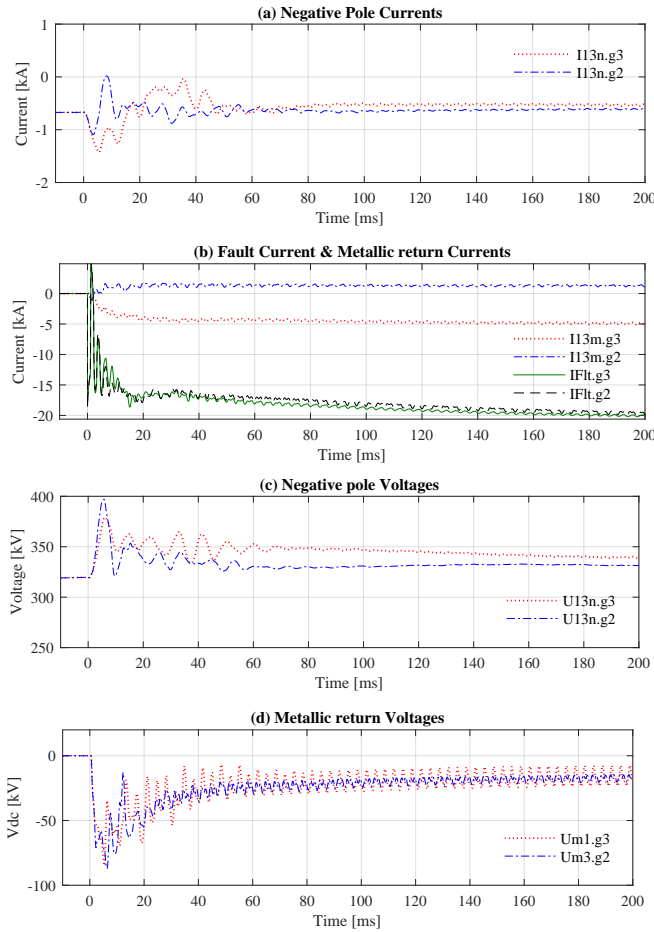


Fig. 7. Currents and voltages of the healthy pole and the metallic return, Case 3 Different grounding location (g3: grounded at station 3, g2: grounded at converter 2)

systems, is not significantly affected by unbalanced conditions and grounding locations. This behavior can be explained by

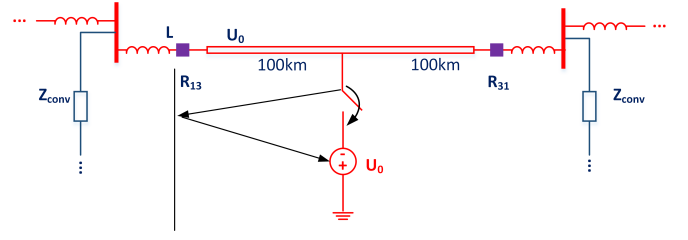


Fig. 8. Traveling wave on a faulted cable terminated with inductor

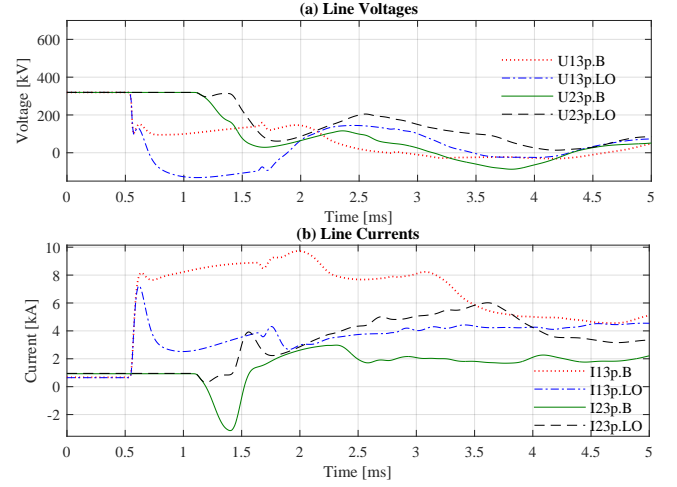


Fig. 9. Fault currents and voltages of the faulted pole, series inductor = 1 mH (B: Balanced operation, LO: Unbalanced configuration, Link 12p open)

the traveling wave theory. Fig. 8 illustrates a simplified path of a traveling wave on a faulted cable terminated with series inductor where solid pole-to-ground fault can be considered as switching in a voltage source with negative polarity at the instant of fault inception. The wave created at the fault location travels to the cable termination, where it is partly reflected back and partly transmitted to the rest of the grid. Until then, the fault waves are identical regardless of unbalances and grounding locations. In the case studies, it takes about 0.55 ms for the fault wave to reach the cable termination which is 100 km from the fault location. Most importantly, the considerably large series inductors at both terminals of the cable reflect most of the first incident wave back, hence the fault wave is largely confined within the faulted cable. As more reflections and refractions happen as the fault develops, fault waves diverge more because the fault paths are different in balanced and unbalanced conditions.

As a comparison, Fig. 9 presents simulations with series inductors of only 1 mH under unbalanced configurations. As shown in Fig. 9, significant differences in voltages and currents can be observed even in the first milliseconds.

V. INFLUENCE ON PROTECTION

If only the first voltage or/and current wave is used to detect and identify the fault in a cable-based system, which is commonly proposed in primary protection [11], [14], [15], then the sensitivity of the protection algorithms to unbalances

or grounding relocation in a bipolar DC grid is mainly determined by the series inductor. If series inductors are installed at the ends of the DC cable, it can be expected that the impact of the unbalances and grounding relocation on the protection algorithms will not be significant. This is especially true in non-unit protection methods [11], which normally involve using fast DC circuit breaker to interrupt the fault current, and the proposed DC circuit breaker are equipped with series inductors to limit the rise rate of the fault current [16], [17]. Therefore, protection concepts which adopt non-unit protection methods can be expected to be relatively insensitive against unbalances and grounding relocation. On the contrary, protection concepts which do not include series inductors or use fault voltage and/or current waves in longer time range will be affected by the unbalances and grounding relocation to a certain extent. In these cases, more detailed simulation studies are required in order to establish robust and selective relay settings.

Since the operation time range of backup protection falls into the region where faults behave differently under unbalanced conditions or grounding relocation [15], [18], detailed parametric studies are needed when developing backup protections for bipolar grids. In addition, failure mode of protection equipment might also change the fault behavior and play an important role in backup protection.

VI. CONCLUSION

This paper analyzed DC fault behavior under unbalanced conditions and different grounding locations in a three-terminal bipolar test system. If series inductors are placed at both ends of the cables, fault behavior in the first milliseconds is not significantly influenced by unbalanced conditions or grounding relocation since the inductors reflect most of the fault waves. The voltages and currents diverge more as fault develops in the grid regardless of the presence of series inductors.

As for the impact on the protection system, as far as the selective primary protection is concerned, the presence of series inductors and time range of signals used for identification are the most determining factors. If large series inductors are placed at the ends of the DC cable, the selective primary protection algorithms are not likely to be affected by the unbalances and grounding relocation. However, the influence on the backup protection systems is implied since the operation time range of the backup protection falls into the region where faults behave differently under unbalanced conditions or different grounding locations.

ACKNOWLEDGMENT

The work of Jef Beerten is funded by a research grant of the Research Foundation-Flanders (FWO).

REFERENCES

- [1] Cigré Working Group B4.52, "HVDC Grid Feasibility Study," *Cigré, Technical Brochure*, Apr. 2013.
- [2] D. Van Hertem and M. Ghandhari, "Multi-terminal VSC HVDC for the European supergrid: Obstacles," *Renewable and Sustainable Energy Reviews*, vol.14, no.9, pp.3156–3163, Dec. 2010.
- [3] X. Li, Z. Yuan, J. Fu, Y. Wang, T. Liu, and Z. Zhu, "Nanao multi-terminal VSC-HVDC project for integrating large-scale wind generation," *Proc. IEEE PES GM 2014*, Washington DC, USA, 27-31 July 2014, 5 pages.
- [4] G. Tang, Z. He, H. Pang, X. Huang, and X. Zhang, "Basic topology and key devices of the five-terminal DC grid," in *CSEE Journal of Power and Energy Systems*, vol.1, no.2, pp.22-35, June 2015.
- [5] S. De Boeck, P. Tielens, W. Leterme, and D. Van Hertem, "Configurations and earthing of HVDC grids," in *Proc. IEEE PES GM 2013*, Vancouver, Canada, 21-25 July 2013, 5 pages.
- [6] W. Leterme, P. Tielens, S. De Boeck, and D. Van Hertem, "Overview of grounding and configuration options for meshed HVDC grids," *IEEE Trans. Power Del.*, vol. 29, no. 6, pp. 2467–2475, Dec. 2014.
- [7] M. K. Bucher, M. M. Walter, M. Pfeiffer, and C. M. Franck, "Options for ground fault clearance in HVDC offshore networks," in *Proc. IEEE ECCE 2012*, Raleigh, NC, USA, 15-20 Sept. 2012, 8 pages.
- [8] M. K. Bucher, R. Wiget, G. Andersson, and C. M. Franck, "Multiterminal HVDC Networks: What is the preferred topology," *IEEE Trans. Power Del.*, vol. 29, no. 1, pp. 406–413, Feb. 2014.
- [9] E. Berne, G. Bergna, P. Egrot, and Q. Wolff, "Earth currents in HVDC grids: An example based on 5 terminal bipolar configurations," in *Proc. EPE'14-ECCE Europe*, Lappeenranta, Finland, 26-28 Aug. 2014, 10 pages.
- [10] E. Kontos, R. T. Pinto, S. Rodrigues, and P. Bauer, "Impact of HVDC Transmission System Topology on Multiterminal DC Network Faults," *IEEE Transactions on Power Delivery*, vol. 30, no. 2, pp. 844–852, Apr. 2015.
- [11] W. Leterme, J. Beerten, and D. Van Hertem, "Non-unit protection of HVDC grids with inductive dc cable termination," *IEEE Transactions on Power Delivery*, to be published.
- [12] A. E. Abu-Elanien, A. A. Elserougi, A. S. Abdel-Khalik, A. M. Massoud, and S. Ahmed, "A Differential Protection Technique for Multi-Terminal HVDC," *Electric Power Systems Research*, vol. 130, pp. 78–88, Jan. 2016.
- [13] W. Leterme, N. Ahmed, J. Beerten, L. Ängquist, D. Van Hertem, and S. Norrga, "A new HVDC grid test system for HVDC grid dynamics and protection studies in EMT-type software," *Proc. IET ACDC 2015*, Birmingham, UK, 10-12 Feb. 2015, 7 pages.
- [14] K. De Kerf, K. Srivastava, M. Reza, D. Bekaert, S. Cole, D. Van Hertem, and R. Belmans, "Wavelet-based protection strategy for DC faults in multi-terminal VSC HVDC systems," *IET Gener. Transm. Distrib.*, vol. 5, no. 4, p. 496–503, Apr. 2011.
- [15] J. Descoux, "Protection contre les courts-circuits des réseaux à courant continu de forte puissance," Ph.D. dissertation, Université de Grenoble, Grenoble, France, Sept. 2013.
- [16] J. Häfner and B. Jacobson, "Proactive hybrid hvdc breakers: A key innovation for reliable HVDC grids," in *Cigré Bologna Symp.*, Bologna, Italy, 13–15 Sep 2011, 8 pages.
- [17] K. Tahata, S. El Oukaili, K. Kamei, D. Yoshida, Y. Kono, R. Yamamoto, and H. Ito, "HVDC circuit breakers for HVDC grid applications," in *Proc. IET ACDC 2015*, Feb. 2015, 9 pages.
- [18] W. Leterme, S. P. Azad, and D. Van Hertem, "Fast breaker failure backup protection for HVDC grids," in *Proc. IPST 2015*, Cavtat, Croatia, 15-18 June 2015, 6 pages.

The Half-Bridge SiC-MOSFET Switching Cell

Implementation in a Three-phase Induction Motor Drive

F. Başkurt
Protonic Holland BV.
Hoorn, the Netherlands
furkan@protonic.nl

dr. K. Boynov and prof. dr. E. Lomonova
Electromechanics and Power Electronics Group
Eindhoven University of Technology
Eindhoven, the Netherlands
k.o.boynov@tue.nl and e.lomonova@tue.nl

Abstract—In this paper, the concept of the Half-Bridge SiC-MOSFET Switching Cell (HB-SC), and its design and test procedures are explained. The HB-SC serves as the basic switching element of scalable power electronic converter. The HB-SC combines the power semiconductor switch, optimized power layout, gate driver, and management circuitry (measurement, protection, and interface blocks).

Keywords—SiC-MOSFET; integrated switch; half-bridge inverter leg; power layout for high switching speed applications; three-phase inverter

I. INTRODUCTION

Electrical machines and variable frequency drives (electric drive systems) are widely used in the industry and they occupy a big and constantly growing market [1,2]. Due to the improvements in renewable energy systems and automotive industry, application areas and power levels of electric drive systems are even increasing [3,4]. In addition, integration of drive systems brings efficiency requirement regulations both for electrical machines and variable frequency drives [5].

The mentioned aspects lead to increasing of the importance of testing environments for electromechanical systems. Because several different types of electrical machines exist and they require different control approaches, the electric drive systems differ for each electrical machine type as well. The commercially available test benches usually have interfaces dedicated to fixed types of electrical machines, and they have restrictions on applicable control algorithms and switching frequencies [6,7].

The PDEng project “*Rapid Prototyping and Testing Environment for Electromechanical Systems*” is conducted to satisfy the need for a test environment with high flexibility concerning the types of the powered machines as well as the control hardware and software. The main focus of the project is designing, manufacturing, and testing of a generic power electronic drive that can be used for a broad range of electrical machines and power electronic systems while reducing the effort required for system reconfiguration. In [8], the topology and semiconductor switch studies resulted that the use of half-bridge SiC-MOSFET inverter legs provide the highest flexibility and scalability in the proposed generic power electronics drive.

In this work, first, the concept of the Half-Bridge Switching Cell (HB-SC) is explained, its internal structure is given, and possible application areas are mentioned. Second, the design steps for the HB-SC are explained, which includes the selection of SiC-MOSFET power switch, design of power circuitry layout, and design of management circuitry. Last, the assembly of the designed HB-SC is shown and three cells are connected in parallel to construct a three-phase inverter to drive an induction motor. Relevant parameters regarding the power layout and measurement circuitry are measured and presented.

II. HALF-BRIDGE SWITCHING CELL CONCEPT

The main purpose of the “*Rapid Prototyping and Testing Environment for Electromechanical Systems*” project was creating a flexible and scalable power electronic drive that can power different types of electrical machines (induction machine and switched-reluctance motor), while requiring low effort for reconfiguration. Besides that, this generic power electronic drive could be used to implement complex control algorithms. The use of half-bridge inverter leg modules provides the highest flexibility in aspect of topology requirements and repairability of the power electronic drive [8]. Table I gives the required specifications for the generic power electronic drive.

TABLE I
GENERIC POWER ELECTRONICS DRIVE REQUIREMENTS

Parameter	Explanation	Value
V_{DC}	DC bus voltage	up to 800V
I_{max}	Maximum phase current	100A
P_{max}	Maximum output power	30kW
f_{sw}	Switching frequency	8kHz – 50kHz

The given specifications lead to use of two possible semiconductor switches: (1) Si-IGBTs and (2) SiC-MOSFETs. Si-IGBTs are widely accepted in high power industrial systems due to their proved reliability, low conduction losses, and low costs. However, their maximum switching frequency is a limiting factor on the flexibility. The intention of complex control algorithms requires switching frequencies up to 50kHz. For this reason, SiC-MOSFETs provide a better solution than Si-IGBTs. Their ratings can reach up to 1.7kV and 300A, while allowing switching frequencies more than 50kHz.

The following solution is, a half-bridge SiC-MOSFET inverter leg that is equipped with its power layout, gate driver, and management circuitry. This integrated power switching unit is called Half-Bridge SiC-MOSFET Switching Cell (HB-SC) and it forms the basic scalable switching element for high power and high speed power electronic applications.

Following facilities are provided by the HB-SC (Fig. 1.):

- a low-inductive power circuitry including the PCB layout, half-bridge SiC-MOSFET, DC link capacitors, and power connectors,
- a low-noise management circuitry including gate drive & interface, measurement, protection, and power management parts,
- galvanic-isolation between the power and management circuitries.

The HB-SC provides an integrated and scalable power electronic solution for various power electronic converters. There are commercially available integrated switching systems in the market [9]. However, these integrated systems are mainly aiming three-phase electric drive applications and have restrictions on control algorithms. The key improvement of the HB-SC is to provide more flexibility respect to the present switching systems.

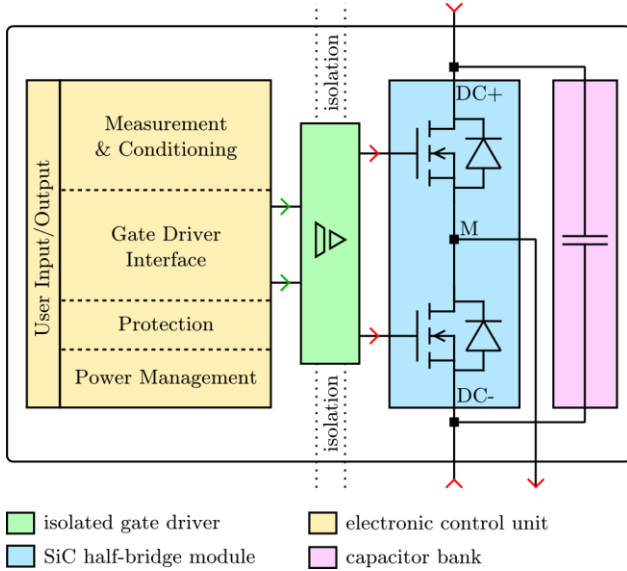


Fig. 1. Internal structure of the Half-Bridge Switching Cell.

III. DESIGN STEPS OF THE HALF-BRIDGE SWITCHING CELL

In this chapter, the design steps of the HB-SC and the decisions given are explained in detail. First, two commercially available SiC-MOSFETs are compared based on their switching performances and one of them is chosen for the final design. Second, the power layout design is explained and last, the management circuitry is presented.

A. SiC-MOSFET Switch Selection

Two SiC-MOSFETs from two different manufacturers are compared based on their switching performances: (1) *CREE CAS120M12BM2* (2) *ROHM BSM120D12P2C005*. Both of the SiC-MOSFETs are rated at 1200V and 120A. The comparison is conducted based on the Double Pulse Test (DPT), which is a widely accepted technique to evaluate the switching performance of the semiconductor switches. In DPT, the device under test is subject to a hard switching under test voltage and test current, and the turn-on and turn-off losses are measured during the switching transitions.

The circuit schematic of the DPT is shown in Fig. 2, where the test voltage is set by the DC supply voltage and the inductor is used to build-up the switch current linearly, until the test current is reached. The gate signal, and the resulting switch voltage and current waveforms of the semiconductor switch are shown in Fig. 3.

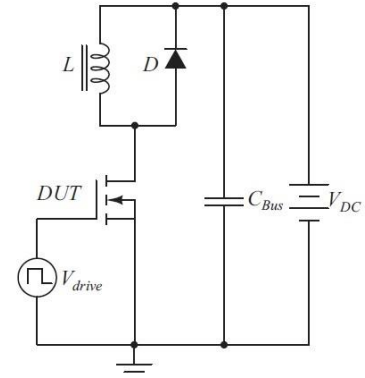


Fig. 2. Double Pulse Test schematic [10].

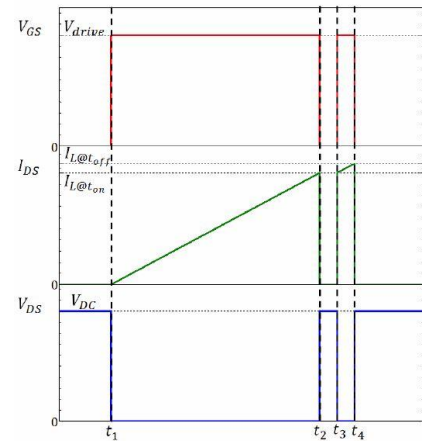


Fig. 3. Double Pulse Test waveforms: gate signal (top), switch current (middle), and switch voltage (bottom) [10].

The test starts when there is no current flowing through the switch. At instant t_1 , the switch is turned on until the switch current reaches test current at t_2 . Then the switch is turned off and the inductor current freewheels through the diode D . The switch is turned on again at t_3 , shortly after t_2 . Since the turn-off and turn-on losses are observable at instants t_2 and t_3 , test period is terminated at t_4 , shortly after t_3 . This test period is repeated once per second in order to avoid heating of the switch.

A DPT setup was created for both of the SiC-MOSFETs and they were tested under 800V test voltage and different test currents. The switching losses were obtained for every condition and the comparison is shown in Fig. 4. In all of the test conditions, *CREE* module resulted around 10% more total switching losses in comparison to *ROHM* module.

Another important aspect is the oscillations during the switching instants. As shown in Fig. 5, oscillations of the current waveform during turn-off were measured two times higher in amplitude for *ROHM* in comparison to *CREE*. Additionally, the turn-off oscillation duration was also observed longer for *ROHM*. This difference was caused by the module layout differences.

Besides the test results, the tested modules have differences in practical aspects as well. One of the differences is that *ROHM* module is 50% more expensive than *CREE* module. The second difference is, a dedicated gate driver is commercially available for *CREE* module. Taking the test results and practical aspects into account, *CREE* module is chosen as the semiconductor switch for the HB-SC.

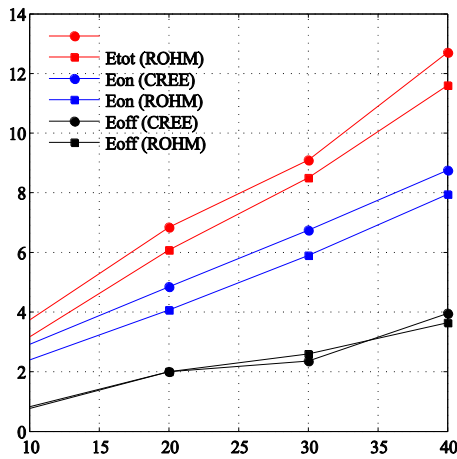


Fig. 4. Comparison of the switching losses of the tested SiC-MOSFETs: total switching losses (top two), turn-on losses (middle two), and turn-off losses (bottom two).

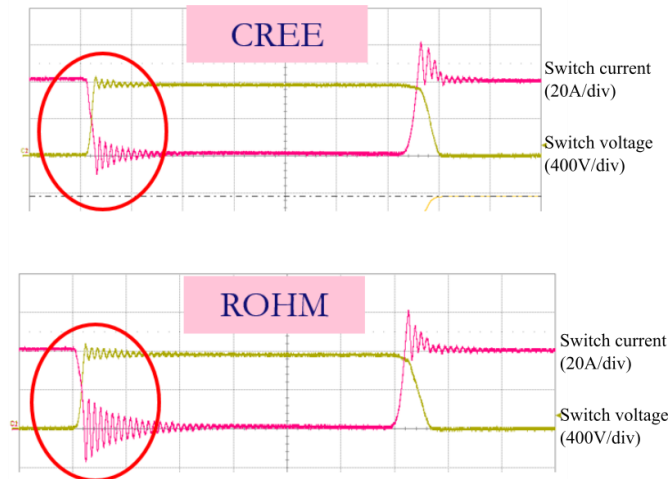


Fig. 5. Switching transition comparison of the tested SiC-MOSFETs.

B. Power Layout Design

The HB-SC utilizes SiC-MOSFETs, which is capable of switching at high speeds under high voltage and current ratings. This requires an extra attention to the parasitic elements, specifically stray inductances and capacitances what is typically incurred for Si-IGBT modules [11]. The HB-SC printed circuit board (PCB) layout should provide a low inductive power plane in order to minimize the consequences of the parasitic elements. This can be achieved by careful consideration of power plane design and good selection of the DC link capacitors.

The following aspects are taken into account during the PCB design;

- PCB involves both high and low power circuitries. Number of layers is important in aspect of current density for high power circuitry, and in aspects of noise and magnetic compatibility for low power circuitry. A 4-layer PCB design is chosen in order to increase the current carrying capacity, obtain low inductive power traces, and reduce the stray capacitances. Taking these aspects into account, three different PCB sections are defined with different layer stack-up planning (Fig. 6).
- The PCB layout for the HB-SC is designed to demonstrate proper insulation up to 1000V. The required clearance and creepage values are calculated referring to IEC 60950 [12].

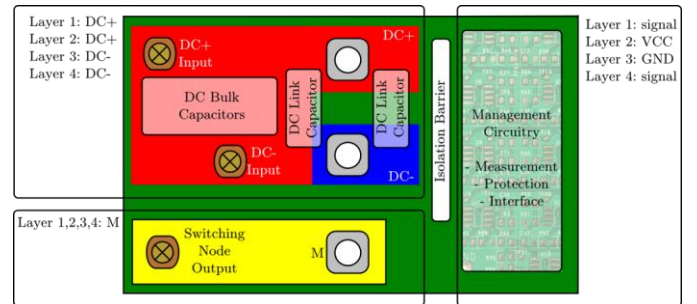


Fig. 6. Printed Circuit Board layout and stack-up planning for HB-SC.

A low inductive power plane is highly crucial for high speed and high power applications. Minimizing the inductance is best achieved by canceling out stray magnetic fields as much as possible [13]. Therefore, power planes for DC+ and DC- are placed on the top left side of the PCB, providing the shortest current path for the SiC-MOSFET (Fig. 6).

Besides that, the selection of the DC link capacitors is also a factor for decreasing the inductance of the power plane. Polypropylene film capacitors are the best candidates for DC link capacitors with their low parasitic inductive structure. To minimize the equivalent series inductance value, three film capacitors (2.2nF, 100nF, and 3μF) are connected in parallel and located directly on top of the SiC-MOSFET pins. The lowest value capacitor shows fastest response to the current transient, therefore it is located as close as possible to the switch pins.

Last, relatively slow changes in the supply voltage are smoothened with the use of DC bulk capacitors. Aluminum electrolytic capacitors offer a good solution for this purpose by

their high capacitance/size ratio. Two parallel branches of two series aluminum electrolytic capacitors are used to decrease the equivalent series resistance. Due to series connection, balancing resistors are used to equalize the voltages on the capacitors.

C. Management Circuitry Design

The *Management Circuitry* of the HB-SC includes four different blocks: (1) measurement & conditioning, (2) protection, (3) gate driver interface, and (4) power management. These blocks and their relations with the power circuitry are shown in Fig.7.

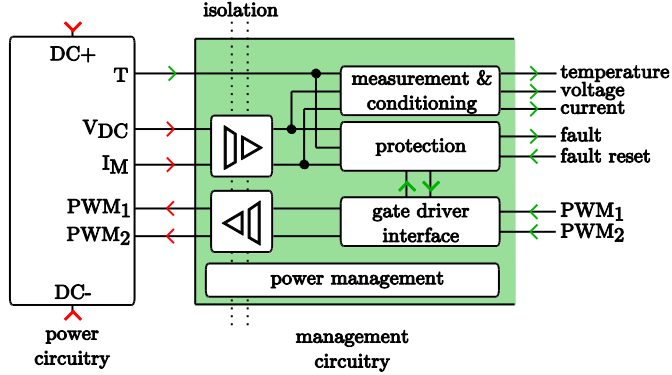


Fig. 7. Internal structure and blocks of the management circuitry.

1) *Measurement and conditioning block*: This block provides the following measurement information isolated from the power circuitry:

a) *DC bus voltage measurement*: The HB-SC senses the DC bus voltage by a resistor divider network on the power circuitry side and transfers the signal to the management circuitry through an isolation amplifier. After that, it conditions the signal and provides it with a gain of 3.3mV/V. Input to output delay of the voltage measurement is around 3.3μs.

b) *Switching node current (phase current) measurement*: The HB-SC equips a magneto-resistive current sensor to sense the switching node current and provides it to the management circuitry through galvanic isolation. After conditioning and filtering, the current sensor output signal is provided with a gain of 90mV/A. High bandwidth (400kHz) and low input to output delay (0.5μs) make this current sensor suitable for complex control algorithms, which requires fast and accurate current measurement.

c) *Temperature measurement*: The temperature of the SiC-MOSFET module is measured by an integrated-circuit CMOS temperature sensor with a gain of -8,2mV/C.

2) *Protection block*: Because SiC-MOSFETs are fast switching devices and not robust as Si-IGBTs, the protection of the SiC-MOSFETs gains importance. Therefore, the reliability of the system can be ensured with a fast and accurately reacting protection approach. For this purpose, the protection block is constructed with fast logic circuits. The following conditions define the thresholds for faults:

- Over-voltage fault : 900V
- Over-current fault : 70A

- Over-temperature fault : 90°C
- Gate-driver fault : shoot-through, missing signal

In case of one of these faults, the protection block takes the following actions: (1) generating a “fault” signal, (2) informing other HB-SCs and the controller/user, (3) disabling all PWM signals, and (4) keeping the fault state until it is reset.

3) *Gate driver and interface block*: Gate drivers are used to isolate and amplify the gating signals between the signal circuitry and gate pins. Besides that, they provide protection against over-current and shoot-through faults. The PT62SCMD12 gate driver is used in this work because of its compatibility with the chosen SiC-MOSFET module. The HB-SC modules accept single-ended PWM signals from the control platform, while the chosen gate driver accepts differential input signals. Besides that, the gate driver does not provide an enable/disable circuitry for the gate signals. Therefore, an interface circuitry block is added between the PWM input and gate driver input. This block is responsible for converting the single-ended PWM signals to differential voltage levels and disabling the PWM signals during a faulty condition.



Fig. 8. Gate driver (PT62SCMD12) and the chosen SiC-MOSFET (CASI20M12BM2).

4) *Power management block*: The management circuitry consists of sensors, operational amplifiers, logic circuits, and gate driver. These blocks require different voltage and power levels. Additionally, an isolated voltage is required for DC bus voltage measurement. In HB-SC, management circuitry is powered with 24V and other circuitries are powered through 24V to 5V (nonisolated) and 5V to 5V (isolated) power supplies.

IV. IMPLEMENTATION OF THE HALF-BRIDGE SWITCHING CELL IN A THREE-PHASE INDUCTION MOTOR DRIVE

Following the design rules and decisions in Chapter III, the HB-SC printed circuit board layout is designed and assembled as shown in Fig. 9 and 10. The numbered areas in Fig. 9 indicates the following functions:

- Area 1 includes the input power connections, DC bulk capacitors, and balancing resistors. As seen in Fig. 9, the power planes are designed as wide as possible to decrease the parasitic inductance of the power traces. DC bulk capacitors are located at the bottom side of the PCB.

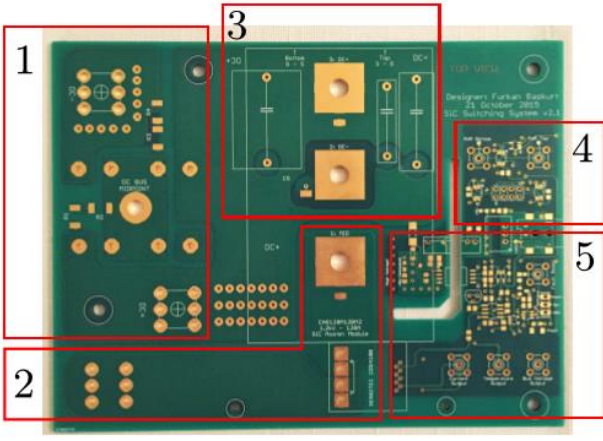


Fig. 9. The designed Printed Circuit Board of the HB-SC.



Fig. 10. Assembled HB-SC (without the gate driver).

- Area 2 includes the switching node of the SiC-MOSFET module and the output connector of the HB-SC.
- The DC link capacitors and gate-driver connections are located in area 3. Capacitors are placed directly on the top of the SiC-MOSFET to provide a low-inductive current path.
- The high-frequency part of the management circuitry occupies area 4. This area includes the PWM signals and gate-driver interface circuitry.
- Area 5, includes low-noise part of the management circuitry.

The HB-SC is implemented in a three-phase induction motor drive. For this purpose, three HB-SCs are connected in parallel and a test setup is constructed. The block diagram of the test and the experimental test setup are shown in Fig. 11 and 12.

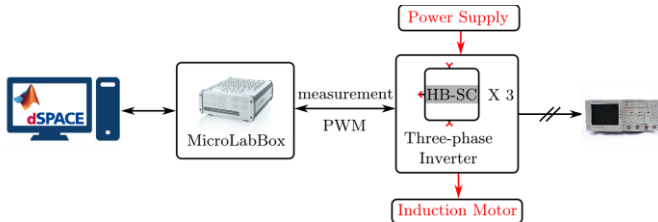


Fig. 11. Block diagram of the test setup.

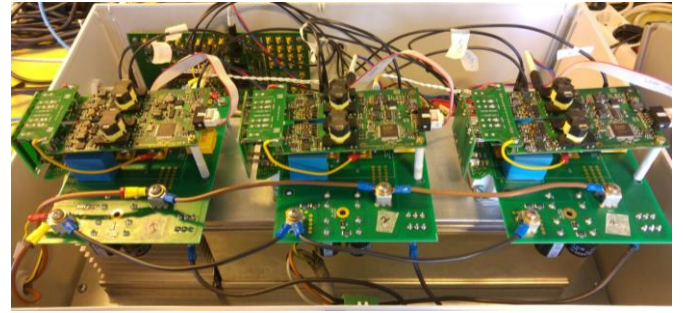


Fig. 12. Three-phase inverter circuit consisting of three HB-SCs in parallel.

First, the induction motor is operated around 2.5kW under two different DC bus voltages: (1) 440V and (2) 700V. During this test, one SiC-MOSFET's drain-source voltage and the switching node current from the same module are measured. As shown in Figs. 13 and 14, the drain-source voltages do not have over-shoot during turn-off transition for both of the conditions. This shows that the power plane design and choice of DC link capacitors ensure a low inductive path for the switches. In Fig. 14, the current ripple is more than the one in Fig. 13. This difference comes from the different dV/dt and changing MOSFET output capacitor values under different DC bus voltages.

Second, a phase current is measured with a current probe and it is compared with the HB-SC current sensor output. As shown in Fig. 15, the HB-SC current sensor output is identical to the current probe measurement in terms of amplitude and it includes only 0.5μs phase shift. This verification indicates that the HB-SC current sensor output provides a fast and accurate current measurement for using in the control algorithms.

Third, the DC bus voltage is measured with a voltage probe and with the voltage sensor of the HB-SC, during a power-up and power-down cycle of the main power supply. The comparison of the two measurements are given in Fig. 16. As shown in the figure, both of the measurements are almost identical. Although the HB-SC voltage sensor output has 3.3μs delay, the delay becomes unimportant when it is considered that a fast voltage measurement is not crucial for the drive applications.

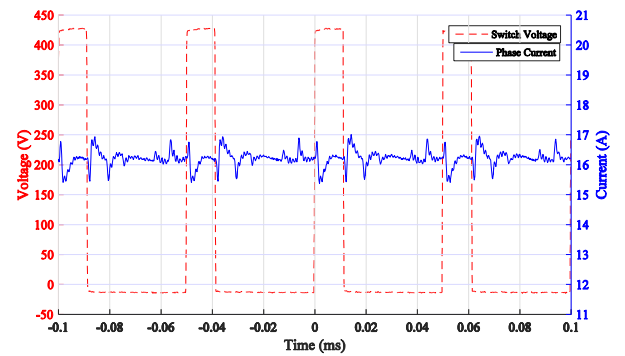


Fig. 13. Drain-source voltage of an upper SiC-MOSFET and the switching node current of the same module under 440V DC bus voltage.

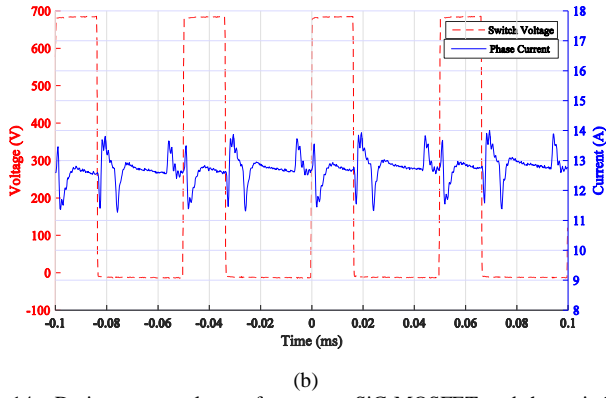


Fig. 14. Drain-source voltage of an upper SiC-MOSFET and the switching node current of the same module under 700V DC bus voltage.

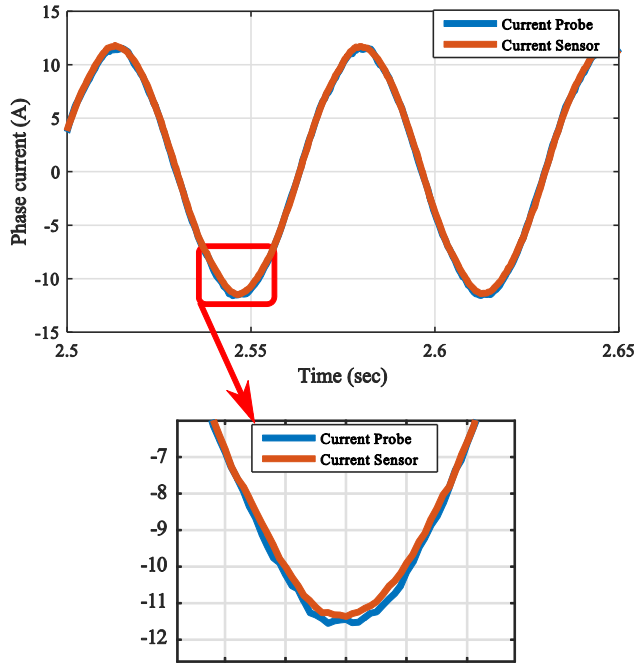


Fig. 15. Comparison of the switching node current measurements between the current probe and the HB-SC current sensor output.

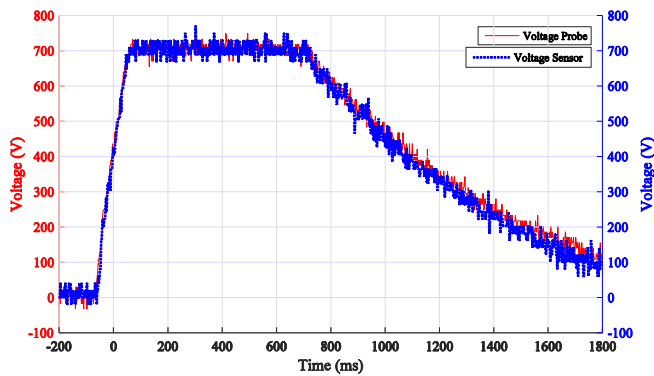


Fig. 16. Comparison of the DC bus voltage measurements between the voltage probe and the HB-SC voltage sensor output.

V. CONCLUSION

In order to create a flexible and scalable generic power electronic drive, half-bridge inverter legs are chosen as power semiconductor candidates. The specifications of the power electronic drive proposes the use of SiC-MOSFETs due to their low losses in high power and high switching frequency applications.

During the implementation of the HB-SC in a three-phase induction motor drive, the switching transition of the SiC-MOSFET demonstrated almost zero voltage overshoot under 440V/16A and 700V/13A switching conditions. This is a result of low-inductive power plane design and it ensures the safe operation of the SiC-MOSFETs in high power high switching frequency applications.

Besides the power switching function, current and voltage measurement facilities of the Half-Bridge Switching Cell are also verified. Current and voltage sensor output signals are consistent with the probe measurements, demonstrating 0.5 μ s delay for the current and 3.3 μ s delay for the voltage measurement. The accuracy and speed of the measurement facilities enable the use of measurements in complex control algorithms. With these features and further improvements on the Half-Bridge Switching Cell design (heatsink, integrated gate driver) will even decrease the reconfiguration effort for high power and high switching frequency applications.

VI. ACKNOWLEDGEMENT

The authors are grateful to Protonic Holland BV. for supporting of the PDEng project “*Rapid Prototyping and Testing Environment for Electromechanical Systems*”, conducted at Eindhoven University of Technology, in the group of Electromechanics and Power Electronics.

VII. REFERENCES

- [1] Unknown, “Electric motor market analysis and segment forecasts to 2022,” Grand View Research, 2015. [Online]. Available: <http://www.grandviewresearch.com/industry-analysis/electric-motor-market>
- [2] Unknown, “Variable frequency drives market by type, power range, voltage, application and geography - global market trends & forecast to 2019,” Markets and Markets, 2014. [Online]. Available: <http://www.marketsandmarkets.com/PressReleases/variable-frequency-drive.asp>
- [3] G. A. Capolino and A. Cavagnino, “New trends in electrical machines technology – part I,” IEEE Transactions on Industrial Electronics, vol. 61, no. 8, pp. 4281-4285, August 2014.
- [4] G. A. Capolino and A. Cavagnino, “New trends in electrical machines technology – part II,” IEEE Transactions on Industrial Electronics, vol. 61, no. 9, pp. 4931-4936, September 2014.
- [5] Unknown, “Electric motors and variable speed drives - standards and legal requirements for the energy efficiency of low-voltage three-phase motors,” ZVEI - Zentralverband Elektrotechnik- und Elektronikindustrie, 2010. [Online]. Available: <http://www.zvei.org/Publicationen/ZVEI%20Electric%20Motors%20and%20Variable%20Speed%20Drives%202nd%20Edition.pdf>
- [6] Triphase, “Triphase PM90P30M60 power modules,” Triphase, 2016. [Online]. Available: <https://triphase.com/products/power-modules/PM90/P30M60/>
- [7] Vogelsang & Benning, “Motor test systems VB-ASB for laboratory and workshop applications,” Vogelsang & Benning, 2016. [Online].

Available: <http://www.vogelsangbenning.de/wp-content/uploads/VB-englisch-Pbl-ASB.pdf>

- [8] F. Başkurt, "Rapid prototyping and testing environment for electromechanical systems – A unified drive system with SiC-Mosfets," PDEng final report, Dept. Elec. Eng., Eindhoven Univ. Tech., Eindhoven, the Netherlands, 2016.
- [9] Semikron, "Semikron SKAI 2HV Flyer," Semikron, 2014. [Online]. Available: <http://www.semikron.com/dl/service-support/downloads/download/semikron-flyer-skai-lv-2014-04-08.pdf>
- [10] A. Anthon, J. C. Hernandez, Z. Zhang, and M. A. E. Andersen, "Switching investigations on a sic mosfet in a to-247 package," in Industrial Electronics Society (IECON 2014), October 2014, pp. 1854–1860.
- [11] Cree, "Minimizing parasitic effects in sic-mosfet modules," 2015. [Online]. Available: <http://www.mouser.com/pdfdocs/CreeCPWRAN12.pdf>
- [12] D. Lorusso, "Insulation calculator," 2016. [Online]. Available: <http://www.creepage.com>
- [13] Cree, "Techniques for minimizing parasitic inductance," 2015. [Online]. Available: <http://www.mouser.com/pdfDocs/Cree-Design-Considerations-for-Designing-with-Cree-SiC-Modules-part-2.pdf>

Comparison of averaged modeling approaches considering a bidirectional boost converter

Ander González, Johan Gyselinck
Bio Electro and Mechanical Systems department
Université Libre de Bruxelles
Brussels, Belgium

Abstract—The bidirectional boost converter is a DC/DC converter able to transmit power between two different voltage level stages using switches and few passive components. This paper presents two detailed and two averaged models which picture out the slower power dynamics of the converters while suppressing the switching behavior, requiring thus less time to be simulated. These models are obtained either from mathematical expressions or extracted from circuit schematics. The times required for simulating different models and their error regarding the average value of the detailed model are presented and compared using different simulation time steps and simulated times.

Index Terms—DC-DC power converters, Semiconductor device modeling.

I. INTRODUCTION

The increasing number of power electronic converters in the electrical grid grows interest in studying grid power flow. Using averaged models of power electronic converters the overall system can be studied in reduced time achieving a good accuracy. This modeling approach brings the possibility to study the power flow within the converter without reproducing the switching dynamics, thus requiring less small time steps [1]. This makes these kind of models convenient when large simulation times, or simulation of complex systems is required such as power transmission or micro-grid modeling.

Different averaging approaches can be found in the literature such as classical averaged model (CAM), generalized averaged model (GAM), and circuit averaging (CA). The CAM approach consists in extracting the DC behavior of the signals to be averaged [2]. This approach is not valid when AC characteristics of the waveform to be averaged are necessary (e.g. when a transformer is used). For these cases a GAM approach, that takes into account some harmonics of the signal, is used [3]. CA consists in keeping unaltered the time-invariant parts of the circuit (eg. capacitors) while substituting the rest (diodes, switches, etc.) by a time-invariant circuit through averaging of the signals comprised [2].

Several approaches applied to different topologies can be found in the literature. In particular, for boost converters unidirectional [4] and bidirectional models [5] can be found, including conduction and/or switching losses [6], [7] or not, and addressing the discontinuous conduction mode (DCM) [8]–[10] or just able to work in continuous conduction mode (CCM).

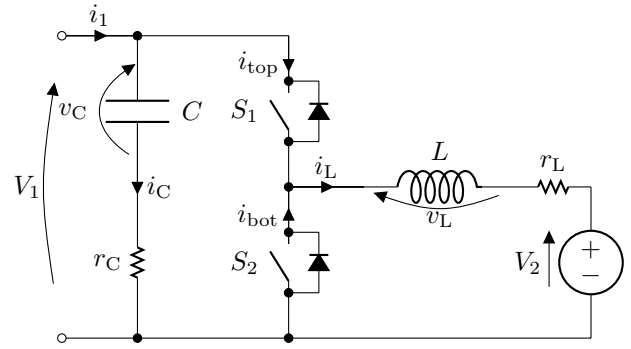


Fig. 1. Bidirectional boost converter with ESR in passive components

II. CONSIDERED MODELS

In this work different models are studied comparing the required simulation time, the achieved accuracy in low frequency dynamic response. Besides the ease of including known phenomena occurring in the converter, the ease of developing the models and other features are discussed as well. The models in this section assumes the following: converter works in CCM and the command of the switches is done in complementary fashion.

The comparisons between the different models are done through the use of different bidirectional boost converter models. This topology comprises two controllable switches S_1 and S_2 in totem-pole configuration with free-wheeling diodes in anti-parallel. This topology uses an inductance L as energy storage device in order to increase the lower voltage V_2 to the higher voltage V_1 that is filtered using a capacitor C (Fig. 1).

A. Detailed model

Two detailed models (including switching behavior) are built for the study. These models are built in order to compare the averaged models to the slow dynamics of a more detailed model. The first switched model has been built using SimPowerSystems library included in Simulink and is expressed with the SPS label. The latter has been developed defining the different states of the converter depending on the two gate signals and the sign of the current in the inductor L (Table I), this model is further referred to with SW label.

TABLE I
DEFINITION OF THE CONVERTER STATES

State	i_L	γ	$\bar{\gamma}$	S_1	S_2	u	\bar{u}
1	≥ 0	1	0	ON	OFF	1	0
2	< 0	0	1	ON	OFF	1	0
3	≥ 0	1	0	OFF	ON	0	1
4	< 0	0	1	OFF	ON	0	1

In this topology the following expressions will always be true regardless of the state:

$$V_1 - v_C - i_C r_C = 0 \quad (1)$$

$$v_L = L \frac{di_L}{dt} \quad (2)$$

$$i_C = C \frac{dv_C}{dt} \quad (3)$$

The current i_1 can be defined as follows:

$$\text{states 1 and 2:} \quad i_1 = i_C + i_L \quad (4)$$

$$\text{states 3 and 4:} \quad i_1 = i_C \quad (5)$$

The low voltage mesh can be also defined as:

$$\text{state 1:} \quad V_1 - V_{S1} - i_L r_{S1} - v_L - i_L r_L - V_2 = 0 \quad (6)$$

$$\text{state 2:} \quad V_1 + V_{F1} - i_L r_{F1} - v_L - i_L r_L - V_2 = 0 \quad (7)$$

$$\text{state 3:} \quad -V_{F2} - i_L r_{F2} - v_L - i_L r_L - V_2 = 0 \quad (8)$$

$$\text{state 4:} \quad V_{S2} - i_L r_{S2} - v_L - i_L r_L - V_2 = 0 \quad (9)$$

where V_{S1} , V_{S2} , V_{F1} and V_{F2} are the forward voltages of the switches 1 and 2 and their anti-parallel diodes respectively during on state, and r_{S1} , r_{S2} , r_{F1} and r_{F2} are the on resistances of the switches 1 and 2 and their anti-parallel diodes respectively. Substituting (1) and (2) into (6)-(9) and then substituting i_C for (3), yields:

$$\text{state 1:} \quad L \frac{di_L}{dt} = -i_L (r_{S1} + r_C + r_L) + v_C - V_2 + i_1 r_C - V_{S1} \quad (10)$$

$$\text{state 2:} \quad L \frac{di_L}{dt} = -i_L (r_{F1} + r_C + r_L) + v_C - V_2 + i_1 r_C + V_{F1} \quad (11)$$

$$\text{state 3:} \quad L \frac{di_L}{dt} = -i_L (r_{F2} + r_L) - V_2 - V_{F2} \quad (12)$$

$$\text{state 4:} \quad L \frac{di_L}{dt} = -i_L (r_{S2} + r_L) - V_2 + V_{S2} \quad (13)$$

and

$$\text{states 1 and 2:} \quad C \frac{dv_C}{dt} = i_1 - i_L, \quad (14)$$

$$\text{states 3 and 4:} \quad C \frac{dv_C}{dt} = i_1. \quad (15)$$

Including the corresponding parameters defining the current sense (γ) and the switching function (u) to each state, yields

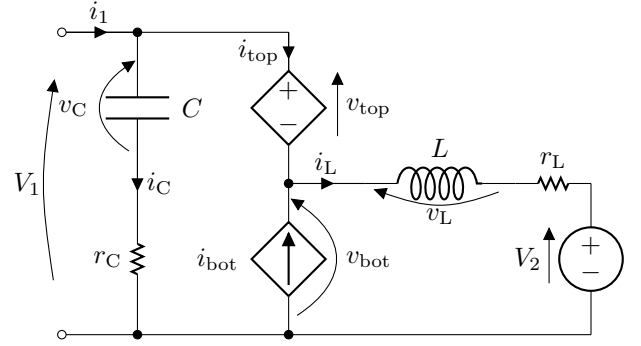


Fig. 2. Circuit averaged model of bidirectional boost converter with ESR in passive components

the model describing the switching behavior of the converter

$$L \frac{di_L}{dt} = -(uA + \bar{u}B + r_L) i_L + uE + \bar{u}F - V_2 \quad (16)$$

$$C \frac{dv_C}{dt} = i_1 - ui_L \quad (17)$$

with $A = \gamma r_{S1} + \bar{\gamma} r_{F1} + r_C$, $B = \gamma r_{F2} + \bar{\gamma} r_{S2}$, $E = v_C + r_C i_1 - \gamma V_{S1} + \bar{\gamma} V_{F1}$, and $F = -\gamma V_{F2} + \bar{\gamma} V_{S2}$.

B. Classical averaged model

The classical averaged model is obtained in the same way used for the detailed model presented above. This model is labeled as CAM throughout the paper. From (16) and (17), the switching function is averaged as follows [3]:

$$D = \langle u \rangle_0 = \frac{1}{T_w} \int_{t-T_w}^t u \cdot dt \quad (18)$$

where T_w is the averaging window. Making T_w to corresponds to the PWM switching period, the duty cycle D will be equal to the average value of u . Doing that, the different states of the converter corresponding to u and \bar{u} , will be averaged as D and $1 - D$ respectively, with $D = \frac{T_{ON}}{T_{sw}}$, and $1 - D = \frac{T_{OFF}}{T_{sw}}$. Applying this to (16) and (17) yields:

$$L \frac{di_L}{dt} = -[DA + (1 - D)B + r_L] i_L + DE + (1 - D)F - V_2 \quad (19)$$

$$C \frac{dv_C}{dt} = i_1 - Di_L \quad (20)$$

C. Circuit averaging model

In this modeling approach the time-invariant part of the topology and the time-variant or switch network are separated. The time-invariant parts of the circuit (e.g. inductances, capacitors...) are left without changes whereas the time-variant (eg. controlled switches, diodes...) is substituted by current and voltage sources to obtain time-invariant circuits. This model is represented with the label CA throughout the paper.

Applying this to bidirectional boost converter results in the new circuit shown in Figure 2, where the controlled voltage and current sources are place interchangeable. Following the same state definition based on the switch function u and

the current sense γ defined in Table I the following current expressions are true:

$$\text{States 1 and 2:} \quad i_{\text{top}} = i_L \quad (21)$$

$$i_{\text{bot}} = 0 \quad (22)$$

$$\text{States 3 and 4:} \quad i_{\text{top}} = 0 \quad (23)$$

$$i_{\text{bot}} = i_L \quad (24)$$

Whereas for the voltage:

$$\text{State 1:} \quad v_{\text{top}} = i_{\text{top}} r_{S1} + V_{S1} \quad (25)$$

$$\text{State 2:} \quad v_{\text{top}} = i_{\text{top}} r_{F1} - V_{F1} \quad (26)$$

$$\text{State 3:} \quad v_{\text{top}} = V_1 + i_{\text{bot}} r_{F2} + V_{F2} \quad (27)$$

$$\text{State 4:} \quad v_{\text{top}} = V_1 + i_{\text{bot}} r_{S2} - V_{S2} \quad (28)$$

Merging equations (25)-(28) using the terms γ and D as defined in equation (18) and substituting the corresponding current equations previously defined (equations (21)-(24)), yields:

$$\begin{aligned} \langle v_{\text{top}} \rangle_0 = & i_L [D(\gamma r_{S1} + \bar{\gamma} r_{F1}) + (1-D)(\gamma r_{F2} + \bar{\gamma} r_{S2})] \\ & + D(\gamma V_{S1} - \bar{\gamma} V_{F1}) + (1-D)(\gamma V_{F2} + \bar{\gamma} V_{S2} + V_1) \end{aligned} \quad (29)$$

Besides, the following expressions are true for every possible state:

$$\langle i_{\text{top}} \rangle_0 = D i_L \quad (30)$$

$$\langle i_{\text{bot}} \rangle_0 = (1-D) i_L \quad (31)$$

III. SIMULATION RESULTS

Simulations were run using the parameters included in Table II and an initial duty cycle equal to 0.7 that ramps down to 0.2 with a constant slope from simulation times 0.2 to 0.7 seconds.

TABLE II
SIMULATION PARAMETERS

Variable	Nomenclature	unit	Value
Inductance	L	μH	640
Coil resistance	r_L	$\text{m}\Omega$	23.4
Capacitance	C	μF	100
Capacitor ESR	r_C	Ω	0.1
Low voltage side voltage	V_2	V	50
High voltage side current	I_1	A	-10
Switching frequency	f_{sw}	kHz	20

Simulations including conduction losses the parameters contained in Table III are used as well.

During the simulation, the models developed using CA trigger an error due to too high time steps. These error appears due to the inclusion of blocks in SimPowerSystems library probably due to the approaching of simulation step times close to the circuit dynamic frequencies.

TABLE III
PARAMETERS REGARDING CONDUCTION LOSSES

Variable	Nomenclature	unit	Value
Switch forward voltage	V_{Sx}	V	0
Switch on resistance	r_{Sx}	$\text{m}\Omega$	16
Diode forward voltage	V_{Fx}	V	1
Diode on resistance	r_{Fx}	$\text{m}\Omega$	13.2

A. Error

The computed steady-state error for i_L is less than 0.01% for both CAM and CA models including or not conduction losses. Regarding V_1 the same result is obtained for CAM models including or not conduction losses while for CA the error rises up to 3.78% in the ideal model and 1.71% in the case including conduction losses. The values of the state variables at the end of the simulation are shown in Figure 3. The steady-state error is computed comparing the value obtained in simulation to the result obtained for detailed model described in section II-A after averaging throughout a switching period. The detailed model was simulated using a time step $T_s = 0.02T_{\text{sw}}$. The steady-state relative error values did not change with the increase of simulation time step. This is expected during steady-state operation since the state variables are not supposed to change in averaged models.

During transients the error lies around 1%. In the figures the voltage (Fig. 5) and current (Fig. 4) values of CAM and CA are compared to the detailed model simulated at $T_s = 0.002T_{\text{sw}}$. The detailed model is averaged for that purpose using a time window equal to the switching period T_{sw} . In the detailed model simulation appears an oscillation close to $t=0.5$. This oscillation is expected to decrease as the simulation step time decreases.

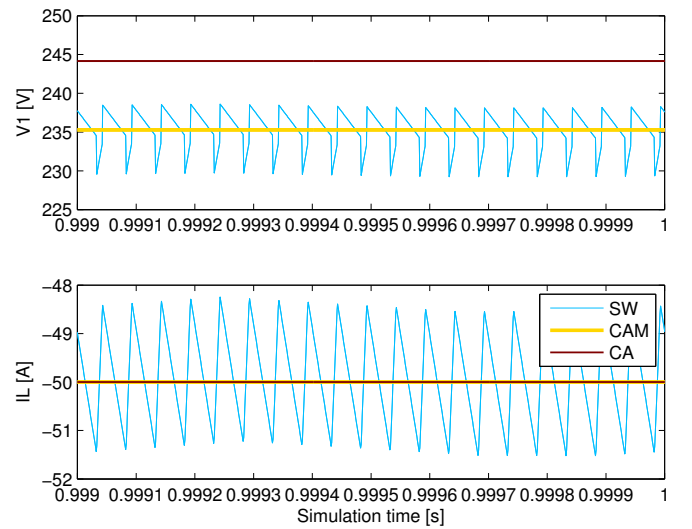


Fig. 3. Steady-state of voltage and current. Detailed model at $T_s = 0.002T_{\text{sw}}$ in cyan, CAM at $T_s = 0.02T_{\text{sw}}$ in yellow and CA at $T_s = 0.02T_{\text{sw}}$ in brown

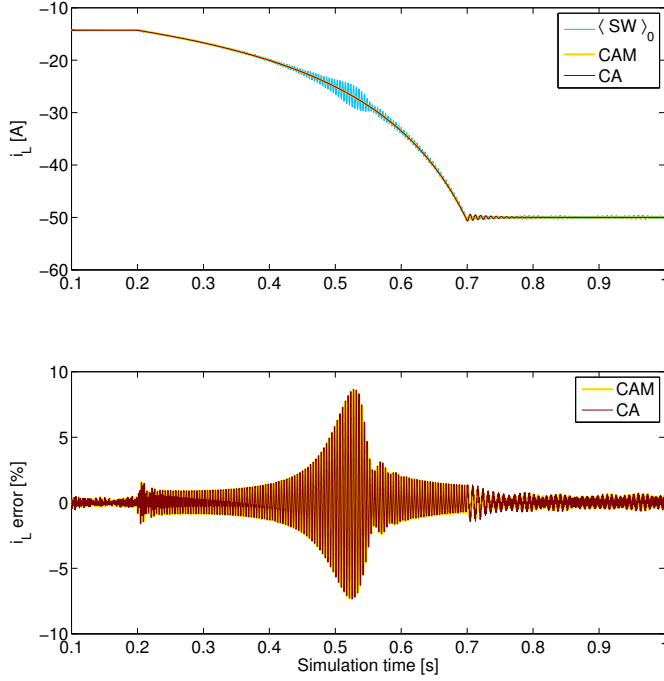


Fig. 4. Low voltage side current at time step of $1\mu s$ for averaged models

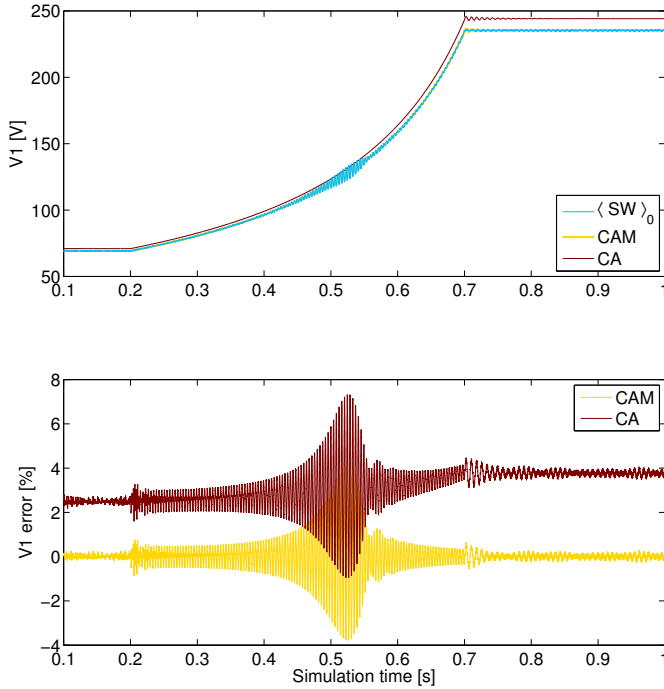


Fig. 5. High voltage side voltage at time step of $1\mu s$ for averaged models

B. Simulation times

Different tables are presented along this section in order to quantize the required time to simulate the different models under certain conditions. Each model/conditions pair has been simulated three times and the average of these is presented in the tables in order to reduce the effect of different tasks

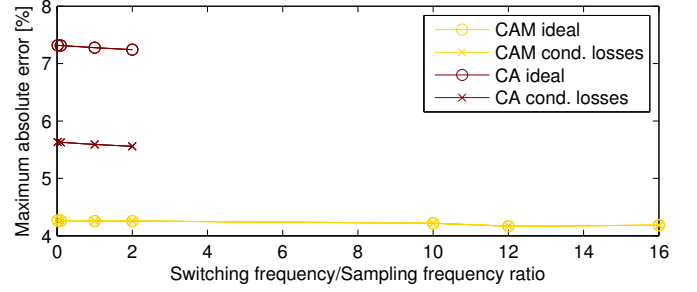


Fig. 6. High voltage side voltage maximum absolute value of relative error for different switching frequency/sampling frequency ratios

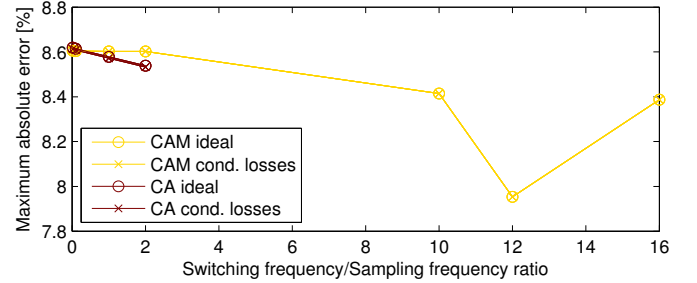


Fig. 7. Low voltage side current maximum absolute value of relative error for different switching frequency/sampling frequency ratios

running in background.

1) *Ideal switches model*: Four different ideal switch models are compared of which two are detailed and other two averaged. Detailed models comprise a SimPowerSystems model using the *Ideal Switch* block (SPS) and the model described in section II-A (SW), while averaged models include the models described in sections II-B (CAM) and II-C (CA) the latter built using SimPowerSystems blocks.

Simulation of the four models was carried out at fixed step of $T_{sw}/10$ ($5\mu s$). Besides the averaged models were simulated at larger step times that are not suitable for switched models following Shannon's theorem. The average time needed to simulate the models under different conditions is gathered in Table IV.

2) *Including conduction losses*: Conduction losses are included in the model using two different ways. When a switch or diode is on (conducting) the device is modeled as a constant voltage drop and a series resistance. These are already included in all model equations in section II. In order to build a detailed model using SimPowerSystems library (SPS), the *Ideal Switch* block was replaced for *Mosfet* block. The average time required for simulating these models is gathered in Table V.

IV. DISCUSSION

CAM and CA models can be obtained in a similar way to the detailed model. CA approach can be easily used as building block for developing more complex models while the CAM approach is not easy to be adapted. Since CA approach only averages the time-variant piece of the circuit this remains

TABLE IV
SIMULATION TIMES OF IDEAL MODELS

t_{sim}	Model	Time step					
		$0.1T_{sw}$	T_{sw}	$2T_{sw}$	$10T_{sw}$	$12T_{sw}$	$16T_{sw}$
0.1s	SPS	1.04	-	-	-	-	-
	SW	2.10	-	-	-	-	-
	CAM	1.25	0.27	0.21	0.17	0.17	0.16
	CA	0.81	0.26	0.24	0.21	0.22	0.21
1s	SPS	7.45	-	-	-	-	-
	SW	19.27	-	-	-	-	-
	CAM	10.27	1.27	0.76	0.25	0.26	0.22
	CA	5.51	0.80	0.53	0.26	0.25	0.24
10s	SPS	72.62	-	-	-	-	-
	SW	194.81	-	-	-	-	-
	CAM	96.01	10.58	5.11	1.21	1.05	0.87
	CA	49.90	5.29	2.83	Failed	Failed	Failed

TABLE V
SIMULATION TIMES OF MODELS INCLUDING CONDUCTION LOSSES

t_{sim}	Model	Time step					
		$0.1T_{sw}$	T_{sw}	$2T_{sw}$	$10T_{sw}$	$12T_{sw}$	$16T_{sw}$
0.1s	SPS	1.13	-	-	-	-	-
	SW	2.19	-	-	-	-	-
	CAM	1.25	0.25	0.20	0.16	0.16	0.16
	CA	0.92	0.27	0.23	0.21	0.21	0.21
1s	SPS	7.87	-	-	-	-	-
	SW	19.82	-	-	-	-	-
	CAM	10.39	1.25	0.74	0.26	0.24	0.25
	CA	6.78	0.93	0.60	0.27	0.26	0.24
10s	SPS	73.80	-	-	-	-	-
	SW	196.76	-	-	-	-	-
	CAM	96.57	10.55	5.04	1.21	1.06	0.85
	CA	62.05	6.44	3.37	Failed	Failed	Failed

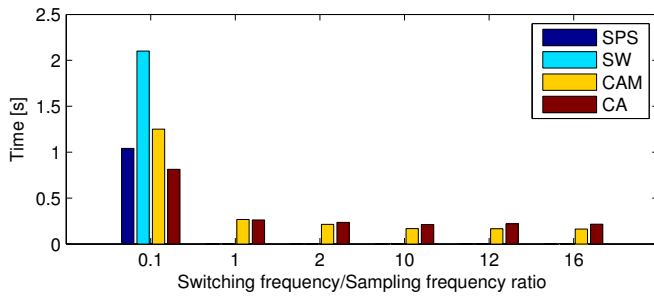


Fig. 8. Required simulation time vs. switching frequency/sampling frequency ratio for 0.1 simulated time.

adaptable to different configurations. On the other hand if a small signal-model is desirable the CA approach is not valid if used to construct more complex systems. Therefore, if a small-signal model is required (i.e. for controller design) the effort required to get the CAM has to be done anyway. In terms of portability, the CAM relies solely on simple mathematical

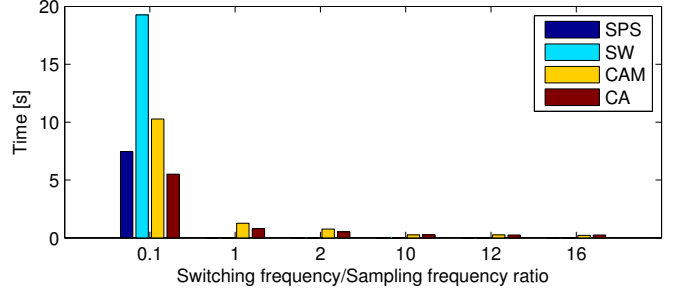


Fig. 9. Required simulation time vs. switching frequency/sampling frequency ratio for 1 simulated time.

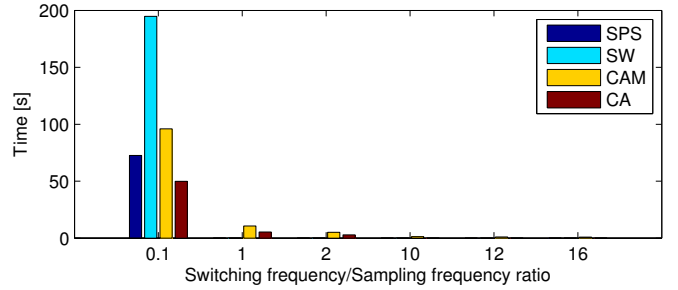


Fig. 10. Required simulation time vs. switching frequency/sampling frequency ratio for 10 simulated time.

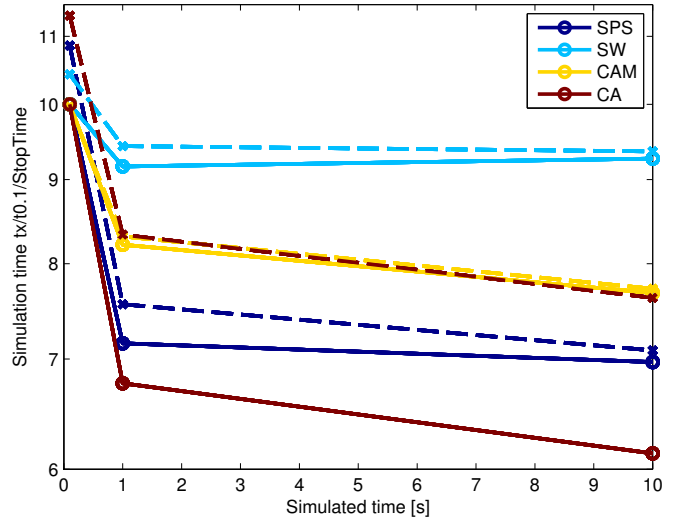


Fig. 11. Required simulation time vs. simulated time at 0.1 switching frequency/sampling frequency ratio. Simulation time referenced to required time to simulate 0.1 seconds (in log scale). Solid lines for ideal models, dashed lines for models including conduction losses.

operations. This makes this modeling approach easier to export to other simulation environments, as well as more robust and flexible (did not trigger any error at high time steps).

The steady-state error of the CAM approach remains very small for the whole simulated range, with no perceptible variation with time step changes. It may decrease the accuracy as the circuit slower natural dynamics are approached with

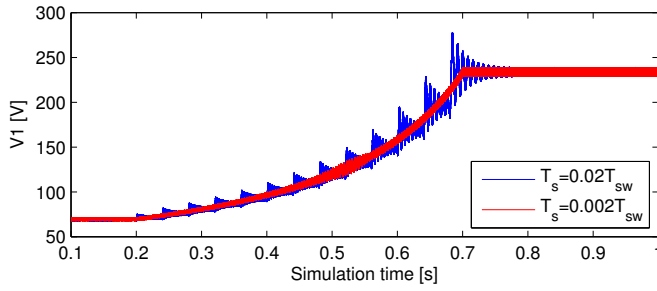


Fig. 12. Output voltage in detailed model SW for different simulation time steps.

the increase of simulation time step. The CA model presents a higher steady-state error which is also not affected by the increase of the simulation time step within an acceptable range. Including the conduction losses of the semiconductor devices did not change considerably any of the errors except the error in V_1 that was reduced from 3.78% to 1.71%.

The relative error during duty cycle changes does not notably change for the selected simulation time step range. The maximum of the absolute value of the relative error of the voltage and the current are shown in figures 6 and 7 respectively. It is predictable that the error will become greater as the time step is increased, specially when circuit natural frequencies are reached.

The time required to simulate any of the models increases nearly in a linear way regarding to the simulated time. A graphical example of this can be found in Figure 11 where it can be seen that for short simulated times initialization time is not negligible anymore. Time measurements are shown starting at simulation step time of $T_s = 0.1T_{sw}$. In the case of detailed models using fixed step the accuracy obtained is not good enough due to low resolution of PWM duty cycle. This makes necessary to further reduce the simulation step time if good accuracy during transients is wanted, making thus averaged models even more valuable when switching dynamics of the converter are not interesting. A graphical example is shown in Figure 12 where the detailed model response is shown for simulation time steps $0.02T_{sw}$ ($1\mu s$) and $0.002T_{sw}$ ($100ns$).

V. CONCLUSION

Averaged models show a relatively high accuracy picturing out the power dynamics of the power converters. Averaged models do not require small simulation time steps compared to detailed models even during transients. This makes averaged models suitable for long simulation times as well as for simulation of complex systems. Time savings is just the most remarkable benefit since some averaged models might be linearized for controller design as well.

ACKNOWLEDGMENT

The work contained in this paper was supported by the government of the Belgian Walloon region under the project BATWAL.

REFERENCES

- [1] D. Maksimovic, a.M. Stankovic, V. Thottuvelil, and G. Verghese, "Modeling and simulation of power electronic converters," *Proceedings of the IEEE*, vol. 89, no. 6, 2001.
- [2] R. W. Erickson and D. Maksimovic, *Fundamentals of Power Electronics*, 2001.
- [3] S. Bacha, I. Munteanu, and A. I. Bratcu, *Power Electronic Converters Modeling and Control*. Springer, 2014. [Online]. Available: <http://link.springer.com/10.1007/978-1-4471-5478-5>
- [4] Y. Lu, G. F. G. Feng, and Y.-F. L. Y.-F. Liu, "A large signal dynamic model for DC-to-DC converters with average current control," *Nineteenth Annual IEEE Applied Power Electronics Conference and Exposition, 2004. APEC '04.*, vol. 2, no. C, pp. 797–803, 2004.
- [5] S. Abid and A. Ammous, "Average modeling of DC-DC and DC-AC converters including semiconductor device non-linearities," *International Conference on Design and Test of Integrated Systems in Nanoscale Technology, 2006. DTIS 2006.*, no. d, 2006.
- [6] G. Gatto, I. Marongiu, A. Mocci, A. Serpi, and I. L. Spano, "An improved averaged model for boost DC-DC converters," *IECON Proceedings (Industrial Electronics Conference)*, pp. 412–417, 2013.
- [7] A. Ammous, K. Ammous, M. Ayedi, Y. Ounajjar, and F. Sellami, "An advanced PWM-switch model including semiconductor device nonlinearities," *IEEE Transactions on Power Electronics*, vol. 18, no. 5, pp. 1230–1237, 2003.
- [8] J. Channegowda, B. Saritha, H. R. Chola, and G. Narayanan, "Comparative evaluation of switching and average models of a DC-DC boost converter for real-time simulation," *IEEE CONECCT 2014 - 2014 IEEE International Conference on Electronics, Computing and Communication Technologies*, pp. 1–6, 2014.
- [9] T. Pavlovic, T. Bjazi, and Ž. Ban, "Simplified averaged models of dc-dc power converters suitable for controller design and microgrid simulation," *IEEE Transactions on Power Electronics*, vol. 28, no. 7, pp. 3266–3275, 2013.
- [10] C. Jaen, R. Pindado, J. Pou, A. Arias, and V. Sala, "Adaptive averaged model applied to PWM DC-DC converters," *EPE-PEMC 2006: 12th International Power Electronics and Motion Control Conference, Proceedings*, pp. 118–123, 2007.

Availability Of The Electric Drive Systems Containing Flux Switching Permanent Magnet Machines

Lie Wang

Electromechanics and Power Electronics (EPE) group
Department of Electrical Engineering
Eindhoven University of Technology (TU/e)
Eindhoven, The Netherlands
L.Wang.1@student.tue.nl

Abstract—This paper investigates how to improve availability of an electrical drive containing a 3-phase 12/10 (12 stator tooth/10 rotor poles) flux switching permanent magnet machine. In this respect, Field-Oriented Control and Space-Vector Pulse-Width-Modulation strategies will be applied with 3-phase operation condition. Availability and reliability require that during faults, such as loss of one inverter phase leg or open-circuit of one machine phase winding, the electrical drive remains operational. Therefore, initial research is given in this paper on the implementation of a fault-free control algorithm that preserves the electromagnetic torque following certain faults. In terms of inter-turn short circuit fault, the machine becomes asymmetric and its behavior such as fault current and output torque are investigated. To further improve system reliability, dual three phase drive is applied by splitting the machine winding, and an extended park transformation is used in machine control.

Index Terms—availability; flux-switching permanent magnet machine; field-oriented control; space-vector pulse-width-modulation; open-circuit fault; inter-turn short circuit fault; dual three phase drive; Pseudo-Park transformation, aerospace.

I. INTRODUCTION

In aerospace, availability of electrical drives is paramount, if ever to replace or augment current alternative systems that accommodate a certain level of redundancy. Further, in automotive, marine and railway applications, electric machines and their drive system also gain more commercial interest as they potentially feature higher energy efficiencies, lower emissions, higher peak powers and faster power response compared to conventional [1].

Usually, availability is considered in these applications in the context of reliability, and serviceability. In this paper, availability is defined as the probability that the

system operates according to the given specifications when required. As such, availability is considered to be the probability that a system does not fail or does not need repair. This research, starts with an elaboration on reliability, and maintaining operation following certain faults.

Flux-switching permanent magnet (FSPM) machines are one candidate for such aeronautics electrical drives as they locate both permanent magnets (PM) and phase windings on the stator side [2]–[5]. This influences availability, as described above, and still provides relatively high torque/inertia and good opportunities for advanced air-cooled configurations. Further, due to the magnetic field being in parallel with the armature field, it inherently has a low demagnetizing characteristic which provides a wide operation range. Additionally, its compact, robust rotor structure and large torque to inertia ratio provide an opportunity for ultra-fast acceleration responses [6]–[9]. All these features concerning FSPM machines are also in good accordance with requirements of electric traction in more general applications such as [10].

The considered electric drive contains a voltage source inverter (VSI) and a control unit which monitors system operation conditions and feeds the desired currents to the electrical machine. In certain cases, such as fuel pumps, aerospace or steering applications, a single failure or malfunction of the electrical system causes severe damage. Therefore, fault-tolerant motor drive system become a necessity with various research institutes and commercial parties focusing on suitable redundant power electronic topologies of VSIs and geometries of electric machines [11].

These safety critical applications demand continuous operation of the electrical drive system that maintains

its equivalent output performance when a fault has happened. These system faults can contain, among many others, switch component short and open-circuit, phase leg short-circuit and machine phase open-circuit [11]. Within this paper, a Field-Oriented Control (FOC) is applied to regulate the phase currents and output electromagnetic torque of the FSPM, which is standard for brushless ac (BLAC) and induction machines that require the maximization of torque-to-ampere (MTPA) ratio and field weakening operation [12]–[14].

In addition, another common fault, intern turn short circuit can happen, caused by the coil insulation breakdown. This will create an extra short circuit path that flows very large current driven with back-emf induced by coupled flux-linkage in the short turns [15], [16]. In this paper, the machine behavior such as fault current, produced torque and required supply voltage will be investigated based on the built up model.

To further improve the drive availability and enhance operation capability such as speed range, machine winding could be separated into six phases and then a dual VSI drive topology is proposed [17]–[20]. Corresponding control and regulation methods are developed with assistant of its specific space vector model.

II. ELECTRIC DRIVE SYSTEM FOR FSPM MACHINE

The machine inductance plays a paramount role in the prediction of the dynamic machine behavior. After acquiring these inductance values, the required specific machine equivalent circuit parameters can be obtained. These are then used to stipulate the machine within the electric drive control strategy to achieve high performance control of the FSPM machine.

A. FSPM Machine Inductance Characteristics

A general mathematical description of the inductance in an electric circuit is given by:

$$\begin{aligned} V &= Ri + \frac{d\psi}{dt} = Ri + \frac{d\psi}{di} \frac{di}{dt}, \\ \Delta L &= \frac{d\psi}{di}. \end{aligned} \quad (1)$$

where R is the resistance of the inductor, ψ is the flux-linkage and ΔL is defined as the incremental inductance obtained from the tangent value of the hysteresis ψ - i curve. It represents the same value as apparent inductance $L = \psi/i$ when the machine operates in the linear region of the ferromagnetic material, but deviates in the saturation region [21]. Incremental inductances rather than apparent inductances have to be implemented in the current controller design in order to accurately predict the transient response of drive system [22].

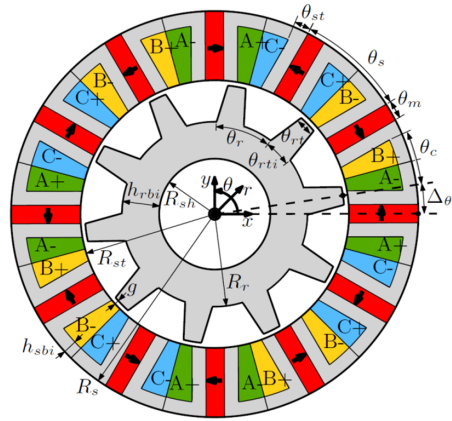


Figure 1: The geometry of the 3-phase 12/10 flux switching permanent magnet machine^[7].

Furthermore, from a machine analysis and control perspective, rotor position is defined by using the dq-axis coordinate, where d-axis alignment occurs when the maximum flux-linkage is achieved by phase A and the q-axis is 90 electric degree leading. However, in case of FSPM machine, the dq-axis definition is modified because of its special machine topology which is shown in Fig. 1.

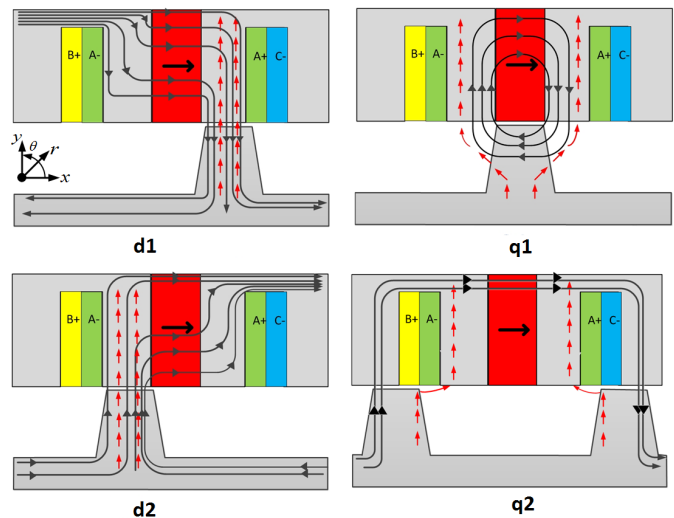


Figure 2: The modified dq-axis in FSPM machine and magnetic field generated by PM and phase winding.

From the knowledge of [23], when the d-axis is aligned, the field ψ_{pm} produced by the permanent magnet is illustrated by black arrows, is strengthening the field ψ_e that is excited by the phase winding, which is illustrated by red arrows for a single rotor position. However, ψ_{pm} is opposing (i.e. field weakening) the phase winding field at another position. Therefore, instead of a periodic d and q-axis throughout the machine, two independent d-axis are applicable with two constant q-axis as illustrated in Fig. 2.

As a result, instead of a periodic dq-axis throughout the FSPM, this paper proposes to use two separate d-axis. This is due to the field of the phase windings being either strengthening or weakening the field of the permanent magnet in the stator teeth. The field strengthening or weakening occurs when the rotor tooth aligns with a stator tooth.

The dq-axis incremental inductances are shown in Fig. 3. On the one hand, L_{d1} is increasing with a phase current increase due to the opposite direction of ψ_{pm} and ψ_e within the “active” right stator tooth. On the other hand, L_{d2} decreases with an increasing current due to saturation of the soft magnetic material, with respect to left stator tooth. L_{q1} and L_{q2} are decreasing with the same rate because of saturation when the current goes higher.

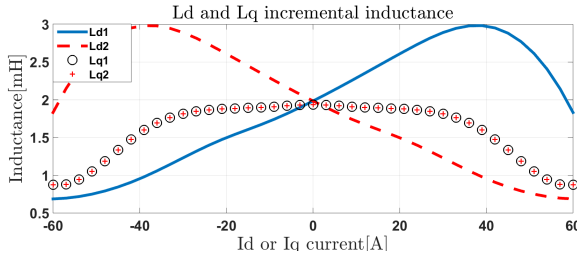


Figure 3: Current dependent dq-axis incremental inductance.

B. The FSPM Machine Model And Control Strategy

Based on the machine inductance characteristics, the FSPM machine is modeled by the following mathematical representation (2), using the synchronous dq reference frame:

$$\begin{aligned} V_q &= R_s i_q + \Delta L_q(i_q, i_d) \frac{di_q}{dt} + \omega_e (L_d i_d + \lambda_{dr}), \\ V_d &= R_s i_d + \Delta L_d(i_q, i_d) \frac{di_d}{dt} - \omega_e L_q i_q, \\ V_{os} &= R_s i_{os} + \Delta L_{ls} \frac{di_{os}}{dt}, \\ T_e &= \frac{3}{2} p (\lambda_{dr} i_q + (L_d - L_q) i_q i_d). \end{aligned} \quad (2)$$

The field-oriented control commands that the d-axis current i_d is zero when not in field weakening. Therefore, inductance $\Delta L_d(i_q, i_d)$ is applied with the average value of the incremental inductances L_{d1} and L_{d2} . The zero sequence voltage V_{os} is then represented by using the zero sequence current i_{os} and the leakage inductance ΔL_{ls} . From this machine model, it is clear that the output torque T_e can be directly controlled using regulation of the dq-axis currents.

The machine is supplied by a full-bridge 3-phase inverter with space-vector PWM strategy, which is specially designed to provide output voltage commands in the dq-axis coordinate system [24] since its switch states

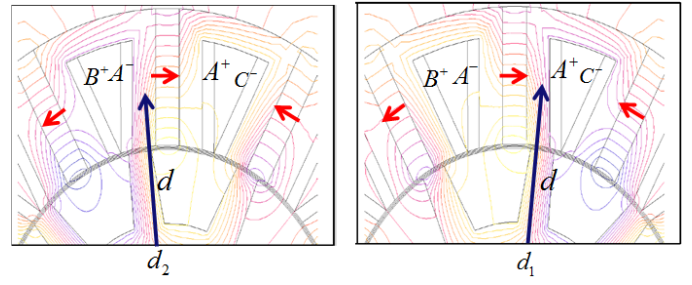


Figure 5: The PM flux-linkage in d-axis of FSPM machine with different position

are represented in the same dq-axis coordinate that is used by the machine.

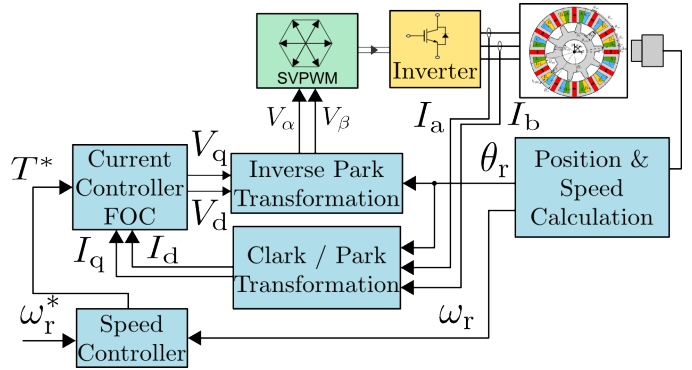


Figure 4: Electric drive system of FSPM machine.

Field-oriented control is implemented for the current control in order to produce the voltage commands in the dq reference frame. A drive system overview with speed control is shown in Fig. 4. This electrical drive system could also be simply modified into torque control mode by only using current control without involving a speed controller.

C. Space-vector and phasor diagram of FSPM machine under Field weakening control algorithm

Because of the VSI DC supply voltage and output phase voltage limitation, field weakening control becomes a necessity when electric machine is commanded to achieve high speed operation, such as in automotive and electric power steering applications. In conventional PMSM machine, the armature currents are controlled to produce an opposing magnetic field to the permanent magnet field [25]. Whereas in the DC-excited flux-switching machines (DCEFSMs), field weakening operation is generally obtained in a similar way except reducing the DC coil currents, which would results in a decrease of output power and electromagnetic torque [26].

In the FSPM machine, phase currents are controlled to produce an opposite field to the PM flux-linkage and thus

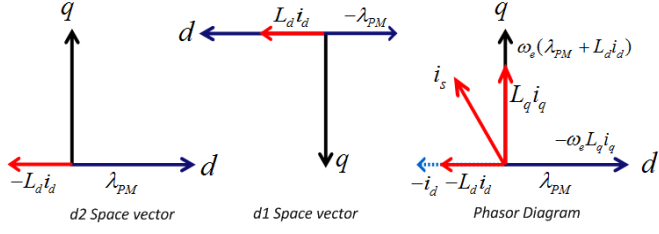


Figure 6: Space vector and phasor diagram of FSPM machine.

reducing the phase back-emf voltage. However, since the PM flux-linkage in both d-axis have the same value with opposite directions, the space-vector diagram also shows an apparent difference with conventional PM machine. From Fig. 5, the PM flux-linkage pointing outward at d_2 which is defined as positive direction and inward at d_1 which is defined as negative direction. Fortunately, the phasor diagram which represents machine voltage equation conserves the same property as PMAC machine.

Fig. 6 depicts the relationship between the space vector and phasor diagram of FSPM machine. In the synchronous rotor dq reference frame, positive PM field is observed by space vector d-axis at d_2 position (0° rotor position), and negative PM field is observed by space vector d-axis at d_1 position (180° rotor position). However, on the other hand, only positive PM field is observed at d-axis in phasor diagram. This is because of the measured three phases back-emf (3) induced by PM field are balanced sinusoidal AC waveforms, through Park transformation, constant positive PM field value is obtained at d-axis.

$$\begin{aligned} V_a &= -\omega_e \lambda_{PM} \sin(\theta), \\ V_b &= -\omega_e \lambda_{PM} \sin(\theta - 2\pi/3), \\ V_c &= -\omega_e \lambda_{PM} \sin(\theta + 2\pi/3). \end{aligned} \quad (3)$$

In order to apply field weakening, the armature currents are controlled to generate magnetic flux pointing inward which is negative $-L_d i_d$ at d_2 position in space vector and pointing outward which is positive $L_d i_d$ at d_1 position, and are illustrated in Fig. 6. Furthermore, due to the direction of flux-linkage that generated by the constant d-axis current is switched while rotor is changing its position among d_1 and d_2 , in phasor diagram, only negative $-L_d i_d$ is necessary for field weakening application.

III. FAULT-TOLERANT DRIVE SYSTEM DURING OPEN-CIRCUIT

In case a breakdown of the transistor in one of the inverter legs or an open-circuit of one of the machine phases encounters, an open-circuit fault will be the consequent electrical machine state. Following such a fault, a modified VSI topology has to be adopted in order

to allow zero sequence current flow that arises due to the summation of the two remaining phase currents. Thus, to preserve continuous operation, an algorithm is applied with two phase operation that maintains the required shaft torque.

A. Torque Maintain Algorithm

Obtained from [27], the torque can be preserved by producing the same magnetomotive force (MMF) with two machine phases in case of a phase open-circuit fault. Because of the open-circuit of an inverter phase leg or machine phase winding, hysteresis modulation in the current controller is adopted instead of SVPWM. The outputs of the current controller are on/off switch gating signals that are obtained from simultaneously monitoring three phase currents and compare them with the corresponding current commands. With certain torque command, three phase current commands (4) can be derived under normal operating condition:

$$\begin{aligned} I_{as}^* &= I_{qs}^{**} \cos \theta + I_{ds}^{**} \sin \theta, \\ I_{bs}^* &= I_{qs}^{**} \cos(\theta - 2\pi/3) + I_{ds}^{**} \sin(\theta - 2\pi/3), \\ I_{cs}^* &= I_{qs}^{**} \cos(\theta + 2\pi/3) + I_{ds}^{**} \sin(\theta + 2\pi/3). \end{aligned} \quad (4)$$

However, with one phase open-circuit, e.g. phase A, the three-phase current commands are modified as following for regaining the same MMF:

$$\begin{aligned} I_{bs}^* &= \sqrt{3} (I_{qs}^{**} \cos(\theta - 5\pi/6) + I_{ds}^{**} \sin(\theta - 5\pi/6)), \\ I_{cs}^* &= \sqrt{3} (I_{qs}^{**} \cos(\theta + 5\pi/6) + I_{ds}^{**} \sin(\theta + 5\pi/6)). \end{aligned}$$

While, in case of phase B or C open-circuit fault, the same current phasor control is applied as illustrated in Fig. 7

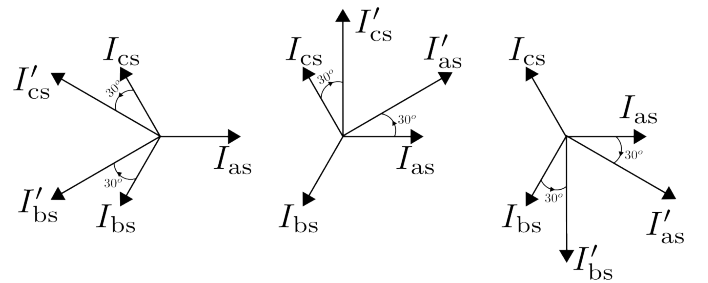


Figure 7: Current phasor control for achieving the same MMF and torque in case of phase A, B or C open-circuit.

B. Topology Of Inverter And Capacitor Voltage Balancing Control

Due to the extreme unbalance of three phase current, one inverter topology is proposed by [27] in Fig. 8. Here, one extra line is connected between the neutral point of the machine and the middle point of a series connected capacitor in the DC-link to provide a path for the zero sequence current. As an alternative, two

resistors are added in parallel to this divided capacitor with interconnection to the middle point to prevent the middle point voltage from drifting.

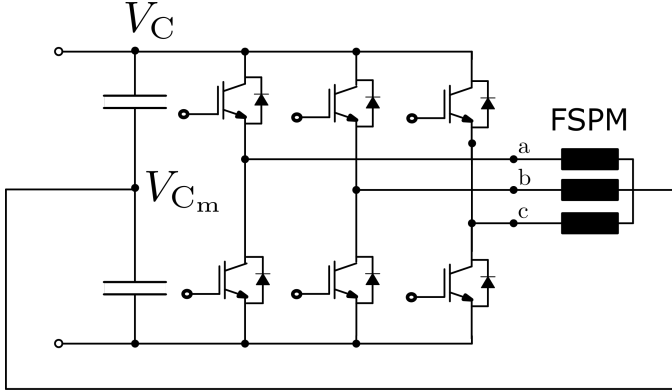


Figure 8: Three phase VSI topology used for open-circuit operation.

The fault-tolerant drive system is shown in Fig. 9, which contains a fault detection function to monitor the system condition and align in with the correct operation mode. A capacitor balancing control block is added in order to keep the middle point voltage potential at the half of the full DC capacitor voltage.

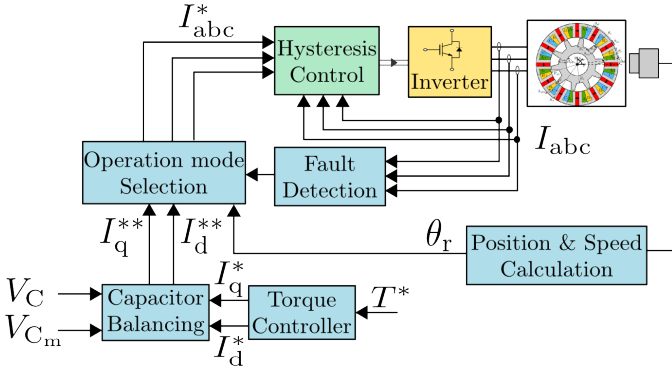


Figure 9: The fault-tolerant drive system for maintaining output torque during phase open-circuit fault.

The capacitor voltage balancing control compares the middle point voltage V_{cm} with half of the full DC capacitor voltage $\frac{1}{2}V_c$. If $\frac{1}{2}V_c > V_{cm}$, the output current I_q^{**} is set higher than I_q^* to discharge the upper capacitor. This modification of q-axis current command will slightly influence the output torque within a certain limit, and the fluctuation of torque will be finally compensated by speed control loop.

IV. FSPM MACHINE MODEL DURING PHASE WINDING INTER-TURN SHORT CIRCUIT FAULT

When machine phase inter-turn short circuit fault happens, the equivalent circuit model of three phase machine is shown in Fig. 10. A low value connection

resistance R_f , coil resistance Δrs , inductance L_f and short turns coupled back-emf forms an extra circuit which provide a path of fault current i_f . Due to inter turn short circuit, the machine phases resistance, inductance and flux-linkage becomes unbalancing, and then negative sequence current is generated which could introduces torque pulsation.

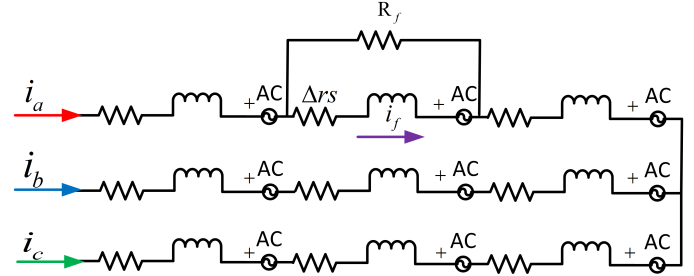


Figure 10: FSPM machine stator circuit model with phase A inter-turn short circuit fault.

A. Three phase machine model

Under short circuit fault, the machine model is reconstructed, where Δ represent fault ratio, L_m and L_l stand for health phase winding magnetizing and leakage inductance, thus phase A inductance under inter turn short circuit fault becomes $(1 - \Delta)^2(L_m + L_l)$.

$$\lambda_{abc} = L_s \begin{bmatrix} I_a \\ I_b \\ I_c \end{bmatrix} + \lambda_{PM} \begin{bmatrix} (1 - \Delta)\cos\theta \\ \cos(\theta - 2\pi/3) \\ \cos(\theta + 2\pi/3) \end{bmatrix},$$

$$L_s = \begin{bmatrix} (1 - \Delta)^2(L_m + L_l) & -\frac{1-\Delta}{2}L_m & -\frac{1-\Delta}{2}L_m \\ -\frac{1-\Delta}{2}L_m & L_m + L_l & -\frac{1}{2}L_m \\ -\frac{1-\Delta}{2}L_m & -\frac{1}{2}L_m & L_m + L_l \end{bmatrix}.$$

Different from the open circuit inverter topology, the machine neutral is opened in this case which results in none zero sequence current. Therefore, phase currents is an combination of both positive and negative sequence current. And similarly, phase flux-linkage is decomposed into positive and negative sequence components. For easy analysis, the inductance matrix is separated into balanced and unbalanced parts where the balanced matrix is the same as healthy winding phase inductance [28], [29].

$$\lambda_{abc} = (L_{bal} + L_{unbal})(I_{abc}^+ + I_{abc}^-),$$

$$L_{bal} = \begin{bmatrix} L_m + L_l & -\frac{1}{2}L_m & -\frac{1}{2}L_m \\ -\frac{1}{2}L_m & L_m + L_l & -\frac{1}{2}L_m \\ -\frac{1}{2}L_m & -\frac{1}{2}L_m & L_m + L_l \end{bmatrix},$$

$$L_{unbal} = \begin{bmatrix} (\Delta^2 - 2\Delta)(L_m + L_l) & \frac{\Delta}{2}L_m & \frac{\Delta}{2}L_m \\ \frac{\Delta}{2}L_m & 0 & 0 \\ \frac{\Delta}{2}L_m & 0 & 0 \end{bmatrix}.$$

The three phase flux-linkage can be transformed into stationary $\alpha\beta$ reference frame:

$$\lambda_{\alpha\beta}^+ = L_{ss}I_{\alpha\beta}^+ + \lambda_{PM}(1 - \frac{\Delta}{3}) \begin{bmatrix} \cos \theta \\ \sin \theta \end{bmatrix} + \frac{2}{3}\Delta_m I_{\alpha}^+,$$

$$\lambda_{\alpha\beta}^- = L_{ss}I_{\alpha\beta}^- - \lambda_{PM}\frac{\Delta}{3} \begin{bmatrix} \cos \theta \\ -\sin \theta \end{bmatrix} + \frac{2}{3}\Delta_m I_{\alpha}^+.$$

In the matrix form representation it becomes:

$$\lambda_{\alpha\beta}^+ = (L_{ss} + B) \begin{bmatrix} I_{\alpha}^+ \\ I_{\beta}^+ \end{bmatrix} + \lambda_{PM}(1 - \frac{\Delta}{3}) \begin{bmatrix} \cos \theta \\ \sin \theta \end{bmatrix},$$

$$\lambda_{\alpha\beta}^- = (L_{ss} + B) \begin{bmatrix} I_{\alpha}^+ \\ I_{\beta}^+ \end{bmatrix} - \lambda_{PM}\frac{\Delta}{3} \begin{bmatrix} \cos \theta \\ -\sin \theta \end{bmatrix}.$$

with

$$L_{ss} = \begin{bmatrix} \frac{3}{2}L_m + L_l & 0 \\ 0 & \frac{3}{2}L_m + L_l \end{bmatrix},$$

$$B = \frac{2}{3}\Delta_m \begin{bmatrix} 1 & 0 \\ 0 & 0 \end{bmatrix},$$

$$\Delta_m = \Delta(\Delta - 3)L_m + \Delta(\Delta - 2)L_l.$$

$I_{\alpha\beta}^+$ and θ represent the positive, negative sequence current in stationary frame and electrical rotor angle. After acquiring the $\alpha\beta$ flux linkage, it can be transformed in the dq rotor synchronous reference frame by using

$$I_{dq}^+ = \begin{bmatrix} \cos \theta & \sin \theta \\ -\sin \theta & \cos \theta \end{bmatrix} I_{\alpha\beta}^+ = e^{-j\theta} I_{\alpha\beta}^+$$

and

$$I_{dq}^- = \begin{bmatrix} \cos \theta & -\sin \theta \\ \sin \theta & \cos \theta \end{bmatrix} I_{\alpha\beta}^- = e^{j\theta} I_{\alpha\beta}^-$$

The flux-linkage in dq frame is then derived as

$$\lambda_{dq}^+ = e^{-j\theta}(L_{ss} + B)e^{j\theta}I_{dq}^+ + \lambda_{PM}(1 - \frac{\Delta}{3}) \begin{bmatrix} 1 \\ 0 \end{bmatrix},$$

$$\lambda_{dq}^- = e^{j\theta}(L_{ss} + B)e^{-j\theta}I_{dq}^- + \lambda_{PM}\frac{\Delta}{3} \begin{bmatrix} -1 \\ 0 \end{bmatrix}.$$

Then, the machine main circuit voltage equation in positive and negative sequence can be represented as :

$$\begin{aligned} V_{dq}^+ &= rI_{dq}^+ + \omega_e J \lambda_{dq}^+ + \frac{d\lambda_{dq}^+}{dt} \\ &= rI_{dq}^+ + \omega_e J L_{ss} I_{dq}^+ + \omega_e J L_{\alpha\alpha} I_{dq}^+ + \omega_e \lambda_{PM} \begin{bmatrix} 0 \\ 1 \end{bmatrix}, \\ &\quad -\omega_e \lambda_{PM} \frac{\Delta}{3} \begin{bmatrix} 0 \\ 1 \end{bmatrix} + L_{ss} \frac{dI_{dq}^+}{dt} + L_{\alpha\alpha} \frac{dI_{dq}^+}{dt} \end{aligned}$$

the negative sequence is :

$$\begin{aligned} V_{dq}^- &= rI_{dq}^- - \omega_e J \lambda_{dq}^- + \frac{d\lambda_{dq}^-}{dt} \\ &= rI_{dq}^- - \omega_e J L_{ss} I_{dq}^- - \omega_e J L_{\beta\beta} I_{dq}^- + \omega_e \lambda_{PM} \frac{\Delta}{3} \begin{bmatrix} 0 \\ 1 \end{bmatrix} \\ &\quad + L_{ss} \frac{dI_{dq}^-}{dt} + L_{\beta\beta} \frac{dI_{dq}^-}{dt} \end{aligned} \quad (6)$$

with $L_{\alpha\alpha} = e^{-j\theta} B e^{j\theta}$ and $L_{\beta\beta} = e^{j\theta} B e^{-j\theta}$. The third terms in (5),(6) can be further expand to :

$$\begin{aligned} &\omega_e J L_{\alpha\alpha} I_{dq}^+ \\ &= \frac{1}{3}\Delta_m \omega_e \left(\begin{bmatrix} 0 & -1 \\ 1 & 0 \end{bmatrix} + \begin{bmatrix} \sin 2\theta & \cos 2\theta \\ \cos 2\theta & -\sin 2\theta \end{bmatrix} \right) I_{dq}^+ \\ &= \frac{1}{3}\Delta_m \omega_e J I_{dq}^+ + \frac{1}{3}\Delta_m \omega_e \begin{bmatrix} 0 & 1 \\ 1 & 0 \end{bmatrix} I_{dq}^- \end{aligned}$$

and

$$\begin{aligned} &-\omega_e J L_{\beta\beta} I_{dq}^- \\ &= \frac{1}{3}\Delta_m \omega_e \left(\begin{bmatrix} 0 & 1 \\ -1 & 0 \end{bmatrix} + \begin{bmatrix} \sin 2\theta & -\cos 2\theta \\ -\cos 2\theta & -\sin 2\theta \end{bmatrix} \right) I_{dq}^- \\ &= -\frac{1}{3}\Delta_m \omega_e J I_{dq}^- + \frac{1}{3}\Delta_m \omega_e \begin{bmatrix} 0 & -1 \\ -1 & 0 \end{bmatrix} I_{dq}^+ \end{aligned}$$

B. Machine model contains short circuit loop

The full circuit model is a combination of main three phase and the inter turn short circuit loop, the full flux linkage equation is

$$\lambda_{abcf} = L_{abcf} i_{abcf} + \lambda_{PMabcf}.$$

Where $L_f = (2\Delta - \Delta^2)(L_m + L_l)$, $L_{phase} = L_m + L_l$ and L_{abcf} is

$$\begin{bmatrix} L_{phase} - L_f & -\frac{1-\Delta}{2}L_m & -\frac{1-\Delta}{2}L_m & L_f - \Delta L_{phase} \\ -\frac{1-\Delta}{2}L_m & L_m + L_l & -\frac{1}{2}L_m & -\frac{\Delta}{2}L_m \\ -\frac{1-\Delta}{2}L_m & -\frac{1}{2}L_m & L_m + L_l & -\frac{\Delta}{2}L_m \\ L_f - \Delta L_{phase} & -\frac{\Delta}{2}L_m & -\frac{\Delta}{2}L_m & -L_f + 2\Delta L_{phase} \end{bmatrix}$$

, the fault i_f is derived with

$$-(R_f + \Delta r s)i_f + R_f i_a = \frac{d\lambda_f}{dt},$$

where

$$\lambda_f = (L_f - \Delta(\frac{L_m}{2} + L_l))i_a + (-L_f + 2\Delta L_{phase})i_f + \Delta\lambda_{PM} \cos \theta.$$

Then fault i_f current can be represented as following at steady state:

$$i_f = \frac{bd + ac\omega_e}{a^2\omega_e^2 + b^2} \sin \theta + \frac{bc - ad\omega_e}{a^2\omega_e^2 + b^2} \cos \theta.$$

The coupled flux-linkage from the fault circuit to machine main phase circuit in $\alpha\beta$ frame is :

$$\begin{bmatrix} \lambda_{\alpha f} \\ \lambda_{\beta f} \end{bmatrix} = \frac{2}{3}(L_f - \Delta(\frac{L_m}{2} + L_l)) \begin{bmatrix} \frac{bd+ac\omega_e}{a^2\omega_e^2+b^2} \sin \theta + \frac{bc-ad\omega_e}{a^2\omega_e^2+b^2} \cos \theta \\ 0 \end{bmatrix}.$$

The flux linkage in $\alpha\beta$ frame is then decomposed into positive and negative sequence for applying dq transformation, and after that the voltage induced by fault flux-linkage in dq reference frame is :

$$\begin{bmatrix} V_{df}^+ \\ V_{qf}^+ \\ V_{df}^- \\ V_{qf}^- \end{bmatrix} = \frac{(L_f - \Delta(\frac{L_m}{2} + L_l))\omega_e}{3(b^2 + a^2\omega_e^2)} \begin{bmatrix} bd + ac\omega_e \\ bc - ad\omega_e \\ bd + ac\omega_e \\ -bc + ad\omega_e \end{bmatrix}, \quad (7)$$

With the following parameters

$$\begin{aligned} a &= -L_f + 2\Delta L_{phase}, \\ b &= R_f + \Delta r_s, \\ c &= (L_f - \Delta(\frac{L_m}{2} + L_l))i_s\omega_e, \\ d &= \Delta\lambda_{PM}\omega_e - R_f i_s. \end{aligned}$$

The machine full mathematic model can be achieved by using equation (5)-(7), which including the healthy phase part and inter-turn short circuit part:

$$\begin{aligned} V_{dq}^+ &= rI_{dq}^+ + \omega_e J \lambda_{dq}^+ + \frac{d\lambda_{dq}^+}{dt} \\ &= rI_{dq}^+ + \omega_e J L_{ss} I_{dq}^+ + \frac{1}{3} \Delta_m \omega_e J I_{dq}^+ \\ &\quad + \frac{1}{3} \Delta_m \omega_e \begin{bmatrix} 0 & 1 \\ 1 & 0 \end{bmatrix} I_{dq}^+ + \omega_e \lambda_{PM} (1 - \frac{\Delta}{3}) \begin{bmatrix} 0 \\ 1 \end{bmatrix} \\ &\quad + L_{ss} \frac{dI_{dq}^+}{dt} + L_{\alpha\alpha} \frac{dI_{dq}^+}{dt} + \begin{bmatrix} V_{df}^+ \\ V_{qf}^+ \end{bmatrix}, \end{aligned} \quad (8)$$

and

$$\begin{aligned} V_{dq}^- &= rI_{dq}^- - \omega_e J \lambda_{dq}^- + \frac{d\lambda_{dq}^-}{dt} \\ &= rI_{dq}^- - \omega_e J L_{ss} I_{dq}^- - \frac{1}{3} \Delta_m \omega_e J I_{dq}^- \\ &\quad + \frac{1}{3} \Delta_m \omega_e \begin{bmatrix} 0 & -1 \\ -1 & 0 \end{bmatrix} I_{dq}^- + \omega_e \lambda_{PM} \frac{\Delta}{3} \begin{bmatrix} 0 \\ 1 \end{bmatrix} \\ &\quad + L_{ss} \frac{dI_{dq}^-}{dt} + L_{\beta\beta} \frac{dI_{dq}^-}{dt} + \begin{bmatrix} V_{df}^- \\ V_{qf}^- \end{bmatrix}. \end{aligned} \quad (9)$$

The output electromagnetic torque under $i_d^+ = i_d^- = 0$ is shown in (10) as following, which contains positive alignment torque, a second order component caused by the back-emf in q-axis of negative sequence, and a torque due the back-emf in short circuit turns $-\omega_e \Delta \lambda_m \sin \theta$ and fault current i_f .

$$T_e = \frac{3}{2} P \lambda_m [(1 - \frac{\Delta}{3} + \frac{\Delta}{3} \cos 2\theta) i_{qe}^+ - \Delta i_f \sin \theta] \quad (10)$$

From equation (11), the short circuit fault can also be further detected by observing the controller negative sequence output voltage by controlling the negative sequence current to zero.

$$\begin{aligned} V_{dq}^- &= \frac{1}{3} \Delta_m \omega_e \begin{bmatrix} 0 & -1 \\ -1 & 0 \end{bmatrix} I_{dq}^+ + \omega_e \lambda_{PM} \frac{\Delta}{3} \begin{bmatrix} 0 \\ 1 \end{bmatrix} \\ &\quad + \begin{bmatrix} V_{df}^- \\ V_{qf}^- \end{bmatrix} \end{aligned} \quad (11)$$

V. DUAL INVERTER DRIVE TOPOLOGY FOR SIX-PHASE FSPM MACHINE

In order to further improve the reliability of electric drive for FSPM machine, a dual inverter drive topology is proposed by splitting the machine into two three phase sets which is illustrated in Fig. 11. Each of the three phase set is independently controlled by one VSI and is shown in Fig. 12, therefore higher fault tolerant

capability and reliability is achieved in case of losing machine phase winding or power inverter leg.

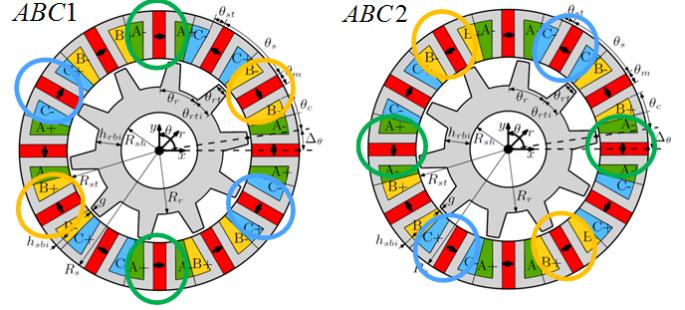


Figure 11: The dual three phase set from separated FSPM machine stator winding.

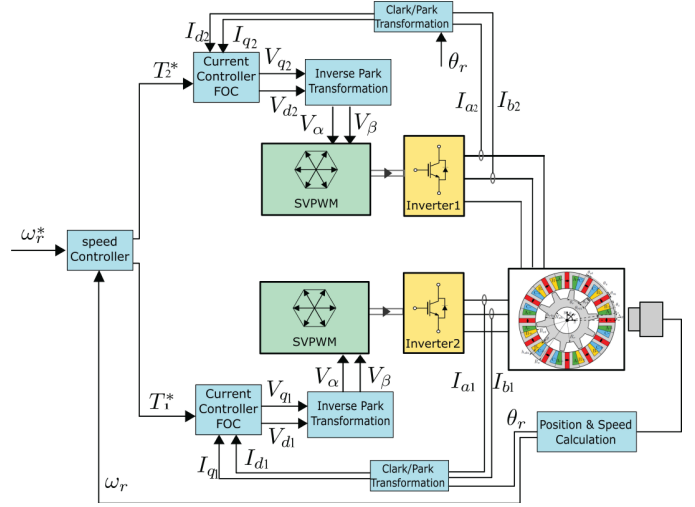


Figure 12: Dual inverter drive algorithm with separated FSPM machine winding.

In addition to that, advantages are accompanying, such as lower risk is guaranteed due to smaller back-emf induced by lower PM flux-linkage in case of inter-turn short circuit. Apart from that, less i_d current is required when applying field weakening control, thus higher speed range might be achieved within certain voltage and current limitation of both VSI and electric machine. Furthermore, less i_d current also gives advantages on minimizing machine resistive losses and VSI losses.

A. Pseudo-Park transformation of each three phase set under MTPA operation region

The back-emf of the separated FSPM machine are investigated and PM flux-linkage for both of three phase set contain second harmonic part which compensates each other, therefore there is no second order component before separation. The existence of second harmonic back-emf in each of the three phase set results in an requirement of two brushless dc (BLDC) machine

operation. Generally, rectangular waveform current is injected with two phase conduction at each commutation cycle.

Taking advantage of the space-vector control algorithm, which allows direct current and flux regulation as well as speed, position control. The ordinary Park transformation is not applicable since back-emf in d-axis is none zero anymore. Thus an extended transformation matrix T_{pp} is created to force zero back-emf on d-axis, which means PM back-emf only exist on q-axis, and after that vector control becomes capable [30]–[32]. The extend matrix is a Park-like or Pseudo-Park transformation, where $\lambda'_{\alpha\beta 0PM}$ and λ'_{dq0PM} are spatial derivative in stationary and Pseudo-Park dq reference frame respectively. The summation of rotor electric angel and displacement angle becomes the position of new dq frame.

$$\begin{bmatrix} \lambda'_{\alpha PM}(\theta) \\ \lambda'_{\beta PM}(\theta) \\ \lambda'_{0PM}(\theta) \end{bmatrix} = T_{pp} \begin{bmatrix} \lambda'_{dPM}(\theta) \\ \lambda'_{qPM}(\theta) \\ \lambda'_{0PM}(\theta) \end{bmatrix},$$

$$T_{pp} = \begin{bmatrix} \cos(\theta + \mu) & -\sin(\theta + \mu) & 0 \\ \sin(\theta + \mu) & \cos(\theta + \mu) & 0 \\ 0 & 0 & 1 \end{bmatrix}.$$

Where $\lambda'_{dPM}(\theta) = 0$ and

$$\begin{cases} \sin(\theta + \mu) = \frac{-\lambda'_{\alpha PM}(\theta)}{\sqrt{\lambda'_{\alpha PM}(\theta)^2 + \lambda'_{\beta PM}(\theta)^2}} \\ \sin(\theta + \mu) = \frac{\lambda'_{\beta PM}(\theta)}{\sqrt{\lambda'_{\alpha PM}(\theta)^2 + \lambda'_{\beta PM}(\theta)^2}} \\ \lambda'_{qPM}(\theta) = \sqrt{\lambda'_{\alpha PM}(\theta)^2 + \lambda'_{\beta PM}(\theta)^2} \\ \theta(t) + \mu(t) = \arctan 2(\lambda'_{\alpha PM}(\theta), \lambda'_{\beta PM}(\theta)) \end{cases}.$$

The position of new dq frame is calculated in previous equation, where spatial derivative of flux-linkage $\lambda'_{qPM}(\theta)$ in q-axis is not an constant value but periodic function due to second harmonic content in back-emf. With the obtained flux-linkage, PM induced back-emf and the dynamic rotating speed of the Pseudo-Park transformed dq reference frame, the entire machine model can be derived in a similar form of BLAC machine model, where dq voltage and output electromagnetic torque are represented as (12). Maximum torque per ampere (MTPA) operation can be achieved once the d-axis current is controlled to zero value and only q-axis current exists which is in line with BLAC machine vector

control.

$$\begin{aligned} V_d &= R_s i_d + L_d \frac{di_d}{dt} - \frac{d(\theta(t) + \mu(t))}{dt} L_q i_q, \\ V_q &= R_s i_q + L_q \frac{di_q}{dt} + \frac{d(\theta(t) + \mu(t))}{dt} L_d i_d + \omega_e \lambda'_{qPM}(\theta), \\ V_0 &= \omega_e \lambda'_{0PM}(\theta), \\ T_e &= \frac{3}{2} \frac{P}{2} \lambda'_{qPM}(\theta) i_q. \end{aligned} \quad (12)$$

B. Dual three phase machine MTPA and Field weakening operation

After separation, each of the three phase set contains two coils rather than four per phase winding, thus the machine parameters are changed where both phase resistance and PM flux-linkage are halved, the inductance becomes one quarter of its original. The dual three phase stator winding are treated in phase and the corresponding two new dq-axis are assumed very close to each other for simplicity of parameter definition. Therefore the dq-axis inductances of dual three phase machine are assumed to be equal as they have the same winding topology and turns number. Thus $L_{d1} = L_{d2} = 1/4 L_d = M_{d12} = M_d = M_{d21}$ and $L_{q1} = L_{q2} = 1/4 L_q = M_{q12} = M_q = M_{q21}$, and the machine equation becomes equation (13):

$$\begin{aligned} \lambda_{d12} &= \begin{bmatrix} L_{d1} i_{d1} \\ L_{d2} i_{d2} \end{bmatrix} + M_d \begin{bmatrix} i_{d2} \\ i_{d1} \end{bmatrix}, \\ \lambda_{q12} &= \begin{bmatrix} L_{q1} i_{q1} \\ L_{q2} i_{q2} \end{bmatrix} + M_q \begin{bmatrix} i_{q2} \\ i_{q1} \end{bmatrix}, \\ V_{d12} &= R_s i_{d12} + \frac{d}{dt} \lambda_{d12} - \omega_{new} \lambda_{q12}, \\ V_{q12} &= R_s i_{q12} + \frac{d}{dt} \lambda_{q12} + \omega_{new} \lambda_{d12} + \omega_e \lambda'_{q12PM}(\theta). \end{aligned} \quad (13)$$

The current command of dual VSI drive in Fig. 12 is directly from speed controller which contains a torque divider and will distribute equal i_q to both controller. Similar to i_q current, i_d current is also regulated to zero before base speed under MTPA region, or distributed with equal negative reference value to achieve same field weakening property. Then for each VSI, the voltage limitation satisfy:

$$(\omega_e L_d i_d + \omega_e \lambda_{PM})^2 + (-\omega_e L_q i_q)^2 \leq \left(\frac{2V_{dc}}{\sqrt{3}}\right)^2. \quad (14)$$

When field weakening is applied in dual three phase machine, d-axis currents can be less negative or even zero with same q-axis current in case of generating same torque. Therefore, less resistive losses are generated by

i_d current.

$$i_d = \frac{\sqrt{\left(\frac{2V_{dc}}{\sqrt{3}\omega_e}\right)^2 - (L_q i_q)^2} - \lambda_{PM}}{L_d}$$

With equation (14), which is illustrated in Fig. 13. We can derived that the center of voltage limit circle is unchanged, however the radius is increased with same electrical frequency, thus higher speed range is achieved with splitted machine winding and dual inverter drive algorithm.

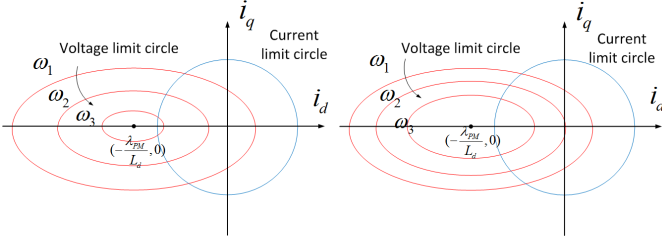


Figure 13: Voltage and current limit circle of three phase machine and splitted phase machine.

As one alternative approach, each of three phase set can also be controlled in two dq frame which are related to 1st and 2nd harmonic in the split phase flux-linkage. The control algorithm is illustrated in Fig. 14, where same flux-linkage are on d_1 -axis for both of three phase set due to same fundamental harmonic and opposite flux-linkage are on d_2 -axis because of opposite 2nd order harmonic. Therefore, when applying field weakening, the i_{d2} in both three phase set also required opposite current and this can be achieved by two PI current controller for V_d or V_q in one set.

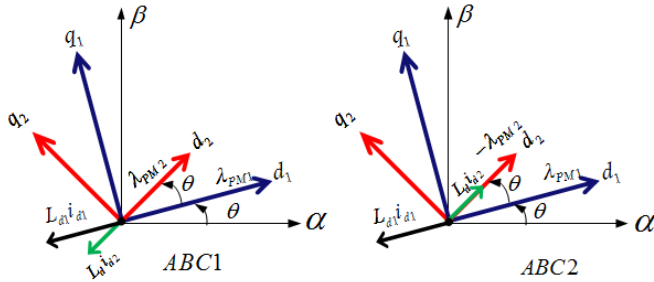


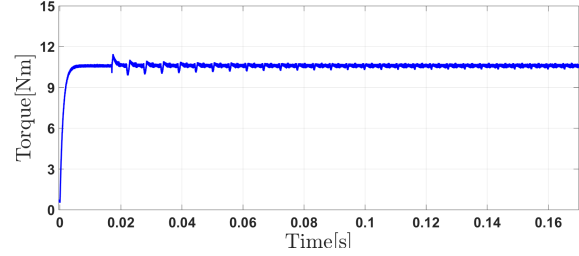
Figure 14: The alternative harmonic based dq reference frame derived from fundamental and 2nd harmonic flux-linkage used for MTPA and field weakening.

VI. SIMULATION RESULTS

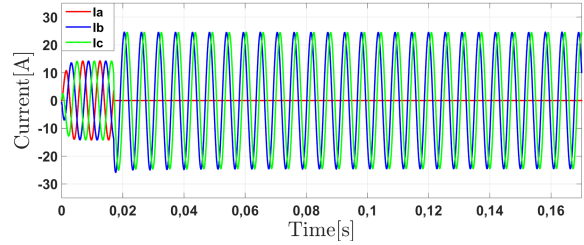
In simulation of phase winding open circuit fault, a 450 V DC source is used to supply the three-phase inverter with a 0.4 A hysteresis band limitation. The FSPM machine is first speed up to 1140 rpm and then a 10 Nm load torque is applied, after that two phase leg

A transistors are turned off and phase A is open circuit at 0.017 s.

In Fig. 15 (a), it can be seen that the output torque is fluctuating immediately following the open-circuit fault, because of the capacitor voltage balancing control algorithm which influences the q-axis current command value. The phase B and C current values are increased with $\sqrt{3}$ times and are phase shifted with 30° electrical to preserve the same torque, which is shown in Fig. 15 (b).



(a)



(b)

Figure 15: (a) Output torque response and (b) Three-phase current response with phase A open-circuit fault at 0.017 s

The terminal voltage of phase winding A, as illustrated in Fig. 16 (a) is a pulse-width modulated waveform before the fault, and becomes a sinusoidal voltage waveform which is induced by the other two phase currents and the PM flux-linkage after a fault has occurred. From Fig. 16 (b), it can be concluded that the both capacitor voltages are not drifting with voltage balancing control and only varies due to charging and discharging from the zero sequence current.

In simulation of phase winding inter turn short circuit fault, the fault ratio Δ is set to be 0.3. The FSPM machine is first speed up to 1140 rpm and then a 5 Nm load torque is applied. In Fig. 17 (a), large fault current is flowing through the short path because of back-emf induced by coupled flux-linkage. This fault current generates a pulsating torque component which is added to the main output torque and illustrated in Fig. 17 (b). In Fig. 18, it can be observed, both negative sequence dq-axis current and positive sequence d-axis current are regulated to zero to avoid negative sequence current.

Fig. 19 shows three phase supply voltage which contains 12 V negative sequence content due to voltage in V_{dq}^- and 113 V in V_{dq}^+ that are observed from sequence analyzer.

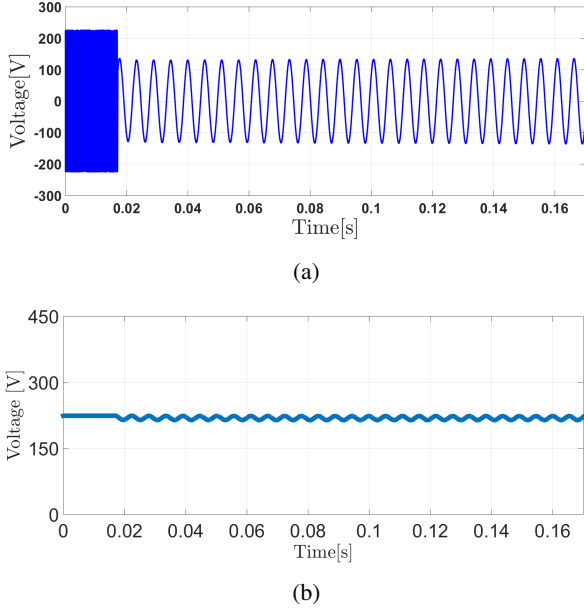


Figure 16: (a) Phase winding A terminal voltage and (b) Lower capacitor voltage with phase A open-circuit fault at 0.017 s

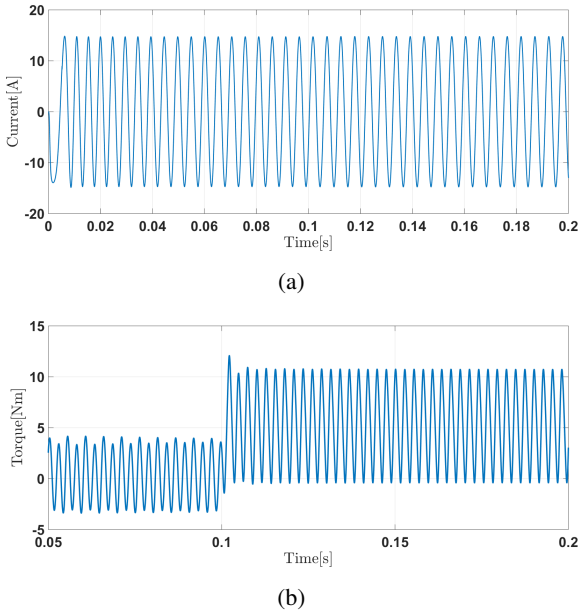


Figure 17: (a) Fault current flowing in inter turn short circuit path and (b) Output torque when one third of phase A winding is shorted.

In simulation of dual three phase drive, the FSPM machine is also first speed up to 1140 rpm and then applying a 10 Nm load torque. The back-emf of first

set in dq-axis is shown in Fig. 21, where $V_{back-q12}$ perform a periodic waveform due to second harmonic in three phase and $V_{back-d12}$ is forced to zero with the specific pseudo-Park transformation. Fig. 20 shows six-phase current in dual three phase set which are all in phase with its phase back-emf waveform to achieve maximum torque per ampere ratio.

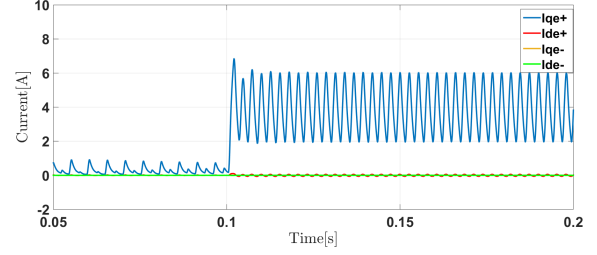


Figure 18: Dq-axis current in positive and negative sequence reference frame when one third of phase A winding is shorted.

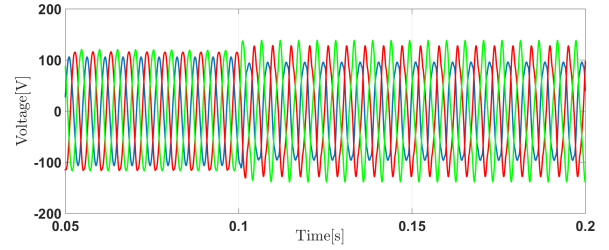


Figure 19: Three phase voltage which contains 12 V negative sequence component and 113 V positive sequence component when one third of phase A winding is shorted

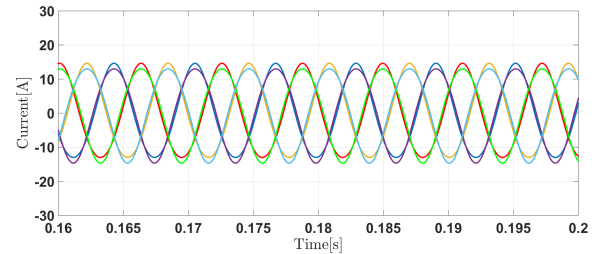


Figure 20: Six phase current in the dual three phase FSPM machine.

For field weakening application, machine is speed up to 5000 rpm and then 10 Nm load torque is applied. Due to high electrical frequency, i_d is regulated to negative value thus to reduce back-emf in normal three phase machine, and i_{d12} could continually kept zero in dual three phase drive since PM flux-linkage and back-emf is halved. i_{q12} current in dual three phase drive is maintained the same as normal i_q because both torque constant and torque command for each three phase set

are halved. The torque output and i_{q12} are shown in Fig. 22 and Fig. 23.

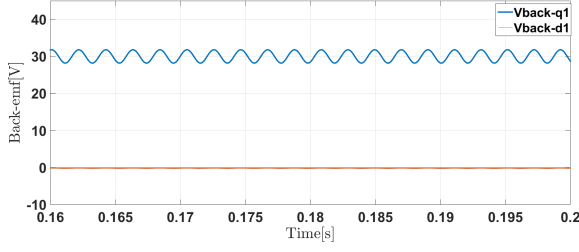


Figure 21: Dq-axis back-emf in pseudo-park reference frame for one of three phase set.

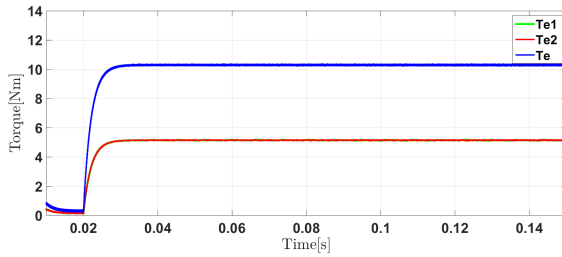


Figure 22: Output torque from both of three phase set and total composed torque.

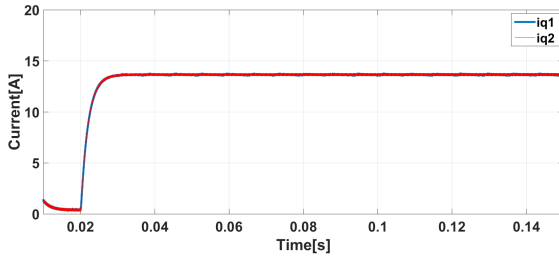


Figure 23: Q-axis current for each of three phase set in the dual drive.

VII. EXPERIMENTAL RESULTS

For experimental verification of the torque control algorithm during open-circuit fault and field weakening characteristics of three phase FSPM machine, a test setup, illustrated in Fig. 24 is built up. The setup consists two three phase VSIs, one FSPM machine prototype, one load machine (Bosch B4.170.050) and a DC power supply. Two VSIs are operated to drive both machine with 10 KHz switching frequency. Rotor position and speed information is obtained from the resolver of FSPM machine, where analog signals are converted by a programmable A/D converter. The control of both power inverter is implemented in dSpace (CP1104) and Simulink platforms, where rotation speed, phase current and thermal control are realized in discrete PI controller.

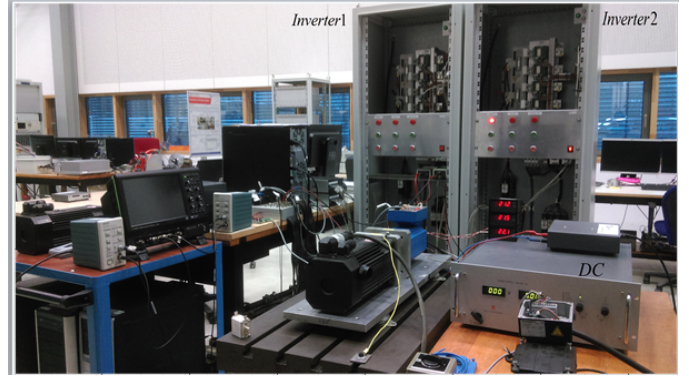
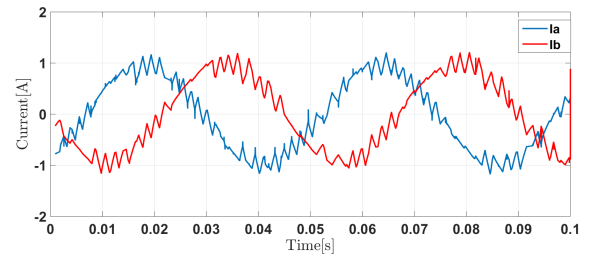
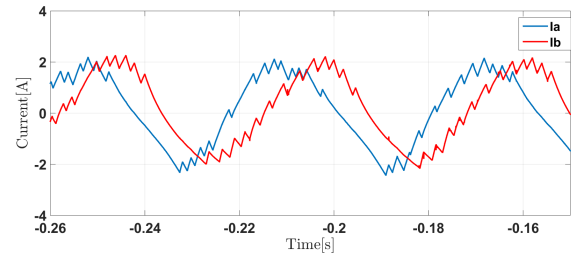


Figure 24: Experimental setups where PMSM and FSPM machine are mechanically coupled together.



(a)



(b)

Figure 25: (a) Phase current before and (b) after phase C open-circuit fault.

The phase winding open-circuit fault is realized by disconnecting phase C supply line. Two extra capacitor bank are used in parallel with the inverter DC-link, and the middle point of two capacitor is connected to neutral point of FSPM machine via a small inductor to prevent high frequency zero sequence current. Three external 50 mH inductors are series connected with three phase winding of FSPM machine to reduce current ripple, as the currents are regulated in delta/Hysteresis control where sampling frequency is 10 KHz. When testing, the machine is supplied with 60 V DC voltage and rotated at 130 rpm with 1 Nm applied by load machine. The measured current and middle point voltage are shown in Fig. 25 - Fig. 27, where phase current at open circuit fault is 1.7 times higher than normal operation. Therefore it verifies the torque control and capacitor voltage balancing algorithm.

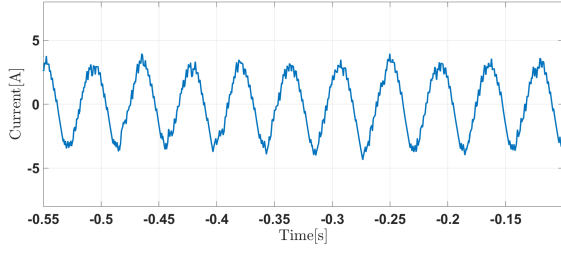


Figure 26: Zero sequence current during phase C open-circuit fault.

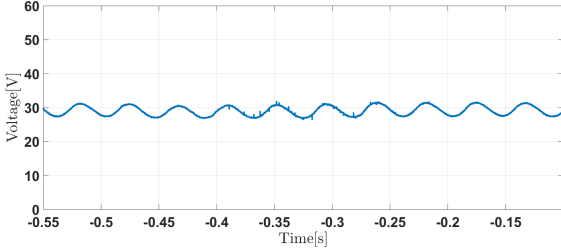


Figure 27: Upper capacitor voltage during phase C open-circuit fault.

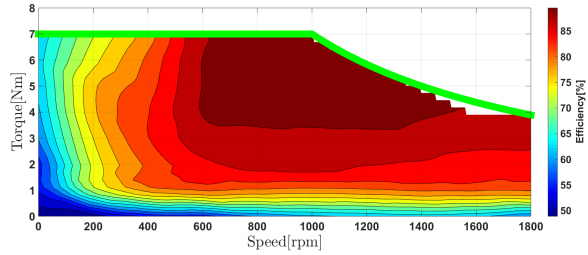


Figure 28: Machine efficiency map under MTPA and field weakening region.

The field weakening operation for three phase PMSM is tested with 100 V DC supply, the based speed is defined with 1000 rpm with 7 Nm torque and the top is speed is 1800 rpm. Machine efficiency is then measured within area of torque-speed curve shown by the green line in Fig. 28, the measuring temperature condition is under steady state operation where coil temperature is around 80°C with 1°C increasing per half hour. The efficiency η is calculated from the ratio of output mechanical power $P_{mech} = T_{out}\omega_{mech}$ to machine input real power $P_{input} = \frac{3}{2} |\vec{V}_s| |\vec{i}_s| \cos \varphi$ through every test point (200 rpm and 1 Nm per step). From Fig. 28, it can be observed that the machine has a high efficiency under field weakening region which proves the negative d-axis current is enough to achieve high speed operation with high efficiency.

VIII. CONCLUSION

The electric drive system for three phase FSPM machine is developed by implementing field-oriented control (FOC) and space-vector pulse-width modulation (SVPWM) strategies in both MTPA and field weakening region, where efficiency contour obtained from measurement shows negative i_d current is enough in field weakening region.

For higher availability of the FSPM machine drive in case of open-circuit fault, one VSI topology is applied which provides a path to flow the zero sequence current. Current vector control is used to obtain the same MMF for preserving the output electromagnetic torque. Because of zero sequence current, the capacitor middle point voltage is fluctuated and the capacitor voltage balancing control is applied to maintain this voltage. Simulation and experimental results show that the torque is maintained after fault happening with slight variation, and that the capacitor voltage is balanced.

The inter-turn short circuit model in rotor reference frame is built up, which contains a healthy phase model and fault circuit model. Because of asymmetry of phase parameters, negative sequence component is injected, and the output torque performs a large ripple because of short-circuit fault current and negative sequence back-emf.

To further enhance reliability, the FSPM machine is split into dual three phase machine which are controlled by two VSIs. Because of the 2nd harmonic in each set, pseudo-Park transformation is applied in MTPA region. In addition, voltage limit circle of dual drive shows a high speed range capability and lower i_d current requirement, which reduces i_d copper losses. Furthermore, an alternative harmonic based dq reference frame is proposed specially for field weakening of the 2nd harmonic content.

REFERENCES

- [1] M. Ehsani, Y. Gao, and J. Miller, "Hybrid Electric Vehicles: Architecture and Motor Drives," *Proceedings of the IEEE*, vol. 95, no. 4, pp. 719–728, April 2007.
- [2] A. Thomas, Z. Zhu, R. Owen, G. Jewell, and D. Howe, "Multi-Phase Flux-Switching Permanent Magnet Brushless Machine for Aerospace Application," in *Industry Applications Society Annual Meeting, 2008. IAS '08. IEEE*, Oct 2008, pp. 1–8.
- [3] A. Thomas, Z. Zhu, and G. Jewell, "Comparison of Flux Switching and Surface Mounted Permanent Magnet Generators for Aerospace Applications," in *Power Electronics, Machines and Drives (PEMD 2010), 5th IET International Conference on*, April 2010, pp. 1–5.
- [4] C. Sanabria-Walter, H. Polinder, and J. Ferreira, "High-Torque-Density High-Efficiency Flux-Switching PM Machine for Aerospace Applications," *Emerging and Selected Topics in Power Electronics, IEEE Journal of*, vol. 1, no. 4, pp. 327–336, Dec 2013.

- [5] C. Sanabria-Walter, "Design of a 600kW Ring-Type Direct-Drive Flux-Switching Permanent Magnet Machine for Aerospace Main Propulsion," in *Power Electronics and Applications (EPE'14-ECCE Europe)*, 2014 16th European Conference on, Aug 2014, pp. 1–10.
- [6] Y. Tang, E. Motoasca, J. J. H. Paulides, and E. A. Lomonova, "Comparison of flux switching machines and permanent magnet synchronous machines in an in wheel traction application," *COMPEL - The international journal for computation and mathematics in electrical and electronic engineering*, vol. 32, no. 1, pp. 153–165, 2012.
- [7] E. Ilhan, "Hybrid Modeling Techniques Embracing Permanent-Magnet-Biased Salient Machines," Ph.D. dissertation, Department of Electrical Engineering, Eindhoven University of Technology, 2014.
- [8] E. Ilhan, J. J. H. Paulides, and E. A. Lomonova, "Fast Torque Estimation of In-Wheel Parallel Flux Switching Machines for Hybrid Trucks," *COMPEL - The international journal for computation and mathematics in electrical and electronic engineering*, vol. 31, no. 1, pp. 40–53, 2011.
- [9] S. Li, Y. Li, and B. Sarlioglu, "Performance Assessment of High-speed Flux-switching Permanent Magnet Machine Using Ferrite and Rare Earth Permanent Magnet Materials," in *Electric Power Components and Systems*, 2015, pp. 711–720.
- [10] Z. Zhu and D. Howe, "Electrical Machines and Drives for Electric, Hybrid, and Fuel Cell Vehicles," *Proceedings of the IEEE*, vol. 95, no. 4, pp. 746–765, April 2007.
- [11] B. Welchko, T. Lipo, T. Jahns, and S. Schulz, "Fault Tolerant Three-Phase AC Motor Drive Topologies; a Comparison of Features, Cost, and Limitations," in *Electric Machines and Drives Conference, 2003. IEMDC'03. IEEE International*, vol. 1, June 2003, pp. 539–546 vol.1.
- [12] J. Espina, A. Arias, J. Balcells, and C. Ortega, "Speed Anti-Windup PI Strategies Review for Field Oriented Control of Permanent Magnet Synchronous Machines," in *Compatibility and Power Electronics, 2009. CPE '09.*, May 2009, pp. 279–285.
- [13] S. Huang, Z. Chen, K. Huang, and J. Gao, "Maximum Torque per Ampere and Flux-Weakening Control for PMSM Based on Curve Fitting," in *Vehicle Power and Propulsion Conference (VPPC)*, 2010 IEEE, Sept 2010, pp. 1–5.
- [14] J. Xuewu and L. Yingchao, "Field weakening control of pmsm used in an electric power steering system," in *Electric Information and Control Engineering (ICEICE)*, 2011 International Conference on, April 2011, pp. 2194–2199.
- [15] C. Zhang, F. Wang, Z. Wang, and J. Yang, "Analysis of stator winding inter-turn short circuit fault of pmsm for electric vehicle based on finite element simulation," in *Transportation Electrification Asia-Pacific (ITEC Asia-Pacific)*, 2014 IEEE Conference and Expo, Aug 2014, pp. 1–6.
- [16] B. Vaseghi, N. Takorabet, F. Meibody-Tabar, A. Djerdir, J. A. Farooq, and A. Miraoui, "Modeling and characterizing the inter-turn short circuit fault in pmsm," in *Electric Machines Drives Conference (IEMDC)*, 2011 IEEE International, May 2011, pp. 551–556.
- [17] Y. Lee and J.-I. Ha, "High efficiency dual inverter drives for a pmsm considering field weakening region," in *Power Electronics and Motion Control Conference (IPEMC)*, 2012 7th International, vol. 2, June 2012, pp. 1009–1014.
- [18] J. Karttunen, S. Kallio, P. Peltoniemi, P. Silventoinen, and O. Pyrhnen, "Dual three-phase permanent magnet synchronous machine supplied by two independent voltage source inverters," in *Power Electronics, Electrical Drives, Automation and Motion (SPEEDAM)*, 2012 International Symposium on, June 2012, pp. 741–747.
- [19] A. Tassarolo, C. Bassi, and D. Giulivo, "Performance of a high-power induction motor supplied by two in-phase voltage-source inverters," in *EUROCON - International Conference on Computer as a Tool (EUROCON)*, 2011 IEEE, April 2011, pp. 1–4.
- [20] Y. Zhao and T. A. Lipo, "Space vector pwm control of dual three-phase induction machine using vector space decomposition," *IEEE Transactions on Industry Applications*, vol. 31, no. 5, pp. 1100–1109, Sep 1995.
- [21] W. Hua and C. Ming, "Inductance Characteristics of 3-phase Flux-Switching Permanent Magnet Machine with Doubly-Salient Structure," in *Power Electronics and Motion Control Conference, 2006. IPEMC 2006. CES/IEEE 5th International*, vol. 3, Aug 2006, pp. 1–5.
- [22] J. H. Jr. and T. Miller, *Design of Brushless Permanent-Magnet Machines*. Motor Design Books LLC, 2010.
- [23] E. Ilhan, M. Kremers, E. Motoasca, J. J. H. Paulides, and E. A. Lomonova, "Sensitivity Analysis for Phase Inductances in Flux-Switching PM Machines," in *Electrical Machines (ICEM)*, 2012 XXth International Conference on, Sept 2012, pp. 763–768.
- [24] P. Krause, O. Wasynczuk, and S. Sudhoff, *Analysis of Electric Machinery and Drive Systems*, 2nd ed. Purdue: Wiley, 2002.
- [25] M. Zordan, P. Vas, M. Rashed, S. Bolognani, and M. Zigliotto, "Field-weakening in high-performance pmsm drives: a comparative analysis," in *Industry Applications Conference, 2000. Conference Record of the 2000 IEEE*, vol. 3, 2000, pp. 1718–1724 vol.3.
- [26] Y. Tang, J. J. H. Paulides, and E. A. Lomonova, "Field weakening performance of flux-switching machines for hybrid/electric vehicles," in *Ecological Vehicles and Renewable Energies (EVER)*, 2015 Tenth International Conference on, March 2015, pp. 1–10.
- [27] T.-H. Liu, J.-R. Fu, and T. Lipo, "A Strategy for Improving Reliability of Field-Oriented Controlled Induction Motor Drives," *Industry Applications, IEEE Transactions on*, vol. 29, no. 5, pp. 910–918, Sep 1993.
- [28] I. Jeong, K. Nam, B. G. Gu, and I. S. Jung, "Dynamic modeling for pmsm with internal turn short fault," in *Power Electronics and ECCE Asia (ICPE ECCE)*, 2011 IEEE 8th International Conference on, May 2011, pp. 2525–2528.
- [29] B. G. Gu, J.-H. Choi, and I. S. Jung, "A dynamic modeling and a fault detection scheme of a pmsm under an inter turn short," in *Vehicle Power and Propulsion Conference (VPPC)*, 2012 IEEE, Oct 2012, pp. 1074–1080.
- [30] D. Grenier, L. A. Dessaint, O. Akhrif, and J. P. Louis, "A park-like transformation for the study and the control of a nonsinusoidal brushless dc motor," in *Industrial Electronics, Control, and Instrumentation, 1995., Proceedings of the 1995 IEEE IECON 21st International Conference on*, vol. 2, Nov 1995, pp. 836–843 vol.2.
- [31] A. Lidozzi, L. Solero, F. Crescimbeni, and R. Burgos, "Vector control of trapezoidal back-emf pm machines using pseudo-park transformation," in *Power Electronics Specialists Conference, 2008. PESC 2008. IEEE*, June 2008, pp. 2167–2171.
- [32] D. Grenier and J. P. Louis, "Use of an extension of the park's transformation to determine control laws applied to a non-sinusoidal permanent magnet synchronous motor," in *Power Electronics and Applications, 1993., Fifth European Conference on*, Sep 1993, pp. 32–37 vol.6.

A Tightly Regulated PWM-PFM-PD Multiple Output DC-DC Converter

Mert Turhan, Marcel A.M. Hendrix, Jorge L. Duarte, Juan C. Castellanos and Julià Delos

e-mail: m.turhan@tue.nl; m.a.m.hendrix@tue.nl; j.l.duarte@tue.nl; j.Castellanos@tue.nl; j.delos-ayllon@tue.nl

Eindhoven University of Technology

Eindhoven, The Netherlands

Abstract—In this paper, a multiple output dc-dc converter is proposed. Pulse frequency modulation (PFM), pulse width modulation (PWM) and phase delay (PD) methods are used to regulate output voltages. Two of the output voltages are regulated by PWM, 2 of them by PFM, and the other one by PD. Five regulated outputs are obtained by using only two active switches. The switches can be operated at different switching frequencies. A hardware prototype was implemented that has 1.5V/0.5A, 3.3V/1A, 12V/0.5A, -12V/0.5A and 5V/1A outputs and the efficiency is 89% at the rated power.

Index Terms—dc-dc converter, multiple outputs, PWM-PD, PWM-PFM, PWM-PFM-PD

I. INTRODUCTION

Multiple output converters have been widely used where individual outputs are required. Their sizes and costs can be less than the individual converters. However, one of the main drawbacks of multiple output converters is cross regulation. They regulate only the output that is defined as master output; the other outputs depend on the load conditions [1]. Therefore, post regulators such as linear, magamp and synchronous switch regulators are used to adjust the additional outputs [2], [3]. The PWM-PFM converters use PFM in order to regulate the second output voltage [4], [5]. One of the converters operates in continuous conduction mode (CCM), and the other operates in discontinuous conduction mode (DCM). Both outputs can be controlled independently by modulating the duty cycle and the switching frequency of a single active switch. In addition, the work in [6] uses the PWM-PFM method to control both outputs. Instead of DCM, the second output is controlled by ZCS quasi resonant mode. The PWM-PD control method produces a regulated third output [7], [8]. In this case, two active switches are used. The active switches are operated at the same switching frequency to implement PD, and the PD enables to adjust the third output voltage. Some researchers have been using the PWM-PFM and the PWM-PD methods with isolated dc-dc converters [9]–[12]. However, more active switches are required to implement these converters. The work in [13] describes a PWM-PFM-PD control method, however this converter can adjust only three output voltages.

In this paper, a PWM-PFM-PD method for multiple output dc-dc converters is proposed. The proposed solution uses two active switches to adjust five-output voltages independently, as two active switches have five independent control parameters which are the duty cycle δ_1 and the switching frequency f_1

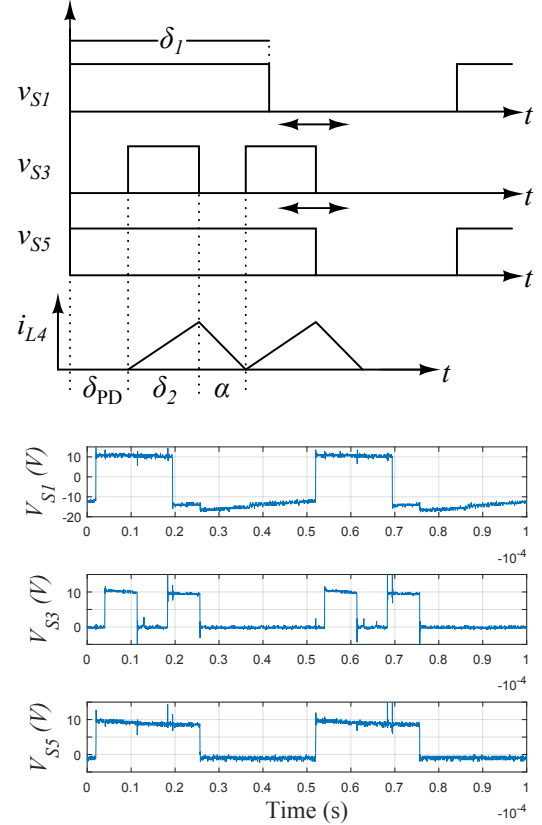


Fig. 1: (a) The waveforms of the applied square voltages to the first converter v_{S1} , the third converter v_{S3} , the fifth converter v_{S5} and (b) their experimental results. The waveforms of v_{S1} in Fig. 1a and Fig. 1b do not match up with each other because of the flyback transformer.

of the first gate signal, the duty cycle δ_2 and the switching frequency f_2 of the second gate signal and the phase delay δ_{PD} between the first and the second gate signals. Two of the outputs are adjusted using PWM in CCM, other two uses PFM in DCM, and one load is regulated by PD. As shown in Fig. 1, using DCM burst mode in one of the two switches enables the PD operation at the same switching frequency. In other words, the active switches do not need to operate at the same switching frequency to use the PD. One possible implementation of PWM-PF-PD controlled multiple output dc-dc converter is shown in Fig. 2.

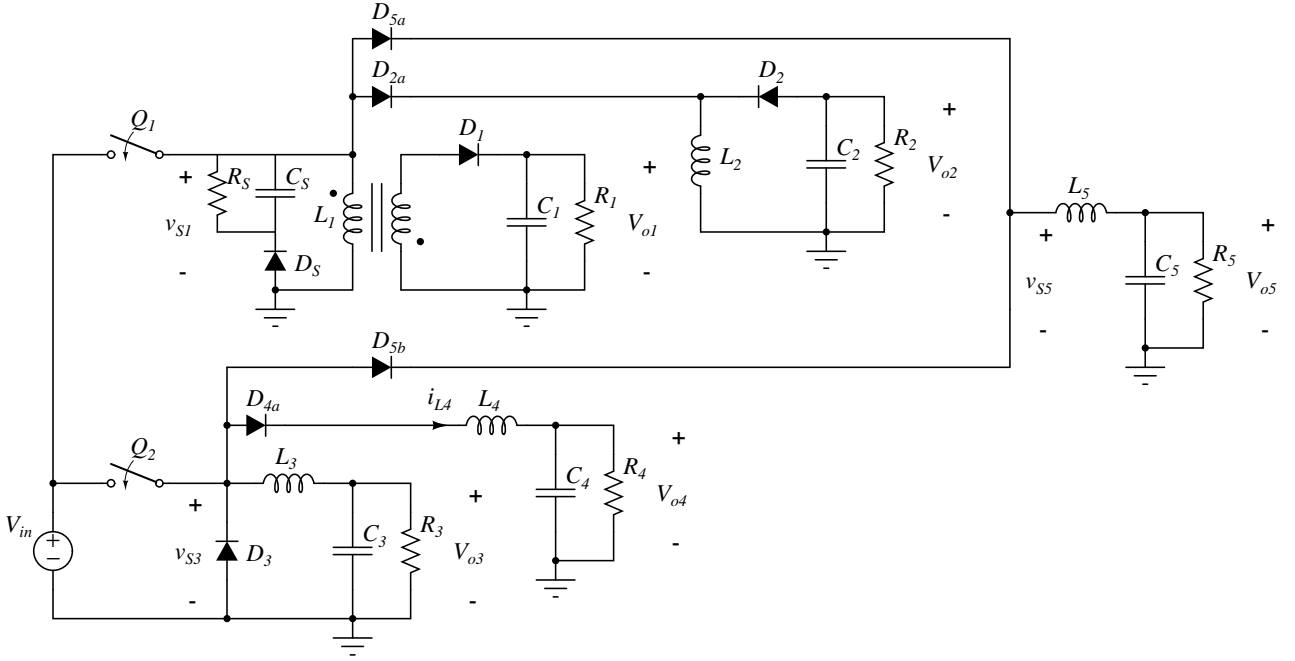


Fig. 2: One possible implementation of the proposed converter.

Section II describes the principle behind the PWM-PFM-PD converter. Section III presents the simulation and the experimental results. Conclusions are given in Section IV.

II. THEORY OF THE PRINCIPLE

The new method is based on a combination of the PWM-PFM and the PWM-PD methods. In order to understand the PWM-PFM-PD method, it is essential to know the PWM-PFM and the PWM-PD methods.

The PWM-PFM method for two-output dc-dc converters with one active switch was proposed in [4]. One output is controlled by PWM and the other output by PFM. One of the inductors is designed for CCM, and the other inductor for DCM as can be seen in Fig. 3. Then, while the duty cycle of the switch determines both output voltages, the switching frequency of the switch determines only one output voltage in DCM. Hence both output voltages can be regulated independently.

The PWM-PD method for three-output dc-dc converters with two active switches was presented in [7], [8]. It requires two square voltages to obtain the third square voltage as shown in Fig. 4a. As it can be seen in Fig. 4b, the first and the second output voltages are controlled by δ_1 and δ_2 , respectively. The third output are adjusted by the third duty cycle δ_3 , which is equal to the total of δ_{PD} and δ_2 . In order to use this method the switching frequencies of the active switches should be the same. Therefore changing the switching frequency to obtain yet another output is not possible.

In order to use the PD method with different frequencies, it is proposed that the second switch operates in burst mode. The second switch is synchronized to the first switch. There can be PD between the starting points of the signals as shown in Fig. 1a. The PD refers to the fifth output voltage V_{o5} . The

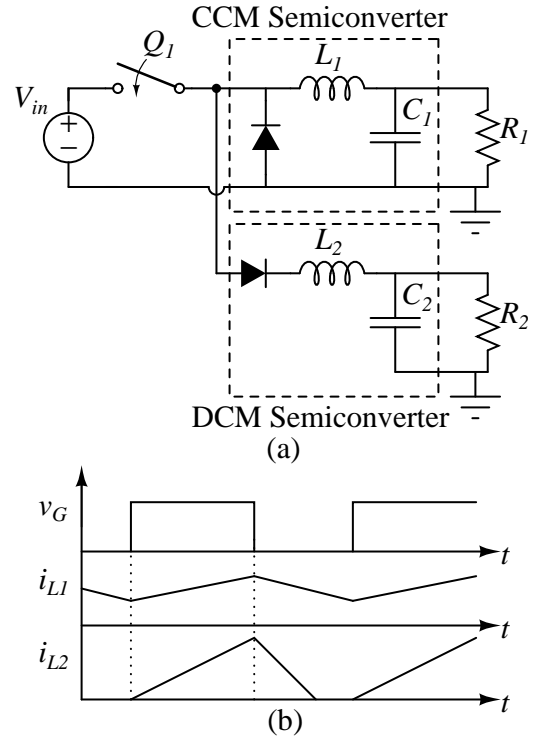


Fig. 3: (a) A two-output buck converter controlled by the PWM-PFM method and (b) the inductors current waveforms.

more this phase difference increases, the more V_{o5} increases. In burst mode, the time delay between two gate signals is determined by the demagnetizing period of the inductor as can be seen in Fig. 1b. When the inductor current drops to zero, the next signal is triggered.

Many different dc-dc converters such as buck, boost, buck-

TABLE I: Ideal conversion ratios of the proposed converter

	V_{o1}/V_{in}	V_{o2}/V_{in}	V_{o3}/V_{in}	V_{o4}/V_{in}	V_{o5}/V_{in}
control variables	$f(\delta_1)$	$f(\delta_1, f_1)$	$f(\delta_2)$	$f(\delta_2, f_2)$	$f(\delta_{PD}, \delta_2)$
Buck Converter	δ_1	$\frac{2}{1 + \sqrt{1 + 8L_2f_1/R_2\delta_1^2}}$	δ_2	$\frac{2}{1 + \sqrt{1 + 8L_4f_2R_4\delta_2^2}}$	$\delta_{PD} + \delta_2$
Boost Converter	$\frac{1}{1 - \delta_1}$	$\frac{1 + \sqrt{1 + 2R_2\delta_1^2/L_2f_1}}{2}$	$\frac{1}{1 - \delta_2}$	$\frac{1 + \sqrt{1 + 2R_4\delta_2^2/L_4f_2}}{2}$	$\frac{1}{1 - (\delta_{PD} + \delta_2)}$
Buck-Boost Converter	$-\frac{\delta_1}{1 - \delta_1}$	$-\frac{\delta_1}{\sqrt{2L_2f_1/R_2}}$	$-\frac{\delta_2}{1 - \delta_2}$	$-\frac{\delta_2}{\sqrt{2L_4f_2/R_4}}$	$-\frac{\delta_{PD} + \delta_2}{1 - (\delta_{PD} + \delta_2)}$
Flyback Converter	$\frac{N_1}{N_2} \frac{\delta_1}{1 - \delta_1}$	$\frac{N_1}{N_2} \frac{\delta_1}{\sqrt{2L_2f_1/R_2}}$	$\frac{N_1}{N_2} \frac{\delta_2}{1 - \delta_2}$	$\frac{N_1}{N_2} \frac{\delta_2}{\sqrt{2L_4f_2/R_4}}$	$-\frac{\delta_{PD} + \delta_2}{1 - (\delta_{PD} + \delta_2)}$

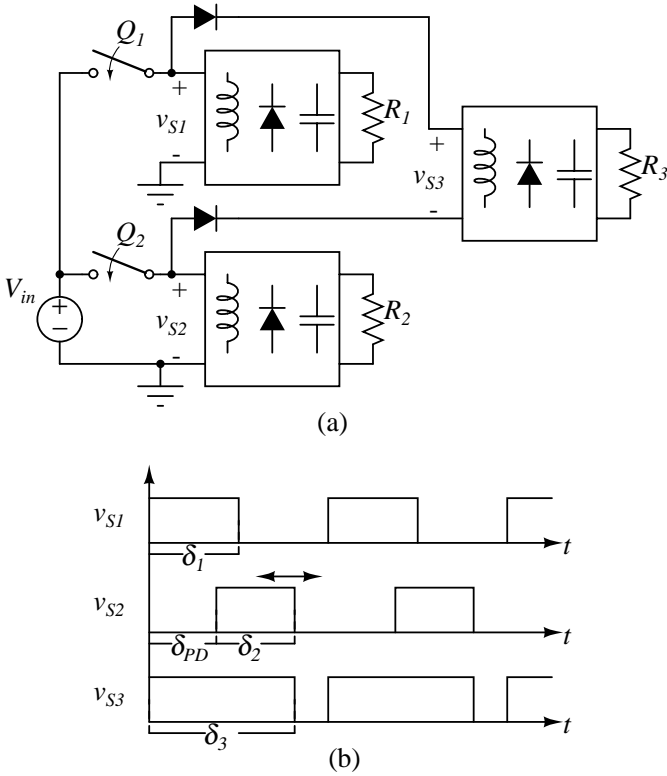


Fig. 4: (a) A three-output dc-dc converter controlled by the PWM-PD method and (b) its main waveforms.

boost and flyback converters can be used depending on requirements and design. The ideal conversion ratios of each output for different types of dc-dc converters are given in Table I.

III. SIMULATION AND EXPERIMENTAL RESULTS

A flyback, a buck-boost, and three buck converters were combined and designed as shown in Fig. 2. Fig. 1b shows

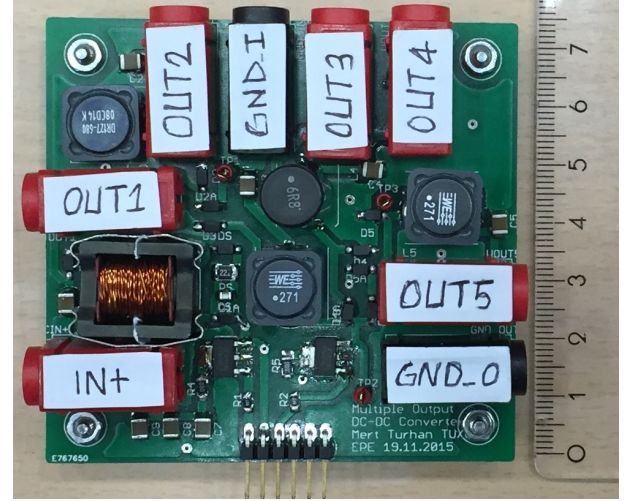


Fig. 5: Experimental setup.

the experimental waveforms of the switching nodes v_{S1} , v_{S3} and v_{S5} . The outputs are 1.5V/0.5A, 3.3V/1A, 12V/0.5A, -12V/0.5A and 5V/1A, respectively. A hardware prototype was built and tested in order to verify the simulation results as shown in Fig. 5. The parameters of the prototype are given in Table II. The measured efficiency was measured as 89% at the rated output power 21W. It should be noted that power loss of the control circuit and gate drivers is not included in the efficiency calculation.

δ_1 is used to control the first output voltage V_{o1} . If δ_1 is lower than the total of δ_2 together with δ_{PD} , the change of δ_1 does not affect V_{o5} as shown in Fig. 6a. In other words, V_{o5} is not independent of δ_1 when there is a gap between the gate signals of the first and the second active switches. However, δ_1 also affects the second output voltage V_{o2} as can be seen in Fig. 6a. f_1 is the control parameter of the second output to adjust V_{o2} as shown in Fig. 6b. At this time, f_1 alters the fourth output voltage V_{o4} since f_2 is synchronized to the first

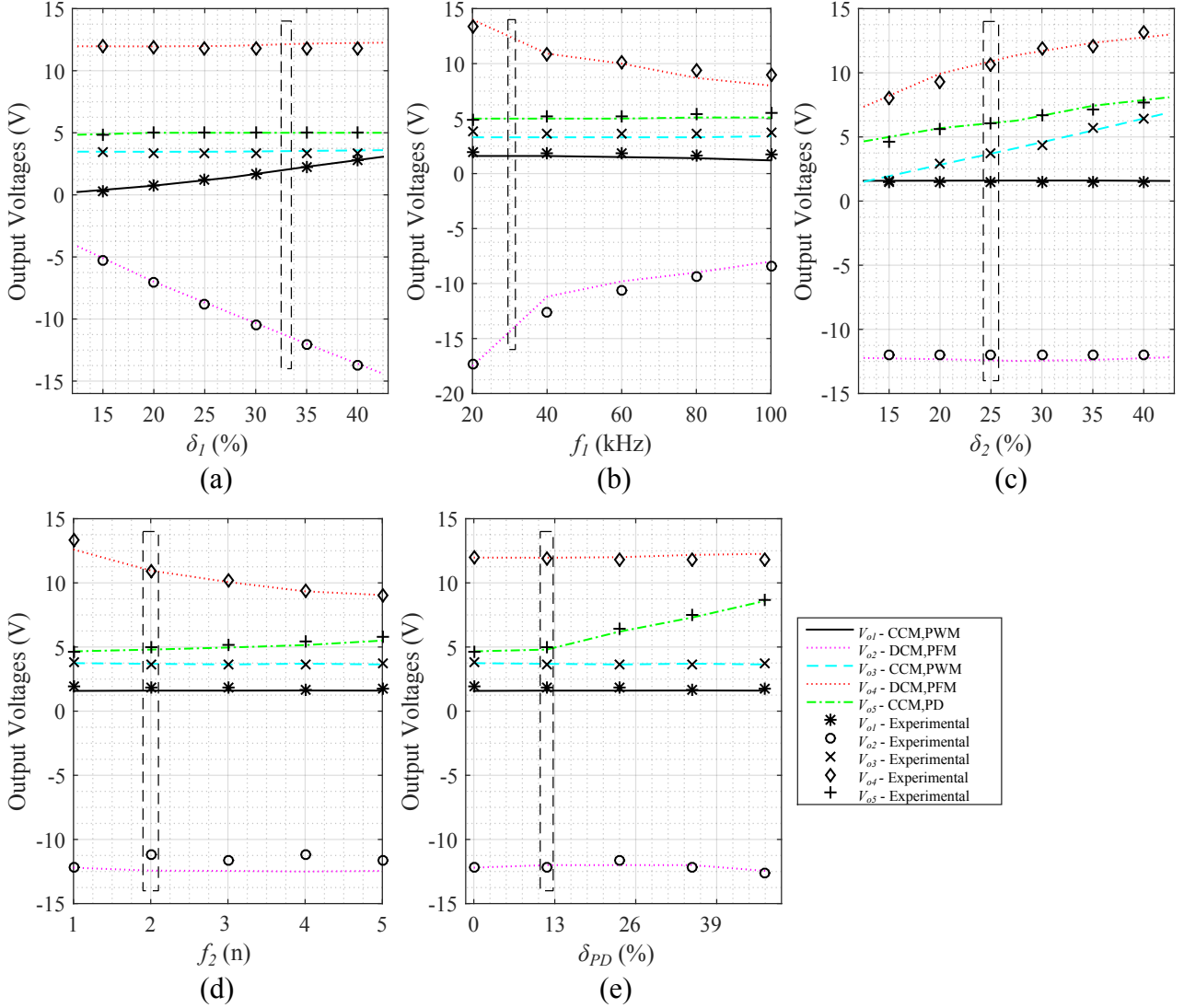


Fig. 6: Simulation and experimental results of output voltages versus (a) δ_1 , (b) δ_2 , (c) f_1 , (d) f_2 and (e) δ_{PD} . It should be noted that f_1 is 25 kHz and is constant in Fig. 6d. The dashed rectangles represent the desired operating points of the converter.

TABLE II: Parameters of the Experimental Prototype

Parameter	Value	Model
C_1, C_2, C_3, C_4, C_5	100 μ F	EMK325ABJ107MM-T
L_1	2000 μ H (turns ratio is 1/3.5)	self-produced
L_2	68 μ H	DR127-680-R
L_3, L_5	270 μ H	SRU1038-5R0Y
L_4	6.8 μ H	744750420068
Q_1, Q_2		ZXMN6A09GTA
$D_1, D_2, D_{2a}, D_3,$ D_{4a}, D_{5a}, D_{5b}		STPS2H100A

switching frequency. f_2 can be represented by

$$f_2 = n f_1. \quad (1)$$

n is the total number of pulses of V_{s3} during the period of V_{s1} . Fig. 6d show that f_2 controls V_{o4} independently, and it does not influence the other output voltages. δ_2 is used in order to control the third output voltage V_{o3} as can be seen in Fig. 6c.

Furthermore, δ_2 affects V_{o4} and V_{o5} marginally, but this can be counteracted in the controller. Phase delay control can be used in order to adjust V_{o5} independently as shown in Fig. 6e.

IV. CONCLUSION

A five-output dc-dc converter and the advanced PWM-PFM-PD control method are proposed in this paper. A prototype was built in order to verify the complex control method. The prototype was composed by a flyback, a buck-boost, and three buck converters. Furthermore, other combinations of dc-dc converters are possible to implement the proposed control method. The proposed converter uses only two active switches to control the five-output voltages, and the measured results show that the different outputs can be controlled independently.

V. ACKNOWLEDGEMENT

This research is supported by the Dutch Technology Foundation STW, which is the applied science division of NWO,

and the Technology Programme of the Ministry of Economic Affairs, Agriculture and Innovation.

REFERENCES

- [1] D. Maksimovic and R. Erickson, "Modeling of cross-regulation in multiple-output flyback converters," in *Applied Power Electronics Conference and Exposition, 1999. APEC '99. Fourteenth Annual*, vol. 2, Mar 1999, pp. 1066–1072 vol.2.
- [2] G. Levin, "A new secondary side post regulator (sspr) pwm controller for multiple output power supplies," in *Applied Power Electronics Conference and Exposition, 1995. APEC '95. Conference Proceedings 1995., Tenth Annual*, no. 0, Mar 1995, pp. 736–742 vol.2.
- [3] A. Ferreres, J. Carrasco, E. Maset, and J. Ejea, "Small-signal modeling of a controlled transformer parallel regulator as a multiple output converter high efficient post-regulator," *Power Electronics, IEEE Transactions on*, vol. 19, no. 1, pp. 183–191, Jan 2004.
- [4] J. Sebastian and J. Uceda, "The double converter: A fully regulated two-output dc-dc converter," *Power Electronics, IEEE Transactions on*, vol. PE-2, no. 3, pp. 239–246, July 1987.
- [5] H. Tacca, "Single-switch two-output flyback-forward converter operation," *Power Electronics, IEEE Transactions on*, vol. 13, no. 5, pp. 903–911, Sep 1998.
- [6] J. Sebastian, J. Uceda, M. Perez, M. Rico, and F. Aldana, "A very simple method to obtain one additional fully regulated output in zero-current-switched quasiresonant converters," in *Power Electronics Specialists Conference, 1990. PESC '90 Record., 21st Annual IEEE*, 1990, pp. 536–542.
- [7] A. Barrado, E. Olías, A. Roldán, R. Vazquez, and J. Pleite, "Multiple output dc/dc converters based on pwm-pulse delay control (pwm-pd)," in *Power Electronics Specialists Conference, 1999. PESC 99. 30th Annual IEEE*, vol. 2, 1999, pp. 1141–1145 vol.2.
- [8] A. Barrado, E. Olías, A. Lazaro, J. Pleite, and R. Vazquez, "Pwm-pd multiple output dc/dc converters: operation and control-loop modeling," *Power Electronics, IEEE Transactions on*, vol. 19, no. 1, pp. 140–149, Jan 2004.
- [9] S.-H. Cho, C.-S. Kim, and S.-K. Han, "High-efficiency and low-cost tightly regulated dual-output llc resonant converter," *Industrial Electronics, IEEE Transactions on*, vol. 59, no. 7, pp. 2982–2991, July 2012.
- [10] C. Liu, B. Gu, J.-S. Lai, M. Wang, Y. Ji, G. Cai, Z. Zhao, C.-L. Chen, C. Zheng, and P. Sun, "High-efficiency hybrid full bridge-half bridge converter with shared zvs lagging leg and dual outputs in series," *Power Electronics, IEEE Transactions on*, vol. 28, no. 2, pp. 849–861, Feb 2013.
- [11] H. Seong, D. Kim, and G.-H. Cho, "A new zvs dc/dc converter with fully regulated dual outputs," in *Power Electronics Specialists Conference, 1993. PESC '93 Record., 24th Annual IEEE*, Jun 1993, pp. 351–356.
- [12] Y. Zhang and D. Xu, "Design and implementation of an accurately regulated multiple output zvs dc-dc converter," *Power Electronics, IEEE Transactions on*, vol. 22, no. 5, pp. 1731–1742, Sept 2007.
- [13] B.-C. Hyeon and B.-H. Cho, "A tightly regulated triple output asymmetrical half bridge flyback converter," *Journal of Power Electronics*, vol. 10, no. 1, pp. 14–20, January 2010.

Impact of Slot Opening on Performance of Axial Flux PMSMs

A. Hemeida, *Student Member*, and P. Sergeant, *Member, IEEE*

Abstract—In this paper, a complete investigation of the impact of the slot opening on the performance of the axial flux permanent magnet synchronous machines (AFPMSMs) is elaborated. The width of the stator slot opening has a major impact on many parameters including the cogging torque, the ripple torque, the mean value of the torque, the permanent magnet (PM) losses, the iron losses, the peak flux density inside the tooth, and the total inductance of the machine. Thanks to the presence of validated analytical models that made it possible to obtain all these parameters. It is found that a good selection of the slot opening width could result in an optimized performance. For a minimum cogging torque, an optimum selection of the slot opening width is required. On one hand, the increase in the stator slot opening width reduces the iron losses. However, the total torque due to the reduced peak flux density inside the tooth increase for large slot openings value. On the other hand, at full load condition, this selection of slot opening on the PM losses might not be an optimum choice and calculation of the PM losses in this case would be mandatory. In addition, Very large slot opening is not a good choice for machine designers due to the total reduction of the total torque. Therefore, a good choice of the slot opening would result in an optimum machine performance and calculation of all machine parameters would be mandatory.

Index Terms—AFPMSM, Analytical Model, Fractional Slot Winding, Machine Design, Slot opening Width.

I. INTRODUCTION

Due to the high performance of the yokeless and segmented armature (YASA) machine, shown in Fig. 1, it has been used in many applications. Owing to the absence of the yoke, this machine provides great robustness in terms of power density and cost. [1]

The slot opening width influences many output parameters in the machine design. In [2], the authors have addressed the effect of slot opening width on the iron and permanent magnet (PM) losses. It has clearly shown major impact on the iron losses. However, it has shown that PM losses is increasing at no load with the increase of the slot opening. Nevertheless, It has not addressed the PM losses at full load conditions. In [3], [4], the authors have studied the effect of all different PM skewing in double rotor axial flux permanent magnet synchronous machines (AFPMSMs). On the other hand, the correct choice of the slot opening width would result in the optimum value for cogging torque and minimum torque ripple.

In [5], the authors studied the impact of slot opening and tooth profile variations on cogging torque and torque profile. In [6], the a stator slot displacement is used to mitigate the cogging torque.

The analytical model in [7] is based on a combined solution of Maxwell's equations based on subdomain model [8] and magnetic equivalent circuit (MEC). This solution is capable

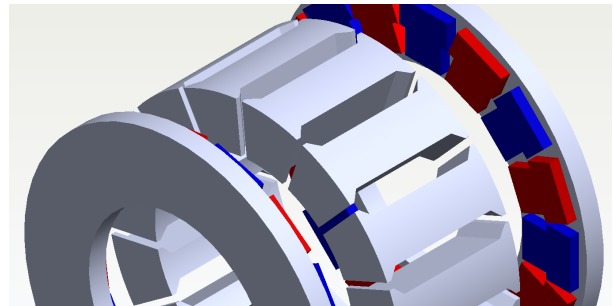


Fig. 1: The YASA topology of the Axial Flux PMSM.

of obtaining the stator iron losses, voltages waveforms, and inductances in a very accurate way. The PM losses is computed using the inductance plus resistance network model developed in [9], [10]. They are based on 2D-2D multi-slice modeling technique. This is done by dividing the machine into slices. On each slice, the flux densities in addition with all the other output parameters are computed.

The cogging torque and ripple torque computations are based on a similar subdomain model developed in [11]. All these models are verified by full 3D finite element (FE) models.

In this paper, a complete investigation of the effect of the slot opening on the main output parameters of the cogging torque, the ripple torque, the mean value of the torque, the permanent magnet (PM) losses, the iron losses, the peak flux density inside the tooth, the total harmonic distortion of the output line voltage, and the total inductances of the machine. Thanks to the presence of a completely verified analytical models [9], [7], [10] that made it possible to obtain all the required data of the machine in a fast appealing time.

This paper is organized as follows. Brief description about analytical models used is done in section II. The effect of slot opening width variation on the cogging torque and ripple torque is studied in section III. Section IV deals with the effect of the slot opening width on the PM and iron losses. In section V, the effect of the slot opening variations on the power quality output of the machine is studied. Finally, conclusions of the paper are drawn in Section VI.

II. ANALYTICAL MODEL DESCRIPTION

The first part of the solution is to obtain the magnetic field in the air gap using the subdomain model based on solution of Maxwell's equations described in [11]. This model divides the machine into the radial direction into multi-slices. This model for the machine consisting of N_s slots and N_m PMs

TABLE I: Parameters of the designed machine.

Parameter	Symbol	Value	Unit
Rated Power	P_n	5	kW
Rated speed	n_m	2500	rpm
Rated torque	T_{FL}	19	Nm
Number of Phases	m	3	
Number of PMs	N_m	16	
Number of Slots	N_s	15	
Rated Current	I_r	7.5	A
Outer diameter	D_o	0.148	m
Inner diameter	D_i	0.1	m
Slot Width	t_s	12	mm
Slot opening	t_{so}	3	mm
PM axial length	Y_m	5	mm
Air gap length	g	1	mm
Copper Losses	P_{co}	65	W
Material Used		M600-50	

is subdivided into three main regions (Slots region where currents are injected, the air gap area, and the permanent magnet (PM) area).

The second part uses the air gap solution of maxwell's equations. This solution is then applied to the stator cores using MEC assuming non linear permeability.

The final stage of the solution is to calculate the permanent magnet (PM) losses. The solution based on Maxwell's equations is then imposed on a resistance and inductance electric network. This network is capable to compute the total eddy current losses in the PMs.

A test case machine of a 5 kW AFPMSM with properties shown in Table I is used. The number of slots and poles are chosen to be 16 poles and 15 slots. This combination has the advantage of very low cogging torque.

III. COGGING TORQUE AND RIPPLE TORQUE

In this section, the effect of slot opening variations on the cogging torque and torque ripple is studied on the AFPMSMs.

Fig. 2 shows the ripple torque and peak to peak cogging torque in percentage of the full load torque. It is clear from Fig. 2, that the cogging torque is a minimum for certain slot openings width.

A natural embedded skewing issues is existing in the axial flux PMSMs that do not exist for radial flux PMSMs. Thus would be explained by Fig. 3. The modeling of this machine is based on dividing the machine in the radial direction into many slices. On each slice the torque is computed individually. Fig. 3 shows the cogging torque for each slice individually at 8.5mm. It is clear that some slices torque cancel each other resulting in a lesser net torque amplitude. This explains the reduction of torque at an explicit slot opening.

Figure 2 also shows the torque ripple. Pulsations in torque occur due to two reasons. One reason is the harmonic contents

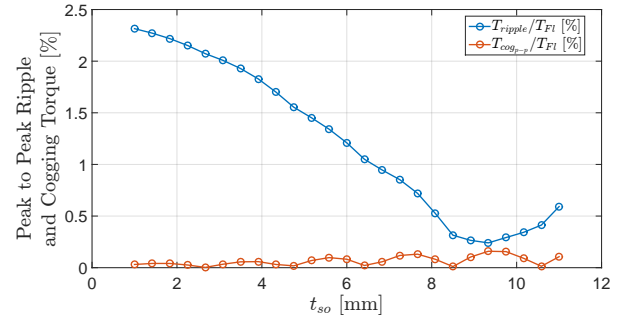


Fig. 2: Impact of slot opening on torque ripple and cogging torque in percentage of the full load torque.

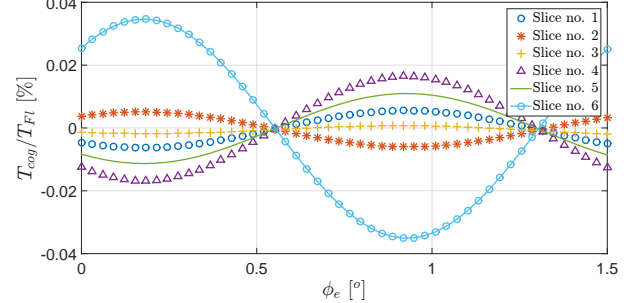


Fig. 3: Cogging torque in percentage of the full load torque for each slice of the machine at 8mm slot opening.

of the stator's magneto motive force (MMF) and additional spatial harmonics existing due to the slots [12]. The torque ripple is minimum at 8.5mm width, where the cogging torque is minimum. For a minimum cogging torque and torque ripple 8.5 mm slot opening width could be selected for the optimum pulsations in torque. However, selecting this value would not be the optimum for other parameters.

IV. IRON AND PM LOSSES

Figure 4 shows the no load air gap flux density at different slot opening of 3mm and 11 mm. It is clear from this figure, that the air gap flux density decreases greatly with the increase of the slot opening.

This significantly reduces the flux density inside the tooth as shown in Fig. 5. The peak no load flux density inside the tooth is about 1.37T at 3mm and 1.17T at 11mm.

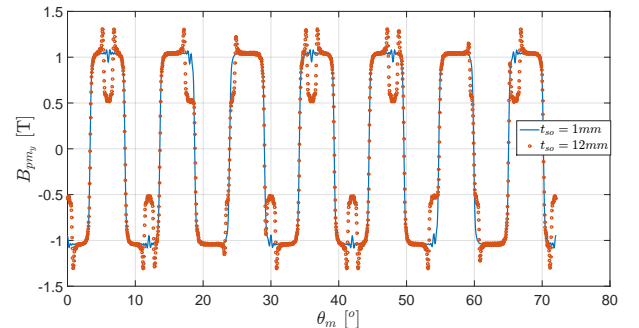


Fig. 4: Flux density variations for different slot opening at no load.

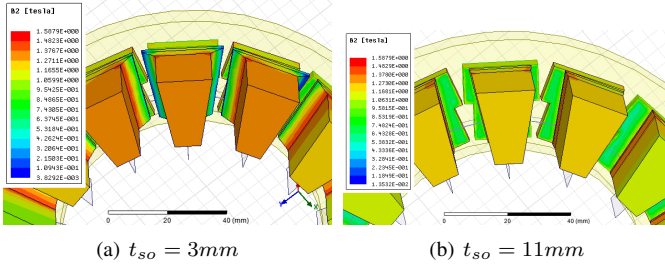


Fig. 5: Flux density variations at no load at different slot openings.

This leads to a reduction of the total stator iron losses as indicated in Fig. 6. Moreover, the difference between no load and full load losses is significantly higher at low slot opening. This is a result from the high leakage inductance associated with low slot opening. As the slot opening increases the difference between no load and full load losses becomes minimal because of the lower leakage inductance. This is more indicative in Fig. 7. This figure shows the full load flux density inside the tooth for slot opening of 3mm and 11mm. It is clear the flux density level inside the tooth reduces from 1.42T to 1.3T from slot opening of 3mm to 11mm. This is a result from the lower leakage inductance.

The no load and full load PM losses is shown in Fig. 8 at different slot opening with different number of segments. Because of the large gradient of the flux density of the air gap flux density, the no load and full load PM losses is increasing accordingly. Fig. 4 shows that flux density the flux density dips under the area of the slot opening. At full load conditions, the PM is increased because of the additional spatial harmonics existing in the space of the armature reaction field.

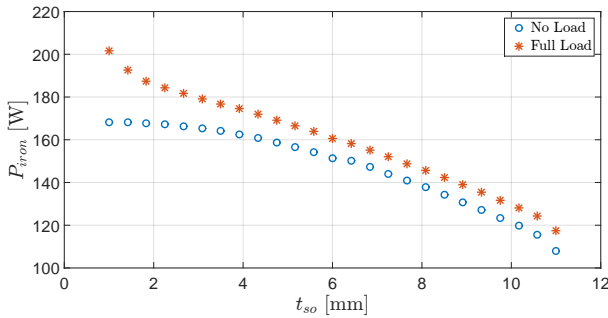


Fig. 6: Impact of slot opening on iron losses.

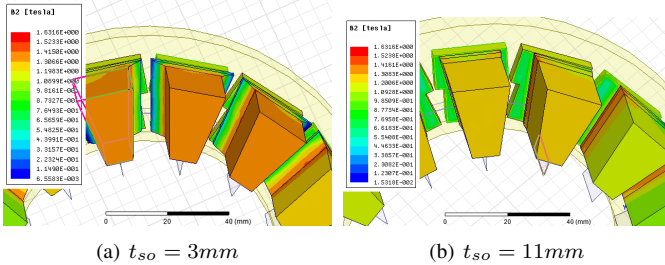


Fig. 7: Flux density variations at full load at different slot openings.

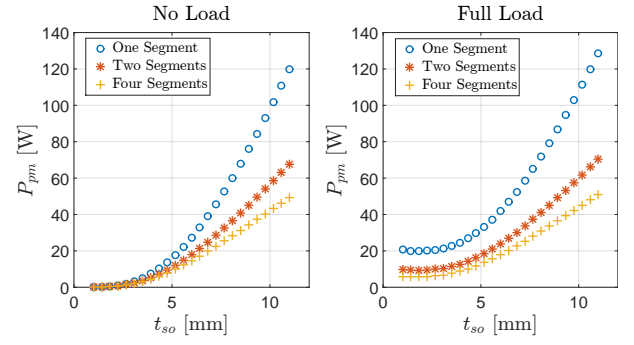


Fig. 8: Impact of slot opening on PM losses.

The PM losses is computed for different number of segments of one, two, and four. Similar trends could be observed. It is clear that for increasing the number of segments, the PM losses decreases. However, it is always mandatory to keep the PM losses as minimum as possible to avoid demagnetization of PMs. Therefore, designing for large slot opening is not a good choice.

Fig. 9 describes that additional PM eddy current loss harmonics exists for the full load conditions that do not exist at no load. Moreover, at no load, only multiples of the slot numbers exist in the eddy current losses. However, at full load, other harmonics exist due to the magneto-motive force (MMF) harmonics. For very large slot openings, the PM eddy current losses increase enormously.

Fig. 10 shows the total efficiency variation including all losses of the machine for different number of PM segments. There is an optimum efficiency that occurs at certain slot openings of 3 to 4 mm. Increasing the slot opening to a large value leads to a very low efficiency. In addition, at low slot openings, the leakage inductance increases leading to less optimized performance and higher iron losses. Therefore, a good choice of 3-4mm for optimum efficiency would be recommended for all losses calculation.

V. POWER QUALITY RESPONSE

In this part, the power quality is studied in terms of mean value of the power.

Figure 12 provides the no load voltage for different slot openings. The slot opening increase leads to a reduction in the air gap flux density indicated in Fig. 4. Consequently, the flux

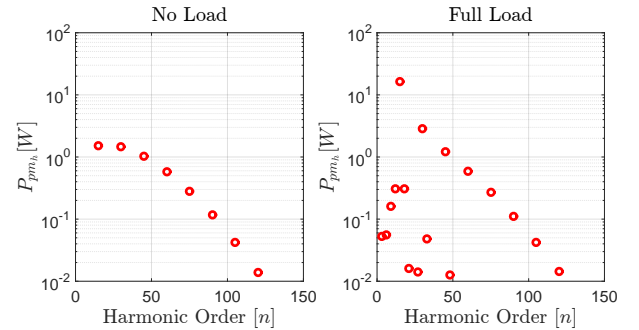


Fig. 9: Harmonics of the power losses spectrum of the eddy current losses in the PMs at $t_{so} = 3mm$.

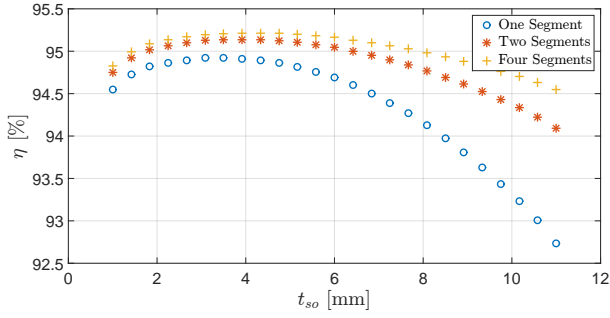


Fig. 10: Total efficiency variations including copper losses.

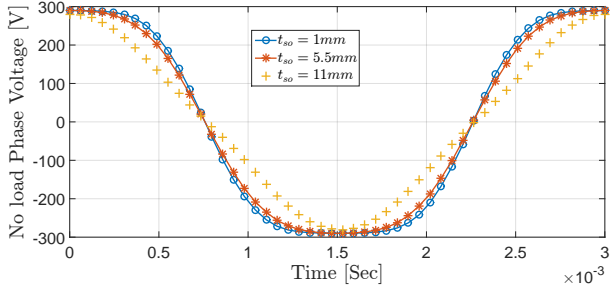


Fig. 11: No load voltage for different slot opening.

linkage reduces and hence, the no load voltage. This lowers the output torque and power of the machine.

Fig. 12 shows the impact of the slot opening variations on the total power output of the machine in per unit. For small a slot opening, the power is higher due to the higher air gap flux density. However, when the slot opening increases, the total power output reduces.

Therefore, for a good output power it is important to keep the slot opening as low as possible to attain the required power.

VI. CONCLUSIONS

This paper investigated the effect of slot opening variations on the total performance of the AFPMSM. Three main parameters (Torque waveforms, Losses, and power quality) are studied in this machine. On the one hand, the right choice of the slot opening width might give the optimum cogging and ripple torque. However, this choice might not be optimum for the iron and PM losses.

Increasing the slot width will always lead to a decrease of the flux density level inside the tooth. In consequence, this leads to a reduction of the iron losses. However, PM

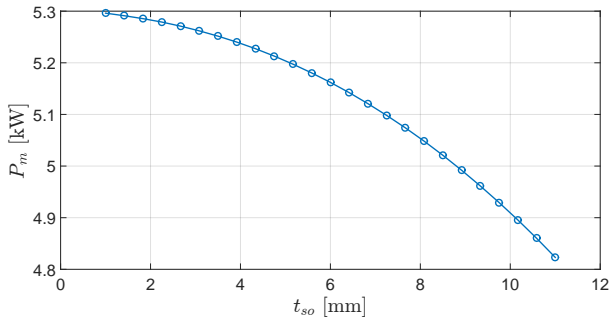


Fig. 12: Impact of slot opening on full load power.

losses at no load and full load increases for large slot opening width. In overall, for a very high slot opening width, the PM losses is observed to rise enormously due to the high gradient change of the magnetic flux density near the air gap area. Therefore, to avoid PM demagnetization, it is mandatory to keep the slot opening as low as possible or to increase the number of PM segments. On the other hand, it is important to deeply investigate the total slot opening variations on the total efficiency of the system.

For a very large slot opening, the total output power of the machine lowers. This is a result of the reduction of the mean air gap flux density.

For the particular studied machine, the choice of the slot opening to give minimum torque ripple is 9mm. However, this choice will lead to an efficiency of 94% for one PM segment. In addition, the output power becomes lesser than the nominal machine power.

Another good choice from efficiency point of view is the 3mm slot opening width which gives an efficiency higher than 95% and the required nominal power. However, the torque ripple becomes 2% of the full load torque. Additional PM skewing would be required to reduce the torque ripple.

Therefore, the slot opening should be strictly determined for all the aforementioned parameters.

REFERENCES

- [1] C. Du-Bar, "Design of an axial flux machine for an in-wheel motor application," *Chalmers Reproservice, Göteborg*, 2011.
- [2] P. Sergeant, H. Vansompel, and L. Dupré, "Effect of stator slot openings in axial flux permanent magnet machines," in *Int. Conf. Model. Simul. Electr. Mach. Convert. Syst. Proceedings.*, pp. 512–517, Universitat Politècnica de València, 2014.
- [3] M. Aydin and M. Gulec, "Reduction of Cogging Torque in Double-Rotor Axial-Flux Permanent-Magnet Disk Motors: A Review of Cost-Effective Magnet-Skewing Techniques With Experimental Verification," *IEEE Trans. Ind. Electron.*, vol. 61, pp. 5025–5034, Sep. 2014.
- [4] M. Aydin, Z. Q. Zhu, T. A. Lipo, and D. Howe, "Minimization of Cogging Torque in Axial-Flux Permanent-Magnet Machines: Design Concepts," *IEEE Trans. Magn.*, vol. 43, pp. 3614–3622, Sep. 2007.
- [5] J. Wanjiku, M. A. Khan, P. S. Barendse, and P. Pillay, "Influence of Slot Openings and Tooth Profile on Cogging Torque in Axial-Flux PM Machines," *IEEE Trans. Ind. Electron.*, vol. 62, pp. 7578–7589, Dec. 2015.
- [6] A. B. Letelier, D. A. Gonzalez, J. A. Tapia, R. Wallace, and M. A. Valenzuela, "Cogging Torque Reduction in an Axial Flux PM Machine via Stator Slot Displacement and Skewing," *IEEE Trans. Ind. Appl.*, vol. 43, no. 3, pp. 685–693, 2007.
- [7] A. Hemeida and P. Sergeant, "Analytical modeling of surface PMSM using a combined solution of Maxwell's equations and Magnetic Equivalent Circuit (MEC)," *IEEE Trans. Magn.*, vol. 50, no. 12, p. 7027913, 2014.
- [8] B. Hannon, P. Sergeant, and L. Dupre, "2-D Analytical Subdomain Model of a Slotted PMSM With Shielding Cylinder," *IEEE Trans. Magn.*, vol. 50, pp. 1–10, Jul. 2014.
- [9] A. Hemeida and P. Sergeant, "Analytical modeling of eddy current losses in Axial Flux PMSM using resistance network," in *2014 Int. Conf. Electr. Mach.*, pp. 2688–2694, IEEE, Sep. 2014.
- [10] A. Hemeida, P. Sergeant, and H. Vansompel, "Comparison of Methods for Permanent Magnet Eddy Current Loss Computations With and Without Reaction Field Considerations in Axial Flux PMSM," *IEEE Trans. Magn.*, vol. 9464, pp. 1–11, Sep. 2015.
- [11] H. Tiegna, A. Bellara, Y. Amara, and G. Barakat, "Analytical Modeling of the Open-Circuit Magnetic Field in Axial Flux Permanent-Magnet Machines With Semi-Closed Slots," *IEEE Trans. Magn.*, vol. 48, no. 3, pp. 1212–1226, 2012.

- [12] M. Aydin, Surong Huang, and T. Lipo, "Torque quality and comparison of internal and external rotor axial flux surface-magnet disc machines," *IEEE Trans. Ind. Electron.*, vol. 53, no. 3, pp. 822–830, 2006.

Candidates of Motor Drives for 48V Automotive Applications

Jing Bao, Konstantin Boynov, Johan Paulides, Korneel Wijnands, Elena Lomonova

Electrical Engineering

Eindhoven University of Technology

Eindhoven, Netherlands

Email: j.bao@tue.nl

Abstract—In automotive systems, reliability and cost are paramount for the success of electrical drive systems. Considering the interior permanent magnet motor, the cost of the rare-earth permanent magnet is becoming a big concern. In this paper, the switched reluctance motor, variable flux reluctance motor and synchronous reluctance motor are analyzed and compared as candidates for the 48V automotive applications. A recommendation is given for the selection of the motor drives.

1. Introduction

Future vehicle electrification needs more electric power to manage more functions, such as electro-mechanical valves, direct electrically driven engine water pump, assisted electrical power steering, etc. As a result, medium power electrical motors are required to assist the main traction drive train. A voltage level of 48V is suitable for such a motor drive considering the safety regulation.

Interior permanent magnet motor (IPM) is commonly considered as a candidate for automotive applications. However, the price rise of the rare-earth permanent magnet tends to restrict the use of the IPM in large scale. Therefore, the utilization of the rare-earth-free motor drive is desired. As a result, the adoption of the switched reluctance motor (SRM) is investigated by researchers and is compared with IPM. Additionally, the current analysis of the variable flux reluctance motor (VFRM) and synchronous reluctance motor (SynRM) also shows a bright prospect. This paper reviews the aforementioned motor drives considering the power electronic circuit, the motor itself and the control algorithm. Finally, the paper is concluded with a summary on the overall performance of different motor drives.

2. MOTOR DRIVE COMPARISON

Interior permanent magnet motor is used by a lot of automakers due to its high efficiency at nominal speeds, high power density, flux-weakening capability and easy cooling. However, the efficiency of the motor decreases in higher speed range since an extra magnetization current is required to suppress the flux. Moreover, at high demagnetization current, there is the risk of magnet demagnetization.

Switched reluctance motor is more and more appealing to researchers as the rival of IPM [1]. It has robust and simple rotor structure, utilizes low cost material and is tolerant towards hostile environment. However, shortcomings of this motor drive are also obvious, for example, it needs complex profiling of phase current waveforms at low speed, requires non-standard power electronic module, demands large DC-link capacitor, generates large acoustic noise, etc.

Three-phase variable flux reluctance motor has been proposed as another candidate recently. [2]- [3] It has simple and robust stator and rotor structures as the SRM. It is concluded in [2] that the VFRM can produce higher output power in flux weakening region compared to IPM while generating lower acoustic noise compared to SRM. Moreover, the conventional three-phase inverter is applicable for this motor, which makes it a competitive option for automotive application.

The synchronous reluctance motor is considered as another competitor. [4] This kind of motor has a shortcoming of the low power factor (with a radially laminated structure). Different methods have been presented to overcome this, such as injecting direct capacitance through an auxiliary winding [5] and adding permanent magnets in the rotor flux barriers [6].

The features of the motor drives from the literature are elaborated in the following, as well as the simulation and analysis for the representatives of the motors.

2.1. Switched reluctance motor

In this subsection, an SRM is analyzed specifically for the aforementioned shortcomings with some possible solutions. To ensure the position-independent starting capability of the machine, it is favorable to have at least four phases in the SRM. It is well known that if the phase windings in SRM are excited by pure square wave current, the torque ripple is large. Therefore, current profiling method is used to smooth the torque and it works effectively for relatively low speed operation [7]. In high speed operation, the SRM may be operated in the continuous conduction mode since the current has to be increased fast enough to reach the desired average torque.

An 8/6 SRM is simulated using the finite element analysis (FEA) for obtaining the flux-current-position character-

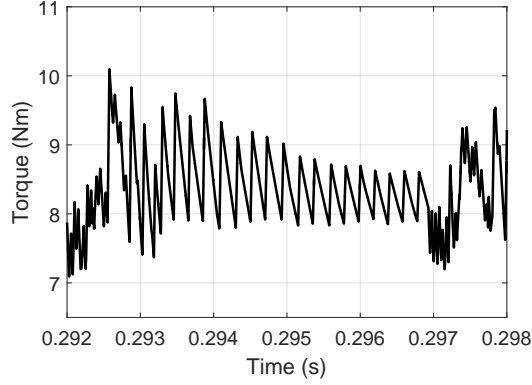


Figure 1. Torque ripple of the SRM by using the torque sharing function when rotational speed is 50 rad/s.

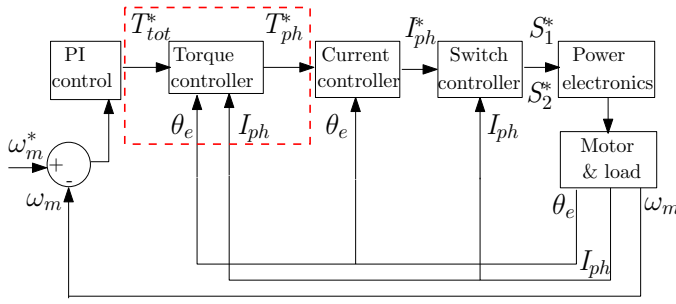


Figure 2. Torque ripple for different number of turns using the same torque sharing function when rotational speed is 50 rad/s.

istic and torque-current-position characteristic. A Simulink model composed of control, power electronic circuit and motor represented by differential equations is created. For low speed operation, torque sharing function is used [8]- [9], as a result, an example of the torque is shown in Figure 1. As can be seen, the torque ripple is around 30%.

For higher speed operation, the torque sharing function is not applicable anymore since the actual phase current is not able to follow the desired current profile. Instead, a speed control is used as shown in Figure 2. T_{tot}^* in the figure represents the drive reference torque and T_{ph}^* represents the desired torque of the incoming phase. During commutation, T_{ph}^* is calculated as a difference between T_{tot}^* and the torque of the outgoing phase that is calculated in the 'Torque controller' block. Turn-on and turn-off angles are tuned in this stage to increase the speed.

To further increase the working envelope, the SRM starts to work in continuous conduction mode. One feasible method in this stage is to control switch S_2 in Figure 3(a) using the control method shown in Figure 3(b). The typical profile of the phase current is shown in Figure 3(c).

In [10], it introduces the feasibility of using merely the bus line current sensor for controlling the SRM, however, if the SRM works in the CCM, a current sensor is required for each phase.

The motor structure of the SRM is simple, however, the intrinsic low kW/kVA ratio of the motor leads to a high

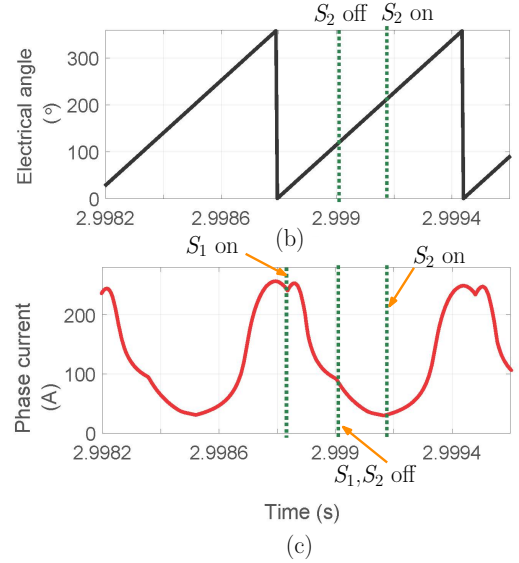
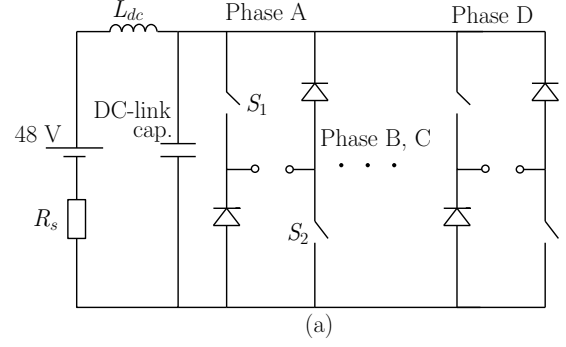


Figure 3. (a) Power electronic circuit of the SRM drive, (b) the control algorithm of S_2 and (c) the current profile of phase A at 15000 rpm.

demand on the power electronic components, such as the DC-link capacitor. Different methods for the minimization of the capacitor size have been reported, including sinusoidal current injection [11], control algorithm for the elimination of bus line current [12]- [13], etc. However, the torque density may decrease using these methods.

Another drawback of the SRM is the large acoustic noise, which is dominantly caused by the radial vibration. An effective method for reducing the noise is introduced in [14] using two-step switching during commutation, other method, such as using sinusoidal bipolar excitation [11], is also investigated.

2.2. Variable flux reluctance motor

Another rare-earth-free candidate for the 48V automotive application is the VFRM. There are a lot of stator and rotor combinations for this kind of motor. The self and mutual inductances of the field and armature windings are simulated in FEA and are shown in Figure 4. For 6 stator poles, the fundamental component of the back-emf with 5 rotor poles is the highest at the same field current, as well

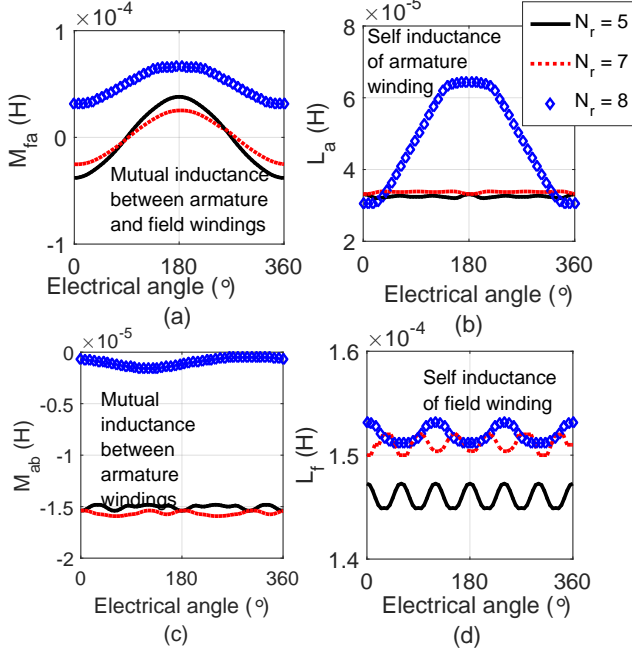


Figure 4. (a) The mutual inductance, M_{fa} , between the armature and field windings (b) the self inductance, L_a of the armature winding (c) the mutual inductance, M_{ab} , between armature windings and (d) the self inductance, L_f of the field winding (N_r is the number of rotor poles).

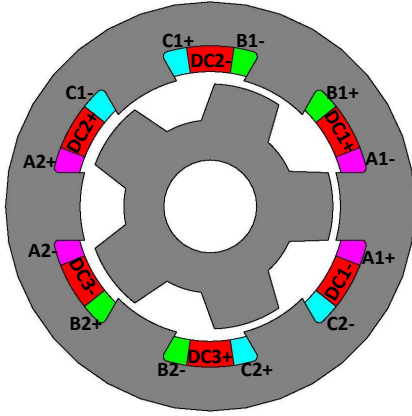


Figure 5. The motor configuration of the 6/5 VFRM.

as the highest torque density [16]. Therefore, only the 6/5 VFRM, shown in Figure 5, is analyzed in this paper.

The self inductance of the armature winding L_a , the mutual inductance between the armature windings M_{aa} and the self inductance of the field winding L_f are almost constant as shown in Figure 4. The ideal expressions of the inductance in a 6/5 motor is [17]

$$\begin{aligned} L_a &= L_0 + L_2 \cos 2\theta + \dots, \\ M_{ab} &= -L_0/2 + L_2 \cos(2\theta + 4\pi/3) + \dots \end{aligned} \quad (1)$$

where L_0 , L_2 are the DC component and second harmonic of L_a , and M_{ab} is the mutual inductance between phase A

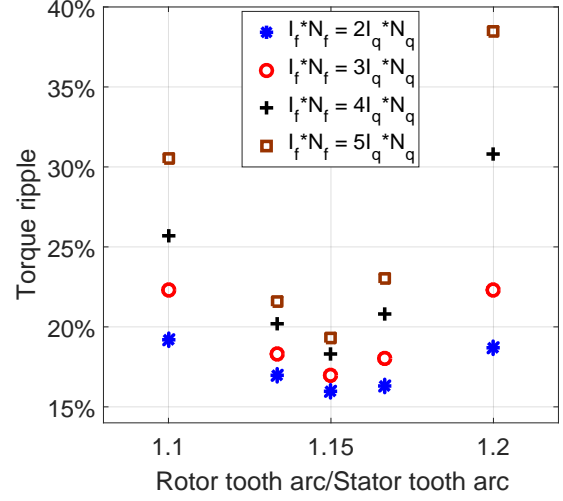


Figure 6. Torque ripple for different motor parameters and currents (N_f and N_{ph} are the number of turns for the field winding and phase winding, respectively).

and B. L_d and L_q are

$$\begin{aligned} L_d &= \frac{3}{2} L_0 + \frac{3}{2} L_2, \\ L_q &= \frac{3}{2} L_0 - \frac{3}{2} L_2 \end{aligned} \quad (2)$$

As can be seen in Figure 4(b), harmonics in L_a are small, as a consequence, L_d and L_q are close when saturation and leakage of the end winding are neglected. This is also verified by simulating L_d and L_q using 2D FEA, namely injecting I_d and I_q respectively, and calculate the inductances as [18],

$$\begin{aligned} L_d &= \frac{\Psi_d}{I_d}, \\ L_q &= \frac{\Psi_q}{I_q}, \\ \Psi_d &= \frac{2}{3} (\Psi_a - \frac{1}{2} \Psi_b - \frac{1}{2} \Psi_c), \\ \Psi_q &= \frac{1}{\sqrt{3}} (\Psi_b - \Psi_c) \end{aligned} \quad (3)$$

The torque and voltage expression is

$$\begin{aligned} \begin{bmatrix} U_d \\ U_q \end{bmatrix} &= \begin{bmatrix} R_s & -\omega_e L_q \\ \omega_e L_d & R_s \end{bmatrix} \begin{bmatrix} I_d \\ I_q \end{bmatrix} + \omega_e M_{fa} I_f \begin{bmatrix} 0 \\ 1 \end{bmatrix}, \\ T &= \omega_e M_{fa} I_f I_q + (L_d - L_q) I_d I_q \end{aligned} \quad (4)$$

where ω_e is the electric speed and I_f is the field current.

The torque ripple of the 6/5 VFRM is shown in Figure 6 for different field currents and rotor arcs. The ripple is calculated using

$$T_{ripple} = \frac{T_{max} - T_{min}}{T_{mean}} \quad (5)$$

As can be seen, the torque ripple increases as the field current rises. However, the torque ripple caused by the

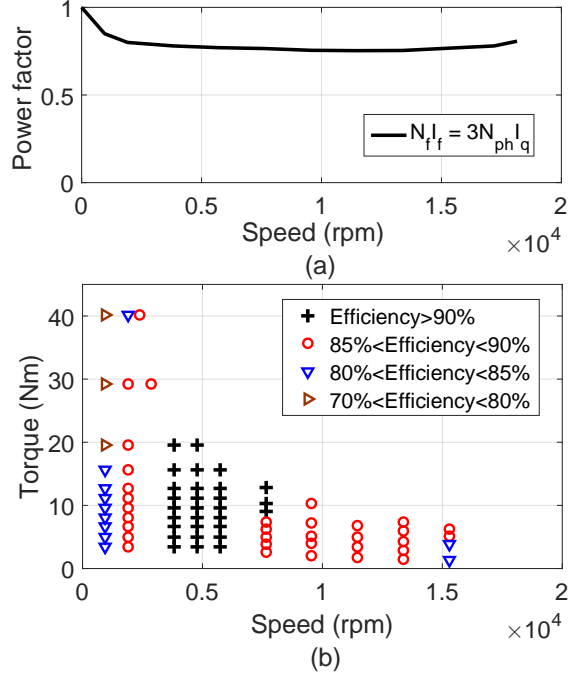


Figure 7. (a) Power factor and (b) efficiency of the 6/5 VFRM.

current fluctuation due to the small inductance in this low voltage application is not considered.

The efficiency and power factor for the 6/5 VFRM are shown in Figure 7. As can be seen, the power factor is relatively high in the overall working range and it can even be further increased by adjusting the ratio between the field current and armature current. However, Figure 7 shows only an indication, because the values are dependent on the control algorithm.

The torque density of the VFRM is relatively low as shown in [2], which is around 75% of the IPM. The acoustic noise of the VFRM is investigated in [19]. A much lower sound pressure level is generated by this motor compared to SRM, although they have similar stator and rotor structures.

2.3. Synchronous reluctance motor

In this subsection, the permanent-magnet-assisted SynRM is briefly introduced. The permanent magnet added in the rotor flux barriers of a conventional SynRM significantly improve the overall performance, such as the operational envelope, efficiency, power factor, etc. The influence of different types of magnets are analyzed and the results are compared with Prius IPM in [21]. By using the ferrite magnet, the torque-speed characteristic, torque density and the efficiency of the SynRM is competitive with Prius IPM. However, the overall power factor is still relatively low, especially in the high speed region based on the result in [21].

In the end, a summary of the performance for different motor drives is listed in TABLE 1. [22]- [23]

TABLE 1. COMPARISON OF THE MOTOR DRIVES.

Note: + good, - bad, o neutral.

	IPM	SRM	VFRM	SynRM	PMA-SynRM
Torque density	+	-	-	-	+
Motor efficiency	+	+	o	o	+
Motor cost	-	+	+	+	o
Demands on power electronics	+	-	o	+	+
Power factor	+	-	+	-	o
Controllability	o	-	o	o	o

3. Conclusion

This paper introduces the comparison between the switched reluctance motor, variable flux reluctance motor, synchronous reluctance motor and permanent magnet assisted synchronous reluctance motor. The strong points and the weakness of each motor drive are analyzed. The switched reluctance motor itself is cheap and robust, however, its low power factor leads to the demands on the large power electronic components, additionally, the high radial force results in large acoustic noise and torque ripple therefore needs complicated control algorithm. The variable flux reluctance motor has good performance for the aspects of power factor, however, the torque density is relatively low. The synchronous reluctance motor has the drawback of relatively low torque density and power factor compared to IPM, however, these are improved by the assisted magnets in the rotor.

The final selection of the motor drive should rely on the specific application and the most important concern in the design, such as the cost limit or the size, etc.

References

- [1] S. Haghbin, A. Rabiei and E. Grunditz, "Switched reluctance motor in electric or hybrid vehicle applications: A status review", IEEE Int. Conf. on Industrial Electronics and Applications. pp. 1017-1022, 2013.
- [2] X. Liu, Z.Q. Zhu and D. Wu, "Evaluation of efficiency optimized variable flux reluctance machine for EVs/HEVs by comparing with interior PM machine", IEEE Int. Electric Machines Drives Conf. pp. 2648-2654, 2014.
- [3] Y. Kano, "Design optimization of brushless synchronous machines with wound-field excitation for hybrid electric vehicles", IEEE Energy Conversion Congress and Exposition. pp. 2769-2775, 2015.
- [4] A. Vagati, B. Boazzo, P. Guglielmi and G. Pellegrino, "Ferrite assisted synchronous reluctance machines: A general approach", IEEE Int. Conf. on Electrical Machines, pp. 1315-1321, 2012.
- [5] A.S.O Ogunjuyigbe, A.A Jimoh and D.V. Nicolae, "Improving synchronous reluctance machine performance by direct capacitance injection through an auxiliary winding", IEEE Int. Conf. on Electrical Machines and Systems, pp. 1055-1060, 2007.
- [6] E. Carraro, M. Degano, M. Morandin and N. Bianchi, "PM synchronous machine comparison for light electric vehicles", IEEE Int. Electric Vehicle Conf., pp. 1-8, 2014.
- [7] S. J. Evangeline and S. Suresh Kumar "Torque ripple minimization of switched reluctance drives - A survey", IET Int. Conf. on Power Electronics, Machines and Drives, pp. 1-6, 2010.

- [8] R.H.S Vrenken, J.L. Duarte, K. Boynov, C.G.E. Wijnands, E.A. Lomonova, S. Bervoets and S. Faid, "Switched reluctance motor drive for full electric vehicles - Part I: Analysis", Int. Conf. and Exhib. on Ecological Vehicles and Renewable Energies. pp. 1-7, 2013.
- [9] R.H.S Vrenken, J.L. Duarte, K. Boynov, C.G.E. Wijnands, E.A. Lomonova, S. Bervoets and S. Faid, "Switched reluctance motor drive for full electric vehicles - Part II: Practical Implementation", Int. Conf. and Exhib. on Ecological Vehicles and Renewable Energies. pp. 1-7, 2013.
- [10] C. Gan, J. Wu, Y. Hu and S. Yang, "Online sensorless position estimation for switched reluctance motors using one current sensor", IEEE Trans. on Power Electronics., no. 99, 2015.
- [11] X. Liu and Z.Q. Zhu, M. Hasegawa, A. Pride and R. Deohar, "DC-link capacitance requirement and noise and vibration reduction in 6/4 switched reluctance machine with sinusoidal bipolar excitation", Energy conversion Congress and Expos. pp. 1596-1603, 2011.
- [12] W. Suppharangsarn and J. Wang, "A new switching technique for DC-link capacitor minimisation in switched reluctance machine drives", IET Int. conf. on Power Electronics, Machines and Drives, pp.1-6, 2010.
- [13] W. Suppharangsarn and J. Wang, "Experimental validation of a new switching technique for DC-link capacitor minimization in switched reluctance machine drives", IEEE Int. Electric Machines Drives Conf., May 2013, pp. 1031-1036.
- [14] C. Pollack and C.Y. Wu, "Acoustic noise cancellation techniques for switched reluctance drives", IEEE Trans. on Industry Applications vol. 33, no. 2, pp. 477-484, 1999.
- [15] Y. Kano, "Design optimization of brushless synchronous machines with wound-field excitation for hybrid electric vehicles", Energy conversion Congress and Expos. pp. 2769-2775, 2015.
- [16] X. Liu and Z.Q. Zhu, "Influence of rotor pole number on electromagnetic performance of novel variable flux reluctance machine with DC-field coil in stator", Power Electronics and Motion Control Conf., pp.1108-1115, 2012.
- [17] Y. Tang, J.J.H. Paulides and E.A. Lomonova, "Field weakening performance of flux-switching machines for hybrid/electric vehicles", Inter. Conf. on Ecological Vehicles and Renewable Energies, pp. 1-10, 2015.
- [18] Y.S. Chen, Z.Q. Zhu and E.A. Lomonova, "Calculation of d- and q-axis inductances of PM brushless ac machines accounting for skew ", IEEE Trans. on Magnetics, vol. 41, no. 10, pp. 3940-3942, 2005.
- [19] X. Liu, Z.Q. Zhu, M. Hasegawa, A. Pride and R. Deodhar "Calculation of d- and q-axis inductances of PM brushless ac machines accounting for skew ", IEEE Trans. on Magnetics, vol. 41, no. 10, pp. 3940-3942, 2005.
- [20] J. Bao, K. Boynov, J.J.H. Paulides and E.A. Lomonova, "Usage of the inductive energy storage in the field winding for driving the variable reluctance motor", IEEE Trans. on Magnetics, no.99, 2016.
- [21] Y.S. Chen, Z.Q. Zhu and E.A. Lomonova, "Design optimisation and performance evaluation of a rare-earth-free Permanent Magnet Assisted Synchronous Reluctance Machine for electric vehicle traction", IET conf. on Power Electronic, Machines and Drives, pp. 1-6, 2014.
- [22] T. Finken, M. Felden and K. Hameyer, "Comparison and design of different electrical machine types regarding their applicability in hybrid electrical vehicles", Int. Conf. on Elec. Machines, pp. 1-5, 2008.
- [23] Z. Yang, F. Shang, I.P. Brown and M. Krishnamurthy, "Comparative study of interior permanent magnet, induction, and switched reluctance motor drives for EV and HEV applications", IEEE Trans. on Transportation Electrification, vol. 1, no. 3, pp. 245-254, 2015.

Performance Evaluation of Synchronous Reluctance Motors With and Without Permanent Magnets

M. N. Ibrahim^{1,2}, *Student Member IEEE*, Peter Sergeant¹, *Member IEEE* and E. M. Rashad³, *Senior Member IEEE*

¹Department of Electrical Energy, Systems and Automation, Ghent University, Ghent 9000, Belgium

²Electrical Engineering Department, Kafrelsheikh University, Kafr el-Sheikh 33511, Egypt

³Electrical Power and Machines Department, Tanta University, Tanta 31527, Egypt

E-mail²: m.nabil@eng.kfs.edu.eg

Abstract— Nowadays, a growing interest in the efficiency and the cost of electrical machines has been noticed. Therefore, Synchronous Reluctance Motors (SynRMs) have become more attractive, thanks to their higher efficiency and nevertheless acceptable cost compared to induction machines. The rotor design of SynRMs with or without permanent magnets (PMs) has a huge effect on the motor efficiency, torque density and power factor. This paper introduces an evaluation for the performance of SynRMs with and without PMs in terms of efficiency, torque and power factor maps. Three different rotor designs for the same machine have been compared. For one machine, the experimental measurements have been obtained and the validation of the simulation results have been confirmed.

Index Terms—PM, Synchronous Reluctance Motors, Design, FEM, sensitivity analysis, flux-barriers.

I. NOMENCLATURE

i_d, i_q	Direct and quadrature axis stator current respectively, A
L_d, L_q	Direct and quadrature axis stator inductance of SynRM respectively, H
P	Number of pole pairs
p	Differential operator (d/dt)
R_s	Stator resistance of the motor, Ω
T_e	Electromagnetic torque of the motor, N.m
V_d, V_q	Direct and quadrature component of stator voltage respectively, V
V_m	Maximum input voltage of the motor, V
λ_s	Stator flux linkage of the motor, V. sec
I_m	Maximum input current of the motor, A
δ, α	Load angle and current angle, rad
ω_r	Mechanical speed of the rotor, rad/s
θ_r	Rotor position, Deg.

II. INTRODUCTION

Recently, Synchronous Reluctance Motors (SynRMs) with or without permanent-Magnets (PMs) are becoming attractive machines for industrial application especially electrical vehicles [1]. This is thanks to their merits of wide constant power speed range and high torque density. The power factor and efficiency are good compared to induction machines [2], [3].

Several papers studied the SynRMs and PMaSynRMs[1], [11]. For example, in [1], SynRM design suitable for electric

vehicles has presented. In addition, a comparison between different flux-barrier design for the same stator is investigated. The effect of four different steel grade on the performance of SynRMs is studied in [2]. It is noticed that the lower thickness steel grade has the higher efficiency, however it has not the higher output torque. In [4], the design characteristics of SynRM with ferrite magnets and stator skew has investigated. In addition, mechanical stress and demagnetization of ferrite has studied as well.

This paper investigates the performance evaluation of SynRMs and PMaSynRMs. The modelling of PMaSynRM is introduced in Section III. Performance evaluation of SynRMs is investigated in Section IV. Experimental results are implemented to validate the simulation results as depicted in Section V. At the end, conclusions are figured out in Section VI.

III. PMASYNRM MODELLING

A. Mathematical dq model of PMaSynRM

The dq model of PMaSynRM can be represented in the rotor reference frame [2], [5], [6]. The dq-axis reference frame rotates at ω_r , so that the voltage equations are represented by:

$$V_d = R_s i_d + p\lambda_d(i_d, i_q) - \omega_r P \lambda_q(i_d, i_q) + \omega_r P \lambda_{pm} \quad (1)$$

$$V_q = R_s i_q + p\lambda_q(i_d, i_q) + \omega_r P \lambda_d(i_d, i_q) \quad (2)$$

The dq-axis flux-linkage relations are given by:

$$\lambda_d(i_d, i_q) = L_d(i_d, i_q) i_d, \quad \lambda_q(i_d, i_q) = L_q(i_d, i_q) i_q \quad (3)$$

The electromagnetic torque can be calculated as follows:

$$T_e = \frac{3}{2} P (\lambda_d(i_d, i_q) i_q - \lambda_q(i_d, i_q) i_d + \lambda_{pm} i_d) \quad (4)$$

The dq-axis currents can be performed as a function of the current angle (α), which is the angle of the stator current space vector with respect to the d-axis of the motor as described in Fig.1.

$$i_d = I_m \cos(\alpha), \quad i_q = I_m \sin(\alpha) \quad (5)$$

The dq-axis supply voltage can be obtained as follows:

$$V_d = -V_m \sin(\delta), \quad V_q = V_m \cos(\delta) \quad (6)$$

where δ is the machine load angle as shown in Fig. 1.

The power factor (PF) of the PMaSynRM can be calculated by:

The authors acknowledge the Egyptian Ministry of Higher Education (Cultural Affairs and Missions Sector) and Special Research Fund of Ghent University (BOF) for the financial support during this work.

$$PF = \cos(\phi) = \frac{V_d \cos(\alpha) + V_q \sin(\alpha)}{\sqrt{V_d^2 + V_q^2}} \quad (7)$$

The torque ripple can be determined as follows:

$$T_{ripple} = \frac{\max(T_e) - \min(T_e)}{\text{avg}(T_e)} \quad (8)$$

where \max , \min and avg are the maximum, the minimum and the average values of the electromagnetic torque respectively.

The SynRM model can be obtained by inserting $\lambda_{pm}=0$ in the previous equations.

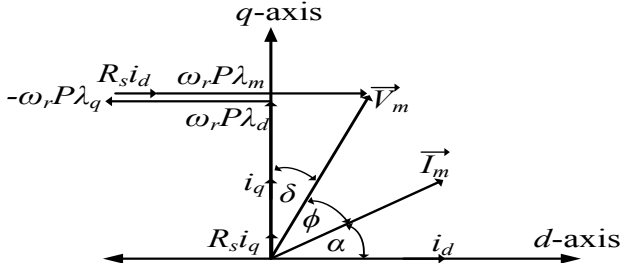


Fig. 1. Vector diagram of PMaSynRM

The iron losses of the SynRM are calculated based on the statistical losses theory of Bertotti. The theory depends on the separation of the losses into hysteresis (hy), classical (cl) and excess (ex) losses [2], [7].

$$\begin{cases} P_{hy} = a_m B_p^{\alpha_m} f \\ P_{cl}(t) = b_m \left| \frac{dB}{dt} \right|^2 \\ P_{ex}(t) = c_m \left(\sqrt{1 + d_m \left| \frac{dB}{dt} \right|} - 1 \right) \left| \frac{dB}{dt} \right| \\ P_{iron} = (P_{hy} + P_{cl} + P_{ex}) \sigma \end{cases} \quad (9)$$

where a_m , α_m , b_m , c_m , d_m and σ are material dependent parameters, and f is the frequency of the applied field.

On the other hand, the SynRM copper losses can be easily computed using the measured phase resistance as follows:

$$P_{copper} = 3 I_{ph}^2 R_{ph} \quad (10)$$

The efficiency of the motor can be obtained by :

$$\eta = \frac{P_o}{P_o + P_{copper} + P_{iron}} \quad (11)$$

where P_o is the mechanical output power of the motor calculated using the computed torque from the FEM model by:

$$P_o = T_e \omega_r \quad (12)$$

IV. PERFORMANCE EVALUATION OF SYNRRMS AND PMASYNRRMS

Three different rotors with the same stator and other geometrical and electromagnetic parameters have been considered. On the one hand, the stator has 36 slots and 15 turns/slot with conventional star-connected windings. The stator design is similar to that of induction machines. Several

specifications for the stator of the machine are listed in table I. On the other hand, all the rotors have 3-flux-barriers per pole as seen in Figs. 2 and 3. The first rotor has been designed by a manufacturing company. This motor is called a reference SynRM and it is the motor for which the experimental validation has been done. The geometrical rotor parameters of the reference motor are shown in table I. The second rotor has been optimized by a conventional optimization technique with 2D FEM for the twelve rotor parameters, depicted in Fig. 2. This motor is called an optimal SynRM and its rotor parameters are given in table II. The final rotor has been obtained by filling all the three flux-barriers of the optimized rotor (second one) with ferrite PMs. The ferrite PM is selected due to the lower cost and the availability in the market. In addition, it can withstand higher temperature [8]. The adopted ferrite PM properties are shown in [8]. This motor is called a PMaSynRM.

TABLE I
PROTOTYPE SYNRM PARAMETERS

Parameter	Value	Parameter	Value
Number of rotor flux barriers per pole	3	Rotor shaft diameter	35 mm
Number of pole pairs	4	Axial length	140 mm
Number of stator slots	36	Air gap length	0.3 mm
Number of phases	3	Rated speed	6000 RPM
Stator outer diameter	180 mm	Rated frequency	200 Hz
Stator inner diameter	110 mm	Rated current	22 A
Rotor outer diameter	109.4 mm	Material grade	M400-50A
θ_1	7.5°	W_1	6 mm
θ_2	20.5°	W_2	4 mm
θ_3	33.5°	W_3	3 mm
L_1	25 mm	p_1	23.5 mm
L_2	19 mm	p_2	36 mm
L_3	12 mm	p_3	46 mm

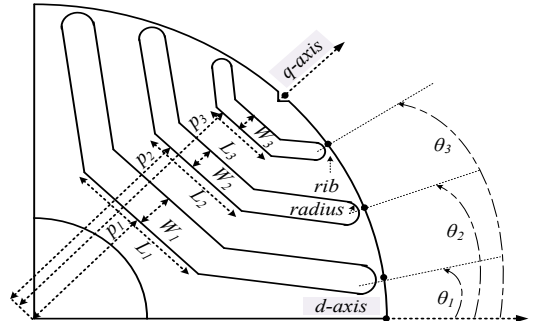


Fig. 2. Quarter rotor geometry of SynRM

The following results have been obtained by 2D-FEM at the same conditions. In FEM, only one pole of the considered four-poles machine needs to be simulated. Sinusoidal currents are injected in the machine windings at different speeds up to the rated value (6000 r/min). The currents have different values up to the rated value ($I_m=30$ A) at fixed current angle $\alpha=56.5^\circ$. The selected value of the current angle (56.5°) is the angle at which the machine can give approximately the maximum output power, for the different currents and speeds.

The FEM field pattern of the reference motor for quarter geometry at rated conditions, is depicted in Fig. 3. It can be noticed that there are some iron regions having higher flux level (red color). These regions are called flux-barrier tangential ribs. The thickness of these ribs has a big influence on the SynRM performance.

TABLE II
OPTIMAL SYNRM ROTOR GEOMETRICAL PARAMETERS

Parameter	Value	Parameter	Value
θ_1	8.08°	W_1	5.5 mm
θ_2	16.43°	W_2	3.5 mm
θ_3	28.4°	W_3	3.5 mm
L_1	28.85 mm	p_1	22.75 mm
L_2	28 mm	p_2	35.5 mm
L_3	13.5 mm	p_3	44.2 mm

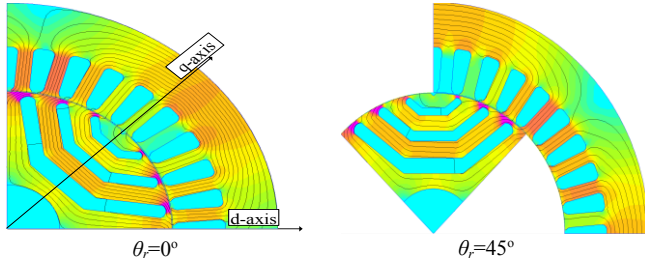


Fig. 3. Flux paths for the reference SynRM using FEM for a quarter geometry for two rotor positions

Figure 4 shows the output torque of the reference, optimal and PM assisted SynRMs at different speeds and currents up to the rated values. On the one hand, for the same current and speed, the output torque of the machine depends on the rotor design which is affected strongly by the design of the twelve rotor parameters, shown in Fig. 2. Therefore, an optimized rotor geometry for the SynRMs is necessary and unavoidable to maximize the machine performance. The SynRM performance mainly depends on the direct (d) and quadrature (q) inductances that depend on the rotor flux-barrier geometrical design. On the other hand, when comparing the subfigs. of optimal SynRM and PMSynRM, it can be noticed that adding ferrite PM in the optimized rotor of the SynRM leads to an increase of about 25% in the motor torque. This is because of the effect of PMs on the q -axis inductance of the SynRM. The PMs saturate the tangential ribs (see: Fig. 2) of the motor. By consequence, reduce the q -axis inductance, this leads to a higher output torque.

Figure 5 shows the computed losses (iron and copper) of the reference, optimal and PM SynRMs for different currents and speeds up to the rated values. The copper losses are constant for all the machines due to the same stator windings and currents. The iron losses depend on the material properties, the currents and the geometry design of the machine. Only, the rotor design is different between the reference, optimal and PM SynRMs. The variation of the flux-barrier parameters, shown in Fig. 2, has a notable effect on the machine iron

losses. This is due to the variation of the saturation regions of the iron especially, the stator teeth and rotor tangential ribs. This can be observed in fig. 5, by comparing the subfigs. (reference, optimal and PMSynRM). For the same current and speed, the iron losses increases for the PMSynRM that has the higher output torque (Fig. 4) compared to the others. In addition, for one machine as expected, the iron losses increases with increasing the speed and current, approximately in proportional way.

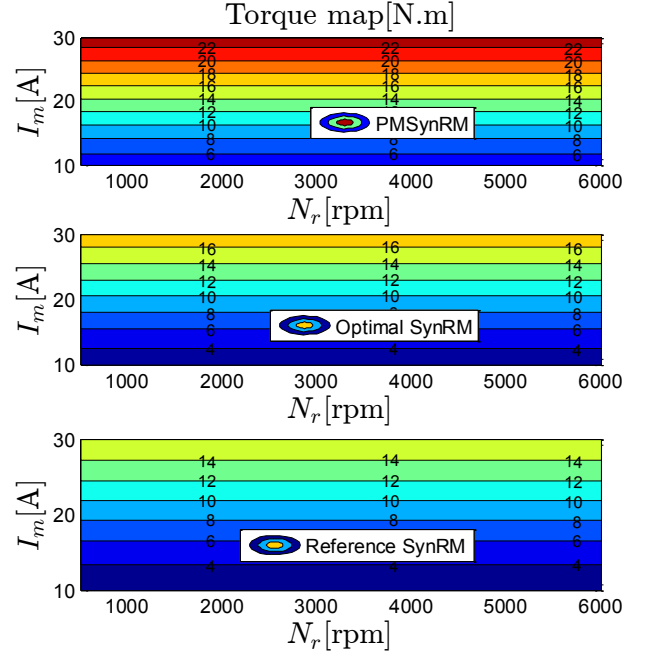


Fig. 4. Motor torque maps for different rotor designs

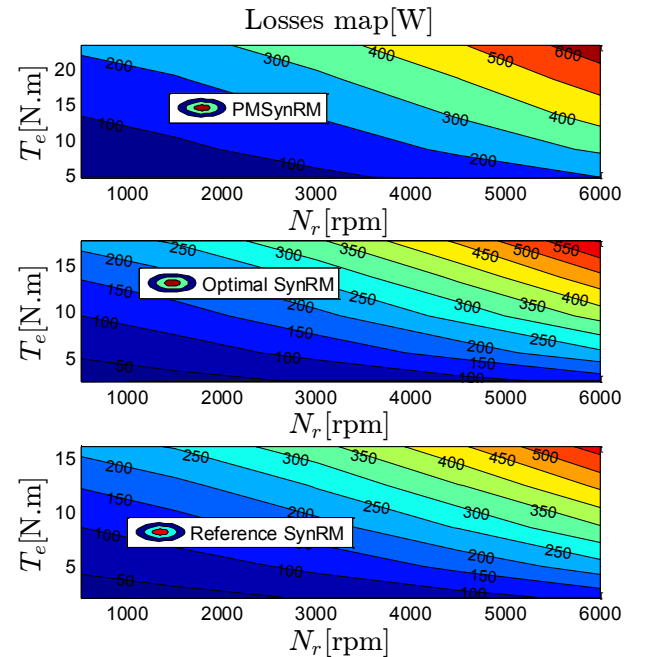


Fig. 5. Motor power losses maps for different rotor designs

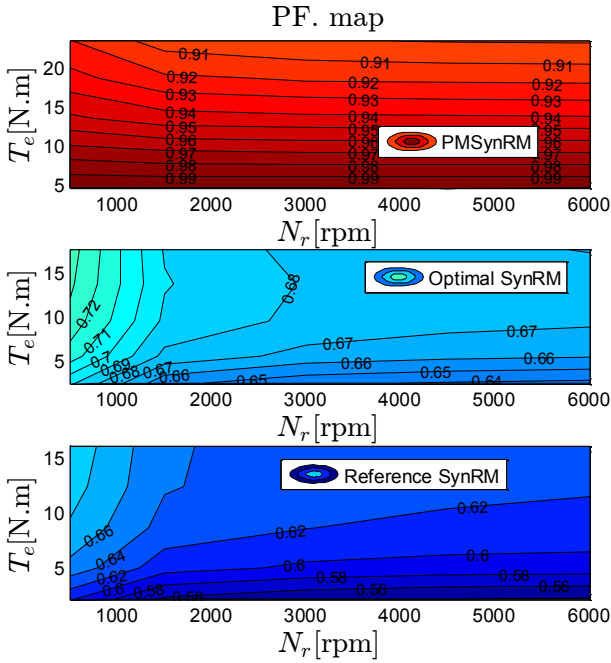


Fig. 6. Motor power factor maps for different rotor designs

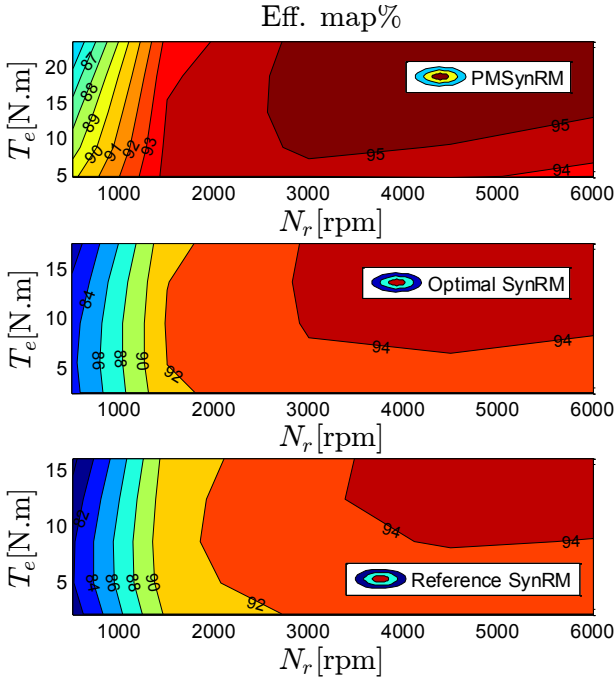


Fig. 7. Motor efficiency maps for different rotor designs

The power factor of the SynRMs depends on the saliency ratio (L_d/L_q) which is affected by the rotor design. As the optimal SynRM has the higher saliency ratio than the reference motor, then it has higher power factor. However, although the SynRM rotor is optimized, the power factor is still low about 0.68 at the rated conditions. Hence, adding PM in the optimized rotor reduces the phase angle between the voltage and current as seen in Fig.1 hence, increases the power factor. The power factor is increased to about 0.91 at the rated conditions as observed in Fig .6 (PMSynRM). This is good

indication for PMSynRM to be attractive motor for industrial applications. Moreover, the efficiency of SynRMs is better than induction motors [3] and is inferior compared to the permanent synchronous motors [9] as deduced in Fig. 7. As the output power and total losses were affected with the rotor design, the efficiency of the machine depends on the rotor design as well (Fig. 7). The efficiency of the PMSynRM can reach 95% for half rated conditions.

V. EXPERIMENTAL VALIDATION

The FEM results have been validated by the experimental measurements. The experimental set up shown in Fig. 8, consists of:

- a three-phase induction motor as a braking load, 10 kW
- a prototype SynRM (reference design), 10 kW and 22 A
- three phase Semikron inverter, 24 A and 500 V
- torque sensor of Lorenz Messtechnik, DR-2112-R
- power analyser Tektronix, PA4000
- a dSpace platform, DS1103
- DC power supply, 17 A and 600 V

The measured and simulated validation results have been obtained at 2000 rpm and 14.14 A.



Fig. 8. Photograph of the experimental setup

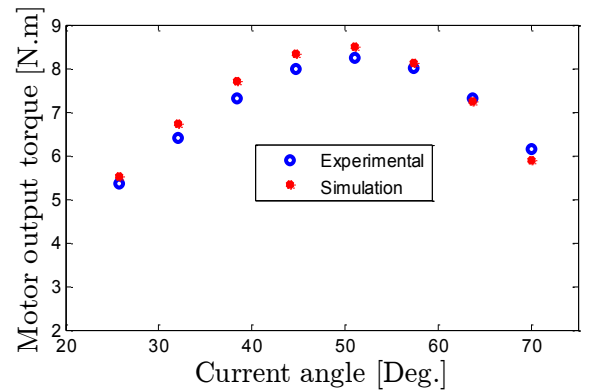


Fig. 9. Computed and measured output torque of SynRM with different current angles

Figure 9 shows the computed (FEM) and the measured

output torque of the SynRM. There is a good agreement between the simulated and the measured values. However, the difference between the measured and computed results is due to different reasons: the cutting and punching effects on the steel properties, the manufacturing tolerance and the measurement error.

VI. CONCLUSION

This paper has discussed the performance evaluation of Synchronous reluctance motors (SynRMs) with and without permanent-magnets. same Three different rotors having the stator design and other geometrical and electromagnetic parameters are considered. The three rotors are reference, optimized and optimized assisted by ferrite PMs (PMA-SynRMs) in its flux-barrier. Different performance indicators for the machine are computed by FEM and compared at the same conditions. The performance indicators are efficiency, torque, total losses and power factor maps. It is found that the PMA-SynRMs can reach efficiency and power factor higher than 95% and 0.91 respectively at the rated conditions. This means that the PMA-SynRMs are much better than both the induction machines and switched reluctance machines. In addition, they can be good competitors compared with the permanent magnet synchronous machines due to lower cost. Finally, measurements are obtained and validated FEM model.

VII. REFERENCES

- [1] M. Ferrari, N. Bianchi, A. Doria, and E. Fornasiero, "Design of synchronous reluctance motor for hybrid electric vehicles," *IEEE Trans. Ind. Appl.*, vol. 51, no. 4, pp. 3030-3040, Jul/Aug. 2015.
- [2] M. N. Ibrahim, P. Sergeant, and E. M. Rashad, "Synchronous reluctance motors performance based on different electrical steel grades," *IEEE Trans. Magn.* vol. 51, no. 11, Nov. 2015, Art. ID 7403304.
- [3] R. Vartanian and H. A. Toliyat, "Design and comparison of an optimized permanent magnet-assisted synchronous reluctance motor (PMA-SynRM) with an induction motor with identical NEMA frame stators," in *Proc. IEEE Electr. Ship Technol. Symp. (ESTS)*, Apr. 2009, pp. 107-112.
- [4] Y. H. Jeong, K. Kim, Y. J. Kim, B. S. Park, and S. Y. Jung, "Design characteristics of PMA-SynRM and performance comparison with IPMSM based on numerical analysis," in *Proc. 20th ICEM*, 2012, pp. 164-170.
- [5] S. Morimoto, M. Sanada, and Y. Takeda, "Performance of PM-assisted synchronous reluctance motor for high-efficiency and wide constant power operation," *IEEE Trans. Ind. Appl.*, vol. 37, no. 5, pp. 1234-1240, Sep./Oct. 2001.
- [6] H. Huang, Y. Sh. Hu, Y. Xiao, and H. Lyu, "research of parameters and antidemagnetization of rare-earth-less permanent magnet-assisted synchronous reluctance motor," *IEEE Trans. Magn.* vol. 51, no. 11, Nov. 2015, Art. ID 8112504.
- [7] G. Bertotti, "General properties of power losses in soft ferromagnetic materials," *IEEE Trans. Magn.*, vol. 24, no. 1, pp. 621 - 630, 1988.
- [8] http://www.bakkermagnetics.com/sites/default/files/downloads/ferrite_-_sintered_1.pdf
- [9] T. Ahonen, J. Tamminen and J. Montonen, "Comparison of electric motor types for realising an energy efficient pumping system," in *Proc. 16th Eur. Con. Power Electronic. Appl. (EPE'14-ECCE Europe)*, 2014, pp. 1-9.

- [10] Ch.T. Liu, T. Y. Luo, Ch. C. Hwang, and B.Y. Chang, "Field path design assessments of a high-performance small-power synchronous-reluctance motor," *IEEE Trans. Magn.* vol. 51, no. 11, Nov. 2015, Art. ID 8206504.
- [11] R. Lohninger, H. Grabner, G. Weidenholzer, S. Silber, and W. Amrhein, "Modeling, simulation, design of permanent-magnet-assisted synchronous reluctance machine," *IEEE Trans. Ind. Appl.*, vol. 51, no. 1, pp. 196-203, Jan./Feb. 2015.

VIII. BIOGRAPHIES



Mohamed N. Ibrahim was born in Kafrelshiekh, Egypt on September 18, 1986. He has graduated from Faculty of Engineering, Kafrelshiekh University, Egypt on 2008. He received his MSc. degree in Electrical Power and Machines Engineering from Tanta University in 2012. Since 2012, he is working as an assistant lecturer at the Department of Electrical Engineering, Faculty of Engineering, Kafrelshiekh University, Egypt. He is currently working towards the PhD at Ghent University, Belgium. His research interests are in Electrical Machines, Electrical Drives, Power Electronics and Renewable Energy.



Prof. Essam M. Rashad was born in Shebin El-Kom, Egypt in 1960. He received his BSc degree from the department of Electric Power and Machines Engineering, Faculty of Engineering, Shebin El-Kom, Menoufiya University, Egypt in May 1983. In 1987 and 1992 he received MSc and PhD, respectively both from faculty of Engineering Alexandria university, Egypt. In 1992 he has joined Faculty of Engineering, Tanta University, Egypt, where he is currently a Professor and Head of Electrical Power and Machines Engineering. From Feb. to Aug 2000, he was a visiting researcher in Faculty of Engineering, Nagasaki University, Japan. In summer 2003, he was a visiting researcher at Faculty of Engineering and Applied Science, Memorial University of Newfoundland, St. John's, NL, Canada. From 2004 to 2009, he was Head of Electrical Technology Department, Buraydah College of Technology, Kingdom of Saudi Arabia. From 2011 to 2014, he was Vice Dean for Education and Student affairs of Faculty of Engineering, Tanta University, Egypt. Prof. Rashad research interests include electrical machine analysis and design, electrical drives, power electronics and renewable energy systems.



Peter Sergeant received the M.Sc. degree in electromechanical engineering in 2001, and the Ph.D. degree in engineering sciences in 2006, both from Ghent University, Ghent, Belgium. In 2001, he became a researcher at the Electrical Energy Laboratory of Ghent University. He became a postdoctoral researcher at Ghent University in 2006 (postdoctoral fellow of the Research Foundation - Flanders) and at Ghent University College in 2008. Since 2012, he is associate professor at Ghent University. His current research interests include numerical methods in combination with optimization techniques to design nonlinear electromagnetic systems, in particular, electrical machines for sustainable energy applications.

Harmonic Model of in Wheel PMSM Machine Dedicated for Optimisation of the Powertrain

Mitrofan Curti, Johannes J.H. Paulides and Elena A. Lomonova
Eindhoven University of Technology, Eindhoven, 5600 MB, The Netherlands
Email: m.curti@tue.nl

Abstract—The fast harmonic modelling technique, which is proved to require low computational power, is used to model an outer rotor in wheel Permanent Magnet Surface Mounted (PMSM) machine for automotive applications. Fast model is prepared to be implemented in an optimisation routine for the whole power train including all principal systems like battery pack, gear ratio, power electronics etc. Primary key features for a model in this case are accuracy and computational time, therefore, the trade of between the accuracy and the speed of the model are discussed.

Index Terms—Harmonic Modelling, PMSM machine, automotive, powertrain.

I. INTRODUCTION

The high performance of a power train depends on how efficient are the components designed. However a better option is to optimise whole powertrain by setting some global objectives such as drivability or gradeability. For this purpose each component of the powertrain has to have a decent model in the optimisation routine, so that the entire system can be modelled based on the specific applications [1].

In order to make a simple and fast PMSM model the limitations of each modelling technique and the assumptions allowed by the given application has to be taken into account [2], from the other hand, all possible assumptions of the model has to be considered for contribution to the model simplicity but, in the same time to keep the results of interest at the required accuracy. Because of the high popularity of PMSM machines, there are various models available [3]–[5], however some of them does not reflect the spatial distribution of the magneto-motive force in the slots, or the field solution is not precise enough to compute the torque using Maxwell Stress Tensor (MST). Therefore, for the current model, the Harmonic Modelling (HM) technique is selected, which is described in [6], [7], and Finite Element Analysis FEA. Both approaches are using the analytical and numerical solution respectively of Poisson or Laplace equations in space domains [8], [9].

In this paper the performance of a PMSM model with a FEA and HM technique is analysed. The principle of the analytical HM technique is described as well as the simplified model in FEM considering the allowed assumptions. The model with both techniques will be analysed in terms of accuracy an computation time, so that the trade off between those parameters could be easily made and the decision on choosing a modelling technique could be taken.

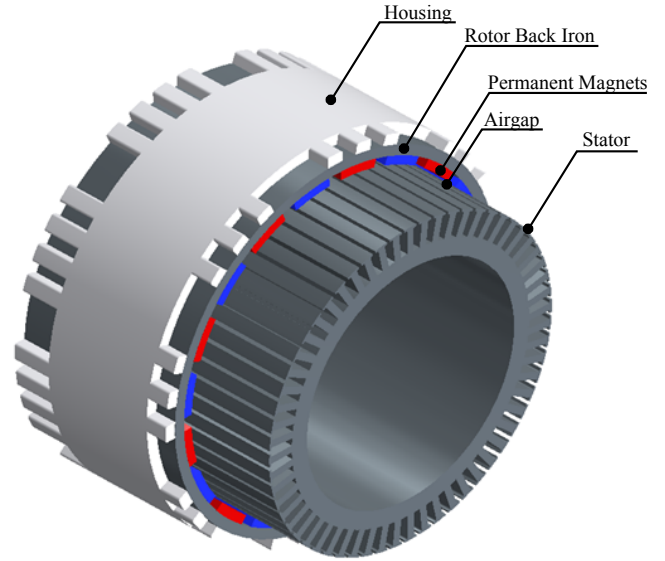


Fig. 1. In wheel motor, PMSM machine

II. PMSM MACHINE

The electrical motor implication in the powertrain system is making a big impact in the automotive technology. Having its strong characteristic of easily decoupling the speed and torque. Apart from that, the electrical motor has a higher efficiency and faster response compared to Internal Combustion Engines (ICE), an important challenge however, still exist - the energy storage technologies [10]. Another important feature of the electrical machines is that they can play three key roles in a powertrain system sense the dynamical quantities, actuate and brake therefore being able to change the energy flow in the system. What makes PMSM (Fig. 1) to withstand among other types of machines is the high power density as well as low weight and increased efficiency, these factors are the key parameters that allow PMSM to be in wheel mounted [11].

III. MACHINE MODELS

Based on powertrain model requirements, and the modelling techniques possibilities and limitations several assumptions were considered. First, the machine geometry is considered long enough such as modelling of only its cross sectional area will give acceptable results, Fig. 2. Secondly, the permeability of the soft magnetic material is considered linear, homogeneous and high enough to be equivalent to infinite permeable

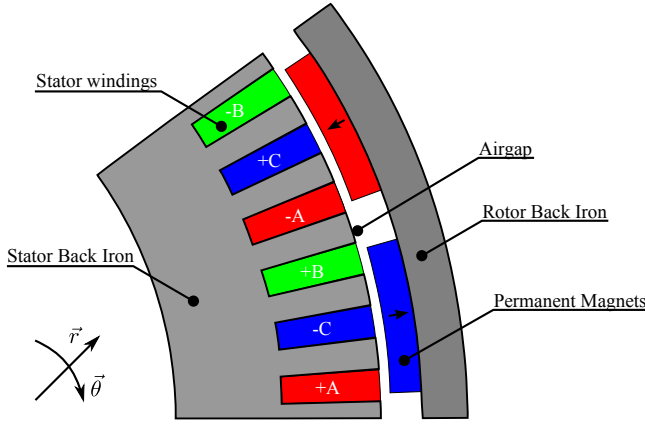


Fig. 2. Simplified geometry of the PMSM machine

material. In the same manner, the stator slots were modified to match the polar geometry so that the implementation of HM can be possible [6]. Main parameters of the given machine can be found in Table I. The comparison study of the two approaches is based on no load analysis.

TABLE I
PARAMETERS OF EXTERNAL ROTOR SURFACE PM MOTOR

Parameters,	Symbol,	Value,	Unit
Number of poles	$2p$	20	-
Slot number	Q_s	60	-
Magnet arc/pole pitch ratio	α_p	0.75	-
Air gap length	g	1.2	mm
Magnet radial thickness	l_m	4.3	mm
Radius of the rotor surface	R_r	85	mm
Radius of the magnet surface	R_m	76.2	mm
Stator outer radius	R_s	75	mm
Magnet remanence	B_r	1.19	T
Relative magnet permeability	μ_{rM}	1.05	-
Core length	l_a	60	mm
Slot depth	d_s	12	mm

A. Harmonic Model

After applying all assumptions for a real machine, Fig. 1, for the resulting geometry, in Fig. 2, it can be seen that clear regions (slotted, airgap and PM region) can be distinguished. In the rotating machine geometry, each region turns out to be annular segments, therefore, the field equations in these domains could be written in polar coordinate system:

$$\mu_r H_r = \frac{1}{r} \frac{\partial A_z}{\partial \theta}; \quad (1)$$

$$\mu_r H_\theta = -\frac{\partial A_z}{\partial r}; \quad (2)$$

$$J_z = \frac{1}{r} H_\theta + \frac{\partial H_\theta}{\partial r} - \frac{1}{r} \frac{\partial H_r}{\partial \theta}. \quad (3)$$

The equations (1) - (3) are the definition of the magnetic vector potential A_z in 2D polar plane and Ampere's circuital law in differential form which is a part of Maxwell's equations set [9], where H and J are the magnetic field strength and current density distribution respectively in r and θ directions. It can be seen that in slotted and PM regions the source terms

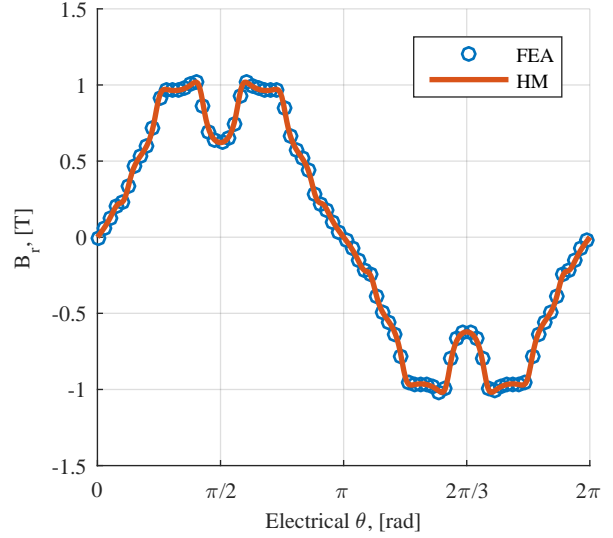


Fig. 3. Solution comparison for radial field B_r component

should be included, whereas in the airgap, the source terms are zero making the use of Laplace equation appropriate. The magnetisation source is coming from the constitutive relation given by:

$$\vec{B} = \mu_0(\vec{H} + \vec{M}). \quad (4)$$

Where \vec{M} is the magnet magnetisation distribution. Solving the equations (1) - (4) for magnetic vector potential we get the field solution:

$$A_z = W r^\lambda a + W r^{-\lambda} b + r^2 G_1. \quad (5)$$

Where G_1 is a constant that contains the source term, W and λ are the eigenvalues and eigenvectors after decomposition of the root of the quadratic equation resulting from second order differential equation. Following the equations (1) and (2) the relationships for the magnetic field can be obtained. It should be noted, that relation 5 is the field solution for a squared domain [7], in this case, since the geometry is described in polar coordinate system, the solution is in a region of the shape of annular sector. In order to couple different regions of motor geometry, like slotted region, airgap region and permanent magnet region, the continuous boundary conditions are applied. Therefore, at the interface with two regions we have the following quantities that are continuous:

$$B_{rI} = B_{rII} \quad (6)$$

$$H_{\tau I} = H_{\tau II} \quad (7)$$

Where the indices I and II stand for two connected regions.

In the Fig. 3 and 4 the comparison of the results between FEA and HM model is presented. It can be seen that a good match is obtained for local quantities such as magnetic field, proving that the HM model is converging towards the correct solution.

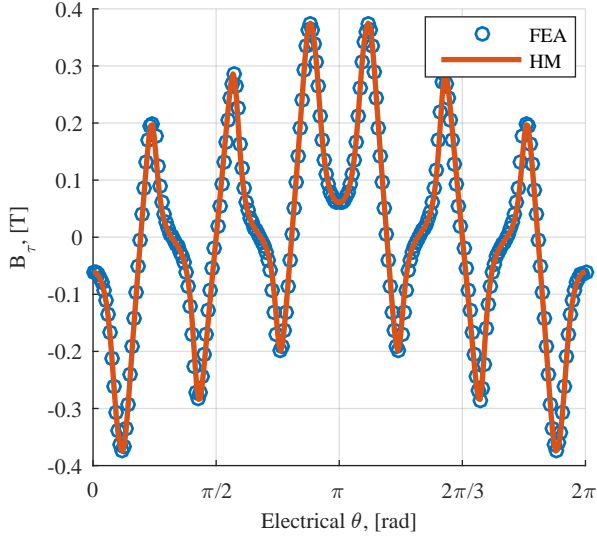


Fig. 4. Solution comparison for tangential field B_τ component

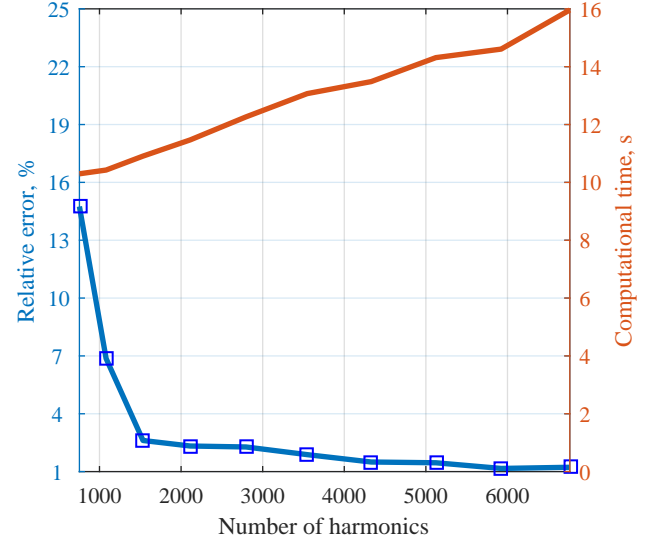


Fig. 6. Performance analysis for FEA model

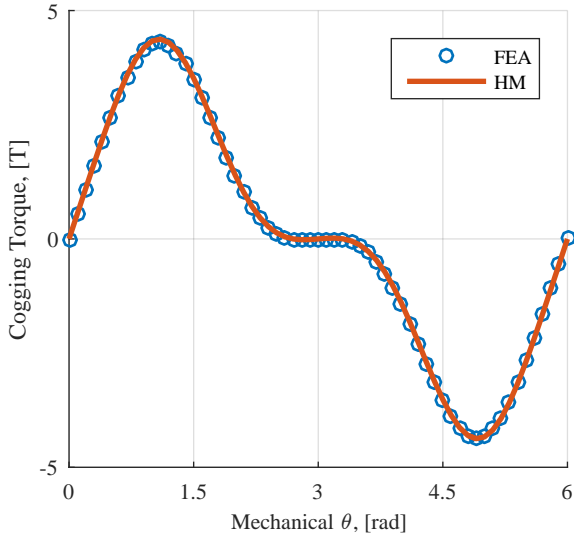


Fig. 5. Solution comparison for cogging torque

IV. FINITE ELEMENT ANALYSIS

In previous section a semi-analytical method for modelling a PMSM geometry is described and its convergence is also shown. However its accuracy and computational requirements should be checked in order to validate its relevance. For this reason the same PMSM geometry is modelled in a FEA software and the convergence of the solution with increasing the number of nodes in the geometry has been analysed. The reference results for both HM and FEA are obtained by solving a FEA model with increased number of nodes, the number of nodes are chosen such that further increasing of them will not considerably improve the results.

In Fig. 5 the comparison of cogging torque is presented.

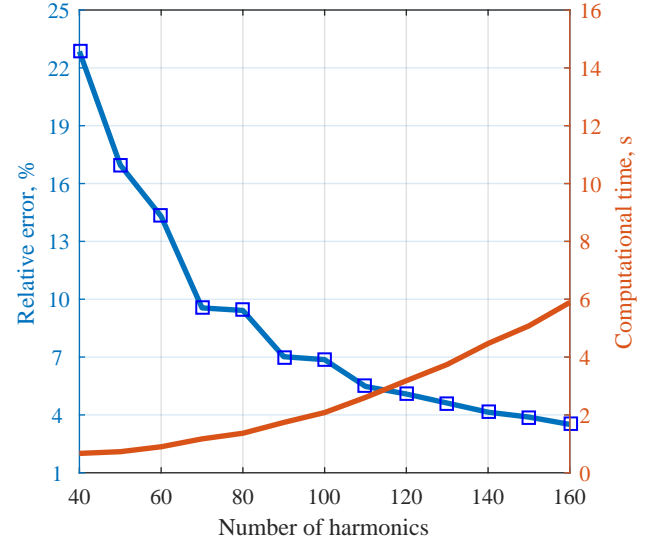


Fig. 7. Performance analysis for HM model

In FEA, the cogging torque is computed based on Virtual Work principle, in HM using the tangential component of MST of the surface covering the stator. It can be seen, that for global quantities the matching is also good. For the comparison of the modelling techniques performances, the results of cogging torque is used. The simulation is performed for a 6° mechanical degrees displacement divided into 60 computational steps.

V. DISCUSSION ON THE RESULTS

In Figures 6 and 7 the performance analysis based on relative error, right y axis and computational time, left y axis is carried out. It can be seen from Fig. 7 that with increasing the number of harmonics which describes the local

field solution, the error is decreasing, but also, in the same time the computational time is increasing in such a way, that for an accuracy of 4% the computational time is 6 seconds. From another hand, the FEA model, from Fig. 6 shows a faster convergence, but the computational time is biased by 10 seconds, which means that for an accuracy of 4% with HM method, the model will run 2.5 times faster than FEA model. These analysis allow to choose the modelling technique for PMSM model in the power train optimisation routine.

VI. CONCLUSION

An analysis over the PMSM model performances implemented with HM and FEA method is presented in this paper. The computational time and the accuracy are the key parameters for a model which is used for optimisation. Using the assumptions that are allowed by the application, a simplified model could be obtained. By changing the number of nodes in FEA and number of harmonics in HM, it could be easily observed that until a certain accuracy, the HM will require less computational effort. Therefore, as a modelling technique for a PMSM model of powetrain optimisation, the HM method is selected.

ACKNOWLEDGMENT

This paper is part of the ADvanced Electric Powertrain Technology (ADEPT) project which is an EU funded Marie Curie ITN project, grant number 607361 [12]. Within ADEPT, virtual and hardware tools are created to assist the design and analysis of future electric propulsions. Especially within the context of the paradigm shift from fuel powered combustion engines to alternative energy sources (e.g. fuel cells, solar cells, and batteries) in vehicles like motorbikes, cars, trucks, boats, planes. The design of these high performance, low cost and clean propulsion systems has stipulated an international cooperation of multiple disciplines such as physics, mathematics, electrical engineering, mechanical engineering and specialisms like control engineering and safety. By cooperation of these disciplines in a structured way, the ADEPT program provides a virtual research lab community from labs of European universities and industries [13].

REFERENCES

- [1] K. Ramakrishnan, M. Gobbi, and G. Mastinu, "Multi-objective optimization of in-wheel motor powertrain and validation using vehicle simulator," in *Ecological Vehicles and Renewable Energies (EVER), 2015 Tenth International Conference on*, March 2015, pp. 1–9.
- [2] M. Curti, J. Paulides, and E. Lomonova, "An overview of analytical methods for magnetic field computation," in *Ecological Vehicles and Renewable Energies (EVER), 2015 Tenth International Conference on*, March 2015, pp. 1–7.
- [3] B. Hague, *The principles of electromagnetism applied to electrical machines: (formerly titled: Electromagnetic problems in electrical engineering)*. Dover Publications, 1962.
- [4] Z. Zhu, D. Howe, and C. Chan, "Improved analytical model for predicting the magnetic field distribution in brushless permanent-magnet machines," *Magnetics, IEEE Transactions on*, vol. 38, no. 1, pp. 229–238, 2002.
- [5] Z. Zhu, D. Howe, E. Bolte, and B. Ackermann, "Instantaneous magnetic field distribution in brushless permanent magnet dc motors. i. open-circuit field," *Magnetics, IEEE Transactions on*, vol. 29, no. 1, pp. 124–135, 1993.

- [6] B. L. J. Gysen, K. J. Meessen, J. J. H. Paulides, and E. A. Lomonova, "General formulation of the electromagnetic field distribution in machines and devices using fourier analysis," *Magnetics, IEEE Transactions on*, vol. 46, no. 1, pp. 39–52, Jan 2010.
- [7] R. L. J. Sprangers, J. J. H. Paulides, B. L. J. Gysen, and E. A. Lomonova, "Magnetic saturation in semi-analytical harmonic modeling for electric machine analysis," *IEEE Transactions on Magnetics*, vol. 52, no. 2, pp. 1–10, Feb 2016.
- [8] K. J. Binns, P. J. Lawrenson, and C. W. Trowbridge, *The analytical and numerical solution of electric and magnetic fields*. John Wiley & Sons, 2001.
- [9] E. P. Furlani, *Electric Machines and Drives*, I. Mayergoyz, Ed. Academic Press, 2001.
- [10] J. G. W. West, "Dc, induction, reluctance and pm motors for electric vehicles," *Power Engineering Journal*, vol. 8, no. 2, pp. 77–88, April 1994.
- [11] Y. K. Kim, Y. H. Cho, N. C. Park, S. H. Kim, and H. S. Mok, "In-wheel motor drive system using 2-phase pmsm," in *Power Electronics and Motion Control Conference, 2009. IPEMC '09. IEEE 6th International*, May 2009, pp. 1875–1879.
- [12] E. A. Lomonova, J. J. H. Paulides, S. Wilkins, and J. Tegenbosch, "Adept: "advanced electric powertrain technology" - virtual and hardware platforms," in *Ecological Vehicles and Renewable Energies (EVER), 2015 Tenth International Conference*, March 2015, pp. 1–10.
- [13] A. Stefanskyi, A. Dziechciarz, F. Chauvicourt, G. E. Sfakianakis, K. Ramakrishnan, K. Niyomsatian, M. Curti, N. Djukic, P. Romanazzi, S. Ayat, S. Wiedemann, W. Peng, A. Tamas, and S. Stipetic, "Researchers within the EU funded Marie Curie ITN project ADEPT, grant number 607361," 2013-2017.